HTML ABSTRACT + LINKS

REVIEW ARTICLE

The physics basis for ignition using indirect-drive targets on the National Ignition Facility

John D. Lindl, Peter Amendt, Richard L. Berger, S. Gail Glendinning, Siegfried H. Glenzer, Steven W. Haan, Robert L. Kauffman, Otto L. Landen, and Laurence J. Suter
Lawrence Livermore National Laboratory, L-637, P.O. Box 808, Livermore, California 94551

(Received 17 May 2001; accepted 10 April 2003)

The 1990 National Academy of Science final report of its review of the Inertial Confinement Fusion Program recommended completion of a series of target physics objectives on the 10-beam Nova laser at the Lawrence Livermore National Laboratory as the highest-priority prerequisite for proceeding with construction of an ignition-scale laser facility, now called the National Ignition Facility (NIF). These objectives were chosen to demonstrate that there was sufficient understanding of the physics of ignition targets that the laser requirements for laboratory ignition could be accurately specified. This research on Nova, as well as additional research on the Omega laser at the University of Rochester, is the subject of this review. The objectives of the U.S. indirect-drive target physics program have been to experimentally demonstrate and predictively model hohlraum characteristics, as well as capsule performance in targets that have been scaled in key physics variables from NIF targets. To address the hohlraum and hydrodynamic constraints on indirect-drive ignition, the target physics program was divided into the Hohlraum and Laser–Plasma Physics (HLP) program and the Hydrodynamically Equivalent Physics (HEP) program. The HLP program addresses laser–plasma coupling, x-ray generation and transport, and the development of energy-efficient hohlraums that provide the appropriate spectral, temporal, and spatial x-ray drive. The HEP experiments address the issues of hydrodynamic instability and mix, as well as the effects of flux asymmetry on capsules that are scaled as closely as possible to ignition capsules (hydrodynamic equivalence). The HEP program also addresses other capsule physics issues associated with ignition, such as energy gain and energy loss to the fuel during implosion in the absence of alpha-particle deposition. The results from the Nova and Omega experiments approach the NIF requirements for most of the important ignition capsule parameters, including drive temperature, drive symmetry, and hydrodynamic instability. This paper starts with a review of the NIF target designs that have formed the motivation for the goals of the target physics program. Following that are theoretical and experimental results from Nova and Omega relevant to the requirements of those targets. Some elements of this work were covered in a 1995 review of indirect-drive [J. D. Lindl, ''Development of the indirect-drive approach to inertial confinement fusion and the target physics basis for ignition and gain,'' Phys. Plasmas **2**, 3933 (1995)]. In order to present as complete a picture as possible of the research that has been carried out on indirect drive, key elements of that earlier review are also covered here, along with a review of work carried out since 1995. © *2004 American Institute of Physics.* [DOI: 10.1063/1.1578638]

TABLE OF CONTENTS

 © 2004 American Institute of Physics

Downloaded 20 Mar 2011 to 69.181.48.121. Redistribution subject to AIP license or copyright; see http://pop.aip.org/about/rights_and_permissions

I. INTRODUCTION

The 1990 National Academy of Science (NAS) final report (NAS Review, 1990) of its review of the Inertial Confinement Fusion (ICF) Program recommended completion of a series of target physics objectives on the Nova laser at Lawrence Livermore National Laboratory (LLNL) as the highest-priority prerequisite for proceeding with construction of an ignition-scale laser facility, now called the National Ignition Facility (NIF). The goal of these physics objectives was to achieve a sufficient understanding of the physics of ignition targets that the laser requirements for laboratory ignition could be accurately specified. This research, as well as additional research on the Omega laser at the University of Rochester, is the subject of this review.

As shown in Fig. 1-1, two principal approaches are used with lasers to generate the energy flux and pressure required to drive an ICF implosion. In the direct-drive approach, the laser beams are aimed directly at the target. The beam energy is absorbed by electrons in the target's outer, low-density corona. Electrons transport that energy to the denser shell material to drive the ablation and the resulting implosion. In the indirect-drive approach, the laser energy is absorbed and converted to x rays by high-Z material inside the hohlraum that surrounds the target (Lindl, 1995; Lindl, 1998).

Because of the x-ray conversion and transport step, indirect-drive is less efficient at coupling energy to a capsule than direct-drive. However, ablation driven by electron conduction is generally less efficient and more hydrodynamically unstable than ablation driven by x rays. Measures taken to mitigate hydrodynamic instability in direct-drive targets (Bodner *et al.*, 1998) partially offset the efficiency advantage. Also, direct-drive targets are very sensitive to intensity variations within individual beams. These variations imprint perturbations on the target that are then amplified by hydrodynamic instability. If adequate beam uniformity can be achieved, calculations for current target designs indicate that direct-drive targets have about the same ignition threshold as indirect-drive targets, but they can have about a factor of 2 higher gain than the best indirect-drive-based designs, depending on the hydrodynamic instability growth that is tolerable. The NIF will be configured with a beam geometry capable of being used for either direct or indirect-drive.

Because of the relaxed beam-quality requirements, as compared to direct-drive, and the reduced Rayleigh–Taylor (RT) growth rates, the Nova laser geometry was chosen for indirect-drive.

For indirect-drive, the hohlraum-wall physics and the capsule physics are essentially the same for any x-ray source. Because of this, indirect-drive experiments on lasers provide much of the target physics basis for heavy ion-driven targets (Lindl, 1998a; Tabak and Callahan-Miller, 1998). Much of what is learned on Nova is also applicable to ICF capsules that use Z-pinch-driven x-ray sources, such as on the Z machine at Sandia National Laboratories (SNL) (Hammer *et al.*, 1999).

The target physics program for indirect-drive was the outcome of a strategy adopted by the U.S. ICF program in the late 1970s when the Nova laser was being designed. This strategy has utilized laboratory tests of the physics of high-gain targets as well as a series of underground nuclear experiments [the Halite/Centurion (H/C) Program] at much higher energy. The H/C experiments remain classified and are not covered in this review.

Downloaded 20 Mar 2011 to 69.181.48.121. Redistribution subject to AIP license or copyright; see http://pop.aip.org/about/rights_and_permissions

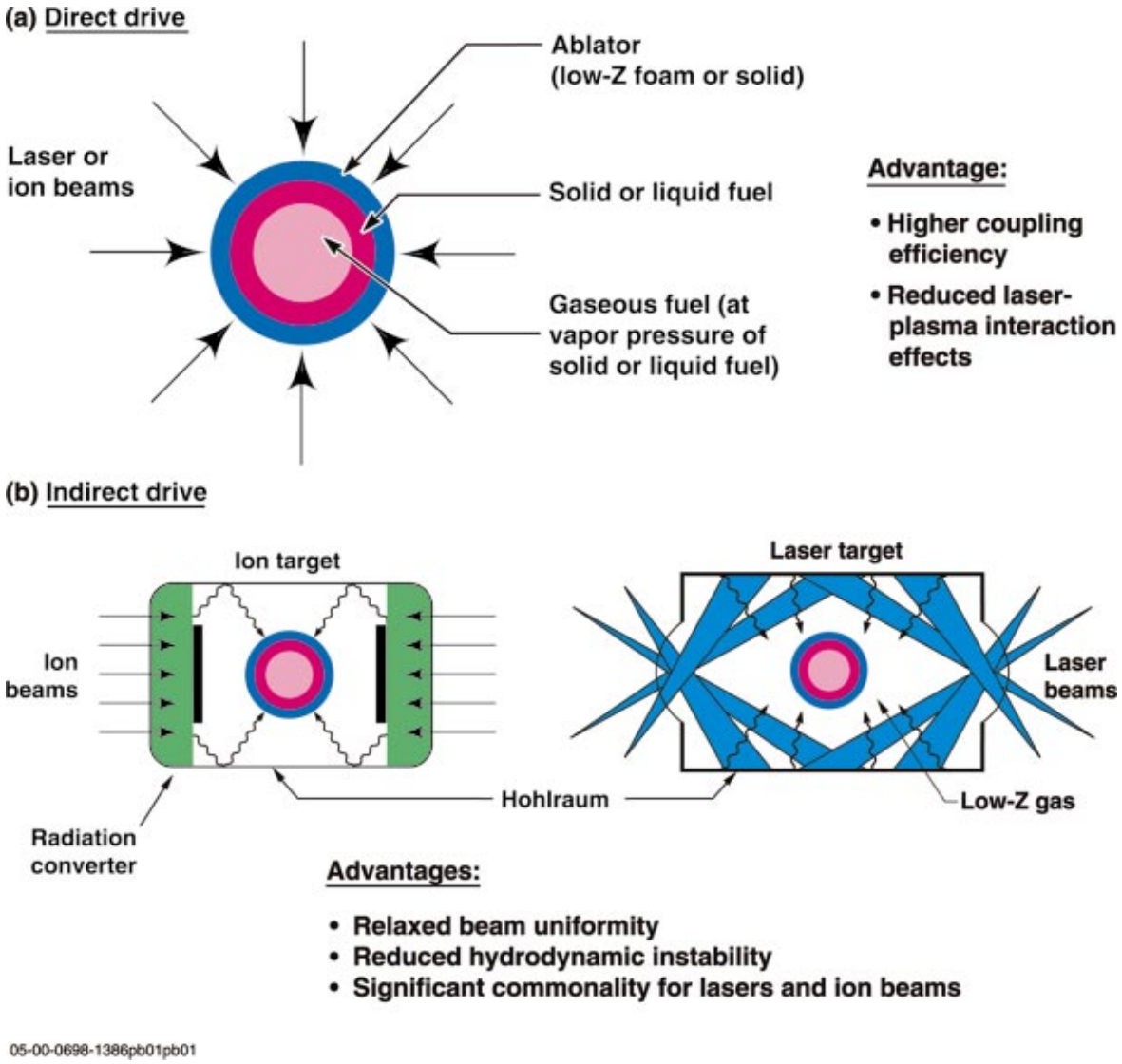

FIG. 1-1. (Color) ICF uses either (a) direct-drive (electron conduction) or (b) indirect-drive (x rays) to produce a high shell-ablation pressure to drive an implosion.

Soon after it became operational in 1985, experiments on Nova achieved their initial temperature goals of 200 to 225 eV with low levels of hot electrons. This goal was established as the temperature that would be required for high gain with a 5- to 10-MJ laser. The Department of Energy (DOE) labeled such a facility the Laboratory Microfusion Facility (LMF) (NTIS Document, 1993).

Between 1986 and 1990, there was rapid progress on indirect-drive target physics (Lindl, 1998b). Nova experiments and modeling-demonstrated basic symmetry control, the first quantitative RT instability experiments, the expected benefits of pulse shaping, and the radiation-drive temperature scaling of implosions.

Based on progress in indirect-drive target physics, the DOE initiated a series of internal reviews of the LMF in 1988. At the request of Congress, an external review of the ICF Program was carried out by the NAS in 1989 to 1990. In its January 1990 interim report, the NAS committee concluded that the LMF, with proposed yields from 200 to 1000 MJ, was too large for the next step and encouraged the laboratories to explore a step between Nova and the LMF (NAS Review, 1990).

Analysis of the relationship between implosion velocity, hydrodynamic instability, and hohlraum temperature indicated that ignition and modest gain would be possible with a 1 to 2 MJ laser if hohlraum temperatures of 300 eV and implosion velocities of 4×10^7 cm/s could be achieved. At this implosion velocity, theoretical modeling concluded that an optimal capsule absorbing 150 kJ of x rays would have sufficient ignition margin to accommodate the level of degradation from hydrodynamic instability and asymmetry expected from an optimized hohlraum and high quality capsule. At a laser energy of 1.8 MJ, which is the NIF baseline, there also is margin to account for uncertainty in the achievable hohlraum coupling efficiency. Early in 1990, 300 eV hohlraums with less than 1% of the absorbed energy in hot electrons were demonstrated. This encouraging result provided some optimism that ignition and gain with the smaller laser recommended by the NAS might be feasible.

Based on the experimental and modeling results, both

Downloaded 20 Mar 2011 to 69.181.48.121. Redistribution subject to AIP license or copyright; see http://pop.aip.org/about/rights_and_permissions

FIG. 1-2. (Color) Nova laser bay.

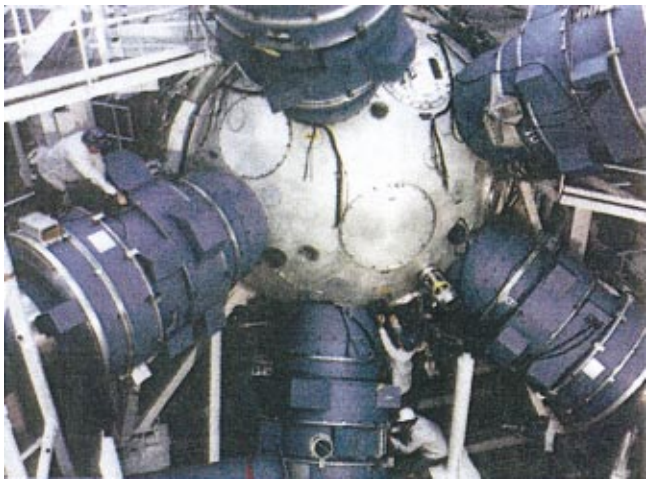

FIG. 1-3. (Color) Nova target chamber.

the September 1990 final report (NAS Review, 1990) of Koonin's NAS committee and the DOE Fusion Policy Advisory Committee (FPAC) report (FPAC Final Report, 1990) endorsed the goal of ignition. This endorsement was made contingent upon successful completion of a series of experiments to be carried out on Nova. These experiments and modeling in hohlraum and laser–plasma-instability physics (HLP) and hydrodynamically equivalent physics (HEP) of capsules constitute what was called the Nova Technical Contract (NTC) (NAS Review, 1990).

The HLP program addresses laser–plasma coupling, x-ray generation and transport, and the development of energy-efficient hohlraums that provide the appropriate spectral, temporal, and spatial x-ray drive.

The HEP experiments address the issues of hydrodynamic instability and mix, as well as the effects of flux asymmetry on capsules that are scaled as closely as possible to ignition capsules (hydrodynamic equivalence). The HEP program addresses capsule-physics issues associated with ignition. This includes the physics associated with ignition (energy gain and energy loss to the fuel during implosion) in the absence of α-particle deposition.

From its completion in 1985 until it was shut down in June 1999, the Nova laser (Emmett *et al.*, 1983; Hunt and Speck, 1989) at Lawrence Livermore National Laboratory (LLNL) was the primary U.S. laboratory facility for radiation-driven experiments. Figure 1-2 is a picture of the laser bay, showing some of Nova's 10 beams. Figure 1-3 shows the Nova experimental area as it was before any diagnostics were installed. The laser beams are arranged so that five beams located along the rim of a 100° cone irradiate each end of a hohlraum, as shown in Fig. 1-4. Nova could deliver 30 to 40 kJ in 1 ns at an output wavelength of 0.35 μm. This energy could also be delivered with a wide variety of pulse shapes. Figure 1-4 shows a typical 1.6-mm-diameter hohlraum used on Nova for implosion experiments. For ease of fabrication, the hohlraum wall for this target is typically made of Au, but other high-Z materials such as W and U are also used. The capsule shown inside is a plastic microballoon about 0.5 mm diameter.

In order to carry out many of the symmetry and explosion experiments spelled out in the NAS review, the ''Precision Nova Project,'' (NTIS Document, 1994) was implemented to achieve improvements in power balance and pointing accuracy. When the upgrades were completed in 1993, the pointing accuracy was improved from about 100 μm to 30 μm [see Fig. 1-5(a)]. The power balance was improved about a factor of two, to 5% during the high-power part of the pulse and to less than 10% during the low-power foot of the pulse [see Fig. 1-5(b)] for a characteristic 20 kJ pulse shape. Figure 1-5(c) shows that Nova was capable of meeting the Precision Nova power balance specifications for a pulse having a 10:1 contrast ratio and delivering more than 40 kJ.

Although the Nova laser is not large enough to achieve ignition, it is possible to design a series of experiments on Nova each of which closely approaches one or more of the requirements critical for ignition, as measured by scaled dimensionless variables. As the NIF ignition concepts have evolved, the elements of the target physics program have also changed. This Introduction summarizes the motivation and objectives of the indirect-drive target physics program in the context of ignition requirements. A much more extensive discussion of the requirements for ignition is contained in (Lindl, 1995; Lindl, 1998).

A. Ignition requirements

There is a strong connection between the compression achievable in a spherical implosion and the ignition threshold (Nuckolls *et al.*, 1972). Because the compression that can be achieved in an implosion is related to the implosion velocity v_{imp}, the ignition threshold depends strongly on v_{imp}. For a fixed-peak driving pressure and fuel entropy, if a laser pulse shape can be achieved that maintains compressibility independent of v_{imp}, the ignition threshold varies (Levedahl and Lindl, 1997) as v_{imp}^{-n}, where $n \approx 5$ to 6 for the target type shown in Fig. 1-6. More generally, for capsules with different peak implosion pressures and fuel entropy, the ignition threshold scales approximately as

$$E_{ign} \propto \beta^{1.8} v_{\mathrm{imp}}^{-6} P^{-0.8} \tag{1-1}$$

Downloaded 20 Mar 2011 to 69.181.48.121. Redistribution subject to AIP license or copyright; see http://pop.aip.org/about/rights_and_permissions

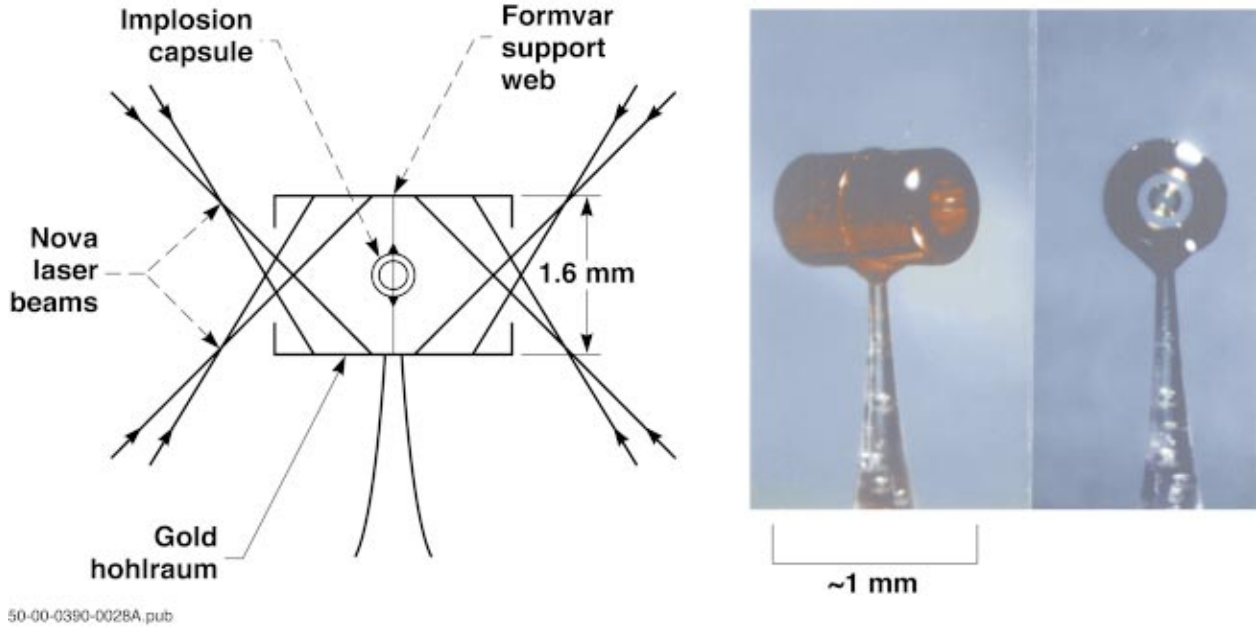

FIG. 1-4. (Color) Nova implosion target illustrating beam geometry. Five Nova beams irradiate each side of the hohlraum. The beams are uniformly distributed around the rim of a 100° cone.

where P is the implosion pressure and β is the ratio of the pressure in the fuel at a given density to the Fermi degenerate pressure (Basko, 1998; Herman *et al.*, 2001).

The implosion of a shell such as that shown in Fig. 1-6 is driven by the ablation of material from the surface of the shell and can be described by a spherical rocket equation. The work W done on the imploding shell is given by $W = \int P\, dV$, where P is the pressure generated by ablation and V is the volume enclosed by the shell. For a given shell mass, generating the highest possible ablation pressure on a shell that encloses the greatest possible volume maximizes the implosion velocity and minimizes the ignition energy.

The ablation pressure is related to the energy flux incident on the surface of the shell. In laser-driven ICF, LPI effects limit the incident flux to about 10^{15} W/cm^2. In ion beam-driven ICF, the pressure is limited by the focused

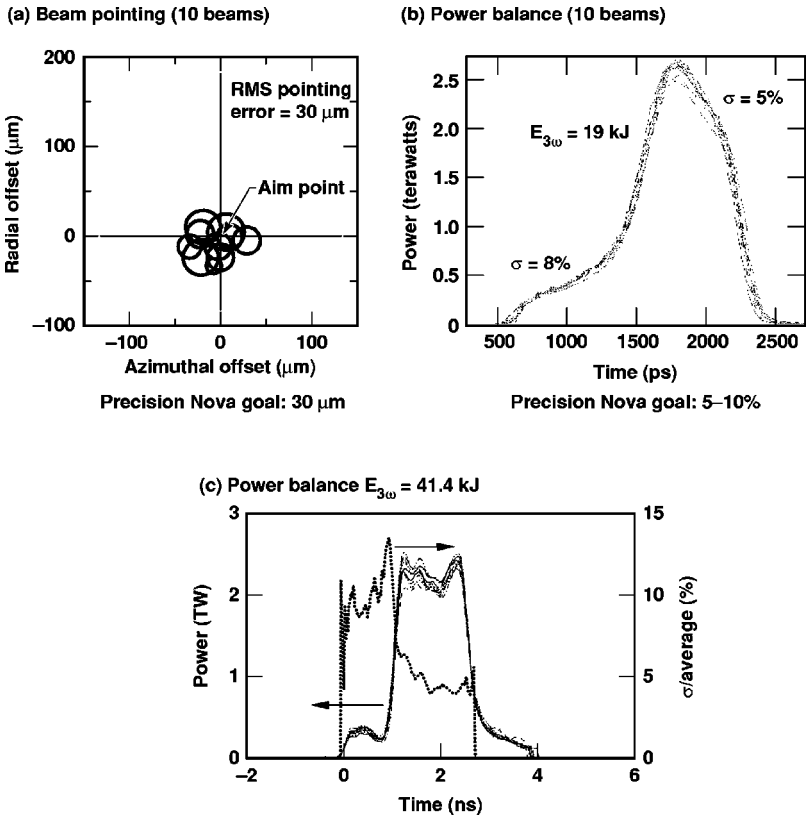

FIG. 1-5. The Nova laser power balance and beam pointing were improved a factor of 2 to 3 in the Precision Nova Project. These improvements were required for high-precision symmetry experiments and high-convergence implosions.

Downloaded 20 Mar 2011 to 69.181.48.121. Redistribution subject to AIP license or copyright; see http://pop.aip.org/about/rights_and_permissions

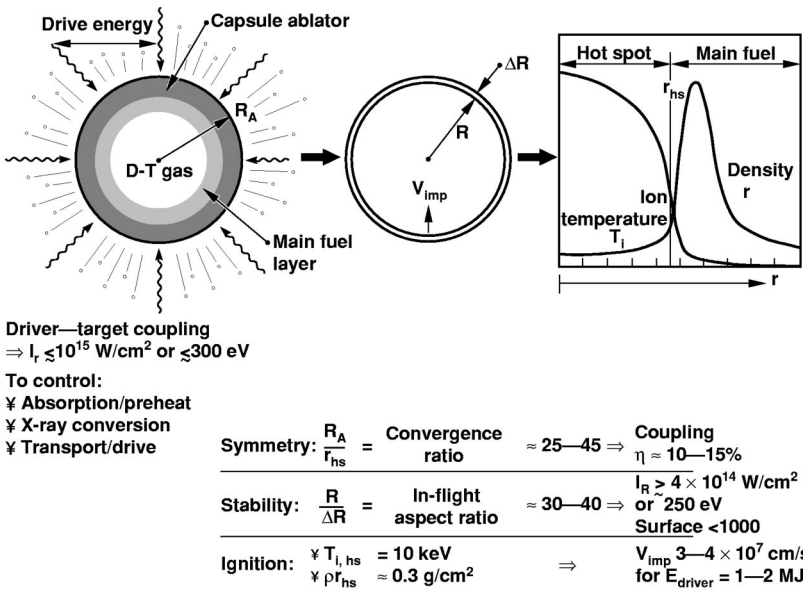

FIG. 1-6. Physics specifications on current ICF ignition targets include constraints on drive intensity, symmetry, stability, and ignition.

intensity achievable. In general, ablation pressures are limited to about 100 to 200 Mbar for current laboratory approaches to ICF.

As the volume enclosed by a shell with fixed mass and density (and thus with a fixed volume of shell material) is increased, the shell must become thinner. Hydrodynamic instabilities during the acceleration and deceleration phases of the implosion limit the so-called in-flight aspect ratio to $R/\Delta R < 30-40$, where R = shell radius and ΔR = shell thickness as it implodes. Perturbations on such shells increase in amplitude during the implosion by 5 to 7 e-foldings (growth factors of 200 to 1000). For thin shells, the shell aspect ratio increases linearly with the volume enclosed. This limitation on the shell aspect ratio and the pressure limitation, as described above, together limit implosion velocities. If driver technology can be developed so that other details of an implosion, such as pulse shaping and drive symmetry, can be controlled, these two limitations ultimately set the ignition threshold for laboratory fusion to a driver of about 1 to 2 MJ for capsules with implosion velocities of 3 to 4×10^7 cm/s. The goal of the indirect-drive ignition physics experiments on hydrodynamic instabilities is to demonstrate quantitative understanding of the growth of perturbations in planar and convergent geometry and an understanding of the effects of these perturbations on implosions that approach NIF perturbation amplification levels and capsule convergence ratios.

Although indirect-drive is less sensitive to individual beam nonuniformities than direct-drive, beam placement inside the hohlraum must be accurately controlled to achieve adequate symmetry. As indicated in Fig. 1-1, typical capsule convergence ratios are $C_r = R_A/r_{\rm hs} \approx 25-45$, where R_A is the initial outer capsule radius and $r_{\rm hs}$ is the final compressed hot fuel radius (the ''hot spot'' radius). Achieving a convergence ratio this high requires x-ray fluxes uniform from 1% to 2%. Use of a relatively large hohlraum (with a ratio of hohlraum radius to capsule radius of 3 to 4) greatly reduces imbalances in irradiation between points close together on the capsule surface (Caruso and Strangio, 1991; Lindl, 1998c); imbalances between points farther apart can be controlled by hohlraum geometry and laser beam placement. In the NIF laser, two rings of beams, each with an independent pulse shape, will enter each end of the hohlraum. (In Nova, a single ring of five beams entered each end.) The two rings on NIF will allow ''beam phasing,'' in which the power in the individual rings is varied independently to control time-dependent asymmetry. The ignition physics symmetry experiments utilize hohlraums with a ratio of hohlraum diameter to capsule diameter that is comparable to that on NIF target designs in order to test both the geometric smoothing of short-wavelength asymmetry and the control of long-wavelength asymmetry by beam placement and hohlraum geometry variations.

For a short-wavelength laser such as Nova (or NIF) (laser wavelength $\lambda = 0.35\ \mu$m in most experiments), 70% to 80% of the incident laser energy is converted to x rays by the high-Z hohlraum material. However, the large hohlraum size resulting from symmetry requirements limits overall coupling efficiency from 10% to 15% of the laser energy into the capsule for the baseline ignition designs.

The laser requirements for ignition by indirect-drive can be shown in a plot of laser power P_L vs total laser energy as indicated in Fig. 1-7. As laser power increases for a given laser energy, the achievable hohlraum temperature T_R increases. The ablation pressure increases approximately (Lindl, 1998d) as $T_R^{3.5}$, so $v_{\rm imp}$ is a strong function of T_R. Generation of plasma in the hohlraum increases as T_R increases; this results in laser–plasma collective effects that limit T_R and the usable power that can be put into the hohlraum. This power depends on laser wavelength, laser beam spatial and temporal uniformity, pulse duration, hohlraum size, and other variables. At $T_R = 400$ eV, for the long pulses required for ignition capsules, the hohlraum plasma density n will approach $n/n_c \approx 1/4$ (the critical density $n_c = 10^{21}\lambda^{-2}$ cm^{-3}, where λ is the laser wavelength in micrometers). Experiments (Lindl, 1998e) at $\lambda = 1\ \mu$m gener-

Downloaded 20 Mar 2011 to 69.181.48.121. Redistribution subject to AIP license or copyright; see http://pop.aip.org/about/rights_and_permissions

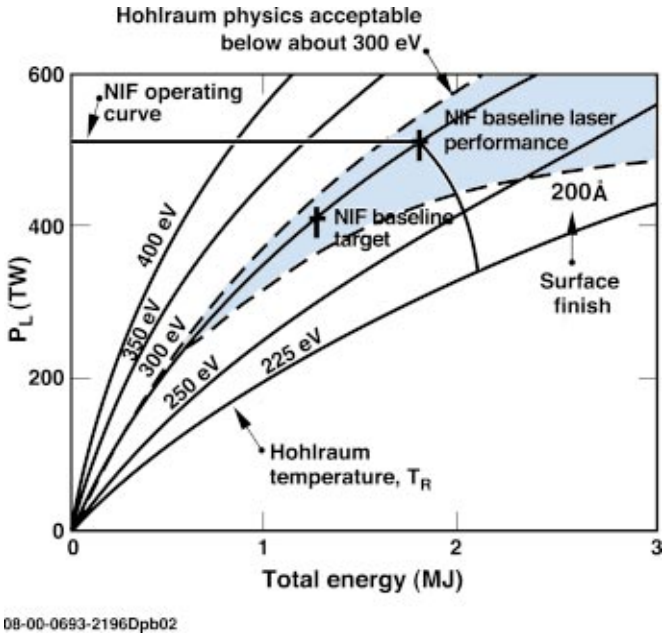

FIG. 1-7. (Color) For laser-driven indirect-drive ignition targets, plasma physics issues constrain the achievable hohlraum temperature and hydrodynamic instabilities (represented here by surface finish) establish the minimum required temperature at a given drive energy. The shaded region constitutes the accessible region in power-energy space where ignition with indirect-direct capsules is predicted. The NIF power-energy operating curve shown here has margin to allow for uncertainty in ignition capsule physics.

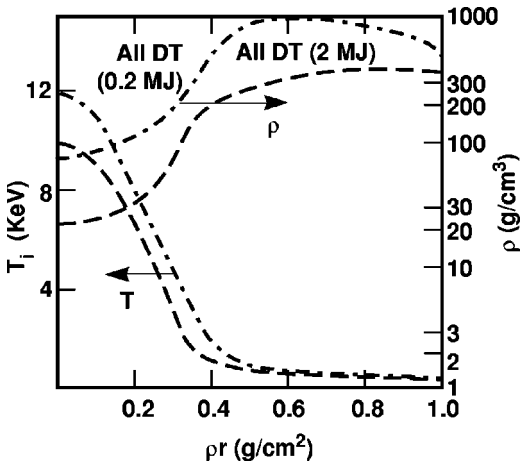

FIG. 1-8. Laboratory ignition and high-gain capsules have very similar ignition conditions. Hot-spot temperature profiles and ρr are nearly independent of size at ignition. Smaller capsules must have higher density to achieve the required hot spot $\rho r \approx 0.3$ g/cm^2.

ated very high levels of scattered light and high-energy electrons for hohlraums as the density approached this value. A simple scaling would suggest that about 400 eV is an upper-limit temperature for ignition hohlraums. (It is possible to achieve higher temperatures for short pulses with reduced plasma filling.) We limit peak hohlraum temperatures in current ignition target designs to $T_R \approx 300-350$ eV, which limits plasma densities to $n/n_c \approx 0.10-0.15$. The goal of the ignition physics experiments on laser–plasma instability (LPI) physics is to better understand ignition-relevant plasmas and to achieve a coupling efficiency of laser light into a hohlraum of about 90% for NIF-type plasmas, laser intensities, and beam geometry.

At a given driver energy, hydrodynamic instabilities place a lower limit on the temperature required to drive a capsule to ignition conditions. A larger capsule with more fuel mass requires a lower implosion velocity, which can be achieved with a lower radiation temperature consistent with the shell aspect-ratio constraints. The value of the required minimum temperature at a given energy will depend on the allowed shell aspect ratio; this depends on the smoothness of the capsule surface, currently limited from 100 to 200 Å rms for Nova capsules. Below a certain size, the required implosion velocity will exceed the velocity achievable within the temperature and capsule uniformity constraints, and ignition is not possible. Above this threshold energy, there is a region in power-energy space where ignition is feasible. This is the shaded area in Fig. 1-7, which encloses the region limited by 300 eV hohlraum temperatures and 100 Å capsule-surface finishes. The analysis for the curves which define the ignition region in Fig. 1-7 follows that in (Lindl, 1995) but with the ignition energy scaling updated using Eq. (1-1).

The NIF laser is being designed to operate at an energy of 1.8 MJ and a power of 500 TW for ignition pulses; both values are about a factor of 2 above the threshold ignition values shown in Fig. 1-7, allowing for remaining uncertainty in the implosion process. Within the ignition region shown in Fig. 1-7, a wide variety of targets have been evaluated. The predicted yields of the baseline NIF targets range from about 1 to greater than 25 MJ. Although the yields expected from NIF targets are less than that required for applications such as inertial fusion energy (IFE), the physics learned from NIF applies to a wide range of capsule sizes and yields.

The targets to be tested on NIF rely on central ignition followed by propagation of the burn via alpha deposition and electron conduction into the surrounding cold fuel. Once the hot central region of the fuel reaches 10 keV with a ρr equal to the range of the α particles (~ 0.3 g/cm^2 at 10 keV), the burn will propagate into and ignite an indefinite amount of surrounding cold fuel. The initiation of a self-sustaining burn wave defines ignition in an ICF target. These ignition and burn propagation conditions are nearly independent of fuel mass over a wide range of sizes.

Figure 1-8 shows the calculated fuel temperature (T_i) and density vs ρr for a 0.2 MJ capsule that could be driven by the NIF and a larger 2 MJ absorbed energy capsule (Lindl, 1998f). Although the capsule energies differ by an order of magnitude, the fuel configuration in temperature and ρr space, the variables that determine burn propagation, are nearly identical. The fuel in the smaller capsule has been compressed to greater density to make up for the reduced mass and energy in the fuel.

Once ignition occurs, the burn wave in these deuterium–tritium (DT) capsules propagates in ρr and temperature space in a way that is essentially independent of size. Figure 1-9 shows the ion temperature-vs-ρr conditions for a 0.2 MJ NIF and the larger 2.0 MJ capsule as the burn wave propagates into the fuel. The two capsules track each other until the smaller capsule starts to decompress. Once started, the burn wave continues to propagate until it runs out of fuel.

Downloaded 20 Mar 2011 to 69.181.48.121. Redistribution subject to AIP license or copyright; see http://pop.aip.org/about/rights_and_permissions

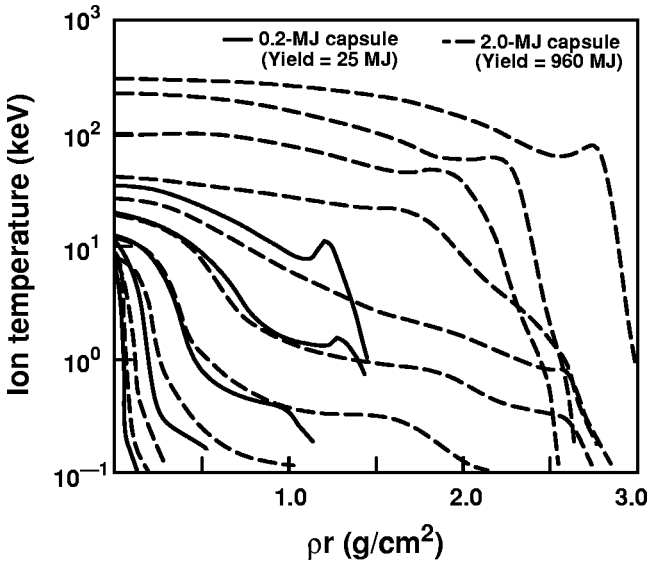

FIG. 1-9. Burn propagation in small capsules tracks that in larger capsules until decompression begins. Pairs of curves are temperature contours at a series of times as the burn wave propagates through the fuel.

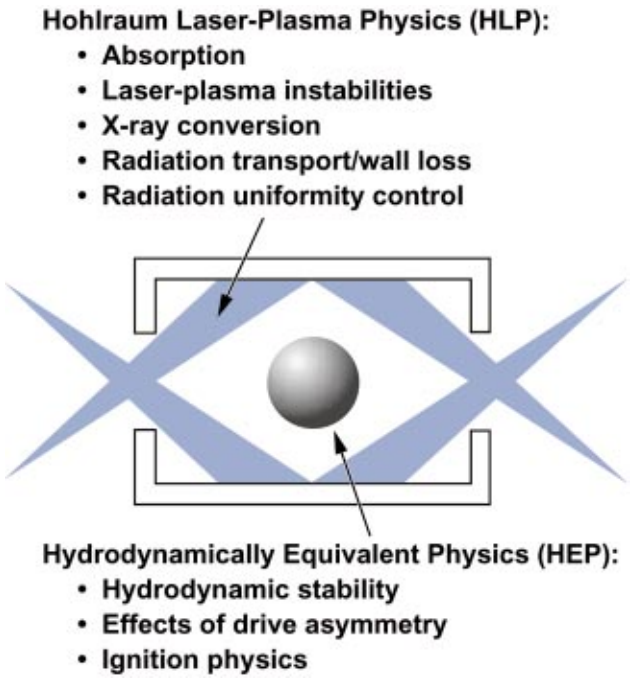

FIG. 1-10. (Color) The Nova Technical Contract (NTC) program comprises two elements that address the hohlraum (HLP) and capsule physics (HEP) of ignition and high gain.

Thus, a demonstration of ignition and burn on the NIF will determine the requirements for high gain with a larger driver.

A high-level summary of some of the key results from the target physics program compared to NIF ignition target requirements is shown in Table I-1. As indicated in the table, the results from the Nova and Omega experiments approach the NIF requirements for most of the important ignition-capsule parameters, including drive temperature, drive symmetry, and hydrodynamic instability.

B. Elements of the indirect-drive target physics program

Section II summarizes the NIF target designs. It covers a variety of target designs using a variety of laser energies, ablator materials, and drive temperatures (from 250 eV to 350 eV). This section also summarizes current capabilities in target shell production and cryogenic-fuel formation.

To address the hohlraum and hydrodynamic constraints on indirect-drive ignition, the ignition program comprises the HLP physics goals, and the HEP goals, as indicated in Fig. 1-10. Sections III–V cover the HLP physics issues, and Secs. VI and VII cover the HEP physics issues.

Section III addresses LPI in hohlraums including laser beam filamentation as well as stimulated Brillouin scattering (SBS) and stimulated Raman scattering (SRS). This section also includes the effects of laser-beam filamentation relevant to hohlraum symmetry. Section IV deals with hohlraum energetics including x-ray production, hohlraum-wall losses and albedo, and hohlraum coupling efficiency. Section V covers hohlraum symmetry including spot motion and hohlraum plasma evolution, and the effects of time-dependent hohlraum albedo.

Section VI deals with RT instability. Most of the experiments are in planar geometry but a few of the experiments are in cylindrical or hemispherical geometry. This section

TABLE I−1. The results from Nova and Omega experiments approach the NIF requirements for most of the important capsule parameters.

Physical parameter	NIF	Nova (Omega)
Drive temperature	250–300	• >300 eV for 1 ns pulse • ~260 eV for shaped pulse in gas-filled hohlraum
Drive symmetry		
Number of beams	192	10 (60)
RMS capsule drive asymmetry (all modes)	1%	4% (2%)
Implosion averaged (P_2)	~1%	~1%
Capsule convergence ratio (CR) with NIF-like hohlraum/capsule ratio	25–45	10 (17–22)
Hydro-instability *e*-foldings		
Acceleration+deceleration for dominant modes (implosion); acceleration only for planar experiments	6–7 spherical	4–5 planar 4–5 spherical (4–5)

Downloaded 20 Mar 2011 to 69.181.48.121. Redistribution subject to AIP license or copyright; see http://pop.aip.org/about/rights_and_permissions

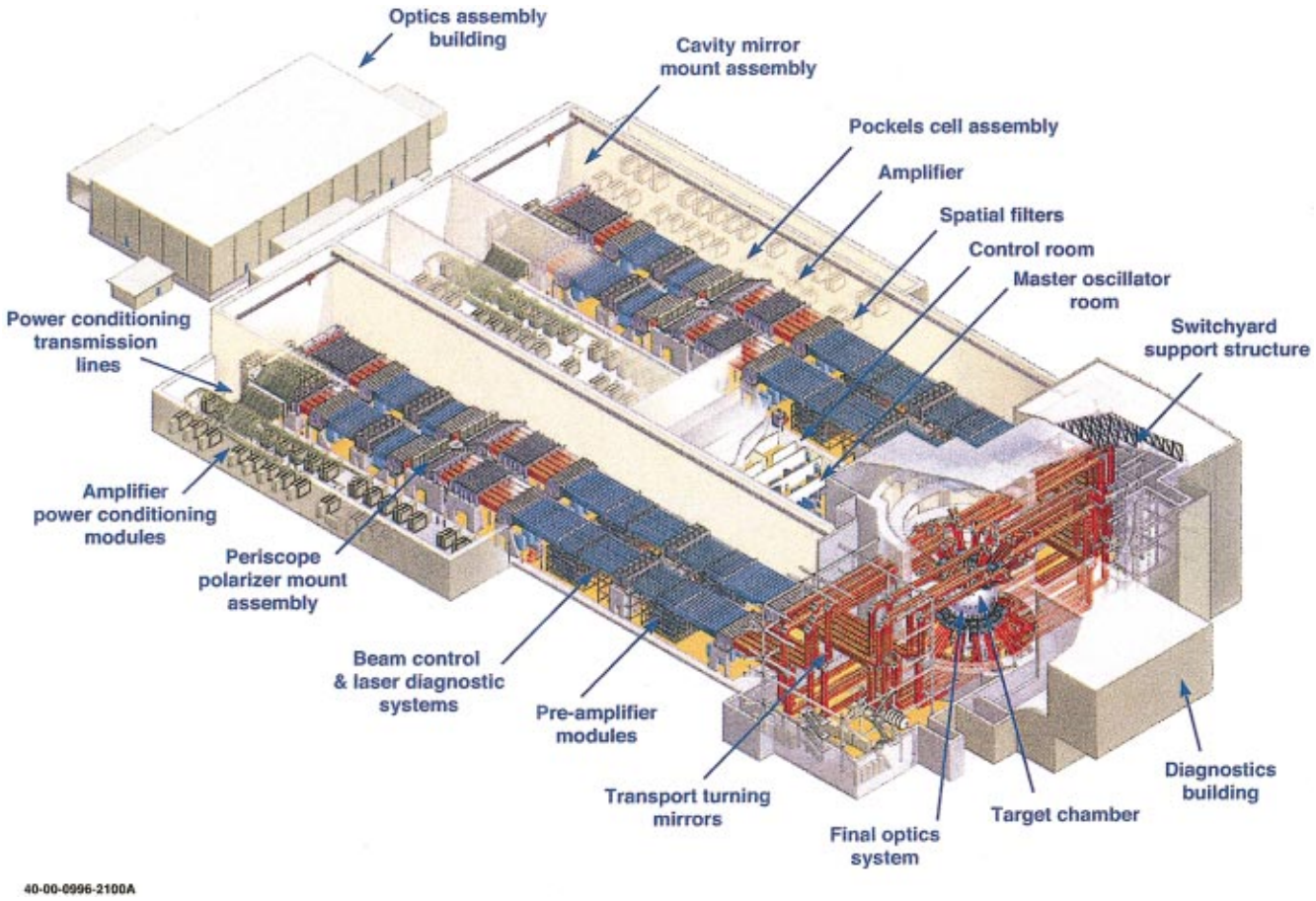

FIG. 1-11. (Color) The NIF is being designed with the energy, power, and precision required to demonstrate ignition and propagating burn in ICF.

covers linear growth rates as well as a number of nonlinear effects in two and three dimensions. Since ICF ignition capsules remain in the linear or weakly nonlinear regime, Sec. VI does not cover much of the recent work on highly nonlinear effects or the transition to turbulence. Section VII deals with implosion experiments designed to approach as closely as possible, the combined hohlraum and capsule requirements of an ignition experiment. The Nova Technical Contract (NTC) spelled out in the 1990 NAS review of the ICF program included a number of quantitative objectives. The indirect-drive target physics program has accomplished most of these objectives. However, as the NIF target designs evolved, the elements of the ignition physics program also evolved beyond the NTC. A detailed description of the NTC is included in the Appendix.

Results from the indirect-drive target physics program experiments and modeling led to the recommendation to proceed with the NIF, which is now under construction at LLNL (NTIS Document, 1994a). The NIF facility is shown schematically in Fig. 1-11. The U.S. indirect target physics program has primarily been the joint responsibility of LLNL and the Los Alamos National Laboratory (LANL). Scientists from the French Commissariat à l'Énergie Atomique (CEA) have participated in several of the later Nova and Omega experimental campaigns.

II. NIF IGNITION TARGET DESIGN

A. Introduction to NIF ignition target design

The NIF design is a 192-beam, frequency-tripled ($\lambda = 0.35\ \mu$m) Nd:glass laser system with a design goal of 1.8 MJ and 500 TW, appropriately pulse shaped, on target (NTIS Document, 1994a; NTIS Document, 1994b). The NIF system-design requirements for indirect-drive, given in Table II-1, have been determined from the NIF baseline target, shown in Fig. 2-1, which is typical of almost all the ignition targets under evaluation (Haan *et al.*, 1995; Krauser *et al.*, 1996; Wilson *et al.*, 1998; Haan *et al.*, 2000). A spherical cryogenic capsule (composed of DT gas, DT solid fuel, and an ablator) is encased in a cylindrical high-Z hohlraum with two laser-entrance holes (LEHs) at opposite ends. The light entering each LEH is in two cones. The relative energy in each cone is varied in time to control time-dependent asymmetry in the x-rays incident on the capsule. Approximately one-third of the energy goes into the cones near the midplane. The NIF target chamber is shown schematically in Fig. 2-2. The beam arrangement for indirect-drive is shown in Fig. 2-2(a). The 192 beams are clustered in 48 quads of four beams. Eight quads make up each inner ring and 16 make up each outer ring. Each cluster of four beams combines to form an effective $f/8$ optic. Each beam is focused to an elliptical spot, which reduces laser intensity and the long

Downloaded 20 Mar 2011 to 69.181.48.121. Redistribution subject to AIP license or copyright; see http://pop.aip.org/about/rights_and_permissions

TABLE II−1. Functional requirements for the indirect drive NIF laser design.

Energy (measured at the entrance hole of the hohlraum)	1.8 MJ
Peak power	500 TW
Wavelength	0.35 μm
Duration	20 ns
Dynamic range	
—Continuous	50:1
—Discrete	10:1
Capsule irradiation symmetry	Hohlraum illumination: Geometry: 2 concentric cones from each side Inner cone (beams incident at 23.5° and 30°) Outer cone (beams incident at 44.5° and 50°) Beamlet distribution: 2/3 on outer cone 1/3 on inner cone
Beamlet energy balance	8% RMS
Beamlet pointing accuracy	50 μm
Prepulse	$<10^8$ W/cm^2
Pulse simultaneity	$<$30 ps
Spot size	500 μm at the laser entrance hole
Beam smoothness	—Phase plates for the control of spatial irradiance on the target —The option to produce different wavelengths for different beams, up to a frequency separation of 1 nm at 1ω —Temporal and spatial smoothing as provided by one-dimensional Smoothing by Spherical Dispersion (SSD), with bandwidth up to 3 Å at 1ω.

axis of the ellipse is chosen so there is no loss of LEH clearance. The nominal spot is 500×1000 μm at best focus. Such a spot can be made with phase-plate techniques (Dixit *et al.*, 1994; Kessler *et al.*, 1996; Lessler *et al.*, 1993; Lin *et al.*, 1995; Lin *et al.*, 1996; NTIS Document, (1994g)). The NIF beams will be initially configured as shown in Fig. 2-2(a). However, by moving 24 of the 48 quads to beam ports closer to the midplane of the chamber [as shown in Fig. 2-2(b)], the NIF will be capable of doing uniformly irradiated direct-drive implosions at a later date.

Three possible ablator materials are currently under evaluation (Haan *et al.*, 1995; Krauser *et al.*, 1996; Wilson *et al.*, 1998; Haan *et al.*, 2000). Capsules with Ge-doped CH, Cu-doped Be, and polyimide ablators are shown respectively

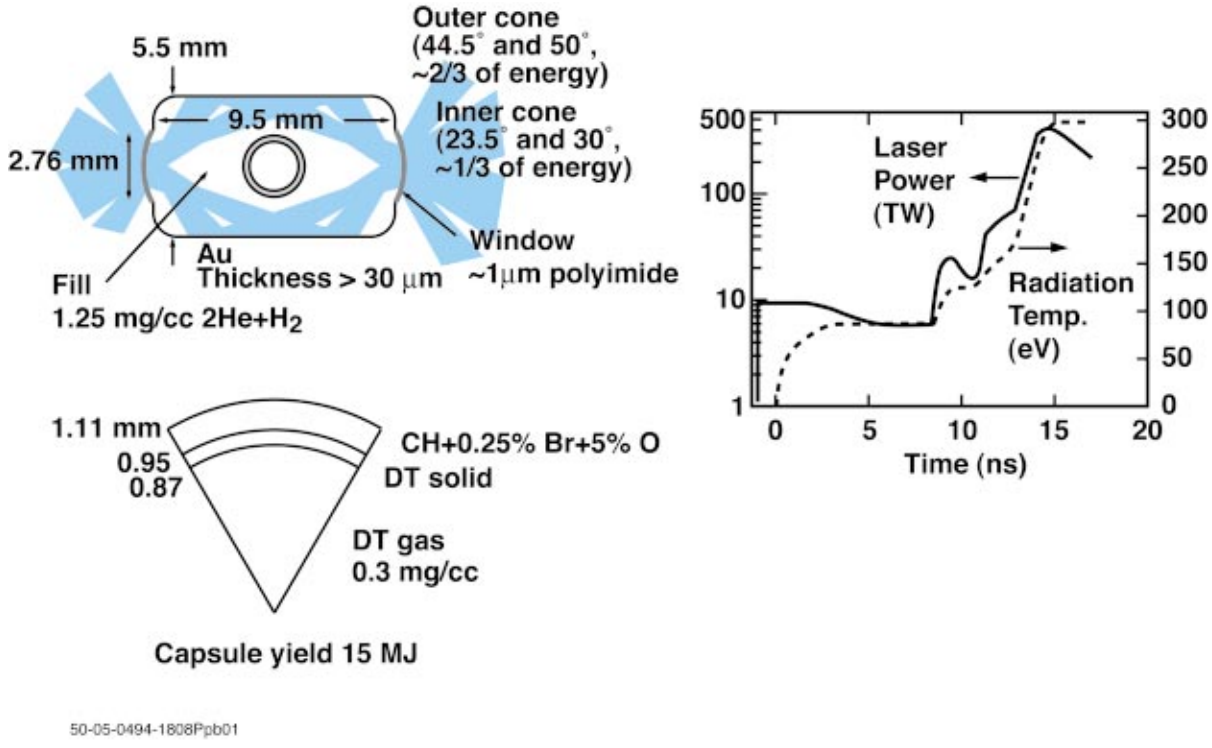

FIG. 2-1. (Color) The most extensive modeling of ignition has concentrated on this target, called the point-design target (PT), that absorbs about 1.3 MJ of light.

Downloaded 20 Mar 2011 to 69.181.48.121. Redistribution subject to AIP license or copyright; see http://pop.aip.org/about/rights_and_permissions

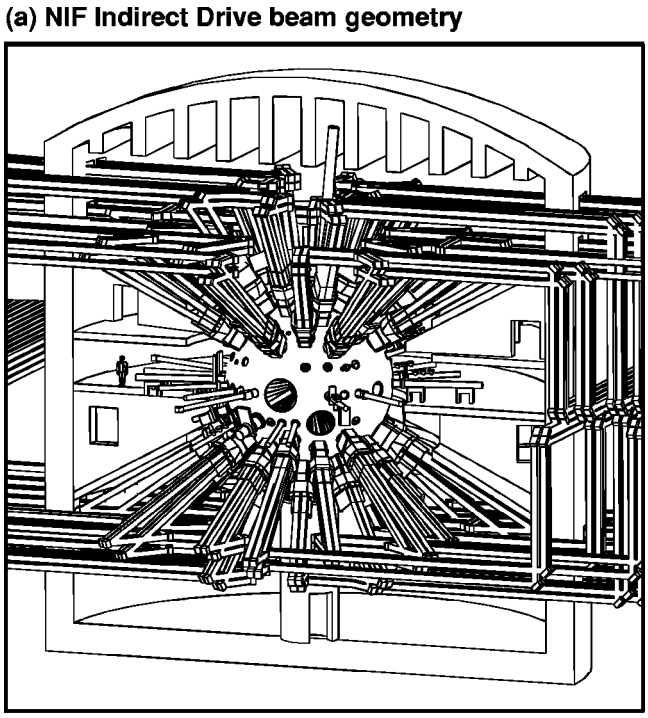

FIG. 2-2. The NIF target-area beam geometry: (a) NIF baseline target area uses 48 clusters of four beams configured for indirect-drive; (b) NIF target-area building and beam transport system can be reconfigured for direct-drive by switching 24 of the four-beam clusters to alternate positions.

in Fig. 2-3. These three designs have similar fuel-implosion characteristics and could be driven in identical 300 eV hohlraums with nearly identical pulse shapes. In the baseline target, the hohlraum material is Au, but a variety of materials or materials mixtures can be used. Designs are being evaluated with hohlraum peak-radiation temperatures (T_r) that range

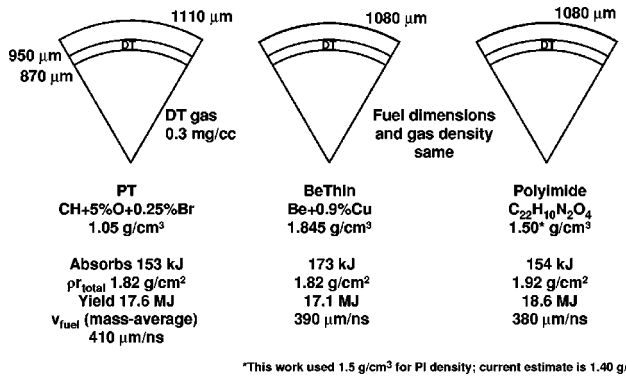

FIG. 2-3. We are evaluating CH, Be, and polyimide as possible ablator materials. These three designs have similar fuel implosion characteristics and could be driven in identical 300 eV hohlraums with nearly identical pulse shapes (1.3 MJ and 400 TW absorbed).

from 250 to 350 eV, with a shaped pulse for a low-entropy implosion. The ablation pressure allows the fuel shell to reach a velocity of 3 to 4×10^7 cm/s. The central part of the DT is then compressed and heated, forming a hot spot that reaches ignition conditions of density$\times$radius $\rho r \approx 0.3$ g/cm^2 and ion temperature about 10 keV. Then, α deposition "bootstraps" the central temperature to >30 keV. The hot-spot density at ignition is typically from 75 to 100 g/cm^3. The hot spot is tamped by a colder main fuel layer, with $\rho\Delta r \approx 1-2$ g/cm^2 and density ≈ 1000 g/cm^3. The burn propagates into the main fuel layer, and from 10% to 25% of the total DT mass is burned. The target shown in Fig. 2-1 produces from 10 to 15 MJ of yield in simulations, depending on the details of pulse shaping, hohlraum asymmetry, and RT instability.

The ignition region in laser power and energy in Fig. 1-7 is bounded on one side by hydrodynamic instabilities. Ultimately, this boundary of the ignition region is determined by the capsule surface smoothness. For Nova capsules described in this review, surface finishes of 100 to 200 Å have been achieved, and similar surface finishes will be required for NIF capsules. This constraint sets a minimum temperature for NIF ignition targets of about 250 eV.

On the high temperature side, the ignition region is bounded by laser–plasma instabilities covered in Sec. III. Laser intensity and other parameters determining the instabilities depend primarily on the desired peak hohlraum T_r. The laser must propagate through 3 to 5 mm of hot ($T_e \approx 3-5$ keV at peak power), low-density ($n_e \leqslant 1\times10^{21}$ cm^{-3}), and low-Z (mixture of He and H) plasma. Near the hohlraum wall, the laser propagates through a few hundred microns of high-Z material. In the NIF-baseline 300 eV hohlraum, the density of the low-Z plasma is 0.05 to $0.10n_c$ (critical density $n_c = 10^{21}\lambda^{-2}$ cm^{-3} where λ is the laser wavelength in microns) over most of the beam path and the temperature is $T_e \approx 4-5$ keV. For the inner ring of beams, the density reaches as high as 15% of critical density for the last millimeter of pathlength. However, this far into the hohlraum the individual laser-beam intensity has decreased substantially from its peak of 2×10^{15} W/cm^2. NIF hohlraums are initially filled with a low-Z gas as a

Downloaded 20 Mar 2011 to 69.181.48.121. Redistribution subject to AIP license or copyright; see http://pop.aip.org/about/rights_and_permissions

symmetry-control technique. Without this low-Z fill, the laser-beam energy is strongly absorbed in high-Z blowoff and does not propagate to positions near the hohlraum wall as required for symmetry.

Without an initial gas fill, for laser pulses as long as those required for ignition, the radiation-driven blowoff has time to fill the hohlraum; it then becomes the dominant source of plasma in the hohlraum. The interaction of the laser with the radiation blowoff determines the plasma conditions in the beam path. A combination of inverse bremsstrahlung absorption along the beam path, electron conduction from the beam path into the surrounding channel, and pressure equilibrium throughout the channel determines the beam-path density and temperature. By balancing these effects, a near equilibrium in temperature and density is established in the laser-propagation channel. A simple theoretical model (Lindl, 1998e) that compares well with the average temperature and density seen in numerical models gives the following scaling for the hohlraum plasma density and temperature:

$$\frac{n}{n_c} \propto \lambda^{12/7} Z^{-2/7} T_r^2 E^{-1/5} \tag{2-1}$$

and

$$T_e \propto \lambda^{2/7} Z^{2/7} T_r^{6/5} E^{1/20}. \tag{2-2}$$

Since the critical density scales as $1/\lambda^2$, the hohlraum plasma density and electron temperature are almost independent of laser wavelength and depend primarily on hohlraum radiation temperature. Also, since the fraction of critical density in the channel scales nearly as the product of the laser wavelength squared and the radiation temperature squared, the achievable radiation temperature at a fixed fraction of critical density is approximately inversely proportional to laser wavelength. An initial gas fill does not significantly change the densities that develop in the hohlraum, but it does provide control of the composition of the material in the hohlraum interior.

Laser scattering or filamentation in the hohlraum affects the target performance in several ways. Of course, energy scattered back out of the hohlraum is unavailable for x-ray conversion. The total energy lost comes out of the energy margin. For the baseline design, NIF has about a 33% margin in laser energy above the 1.3 MJ absorbed energy required. The irreproducible part of scattering becomes a pulse shape and power balance or pointing uncertainty, and any resultant geometrical nonuniformity can affect the symmetry of the irradiation on the capsule. If the overall level of these instabilities can be kept to 10% or less, their impact on the hohlraum performance will be small. At this level, even if the scattering had a large variation from beam to beam, the effects on power balance would be less than that from the expected 8% RMS statistical variation in the input energy of the laser beams (see Table II-1). Because of the relatively thick capsules on NIF and the relatively low energy of the electrons produced under typical NIF plasma conditions, we do not expect hot electrons produced by SRS to have any effect on target performance (Lindl, 1998g). The upper boundary of the radiation temperature is still somewhat uncertain, but as discussed in Sec. III, hohlraums with temperatures of 300 eV, and perhaps somewhat more, are consistent with the experiments and modeling that have been carried out on Nova to emulate the plasmas that are expected in NIF targets.

The region between the NIF laser design performance and the intersection of the achievable hohlraum temperature and achievable capsule surface finishes defines the operating space for ignition targets, as shown in Fig. 1-7.

The most complete target analysis (Haan *et al.*, 1995; Krauser *et al.*, 1996; Lindl, 1998h) has been carried out on the baseline 300 eV hohlraum and capsule shown in Fig. 2-1. This combination of hohlraum and capsule is referred to as the point-design target (PT). At 1.35 MJ, this point design is about midway between the 1.8 MJ, 500 TW NIF laser-design performance and the ignition energy minimum. This design allows for uncertainty in both laser-capsule coupling efficiency and ignition threshold.

B. NIF ignition capsules

The most detailed one-dimensional (1D) capsule simulations are done with the LASNEX code (Zimmerman and Kruer, 1975) using P_N radiation transport (NTIS Document, 1976), equations of state (EOS) calculated in-line with a ''Quotidian EOS'' model (More *et al.*, 1988), and average-atom XSN opacities (NTIS Document, 1977). Other radiation-transport schemes predict the same capsule performance, as do other opacity models such as OPAL (Iglesias and Rogers, 1996) and super transition arrays (STA) (Bar Shalom *et al.*, 1989). For separate implosion calculations that explore RT instability in detail, a non-Planckian frequency-dependent radiation source is obtained from two-dimensional (2D) hohlraum simulations. The spectrum used affects the short-wavelength hydrodynamic-instability growth. Other than this effect, which can change short wavelength perturbation amplitudes by about a factor of 2 in some capsule designs, the spectrum has little effect on target characteristics. The deposition of α particles produced by the burn is normally calculated with the multigroup diffusion (Corman *et al.*, 1975) model in LASNEX. Calculations (Hatchett, 1993) of the PT capsule using a Monte Carlo charged-particle transport model (NTIS Document, 1990a) produce ignition and burn that are essentially the same as produced by multigroup charged-particle diffusion.

The pulse shape shown in Fig. 2-1 creates four shocks. This series of shocks brings the ablator up to peak pressure while maintaining sufficiently low entropy in the DT that it remains in a near-Fermi degenerate state (Lindl, 1998i). For optimal performance, the shocks must be timed within about 100 to 200 ps. Given uncertainties in opacity and EOS, adequate shock timing may not be predictable *a priori*, but it is achievable with an experimental program (Munro *et al.*, 2001). The absolute value of the shock strengths at each step can be varied over a fairly wide range as long as the timing is adjusted to maintain the appropriate timing between successive shocks. Figure 2-4 shows the tolerable variation in individual shock strengths, assuming the timing of all the

Downloaded 20 Mar 2011 to 69.181.48.121. Redistribution subject to AIP license or copyright; see http://pop.aip.org/about/rights_and_permissions

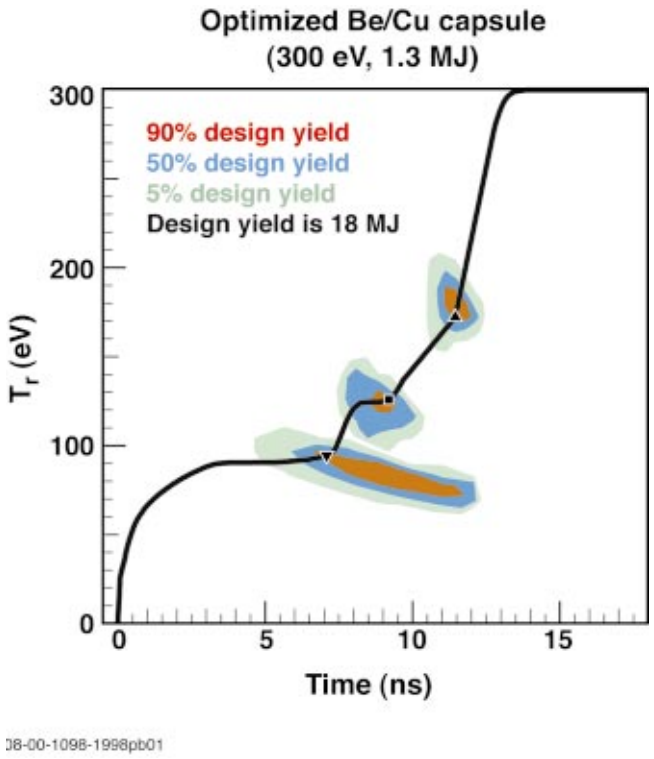

FIG. 2-4. (Color) Sensitivity of NIF ignition targets to pulse shape: the color scale shows yield variation as the drive profile is varied by moving the ''peg-points'' indicated by the small triangles. A wide range of pulse shapes provides good performance, but for a given pulse shape, the shocks generated must be accurate to 2%.

other shocks has been optimally adjusted (Munro, 1998). For example, the radiation temperature driving the first shock can be varied from 65 to 90 eV as the length of the pulse prior to generation of the second shock is varied from 13.5 to 8.0 ns. The NIF point design was chosen near the high-temperature end of this range in order to minimize the overall laser pulse length into the hohlraum. Typically, the pressure ratio between successive shocks must be kept below about a factor of 4 to minimize the entropy increase (Lindl, 1998i).

All the single-shell-ignition target designs for NIF require that the bulk of the fuel be in a cryogenic layer on the inside surface of the ablator. Bulk heating of the DT by β decay of the tritium provides an effective technique for producing uniform layers of DT in ICF targets (Hoffer and Foreman, 1988; Martin *et al.*, 1988; NTIS Document, 1991a). If the capsule outer surface is at a uniform temperature, β decay will cause thick regions of DT to be at a higher temperature than thinner regions. These hotter regions will sublime more rapidly and become thinner. This process continues until the layer has a nominally uniform thickness. However, the DT tends to deposit as a large number of small crystallites. The β-heating process does not completely eliminate discontinuities that arise at the boundaries of these crystallites, resulting in about <1 μm microscale roughness near the triple point of DT (Hoffer *et al.*, 1992; Hoffer *et al.*, 1995). The β decay in 50/50 DT produces about 0.16 W/g. If external heating is applied to augment the β decay, smoother layers can be produced. Both optical techniques that couple to rotational/vibrational transitions in DT and radio-frequency heating that couples to the free electrons produced by β decay have been shown to produce smoother DT layers (Collins *et al.*). The optical absorption technique applies equally well to DD or DT fuel. This will be important in nonignition experiments that may utilize DD fuel. However, the optical technique requires transparent shells, and the radio-frequency approach requires nonconducting shells. Hence, neither approach applies to Be shells.

A uniform layer may also be produced by applying a temperature gradient to a liquid cryogenic layer (Kim *et al.*, 1985). Because both surface tension and evaporation rates are temperature dependent, it is possible under some conditions to obtain a uniform layer by adjusting these two properties with an appropriate temperature gradient.

In a final technique, low-density foam is used as a matrix for the cryogenic-fuel layer (Sacks and Darling, 1987). A foam-filled fuel layer has a higher ignition temperature, which depends on the foam density and material composition. Hence, most foam designs require a thin layer of pure DT on the inside of the foam to aid ignition.

The Omega laser will be used as a test bed for developing targets with thick cryogenic layers. Initial experiments began in calendar year (CY) 2000 (Stoeckl *et al.*, 2002).

Initiation of a self-sustaining burn wave constitutes ignition in ICF. Beyond a threshold implosion velocity for a given capsule size, $P\,dV$ work can compress the hot spot to the ρr and temperature at which α-particle deposition can initiate a burn wave. For the baseline NIF-scale capsules, the threshold implosion velocity for ignition is expected to be 3.5 to 4.0×10^7 cm/s. Ignition results in a rapid increase in yield as implosion velocity is increased gradually beyond the ignition threshold velocity. Experimentally, the implosion velocity can be increased, while keeping the fuel on the same isentrope and maintaining the low temperature foot of the pulse, by varying either the peak-drive temperature at the end of the pulse or the length of the pulse. Alternatively, the ablator thickness and mass could be varied using the same peak power part of the pulse while varying the lower-temperature foot to maintain the fuel entropy.

As shown in Fig. 2-5 for the baseline polyimide capsule, without α-particle deposition and the resulting burn propagation, NIF targets are expected to produce no more than 10 to 100 kJ (Lindl, 1998h), whereas a target with ignition and successful burn propagation will produce from 1 to 20 MJ of thermonuclear energy, depending on capsule and hohlraum design.

Below a burn-averaged temperature of about 3 keV, negligible α-particle deposition occurs, and the observed increase in fusion yield with implosion velocity follows that expected for the purely hydrodynamic increase in fusion cross section. By the time the fuel temperature doubles due to α-particle deposition, the fusion burn rate has increased by an order of magnitude (White *et al.*, 1992) or more beyond what could be achieved with pure hydrodynamic compression. Target performance below a central temperature of a few keV will provide an experimental baseline for determining the purely hydrodynamic increase in fuel temperature as a function of implosion velocity; against this the measured departure due to α-particle deposition can be determined.

Downloaded 20 Mar 2011 to 69.181.48.121. Redistribution subject to AIP license or copyright; see http://pop.aip.org/about/rights_and_permissions

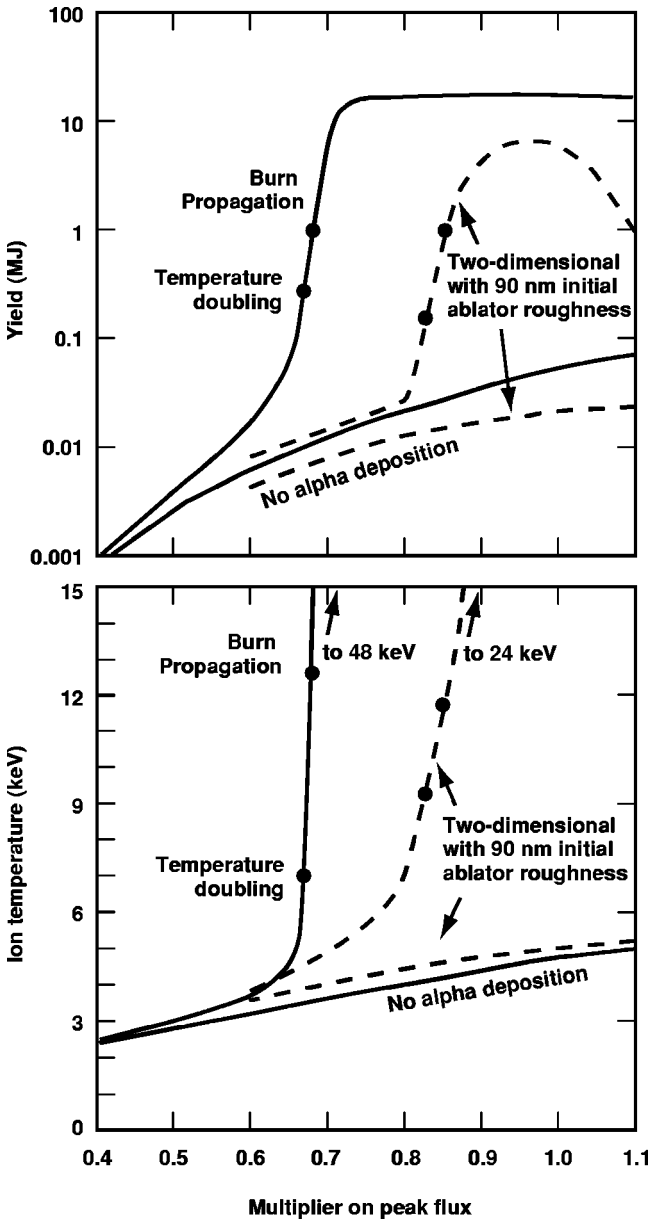

FIG. 2-5. Ignition could be diagnosed as a rapid increase in yield and neutron-width burn temperature as drive is varied. The horizontal axis is a multiplier on the peak drive, with the first 13 ns of the pulse unchanged, and the flux smoothly interpolated between 13 ns and the multiplied flux for times 14 ns and greater. Solid lines show one-dimensional simulations, and dashed lines show a heavily perturbed two-dimensional simulation. (The 90 nm initial roughness in the 2D simulations is about four times the surface roughness specification.) Temperature doubling, above what would occur without bootstrapping via α deposition, occurs at a yield of a few hundred kJ, and yields above about 1 MJ require propagation of the burn into the main fuel region. The appearance of ignition as a threshold in yield and ion temperature is similar in 1D and 2D, although in 2D the capsule has less margin and lower yields.

A complementary set of experiments could be done with a nonigniting fuel layer. For example, above or below some ratio of D to T, the targets will not ignite at any implosion velocity reached on the NIF. Assuming a comparable cryogenic-layer quality and a slightly revised pulse shape to account for initial fuel density differences, a curve of yield vs implosion velocity with a nonigniting fuel mixture, normalized for cross section differences, would provide an additional baseline for comparison with the ignition experiments. Changing the D to T ratio could affect a cryogenic layering process, which would complicate direct comparison with the 50/50 DT case. For example, β layering will not work with a pure D_2 fuel layer but might work with a pure or nearly pure T_2 layer. However, RF or IR heating will work with all fuel combinations in transparent shells.

The NIF baseline capsule designs absorb 150 kJ, of which about 25 kJ ends up in the compressed fuel. As shown in Fig. 2-5, the ion temperature, obtained here from the neutron energy width, gets to about 10 keV when the capsule has produced about 400 kJ (on about 20% of this or 80 kJ is in α particles which are absorbed in the central hot spot and surrounding fuel). Therefore, ignition occurs when the fuel-energy gain is about 16, or when the α-particle deposition is about $3\times$ the initial energy delivered to the compressed fuel. Since the NIF baseline targets are expected to yield up to 15 MJ, these targets would have a fuel energy gain of about 600.

At the ablation front, short-wavelength RT growth in the NIF capsules is stabilized by ablation of material at the unstable interface and by the finite density-scale length as discussed in Sec. VI. As a result, the ignition targets can be designed to remain in the linear or weakly nonlinear regime for hydrodynamic instabilities. Because of this, much of the instability modeling can be based on linear analysis that is as accurate as possible, with an extension into the weakly nonlinear regime as necessary. In this regime, the principal nonlinear effect is mode-shape changes. Other mode coupling effects are, in general, not important. The linear analysis is based on a decomposition of the surface perturbations into spherical harmonics, which are eigenmodes of the linear evolution. Single-mode growth is determined by running many 2D simulations, each of one single mode in the linear regime throughout the simulation. This provides the most accurate calculation of all known effects in the linear regime, including ablation and density-gradient stabilization, Richtmyer–Meshkov growth, and convergence effects. This set of calculations, combined with a nonlinear saturation model (discussed further in Sec. VI), provides a spectrum of growth factors that vary from several hundred to approximately 1000. Time-dependent growth factors are combined with an assumed initial-surface spectrum to determine the root-mean-square (rms) perturbation σ as a function of time, near ignition time. As described in Sec. VI, the bubble amplitude is taken to be $\sqrt{2}\sigma$, and the spike amplitude to be $(1+A)\sqrt{2}\sigma$, where the Atwood number A is nearly unity in this case.

In this approach, the effects of the perturbed layer on the ignition hot spot are evaluated using a 1D model in which mixing is represented only as an enhanced thermal conductivity in the perturbed region. Because the mixing occurs between hot and cold DT, material mixing of different elements does not occur. The effect of this 1D mixing model is to distribute the energy in the mixed region nearly uniformly over all the mass in the mixed region. LASNEX models this heat flow with an enhanced thermal diffusivity given by $\alpha_D L(dL/dt)$ over the 1D mix layer of width L, where α_D is a heat-diffusivity multiplier and L is the size of the mixed layer determined as described above and in more detail in

Downloaded 20 Mar 2011 to 69.181.48.121. Redistribution subject to AIP license or copyright; see http://pop.aip.org/about/rights_and_permissions

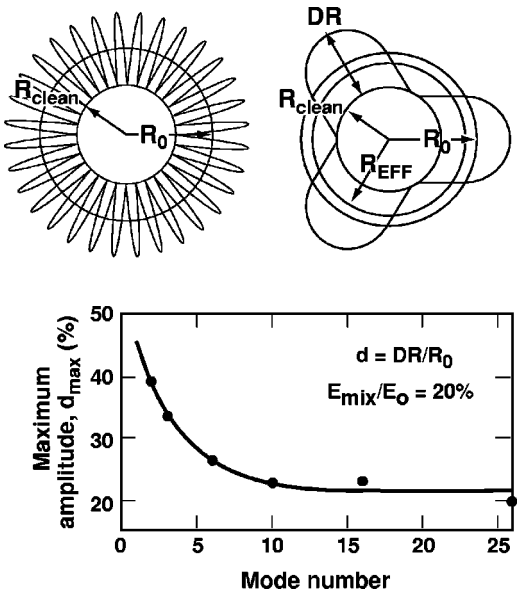

FIG. 2-6. At high l-mode numbers ($l>10$), the DT contained within the bubbles does not contribute to ignition—only the clean inner part of the hot spot ignites (Kishony, 2001). As the l-mode decreases below 10, the ratio of the surface area of the cold spikes to hot-spot volume decreases, allowing a larger effective radius to contribute to ignition. The case shown is for $E_{\mathrm{mix}}/E_0=20\%$, an implosion with a 20% ignition margin (Kishony, 2001).

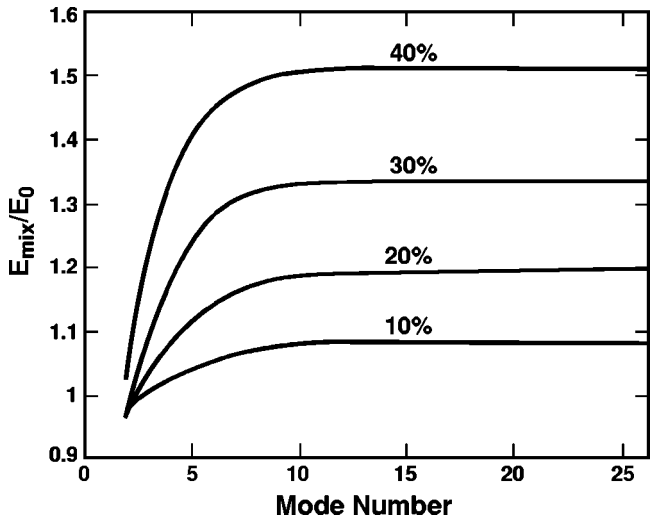

FIG. 2-7. The increase in the required driver energy vs the perturbation mode number for perturbation amplitudes as a fraction of the hot-spot radius of 10%, 20%, 30%, and 40% at peak compression (Kishony, 2001).

Sec. VI. This extra heat flow is used to mimic the heat lost from the hot spot that occurs as the surface area of a more realistic RT-modulated interface grows. Calculations typically use $\alpha_D=1$, but the result changes little for α between 0.5 and 2.0. Full simulations of multimode perturbations with realistic initial amplitudes are also run in both two and three dimensions. A variety of multimode simulations have been run on several capsules, at solid angles ranging from relatively small conic sections to half-spheres. Amplitudes obtained this way are consistent with the weakly nonlinear analysis. These calculations can be continued through burn time to model the effects of the perturbations on the capsule yield.

The multimode RT calculations and the 1D thermal mixing model give very similar results. Even though the multimode calculations do not result in a fine-scale mix of hot and cold material, heat conduction into the spikes for mode number greater than about 10 is sufficiently large that only the clean DT inside of the spike tips contribute to ignition. This is equivalent to what happens in a 1D-mix model. For a given kinetic-energy margin above the ignition threshold, some penetration of the perturbed spikes is tolerable. Below an l-mode of about 10, the ratio of the surface area of the cold spikes to hot-spot volume decreases, allowing a larger effective radius to contribute to ignition. These effects are shown in Fig. 2-6 for calculations in which a large-amplitude single-mode perturbation was applied to the imploding fuel configuration (Kishony, 2001). Figure 2-7 is a plot of the increase in the required ignition margin (driver energy) vs perturbation mode number for various perturbation penetration fractions. The dominant contribution to the perturbed region between the hot spot and cold-DT main fuel is for modes in the range of $l=15-40$ for NIF capsules. Because of this, there is very little difference in the effects of thermal conduction between a spatially detailed calculation that resolves these modes in the perturbed region and an atomic mix approximation with the same spatial depth (Levedahl and Lindl, 1997). For the NIF baseline capsules, the kinetic energy of the imploding fuel is about 40% above the minimum required for ignition. Detailed multimode 2D calculations, as well as the 3D calculations discussed below, predict that a maximum spike amplitude can be about 10 μm in amplitude compared to a hot-spot radius of 30 μm. This is consistent with the single mode calculational results in Fig. 2-7 and a 1D mix model.

The modeling above focused on surface perturbations that are initially on the outside of the ablator or on the inner surface of the DT. Of course, there will be perturbations on the other interfaces, as well as material inhomogeneity and other fabrication defects. Any of these can be modeled in a conceptually identical way. These calculations predict that the capsule is most sensitive to perturbations that are initially on the outside of the ablator. Perturbations on the DT gas/solid interface can be significantly larger than those on the outer ablator surface. These perturbations contribute to the growth by seeding perturbations at the ablation front during the acceleration phase or during the deceleration phase (when the amplification factors are relatively small). In either case, the impact of perturbations of a given size on the inner surface is reduced compared to those on the outer surface. When perturbations from multiple sources are included, a combined specification is given approximately by

$$\left(\frac{\mathrm{DT-ice-rms}}{\text{``max-tolerable''}}\right)^2+\left(\frac{\mathrm{Ablator-rms}}{\text{``max-tolerable''}}\right)^2+\left(\frac{\mathrm{Radiation-symmetry}}{\text{``max-tolerable''}}\right)^2<1. \tag{2-3}$$

Development of the 3D HYDRA code (NTIS Document, 1995b) has allowed us to perform 3D-multimode simulations

Downloaded 20 Mar 2011 to 69.181.48.121. Redistribution subject to AIP license or copyright; see http://pop.aip.org/about/rights_and_permissions

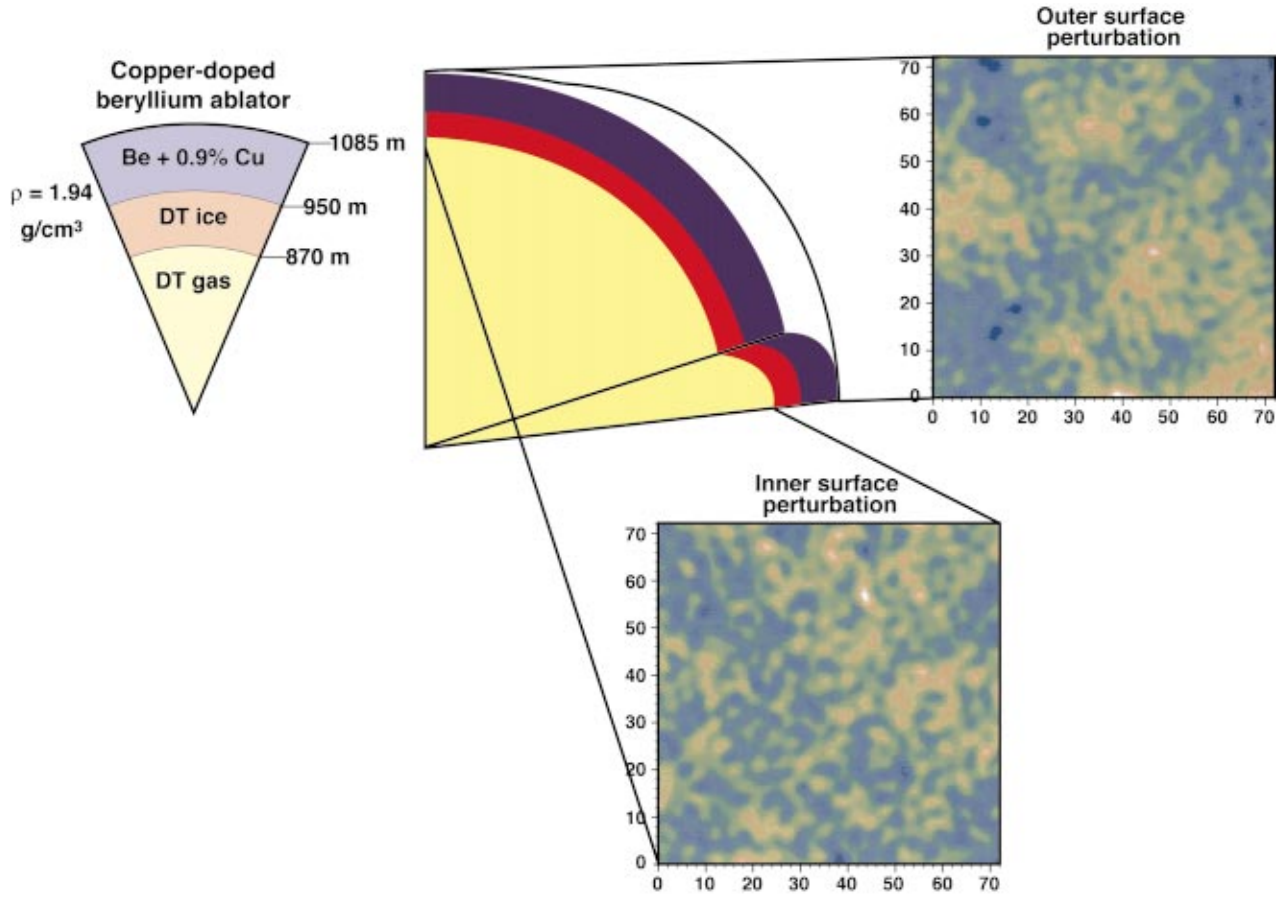

FIG. 2-8. (Color) Capsule-only simulations in 3D examine the effect of multimode surface perturbations. Both the inner ice and outer ablator surfaces are perturbed with modes over the range responsible for mix. Perturbations shown are derived from measured spectra of DT ice and a Nova capsule ablator, respectively.

(Lindl and Marinak, 1996b; Haan *et al.*, 2000) of various ignition capsule designs. HYDRA uses arbitrary Lagrange–Eulerian hydrodynamics. It has second order accurate laser raytracing with inverse bremsstrahlung absorption. Radiation transport can be either flux-limited multigroup diffusion or implicit Monte Carlo transport. The ignition capsule simulations use a thermonuclear burn model to treat the depletion and production of isotopes. An efficient multigroup routine transports energetic charged particles produced during the burn phase. Because the capsules are thin to neutrons, an accurate treatment of neutron-energy deposition is obtained with a neutron transport model derived in the free streaming limit. As energetic particles slow down, they deposit energy in separate electron and ion channels. Electron and ion conduction are treated, as well as electron-ion energy exchange.

Hydrodynamic instabilities are simulated over a portion of the capsule solid angle, which extends equal amounts in the polar and azimuthal angles $(\Delta\theta,\Delta\phi)$, with one boundary coincident with the capsule equator. Multimode surface perturbations imposed are of the form $G(\theta,\phi) = \Sigma_m \Sigma_n \cos(m\pi\theta/\Delta\theta)\cos(n\pi\phi/\Delta\phi)$, with symmetry boundary conditions at transverse boundaries. These are analogous to modes used in the 2D axisymmetric simulations over a portion of a quadrant. Perturbations on the outer ablator surface are based on traces from a Nova capsule, while those on the inner DT surface are based on a trace of cryogenic ice. These traces are converted to an estimated 3D power spectrum (NTIS Document, 1994c); power is distributed isotropically among the 3D modes with equivalent wave number. Using the Pacific Blue ASCI machine at LLNL, HYDRA simulations have been carried out for sectors of a sphere as large as 72° in both angular directions (Haan *et al.*, 2000). The initial conditions for such a calculation on the 300 eV Be capsule in Fig. 2-3 are shown in Fig. 2-8. This simulation resolves the full range of the most dangerous modes ($l \approx 2-100$), that grow from surface roughness on a NIF capsule. (Perturbations on the ablator had spherical harmonic amplitudes $10/l^{1.5}+1.5/l^{0.7}$, in nm, and on the DT ice $1.0/3l^{0.6}+2.2e-7l^4$, in μm.) During the implosion phase, the shell areal density strongly resembles the initial outer-surface perturbation, demonstrating that the modes that grow in the ablator are seeded predominantly by initial ablator surface perturbations, not from the rarefaction wave returning from the ice surface. Depressions initially on the surface develop into bubbles on the ablator surrounded by interconnecting spike sheets and larger individual spikes. Figure 2-9(a) shows density iso-contours of 13.8 g/cm^3 near peak implosion velocity. As the capsule approaches ignition, the perturbation structure on the inner surface evolves toward lower mode numbers. This behavior is strongly influenced by conductive ablation during deceleration and the effect of convergence, rather than by mode coupling. Figure 2-9(b)

Downloaded 20 Mar 2011 to 69.181.48.121. Redistribution subject to AIP license or copyright; see http://pop.aip.org/about/rights_and_permissions

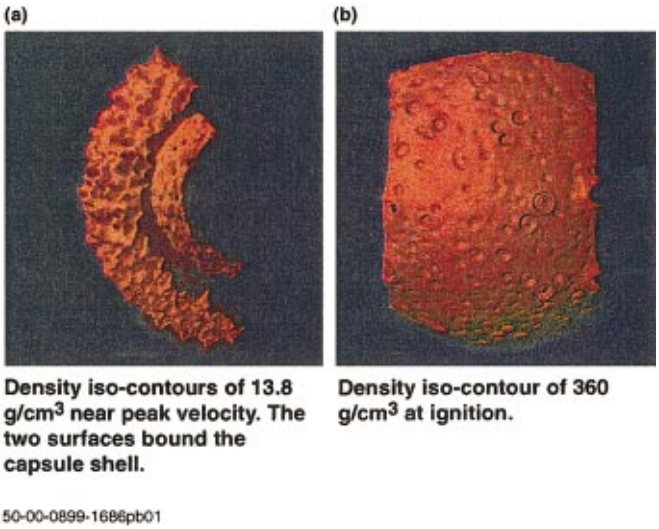

FIG. 2-9. (Color) A HYDRA simulation has resolved the full range of the most dangerous modes ($l \approx 2-100$) that grow from surface roughness on a NIF capsule. (a) Density iso-contours of 13.8 g/cm^3 near peak velocity. The two surfaces bound the capsule shell. (b) Density isocontour of 360 g/cm^3 at ignition.

shows a density iso-contour of 360 g/cm^3 in the dense fuel at ignition. This calculation shows that the largest amplitude modes are those with an $l \approx 30$ as expected from the single mode calculations, consistent with an implosion in a weakly nonlinear regime with little mode coupling other than that caused by mode shape change. Calculations with only an 18° sector of the sphere, which resolve modes in the range of $l = 10-40$, give essentially the same yield and are used for most of the 3D calculations. RT unstable modes in the range $40 < l < 120$ are much less capable of feeding through the shell and producing spikes upon deceleration than these longer wavelength modes. But they can threaten the shell integrity during the implosion phase, when the shell aspect ratio is higher. The longer wavelength perturbation from intrinsic hohlraum asymmetry, the power balance, and pointing errors have not yet been included in these 3D calculations.

Figure 2-10 shows the results of a series of HYDRA calculations on the three capsules in Fig. 2-3. Generally, Be performs better than CH as an ablator with the same perturbation level. At 300 eV, Be must be doped with higher-Z materials for optimal performance. The dopants suppress primarily the effects of preheat caused by higher energy photons in the tail of the x-ray distribution. Radially varying the doping allows for more complete optimization. Doping the Be with Cu appears attractive from a fabrication point of view.

Other Be capsules with a mixture of Na and Br dopants have been evaluated. Also, Be has a lower albedo than CH. As a result it absorbs energy more efficiently than CH and has a higher ablation rate at a given hohlraum temperature. Because of the higher ablation rate, Be shells are more stable. In the most highly optimized targets, the additional performance margin obtained by using Be instead of CH is equivalent to about 25 eV in peak hohlraum T_r. The advantage is greater at 250 eV than at 300 eV. Polyimide is inter-

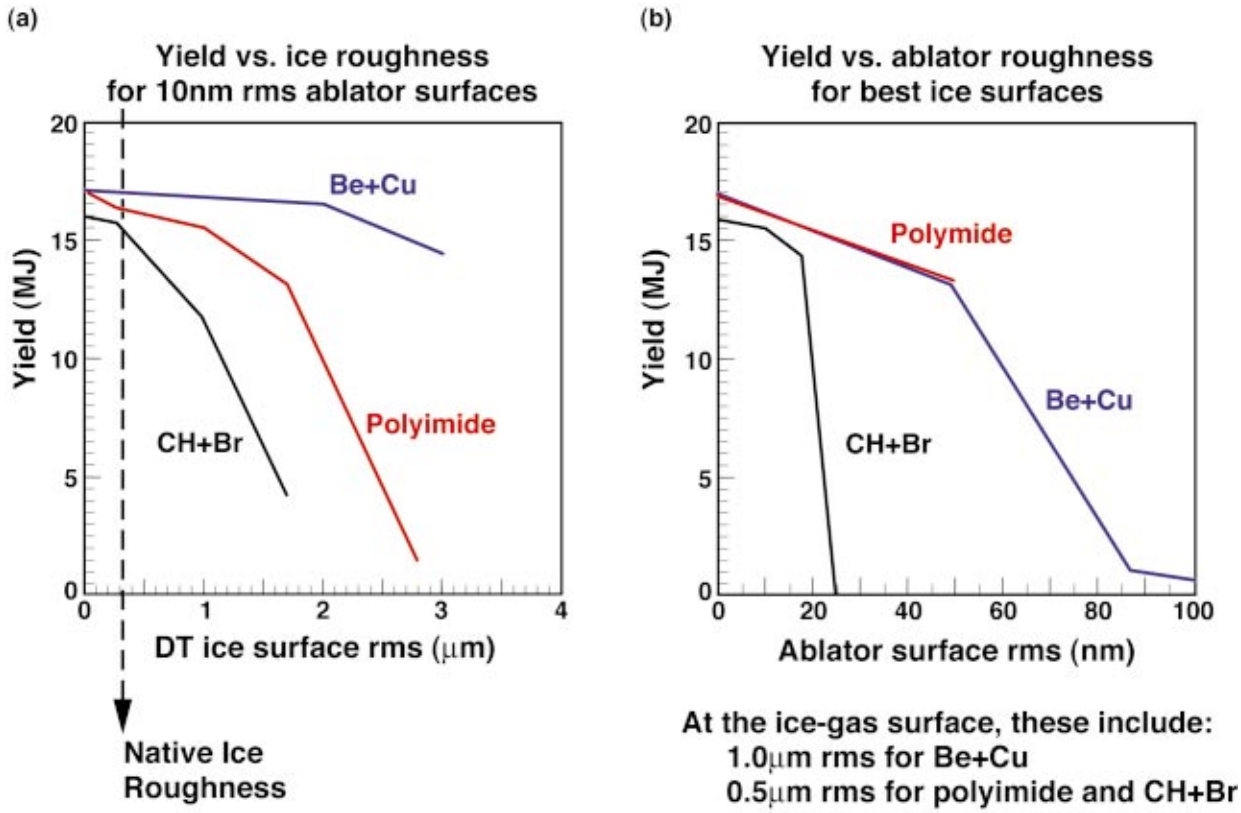

FIG. 2-10. (Color) 3D simulations with HYDRA show that at 300 eV drive, the BeCu NIF capsule can tolerate the roughest ice-gas and ablator surfaces. (a) Yield vs ice roughness for 10 nm rms ablator surfaces. (b) Yield vs ablator roughness for best ice surfaces.

Downloaded 20 Mar 2011 to 69.181.48.121. Redistribution subject to AIP license or copyright; see http://pop.aip.org/about/rights_and_permissions

mediate between CH and Be. Because Be is more efficient and has a higher ablation rate, Be shells in a given hohlraum with a given laser energy generally have more mass and have higher absorbed energy. The initial mass of the Be ablator in Fig. 2-2 is nearly twice that of the CH. An additional effect, which varies between the three capsule ablators is the effect of x-ray preheat. X-ray preheat, which is preferentially absorbed in the ablator, can result in an ablator density that is less than that of the fuel density during acceleration. There is then an interior interface between the fuel and the ablator, which can also grow. This effect is the most severe for the CH ablator PT capsule which has the thinnest ablator. Growth at this interface is seeded by feedthrough from the ablation front. To reduce this effect, the PT capsule is currently being reoptimized with a thicker ablator and/or thicker fuel layer and possibly a graded ablator preheat dopant. This effect is further discussed in Sec. VI C.

In Fig. 2-10(a), the roughness of the inner surface of the DT ice is varied for a constant ablator roughness of 10 nm. As seen from these calculations, the Be ablator capsule can tolerate about a factor of 4 rougher ice layer than a doped CH capsule. Perturbations initially on the ice grow by coupling to the unstable ablation front during acceleration; this coupling is much less effective through the more massive Be shell (Wilson *et al.*, 1998). Polyimide is intermediate between these two materials. However, both the CH capsule and polyimide may be suitable for enhanced smoothing while Be, which is not transparent, is not. If the achievable layer smoothness is a factor of 2 better for a polyimide capsule, then the relative safety factor for a Be and polyimide ablator would be similar. Figure 2-10(b) shows the sensitivity of the three capsules to ablator roughness. Be and polyimide are both substantially more tolerant than the doped CH capsule. Clearly, for equal quality ablator and DT ice surface roughness, a Be ablator shell is preferred. Most Nova capsules were made largely from CH plastic. A CH plastic ablator was chosen for the original baseline NIF capsules because developing, characterizing, and filling NIF capsules would be more straightforward by means of techniques similar to those already developed for Nova capsules. Techniques are now being evaluated to develop high-quality Be and polyimide shells. The relative merits of Be shells compared to CH or polyimide shells will be determined by the fabrication quality that can be achieved.

Another important issue in ablator selection may turn out to be the bulk homogeneity of the ablator. The implosion is very sensitive to nonuniformities in density or opacity. As a rough estimate of this sensitivity, note that a 30 nm surface roughness perturbation corresponds to a 1:5000 perturbation in column density for a 150 micron shell. It is likely that the implosion will be sensitive to column density variations of this order; quantifying this sensitivity is an area of current research. Also, the sound speed in crystalline beryllium is known to depend on crystal orientation, and it is possible the first shock will be perturbed as it propagates through the grain structure of a beryllium ablator. Again, this is an area of current research.

Modeling of a wide variety of other targets has been performed at various levels of detail. Several important aspects of the target can be varied, providing different trade-offs of the remaining uncertainties in our understanding.

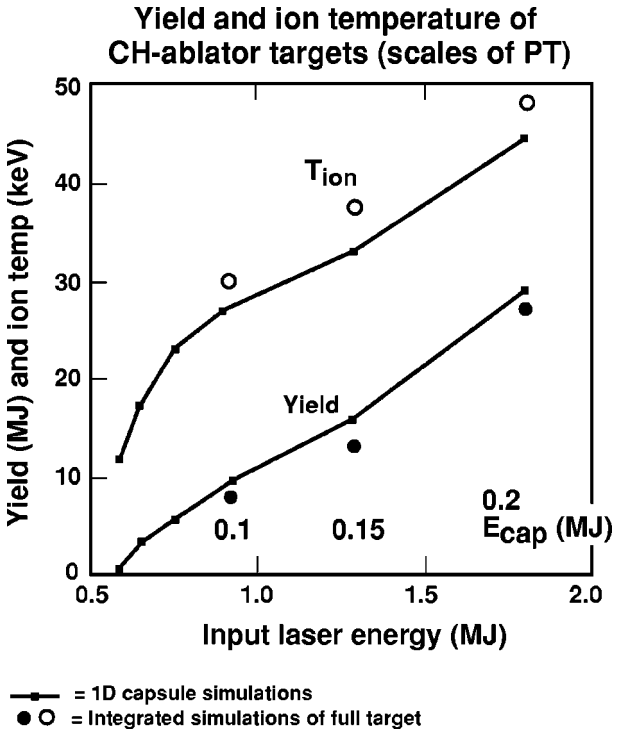

FIG. 2-11. Scales of the PT point design ignite in 1D above about 0.7 MJ. For the 1D capsule simulations, capsule dimensions and times are scaled by s, and the effective laser energy is given by $E_{\mathrm{eff}}(\mathrm{MJ}) = 1.35 s^3$, where $s = 1$ is the PT design. For the integrated hohlraum and capsule simulations, dimensions and times are proportional to s, and powers are proportional to s^2.

We can vary the size of the target and the energy it uses. Direct geometric scales of the PT produce good burn at any laser energy above about 700 kJ, as shown in Fig. 2-11. The 1D results are from hydrodynamically scaled targets with the required laser energy given by $E\ (\mathrm{MJ}) = 1.35\ s$ (Haan *et al.*, 1995) where s is the spatial scale factor compared to the PT. The 2D results are from integrated hohlraum and capsule calculations described below but do not include RT perturbation calculations for the smaller capsules. This energy margin allows for loss of energy to stimulated scattering processes and laser coupling. Also, it allows us, if necessary, to change the relative size of the hohlraum and capsule. This allows a trade-off of the capsule ignition physics, and hydrodynamic instability, with symmetry and hohlraum filling.

Figure 2-12 compares the characteristics of capsules with a drive temperature that varies from 250 (Dittrich *et al.*, 1999) to 350 eV (Hinkel *et al.*). The higher temperature designs stress the hohlraum–plasma physics and the achievable laser power while the lower-temperature designs stress the hydrodynamic instabilities. The greater sensitivity to hydrodynamic instabilities as the radiation temperature decreases is apparent from the capsule in-flight aspect ratios. One interesting observation from Fig. 2-12 is that the convergence ratio increases as the capsule temperature increases, even though the initial radius scaled to the fuel mass decreases with temperature. This occurs because the fuel in the smaller,

Downloaded 20 Mar 2011 to 69.181.48.121. Redistribution subject to AIP license or copyright; see http://pop.aip.org/about/rights_and_permissions

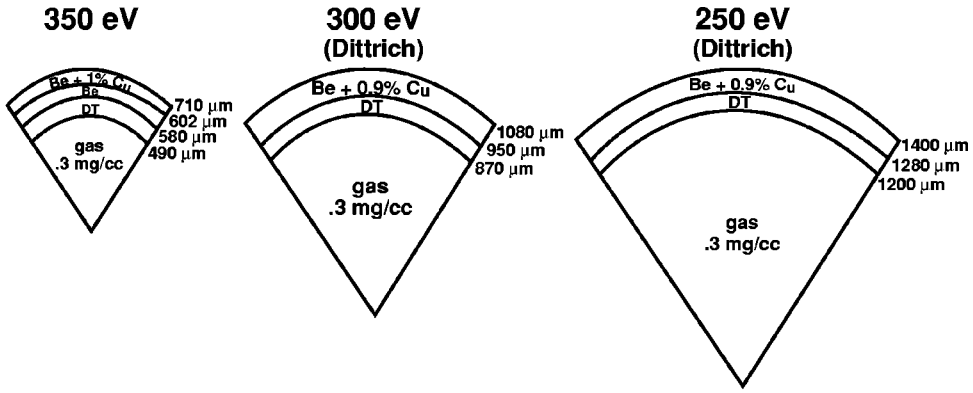

Estimated Peak Power	**450–600 TW**	**410 TW**	**300 TW**
Estimated laser energy	**1–1.4 MJ**	**1.3 MJ**	**1.3–1.6 MJ**
Abs. Cap. Energy	**75 kJ**	**173 kJ**	**192 kJ**
peak ρr (gm/cm^2)	**1.9**	**1.82**	**1.75**
v (fuel), 10^7 cm/s	**3.9**	**3.9**	**3.4**
Yield (MJ)	**5.8**	**17.1**	**22**
Convergence Ratio	**~43**	**~35**	**~33**
In-Flight Aspect Ratio	**~30**	**~46**	**~62**
Remaining kinetic energy	**41%**	**38%**	**2%**

FIG. 2-12. Capsules being designed for NIF span a range of temperatures from 250 eV to 350 eV.

higher temperature, higher-pressure capsule has a higher fuel density in the final compressed state.

To accommodate changes in the hohlraum–plasma physics, and the laser peak-power limits, the capsule at 350 eV had to be designed with a significantly smaller absorbed energy than the lower temperature capsules. The 250 eV capsule has more instability growth for a given implosion velocity. With a velocity of about 3.4×10^7 cm/s, it will have about the same growth during acceleration as the 300 eV capsule at a velocity of 3.9×10^7 cm/s. Capsules with an absorbed energy closer to 1 MJ that have this implosion velocity can be quite robust. However, at the NIF size this lower velocity 250 eV capsule has almost no remaining ignition margin, as indicated in Fig. 2-12, and is much more sensitive to mix. Figure 2-13 shows the sensitivity of the yield of these capsules to perturbations on the ablator or inner DT ice surface. In spite of its small size, the 350 eV capsule is the most robust. The thicker shell and higher ablation rates at this temperature more than compensate for the smaller size. The 250 eV design, by contrast, requires ex-

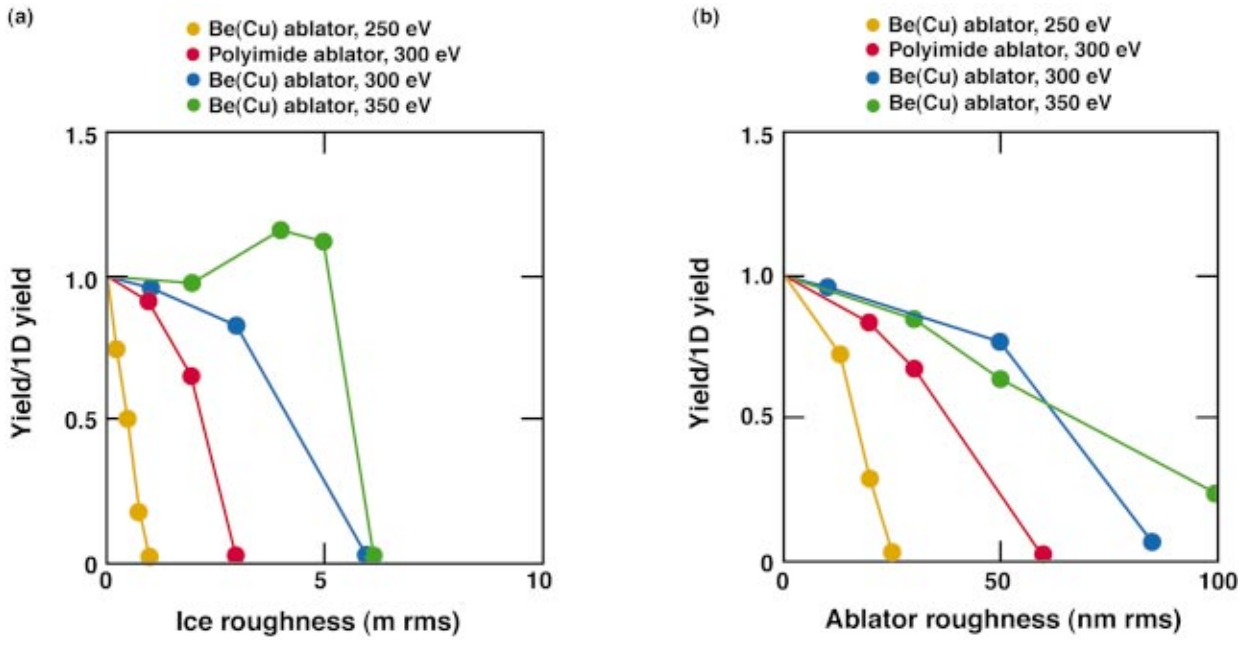

FIG. 2-13. (Color) For the current designs, tolerance to RT instability is a strong function of peak-drive temperature and capsule ablator material.

Downloaded 20 Mar 2011 to 69.181.48.121. Redistribution subject to AIP license or copyright; see http://pop.aip.org/about/rights_and_permissions

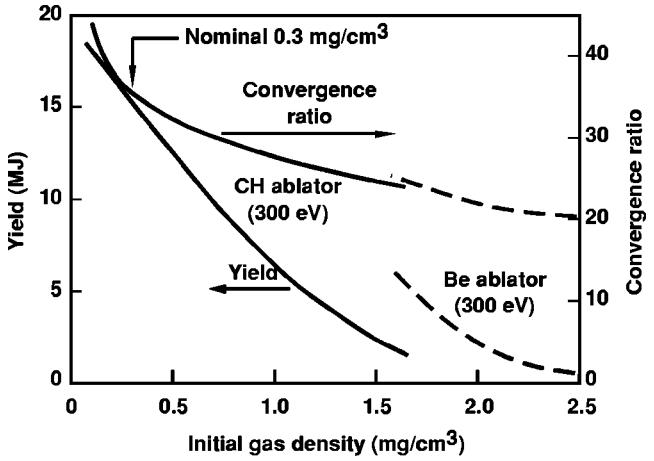

FIG. 2-14. Capsule gas fill provides direct control of convergence ratio. Increasing the initial gas fill reduces convergence ratio (and yield). However, ignition margin also decreases as gas fill increases. The higher-fill-pressure capsules are more sensitive to asymmetry and instability even though they have lower convergence.

tremely smooth surfaces. More optimization may be possible for the 250 eV design, but it is clearly more susceptible to instability growth than the higher temperature designs.

The initial gas-fill density in the capsule is determined by the temperature of the cryogenic fuel. Figure 2-14 shows the result of varying the initial fill on the convergence ratio and the 1D yield for the 300 eV baseline CH capsule. As shown, the convergence ratio can be decreased approximately from 35 to 25 before the yield drops below 1 MJ. This reduction in the convergence ratio would reduce the capsule sensitivity to flux asymmetry if the ignition margin could be maintained. However, the yield decreases as the initial gas fill is increased because the total fuel ρr decreases. This reduction in total ρr occurs because stagnation starts earlier in the implosion process when less compression of the main fuel has occurred due to convergence. More of the imploding kinetic energy ends up in thermal energy in a larger fraction of the fuel mass and less goes into compression. The reduced ρr results in a smaller ignition margin for a given fuel mass, implosion velocity, fuel adiabat, and implosion pressure. The reduced ρr of capsules with higher gas fill makes them more sensitive to growth of perturbations due to RT instability. Figure 2-15 shows the yield vs DT ice roughness and ablator roughness for gas fills of 0.3 and 0.6 mg/cm^3. These fills correspond to a DT layer temperature of about 1.5 and 0.5 K, respectively, below the DT triple point. The calculations are for a polyimide capsule driven at 300 eV. For a given level of roughness, the fractional reduction in yield is larger for the higher fill. However, in current experiments on β-layered DT, substantially better layers are produced at the higher temperature. The optimal choice for the DT gas fill will be determined by this tradeoff in fabrication quality and performance sensitivity.

C. NIF hohlraums

Currently, the best way to model radiation transport and coupling efficiency in ICF hohlraums is with detailed 2D calculations using a radiation-hydrodynamics code. The HYDRA code is able to do 3D hohlraum calculations but needs further development of some of the physics models. The calculations described here use LASNEX, with detailed radiation transport for the hohlraum/capsule coupling. The simulations track the laser beams, calculating inverse bremsstrahlung energy deposition and any refraction that occurs. The calculations typically use XSN non-local-thermodynamic-equlibrium (non-LTE) multigroup opacities (NTIS Document, 1977) although simulations with an opacity table derived from the STA opacity model are also done (Bar Shalom *et al.*, 1989). Any coupling to the capsule via hydrodynamic pressure or electron conduction is included.

The size of the hohlraum relative to the capsule is determined by a variety of trade-offs. The required profile of T_r vs time is determined by the capsule, and any hohlraum larger than some minimum size could provide the needed T_r vs time profile. A larger hohlraum takes more laser energy and power, and the optimal size is a trade-off of the energy and power requirements and the need for symmetry and acceptable plasma filling.

Even with perfect laser pointing and beam-to-beam power balance, there is some asymmetry. This asymmetry arises because of the LEH and the bright laser-irradiated spots (if uncorrected the LEH alone causes a 15% peak-to-valley P_2 asymmetry for a typical size LEH). The bright laser spots are placed to cancel the deficit in flux caused by the LEH. As discussed further in Sec. V, the symmetry can be adjusted by changing the hohlraum length and the point-

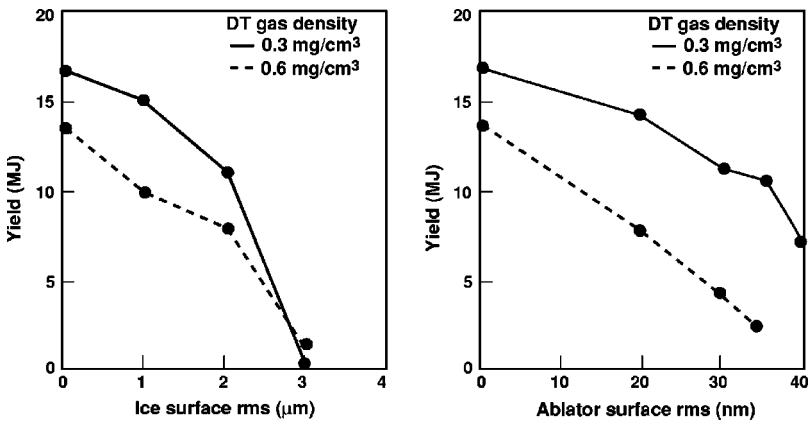

FIG. 2-15. The central gas density must be optimized in coordination with target fabrication. DT layer quality from β-decay is better at 0.5 K below the triple point than at 1.5 K below the triple point. However, the higher fill density of 0.6 mg/cm^{-3} near the triple point also increases sensitivity to ice roughness. Supplementing the β-decay heating with an external IR source results in improved layer smoothness at lower temperatures and lower gas vapor pressures.

Downloaded 20 Mar 2011 to 69.181.48.121. Redistribution subject to AIP license or copyright; see http://pop.aip.org/about/rights_and_permissions

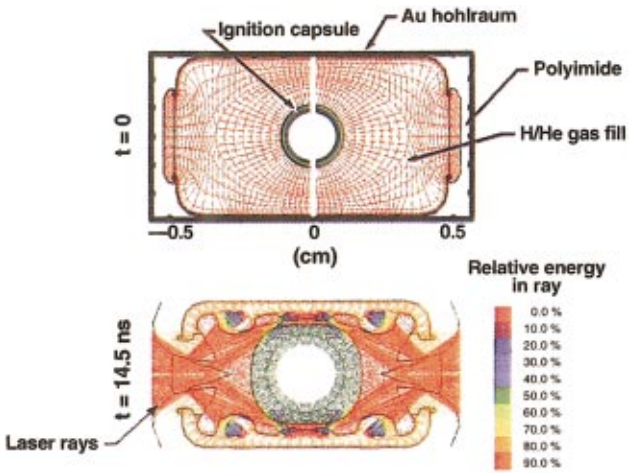

FIG. 2-16. (Color) 2D LASNEX calculations of NIF ignition targets are performed in order to accurately model the laser propagation and collisional absorption, the hohlraum, and the capsule. (a) The initial numerical grid from a typical calculation (Krauser *et al.*, 1996) of the PT ignition point design. (b) The numerical grid and material boundaries near the peak of the laser pulse. The numerical grid for the interior of the fusion capsule is not shown but is included in the calculation. The color tables for the laser rays indicate the remaining fraction of the incident laser energy. Most of the laser energy is transmitted through the H/He gas fill and is absorbed in the Au wall.

ing of the beams. A number of effects determine the intrinsic symmetry change in time: the LEH shrinks, the laser spots move due to plasma evolution, and the spots become less bright relative to the overall hohlraum brightness because of the changing albedo of the hohlraum wall (Wilson *et al.*, 1998; Haan *et al.*, 2000).

Shown in Fig. 2-16 is the numerical grid from a typical LASNEX calculation (Krauser *et al.*, 1996) of the baseline PT ignition target. The upper image is the initial grid. The lower image is near the peak of the laser power and shows the grid, the material boundaries, and the laser rays. The color table for the lower image indicates the fractional absorption of the laser rays along their propagation path. This shows that the laser rays propagate through the H/He gas fill and are absorbed predominantly in Au near the hohlraum wall. The interior grid of the capsule is removed from the lower image but is included in the calculation.

Adequate symmetry and near 1D burn performance have been achieved in such integrated simulations for a variety of designs at several sizes, with temperatures ranging from 250 to 350 eV. Figure 2-11 shows the 1D and 2D yield and burn temperature for the PT target and targets scaled from this design.

Figure 2-17 shows sketches for hohlraums at 250 eV and 350 eV in comparison with the hohlraum for the PT capsule. These hohlraums drive the 300 and 350 eV capsules shown in Fig. 2-12. The capsule used in the 250 eV hohlraum was an earlier design with an initial outer radius $r = 0.123$ cm. Below about 300 eV, it is relatively easy to adjust hohlraums for various radiation temperatures. The hohlraums for 250 and 300 eV are essentially geometric scales of each other with the same ratio of hohlraum-to-capsule size and the same LEH-to-hohlraum diameter. Since the coupling efficiency for

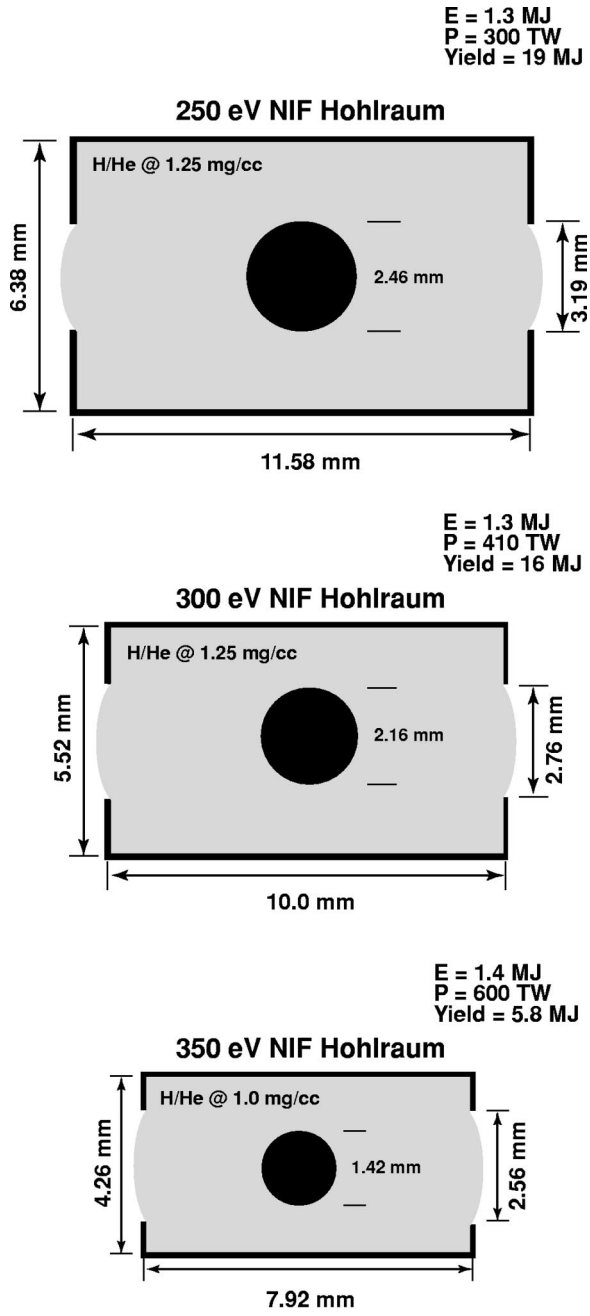

FIG. 2-17. Hohlraum designs have been developed for drive temperatures ranging from 250 eV to 350 eV. LASNEX 2D calculations have adequate symmetry for all three designs shown.

ignition designs is primarily a function of these two geometric ratios, and only a weak function of drive temperature (Lindl, 1998c), these designs have very similar coupling efficiency. If nonlinear plasma physics effects can be ignored, the symmetry is also largely determined by geometric effects so the beam geometry also scales. However, for the 350 eV capsule, significant changes to the hohlraum were required, even without accounting for possibly worse levels of parametric instabilities or filamentation. In order to keep the Au plasma sufficiently far from the capsule blowoff to allow symmetry control, it is necessary to increase the hohlraum size relative to the capsule. At 350 eV, as shown in Fig. 2-17, this ratio is a minimum of 3.0 at the hohlraum waist, com-

Downloaded 20 Mar 2011 to 69.181.48.121. Redistribution subject to AIP license or copyright; see http://pop.aip.org/about/rights_and_permissions

pared to 2.5 for the 300- and 250-eV designs. The gas fill in the hohlraum also must be carefully optimized. With too little gas fill, the Au wall moves too far and symmetry is degraded. With too much fill, the pressure in the gas becomes large enough to cause a pressure spike near the hohlraum axis, which degrades symmetry. The optimum for the target shown appears to be about from 1.1 to 1.2 mg/cm^3 of He, just a little higher than the baseline of 1.0 mg/cc. The 350 eV hohlraum also has relatively larger LEHs, 60% of the hohlraum diameter rather than 50% in the lower temperature designs. This requirement arises because there is relatively more radiation-driven blowoff from the lip of the LEH at 350 eV, and because the NIF beams are constrained to a minimum focal size of about 600 μm. The larger LEH increases the radiative loss by almost 50% relative to a design with the smaller hole.

The 350 eV target, by intent, stresses the laser–plasma instabilities. The hohlraum interior electron density is from 10% to 15% of critical density for most of the laser path. The laser intensity is about 50% higher than for the 300 eV hohlraum. The relatively larger spot size and LEH in this hohlraum, required because of NIFs focusing limitations, keeps the intensity from being as high as it would be for a direct geometric scale but this does result in a hohlraum efficiency penalty.

We have imposed a wide variety of asymmetries on 2D capsule implosions to ensure that the specified asymmetry levels are acceptable. Asymmetry can affect ignition in a variety of ways: the obvious kinematic effects of differing velocities; initiation of RT instability growth, especially evident during deceleration; mass flow toward less driven regions, seeding RT instability; irregular hot-spot compression, sometimes forming jets that protrude from the core and disrupt the imploded configuration; and delayed ignition, resulting in more RT growth. Capsules with a time-varying asymmetry cannot be corrected simultaneously in velocity and position without introducing initial spatial variations in composition or thickness. Azimuthal variations in radial velocity introduce azimuthal pressure variations, which generate azimuthal mass flow. For small-amplitude or short-duration intensity variations, these effects are largely reversible if the sign of the flux variations is reversed to give a uniform time-averaged flux. However, after an azimuthal flux variation that persists for a substantial fraction of the pulse, subsequent reversal of the flux nonuniformity will not adequately remove the effects of the earlier asymmetry. If the effect of the asymmetry is tuned so that the capsule is spherical at ignition, then velocity and density generally will vary from pole to waist. If the capsule is tuned to minimize velocity and density variations at ignition, then the implosion will be asymmetric. Excessive time-dependent asymmetry can cause jetting of material in the azimuthal direction. The maximum tolerable asymmetry depends on its temporal and spatial specifics. In summary, the capsule can tolerate less than about 1% time-averaged asymmetry, from 5% to 10% time-dependent swings in asymmetry that last for about 2 ns, and larger swings if they last much less than 2 ns.

The maximum tolerable asymmetry depends on temporal and spatial specifics. In detailed simulations, a P_2 asymmetry that varies between $+4\%$ (constant until numerically switched) and -4% (for the remainder of the pulse) produces a marginally acceptable implosion. (In this, and in all of the following, the P_2 coefficient is quoted so that the peak-to-valley asymmetry in flux is $1.5\times$ the number quoted.) If the switching time is chosen so that the average asymmetry is zero, the imploded configuration is, on average, round but shows a jet. With a swing from $+2$ to -2%, the asymmetry is small. In this case, the peak pressure generated in the fuel (when no thermonuclear burn is allowed) is reduced by about 12% compared to a perfectly spherical implosion. The yield (in a burn-on simulation) is not reduced by the asymmetry.

In this simulated implosion with a $\pm 2\%$ time-dependent asymmetry, the shell is as much as 10 μm out-of-round while at radii between 500 and 100 μm. It is as much as 10% out-of-round ($\Delta R = 10$ μm for $R = 100$ μm) toward the end of the implosion. This degree of asymmetry in the implosion could be measured with a backlighted imaging diagnostic similar to those that have been used on Nova as discussed in Sec. V.

The jetting asymmetry effect is maximized (at a given percent of peak flux asymmetry) by having the asymmetry be constant for the first part of the pulse and then switching to another constant value, with the opposite sign, for the remainder of the pulse. For that kind of time dependence, the baseline NIF capsule can tolerate 4% P_2 asymmetry as described above. Typical detailed 2D calculations have a more gradual variation in asymmetry with a lower average perturbation for a given peak.

If the period of the symmetry swings is shorter, such as would be the case in an experimental program that was designed to obtain a uniform average flux over some fraction of the implosion, still larger symmetry swings are tolerable. For example, with a P_2 of form

$$A_2(t) = A_0(t)\varepsilon_{20}\sin[\omega(t-t_0)], \tag{2-4}$$

where $A_0(t)$ is the total flux, $\omega = \tau$ (a 2 ns period), implosion symmetry is tolerable with ε_{20} larger than 10%. The time t_0, which is present to set the phase of the time dependence, also affects the average A_2 because of the $A_0(t)$ time dependence. The choice of t_0 must be such that the average asymmetry is about 1% or less. This is the only significant effect we see if we change the phase t_0. If the sinusoidally time-dependent asymmetry is too large, the failure mechanism for this short-duration asymmetry is a jet coming from the center of the implosion outward, as a result of irregular shock convergence in the center, rather than the azimuthal mass variation seen for the longer duration asymmetry described above.

The maximum tolerable asymmetry levels for the 300 eV peak-temperature ignition-hohlraum drives are approximately (Jones, 1998; Pollaine *et al.*, 2001) 1% for the time-integrated P_2, $10/\tau$(ns)% for the time-dependent P_2 averaged over any time interval τ, from 0.25% to 0.5% for the time-integrated P_4, P_6, and P_8. Averaging over just the 10 ns foot of the NIF pulse, the tolerable asymmetry levels are from 1% to 2% for modes P_2 through P_6 and from 0.5% to 1.0% for mode P_8. The range in requirements reflects the fact that ignition also depends on reducing imbalances and

Downloaded 20 Mar 2011 to 69.181.48.121. Redistribution subject to AIP license or copyright; see http://pop.aip.org/about/rights_and_permissions

TABLE II−2. Several parameters are available to control symmetry with two cones of beams.

		P_2 (%)[a]	P_4 (%)[a]
Power balance inner vs outer			
Change inner/outer power by 5%	Foot	1.7	−0.4
	Peak	1.0	−0.1
Hohlraum aspect ratio (fixed hohlraum area and LEH, beams central in LEH)			
Make hohlraum 100 μm longer	Foot	1.8	1.6
	Peak	1.6	0.7
Make hohlraum 100 μm longer, use power to correct P_2 change	Foot		2.0
	Peak		0.8
Outer beam pointing			
Move spots 100 μm out	Foot	1.2	1.2
	Peak	1.2	0.5
Inner beam pointing			
Move spots 100 μm out	Foot	1.4	−1.2
	Peak	0.9	−0.5

[a]Estimates made using the Walle 3D view factor radiation transport code.

inefficiencies on other laser and target parameters; hence, tolerances on asymmetries are partially dependent on tolerances on other specifications.

Since LEH effects and laser-spot motion from refraction, wall blowoff, and LPI are the primary causes of time-dependent asymmetry, the issue for the NIF is whether uncertainty in these variations could lead to a failed implosion. Experimental measurements of the wall loss and laser-spot position on Nova establish the time-dependent asymmetry to a few percent. Similar experiments can be done on the NIF. Further, as discussed in Sec. V, several techniques were developed on Nova that would apply to the NIF for directly measuring the time-dependent asymmetry on the capsule.

We find little variation in sensitivity to asymmetry among the various targets. Smaller capsules are slightly more sensitive to asymmetries that couple to deceleration RT growth. The difference is not large, and symmetry sensitivity is not an issue that is important in deciding the overall tradeoffs of laser size and power. Varying the hohlraum size, with a given capsule, is the symmetry issue likely to be more important in the tradeoffs.

Both view factor and 2D detailed, integrated calculations have been carried out to evaluate the sensitivity of symmetry to changes in hohlraum geometry and beam cone positions. Table II-2 gives the results for the view factor calculations, which are generally consistent with analytical analysis such as Eq. (5-14) in Sec. V.

Figure 2-18 shows an example of the 2D sensitivity determined from the integrated calculations, in this case for a Be-ablator target driven with a step laser power profile. The target can tolerate beam movement of the average ring location of ± 200 μm, well outside the expected deviation, given the pointing specification on the laser.

To estimate the sensitivity of NIF ignition targets to random pointing and power imbalance between the beams, and to set the specifications on components and NIF subsystems, a model of the performance of NIF beamlines was developed (NTIS Document, 1998). This model incorporates both systematic variations from beamline to beamline and random variations. The systematic variations arise from component differences in the beamlines, such as transmission of optics and frequency-conversion crystal thickness, which are repeatable from shot to shot. The random variations arise from such things as amplifier gain, which can vary from shot to shot. The NIF is configured to have 48 quads. The four beamlets in each quad are all driven with a single preamplifier module. Because of this the power in each beamlet is not completely independent of the other beamlets in a quad. Each of the beamlets in a quad is independently pointed, but the spots from each beamlet in a quad partially overlap on the hohlraum wall. Figure 2-19 shows the power imbalance calculated by the model. Power imbalance is reduced late in the pulse because of saturation effects in the 1ω output and reduced sensitivity to 1ω power imbalance in the frequency conversion crystals near peak power.

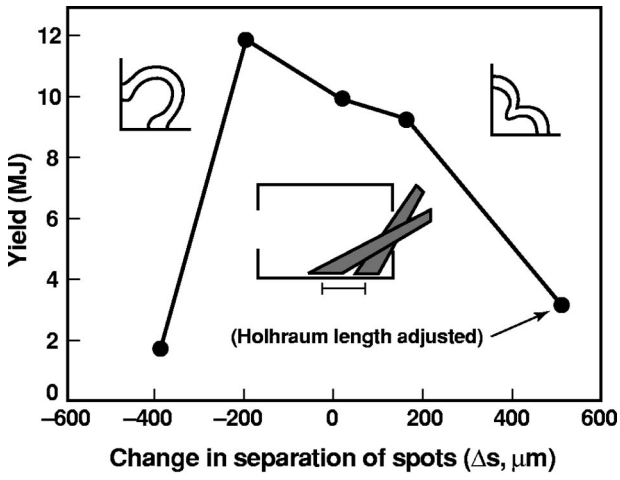

FIG. 2-18. Integrated calculations are being used to confirm acceptable sensitivity to pointing. Laser ring separation controls P_4. The pointing sensitivity is large enough that we can use it to control P_4, but small enough for the specified pointing accuracy.

Downloaded 20 Mar 2011 to 69.181.48.121. Redistribution subject to AIP license or copyright; see http://pop.aip.org/about/rights_and_permissions

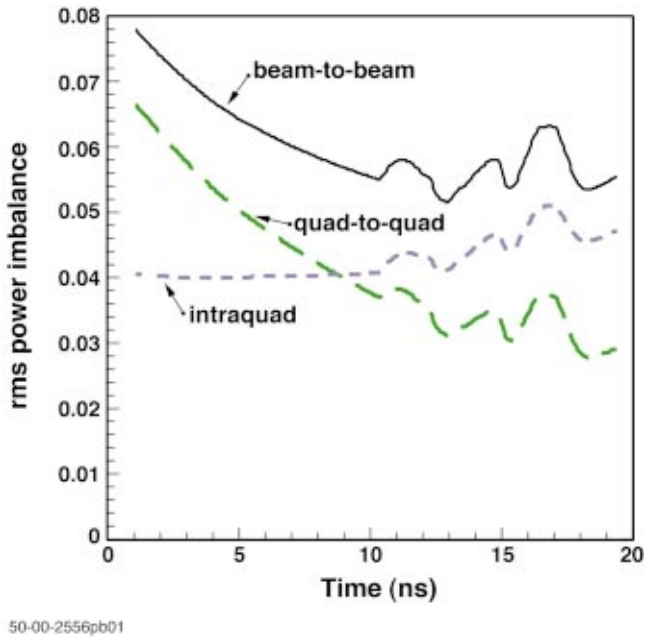

FIG. 2-19. (Color) The calculated total rms power imbalance vs time on NIF for a 1.8 MJ scale of the PT pulse meets the power balance functional requirements specified in Table II-1.

Given the power imbalance in Fig. 2-19, the 3D viewfactor code Gertie (Kirkpatrick and Wingate, 1980; Bailey, 1981; Munro and Zimmerman, 1993) is used to estimate flux asymmetry on the capsule. Figure 2-20(a) shows the sensitivity of total rms capsule flux to the amount of quad-to-quad power imbalance using the viewfactors midway through the foot and peak of the pulse. Because the capsule is larger and the hohlraum albedos are lower during the foot, there is a larger flux asymmetry on the capsule for a given power imbalance during the foot than during the peak. The average quad-power imbalance during the foot of the pulse is approximately 4% and about 3% during the peak. Thus the resulting power imbalance at the capsule will be about 0.6% during the foot and 0.2% during the peak. Figure 2-20(b) gives the fractional contribution of each Legendre mode to total variance of the capsule flux due to power imbalance. This shows that the effect of power imbalance is predominantly in very low-order modes.

The other contributor to random flux asymmetry is pointing errors. Figure 2-21(a) shows the rms flux asymmetry on the capsule as a function of rms quad pointing error. The NIF specification for allowable beam-to-beam pointing errors is 50 μm. If we assume that the pointing errors are uncorrelated, then a 50 μm, beam-to-beam error corresponds to a 25 μm quad-to-quad error. The corresponding capsule flux asymmetry is about 0.4% during the foot and less than 0.2% during the peak. It is likely that there will be some sources of pointing error that are common to beams within a quad. However, the breakdown has not been determined at this time. Figure 2-21(b) shows fractional contribution by Legendre mode.

Asymmetries might also arise from LPI processes, which are currently predicted not to be significant, but for which uncertainty remains. Light can be scattered, or it can be absorbed, with different efficiencies at different positions in the hohlraum. The effect in all cases is equivalent to a power-balance change, a movement of the x-ray emission spots, or perhaps a spreading of the laser-deposition spots (for small-angle side-scattering). Difficulties arise only if these effects

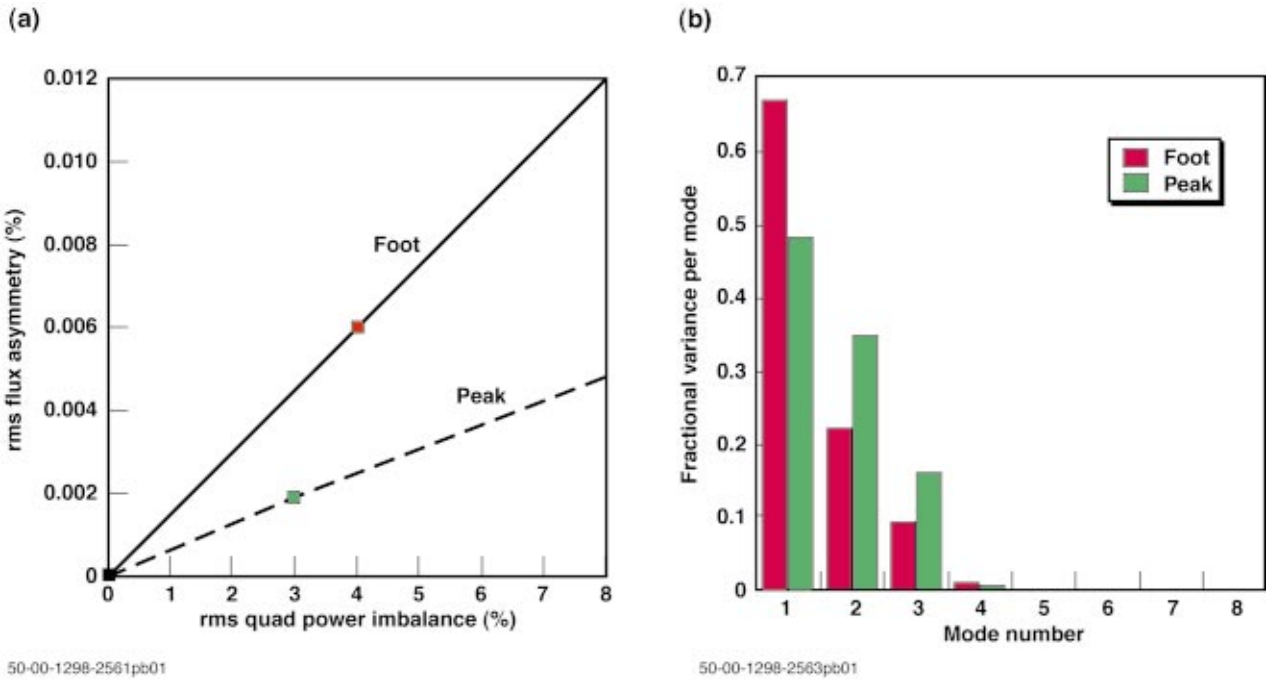

FIG. 2-20. (Color) (a) The rms capsule-flux asymmetry as a function of amount of quad-to-quad power imbalance. The red and green squares indicate the rms quad power imbalance estimated for NIF from Fig. 2-19. (b) Fractional contribution of each Legendre mode to total variance of the capsule flux due to power imbalance.

Downloaded 20 Mar 2011 to 69.181.48.121. Redistribution subject to AIP license or copyright; see http://pop.aip.org/about/rights_and_permissions

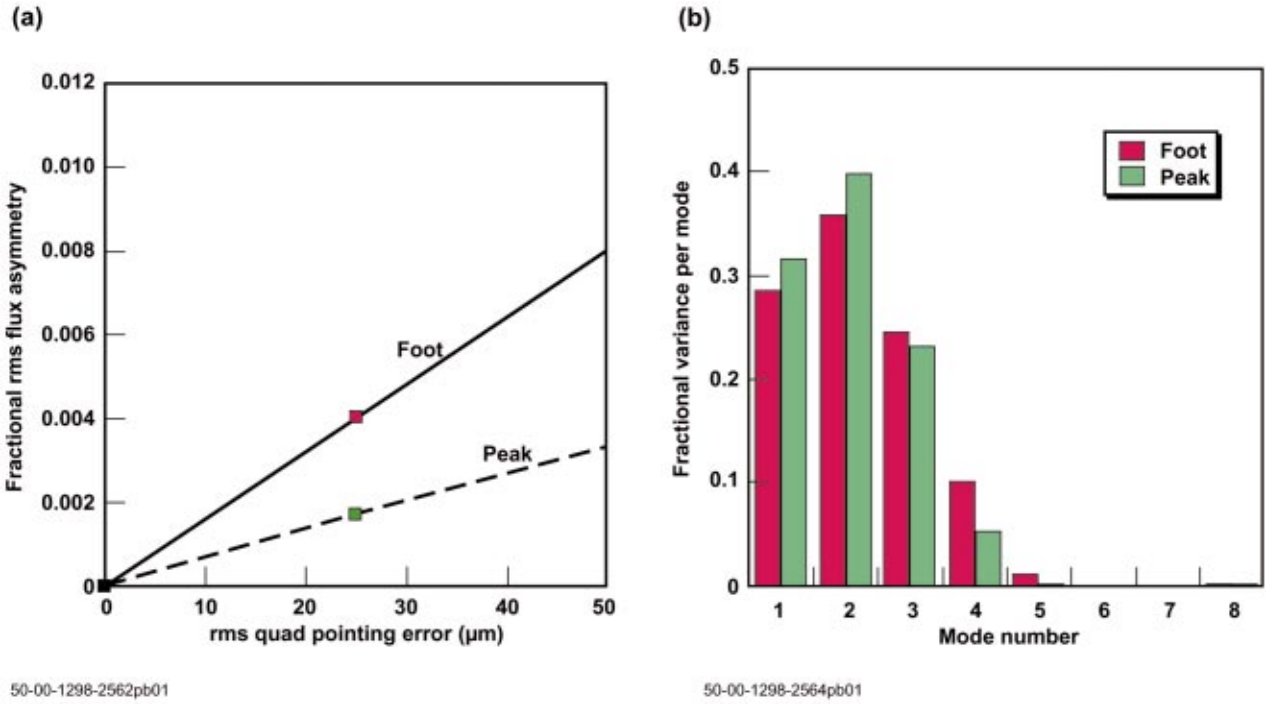

FIG. 2-21. (Color) (a) The rms capsule-flux asymmetry as a function of quad-to-quad pointing errors. The red and green squares indicate the estimated quad-to-quad pointing error for NIF. (b) Fractional contribution of each Legendre mode to total variance of the capsule flux due to beam pointing errors.

are sufficiently large that their irreproducible part is larger than the limits described above. If any of these processes occur but are reproducible and not too large, the effect can be mitigated by changing the hohlraum design parameters. Based on Nova experiments and modeling, we expect that these processes can be kept within acceptable limits for 300 eV hohlraums. If we cannot do this for the 300 eV PT target, we can increase the hohlraum size, reduce the laser intensity, and correspondingly reduce the hohlraum drive temperature to the 250 eV design, which has significantly less plasma.

D. Hohlraums and capsules for enhanced performance from NIF

The NIF hohlraums described above used the concepts most thoroughly tested on Nova and used relatively conservative assumptions for hohlraum materials, LEH sizes, and hohlraum geometry. Advances in target physics understanding makes it feasible to develop hohlraum designs with improved coupling efficiency (Suter *et al.*, 2000).

As described above, the baseline NIF targets require about 1.3 MJ of laser light absorbed into the hohlraum. This allows a margin of about 33% in energy to accommodate losses due to LPI and hohlraum coupling uncertainties. Nova experiments on surrogate plasmas discussed in Sec. III indicate that, with adequate beam smoothing, it may be possible to keep LPI losses to $\leqslant 5\%-10\%$. Figure 2-22 shows the distribution of energy for a NIF ignition target. Including 0.45 MJ for contingency, the overall coupling efficiency from the 1.8 MJ output to the 0.15 MJ capsule is 8.3%. It is likely that the hohlraum efficiency can be significantly increased as discussed below.

The baseline hohlraum designs use Au for the hohlraum wall material in order to relate to the predominant Nova database. Modeling and experiments, discussed in Sec. IV, indicate that the hohlraum wall losses can be decreased substantially by using mixtures of materials. Losses into the hohlraum wall are dominated by photon energies at which the opacity is relatively low. By using materials for which

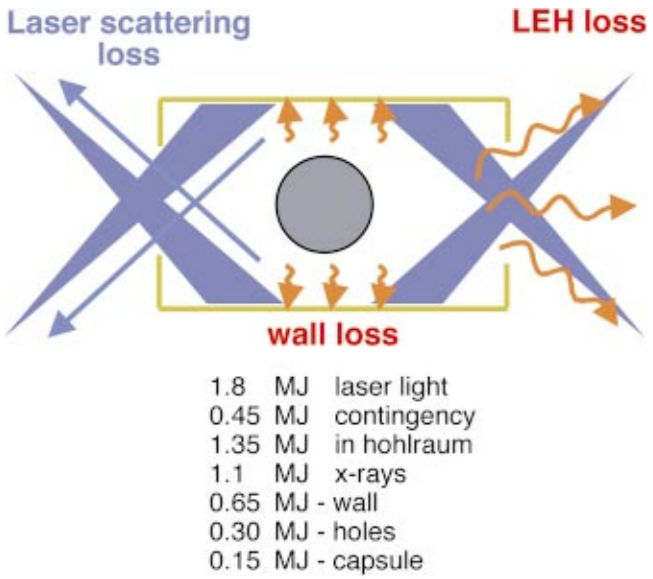

FIG. 2-22. (Color) The NIF ''point design'' achieves a calculated coupling efficiency to the fuel capsule of 8.3% relative to 1.8 MJ of laser output or 11% relative to a calculated 1.3 MJ of absorbed energy. Recent advances in target physics project coupling efficiencies of 20% to 30%. These calculations rely on material mixtures to reduce hohlraum-wall losses and improved understanding of hohlraum symmetry to reduce case-to-capsule area ratios and LEH areas.

Downloaded 20 Mar 2011 to 69.181.48.121. Redistribution subject to AIP license or copyright; see http://pop.aip.org/about/rights_and_permissions

the high opacity photon energies of one material overlap the low opacity photon energies of another material, calculations indicate that wall losses can be reduced by as much as one-third. Because the dominant sink of energy is the hohlraum wall, reducing the loss has large leverage on the overall efficiency.

For the same reason, decreasing the hohlraum size relative to the capsule size can have large leverage. The NIF baseline hohlraum size was chosen in order to maximize confidence in the capsule-flux symmetry. Recent calculations indicate that it may be possible under some circumstances to reduce the hohlraum area by 20% or more and maintain adequate symmetry. The higher albedos of the hohlraum wall obtained with mixtures can also help reduce the source level for asymmetry, allowing a concomitant decrease in case-to-capsule ratio. The laser LEHs were made larger than necessary for many of the hohlraum designs, to insure beam clearance. Calculations indicate that the LEH losses can be reduced by as much as 40% in some designs.

These improvements in hohlraum-coupling efficiency are more accessible for targets with lower peak-drive temperature. At the highest drive temperatures considered likely on NIF, about 350 eV, the only likely improvement is the use of mixtures for the wall material. There appears to be little room to decrease the LEH size or the case-to-capsule ratio at the higher temperatures. At the other extreme, these possible improvements may make it possible to implode significantly larger capsules at 250 eV. Then, an additional advantage also appears possible: the lower hohlraum temperatures and larger capsules require lower power and longer pulse output from the laser. This results in additional energy being possibly available from the laser. As indicated in Fig. 2-23, longer pulses may result in more output energy from NIF and also result in improved coupling efficiency. For the point-design capsule operating at 300 eV, the NIF laser is being designed to deliver 1.8 MJ and 500 TW in an effective high-power pulse length of 3.6 ns. For a 7.5 ns equivalent high-power pulse suitable for a capsule operating at 250 eV and absorbing 600 kJ, the NIF is capable of an output energy from 2.1 to 2.5 MJ. The larger output utilizes two additional laser slabs in the NIF output amplifiers. The two columns in the table refer to the number of laser slabs in the main amplifier, 11 in both cases, and the booster amplifier, either five or seven. NIF is being designed so that the additional slabs can be added. The shorter, higher power pulse of the nominal hohlraum target does not benefit from the added slabs because the output is more limited by the output damage fluence than by the stored energy available. The ability to utilize this increased energy will depend on advances in 3ω optical damage, a topic of current research. Also for the larger longer-pulse hohlraums, the hohlraum wall loss is further reduced because of an increase in albedo as indicated in the sketch in Fig. 2-23. Because the ratio of the capsule energy to wall loss scales approximately as $T^{0.7}\tau^{0.38}$, as discussed in Sec. IV, the coupling efficiency is improved by about 15% for the higher energy, lower temperature design.

These ideas have been applied to the 600 kJ capsule shown in Fig. 2-24, which is capable of yields of 70 to 150 MJ depending on pulse shape. Figure 2-25 shows the x-ray

	11/5* Performance	11/17* Performance
NIF Point design (300 eV, 3.5 ns)	1.8 MJ 500 TW	1.8 MJ 500 TW
Longer pulse design region (250 eV, 7.5 ns)	2.1 MJ 260 TW	2.5 MJ 330 TW

*11/5 and 11/7 refer to the number of laser slabs in the NIF main amplifier and booster amplifier. The NIF design can accommodate either.

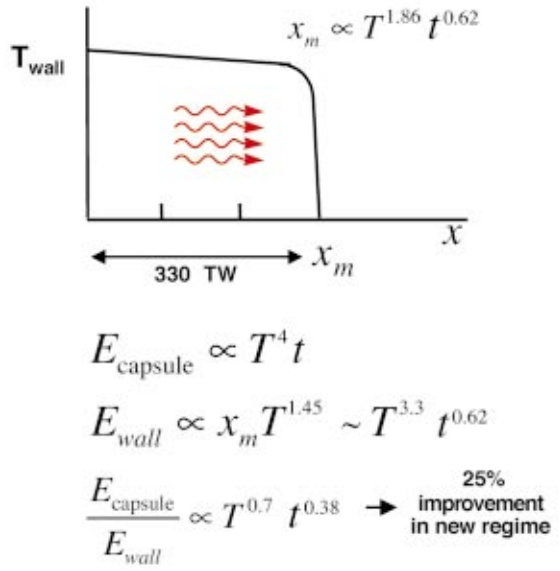

FIG. 2-23. (Color) At longer pulses, NIF is capable of delivering more laser energy and the longer pulses result in improved capsule coupling efficiency because of higher hohlraum wall albedo.

energy required to drive this capsule. Figure 2-25(a) shows that it would be impossible to drive this capsule in NIF with a standard hohlraum: this calculation uses a pure Au hohlraum, a standard LEH, and a standard ratio of the hohlraum size to capsule size. This target would require 3.3 MJ of x rays and from 3.8 to 4.0 MJ of laser light, well beyond NIFs capabilities. Figure 2-25(b) shows that this is reduced to 2.3 MJ by using an optimal mixture of materials for the wall and allowing the LEH to close during the pulse. If the hohlraum dimensions and LEH diameter are reduced by 10%, the total x-ray energy is further reduced to 2.0 MJ as indicated in Fig. 2-25(c). The absorbed laser light required is from 2.3 to 2.4 MJ and this is within NIFs capabilities if the laser scattering losses are limited from 5% to 10%. Although the symmetry has not yet been optimized and is worse than for the NIF baseline target, integrated calculations of the hohlraum and capsule have achieved near 1D yields with all the changes indicated in Fig. 2-25(c). Although significantly more work is required both in target design and in experiments, these energetic improvements would move us far above the ignition threshold on NIF for both 250 eV and 300 eV capsules as indicated in Fig. 2-26. The gains of 30 to 60 for the 250 eV capsule are approaching those required for inertial fusion energy (IFE) applications.

Downloaded 20 Mar 2011 to 69.181.48.121. Redistribution subject to AIP license or copyright; see http://pop.aip.org/about/rights_and_permissions

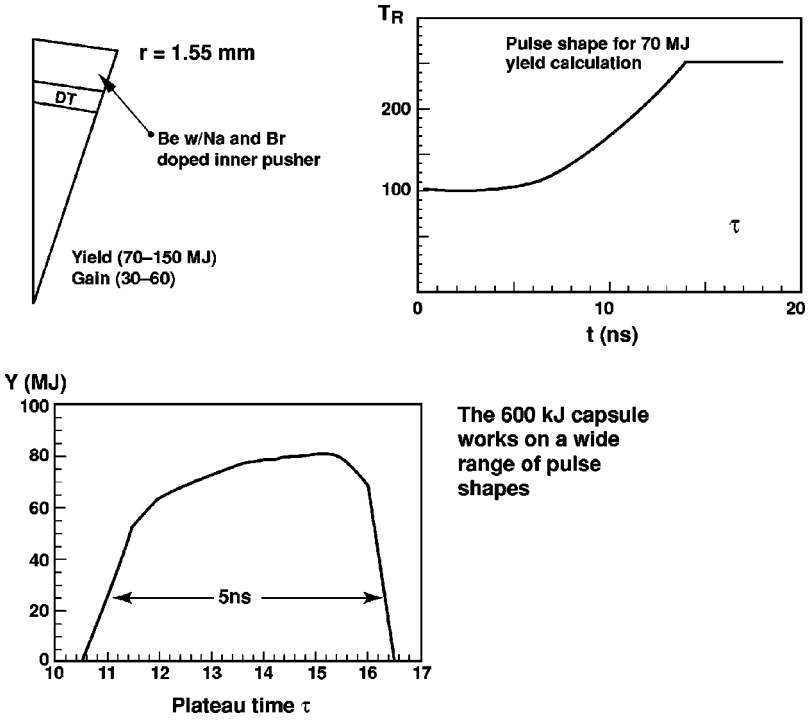

FIG. 2-24. With improved hohlraum coupling efficiency, it may be possible to drive a 250 eV Be design with ~100 MJ yield on NIF.

III. LASER–PLASMA INTERACTIONS IN NIF-SCALE PLASMAS

A. Introduction to laser–plasma interactions in NIF-scale plasmas

The success of an indirect-drive ICF ignition experiment depends on the ability to predict and control the temporal and spatial absorption of the laser light by the high-Z plasma at the hohlraum wall. The hohlraum size and long time scale ($\sim 10-20$ ns) required for ignition targets result in the presence of several millimeters of plasma (electron density $n_e \approx 0.1 n_c \approx 10^{21}\ \mathrm{cm}^{-3}$ where the critical density $n_c = 10^{21}\lambda^{-2}\ \mathrm{cm}^{-3}$ with λ the laser wavelength in microns), through which the 3ω ($\lambda_0 = 351$ nm) laser beams must propagate before they are absorbed at the hohlraum wall. The light absorption rate, $v_{\mathrm{abs}} = n_e v_{ei}/2n_c$ where the electron–ion collision frequency, $v_{ei} = (4\sqrt{2\pi}/3\sqrt{m_e T_e^3})\Sigma_j n_j Z_j^2 e^4 \ln(\Lambda)$, depends on the electron density, n_e, the electron temperature, T_e, and the charge state Z_j and density n_j of each ion species. Here, m_e is the electron mass, e is the electron charge, n_c is the critical density, and $\ln(\Lambda)$ is the Coulomb

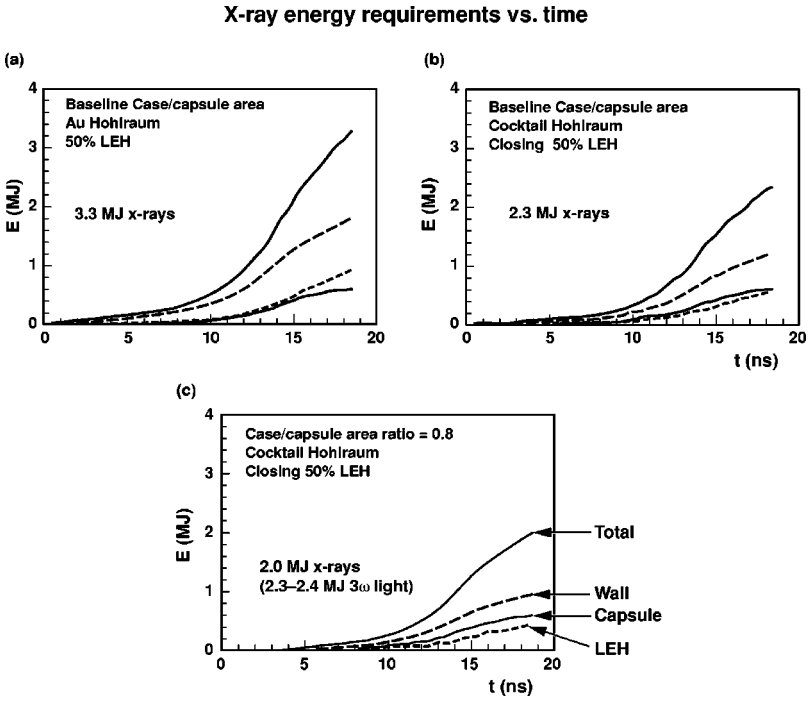

FIG. 2-25. Use of cocktails, LEH reduction, and smaller case-to-capsule area ratio leads to reduced radiation requirements, which might make a 600 kJ absorbed-energy capsule feasible on NIF.

Downloaded 20 Mar 2011 to 69.181.48.121. Redistribution subject to AIP license or copyright; see http://pop.aip.org/about/rights_and_permissions

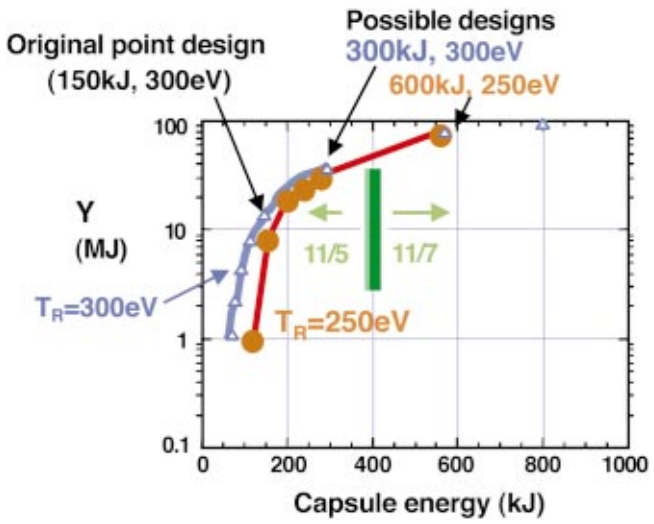

FIG. 2-26. (Color) Improvements in target physics and 11/7 amplifiers will move us far above the ignition threshold on NIF. (11/7 refers to 11 laser slabs in the main amplifier and 7 slabs in the booster amplifier. An 11/5 configuration has 5 slabs in the booster.)

logarithm. The laser light is strongly absorbed in the high-Z plasma near the wall but weakly absorbed in the low-Z gas fill.

The propagation of the beams to the hohlraum wall can be affected by various laser scattering and self-focusing (filamentation) processes within the low-density plasma inside the hohlraum. For example, while traversing such a plasma, the incoming light wave can resonantly decay into a backscattered light wave and an internal mode of the plasma, either an ion sound wave or an electron plasma wave. The backscattered light wave can beat with the incident light wave at a frequency that pumps the internal mode; this process can increase the amplitude of the plasma wave, increasing its scattering efficiency. Hence an unstable feedback loop is formed that can cause the amplitudes of the internal mode and scattered light waves to grow exponentially on time scales of 0.1 to 10 ps. For scattering from ion sound waves, these parametric scattering instabilities are stimulated Brillouin scattering (SBS); for scattering from electron plasma waves, they are stimulated Raman scattering (SRS) (Rosenbluth and Sagdeev, 1991). Both of these instabilities can lead to undesirable effects, including significant amounts of light reflecting from the plasma or shining directly onto the capsule, spoiling the illumination symmetry. Also, the damping of high-phase-velocity plasma waves can produce energetic electrons capable of preheating the fusion fuel and reducing its compressibility (Lindl, 1998g).

Another instability, filamentation or self-focusing (Cohen *et al.*, 1991), that can affect laser beam propagation, occurs when individual speckles (''hot spots'') within the beam self-induce refractive index changes. The ponderomotive pressure of the laser depresses the plasma density approximately in proportion to the local laser intensity. Additionally, the creation of these density channels by the laser is reinforced by localized laser deposition, which creates electron temperature and thermal pressure perturbations in phase with ponderomotive pressure. Since the light waves are refracted towards the lowered density, the laser propagation is modified by the self-consistent density response to the laser's intensity profile. With sufficient power, the entire beam can self-focus (Max, 1976; Anderson and Bonnedal, 1979; Coggeshall *et al.*, 1988), or perturbations to the beam intensity can grow exponentially giving rise to filamentation and beam breakup. The concentration of the laser power by refraction into the lowered density is opposed by diffraction. The related process of beam deflection is influenced by filamentation in flowing plasma.

In many laser-produced plasmas, SBS and SRS are limited by plasma inhomogeneity (Kruer, 1988). However, hydrodynamic simulations show the NIF ignition hohlraum plasma to be very uniform [density-gradient scale length $L_n = n_e(dn_e/dx)^{-1} \approx 2$ mm where n_e is the electron density] and to exhibit low velocity gradients [velocity-gradient scale length $L_v = C_s(dv/dx)^{-1} > 6$ mm where C_s is the sound speed and v is the flow velocity] (Kruer, 1991). Thus, in the plasmas expected in the NIF hohlraums, either wave damping, pump depletion, or nonlinear saturation mechanisms would be the primary limitations on instability growth. Some of the 351 nm Nova interaction experiments in homogeneous low-density plasmas have shown as much as 35% of the incident laser energy backscattered as SBS; in other experiments, SRS-reflected energy fractions as high as 25% have been observed. Although these extreme cases represent scattering from plasmas that have less linear damping of instabilities than is expected in the NIF plasma, they illustrate the potential of parametric instabilities to cause problems. This amount of backscattering would obviously reduce coupling to the hohlraum wall, reducing the x-ray drive and increasing the laser energy required to drive a target to ignition. In addition, in a number of experiments on the Nova laser facility, the backscatter at relatively low laser intensity, although not energetically significant ($<1\%$) and lower than at higher laser intensities for similar conditions, was much larger than expected from linear instability theory. SRS could cause additional problems, because the process not only transfers energy into backscattered light and electron plasma waves but also produces suprathermal electrons with tens of keV energy (Glenzer *et al.*, 1998). Significant energy scattering due to instabilities such as SBS and SRS, if it varied randomly from beam to beam, would also make it more difficult to meet the NIF power-balance specification of $<8\%$ rms variation in power between beams, which is needed to meet the symmetry requirements for a high-convergence implosion (Lindl, 1995; Haan *et al.*, 1995; Lindl, 1998).

B. Theory and code development for NIF plasmas

1. Linear theory

The resonant three-wave instabilities, SBS and SRS, require phase matching in time and space, which imposes frequency and wave-number matching conditions. In turn, these conditions make the instabilities sensitive to spatial inhomogeneity and temporal incoherence.

The wave-number-matching condition for SBS requires that

Downloaded 20 Mar 2011 to 69.181.48.121. Redistribution subject to AIP license or copyright; see http://pop.aip.org/about/rights_and_permissions

$$\mathbf{k}_0 = \mathbf{k}_s + \mathbf{k}_{ia}, \tag{3-1}$$

where $\mathbf{k}_0$ and $\mathbf{k}_s$ are the incident and scattered light wave vectors, respectively, in the plasma. The wave number of the ion–acoustic wave $\mathbf{k}_{ia}$ has a magnitude equal to $2k_0$ for direct backscattering (since $\mathbf{k}_s \approx -\mathbf{k}_0$), where k_0 is related to the vacuum wave number $k_{\mathrm{vac}} = \omega_0/c = 2\pi/\lambda_0$ of the incident laser light by

$$k_0 = k_{\mathrm{vac}}(1 - n_e/n_c)^{1/2}, \tag{3-2}$$

where n_e is the local electron density, n_c is the critical density, and c is the speed of light. This is a minor correction for densities near $0.1n_c$.

The resonance matching depends most strongly on the sound speed and Mach number of the plasma in which the scattering is occurring. The ion–acoustic wave dispersion relation in a cold ion plasma $T_i \ll Z_j T_e$, where T_i, T_e is the ion/electron temperature, and Z_j is the charge state of ion species j, is

$$\omega^2 = k^2 \lambda_{\mathrm{De}}^2 \sum_j \omega_{pj}^2, \tag{3-3}$$

where $\omega_{pj} = (4\pi n_j Z_j^2 e^2/m_j)^{1/2}$ is the ion plasma frequency for ion species j of number density n_j, and mass m_j, $\lambda_{\mathrm{De}} = v_e/\omega_{pe}$ is the electron Debye length, $\omega_{pe} = (4\pi n_e e^2/m_e)^{1/2}$ is the electron plasma frequency, and $v_e = \sqrt{T_e/m_e}$ is the electron thermal velocity. In the single species limit and for $k\lambda_{\mathrm{De}} \ll 1$, $Zn = n_e$, and the familiar dispersion relation is recovered, $\omega = k\lambda_{\mathrm{De}}\omega_{pj} = kC_s = k(ZT_e/m_i)^{1/2}$, where C_s is the sound speed.

Although most of the incident photon energy goes into the backscattered photon, the ion–acoustic wave takes away some energy according to

$$\omega_0 = \omega_s + \omega_{ia}; \tag{3-4}$$

the frequency shift $\Delta\omega$ in the scattered light wave for direct backscatter is therefore approximately

$$\Delta\omega = \omega_{ia} \approx 2k_0 C_s \tag{3-5}$$

resulting in a wavelength shift

$$\Delta\lambda \approx 2\lambda_{\mathrm{vac}}(1 - n_e/n_c)^{1/2} C_s/c, \tag{3-6a}$$

in a stationary plasma. For a plasma flowing towards the observer with Mach number $M = v/C_s$, one observes an additional Doppler shift with combined effect

$$\Delta\lambda \approx 2\lambda_{\mathrm{vac}}(1 - n_e/n_c)^{1/2}(1 - M) C_s/c. \tag{3-6b}$$

In a mixture of light and heavy species, the sound speed, and thus the wavelength shift in Eq. (3-6), will be determined predominantly by the heavy species charge-to-mass ratio and the electron temperature. (This is not true if the heavy species is a very small fraction.)

The wavelength of the SRS optical light carries information about the density and temperature of the plasma from which it scattered because the electron plasma wave from which it scatters must satisfy the dispersion relation, given in the fluid limit ($k_\ell \lambda_{\mathrm{De}} \ll 1$) by

$$\omega_\ell^2 = \omega_{pe}^2 + 3v_e^2 k_\ell^2, \tag{3-7}$$

where ω_ℓ and k_ℓ are the frequency and wave number of the Langmuir electron plasma wave. The plasma frequency introduces density dependence, and the electron thermal velocity, v_e, introduces temperature dependence. The incident and scattered wave numbers are related by energy and momentum conservation

$$\omega_0 = \omega_s + \omega_\ell, \tag{3-8}$$

$$\mathbf{k}_0 = \mathbf{k}_s + \mathbf{k}_\ell, \tag{3-9}$$

where $\mathbf{k}_0(\omega_0)$ and $\mathbf{k}_s(\omega_s)$ are the incident and scattered light wave vectors (frequencies). The wavelength of the scattered light that satisfies these conditions is strongly dependent on density and less strongly dependent on electron temperature.

A useful measure of the probability for SRS and SBS is the gain exponent for linear amplification. For weakly inhomogeneous plasmas, the intensity gain exponent is given by

$$G(\omega_s) = \frac{1}{4}\frac{k_\ell^2 v_0^2}{v_{gs}\omega_s}\int_{\mathrm{path}} dz\, \mathrm{Im}\left(\frac{\chi_e(1+\chi_i)}{\varepsilon(k_s - k_0, \omega_s - \omega_0)}\right), \tag{3-10}$$

where $\varepsilon = 1 + \chi_e + \chi_i$ is the dielectric function for the plasma wave of frequency $\omega_s - \omega_0$ and wave number $k_0 - k_s$. The gain peaks at those frequencies for which the dielectric function is nearly zero, i.e., when the light scatters from a natural mode of oscillation of the plasma, such as an ion–acoustic or Langmuir wave.

For ponderomotively driven SBS, the intensity gain exponent is

$$G_{\mathrm{SBS}} = \frac{1}{8}\frac{v_0^2}{v_e^2}\frac{n_e}{n_c}\frac{\omega_a}{v_a}\frac{\omega_0}{v_{gb}}L \tag{3-11}$$

and for SRS, it is,

$$G_{\mathrm{SRS}} = \frac{1}{8}\frac{k_\ell^2 v_0^2}{\omega_0\omega_r}\frac{\omega_\ell}{v_\ell}\frac{\omega_0}{v_{gr}}L, \tag{3-12}$$

where the fluid limit of the plasma dispersion function has been used. Here, v_0 is the oscillatory velocity of an electron in the laser electric field, and L is the smaller of the plasma length or, in an inhomogeneous plasma, the length over which the three-wave resonance is maintained. The group velocities of the laser light and the Brillouin and Raman scattered light are v_{g0}, v_{gb}, v_{gr}, respectively, and $v_{g0} = c^2 k_0/\omega_0$, $v_{gb} = C_s$, and $v_{gr} = 3k_\ell v_e^2/\omega_\ell$ in the fluid limit. The important parameters are the laser intensity, the electron temperature, the electron density, the relevant damping rate, and the length L over which the matching conditions are maintained. The damping rate v_ℓ for the plasma wave of frequency ω_ℓ that Raman scatters the light is very sensitive to $k_\ell\lambda_{\mathrm{De}}$, the product of the wave number and the Debye length. If $k_\ell\lambda_{\mathrm{De}} < 0.2$, the Landau damping is very small but collisional damping remains. In sub-keV electron temperature plasmas, this collisional rate may be significant. In NIF relevant 3 to 6 keV plasmas, this collisional damping rate is very weak. The damping rate v_a for the acoustic wave that Brillouin scatters the light is weak for single species plasmas if $ZT_e/T_i \gg 1$, e.g., for a Au plasma because there are few

Downloaded 20 Mar 2011 to 69.181.48.121. Redistribution subject to AIP license or copyright; see http://pop.aip.org/about/rights_and_permissions

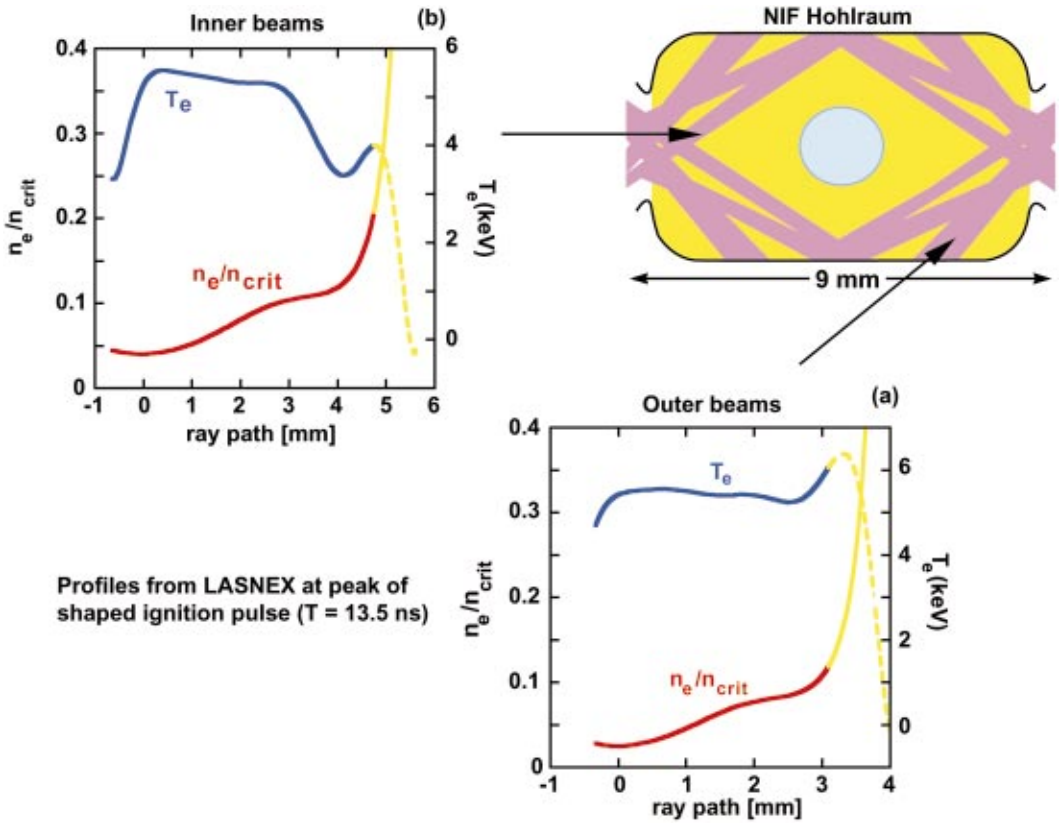

FIG. 3-1. (Color) A schematic of a NIF hohlraum with a capsule and an inner and an outer ring of beams are shown. Also shown are the electron density and temperature along the path of the outer (a) and inner (b) beams. There are distinct low-Z and high-Z NIF plasma conditions of concern for LPI. The low-Z gas fill is most important for the NIF inner beams which have a longer pathlength at somewhat higher density than the outer beams. The high-Z hohlraum-wall plasma is most important for the outer beams which have higher intensity near the hohlraum wall than the inner beams. The interface between the low-Z fill and the gold blowoff is indicated by change in color to yellow from blue or red.

ions with velocities near the phase velocity C_s. For mixed species plasmas, especially ones with significant percentages of protons as in some NIF hohlraums gasfills, the damping is typically strong, namely $v_a/\omega_a \geqslant 0.1$ because there are many protons at the phase velocity. Because both the growth and saturation of SRS and SBS depend on these damping rates, the scaling of results from current experiments to NIF is complex. In order to minimize the scaling required, the Nova LPI experiments were designed to reproduce the NIF ignition hohlraum plasma conditions as closely as possible.

The current NIF point design in Fig. 2-1 has two cones of beams on each side of the hohlraum. Figures 3-1(a) and 3-1(b) show the density and electron temperature along the outer- and inner-beam paths at the time of peak power, 13.5 ns. The absolute and relative amount of He and H gas in the hohlraum interior are design options. The laser beam intensity along the beam paths for the inner and outer beams are shown in Fig. 3-2 along with the electron density.

The output from the 2D LASNEX (Zimmerman and Kruer, 1975) radiation-hydrodynamics simulations of the NIF target can be analyzed with the Laser Interactions with Plasma post-processor (LIP) (Berger *et al.*, 1989) to obtain the total gain exponent for SBS and SRS [Eqs. (3-11) and (3-12)] as a function of time and scattered-light wavelength. The calculated peak gain exponents along the path of a 2×10^{15} W/cm^2 NIF beam are 25 for SRS along the inner-beam path and 30 for SBS along the outer-beam path for the point design (Powers *et al.*, 1995).

Some of the spectral features of the SBS gain calculations and differences between the inner-beam and outer-beam cases can be understood in terms of the plasma conditions under which the scattering would occur. For instance, Fig. 3-1 indicates that the inner beams traverse a longer length of low-density fill plasma than the outer beams. The sound speeds in Au and He/H are very different, because the sound speed is proportional to $[(Z_{\text{eff}}T_e+3T_i)/A]^{1/2}$ and Au is a heavy atom ($Z<A/2$) that is not completely ionized (i.e., $Z<Z_{\text{nucleus}}$) while the low-Z plasma is fully ionized and has $Z\geqslant A/2$ (Foord *et al.*, 2000). Typical sound speeds are from 3 to 4×10^7 cm/s for Au and from 6 to 7×10^7 cm/s for He/H for the temperatures ($T_e=3-6$ keV) expected in the NIF plasma. The shifts in wavelength for SBS backscattering from Au and He/H are then 7 and 14 Å, respectively, for stationary plasmas. Flows in the plasma will also shift the scattered-light wavelength according to the $(1-M)$ term in Eq. (3-6b). The SBS gain peaks at a wavelength of $\Delta\lambda \approx 14$ Å for the inner-beam case because most of the gain occurs in the nearly stationary He/H mixture; for the outer beam, which has less path length in the low-Z plasma, the main spectral feature is a narrow gain spike at $\Delta\lambda\approx7$ Å because most of the gain occurs in the Au plasma.

Downloaded 20 Mar 2011 to 69.181.48.121. Redistribution subject to AIP license or copyright; see http://pop.aip.org/about/rights_and_permissions

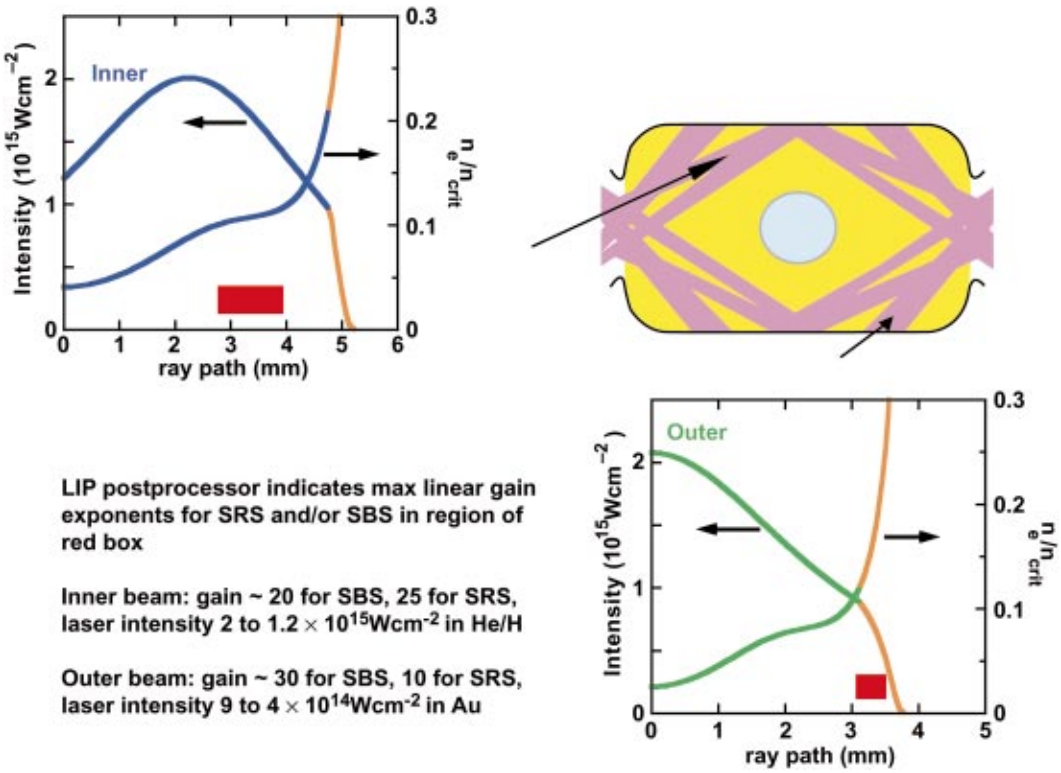

FIG. 3-2. (Color) A schematic of a NIF hohlraum with a capsule and an inner (blue) and an outer (green) ring of beams are shown. Also shown are the electron density and laser intensity along the path of the outer and inner beams. The $f/8$ inner and outer NIF beam quads interact with NIF plasmas at average irradiances of $<2\times10^{15}$ W/cm^2. The linear gain for stimulated Raman scattering is maximum in the low-Z interior for the NIF inner beams while gain for the outer beams is maximum for stimulated Brillouin scattering in the high-Z hohlraum blowoff. The interface between the low-Z fill and the gold blowoff is indicated by change in line color to yellow from blue or green.

The large outer-beam SBS gain occurs in the Au plasma with a peak gain exponent of 30. The gain peak in the inner-beam case represents gain in the low-Z plasma with a peak gain exponent of 20. Although there is a small amount of gain in the Au in the inner-beam case, the main SBS threat is from the low-Z fill gas. Hence the SBS problem is decomposed into a high-Z problem, which is best addressed in experiments with Au walls, typically standard Nova hohlraums and a low-Z plasma SBS problem, which can be addressed in larger gas-filled hohlraums or with open-geometry gas targets called gasbags.

For the Nova experiments, the low-Z gas fills were primarily hydrocarbons which, when fully ionized, had a range of densities from about 0.03 to 0.17 n_c, where n_c is the critical density for 351 nm laser light. In such mixtures (Vu *et al.*, 1994; Williams *et al.*, 1995), the ion temperature for each species is nearly the same with the consequence that there are many light hydrogen ions at the phase velocity of the ion–acoustic wave, thereby Landau damping the wave. There are in fact two modes, the usual fast wave with phase velocity, $C_{sf}\approx(ZT_e/A)^{1/2}$ with $Z/A=\Sigma Z_j^2/A_j/\Sigma Z_j$ and a slow wave with phase velocity $C_{SS}\approx(T_i/A)^{1/2}$. The acoustic wave damping is sensitive to the ratio of the ion to electron temperature. Shown in Fig. 3-3 is the calculated ratio of the damping rate to the frequency of the least damped wave, for a variety of gas mixtures in Nova gasbags and in NIF hohlraums. In the Nova gasbags, the fast wave is least damped ($T_i/T_e<0.2$ in C_5H_{12} at an electron density of $0.1n_c$ up to 1 ns) but the Landau damping rate is nonetheless much higher ($v/\omega\approx0.1$) than in the pure Au plasma where $v/\omega\approx0.01$. In NIF hohlraums and in typical Nova hohlraums, $T_i/T_e\approx1/2$ which means that the acoustic waves in the low-Z plasma will be strongly damped. Thomson scattering experiments on Nova have confirmed the existence of these two acoustic modes (Glenzer *et al.*, 1996; Glenzer *et al.*, 1997). Furthermore, the shape of the ion feature from two species plasmas can be used to determine the ion temperature as well as ZT_e/A (Glenzer *et al.*, 1999).

In NIF hohlraums, the fill gas is a mixture of He and H for which the ion wave damping at the ion and electron temperatures expected may be larger than the ion damping in hydrocarbon plasmas used on Nova (Moody *et al.*). This level of damping reduces the linear SBS gain exponents for the low-Z gas region in NIF hohlraums. However, this heavy damping affects the threshold of the Langmuir decay instability (LDI), one of the channels by which SRS could saturate, and the two ion wave decay, one of the channels by which SBS could saturate, as is discussed in Sec III B 3. By changing the ratio of H to He, the damping rate could be adjusted as shown in Fig. 3-3 to vary SRS or SBS. Some of the last gasbag experiments on Nova used HeH mixtures.

When the laser beams reach the Au plasma they are absorbed by inverse bremsstrahlung, or collisional, absorption in a short distance ($L_{abs}=c/\nu_{abs}\approx300$ to 500 μm) in a region with steep density gradients. Since SRS gain is higher in large, homogeneous regions with shallow density gradients,

Downloaded 20 Mar 2011 to 69.181.48.121. Redistribution subject to AIP license or copyright; see http://pop.aip.org/about/rights_and_permissions

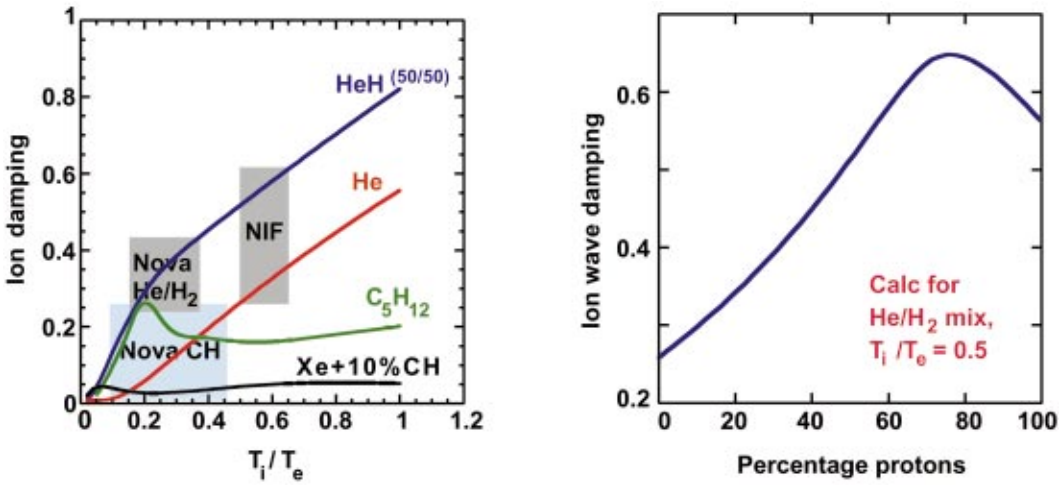

FIG. 3-3. (Color) The ratio of the damping rate to the frequency of the least-damped ion acoustic wave is shown as a function of the ratio of the ion temperature over the electron temperature (left-hand figure) and as a function of the percentage of protons in a helium–hydrogen mixture (right-hand figure). The damping rate is defined as the rate that yields the correct steady-state stimulated Brillouin gain exponent.

most of the calculated SRS gain is in the low-density, low-Z plasma. Beams in the inner cone have a calculated maximum SRS gain exponent of 26 while the outer beams gave an SRS gain of 11. The inner beams have more gain because they have longer paths in the low-Z plasma than the outer beams, and the beam intensity is higher for the focusing strategy shown in Fig. 3-2. In this case, for symmetry reasons, best focus for the inner beams occurs inside the hohlraum.

The large gain exponent for the NIF inner beam occurs at a scattered light wavelength of 590 nm, which corresponds to SRS growing at $n_e \approx 0.1 n_c$ and a $T_e = 3$ to 4 keV. The long-scalelength targets described below (Sec. III C 4) were designed to investigate this SRS gain region.

For ponderomotive self-focusing, the intensity gain exponent is

$$G_{\text{fil}} = \frac{1}{4} \frac{v_0^2}{v_e^2} \frac{n_e}{n_c} \frac{\omega_0}{v_{g0}} \ell_s \tag{3-13}$$

which is obtained by multiplying the linear gain rate (maximized with respect to perturbation wavelength) by the speckle length. The filamentation threshold occurs when $G_{\text{fil}} = 1$ which is equivalent (within a factor of order one) to the condition that the power in a speckle be greater than the critical power for self-focusing (Max, 1976), namely,

$$P_{\text{crit}} = \left(\frac{m_e c^3 (T_e + T_i/Z)}{e^2} \right) \frac{n_c}{n_e} \sqrt{1 - \frac{n_e}{n_c}}. \tag{3-13'}$$

Self-focusing or filamentation is of particular concern for NIF hohlraums, because its intensity threshold is affected by the length and transverse scale of the hot spots. For a beam smoothed with a random phase plate (Kato *et al.*, 1984) or kinoform phase plates (Dixit *et al.*, 1994), these scales are determined by the beam f/number. The coherence length of a speckle is approximately the Rayleigh range for the lens and is given by $\ell_s = 8 f^2 \lambda_0$ where λ_0 is the laser wavelength and f is the f/number. A speckle diameter full width at half-maximum (FWHM) is approximately equal to the diffraction limited spot width for the lens or $\ell_\perp \approx f \lambda_0$. The $f/8$ focusing geometry planned for the NIF will have speckles 180 μm long for 351 nm light, contrasting with 50 μm speckles for the $f/4.3$ optics normally used at the LLNL Nova laser. This effect is shown in the simulation (Berger *et al.*, 1995) in Fig. 3-4. Calculations and simulations indicate that at the laser intensity of 2×10^{15} W/cm^2 planned for the NIF, a significant fraction of an $f/8$ beam would be above the intensity threshold for self-focusing, in the absence of any further beam smoothing beyond the use of an RPP (NTIS Document, 1991; Berger *et al.*, 1993; Dixit *et al.*, 1993; NTIS Document, 1995). Self-focusing increases the growth rate and gain rate of SBS and SRS and, in the advent that filamentation and beam breakup occur, leads to uncontrolled propagation and laser energy deposition. The f-number dependence predicted by the filamentation process was tested experimentally by configuring one Nova beam with an $f/8$ lens.

2. Effects of non-Maxwellian electron distributions and nonlocal transport

If the electron mean free path ($\lambda_{ei} = v_e / v_{ei}$) were larger than the transverse scale size of the laser intensity, thermal pressure gradients caused by the nonuniform deposition of laser energy would be smoothed according to the classical theory of thermal transport. Thus, thermal filamentation (Sodha *et al.*, 1976; McMullin *et al.*, 1981) should be weaker than ponderomotive at small spatial scales. However, because inverse bremsstrahlung preferentially heats electrons with velocity lower than the thermal velocity, the laser intensity nonuniformity is imprinted initially on the distribution of electrons with low velocity. This pressure gradient can be maintained because the mean free path of these inverse bremsstrahlung-heated electrons can be much smaller than the speckle width. Moreover, the electron–ion scattering rate is a factor of Z faster than the electron–electron scattering rate. It is this latter rate, which determines how fast the population of higher velocity electrons, which transport energy over large scales quickly, is increased. There are two effects

Downloaded 20 Mar 2011 to 69.181.48.121. Redistribution subject to AIP license or copyright; see http://pop.aip.org/about/rights_and_permissions

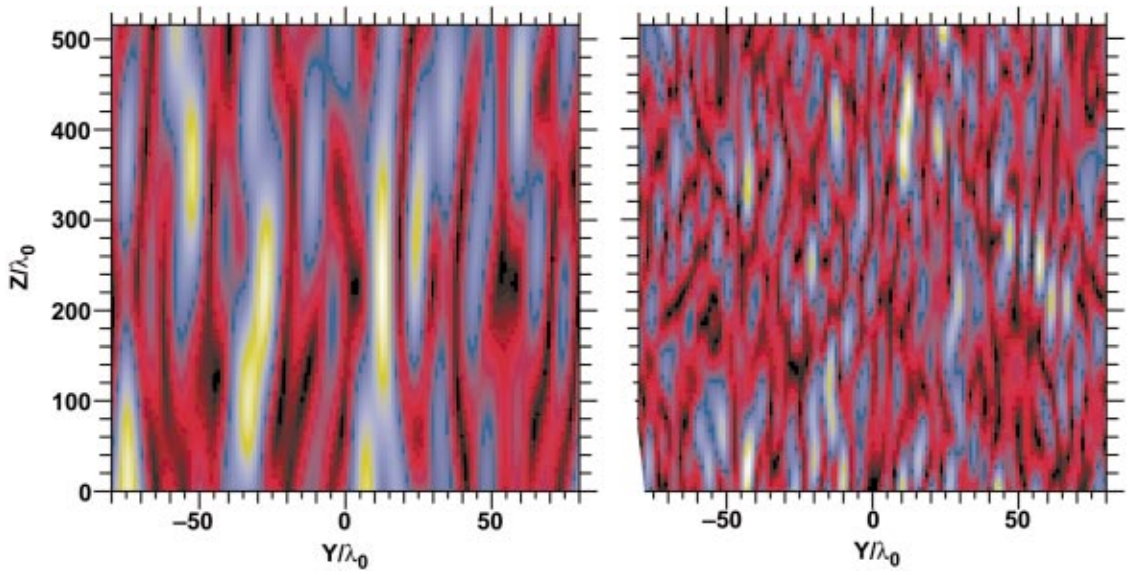

FIG. 3-4. (Color) Near "best focus," the field of a random phase-plate beam consists of long, narrow speckles whose size depends on lens f number and laser wavelength. A simulated $f/8$ far field is shown on the left-hand side, an $f/4$ on the right-hand side. The transverse width of the speckles is linearly proportional to the f number while the axial length is quadratic in the f number.

that come into play: a modification (generally a reduction) in the electron thermal conduction and the other transport coefficients for small spatial scales ($k\lambda_{ei}>1$) and a distortion of the distribution function from a Maxwell–Boltzmann. The former effect occurs for small scales and occurs even for small laser intensity (Bell, 1983; Luciani *et al.*, 1983; Albritton *et al.*, 1986); the latter is a function of the ratio of the heating rate to the thermalization rate, which is proportional to $\alpha=Z(v_0^2/v_e^2)$, a useful measure of the degree of distortion (Langdon, 1980). If this parameter is greater than one, the electron velocity distribution (often called a Langdon distribution) is similar to a super-Gaussian.

The dependence of transport coefficients on the ratio of the electron–ion mean free path, λ_{ei}, to the scale length of the temperature and density perturbation, $\lambda_t=2\pi/k$, has been calculated with Fokker–Planck codes (Epperlein, 1990; Epperlein and Short, 1992; Epperlein and Short, 1994; Epperlein, 1994; Brunner and Valeo, 2002) and analytically (Epperlein *et al.*, 1992; Bychenkov *et al.*, 1995; Brantov *et al.*, 1996; Brantov *et al.*, 1998) for small amplitude perturbations. Significant modifications occur to the classical transport coefficients for electrical conductivity, thermal conductivity, and friction force and also to the ponderomotive force and inverse bremsstrahlung. The electron heat conductivity for a temperature perturbation of wave number k takes the form (Epperlein, 1990) $K_{nl}=K_{\mathrm{cl}}/[1+b(k\lambda_{ei})^d]$, where $b\approx 50$, $d\approx 1.3$, and K_{cl} is the classical Spitzer–Härm heat conductivity. The reduction in the thermal transport increases the growth rate of filamentation (Epperlein, 1991), and stimulated forward Brillouin scattering (Rose and DuBois, 1992; Bychenkov *et al.*, 2000) especially in high-Z plasmas because the temperature perturbation produced by the absorbed wave energy is bigger than it would be for Spitzer–Härm. These effects influence the damping rate and, to a lesser extent, the dispersion properties of ion–acoustic waves in the intermediate range of spatial scales, $k\lambda_{ei}\approx 0.1-20$. At very short spatial scales, $k\lambda_{ei}\gg 1$, and time scales much shorter than the electron–ion collision frequency, $\Delta t<1/v_{ei}$, the usual collisionless description applies where these nonlocal thermal transport effects can be neglected. The collisionless description should apply to the conditions we expect in NIF plasmas where $v_{ei}\sim\langle Z^2 n_i\rangle/T_e^{3/2}\sim 2-1\times 10^{11}\ \mathrm{s}^{-1}$ and $\lambda_{ei}\sim T_e^2/\langle Z^2 n_i\rangle\sim 100-300$ microns for $T_e=3-5$ keV for a HeH plasma at $n_e=9\times 10^{20}\ \mathrm{cm}^{-3}$. For comparison, typical speckles in the beam focal spot are a few microns in diameter as discussed above. However, many important experiments (Labaune *et al.*, 1996; Renard *et al.*, 1996; Labaune *et al.*, 1998; Labaune *et al.*, 1999; Montgomery *et al.*, 2000) that provide the scientific basis for understanding laser–plasma interactions are done with laser and plasma parameters for which $\lambda_{ei}\sim 1$ micron and these nonlocal transport effects can have a large impact on thermal filamentation and the propagation of the incident laser beam. The modeling of these experiments is very problematic at this time given that simulations of heat transport and inverse bremsstrahlung for a single hot spot (Brunner and Valeo, 2002) show that 10% deviations of the transport coefficients from the analytic theory appear for temperature perturbations as little as 1%. Much larger discrepancy occurs as larger perturbations are driven.

Non-Maxwell–Boltzmann distributions (NMBDs) produced by inverse bremsstrahlung have fewer electrons at low velocity than a Maxwell–Boltzmann with the same density and internal energy. Therefore the rate of collisional absorption of light and Langmuir waves, both of which depend on the electron–ion collision frequency at low velocity, are reduced (Langdon, 1980). In spatially uniform calculations which neglect self-collisions, no steady state exists and, for long times, the distribution becomes super-Gaussian NMBDs, $f(v)\sim\exp(-(v/u)^5)$, with $u^5\sim v_0^2 t$. Because the "temperature" increases until the heating rate is smaller than

Downloaded 20 Mar 2011 to 69.181.48.121. Redistribution subject to AIP license or copyright; see http://pop.aip.org/about/rights_and_permissions

the thermalization rate, i.e., $\alpha \ll 1$, it is clear that the long time *physical* solution will again be Maxwellian. Spatially uniform calculations (Matte *et al.*, 1988) that use a Fokker–Planck code (with self-collisions which tend to restore a Maxwell–Boltzmann) also demonstrated NMBDs of the form, $f(v) \sim \exp(-(v/u)^{m(\alpha)})$ for inverse bremsstrahlung heating and showed that $m(\alpha) \sim 2$ when $\alpha \ll 1$ and evolves smoothly to $m(\alpha) \sim 5$ when $\alpha \gg 1$. More recent calculations (Afeyan *et al.*, 1998), done with a nonuniform laser driver but spatially periodic boundary conditions, showed a local distortion of the velocity distribution in the intense laser hot spots. This distortion of the distribution function locally increases the acoustic frequency, effectively by increasing the electron Debye length. As a result, the ion Landau damping of the acoustic wave is reduced. Whereas SRS and SBS may be increased by NMBD in weakly unstable experiments because the linear growth or gain rate may be increased (Bychenkov *et al.*, 1997; Afeyan *et al.*, 1998), they may also be decreased in strongly driven cases because the thresholds for saturation processes (that also depend on the damping rates) are reduced. Additionally, if the laser intensity nonuniformity causes the shape of the NMBD to vary in space, the acoustic dispersion will vary in space, which may be enough in some cases to detune SBS and lower overall its gain in otherwise uniform plasmas.

Recent calculations (Fourkal *et al.*, 2001) and calculations for a single hot spot (Brunner and Valeo, 2002), supported by Thomson scattering experiments in high-*Z* plasma (Glenzer *et al.*, 1999), have shown that the distribution is super-Gaussian at low velocity but Maxwellian at high velocity. These calculations identify the additional parameter, $\sigma = r_{\text{spot}}/\lambda_{ei}$, when the energy can be transported out of the heated region. This parameter measures the importance of transport to the value of the distribution function. If σ is small, then the electrons are not localized to a single hot spot and transport is important. Since $\lambda_{ei} \sim v^4$, the higher velocity electrons can sample multiple hot spots and are influenced by the spatially averaged intensity where $\alpha \ll 1$. These higher velocity electrons are therefore Maxwellian although $\alpha \sim 1$ for the low velocity electrons which are non-Maxwellian. Thus, electron Landau damping of Langmuir waves, although reduced, is less affected by inverse bremsstrahlung heated distributions than the predictions based on superGaussians for all velocities.

3. Nonlinear effects on scattering

Amplification of thermal fluctuations (Oberman and Auer, 1974; Seka *et al.*, 1984) by 20 *e*-foldings is sufficient to produce both significant backscattering and plasma waves of sufficient amplitude that nonlinear saturation mechanisms are important. The NIF quads are composed of four $f/20$ beams which cluster together to form an effective $f/8$ beam which interacts with the plasma at intensities up to 2×10^{15} W/cm^2 for the baseline 300 eV hohlraum target, with a variation of intensity along the beam path as shown in Fig. 3-2. In the transverse direction, the laser intensity is assumed to be averaged over the beam profile, and the LIP calculations use this spatially averaged intensity. However, each beam is composed of small (about 3 μm diameter) speckles with a distribution of intensities above and below the average. SRS and SBS grow faster in the intense speckles with the result that, even for average gain exponents smaller than 20, significant reflectivity is expected (Rose and DuBois, 1994; Berger *et al.*, 1995). The speckles can self-focus as they interact with the plasma, increasing the intensity within individual ''hot spots,'' further enhancing the reflectivity. Laser beam smoothing such as smoothing by spectral dispersion (SSD) (Skupsky *et al.*, 1989; Rothenberg, 1997), which changes the speckle pattern on the laser bandwidth time scale, or polarization smoothing (NTIS Document, 1990; Tsubakimoto *et al.*, 1992; Tsubakimoto *et al.*, 1993; Pau *et al.*, 1994; Boehly *et al.*, 1999), which instantaneously reduces the power in high intensity speckles, can reduce filamentation (Lefebvre *et al.*, 1998), SRS, and SBS (Hüller *et al.*, 1998; Berger *et al.*, 1999).

The levels of SBS and SRS are influenced by nonlinear processes, e.g., by secondary decay of the primary Langmuir wave driven by the SRS process (Fernandez *et al.*, 1996; Kirkwood *et al.*, 1996; Fernandez *et al.*, 1997). Once the instability threshold is exceeded, the Langmuir decay instability (LDI) (DuBois and Goldman, 1965; DuBois and Goldman, 1967; Bonnaud *et al.*, 1990) rapidly transfers energy, to another Langmuir wave and an acoustic wave, from the Langmuir wave driven directly by the incident laser and Raman reflected light wave. The threshold Langmuir wave charge density $\delta n_{\text{th}}^{\text{LDI}}$ for driving the LDI is given by

$$\left| \frac{\delta n_{\text{th}}^{\text{LDI}}}{n_e} \right|^2 = 16 (k\lambda_{\text{De}})^2 \frac{v_e}{\omega_\ell} \frac{v_a}{\omega_a}, \tag{3-14}$$

where n_e is the background density, $v_e = v_e^c + v_e^L$ is the sum of the collisional damping rate, $v_e^c = 1/2 v_{ei} \omega_{pe}^2 / \omega_\ell^2$, and the Landau damping rate v_e^L of the Langmuir wave of frequency ω_ℓ. Here, ω_a and v_a are the local acoustic frequency of the least damped mode and acoustic wave damping rate, respectively, and $k_\ell \lambda_{\text{De}}$ is the wave number of the Langmuir wave times the electron Debye length. The threshold depends on the damping rate of the acoustic wave and thus, if the damping rate of the acoustic wave were increased while other plasma parameters are kept constant, the Langmuir wave can be driven to larger amplitude and more SRS would be expected for the same linear gain exponent. In simulations (Bezzerides *et al.*, 1993), the amplitude of the primary Langmuir wave continues to increase above the LDI threshold but at a slower rate. Analysis of the results supports a scaling of the dissipation on the Langmuir wave above the LDI threshold to the enhanced value, $v_e^{nl} = v_e |\delta n_\ell / \delta n_{\text{th}}^{\text{LDI}}|^2$. From this modeling, one obtains a reflectivity that is dependent on the ion wave damping but weakly dependent on the Langmuir wave linear damping rate (DuBois, 1998). This scaling with ion wave damping is observed in a number of experiments, including the Nova gasbag (Kirkwood *et al.*, 1996) and toroidal experiments (Fernandez *et al.*, 1996; Fernandez *et al.*, 1997) discussed below.

In the fluid simulations of LDI just discussed, the plasma parameters were generally chosen such that SRS was absolutely unstable ($k_\ell \lambda_{\text{De}} < 0.15$) because computational con-

Downloaded 20 Mar 2011 to 69.181.48.121. Redistribution subject to AIP license or copyright; see http://pop.aip.org/about/rights_and_permissions

straints precluded simulating regions large enough for convective instability to reach nonlinear levels. With the advent of more computational resources, PIC simulations have been done that indicate that SRS saturates by different mechanisms if $k_\ell \lambda_{De} > 0.15$, that is, particle trapping occurs (Mourenas, 1999; Vu *et al.*, 2001). As a result of the flattening of the distribution at the phase velocity of the Langmuir wave, Landau damping and the plasma wave frequency are reduced (Willis and Deardorf, 1965). In these simulations, LDI may be observed but is not the dominant saturation channel in this parameter range. There are several effects of trapping that reduce the growth of SRS: the detuning effect of a nonlinear frequency shift (Cohen and Kaufman, 1978; Vu *et al.*, 2001) and the parasitic effect of a sideband instability (Brunner and Valeo; Kruer *et al.*, 1969).

NIF-like high-Z plasmas generally have weaker SRS than low-Z plasmas (see, for example, Fernandez *et al.*, 1996; Kirkwood *et al.*, 1996). The electron temperature is higher than in the low-Z plasmas and collisional damping is stronger. These effects reduce the linear gain. In addition, the acoustic waves are weakly damped, leading to a lower secondary decay instability threshold and a lower nonlinear saturation level. Moreover, the low ion wave damping increases the level of SBS which is often observed to correlate with low levels of SRS as will be discussed subsequently.

Some semianalytic models of SRS saturation have been proposed which limit the amplitude of the primary Langmuir wave to values near the LDI threshold (Drake and Batha, 1991; Kolber *et al.*, 1995). In the Drake model, the SRS reflectivity scales with the product of the ion–acoustic wave damping times the Langmuir wave damping (Landau and collisional). Since Landau damping decreases with density increase (at constant electron temperature) and is typically much larger than collisional damping whereas the observed SRS increases with density in Nova gasbags, the consistency of this model requires the elimination of Landau damping of Langmuir waves. Only collisional damping remains which increases with density. With that Ansatz, this model is also consistent with the data scaling. In the Kolber *et al.* model, the reflectivity depends on the ion wave damping but not on the damping of Langmuir wave.

Although the scaling of the SRS reflectivity with ion damping given by these models agrees with the data, it applies only when the threshold given in Eq. (3-14) is exceeded. For the 351 nm Nova experiments (Fernandez *et al.*, 1996; Kirkwood *et al.*, 1996; Fernandez *et al.*, 1997), the linear electron Landau damping for a Maxwell–Boltzmann distribution at the measured temperature is so large that the threshold would not be exceeded. However, a super-Gaussian electron distribution produced by inverse bremsstrahlung or distribution flattened at the phase velocity by trapping have been invoked as possible explanations for drastically reduced Landau damping. However, super-Gaussians for the electrons with $v = \omega/k > v_e$ disagree with the best theory and data (as discussed in Sec. III B 2) and reduction of damping by trapping would not affect the LDI threshold because trapping affects waves traveling along the direction of the incident laser beam only.

The association of the LDI with SRS has been directly observed in time-integrated (Baker *et al.*, 1997) and time-resolved (Labaune *et al.*, 1998) Thomson scattering measurements of the decay Langmuir wave amplitudes in sub-keV plasmas. The ion–acoustic wave product of LDI was also measured in these plasmas (Depierreux *et al.*, 2000; Salcedo *et al.*, 2003; Montgomery *et al.*, 2002). Recently, the decay of ion–acoustic waves associated with LDI was measured far above thermal levels at the Nova facility in $T_e > 2.2$ keV gasbag plasmas illuminated at 527 nm, the second harmonic of the laser wavelength (Geddes *et al.*, 2003; Young *et al.*, 2000). In this case, the nominal LDI threshold was exceeded in the calculations. However, these same calculations produced more SRS than the experiments observed which leaves open the possibility that LDI is not the primary saturation mechanism.

Both the primary and secondary Langmuir waves dissipate their energy by producing energetic electrons whether by linear Landau damping (Short and Simon, 1998; Short and Simon, 1998a) or electron trapping (Vu *et al.*, 2001). Trapping also produces modifications to the distribution function that produce frequency shifts in the Langmuir wave, which may detune and saturate SRS (Morales and O'Neil, 1972). The number and energy of hot electrons predicted by the SRS spectrum matches very well with measurements that used spectroscopy in hohlraum targets (Glenzer *et al.*, 1998).

The amplitude of the acoustic wave directly driven in SBS is also limited by wave–wave instabilities (Cohen *et al.*, 1997; Williams *et al.*, 1997; Riconda *et al.*, 2000) once its amplitude exceeds the two-ion-wave decay (TIWD) instability. In this instability, one large amplitude ion–acoustic wave decays into two other ion waves of higher or lower frequency. Higher frequencies are the result of harmonic generation (Heikkinen *et al.*, 1984), which occurs when the ion wave steepens until the gradient in the amplitude is comparable to the Debye length. The higher spatial frequencies are out of phase with the incident and SBS reflected light. If the primary ion wave has a wavelength comparable to the Debye length, decay into lower frequency ion waves is favored. This process has a high threshold if the acoustic waves are strongly damped which is the case in the hydrocarbon gasbag or HeH plasmas.

Particle-in-cell (PIC) simulations with EPIC (Wilks *et al.*, 1995) of the nonlinear saturation of SBS with multiple species ions were initially done in 1D with a Boltzmann fluid electron response. These simulations showed the importance of the light ion species (protons) in saturating SBS as they are easily trapped by the large amplitude ion–acoustic wave. Although the PIC simulations showed much larger reflectivities than observed, they showed lower reflectivity after the trapping occurred than at first both because of enhanced damping and nonlinear frequency shifts (Andreev and Tikhonchuk, 1989). This work was extended to 2D where additional saturation mechanisms, in particular the TIWD, can occur. In 2D PIC simulations using BZohar (Cohen *et al.*, 1997; Williams *et al.*, 1997), the reflectivity initially follows the 1D behavior but then ''crashes'' to a much lower level where it remains for the duration of the simulation. The ''crash'' occurs just after the TIWD saturates.

In addition to these wave–wave nonlinearities for SBS,

Downloaded 20 Mar 2011 to 69.181.48.121. Redistribution subject to AIP license or copyright; see http://pop.aip.org/about/rights_and_permissions

there are the kinetic effects of particle trapping and the fluid nonlinearities such as bulk heating, and induced flow velocities (Rose, 1997). These flows result from the transfer of light momentum to the plasma as the acoustic waves involved in the SBS process scatter the light backward and reverse a portion of light's momentum. It is more important when SBS is driven in localized hot spots than when the pump is uniform. It is the flow velocity gradient that is important, and a steepening of the gradient occurs because the momentum transfer is concentrated in the last exponentiation length of SBS light. In addition to the momentum transfer, the energy lost to the acoustic wave subsequently heats the plasma (mostly the ions), which can change the damping and natural frequency of the acoustic wave, especially in multispecies plasmas, which are sensitive to the ratio of the ion to electron temperature. Both of these effects weaken the growth of SBS and are included naturally in PIC simulations (Kruer *et al.*, 1975; Estabrook *et al.*, 1989). In such simulations, the momentum and heating are initially exchanged with particles with velocities near the ion–acoustic wave's phase velocity. In multispecies plasma, where the least damped ion wave's phase velocity is above the lightest ion's thermal velocity, it is the light ions that are trapped. On the time scale short compared to the ion–ion collision time but longer than the bounce time of an ion in the ion wave, trapping reduces the Landau damping but lowers the acoustic wave frequency. These kinetic effects appear to allow the fluid TIWD instability discussed previously to satisfy the frequency matching conditions and exceed threshold (Cohen *et al.*, 1997; Williams *et al.*, 1997; Riconda *et al.*, 2000). Over a longer collisional time scale, the bulk ions are heated. By using the fact that the ratio of Thomson scatter signal from the slow and fast modes of beryllium-gold plasmas is sensitive to the bulk ion temperature, this SBS-correlated ion heating has been measured with Thomson scattering (Froula *et al.*, 2002).

The gain exponent for SBS in NIF targets is largest in the Au blowoff, not the HeH gas. For high-Z plasmas, the most relevant work to date with PIC codes was done in 1D with ion–ion collisional effects included (Rambo *et al.*, 1997). The Au plasma is collisional enough that, although the ions are heated with a nonthermal tail, trapping does not occur. The nonthermal tail provides the only significant damping of the acoustic waves. Subsequent work in 2D awaits the development of a 2D code with collisional effects included (Caillard and Lefebvre, 1999).

Developing a comprehensive computational model for laser plasma interactions which will reliably predict the reflectivity for NIF targets is a goal of the ICF Program. At LLNL, the three-dimensional, time-dependent fluid code F3D has been developed for this purpose (Berger *et al.*, 1998). F3D couples light propagation to a single-fluid, two-temperature (electron and ion) nonlinear hydrodynamics code to calculate the stimulated scattering and self-focusing of laser light. The light propagation is usually done within the paraxial approximation for both the incident laser light and the Raman and Brillouin backscattered light waves. The charge density waves, Langmuir and acoustic waves, are time and space enveloped. Other options which relax these approximations are also being developed as appropriate for studying specific problems. In general, the nonlinear processes that can act to limit the amplitudes of the plasma charge-density waves that scatter the laser light are of three types: in the first type, the waves modify the plasma parameters of temperature, density, or flow velocity such as to reduce the gain rate; in the second type, the waves grow to sufficient amplitude to decay themselves which slows their rate of growth; in the third type, the particle distribution function is modified by the large amplitude waves such that the Maxwell–Boltzmann assumption is no longer valid. The first two types are included in F3D: the first by including the appropriate physics in the nonlinear hydro; the second by introducing anomalous damping rates when the plasma wave amplitudes exceed the decay thresholds. Kinetic nonlinear processes are also important (Forslund *et al.*, 1975; Forslund *et al.*, 1975a; Langdon and Lasinski, 1975; Langdon *et al.*, 1979; Estabrook *et al.*, 1980; Wilks *et al.*, 1992; Wilks *et al.*, 1995; Sanbonmatsu *et al.*, 1999; Sanbonmatsu *et al.*, 2000; Vu *et al.*, 2001) and models of these effects will be incorporated into F3D in the future.

Nonlinear kinetic processes that limit SRS or SBS typically increase the damping of the Langmuir or acoustic wave when the plasma wave amplitude is large enough to accelerate thermal particles up to the phase velocity, ω/k and wave breaking occurs (Kruer, 1988). If the plasma waves are less strongly driven, trapping may still occur with a decrease in the damping and a nonlinear frequency shift near the phase velocity (Cohen and Kaufman, 1978; Andreev and Tikhonchuk, 1989; Cohen *et al.*, 1997; Vu *et al.*, 2001; Williams *et al.*, 1997; Riconda *et al.*, 2000). These processes are studied with particle-in-cell codes (Morse and Nielson, 1970; Langdon and Lasinski, 1976; Birdsall and Langdon, 1985; Hemker *et al.*, 1999; Hemker, 2000) or (less often) with Vlasov codes (Hiob and Barnard, 1983; Ghizzo *et al.*, 1990) that solve Maxwell equations and evolve the particle distribution functions. Because the length and time scales of the Debye length and the plasma or laser frequency, respectively, are resolved and the particle distribution rather than a few moments are evolved, the increase in physical detail is accompanied by a substantial decrease in the physical system size that can be modeled. However, the ever increasing speed and memory of computers make this tool more and more useful for developing the basic physics understanding needed for F3D.

At LANL, 2D Langmuir fluid turbulence codes (Russell *et al.*, 1999) have been developed and used to predict the scaling of SRS. Some of these results have motivated reduced models in F3D. LANL has also developed PIC and hybrid PIC-fluid codes (Vu, 1996; Vu, 2000) to study beam deflection of single speckles, nonlinear SBS with kinetic effects, and LDI. The LANL PIC code has used special techniques to reduce the PIC electrostatic noise from which SRS and SBS grow so that wave–wave nonlinear processes can compete with particle distribution modifications without using a prohibitive number of particles.

One of the difficulties of empirically scaling to NIF is the fact that these nonlinear processes depend on the same plasma parameters as the linear gain exponents but with a

Downloaded 20 Mar 2011 to 69.181.48.121. Redistribution subject to AIP license or copyright; see http://pop.aip.org/about/rights_and_permissions

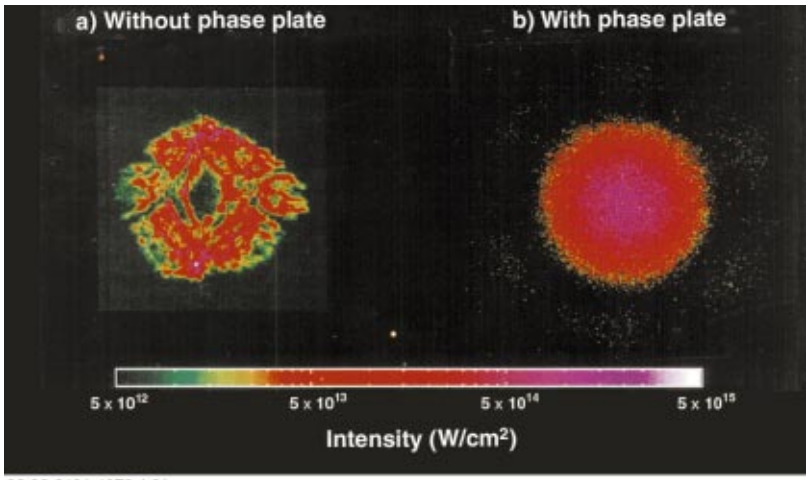

FIG. 3-5. (Color) Two laser beam spots with the same spot-averaged intensity are shown. On the left-hand side is an $f/4$ Nova spot 1 mm past best focus, typical of the unsmoothed beam in Nova hohlraums at the LEH. On the right-hand side is an RPP-smoothed beam. A phase plate produces a more uniform focal spot distribution and smaller speckle sizes for the same spot-averaged intensity.

different functional form. Hence, the plasma emulation experiments at the Nova Laser Facility were designed to reproduce the actual calculated NIF plasma conditions as well as the NIF linear instability gain, as closely as possible, in order to properly incorporate saturation and other plasma effects that are omitted by the simple linear gain analysis. At the same time, the models have been tested not only on the NIF-relevant experiments but also on a limited number of other experiments with very different parameters (Labaune *et al.*, 1996; Young *et al.*, 1998; Montgomery *et al.*, 2000; Froula *et al.*, 2002; Labaune *et al.*, 1998; Labaune *et al.*, 1999; Renard *et al.*, 1996).

4. Beam smoothing effects on LPI

To better emulate NIF-like laser–plasma interactions, a laser beam with the intensity, smoothing, and f/number appropriate to a NIF beam was installed on the Nova Laser Facility (Campbell *et al.*, 1991).

Because of aberrations, the focus of the laser beam is far from diffraction limited but it typically contains coherent regions of high intensity within the focal region. The radiation pattern needed for indirect-drive of capsules within a hohlraum does not necessarily require a smooth focal spot but laser–plasma instabilities, being nonlinear intensity-dependent phenomena, are sensitive to the laser beam intensity nonuniformity. Random phase plates (RPPs) (Kato *et al.*, 1984) were introduced to eliminate long-wavelength spatial coherence of the laser beam phase front and produce a globally smooth intensity pattern near focus as indicated in Fig. 3-5. In the simplest form, RPPs are transmissive optical elements of transverse size, $\Delta x \approx 1$ to 10 mm, through which the light passes and acquires a phase shift of 0 or π. At focus the light intensity has high-intensity speckles of width $f\lambda_0$, length $8f^2\lambda_0$, and an overall envelope of width $A_{\text{spot}} \approx fD\lambda_0/\Delta x$ and shape $\{[\sin(\xi)/\xi]\times[\sin(\zeta)/\zeta]\}^2$ where $\xi = \pi x/A_{\text{spot}}$, $\zeta = \pi y/A_{\text{spot}}$, and D is the beam diameter at the aperture of a square lens. A circular lens has a Bessel function shape at focus. The stationary fine-scale intensity structure of size $f\lambda_0$ within the focal envelope has an approximately speckle (areal) distribution, $P(I) = I_0^{-1}\exp(-I/I_0)$.

An unfortunate consequence of RPP smoothing is that about 20% of the light is diffracted outside the central spot. Recent developments improve on this design by changing the phase continuously in the near field with the result that up to 95% of the light can be contained within a super-Gaussian central spot (Lessler *et al.*, 1993; Dixit *et al.*, 1994; Lin *et al.*, 1995; Kessler *et al.*, 1996; Lin *et al.*, 1996). These Kinoform phase plates (KPPs) will be used on NIF. The difference between KPP and RPP illumination appears at long wavelengths. F3D calculations of KPPs and RPPs with the same power in the central spot found slightly less self-focusing with KPPs than RPPs because the flatter envelope of the KPP slightly reduces the percent of the power at intensities far above the mean (Williams, 2000). Experiments have shown that laser–plasma instabilities respond to KPP smoothing in a manner similar to RPP smoothing (MacGowan *et al.*, 1998).

Two other smoothing techniques have been used on the Nova Laser Facility to control LPIs: SSD (Lehmberg and Obenschain, 1983; Skupsky *et al.*, 1989; Rothenberg, 1997) and polarization smoothing (PS) (NTIS Document, 1990; Pau *et al.*, 1994; Boehly *et al.*, 1999). In SSD (Skupsky *et al.*, 1989), the laser pulse is spectrally broadened by frequency modulated phase modulation and is angularly dispersed by a diffraction grating so that the different frequency components produce speckle patterns shifted in space with respect to one another. At a given time there is one speckle pattern from the coherent sum of the Fourier components which, however, changes at a rate determined by the total bandwidth, $\Delta\omega$. Polarization smoothing (NTIS Document, 1990) consists of dividing the light power into two polarizations each of which effectively has an independent phase plate and thus an uncorrelated speckle pattern in the plasma. In the limit of two uncorrelated speckle patterns, the distribution of intensities is given by $P(I) = 4I/I_0^2\exp(-2I/I_0)$. SSD and PS can be used in conjunction as discussed below for the Nova experiments.

For frequency modulated (FM) SSD, which was used on Nova, the phase of the electric field in the near field (the lens aperture) is $\phi = \alpha\sin[\Omega(t-\beta k_x)]$, where Ω is the FM modulator frequency, β is the grating dispersion parameter, k_x is a

Downloaded 20 Mar 2011 to 69.181.48.121. Redistribution subject to AIP license or copyright; see http://pop.aip.org/about/rights_and_permissions

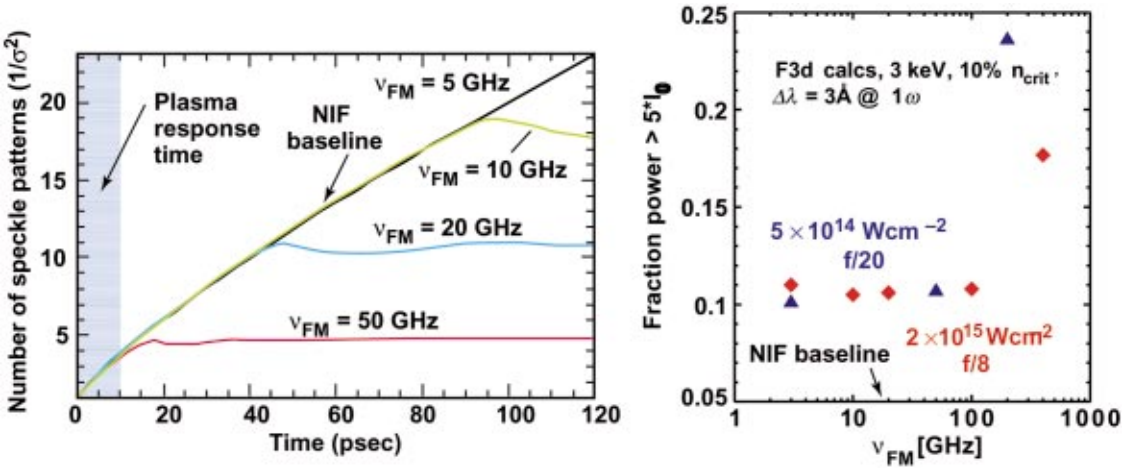

FIG. 3-6. (Color) The dependence of SSD smoothing on the FM modulator frequency (17 GHz for NIF) and time is shown. On the left-hand side, the number of independent speckle patterns that contribute to the smoothing is shown versus time. On the right-hand side, the fraction of the laser power with intensity above five times the average in a NIF-like plasma (0.04 in vacuum) is shown vs modulator frequency for a fixed laser bandwidth. NIF SSD will use a high-frequency modulator (17 GHz) to minimize dispersion required for SSD. A higher-frequency modulator reduces pinhole and LEH clipping as less dispersion is required for SSD. With fewer independent speckle patterns, the smoothing approaches its asymptotic value earlier for high-frequency modulators. F3D calculations show that since filaments only respond to the smoothing achieved by about 10 ps, filamentation is insensitive to modulator frequency up to about 100 GHz.

measure of the distance from the center of the aperture, and α is the modulation depth. The bandwidth is given by $\Delta\omega = 2\alpha\Omega$. In order for the full bandwidth of the SSD to be sampled at each instant, $\Omega\beta k_x$ must change by at least 2π across the lens aperture, defined as one ''color cycle'' across the lens. The grating introduces a time delay of the laser beam arrival from one edge of the laser beam to the other of $\tau = \beta\omega_0/fc$. One color cycle requires a time delay of $\tau = 2\pi/\Omega$. In one view of SSD obtained by decomposing the field in a Fourier series, the laser field consists of a number of lines, separated from the fundamental frequency by $j\Omega$, with amplitude $J_j(\alpha)$. The amplitude of the Bessel function decays rapidly for $j > \alpha$ with the result that $\Delta\omega = 2\alpha\Omega$. As the modulator frequency, Ω, increases, the number of sidebands decreases and the duration of smoothing decreases as shown in Fig. 3-6; in other words, the number of independent speckle patterns decreases.

As shown in Fig. 3-6, the F3D-simulated laser beam filamentation did not depend on modulator frequency, up to 100 GHz, for fixed bandwidth and at least one color cycle. This outcome is a consequence of the fact that beam filamentation occurs in a time of 10 to 20 ps. Up to this time, the higher and lower frequency modulators achieve the same smoothing. Beam smoothing that occurs over times longer than this is ineffective in reducing filamentation. If a less dispersive grating was used such that less than one color cycle was present across the lens aperture, F3D simulations showed SSD was less effective in controlling filamentation. Using a more dispersive grating to produce more than one color cycle has the effect of smoothing a wider range of wavelengths. The longest wavelength smoothed is $fD\theta$, where D is the lens diameter and θ is the angular dispersion of the grating. However, F3D simulations found no benefit for more than one color cycle (Hinkel, 1996).

A smaller modulation frequency requires a grating with more dispersion, a longer delay, to realize at least one color cycle across the lens. Increased dispersion has two negative consequences: (1) the pinholes in the laser spatial filters have to be larger, because of the larger angular spread of the beam, resulting in greater nonlinear B-integral effects (NTIS Document, 1975) in the laser propagation and reduced output power, and (2) the laser spot produced by the KPP is smeared to a larger spot in the LEH. The gratings used for the 3 GHz modulator on Nova also limited the rate at which the laser power on target could be changed. A modulator frequency of 17 GHz was tested in Nova experiments (discussed in Sec. III C), showed little difference from the 3 GHz backscatter results, and has been chosen as the NIF baseline. To this point, only 1D SSD has been discussed and only 1D SSD was used in experiments that explored the effect of SSD on LPI. Not discussed was the option of 2D SSD (Skupsky and Craxton, 1999) wherein two FM modulators with different FM frequencies and two gratings that disperse the beam in two orthogonal directions are used. Although 2D SSD smoothes intensity modulations more effectively than 1D SSD, it does so on a long time scale. On the shorter time scales on which LPI grow and saturate, there is little difference between 1D and 2D SSD provided the total bandwidth is the same and there is at least one color cycle.

Filamentation is of more concern for NIF ignition targets than for typical Nova implosion targets primarily because of NIFs higher f number. The distribution of intensities near focus is independent of f number but the laser light power in a typical speckle is proportional to the area of the speckle or to the square of the f number. Thus, a laser beam of a given power focused to a given spot size with an $f/8$ NIF lens will have more speckles above the threshold power for ponderomotive self-focusing than with an $f/4$ lens. The power threshold for self-focusing [Eq. (3-13′)] is equivalent to the criterion that the product of the spatial growth rate (at the most unstable wavelength) and the speckle length exceed one (Dixit *et al.*, 1993). Thermal filamentation may be nearly

Downloaded 20 Mar 2011 to 69.181.48.121. Redistribution subject to AIP license or copyright; see http://pop.aip.org/about/rights_and_permissions

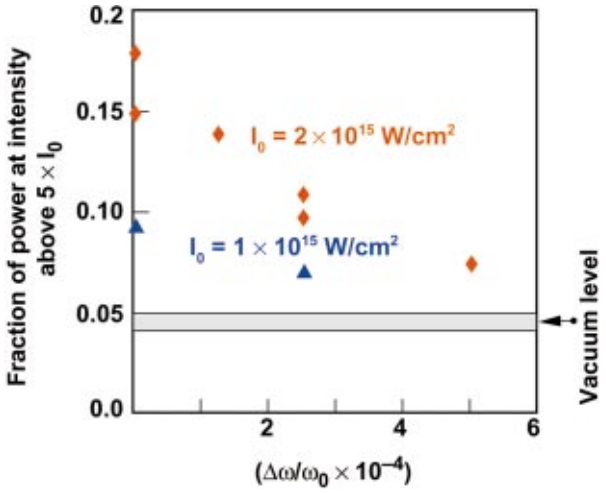

FIG. 3-7. (Color) The reduction of self-focusing by SSD smoothing is shown as a function of the laser bandwidth as a percentage of the laser frequency. The reduction is characterized by plotting the fraction of the laser power above five times the mean intensity (0.04 in vacuum) after self-focusing in the plasma for the mean intensities, I_0, as indicated. Simulation parameters: $T_e=3$ keV, $n_e=0.1n_c$, $I_0=2\times10^{15}$ W/cm^2, $\lambda_0=351$ nm in a C_5H_{12} plasma.

as important as ponderomotive if the thermal transport is inhibited (Epperlein, 1990) and the criterion for instability given by the product of the spatial growth rate and the speckle length is more useful if the total spatial growth rate is used.

Simulations of laser beam filamentation with F3D in three dimensions and other codes (Schmitt and Afeyan, 1998) in two dimensions confirmed the f-number scaling of filamentation and predicted a noticeable angular spreading of the light that is transmitted through a millimeter-scale, low-Z, underdense plasma with a threshold [see Eq. (3-13)] for an $f/8$ beam at an intensity near 2×10^{15} W/cm^2 if the plasma parameters are NIF-like, i.e., $T_e=3-6$ keV, $n_e=0.1n_c$. The spreading for $f/4$ beams is predicted to be much less. Temporal beam smoothing reduces the self-focusing of the speckles; it is most effective on the lower power speckles. The calculated level of filamentation for $f/8$ illumination, with plasma and laser parameters chosen to be representative of those encountered in Nova hydrocarbon-filled gasbags [e.g., neopentane (C_5H_{12}), $T_e=3$ keV, $n_e=0.1n_c$, $I=2\times10^{15}$ W/cm^2, $\lambda_0=351$ nm], decreases with increase in laser bandwidth as shown in Fig. 3-7 (Riazuelo and Bonnaud, 2000). Polarization smoothing also reduces the amount of filamentation because the number of high intensity speckles is significantly and instantaneously reduced, e.g., for a typical NIF beam with an intensity of 2×10^{15} W/cm^2, the fraction of the beam power at intensities above $5\times I_0$ (where I_0 is the mean intensity) is 4% for an RPP beam with one polarization but 0.3% for two polarizations. In Fig. 3-8(a), the power probability distribution function in vacuum at focus is shown for one polarization and for two uncorrelated polarizations as appropriate for PS. The spatially averaged intensity in both cases is 2×10^{15} W/cm^2. PS narrows the distribution about the mean intensity so that there is actually more power in speckles only a few times the mean intensity. However, there is much less power at very high intensity. The power distribution for an RPP distribution at half the mean intensity in Fig. 3-8(a) makes it clear that PS is not as effective in lowering the power at high intensity as simply halving the intensity.

The effect of PS and SSD on stimulated Brillouin and Raman backscatter while allowing for the self-focusing of the incident and reflected light has been simulated with F3D (Berger *et al.*, 1998) in homogeneous plasma (Lefebvre *et al.*, 1998; Berger *et al.*, 1999) with plasma and laser parameters as given for Fig. 3-7. Both $f/4$ and $f/8$ focusing were simulated. Because filamentation grows on a time scale

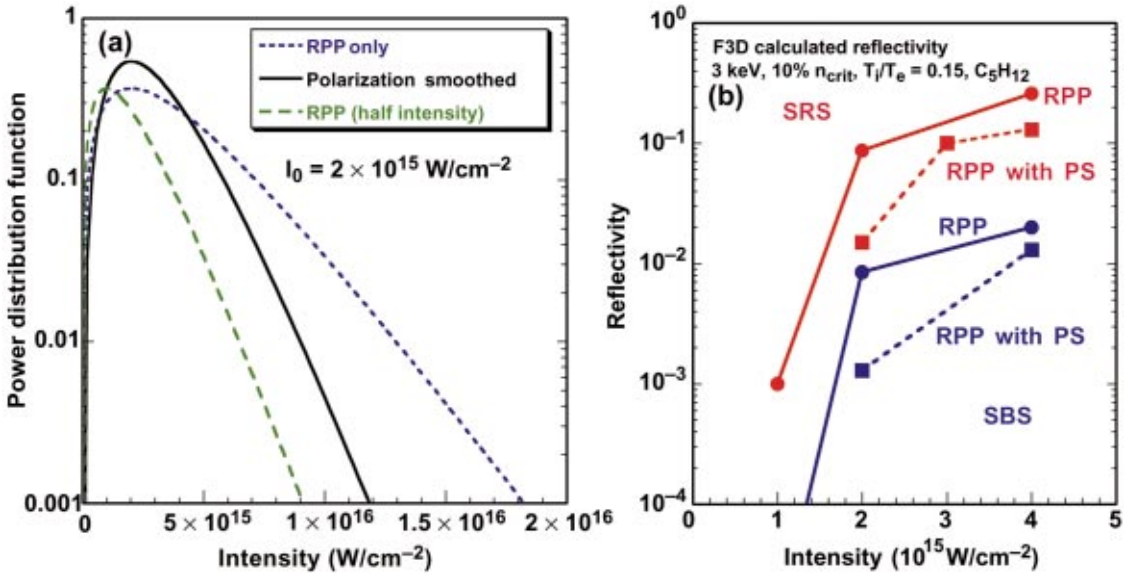

FIG. 3-8. (Color) Polarization smoothing (PS) reduces the fraction of the laser beam power at high intensity and hence reduces backscatter. (a) The distribution of laser power at the focal spot is shown vs intensity for one polarization (RPP), for two independent polarizations (PS) and for one polarization with half the total power. PS reduces the number of high-intensity hot spots, and narrows the distribution about the mean intensity. (b) In F3D calculations, PS reduces SRS and SBS backscatter.

Downloaded 20 Mar 2011 to 69.181.48.121. Redistribution subject to AIP license or copyright; see http://pop.aip.org/about/rights_and_permissions

which can be comparable to the SSD smoothing time, temporal beam smoothing can suppress it directly as shown in Fig. 3-7.

Although self-focusing in high-temperature plasma is undesirable and generally increases backscatter, there are conditions where the temperature and density perturbations induced by the laser may reduce or at least lessen the severity of the backscatter (Kruer *et al.*, 1999; Tikhonchuk *et al.*, 2001).

Although the SSD bandwidth is typically too small to reduce the SBS and SRS growth rate directly (Laval *et al.*, 1977), the F3D simulations show that reducing filamentation reduces the nonlinear enhancement of the gain exponent for these instabilities in the Nova gasbag conditions. Moreover, if the bandwidth is big enough that a speckle dissolves before SBS grows to saturation, SSD can also reduce the SBS reflectivity (Mounaix *et al.*, 2000). Dramatic reductions in SRS and SBS are calculated under conditions when the intensity gain exponents are less than 20. Much less reduction is calculated for the higher gain exponents anticipated for NIF and simulated by the Nova experiments. However, reduction of a factor of about 2 is calculated and this is significant if the reflectivity is from 10% to 30% as experienced in some experiments on Nova.

The growth rate for SRS is typically about 10^{13} s^{-1}, an order of magnitude larger than the maximum bandwidth (about 3×10^{-4} to $10^{-3}\omega_0$ which is 3×10^{11} to 10^{12} s^{-1} or 1–3.5 Å at 0.351 μm laser wavelength) achievable with NIF. Thus, SSD can have no direct effect on SRS. On the other hand, PS is instantaneous and can reduce the growth of SRS that depends on the higher intensity speckles. SBS with growth rates not much larger than the maximum bandwidths may be affected by both SSD and PS.

F3D calculations of the SRS and SBS reflectivity as a function of the mean laser intensity are shown in Fig. 3-8(b) with and without PS for the same plasma parameters as in Fig. 3-7 ($n/n_c=0.1$, $T_e=3$ keV, and $T_i/T_e=0.15$) parameters appropriate for low-Z gasbags. With a simulation plasma length of 0.35 mm ($1000\lambda_0$), less than the length of the plateau region in a gasbag, the linear intensity gain exponents of 12 for SRS and 10 for SBS at 2×10^{15} W/cm^2 were less than calculated for NIF or gasbags. The gains at 4×10^{15} W/cm^2 are comparable to those expected for NIF and for the Nova gasbags, but the effects of self-focusing and plasma induced laser beam incoherence are bigger than in the experiment. Although the biggest reductions are at the lower intensities, there is still a noticeable reduction at 4×10^{15} W/cm^2 where the gain exponents are comparable to those for NIF and gasbags (Berger, 2001).

Although these F3D simulations were able to predict the qualitative behavior of the effects of beam smoothing, quantitative predictions await the further development of models of wave-particle and wave–wave nonlinearities that can reproduce the essential ingredients of these processes in the evolution of SRS and SBS. As discussed in Sec. III B 3, nonlinear modification of the density and flow velocity by ponderomotive forces from the plasma and light waves and some simple models of wave–wave interactions have already been included in F3D. Models of effects of trapping in reducing the linear damping and inducing frequency shifts are in development.

5. Laser beam deflection

Laser–plasma interactions have effects on NIF hohlraums beyond the loss of laser power caused by stimulated backscatter. Two processes which have been examined in detail are laser beam deflection (Short *et al.*, 1982; Hinkel *et al.*, 1996; Moody *et al.*, 1996; Rose, 1996; Ghosal and Rose, 1997; Hinkel *et al.*, 1998; Young *et al.*, 1998) and energy transfer between crossing beams (Kruer *et al.*, 1996; Kirkwood *et al.*, 1996a; Kirkwood *et al.*, 1997). Both of these processes have been observed in Nova experiments.

In the hot spots of the laser beam, density depressions are formed ponderomotively (or thermally) and light is refracted into them, which can cause filamentation as discussed previously. In the presence of a transverse plasma flow, these density depressions form downstream from the laser beam's high intensity regions. Light refracted into the lowered density is thus deflected in the direction of the flow. This process is strongest when the transverse flow is nearly sonic, which happens near the laser entrance hole (Hinkel *et al.*, 1998). There is no threshold for this process, unlike filamentation or whole beam self-focusing. However, the presence of filamentation or self-focusing can enhance the beam bending effect by locally increasing the intensity and the density gradient.

By taking transverse position and momentum moments of the paraxial wave equation one can readily show that the rate of change of the mean propagation direction, $d\langle\alpha\rangle/dz$ is given by (Williams, 2002)

$$\frac{d\langle\alpha\rangle}{dz}=-\frac{1}{1-n_e/n_c}\frac{\langle\nabla_\perp n_e\rangle}{2n_c}, \tag{3-15}$$

where n_e is the electron density and n_c is the critical density. The average $\langle\,\rangle$ is weighted by the laser intensity. Performing this average, the beam bending scales as

$$\frac{d\langle\alpha\rangle}{dz}\approx-\frac{1}{1-n_e/n_c}\frac{n_e}{n_c}\left(\frac{v_0}{v_e}\right)^2\frac{1}{L_\perp}F \quad \text{(beam, plasma)}, \tag{3-16}$$

where α is the angle of deflection and $L_\perp$ is the transverse scale size of the laser intensity (the speckle size for an imperfect or RPP beam). Here, the $(v_0/v_e)^2$ dependence of ponderomotively induced density fluctuations on the laser intensity has been factored out. The dimensionless function F contains the detailed dependence of the bending rate on the beam characteristics (e.g., Gaussian, RPP, SSD) and the plasma conditions, particularly its transverse Mach number and ion–acoustic damping rate. In collisional plasmas, it contains a factor quantifying the enhancement of the ponderomotive force by thermal effects. This function has been investigated in some detail for a variety of analytically tractable beam and plasma models (Rose, 1996; Bezzerides, 1998; Hinkel *et al.*, 1998).

These analytical studies and simulations using F3D conclude that the greatest bending occurs when the transverse flow is near sonic or mildly supersonic, in which regime it is

Downloaded 20 Mar 2011 to 69.181.48.121. Redistribution subject to AIP license or copyright; see http://pop.aip.org/about/rights_and_permissions

only weakly dependent on the ion–acoustic damping rate. In this near-sonic regime, beam bending can be thought of as internal forward Brillouin scattering, in which there is a resonant interaction between different k components of the laser, where ion waves at the different k's are Doppler shifted by the flow to zero frequency. In steady state, when the transverse flow is subsonic, the beam-bending rate is proportional to the ion-damping rate. However, time-dependent simulations with F3D with (static) RPP beams indicate that the time to reach steady state increases with decreasing damping and with increasing laser propagation distance. Because of this, subsonic beam deflection does not vanish in the limit of zero ion–acoustic damping as would be inferred from steady state theory.

For a ''statistical'' beam with random or kinoform phase plates, perhaps with additional temporal smoothing, such as SSD, the $\langle \nabla_\perp n_e \rangle$ is additionally averaged over the beam statistics. With temporal smoothing, the speckle distribution in the plasma is no longer stationary. Typical speckles have a residence time given by the inverse of the temporal bandwidth, $\Delta\omega^{-1}$. This changes (mostly reducing) the density perturbations in the plasma induced by the imposed intensity fluctuations.

Beam bending transfers transverse momentum from the flowing plasma to the light, slowing the flow. Rose (Rose, 1996) has pointed out that a beam with many speckles can represent a substantial impediment to the flow. In a supersonic flow, a bow shock can form upstream of the beam, putting the beam in a subsonic flow in which the bending is reduced. Crossing beam energy transfer discussed in the next section could also be affected.

Significant reduction in beam deflection through plasmas containing sonic and supersonic transverse flows is obtained once the bandwidth $\Delta\omega$ becomes of order of the characteristic ion–acoustic frequency $C_s k_0/2f$ of speckle sized perturbations. In subsonic transverse flow, where the beam bending rate is smaller, proportional to the ion damping rate, the addition of bandwidth can *increase* the rate. This can occur because the speckle motion induced by SSD can combine with the plasma flow to give supersonic relative motion. In effect, with SSD, the beam bending rate gets averaged over the distribution of relative velocities between the speckles and the flow. However, in a hohlraum, where the laser beam path traverses both supersonic and subsonic flows, the net effect of SSD bandwidth is to decrease the beam bending, because the major contribution, from the supersonic portion of the trajectory, is reduced (NTIS Document, 1997). Of the various SSD parameters, the bandwidth is the most important, but there is a predicted decrease in bending rate as the number of color cycles increases. There is also dependence on the direction of the SSD smoothing with respect to the flow (Rose and Ghosal, 1998).

The analytical calculations described above provide useful guidance and insight to the scaling of beam bending with plasma parameters and the choice of smoothing scheme, but more detailed numerical calculations are required to accurately quantify the effect. The most significant limitation of the analytic theory is that it does not account for changes to the statistics of the laser beam which evolves from the vacuum values as it propagates through the plasma. These effects can be modeled with a laser–plasma interaction code such as F3D. Filamentation broadens the k spectrum of the waves. Time dependent fluctuations in the plasma increase the beam's temporal bandwidth. SBS and SRS can extract energy from the beams higher intensity regions.

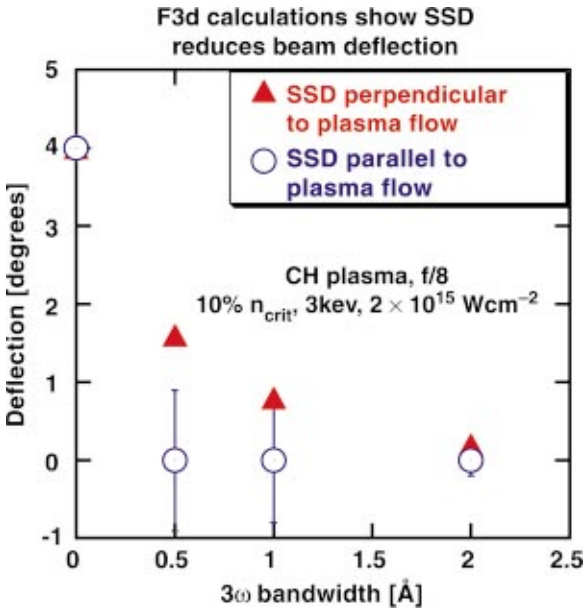

FIG. 3-9. (Color) SSD will be used to reduce beam deflection in flowing plasma. The current NIF baseline has SSD perpendicular to plasma flow in the hohlraum in order to minimize the focal spot smearing in the short direction of the elliptical NIF focal spot. Either orientation of SSD relative to the plasma flow will reduce beam deflection with modest bandwidth. Either orientation will be available on NIF with minimal setup requirements.

F3D simulations with $f/8$ beams show a preference for smoothing parallel to the flow as shown in Fig. 3-9 (Hinkel, 1996). Corresponding simulations at $f/4$, where nonlinear effects from speckle self-focusing no longer played a role, agreed with the (linear) analytic theory, showing no significant dependence on direction of smoothing or increasing the number of color cycles beyond one.

An effect of SSD smoothing is to broaden the vacuum beam spot in the smoothing direction. In order to focus through a minimal laser entrance hole of a hohlraum, it is desirable to put the SSD smoothing direction along the long axis of the elliptical beam spot (see Fig. 3-14 for an example of a NIF beam elliptical focal spot). Assuming azimuthal symmetry, plasma flows would be along the short axis of the ellipse, or perpendicular to the smoothing direction, which is the less desirable smoothing direction for the reduction of beam bending. Figure 3-9 shows the difference between the smoothing directions is insignificant for 2 Å of bandwidth at 351 nm. Increasing SSD bandwidth to this level or adding PS are options if smoothing perpendicular to the flow is required. In addition, filamentation near the LEH in NIF, the source of the difference between the smoothing directions, might be less in NIF since the NIF electron temperature is higher than in these calculations. An important bending saturation effect is observed if filamentation is controlled. Energy is then primarily transferred between existing k components

Downloaded 20 Mar 2011 to 69.181.48.121. Redistribution subject to AIP license or copyright; see http://pop.aip.org/about/rights_and_permissions

of the laser, that is, within the beam cone, limiting the maximum deflection. If filamentation is important, as in the high intensity regions of an unsmoothed (no RPP) beam, the k-spectrum spreads and deflection to larger angles ensues. This was observed in simulations modeling the deflection of smoothed and unsmoothed beams in Nova hohlraums (Hinkel *et al.*, 1998).

The most significant portion of the laser deflection typically occurs near the LEH. It is there that the transverse flows are near sonic. In addition, it is there that the deflection has the greatest lever arm. An equal deflection occurring later in the beam path near the wall gives rise to a smaller displacement of the laser spot. The inner and outer NIF beams encounter similar plasma conditions near the LEH, but because of this lever arm effect, the inner beams are the most critical for deflection.

In general, F3D simulations for filamentation and beam deflection angle for NIF show a smaller angular deflection and less filamentation than for the Nova scale-1 methane-filled hohlraums or for the gasbags discussed below (Hinkel, 1996). At peak power, the factor $(v_0/v_e)^2(n/n_c)$ in Eq. (3-16) is ten times smaller for NIF than Nova hohlraums because, at the sonic point, the NIF density is three times smaller, the NIF electron temperature is almost two times larger, and the mean intensity in NIF designs is 50% smaller than Nova hohlraums. This counterbalances the transverse flow scalelength which is about 4.5 times longer in NIF.

With the current Accelerated Strategic Computing Initiative (ASCI) machines, full-Nova-scale F3D simulations have been done (without transverse flow) (Still *et al.*, 2000) Complete F3D simulations of NIF scale beams are not yet computationally feasible. With the next ASCI upgrade (Still, 2002), filamentation only NIF-scale runs should become possible. However, by piecing together a series of F3D runs, each characteristic of successive parts of the beam path, beam deflections of 550 and 230 μm were estimated for the inner and outer RPP beams, respectively, at the hohlraum wall, with no SSD. With 3 Å of SSD, these are reduced to 150 and 58 μm, respectively.

Control of beam deflection has been demonstrated by spatial beam smoothing in 10-beam Nova symmetry experiments, as discussed in Sec. V. In these experiments, the observed shift in the optimal pointing for symmetry, with and without beam smoothing, was consistent with F3D calculations. Experiments on Nova with a single smoothed beam also showed the expected shift in the location of x-ray emission from the hohlraum wall. In these experiments, addition of an RPP, by itself, to the $f/4$ beam was sufficient to eliminate the deflection within the experimental uncertainty (± 50 μm) (Delamater *et al.*, 1996) in agreement with F3D simulations (Hinkel *et al.*, 1998). Thus, the additional effects of SSD on beam bending were not testable in scale-1 hohlraums.

The near field images of the SBS from Nova hohlraums are also deflected in a direction consistent with deflected incident laser light (Kirkwood *et al.*, 1997a; Glenzer *et al.*, 2000). Such images inspired Rose to conclude that beam deflection was responsible for asymmetric capsule implosions. The SBS is produced in the high-Z gold blowoff plasma near the hohlraum wall after the incident laser beam has been deflected near the LEH. A fluid model is sufficient to describe the beam bending effect, so most studies have made use of this simplification in description. Because of flow, and because the plasma charge state, atomic number, and temperature in the gold differ from those in the low-Z plasma near the LEH, the SBS produced in the gold is not amplified near the LEH nor does it retrace the path of the incident light. Thus, it is aligned along the direction of the deflected incident light and is diagnostic of beam deflection. Fluid simulations of beam deflection and backward SBS (Hinkel *et al.*, 1999), which include the axial flow and density gradients as well as the transverse flow, reproduce the experimental observations. Even tour de force PIC simulations, such as those carried out by Vu (Vu, 1997) generally do not capture the differences between the Au where the SBS growth occurs and low-Z regions of a hohlraum responsible for the beam deflection. The simulations of Vu did include both beam bending and SBS but showed no deflection because most of the SBS gain occurred before the beam bending.

6. Crossing-beam energy transfer theory

Closely related to filamentation, stimulated Brillouin forward scatter is an instability in which the light is scattered in the near forward direction to larger angles with a small frequency shift. This has generally been observed to be a weak instability. However, for two laser beams crossing in a plasma, if the difference of the frequencies equals the acoustic frequency ($\Delta\omega = C_s|\Delta\mathbf{k}|$), some of the power in the higher-frequency beams will be transferred to the lower-frequency beam. Here, C_s is the acoustic speed and $\Delta\mathbf{k}$ the difference in wave vectors between the two beams. In a flowing plasma, there will be a Doppler shift in the relative frequencies of the beams. In appropriate flow conditions (where the perpendicular flow velocity equals the sound speed), the crossing beam energy exchange can occur for equal-frequency beams. The Doppler shift of each light wave will depend on its angle relative to the flow. If $\Delta\mathbf{k}\cdot\mathbf{U} = kC_s$, the Doppler shifted higher-frequency wave can resonantly decay locally into the other. In some cases, significant power can be transferred from one beam to another by this process.

The first case of crossing-beam energy transfer evaluated theoretically for NIF was the case in which the inner and outer cones of NIF beams had an array of four frequencies (Kruer *et al.*, 1996). [The multiple frequencies were originally envisioned as part of a four-color smoothing scheme (Pennington *et al.*, 1994; NTIS Document, 1996), which was abandoned when calculations (NTIS Document, 1995) and experiments showed it was ineffective in controlling laser plasma instabilities (NTIS Document, 1995a).] The higher frequency components of one beam could then scatter via stimulated forward Brillouin scatter (SFBS) into the other beam. Velocity inhomogeneity was shown to be an important limit on the transfer but not enough of a limit to render the effect unimportant. A large energy exchange would compromise NIF's ability to control symmetry by separately control-

Downloaded 20 Mar 2011 to 69.181.48.121. Redistribution subject to AIP license or copyright; see http://pop.aip.org/about/rights_and_permissions

ling the power and pulse shape on the inner and outer cone of beams. Two-dimensional fluid simulations of the energy exchange (Eliseev *et al.*, 1996) between two Gaussian light beams that cross at an angle of 20° showed that filamentation of each beam as well as Brillouin scatter to larger angles ($-20°$ and 40°) play an important role in the nonlinear dynamics.

The theoretical understanding of this process was enhanced by considering (McKinstrie *et al.*, 1996) in a homogeneous plasma the 2D interaction of crossing light waves with a frequency difference near an ion–acoustic wave resonance and by including (McKinstrie *et al.*, 1997) a number of frequency components as appropriate for the four-color smoothing scheme or SSD.

The distinction between beam deflection and energy exchange is somewhat artificial theoretically although the distinction in the NIF application is clear. Here, energy exchange is restricted to beams where the mean wave number between beams is bigger than the spread in wave numbers within the beam, $k_0/2f$. In a steady-state analysis (Rose and Ghosal, 1998a), the important case with both a frequency difference between the beams and uniform flow for RPP smoothed laser beams was considered so that both deflection and energy transfer occur. Since flow can affect self-focusing and the wave number composition of the beams, the interaction of unequal frequency beams in a stationary plasma and interaction of equal frequency beams in a flowing plasma are not completely equivalent.

Crossed-beam experiments on Nova, described below, resulted in significant energy transfer but less than estimates based on theory and fluid simulations. Thus, the PIC code Zohar was used to examine how nonlinear effects on the acoustic wave driven by the crossing beams might limit the transfer (Cohen *et al.*, 1998). These simulations found that trapping and wave–wave nonlinearities do have a substantial effect in reducing the transfer. This is also an active area of research and work remains before we can scale confidently to NIF. It is a considerable challenge to simulations because the angle between the beams can strain the validity of the paraxial approximation and the driven resonant ion waves demand more resolution than ion waves driven by speckle self-focusing of each beam. Yet, there is not the clear separation in scales that is used effectively in treating filamentation and backscatter in paraxial codes.

C. LPI experiments on Nova

Laser–plasma interaction experiments have been carried out with a variety of beam smoothing approaches and a variety of plasma conditions. The plasma conditions were as close to those expected in the NIF 300 eV baseline targets, as well as conditions expected in both higher and lower radiation-temperature hohlraums, as could be produced with Nova. These studies were intended to provide a broad database for optimizing the ignition design.

To emulate the low-Z regions of NIF hohlraums, various targets were explored, including low-density foams and thin exploding foils. The most promising targets were ''gasbags'' and large gas-filled hohlraums (of which two types were developed). The plasmas were created by irradiating a thin-walled gas balloon or a sealed hohlraum (Powers *et al.*, 1995) containing of order 1 atm of a low-Z gas. In hohlraum targets large enough to emulate the NIF low-Z plasma, LASNEX simulations show that almost all the laser light is absorbed in the gas, and very little of the Au wall is heated. Thus, the Au wall laser–plasma interaction is best studied in the standard Nova 1.6 mm diameter scale-1 hohlraum. The scale length of plasma in the high-Z wall is determined by the inverse bremsstrahlung absorption length rather than the hohlraum size, and the high-Z plasma in a standard Nova scale-1 hohlraum is similar to that in NIF hohlraums. Figure 3-10 compares the LASNEX simulations of the gasbag and scale-1 hohlraums to simulated conditions in NIF hohlraums. Because of the longer pathlength in low-Z material, LPI effects in the low-Z gas should be greater for the inner beams than for the outer beams. Calculated gains for SBS and SRS in gasbags are similar to that for the inner beams as shown in Fig. 3-10. The NIF outer beam intensity at the wall is higher than that of the NIF inner beams so high-Z LPI effects are larger for the outer beams than for the inner beams. Most of the calculated SBS gain for the outer beams occurs in the high-Z plasma and the SBS gain for the NIF outer beams and a Nova scale-1 hohlraum are similar, as shown in Fig. 3-10.

1. LPI plasma diagnostics

Figure 3-11 shows the placement of the various light scattering diagnostics in the Nova target chamber. The beam shown is the interaction beam (beamline 7), on which the NIF beam smoothing and f/number were replicated.

The Full Aperture Backscatter Station (FABS) (Kirkwood *et al.*, 1997a) viewed the scattered light that propagates back down the beamline and is transmitted by the 1ω (1054 nm) turning mirror closest to the chamber. This mirror has high reflectivity (about 95%) for the incident 1ω light but transmits about 30% of backscattered 3ω (351 nm) light. A large hole was cut in the back of the mirror mounting box, allowing access to the scattered light transmitted by the mirror. Since light scattered from the target passes back through the Nova focusing lens, it is recollimated and is 70 cm in diameter when it emerges from the back of the mirror box. A second $f/4.3$ Nova lens was then used to focus the beam into the various diagnostic packages to allow analysis of the scattered light. A time-resolving SBS spectrometer, which was calibrated with a time-resolving diode, allowed the power history for SBS to be recorded. A CCD camera also recorded a time-integrated image of the SBS backscatter angularly resolved within the diagnostic acceptance angle (i.e., SBS imaged in the plane of the Nova lens).

A diffuser placed in the FABS soon after the focusing lens was used to monitor SRS scattering. The scattered light was then recorded by a filtered diode. A complication was introduced by severe spectral modulations in the transmission of the turning mirror. The modulation is due to the multilayer coating on the mirror, which is optimized to reflect narrow-band 1ω laser light efficiently, not to transmit a broadband signal. This modulation makes quantitative measurements of SRS difficult. The difficulty was addressed by using a streaked optical spectrometer to spectrally resolve the

Downloaded 20 Mar 2011 to 69.181.48.121. Redistribution subject to AIP license or copyright; see http://pop.aip.org/about/rights_and_permissions

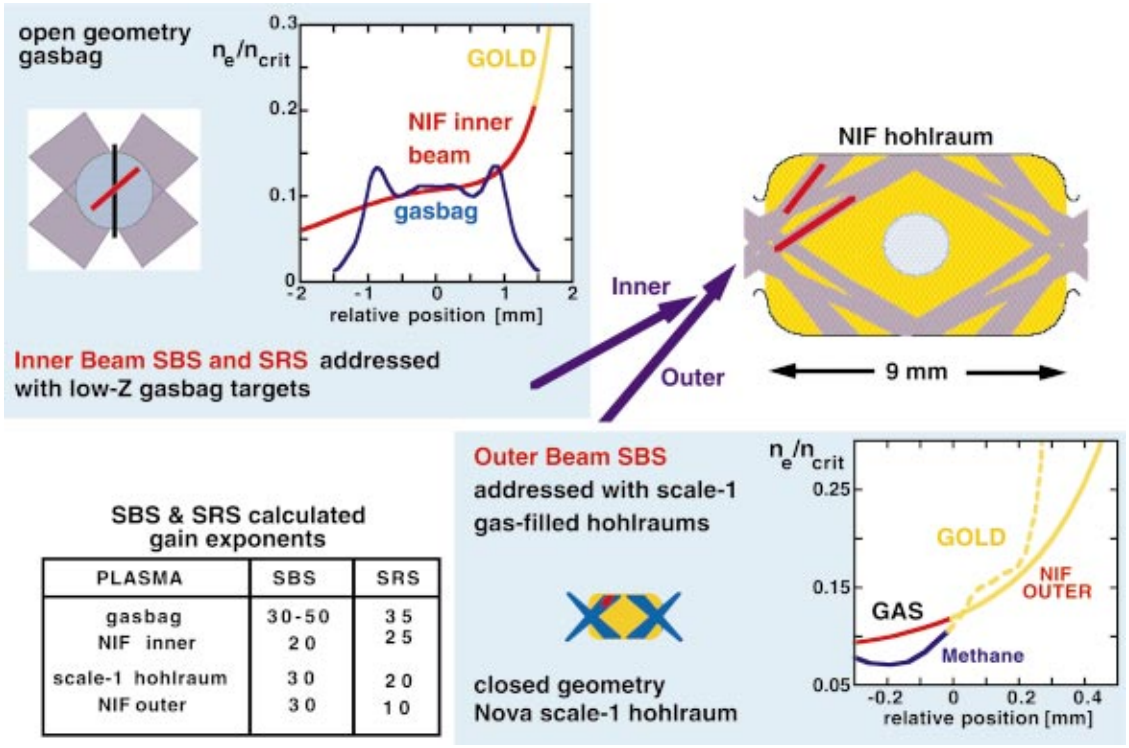

FIG. 3-10. (Color) Nova gasbags and scale-1 hohlraums develop plasma conditions and linear LPI gains (calculated by the postprocessor LIP with LASNEX plasma conditions) similar to NIF plasma conditions for the most unstable regions of the inner beams and outer beams, respectively. The interface between the low-*Z* fill and the gold blowoff is indicated by change in color to yellow from blue or red. The red bars along the beam paths on the NIF hohlraum schematic show what part of the NIF laser plasma interaction is simulated either by the gasbag or by the scale-1 hohlraum.

SRS signal seen by the diode. The spectrum could then be corrected using the calibrated mirror transmission function, and the diode signal (which represents an integral of the spectrum) could be corrected accordingly.

The FABS diagnostic was calibrated *in situ* by using an uncoated spherical mirror placed on the far side of the chamber. Beam 7 was then focused through a large hole (4 mm diameter) in a plate positioned at chamber center. The plate rejected the unwanted harmonics of the laser beam (e.g., 1054 nm and 527 nm in the case of a 351 nm calibration shot), because the chromatic aberration in the Nova lens and the hole in the center of the Nova beam meant that only one color was focused at the hole. The light then diverged before it was reflected by the uncoated mirror (metrologized off-line) and sent back down the beam line, where it was recorded as a known amount (about 8% of the incident power) of light.

The SBS detectors were calibrated using the 3ω calibration shots that were run routinely to maintain confidence in the precision Nova incident-beam diagnostics. To calibrate the SRS detectors, 2ω (527 nm) light was used, since its wavelength is in the middle of the spectral range of SRS light from most of the experiments. The sensitivity of the other components in the diagnostic relative to their sensitivity at 2ω was calibrated off-line. This process resulted in a typical uncertainty of 10% to 20% in the SBS and 20% in the FABS SRS measurements.

To complement the FABS, the diagnostic set included time-integrated diodes spaced at about 10° intervals around the chamber to look at sidescattered light (Fernandez *et al.*, 1995; Kyrala *et al.*, 1997).

The near-backscattering imager (NBI) extended the continuous coverage of SBS and SRS backscattering outside the lens to 20° from the lens axis. This was achieved by placing a large annular plate of bead-blasted aluminum around the outside of the lens assembly within the target chamber. The near-backscattered light from the target scatters from the plate as if from a diffuse screen and is then imaged by two TV cameras on the far side of the target chamber. Filters on the TV cameras allowed us to separately measure SBS (near 351 nm) and SRS (400 to 700 nm). Off-line calibration of the plate reflectivity and the known filter and TV camera throughput made it possible to spatially integrate an image frame at shot time to determine the total amount of scattered light. The images could also be combined with the images recorded by the FABS SBS and SRS cameras to provide an image of the angular distribution of scattering inside and outside the interaction beam solid angle. The diagnostic was supplemented by time-integrating diodes and fiber optics viewing the target through holes in the plate. The fiber optics allowed samples of the scattered light to be transported to an optical streak camera, where differences in time history as a function of scattering angle could be quantified.

The calibration of the plate reflectivity plus camera sensitivity could be checked *in situ* by comparing the scattered intensity with that recorded on the diodes. The sensitivity of the FABS and the NBI could also be compared by using a Au foil target at the chamber center to reflect energy from one of

Downloaded 20 Mar 2011 to 69.181.48.121. Redistribution subject to AIP license or copyright; see http://pop.aip.org/about/rights_and_permissions

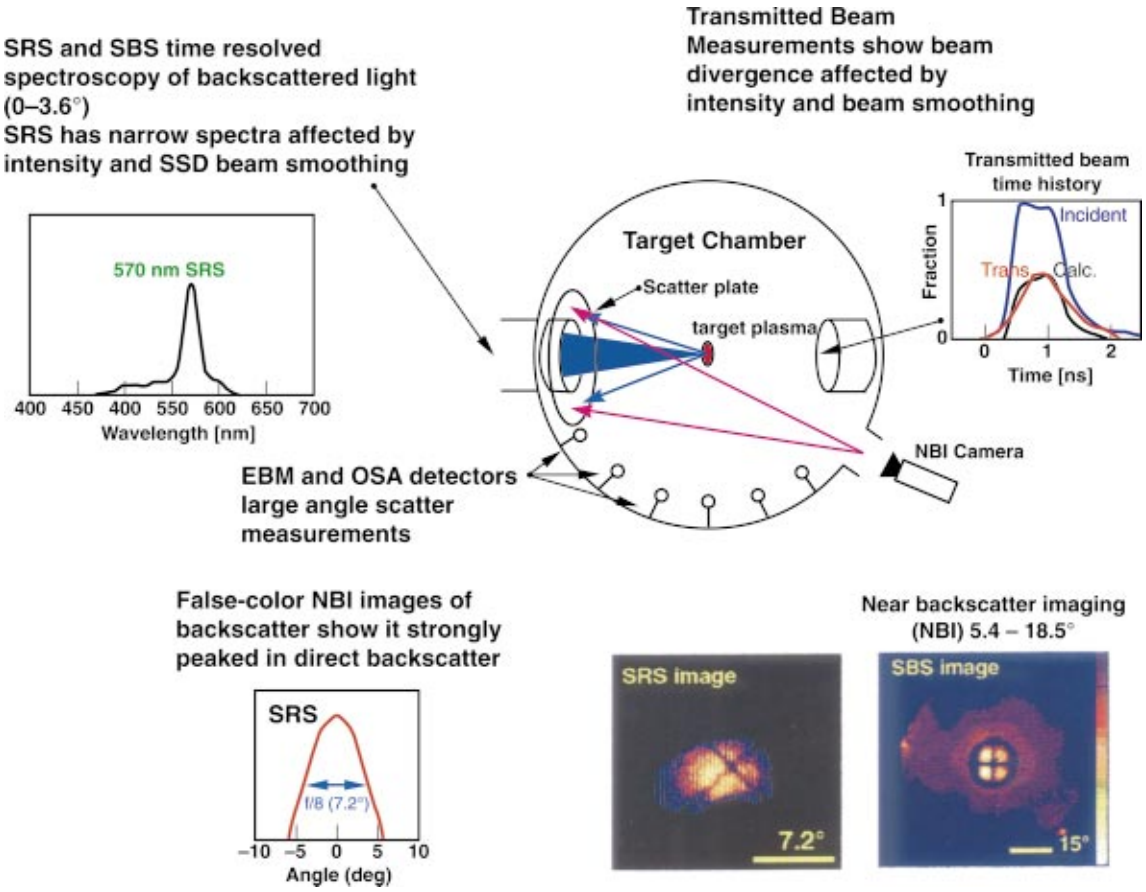

FIG. 3-11. (Color) Several diagnostics were implemented on Nova to study scattered light over a wide range of angles and frequencies. Also used but not shown on this schematic is Thomson scattering.

the other beam lines towards beam 7. This technique uses the ''glint'' reflected from the Au foil to fill both diagnostics with light. Comparison of the glint imaged in both diagnostics then revealed any inconsistencies as sharp jumps in image intensity where the coverage of the two diagnostics abutted one another. Contamination of the plate by target debris is a potential source of inconsistency. The uncertainty in the NBI SRS and SBS numbers is about 30% for the data discussed below.

Sidescattered SBS light in these experiments was studied with a diode array. The diodes were time integrating, so they could not distinguish the contributions due to sidescattering from the heater beams. The solution to this problem was to put fiber optics inside the chamber beside each diode to relay the SBS light from there to an optical streak camera, which then provided a time-resolved history of the sidescattering that could be normalized with the time-integrated diode signal (Fernandez *et al.*, 1995). The contributions due to sidescattering from the heater beams could then be seen occurring early in time; those due to the interaction beam would come later. This system of combined diodes and fiber optics was called the oblique scattering array (OSA). In all applications involving diode measurements, it was necessary to absolutely calibrate the detectors, filters, and blast shields off-line and then monitor how their calibration changed in the target chamber due to debris buildup by frequent recalibration and replacement of debris shields and filters.

Another scattered light diagnostic shown in Fig. 3-11 is the Transmitted Beam Diagnostic (TBD) (Moody *et al.*, 1997; Moody *et al.*, 1999), whose purpose was to measure the amount of light transmitted by the open-geometry plasmas and to study the effect of processes such as diffraction from filaments on the divergence of the transmitted beam. The device was a frosted glass plate mounted on the opposite side of the chamber from Beam 7. In its original form, the plate intercepted transmitted and forward-scattered light over an angle equivalent to $f/7.2$. However, the TBD was enlarged to detect light over a $f/3.6$ cone since the beam expanded beyond the $f/8$ original beam divergence as a consequence of refraction, diffraction in filaments, or forward SBS. The plate was viewed by an optical framing camera that recorded the beam angular spread at four distinct times, together with a streak camera that resolved the divergence in one dimension continuously in time. Absolute measurement of the transmitted light was made using a fast diode that gave the history of the beam integrated in both spatial dimensions. The system was calibrated by firing a shot with known 3ω laser energy through an aperture placed at chamber center that removed the 1ω and 2ω light. A secondary measurement made with the TBD system was quantification of forward Raman scattering by injecting some of the transmitted light through a fiber optic into a low-resolution streaked optical spectrometer. Fiber-optic coupling was also used to inject the forward-scattered light into a high-resolution spectrometer to

Downloaded 20 Mar 2011 to 69.181.48.121. Redistribution subject to AIP license or copyright; see http://pop.aip.org/about/rights_and_permissions

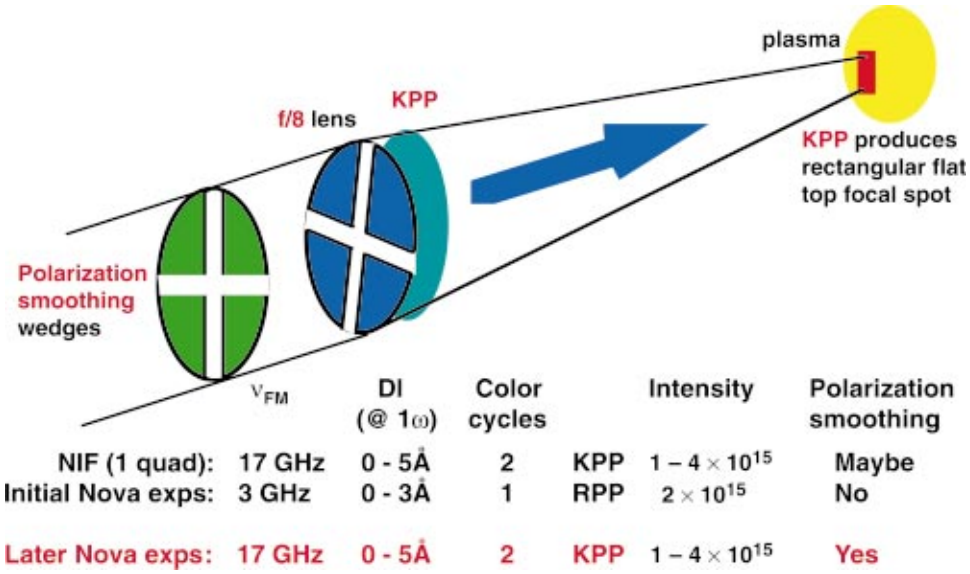

FIG. 3-12. (Color) A Nova beam was converted to $f/8$ to simulate a NIF quad and to test the planned implementation of NIF beam smoothing. Experiments have been done using a 17 GHz modulator with up to 5 Å (1ω) of bandwidth. This is similar to the smoothing approach planned for NIF. KDP wedges are added before the KPP for PS; more details are shown in Fig. 3-13 for SSD and Fig. 3-15 for PS.

investigate the effects of filamentation on laser wavelength.

The Thomson scattering (TS) diagnostic (Glenzer, 2000) was implemented at Nova in 1996 to investigate the properties of two-ion species plasmas (Glenzer *et al.*, 1996) and to measure temperatures and densities in underdense large-scale length plasmas. This diagnostic has provided important data for testing our radiation-hydrodynamic modeling capability (Glenzer *et al.*, 1996; Glenzer *et al.*, 1999) as well as atomic physics codes (Zimmerman and More, 1980; Lee, 1987). Thomson scattering spectra provide a direct measurement of the plasma properties without the need for modeling. Moreover, the temporal and the spatial resolution of the measurements was greatly improved compared to data obtained with spectroscopy. Using TS, we have obtained the electron temperature T_e, the electron density n_e, the averaged ionization state Z, and the plasma flow velocity at known positions in both gasbag and hohlraum targets. In addition, in plasmas with large ion Landau damping such as in low-Z or two-ion species plasmas, the ion temperature T_i of the plasma can also be determined with TS. These data are obtained by focusing a probe laser into the plasma and by imaging the scattered light onto spectrometers which show scattering resonances at the ion–acoustic wave and at the electron plasma wave frequencies. Initially these measurements were performed with one beam of the Nova laser with frequency doubled light at 527 nm. The use of 527 nm light limited TS to experiments where stray light levels could be minimized either by shields or by special heater and probe beam configurations. The TS capability at the Nova Laser Facility was upgraded by implementing a high-energy 4ω probe laser operating at 263 nm. A total energy greater than 50 J at 4ω, a focal spot size of order 100 μm, and a pointing accuracy of 100 μm was demonstrated for target shots (Glenzer *et al.*, 1999a; Glenzer *et al.*, 1999b). This laser provides intensities of up to 3×10^{14} W/cm^2 and meets the high-power requirements for laser–plasma interaction experiments in hohlraums. Stray light is much less important at 4ω since there is no residual 4ω light in the chamber produced by the heater beams. Moreover, the 4ω probe laser made it possible to probe higher density plasmas of $n_e > 2\times10^{21}$ cm^{-3}, a capability that has allowed the study of gradients which is important for high-Z plasmas from disk targets (Glenzer *et al.*, 1999) as well as for hohlraums (Glenzer *et al.*, 1999c; Glenzer *et al.*, 1999a; Glenzer *et al.*, 1999b). In addition, our capability to characterize higher-density plasmas with TS made experiments possible to study non-LTE radiation physics in steady-state Au plasmas (Foord *et al.*, 2000) and the temperatures of Au jet plasmas (Farley *et al.*, 1999) relevant to astrophysical phenomena.

2. Beam smoothing approaches on Nova

The beam smoothing techniques tested on Nova, indicated schematically in Fig. 3-12, have evolved to match planned NIF capabilities and potential modifications. Early experiments used RPPs (Kato *et al.*, 1984) for beam smoothing, with or without SSD. A schematic representation of SSD as implemented on Nova is shown in Fig. 3-13. The first SSD experiments on Nova used a 3 GHz modulator capable of generating bandwidths up to 3 Å at 1ω (1.0 Å or 0.25 THz at 3ω). RPPs produce an intensity distribution in the target plane that is an Airy function with as much as 16% of the light missing the LEH of a typical Nova hohlraum. Later experiments were performed with KPPs (Dixit *et al.*, 1994) and SSD using a high-frequency modulator (17 GHz) capable of generating bandwidths up to 5 Å at 1ω (1.6 Å or 0.4 THz at 3ω). KPPs can be designed so that the intensity distribution is essentially flat topped with up to 95% of the light entering the LEH (Dixit *et al.*, 1994). A potential problem with KPPs is that the focal spot may have more long-scale-length intensity inhomogeneities. As shown in Fig. 3-14, the KPP implemented on Nova has an intensity distribution similar to that for the current NIF KPP design. As discussed above, the laser bandwidth is the product of the FM modulator frequency, Ω, and the depth of modulation, α. To have the entire spectrum of bandwidth at any time requires a full color cycle across the lens so that smaller FM frequencies require more grating dispersion, β, and a time delay of τ

Downloaded 20 Mar 2011 to 69.181.48.121. Redistribution subject to AIP license or copyright; see http://pop.aip.org/about/rights_and_permissions

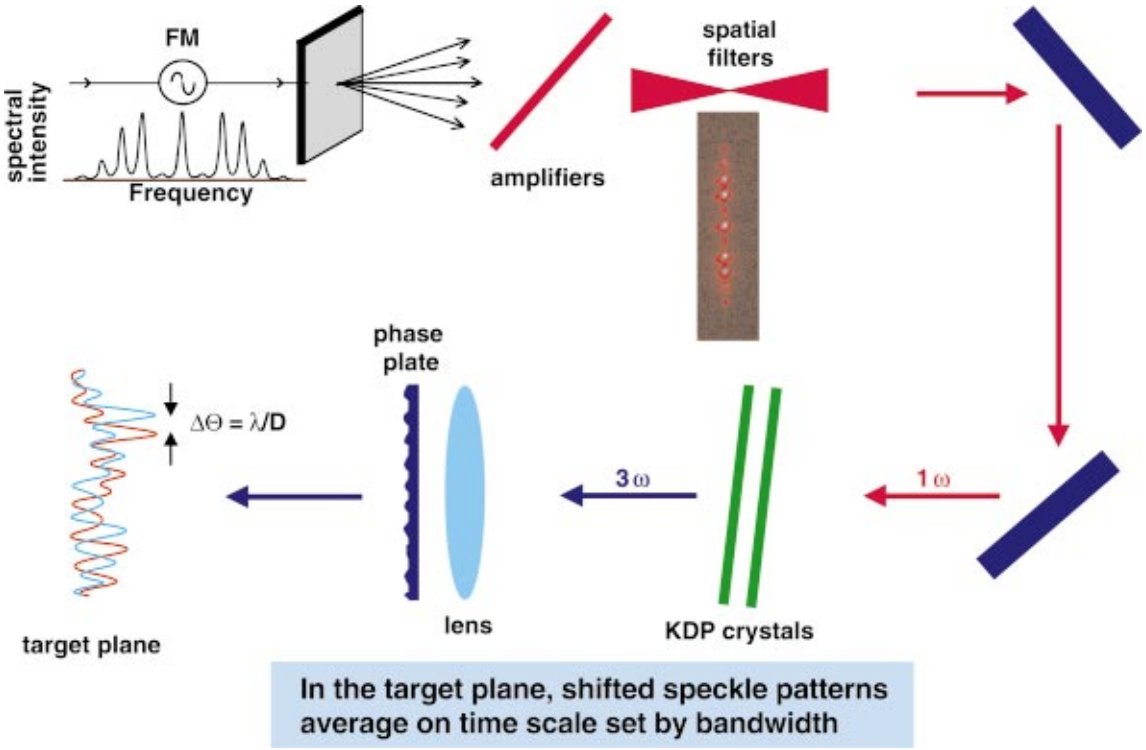

FIG. 3-13. (Color) SSD on Nova is applied by frequency modulating and dispersing the pulse (FM SSD) prior to amplification and conversion to 3ω.

~400 ps at 3 GHz. The dispersion smears the focal spot of a KPP along the smoothing direction and limits the maximum intensity available with SSD. The time delay also adds a rise and fall time to a pulse that, at 3 GHz, significantly changes the pulse shape which, among other effects, complicates interpretation. The 17 GHz modulator developed for the later experiments is needed for NIF and removes the limitations on experiments imposed by the 3 GHz modulator. A 1200 mm^{-1} grating was used to skew the pulse front by 150 ps, corresponding to two color cycles of SSD (Skupsky *et al.*, 1989; Rothenberg, 1997). (Each $f/20$ NIF beamlet will have one full color cycle of SSD, so NIF $f/8$ ''quads'' will have two color cycles of SSD across their width.) One goal of these later experiments was to verify that the combination of a high-frequency modulator and low-dispersion SSD with a KPP focal spot gives results similar to those obtained with RPPs and the lower frequency modulator.

The later experiments also tested polarization smoothing (NTIS Document, 1990; Lefebvre *et al.*, 1998; Pau *et al.*, 1994; Boehly *et al.*, 1999), which was implemented by using an array of Type I KDP doubler crystals cut at a wedge angle of 270 μrad as indicated in Fig. 3-15. The crystal wedges were inserted in the beam after the frequency tripling conversion crystals and were oriented such that the 3ω polarization vector was at 45° to the *e* and *o* axes of the crystals. The wedges deflected the beam 0.8 mm in the target plane with the speckle patterns due to the two polarization components displaced 30 μm relative to each other, leading to the averaging of intensity variations as the two speckle patterns are added incoherently. The 1D SSD displaced the laser speckle patterns in the target plane in a direction orthogonal to the direction of displacement due to the polarization smoothing wedges.

3. Gasbag experimental results

Gasbag targets are heated by nine unsmoothed Nova beams with 22 kJ of laser energy delivered in 1 ns (Glenzer *et al.*, 1997b). The mean heater beam intensity over the laser spot at the target is from 1.5 to 3×10^{14} W/cm^2, but there are large areas within the spot where the intensity is much higher. As a result, about 20% of the heater beam energy is backscattered. The time history of the gasbag electron temperature for a C_5H_{12} neopentane-filled target near the target center is shown in Fig. 3-16 from LASNEX calculations along with TS data taken at 200 microns from the gasbag center. When fully ionized, this gas fill gives an electron density of 9×10^{20} cm^3. The LASNEX calculations account for the measured backscatter losses from the heater beams by subtracting that power from the heater beams before illuminating the target (Glenzer *et al.*, 1997b). The electron temperature peaks at 1 ns at 3 keV just when the heater beams turn off and then cools. Temperatures obtained from spectroscopy, shown in Fig. 3-17, are similar. The measured ion temperature peaks at 700 eV also at 1 ns and decays 200 eV over the next 400 ps whereas in LASNEX it continues to increase from 620 to 780 eV. The reason for this discrepancy has not been determined. The 1 ns long square pulse, $f/8$ interaction beam turns on at 500 ps with an intensity of 2×10^{15} W/cm^2 (1.8 kJ in 1 ns).

Electron temperatures obtained (Marjoribanks *et al.*, 1992; Kalantar *et al.*, 1995; Kalantar *et al.*, 1995a; Klem,

Downloaded 20 Mar 2011 to 69.181.48.121. Redistribution subject to AIP license or copyright; see http://pop.aip.org/about/rights_and_permissions

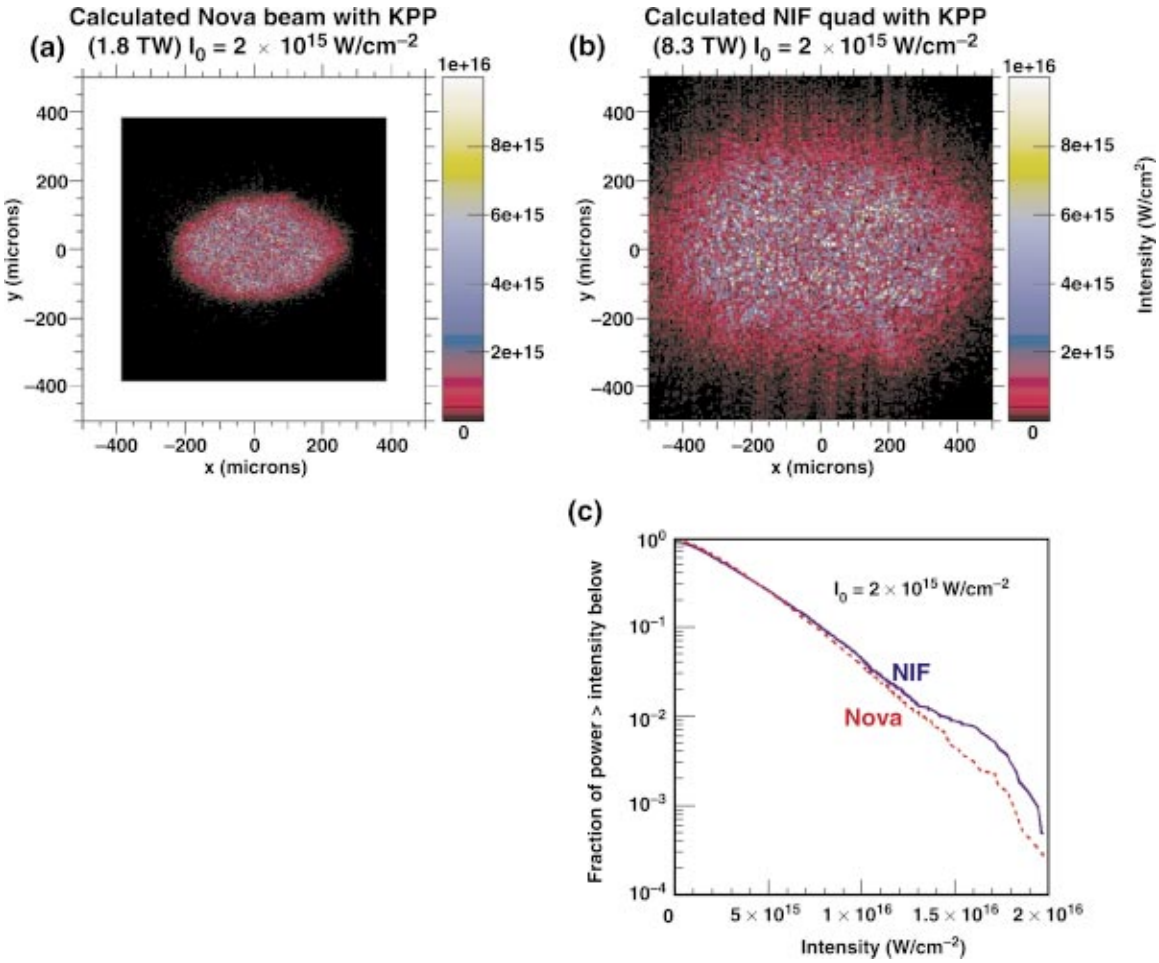

FIG. 3-14. (Color) A kinoform phase plate (KPP) is used to produce a focal spot for experiments at Nova and Omega (upper left-hand side) and NIF (upper right-hand side) with an intensity distribution (lower right-hand side) similar to that planned for NIF.

1995; Marjoribanks *et al.*, 1995) from x-ray spectroscopy use *K*-shell line spectra from mid-*Z* elements [such as 2000 Å of co-sputtered Ti and Cr or 2500 Å of potassium chloride (KCl)] on fibers placed in different locations inside the gas-filled targets. Analysis of the line intensity ratios uses a time-dependent collisional-radiative model of the plasma (Lee *et al.*, 1984). Isoelectronic ratios of the He-like emission were used because they are less affected by time-dependent ionization effects. Density variations are not expected to introduce large effects in the analysis and are included in the error estimates of the results.

The electron temperature in the C_5H_{12}-filled gasbag was measured with TiCr dopants and with Ar/Cl gas dopants (Back *et al.*, 1995). These spectroscopic measurements, using three different line ratios, consistently indicate that peak temperatures of 3.0 ± 0.5 keV, slightly below the nominal LASNEX predictions, are achieved in the gasbags. Measurements of Ar and Cl satellite and resonance lines over several shots have enabled us to obtain a history of the temperature rise (Glenzer *et al.*, 1997b). The measured temperature lags behind the temperature rise indicated by the simulation. Gasbags attain their peak electron temperature at 1 ns, when the

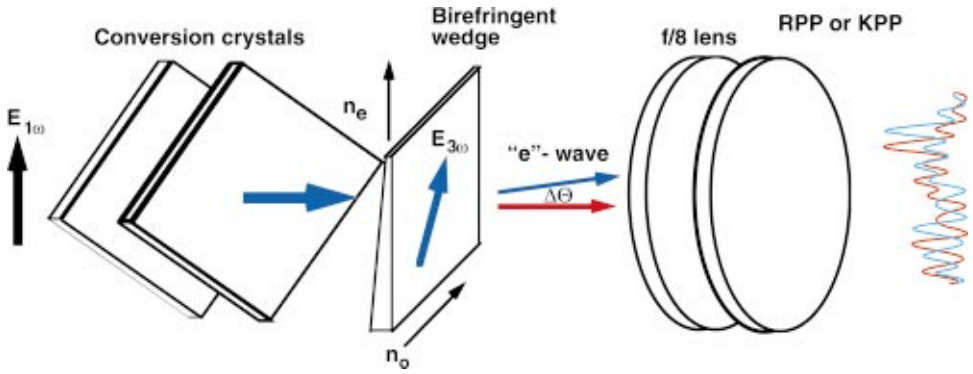

FIG. 3-15. (Color) Polarization smoothing was introduced through the use of a birefringent wedge.

Downloaded 20 Mar 2011 to 69.181.48.121. Redistribution subject to AIP license or copyright; see http://pop.aip.org/about/rights_and_permissions

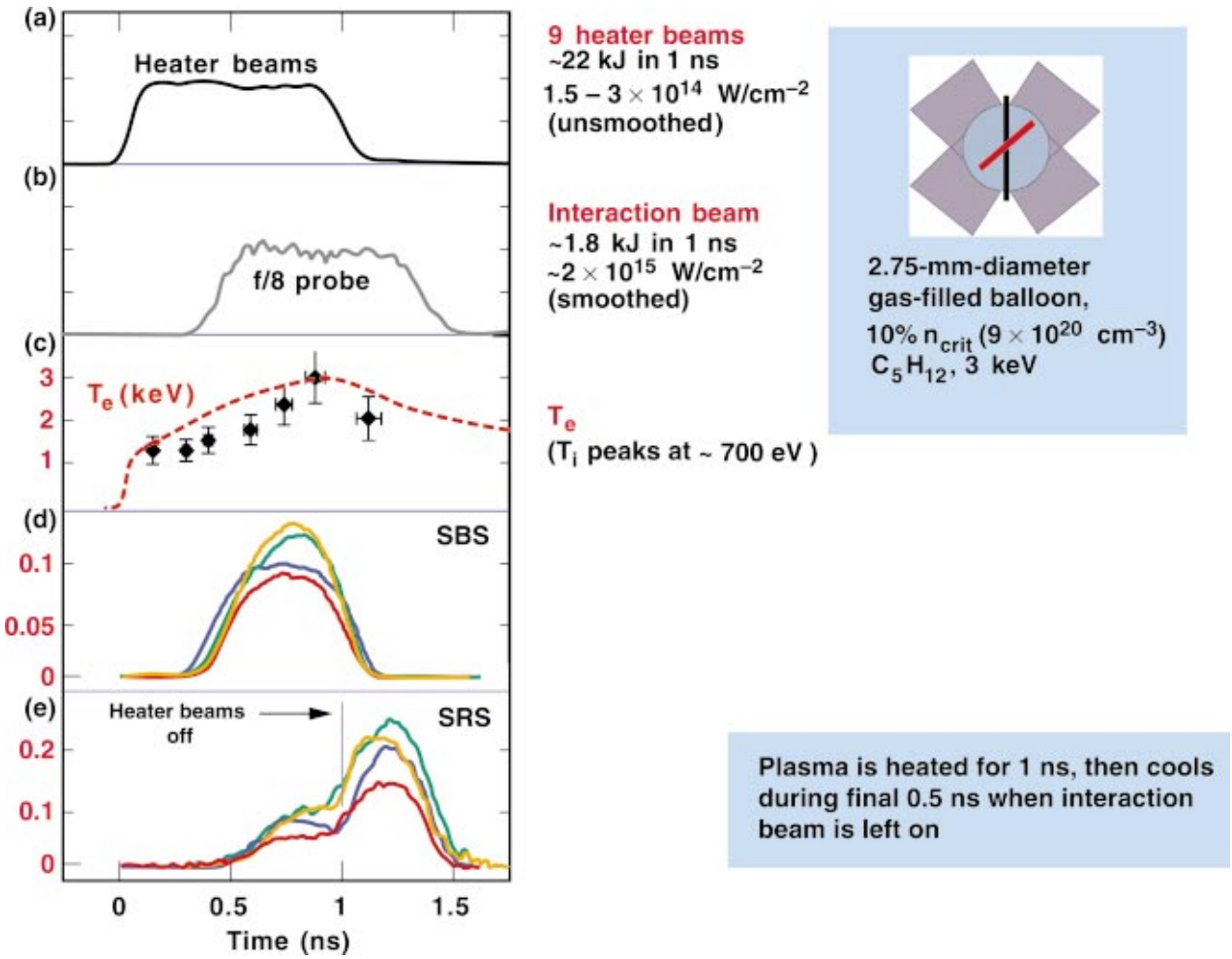

FIG. 3-16. (Color) Gasbag plasmas were developed to approximate the NIF inner beam plasma conditions. Shown are (a) the typical pulse shape of the heater beam power, (b) the $f/8$ probe incident power, (c) the computed and Thomson scattering measurement of the electron temperature, (d) the fractional SBS reflected power, and (e) the fractional SRS reflected power. The multiple curves in (d) and (e) are the scattering levels from different shots and indicate typical shot-to-shot scatter [S. H. Glenzer *et al.*, Phys. Rev. E **55**, 927 (1997)].

heater beams turn off, but they are homogeneous after about 400 ps when they are heated with 3ω heater beams (Back *et al.*, 1995; Glenzer *et al.*, 2000a).

Figure 3-18 shows a gasbag target along with the three 2D images of x-ray emission for energies greater than 2 keV. By 500 ps, when the 1 ns interaction beam is turned on, the plasma is quite uniform. The explosion of the gasbag membrane perturbs the interior gasbag densities somewhat. The membrane is about 2000 to 3000 Å thick after the bag has been inflated and the material has stretched. The lasers heat the membrane, causing it to expand and rarefy, much like an exploding foil (Rosen and Nuckolls, 1979). That process launches a shock into the bag, which propagates into the center of the target at about the sound speed. Unlike solid or exploding-foil targets, the gas balloon targets convert most of the incident heater laser energy into thermal energy of the electrons and less into kinetic energy of bulk plasma motion. The energy budget for a typical gas balloon simulation is 22 kJ incident, 12.5 kJ absorbed, 8.8 kJ in electron thermal energy ($T_e = 3.2$ keV) and only 2.6 kJ (21% of absorbed energy) in kinetic energy. For a typical exploding-foil plasma, calculations (to produce a $0.1n_c$ plasma) show 22 kJ incident, 8 kJ absorbed, 3.1 kJ in electron thermal energy ($T_e = 2.4$ keV), and 4.5 kJ in kinetic energy (56% of absorbed energy). The heating of a stationary low-density target is therefore a much more efficient way of producing a high-temperature plasma. Also, the density and velocity gradients in a gasbag plasma are much less severe and therefore more suitable for interaction experiments that mimic laser–plasma interactions within indirect-drive ICF hohlraums.

The electron temperature has been measured as a function of radius from the gasbag center as shown in Fig. 3-18. The Thomson scattering and the spectroscopic measurements are consistent. Two-dimensional hydrodynamic simulations with LASNEX and FCI2 (Buresi *et al.*, 1986; Schurtz *et al.*, 2001) model the data well as shown. Very early in the evolution the heat wave has penetrated to the center of the bag and produced a very uniform electron temperature and pressure. These conditions minimize plasma gradients and favor the growth of SRS and SBS. In addition to the electron temperature, the ion temperature and flow velocity can be obtained from the TS data. By fitting the data with the known shape of the TS spectrum in the collisionless plasma limit,

Downloaded 20 Mar 2011 to 69.181.48.121. Redistribution subject to AIP license or copyright; see http://pop.aip.org/about/rights_and_permissions

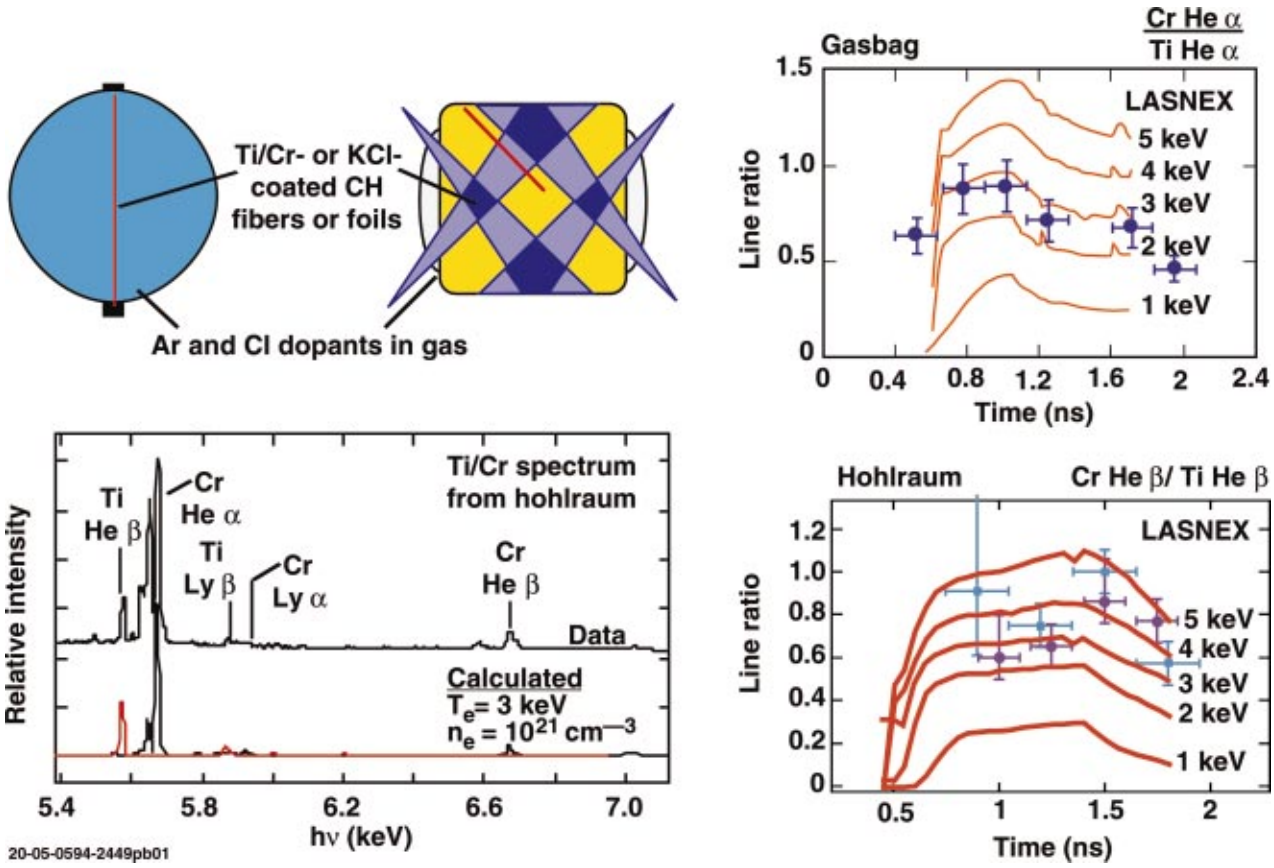

FIG. 3-17. (Color) X-ray spectroscopy indicates $T_e \approx 3$ keV for both open and closed geometries designed to approach NIF low-Z inner beam conditions on Nova. The theoretical time history of the line ratios for the gasbags and hohlraums is calculated for plasmas with the peak temperature indicated and with a time history of the temperature from LASNEX calculations. The nominal LASNEX calculations predict peak temperatures of slightly more than 3 keV.

one finds the ion temperature increases from 0.17 keV at 0.35 ns to 0.62 keV at 0.9 ns as the ion temperature slowly equilibrates with the electron temperature in this low-*Z* plasma. A mean plasma flow velocity in the Thomson scattering volume will add an overall Doppler shift to the spectrum (not seen here) as will be seen in TS data from hohlraums discussed in Sec. III C 5. Random velocity perturbations, caused by nonuniform heating or by ponderomotive forces of the heater beams, broaden the line shape and are less than 5% of the sound speed in this typical example.

Figure 3-16 shows the typical time history of the SBS and SRS in a C_5H_{12} gasbag plasma at $n/n_c \approx 0.1$. The SBS peaks at about 0.75 to 0.8 ns while the heater beams are still on, and then drops to very small levels by the end of the heater pulse. The SRS generally increases throughout the heater pulse and continues to increase for a couple of hundred picoseconds after the heater pulse is turned off. Without a detailed understanding of the mechanisms controlling the magnitude of the scattering in gasbags and its relation to NIF laser and plasma conditions, it is difficult to conclude when the scattering from these gasbag plasmas is most "NIF-like." The highest electron temperature of about 3 keV is reached at 1 ns at the end of the heater pulse. Although this is 1 to 2 keV lower than a typical NIF plasma, the linear gain for SRS is comparable to NIF at this time. However, as discussed below and in Sec. III B 3, a nonlinear saturation mechanism of SRS is strongly affected by ion–acoustic damping, which scales with T_i/T_e. Near the end of the heater pulse, $T_i/T_e \approx 1/4$ as measured by Thomson scattering (see Fig. 3-18). For NIF, this value is calculated to be about 1/2. For the gasbag plasmas, T_i/T_e remains below 1/2 but continues to increase (mainly because the electron temperature decreases) and gets closer to NIF ratios after the heater beams are turned off. By this criterion, the gasbag plasmas are arguably most NIF-like shortly after the heater beams are turned off. The effect of ion wave damping on SRS levels in gasbags at early times while the heater beams are on and at late times after the heater beams are off, is further discussed below.

At their peak level after the heater beams are turned off, the SRS scattering is typically a factor of 1.5 to 2 higher than at the end of the heater beams. The measured electron temperature after the heaters turn off drops such that the SRS growth rate is similar to a value before the heaters turn off. Moreover, the length of the plateau in electron density between the blast waves is shorter than before the heaters turn off. Thus, there is more linear gain before 1 ns than after at comparable electron temperature. Because an increase in the ion–acoustic wave damping after 1 ns will increase the LDI threshold, this nonlinear SRS saturation mechanism might explain this difference between the SRS levels. In addition, this damping along with the decrease of the plasma length lowers the gain of SBS and eliminates the competition between SRS and SBS which has been observed in a number of

Downloaded 20 Mar 2011 to 69.181.48.121. Redistribution subject to AIP license or copyright; see http://pop.aip.org/about/rights_and_permissions

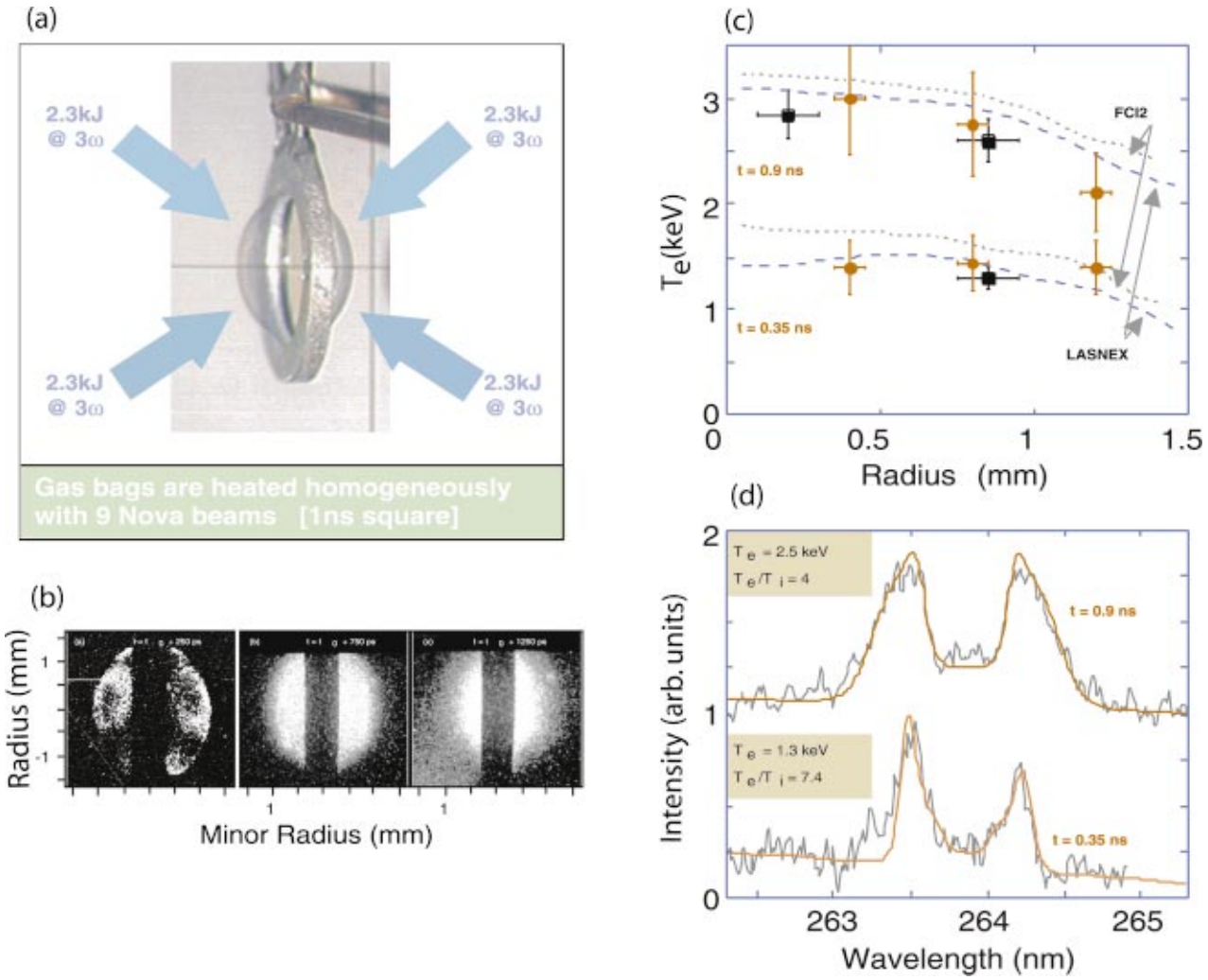

FIG. 3-18. (Color) (a) Gasbag target before it is pressurized. The thickness and the inner diameter of the washer is ~0.4 mm and ~2.75 mm, respectively. (b) Two-dimensional x-ray images measuring emission energies, $E>2$ keV, indicate that the gasbags are homogeneously heated after ~0.35 ns. (c) Experimental electron temperature data for various radial positions measured at $t=0.35$ ns and at $t=0.9$ ns. The temperatures from Thomson scattering (solid circles) show excellent agreement with the results from x-ray spectroscopy (squares). At $t=0.35$ ns, the electron temperature profile becomes flat indicating the utility of gas bags for studying NIF-like laser plasma interactions. The data are consistent with two-dimensional hydrodynamic modeling using the codes LASNEX and FCI2. (d) Experimental Thomson scattering spectra from a C5H12-filled gasbag measured from a radial distance of 0.8 mm from the gasbag center. The spectra taken at $t=0.35$ ns and at $t=0.9$ ns show increasing electron temperatures and decreasing electron-to-ion temperature ratios. The parameters are inferred from the theoretical fits to the experimental data.

experiments. Acoustic wave fluctuations can inhibit LDI and the growth of SBS (Cohen *et al.*, 2001). To simulate the SBS reflectivity in gasbags, fluctuations of magnitude $\delta V/C_s \sim 0.3$ (Montgomery *et al.*, 1998) are required absent nonlinear saturation, but the TS measurements shown in Fig. 3-18 rule out such large perturbations. Nonlocal thermal effects and non-Maxwell–Boltzmann electron distributions have also been invoked to explain the SRS behavior when the electron temperature decreases (Kirkwood *et al.*, 1996). However, for these plasma conditions, theory and experiments do not support NMB distributions.

In the data summaries shown in Figs. 3-19 and 3-20, the peak SBS (at about 0.8 ns) and the SRS at peak T_e (averaged over the 50 ps diagnostic resolution) at the end of the heater pulse is plotted.

Figure 3-19 shows the SRS and SBS backscatter data for gasbags, using RPPs and the 3 GHz modulator (MacGowan *et al.*, 1996). The effect of SSD bandwidth is shown in Fig. 3-19(a) for the $0.1n_c$ targets. SSD reduces SRS slightly from 7% to 4%; the effect on SBS is similar, 6% to 3%. For the lower-density, $0.075n_c$ data in Fig. 3-19(b), SBS decreases from 10% to 6% while SRS decreases from 4% to 1%. At $0.1n_c$, there is a slight benefit to increasing the bandwidth from 0.5 to 1 Å at 3ω, while for the lower density plasmas, backscatter is minimized with 0.5 Å bandwidth.

Figure 3-20 shows scattering results using KPPs and the 17 GHz modulator as well as tests of polarization smoothing performed in gasbag plasmas (MacGowan *et al.*, 1999; MacGowan *et al.*, 1997; Moody *et al.*, 2001). Most of the data in Fig. 3-20 had a probe beam irradiance of 2×10^{15} W/cm^2 corresponding to the NIF 300 eV point design (see Fig. 2-1). The data in the range from 0.13 to $0.15n_c$ had an interaction beam irradiance of 4×10^{15} W/cm^2, consistent with that in higher radiation temperature (350 eV) NIF hohl-

Downloaded 20 Mar 2011 to 69.181.48.121. Redistribution subject to AIP license or copyright; see http://pop.aip.org/about/rights_and_permissions

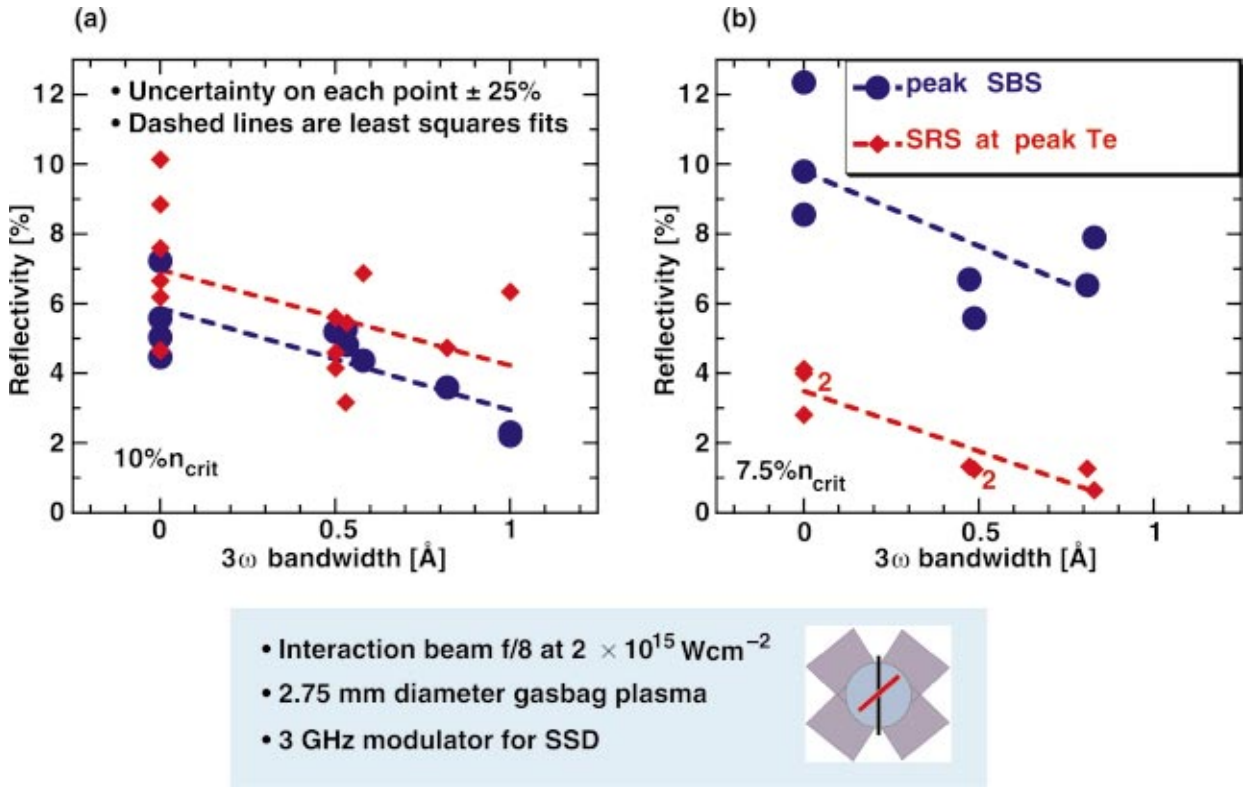

FIG. 3-19. (Color) Experiments using gasbag plasmas with the interaction beam outfitted with RPPs and 3 GHz SSD showed the benefit of SSD in reducing scattering. The SRS (♦) and SBS (●) reflectivity vs SSD bandwidth are shown for (a) 10% critical and (b) 7.5% critical gasbags filled with mixtures of C_5H_{12} and C_3H_8.

raum designs, which would have this higher density. The bulk of the data with PS lie below the unsmoothed data (open circles), while the experiments with PS and 1 Å SSD have the lowest backscatter levels (total scatter is less than 6%), especially for the case of SBS indicating that there is some benefit to PS for this case which primarily addresses backscatter for the inner beams of the NIF hohlraum geometry. While the SRS is seen to increase with density in the

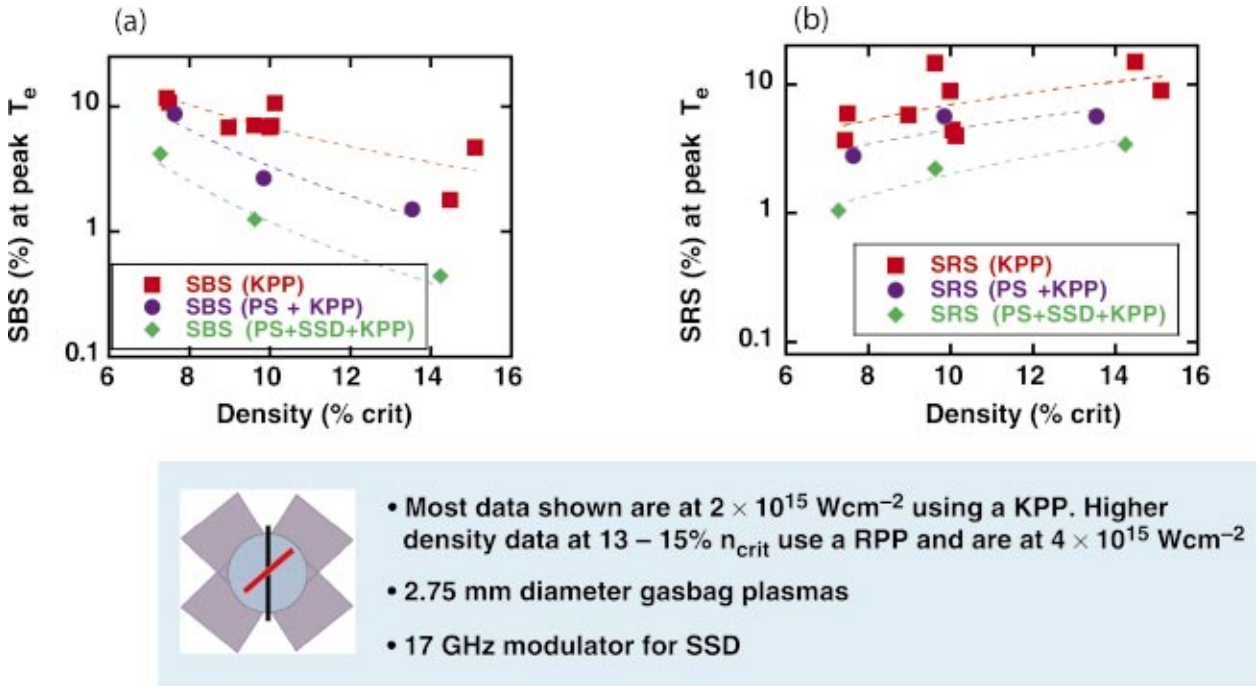

FIG. 3-20. (Color) Gasbag experiments using a KPP and 17 GHz SSD for beam smoothing show that SBS (a) and SRS (b) from gasbags filled with mixtures of C_5H_{12} and C_3H_8 are consistent with experiments using an RPP and 3 GHz SSD (see Fig. 3-19).

Downloaded 20 Mar 2011 to 69.181.48.121. Redistribution subject to AIP license or copyright; see http://pop.aip.org/about/rights_and_permissions

gasbag experiments above, consistent with linear gain theory, the SBS decreases with increasing density even though the linear gain is about constant or increasing. Besides being observed in the Nova gasbags (Montgomery *et al.*, 1998), an ''anticorrelation'' between SRS and SBS has been observed in a number of experiments including exploding foils at Laboratoire pour l'Untilisation des Lasers Intenses (LULI) (Baldis *et al.*, 1993), and the Trident Laser Facility at LANL (Montgomery *et al.*, 1999). The former two experiments used RPPs and the interaction region had a large number of hot spots obeying speckle statistics. The anticorrelation was observed for both $f/4$ and $f/8$ optics on Nova although there was some difference in the absolute reflectivities. The Trident experiment used an almost diffraction-limited interaction beam, i.e., a single hot spot. In all three experiments, there is an anticorrelation in time during the laser pulse with the transition from SRS dominance to SBS dominance occurring over hydrodynamic time scales, namely, from 50 to 500 ps.

One interpretation of these results is that the instability with the largest gain exponent will have the larger reflectivity and lower the reflectivity of the other. This effect is a straightforward 1D theoretical result obtained by coupled mode equations (Berger, 1983) and 1D PIC simulations (Estabrook *et al.*, 1989). However, these 1D calculations have reflectivities far in excess of the observed ones. Imaging of the reflected light has shown that, in the plasma, the reflected light is concentrated in ''clumps'' much less dense than the hot spots of the incident light (Baldis *et al.*, 1998). Clumps of reflected light are regions of the plasma whose transverse size is much less than the laser spot but greater than a speckle width. The imaging system cannot resolve a speckle and the SBS may be coming from individual speckles. In fact, the overall reflectivity is consistent with large reflectivity in a few hot spots (Tikhonchuk *et al.*, 1997). F3D simulations confirm this as a plausible explanation for the LULI experiments and also for the Nova density scaling of SRS and SBS (Cobble *et al.*, 2000). Thus if the more intense speckles, that have only a fraction of the total power, account for most of the reflectivity, SRS and SBS competition in the speckles can explain the observed anticorrelation.

Shown in Fig. 3-21(a), for the Nova gasbag experiments, are the SRS and the SBS reflectivity at the time of peak SBS reflectivity plotted against the electron density from Nova experiments. LASNEX simulations and the post-processor LIP, predict that the SBS gain exponent for these experiments was roughly constant with density while the SRS gain exponent rapidly increased. The behavior of the SRS gain exponent [see Eq. (3-12)] is expected because v_e, the Landau damping of the resonant Langmuir wave, is a strongly decreasing function of the density. The SBS gain exponent [see Eq. (3-11)] has an explicit dependence on density but also an implicit one because of the density dependence of the ratio of the ion–acoustic wave damping to its frequency, v_α/ω_α. The dependence of v_α/ω_α on density arises from its dependence on T_i/T_e and the density dependence of the temperature equilibration which causes T_i/T_e to increase with density (and time). F3D simulations (2D) of the density dependence of the reflectivity, shown in Fig. 3-21(b), are qualitatively in agreement with the experimental results. Important ingredients in the simulations, in addition to the correct plasma parameters that determine the growth of SRS, SBS, and filamentation, are the saturation mechanisms in F3D that limit the amplitude of the plasma waves. As described in Sec. III B 3 [see discussion following Eq. (3-14)], the saturation of SRS and SBS is accomplished in F3D by introducing an amplitude-dependent damping on the Langmuir and acoustic waves, respectively, when these plasma waves exceed the threshold for nonlinear decay. These thresholds are determined by PIC simulations or nonlinear fluid simulations. This is an active area of current research.

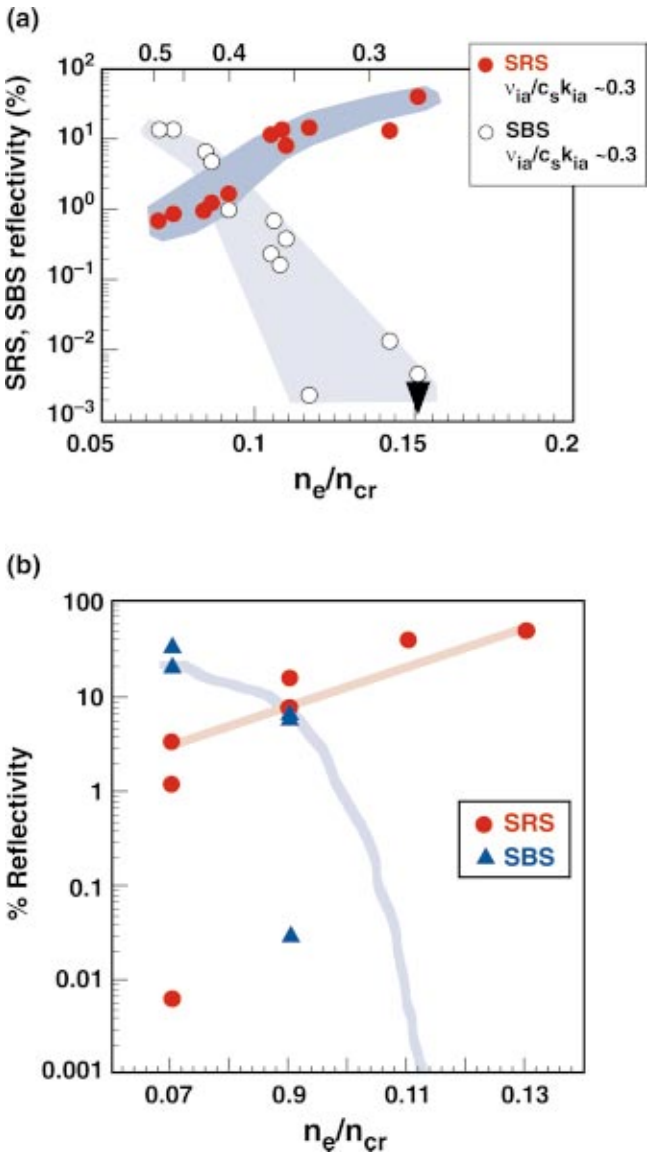

FIG. 3-21. (Color) Data (a) [D. S. Montgomery *et al.*, Phys. Plasmas **5**, 1973 (1998)] and F3D simulations (b) show an anticorrelation of the SRS and SBS reflectivity as a function of electron density. The SBS and SRS reflectivity for a given density was varied in the simulations by changing the ion wave damping which affects the linear SBS gain and the SRS and SBS saturation. For each density, a higher SBS reflectivity is paired with a lower SRS reflectivity.

The light transmitted through the gasbag plasma is influenced by collisional absorption (inverse bremsstrahlung), filamentation or stimulated Brillouin forward scatter, as well

Downloaded 20 Mar 2011 to 69.181.48.121. Redistribution subject to AIP license or copyright; see http://pop.aip.org/about/rights_and_permissions

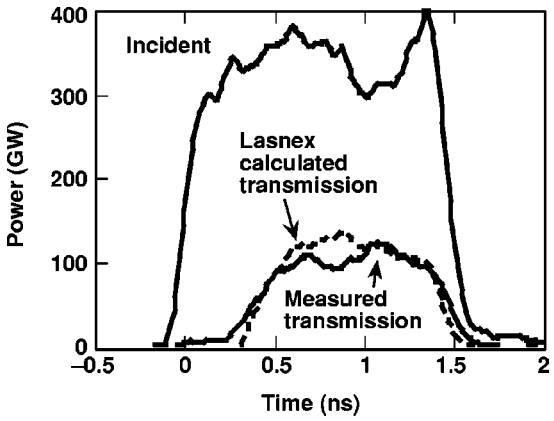

FIG. 3-22. The incident laser power, measured transmitted power (solid), and the calculated transmitted power (dashed) are shown for low laser intensity ($I=10^{14}$ W/cm^2) [J. D. Moody *et al.*, Phys. Plasmas **7**, 3388 (2000)].

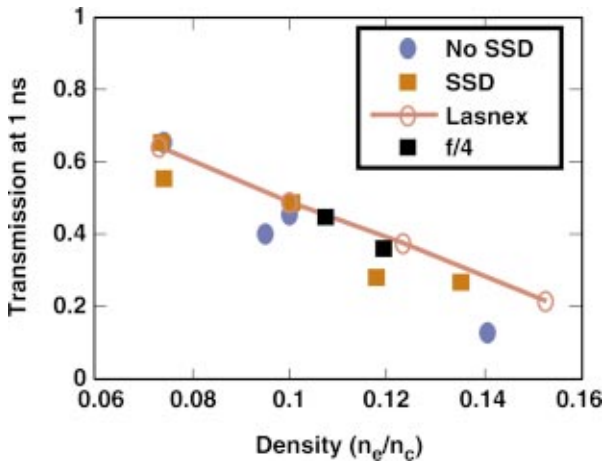

FIG. 3-24. (Color) The transmitted power fraction at 1 ns is compared to the LASNEX calculated fraction as a function of electron density for $f/8$ focusing with and without SSD and for $f/4$ focusing. The agreement is better for $f/4$ and SSD, both of which reduce filamentation [J. D. Moody *et al.*, Phys. Plasmas **7**, 3388 (2000)].

as stimulated backscatter. The TBD measures the time-dependent transmission within the initial cone angle of the $f/8$ lens and the light scattered to larger angles both with the fused-silica scatter plate and with optical fibers coupled to streak cameras as described above. In Fig. 3-22, the measured and LASNEX-calculated transmitted light time history agree very well for a low intensity ($I=10^{14}$ W/cm^2) interaction beam. However, at higher laser intensity ($I=2\times10^{15}$ W/cm^2) shown in Fig. 3-23, the measured transmitted laser power lags the LASNEX-calculated power early in the pulse although the agreement is good later in time. The difference can probably be accounted for by the fact that the measured temperature early in the pulse (see Fig. 3-16 for TS data) is lower than calculated which increases the absorption, and that the laser beam is more unstable to filamentation and beam spraying early in the pulse. There is more scatter to larger angles measured by the TBD earlier in the pulse, possibly to angles beyond the edge of the scatter plate. Moreover, because the area increases rapidly with angle while the power of the scattered light is decreasing, accurate measurements of the power scattered to large angles is difficult. Very early in time ($t<0.35$ ns) the gasbag temperature is less uniform and light scattered out of the beam may be absorbed by cold plasma not yet heated by electron conduction.

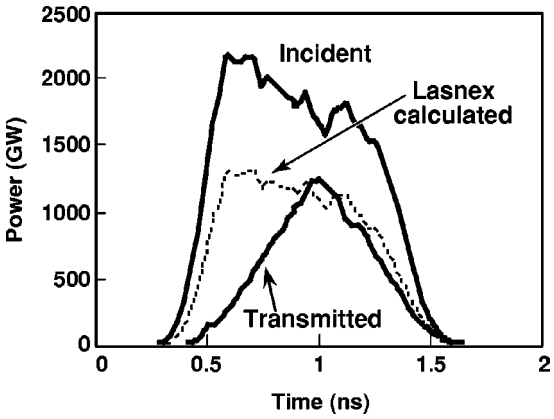

FIG. 3-23. The incident laser power, measured transmitted power (solid) and the calculated transmitted power (dashed) are shown for high laser intensity ($I=2\times10^{15}$ W/cm^2) [J. D. Moody *et al.*, Phys. Plasmas **7**, 3388 (2000)].

The spectrum of the light scattered to larger forward angles is consistent with stimulated Brillouin forward scatter (Moody *et al.*, 1999a). The amount of light scattered to large angles is reduced by the use of beam smoothing, both SSD and four color, and possibly PS. In the experiments, the amount of large angle scatter is reduced by a factor of 2 to 3 by either SSD and PS separately and is reduced by about a factor of 10 by the combination of SSD and PS. Filamentation, which plays an important role in beam spray, has a higher gain for higher f numbers as indicated by Eq. (3-13). F3D calculations of both $f/4$ and $f/8$ beams which model only a representative portion of the laser beam, are in good agreement with the data for angles out to a few times the incident cone angle. However, there is less calculated scatter at even larger angles than in the data, possibly because the axial length of the simulated plasma is too short to allow forward Brillouin to grow fully. The results from a large number of shots, shown in Fig. 3-24, show that temporal beam smoothing improves the agreement between LASNEX and the measured transmission over a range of densities from $0.07n_c$ to $0.15n_c$.

A number of experiments measuring the spreading of the transmitted light have been done with the TBD. In general, the spreading agrees with the theoretical and simulation scaling. Detailed comparisons of the spreading of the light transmitted through gasbags with the $f/4$ Nova beam vs predictions of the massively parallel code pF3D are in good agreement out to 15°. Comparisons at larger angles, which require greater spatial resolution and thus more memory in the simulations, are planned (Williams, 1999). However, the amount of power scattered to these larger angles is energetically insignificant for ICF.

To understand the dependence of SRS saturation on ion–acoustic wave damping, experiments were carried out with gasbags filled with Xe mixed with varying amounts of C_5H_{12}

Downloaded 20 Mar 2011 to 69.181.48.121. Redistribution subject to AIP license or copyright; see http://pop.aip.org/about/rights_and_permissions

to systematically vary the ion–acoustic wave damping (Kirkwood *et al.*, 1996). LASNEX simulations show that the Xe gas ionizes to a charge state of about 40, similar to the charge state of 50 for Au in the hohlraum plasmas, and therefore Xe has very similar collisional properties. The fraction of C_5H_{12} can be varied between 0 and 30% without affecting the electron density significantly, while changing the ion–acoustic wave damping by a factor of 15.

The electrons are heated to a temperature of $T_e = 3.6$ keV during the last half of the 1.0 ns square heater pulse when the plasma parameters are most constant in space and time (Glenzer *et al.*, 1997b). The electron density is $n_e = 8.5\times10^{20}$ cm^{-3}, determined by the initial gas density and ionization state. The temperature is determined from measurements of x-ray line ratios and x-ray transport modeling and is in agreement with LASNEX simulations. The variation in measured transmission of a beam through the plasma (Moody *et al.*, 1994) is only 1% to 2% when the C_5H_{12} concentration is varied from 0% to 30%, also in agreement with the simulations, indicating that the electron temperature variations are small ($\leqslant \pm 6\%$). Measurements of the radiated x-ray power in the photon energy range from 0.2 to 2 keV indicate that the radiated power is also constant within $\pm 15\%$ over the same range of C_5H_{12} concentration. Keeping the electron density and temperature constant while the C_5H_{12} concentration is varied ensures that the frequency and damping rate of the Langmuir wave is also constant. This assumes that Landau damping dominates the damping since collisional damping does depend on the charge state Z.

For these experiments, the interaction beam power was 1.5 TW for 1.0 ns. This beam was delayed 0.5 ns with respect to the heaters and focused at the plasma center. Reflectivity measurements were made during the 0.5 to 1.0 ns (early) period when the heaters were on, as well as during the 1.0 to 1.5 ns (late) period when the plasma was cooling. The interaction beam was smoothed by an RPP and 1 Å (3ω) FM bandwidth dispersed across the beam with the 1200 lines/mm grating, so that its peak intensity and spot size in vacuum are 7.0×10^{15} W/cm^2 and 177 μm FWHM (345 μm between first Airy minima). The plasma properties encountered by the interaction beam during the early period are calculated by LASNEX for a 90% Xe, 10% C_5H_{12} gas mix, indicating a temperature, and density plateau near the plasma edge as shown in Fig. 3-25. The collisional absorption length for 351 nm light in Xe with a 3.6 keV electron temperature and 8.5×10^{20} cm^3 electron density is 800 μm. Therefore, the majority of the backscattering occurs outside $r = 0.5$ mm. The downshifted light scattered within 20° of direct backscatter is measured with a streaked optical spectrometer in the visible, with a spectral range from 400 to 700 nm, and a second spectrometer in the UV, with a spectral range from 346 to 361 nm. The case of Xe with 5.5% C_5H_{12} mixture is shown in Fig. 3-26. During the early period the peak of the spectrum is at 575 nm consistent with scattering from a Langmuir wave propagating in a plasma with a density equal to 10% of the critical density and a 3.0 keV electron temperature comparable to the simulated plasma parameters near $r = 1.2$ mm. After the heaters turn off at 1.0 ns, the peak shifts to shorter wavelengths, indicating the cooling of the plasma or a density decrease in the scattering region.

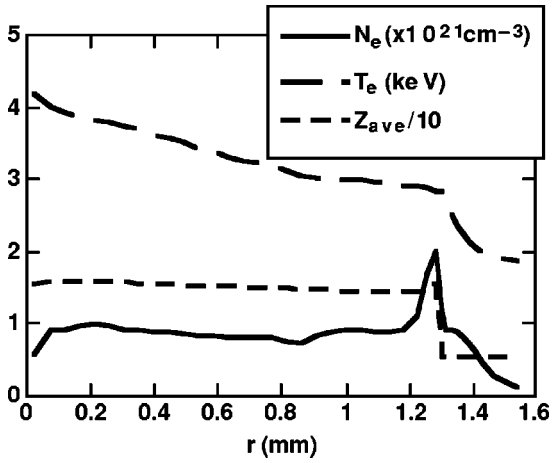

FIG. 3-25. The calculated electron density, temperature, and average ionization state at $t = 0.9$ ns for a gasbag target containing 90% Xe and 10% C_5H_{12}. These conditions were insensitive to the percent of C_5H_{12} content, which was varied from 0% to 30% [R. K. Kirkwood *et al.*, Phys. Rev. Lett. **77**, 2706 (1996)].

Experiments, performed with six different mixtures of Xe and 0% to 30% C_5H_{12}, exhibit a strong dependence of the SRS reflectivity on the concentration of C_5H_{12}. The integrated energies from the two time periods are expressed as percent reflectivity of the incident beam power due to SRS and plotted in Fig. 3-27. In the integrated data it is clear that late time SRS reflectivity is approximately proportional to the C_5H_{12} concentration for all concentrations studied. The early time reflectivity is proportional to concentration up to 10% and becomes independent, or a mildly decreasing function, of concentration between 10% and 30%. Because the ion–acoustic damping rate is expected to be linear with C_5H_{12} concentration in this case (Williams *et al.*, 1995; Vu *et al.*, 1994), a linear dependence of reflectivity on C_5H_{12} concentration is interpreted as a linear dependence on the damping of the ion–acoustic wave.

For the early time data, during the time when the heater beams are still on, the linear dependence of the SRS reflectivity on the C_5H_{12} concentration is only seen when the C_5H_{12} concentration is less than 10%. For C_5H_{12} concentrations above 10%, or normalized ion-wave damping of 5%, the early time SRS reflectivity is not very dependent on the ion-wave damping, and the inferred Langmuir wave ampli-

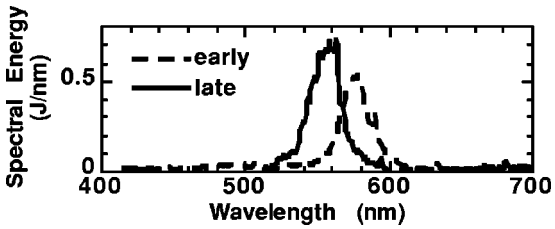

FIG. 3-26. Time-integrated SRS spectra from a Xe-filled gasbag with a 5.5% C_5H_{12} content for the ''early phase'' from 0.5 to 1.0 ns while the heater beams are on, and from the ''late phase'' from 1.0 to 1.5 ns after the heater beams have turned off. The frequency shift after the heater beams turns off is consistent with cooling of the plasma [R. K. Kirkwood *et al.*, Phys. Rev. Lett. **77**, 2706 (1996)].

Downloaded 20 Mar 2011 to 69.181.48.121. Redistribution subject to AIP license or copyright; see http://pop.aip.org/about/rights_and_permissions

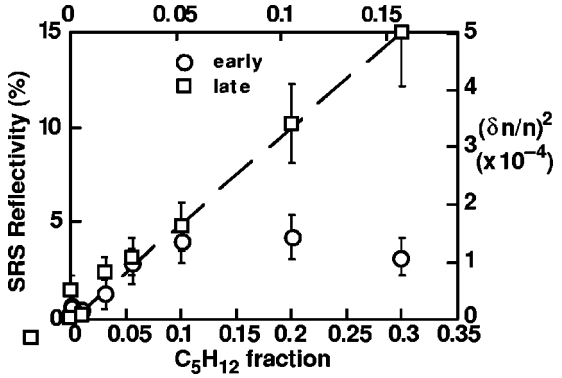

FIG. 3-27. SRS reflectivities from Xe-filled gasbag targets averaged over the "early period" and the "late period" are shown vs C_5H_{12} concentration. The calculated ion-wave damping is proportional to the C_5H_{12} concentration. The square of the fluctuation amplitude is estimated from the reflectivity [R. K. Kirkwood *et al.*, Phys. Rev. Lett. **77**, 2706 (1996)].

tude falls below the threshold for the secondary decay. One possible explanation for this behavior is that the SRS generated Langmuir wave is convectively saturated before it reaches the secondary decay threshold. The secondary decay mechanism will only determine the SRS reflectivity when the primary three wave process is sufficiently strong to drive the Langmuir wave amplitude to the threshold for the secondary decay. The late time data show linear dependence of the reflectivity on the C_5H_{12} concentration up to much higher concentration than at early time. At late time the plasma has cooled and SRS has a higher convective saturation level for the three wave process because of the reduced Landau damping of the Langmuir wave at low T_e. A high convective saturation level allows the Langmuir waves to grow to the secondary decay threshold even when ion-wave damping is large, resulting in a reflectivity that follows the linear scaling with ion-wave damping up to at least 30%, as shown in Fig. 3-27.

Additional evidence for the importance of the LDI is provided in hydrocarbon plasmas in which a 3ω laser beam beats with a 2ω beam to drive a resonant Langmuir wave (Kirkwood *et al.*, 1999). The plasma density was varied until the maximum response was obtained. As the incident power of the 2ω beam is increased, the transferred power increases until the threshold for LDI is exceeded, after which the transferred power shows no further increase.

For LPI effects, the primary differences between the hydrocarbon plasmas used in most of the Nova gasbag experiments and the He/H_2 plasma hohlraum fills planned for NIF are the different ion–acoustic damping rate v_i and the different ion charge value Z. As discussed above, gasbag experiments which explored the effect of ion–acoustic damping on SRS and SBS in CH and Xe plasmas found that increasing v_i led to an increase in the SRS, particularly during the late phase after the heater beams were turned off. This effect is also seen in the LANL toroidal hohlraum experiments discussed below.

The effect of ion charge value is twofold. First, a lower value of Z reduces the effects of thermal filamentation that affect the laser beam spray. In addition, the multispecies ion–acoustic modes are different in an He/H_2 plasma from the modes in a hydrocarbon plasma so that the SBS thresholds and growth rates may be different. Extrapolation of the late time scattering results for the Xe/C_5H_{12} gasbag results, or the LANL toroidal hohlraum results to the ion–acoustic wave damping values expected in an indirect-drive hohlraum designed for ignition on the National Ignition Facility (NIF) imply SRS reflectivity in the range of 50%. However, measurements in gasbags with a He/H or a He/H/Ne fill discussed below (Moody *et al.*) show relatively little change in scattering as the ion–acoustic damping increases from 0.1 to 0.4 of the acoustic frequency.

As with other gasbags, nine Nova beams were used to heat the He/H/Ne gasbags and the tenth beam drives the backscatter instabilities. The heater beams were $f/4.3$, do not use a phase plate, and were defocused to a diameter of about 1.5 mm to illuminate a large section of the gasbag surface at an intensity of about 10^{14} W/cm^2. The probe beam, with intensity between 1.8 and 2.2×10^{15} W/cm^2, was configured as an $f/4.3$ beam for these experiments. Laser light from the probe always passes through a KPP. This KPP produced a focal spot in the shape of an ellipse whose diameter is about 400 μm along the major axis and 260 μm along the minor axis. The intensity envelope of the focal spot was fairly flat and drops off rapidly near the edges. The vacuum transverse speckle size at focus is $f\lambda_0\approx1.3$ μm and the longitudinal depth of focus is $8f^2\lambda_0\approx50$ μm, where $f=4.3$ is the f number of the probe beam focusing geometry.

The targets were filled with 1 atm of a mixture composed of He, H, and Ne gases and then the entire target was cooled to about 27 K while keeping the pressure at 1 atm. The resulting ionized electron density was about 0.07 to $0.08n_c$ for 351 nm laser light. Three gas mixtures were chosen to provide a range of both v_i and T_e. The three mixtures were (1) 90% He, and 10% Ne; (2) 40% He, and 60% H_2; (3) 33% He, 52% H_2, and 15% Ne. Hydrogen increases v_i and Ne increases T_e compared to pure He. To achieve a large v_i, the targets were also designed to give a higher T_i than in the hydrocarbon gas fill targets. This was done by increasing the gas balloon size by 1.25 times that used for hydrocarbon gas fill experiments and heating the target for 1.5 ns rather than only 1 ns. These changes gave more time for the electron and ion temperatures to equilibrate, leading to a higher T_i and higher v_i. Figure 3-28 shows the calculated electron temperatures and ion damping for the three mixtures. The dots along the curves are at 100 ps intervals along the 1.5 ns interaction pulse. The plasma electron temperature near the end of the heater pulse, characterized using TS, is about 1.5 keV for the HeH mixture. This is about 0.5 keV lower than the LASNEX/FCI2 calculations. For the HeHNe mixture, the electron temperature is about 2.2 keV, which is almost 1 keV lower than calculated. Because the Nova facility shut down shortly after these experiments were conducted, the reason for this difference between measured and predicted temperature was not determined. Gated x-ray pinhole camera measurements showed the targets becoming relatively uniformly heated after 0.5 ns.

Figure 3-29 shows the time history of a typical back-

Downloaded 20 Mar 2011 to 69.181.48.121. Redistribution subject to AIP license or copyright; see http://pop.aip.org/about/rights_and_permissions

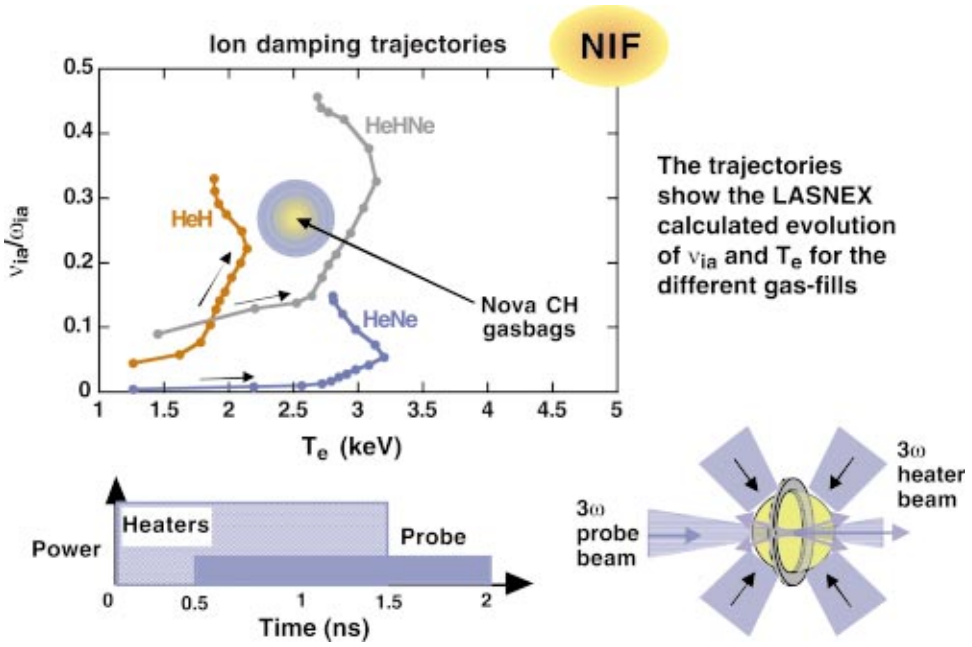

FIG. 3-28. (Color) Three mixtures of He, H, and Ne gas provided ion damping and electron temperature scaling in a NIF-like composition low-Z plasma. The dots along the curves represent 100 ps intervals in time along the 1.5 ns heater pulse [J. D. Moody *et al.*, "First measurement of backscatter dependence on ion acoustic damping in a low-Z, high density laser-plasma," Phys. Plasmas (to be submitted)].

scattering signal from the HeNe, HeH, and HeHNe fills. In all cases, the time history is qualitatively similar to that seen in the hydrocarbon-filled gasbags. The SBS peaks slightly before the time of peak electron temperature. The SRS peaks a couple of hundred picoseconds after the heater beams are turned off. As for the earlier gasbag experiments, there is typically a factor-of-2 difference between the SRS at peak T_e just before the heater beams turn off and the peak during the cooling phase. However, for the HeHNe plasma, which has the most NIF-like ion–acoustic damping, the peak SRS scattering at any time during the pulse is 10% or less, and the SBS is always less than a few percent. As shown, the addition of 3 Å (1ω) SSD has relatively little effect on the total scattering. The SBS is suppressed by about a factor of 2 while the peak SRS is essentially unchanged but reaches a higher value earlier.

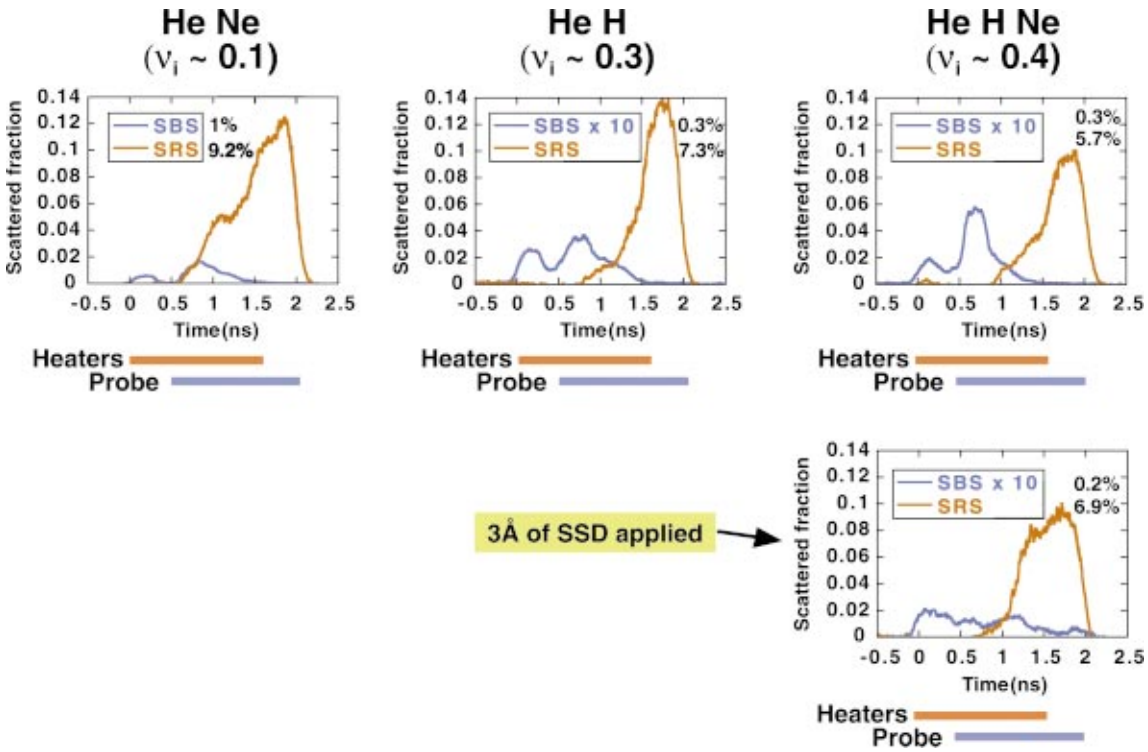

FIG. 3-29. (Color) Time histories of SRS and SBS in HeH (v_i=0.3), HeNe (v_i=0.1), and HeHNe (v_i=0.4) gasbag plasmas are similar to those in gasbags with hydrocarbon fills. The time-integrated reflectivity is also given on each figure. The peak scattering only depends weakly on the ion damping for these low-Z NIF-like gas fills [J. D. Moody *et al.*, "First measurement of backscatter dependence on ion acoustic damping in a low-Z, high density laser-plasma," Phys. Plasmas (to be submitted)].

Downloaded 20 Mar 2011 to 69.181.48.121. Redistribution subject to AIP license or copyright; see http://pop.aip.org/about/rights_and_permissions

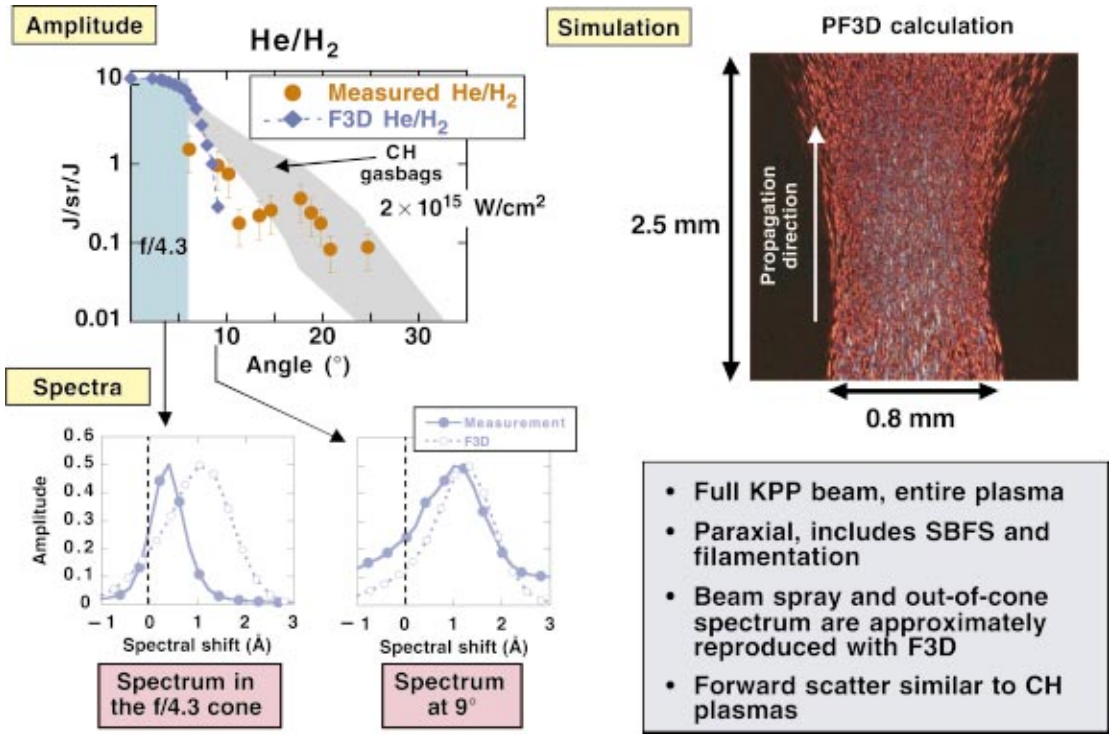

FIG. 3-30. (Color) Calculations of the forward scatter from the HeH experiments using the parallel F3D code. These results are in good agreement with the observed scattering out to about 10°. The experiments show somewhat more scattering at larger angles where the calculations have poor statistics [J. D. Moody *et al.*, "First measurement of backscatter dependence on ion acoustic damping in a low-*Z*, high density laser-plasma," Phys. Rev. Lett. (submitted)].

Figure 3-30 shows the measurements of the transmitted light from the probe beam. This light is measured using the TBD described above. The beam spray is similar to that measured on hydrocarbon-filled gasbags and shows that the majority of the sprayed light remains within about an $f/3$ or $f/2$ cone angle with a small amount of light beyond this. The redshift of the forward scattered light indicates that forward SBS is responsible for the spray.

The forward scattered light was calculated using PF3D to analyze transmission through the entire He/H plasma. The calculation is compared to the measurement in Fig. 3-30. The calculated and measured beam spray show good agreement out to about 10° (the resolution of the calculation was such that scattering beyond 15° was suppressed). Agreement between the measured and calculated transmitted light spectral shift is good outside of the $f/4$ cone angle, but the calculated shift is larger than the measured shift inside of the cone angle.

4. Toroidal hohlraums

An alternative approach to producing long-scale-length, low-*Z* plasmas on Nova was pursued that used large toroidally shaped gas-filled hohlraums (Fernandez *et al.*, 1996a; Wilde *et al.*, 1996; Fernandez *et al.*, 2000). The hohlraum is illustrated in Fig. 3-31. Nine of the 10 $f/4.3$ beams (heater beams) turn on at time 0, reaching approximately 2 TW each in 0.1 ns. Subsequently the power ramps up to 3 TW at time 1.4 ns, when all beams are turned off. An interaction beam is turned on at 0.4 ns and is kept at constant power for another 1 ns. The interaction beam in these experiments is smoothed spatially with a binary RPP (NTIS Document, 1991). Depending on the experiment, the size of the square phase-plate element was either 3.1 or 5.8 mm. The interaction beam best focus is placed near the hohlraum midplane, about 1 mm forward from the beam-crossing location which is near the LEH, but the intensity values quoted below are those at the hohlraum LEH unless otherwise noted. In vacuum, the peak intensity at the midplane would be about a factor of 1.6 higher at the midplane than at the LEH with the 3.1 mm phase plate, and about 2.8 for the 5.8 mm phase plate. Inverse bremsstrahlung absorption of the beam decreases the difference.

The hohlraum gas fill, with pressures of up to 2.2 atm, is contained by thin windows covering the two LEHs. The gas fills were C_3H_8 (propane) at about 1 atm, C_5H_{12} (neopentane) at about 1 atm, and C_4H_{10} (isobutane) at up to 2.2 atm. The LEH window is made of silicon nitride 0.3 μm in thickness except in the case of isobutane gas fills, where the higher pressure requires a polyimide window 0.7 μm in thickness. When the gas is fully ionized, the nominal density for these fills is $n_e/n_c = 0.065$ for C_3H_8, $n_e/n_c \approx 0.11$ for C_5H_{12}, and $n_e/n_c \approx 0.17$ for C_4H_{10}.

The shapes of the n_e, T_e, and T_i profiles predicted by LASNEX are similar for the range of n_e/n_c in this study, as shown in Fig. 3-31, bottom. Note that the n_e/n_c plateau is about 1 mm in length, with a value dependent on the gas fill. For C_5H_{12}, $T_e \approx 3$ keV has been measured spectroscopically (Fernandez *et al.*, 1996a; Wilde *et al.*, 1996), and $T_e = 2.50 \pm 0.25$ keV has been measured by collective Thomson scattering (Glenzer, 1998) along the hohlraum axis near the hohl-

Downloaded 20 Mar 2011 to 69.181.48.121. Redistribution subject to AIP license or copyright; see http://pop.aip.org/about/rights_and_permissions

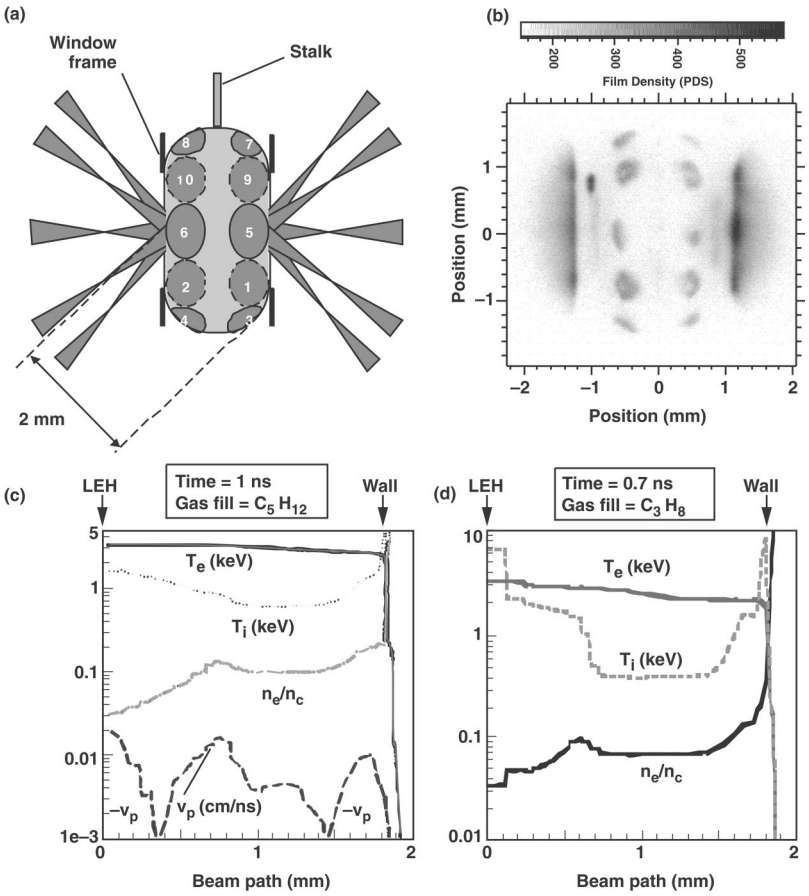

FIG. 3-31. (a) The gas-filled hohlraum and beam footprints are illustrated. The hohlraum is 1.6 mm in length and 3.2 mm in diameter. (b) Hohlraum x-ray image (0.08 ns frame time) taken at time 0.12 ns is shown. For this picture only, the hohlraum had thin (2 μm) Au walls, and the gas fill was suppressed to allow a sufficient production of L-shell photons that reach the pinhole camera to record an image. (c), (d) Profiles within the hohlraum along a beam path, as calculated with LASNEX, are plotted for neopentane (c) and propane (d) gas fills [J. C. Fernandez *et al.*, Phys Plasmas **7**, 3743 (2000)].

raum midplane (Fig. 3-31, bottom left). In the homogeneous region, LASNEX predicts $T_e = 2.5$ keV for the propane fill due to decreased laser absorption at lower n_e, and $T_e = 3$ keV for the high-pressure isobutane due to increased laser absorption at higher n_e. Besides the changes predicted in T_e, varying the gas fill is a straightforward way to vary n_e, and consequently to vary v_e at constant I and v_i over the range of interest for ignition hohlraums. These nominal plasma conditions correspond to $k\lambda_D \approx 0.43$ for propane, $k\lambda_D \approx 0.325$ for neopentane and $k\lambda_D \approx 0.25$ for the high-pressure isobutane where k is the wave number of the Langmuir wave. Although T_e is designed to remain fairly constant over the period when the interaction beam is on, T_i is predicted to increase in time (Fernandez *et al.*, 1996a) due to electron–ion collisions, reaching $T_i/T_e \approx 1/4$, compared to about 1/2 expected with the longer laser pulse in the NIF.

The measured reflectivity includes all of the backscattered light within an 18° cone from the interaction beam propagation direction, significantly larger than the interaction beam cone. In practice, the SRS light outside the interaction cone is always negligible whenever an $f/4.3$ interaction beam is used, which is the case here.

Time-integrated measurements of SRS, R_{SRS}, as the interaction beam intensity is varied are shown in Fig. 3-32 for two different gas fills. Significant SRS is measured for laser intensity above $I \approx 10^{14}$ W/cm^2. The observed onset intensity is consistent with a model which computes the response of a statistical ensemble of hot spots from an RPP beam (Rose and DuBois, 1994), provided SRS is in the strong damping regime. In this model, significant reflectivity occurs when a critical intensity is exceeded. The change in the onset intensity seen in Fig. 3-32 as the electron density n_e is changed, is consistent with the expected change in the critical intensity I_c defined as the intensity at which the SRS gain at the mean intensity is one for a length equal to the speckle length. Examining Eq. (3-12) for the SRS gain with collisionless damping, the dominant contributor to v_e here, and one sees that the critical intensity decreases with density because the Landau damping decreases with increase in density. For intensities of interest for NIF, $I \approx 2 \times 10^{15}$ W/cm^2, the SRS reflectivity R_{SRS} is insensitive to the exact value of intensity I, which is one manifestation of nonlinear SRS saturation. In these experiments, the two reflectivity measurements from neopentane plasmas in which the interaction beam was temporally smoothed by spectral dispersion (3 Å at 1.053 μm) are lower than the measurements in experiments which used only random phase plates but still higher than 10% and higher than typical in gasbags.

The SBS reflectivity, much lower than the SRS, is also shown in Fig. 3-32 for the same shots, including the contribution near but outside the interaction beam cone. The onset intensity for SRS lies significantly below that for SBS. Also, as expected, the onset intensity for SRS changes with n_e while for SBS it does not.

Figure 3-33 shows time resolved spectra from two toroidal hohlraum experiments (Montgomery *et al.*, 1998), a standard hohlraum and one which was lengthened by 0.25 mm. The wavelength of the Raman scattered light from the three

Downloaded 20 Mar 2011 to 69.181.48.121. Redistribution subject to AIP license or copyright; see http://pop.aip.org/about/rights_and_permissions

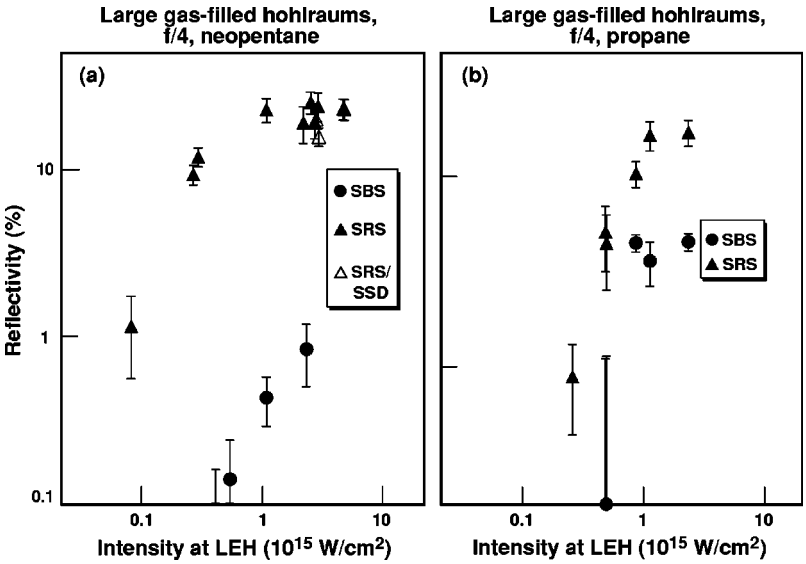

FIG. 3-32. Time-averaged reflectivity for stimulated Raman scattering, R_{SRS}, and for stimulated Brillouin scattering, R_{SBS} is plotted versus interaction beam intensity I for gas fills of neopentane, $n_e/n_c=0.11$ (a), and propane, $n_e/n_c=0.065$ (b). The nominal plasma conditions correspond to $k\lambda_D\approx 0.325$ for neopentane (a) and $k\lambda_D\approx 0.43$ for propane (d) [J. C. Fernandez *et al.*, Phys Plasmas **7**, 3743 (2000)].

gas fills can be matched using the kinetic SRS dispersion relation by assuming $[n_e/n_c, T_e\ (\mathrm{keV})]=(0.055,2.5)$, (0.11, 2.75), and (0.13, 3.0), respectively. The density values are somewhat lower than the nominal gas fill values corresponding to the expected initial densities.

At a time of about 0.8 ns in the smaller hohlraum and 1.0 ns in the stretched hohlraum, there is a disruption in the spectrum. There is a decrease in the Raman scattering at the wavelength corresponding to the gas fill and significant scattering at a longer wavelength corresponding to a higher density perturbation from the blast wave of the hohlraum window. The measured SBS also peaks at this time. It is tempting to assume that the blast wave, generated by the explosion of the hohlraum window, is causing these spectral features (Montgomery *et al.*, 1998). However, the disruption in the scattered spectrum occurs only in a relatively narrow time interval while the interaction beam passes through this blast wave throughout its time duration. A calculation of the linear gain for SRS along the entire interaction beam path shows no discontinuity as a function of time. However, if the linear gain is calculated over a restricted region of the interaction beam path, from 0.6 to 1.2 mm, the calculated spectrum is similar to that which is observed. Also the time at which the blast wave would get to this region is consistent with the time at which the spectral change is observed. This is possibly evidence that the observed scattering is coming from a restricted region in the hohlraum. There is nothing in the LASNEX calculations of the hohlraum conditions which would pick out this region as more important than any other for the effects of the blast wave. However, this region does coincide approximately with the region where the interaction beam intersects a beam coming from the opposite side of the hohlraum. More work will be required to understand these features of the scattering from toroidal hohlraums. Early gasbag experiments, which used a thicker gasbag wall also showed a disruption in the scattering spectrum. Later experiments with thinner walls showed no such features.

Figure 3-34(a) shows the highest instantaneous SRS reflectivity versus electron density from any given shot during

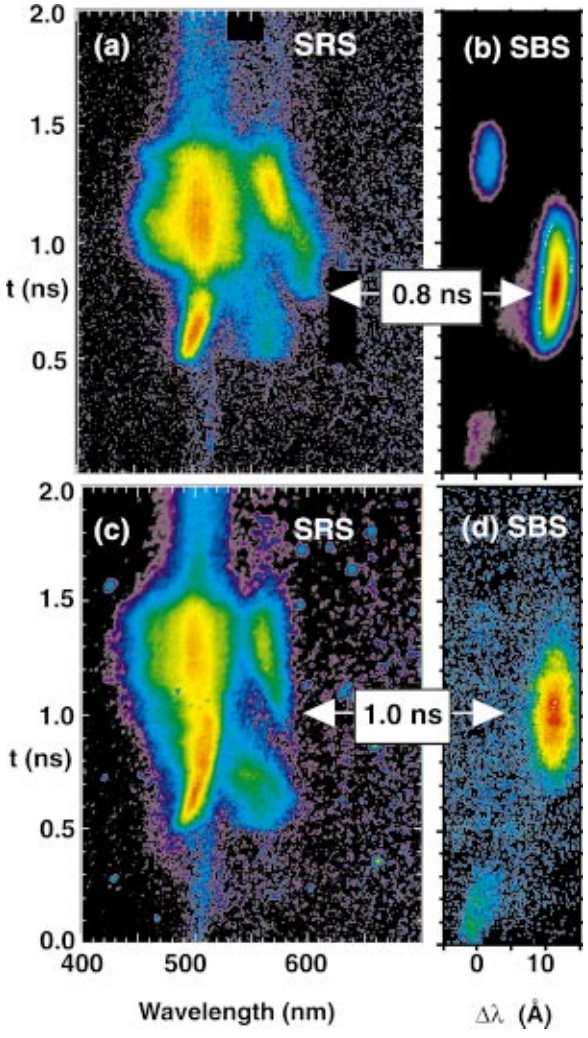

FIG. 3-33. (Color) The time history of the SRS spectrum (a) and the SBS spectrum (b) in propane-filled (C3H8) hohlraums for the standard toroidal hohlraum length shows an earlier onset of SBS and disruption of SRS than that of the SRS spectrum (c) and SBS spectrum (d) of a toroidal hohlraum whose length was increased by 0.25 mm [J. C. Fernandez *et al.*, Phys Plasmas **7**, 3743 (2000)].

Downloaded 20 Mar 2011 to 69.181.48.121. Redistribution subject to AIP license or copyright; see http://pop.aip.org/about/rights_and_permissions

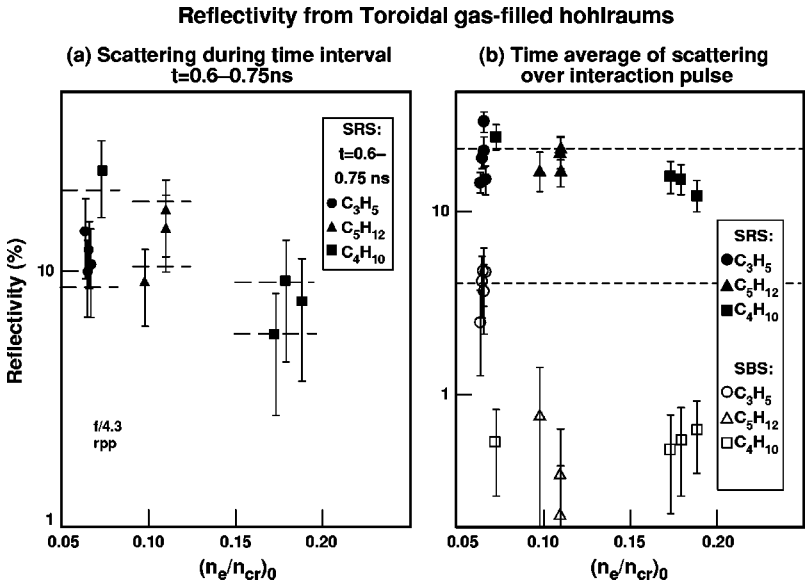

FIG. 3-34. (a) Instantaneous R_{SRS} at time $=0.675 \pm 0.075$ ns based on the measured light leaving the hohlraum are plotted vs initial n_e/n_c of the gas fill. A range equal to one standard deviation above and below the average reflectivity for each density is indicated. (b) Similar plot of the time-averaged R_{SRS} and R_{SBS}. For all these shots, the laser intensity at the hohlraum laser entrance hole is 2 to 3×10^{15} W/cm^2 [J. C. Fernandez *et al.*, Phys Plasmas **7**, 3743 (2000)].

the period 0.6 to 0.75 ns. This is a period during the interaction pulse just before the disruption in the spectrum. Only the fraction of the SRS backscatter near the wavelength of the gas fill is included in order to exclude any SRS associated with plasma outside of the density plateau region.

The time-integrated SRS reflectivity shown in Fig. 3-34(b) was saturated at 15–20 % for laser intensity above 10^{15} W/cm^2 and weakly dependent on electron density. The density was varied systematically in order to vary the linear damping rate of plasma waves. The SRS reflectivity from the toroidal hohlraums is sizable even for the low-density gas fill. From the SRS spectrum in the propane fills, the matching electron density is $n_e=0.055n_c$ for the measured electron temperature of 2.5 keV whereas the matching temperature is 1.65 keV for $n_e=0.065n_c$, the electron density corresponding to the initial fill. The Langmuir wave–wave number, $k_e=k_0+k_{SRS}$, is also determined from the SRS spectrum which has $k_e\lambda_D\approx0.35$ for the lower temperature but $k_e\lambda_D\approx0.5$ for the higher temperature. The measured SRS onset intensity and the spatial gains needed to explain the high reflectivities observed for the large $k_e\lambda_D\approx0.5$ imply much lower values of Langmuir wave damping rates than expected from the LASNEX-calculated plasma temperatures (assuming Maxwellian electron distributions). Trapping of electrons in the driven Langmuir waves has the required effect of lowering the damping rate (Vu *et al.*, 2001). The measured SRS tends to increase in time, a trend that correlates with the increase of the ion temperature over time as the ions are heated by the electrons. Higher ion temperature should increase the damping rate of ion–acoustic waves. Therefore these observations are consistent with previous observations that the Raman reflectivity in these plasmas depends on the damping rate of ion–acoustic waves as discussed above for gasbag plasmas.

5. Scale-1 Nova hohlraums

As shown in Fig. 3-35, scale-1 gas-filled hohlraums are also heated with nine $f/4$ beams and one smoothed $f/8$ or $f/4.3$ interaction beam, both with 2.4 ns shaped pulses. Five laser beams enter from each side, overlap in the LEH, and are distributed on the hohlraum wall uniformly over the azimuth but covering only about half the circumference. In the axial view in Fig. 3-35, the footprints of the individual laser beams are seen in the x-ray emission from the heated gold. The interface between the gold blowoff and low-Z gas fill, also visible in the x-ray emission, is similar to the LASNEX lineout in Fig. 3-10. In the first set of experiments, the heater beams were unsmoothed. After control of laser beam deflection by beam smoothing was demonstrated, phase plates were used on all beams for hohlraum experiments. The nominal intensity of the unsmoothed $f/4$ heater beams on the hohlraum wall is 5×10^{14} W/cm^2. The $f/8$ RPP-smoothed beams have an intensity of about 2×10^{15} W/cm^2 and have roughly the same intensity in the LEH and at the wall without accounting for inverse bremsstrahlung absorption.

LPI experiments in scale-1 gas-filled Nova hohlraums used a shaped drive pulse that has a rapid rise to a ''foot'' power of about 1 TW/beam, followed by a gradual ramp up to a peak of about 2 TW/beam at about 1.6 ns. This is the standard pulse-shape 22 pulse used in the symmetry experiments discussed in Sec. V. The electron temperature was determined initially by spectroscopic methods (Back *et al.*, 1996) and later by Thomson scattering (Glenzer *et al.*, 1999a). Figure 3-35 shows the plasma volume probed with 4ω (261 nm) Thomson scattering and the measured electron temperature and axial flow velocity along the hohlraum axis. The measurement shows larger gradients in the temperature and the flow velocity than is consistent with LASNEX simulations unless heat flux inhibition by self-generated magnetic fields is included in the simulations (Glenzer *et al.*, 1999b).

Measurement of the backscattering from such hohlraums showed that energy loss due to reflection by SBS and SRS played a significant role in determining the hohlraum energetics (Glenzer *et al.*, 1998a). For the scale-1 gas-filled hohlraums, the near-backscatter imager detects a large fraction of the SBS, which appears in a localized spatial region. This

Downloaded 20 Mar 2011 to 69.181.48.121. Redistribution subject to AIP license or copyright; see http://pop.aip.org/about/rights_and_permissions

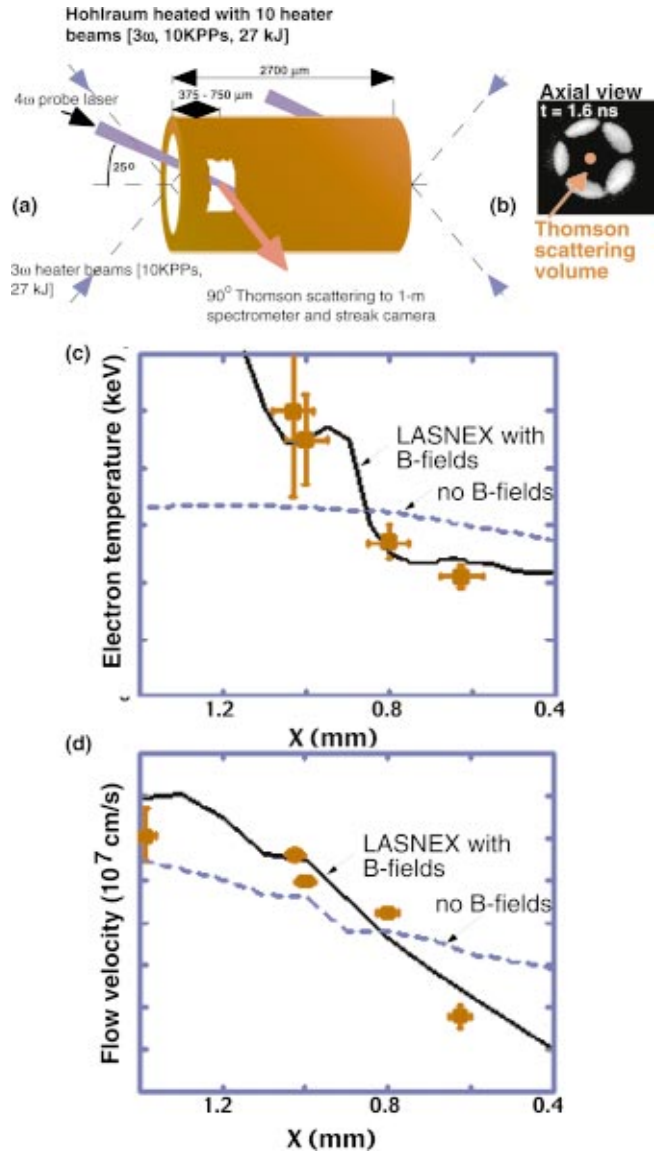

FIG. 3-35. (Color) (a) The 2.4 ns $f/4$ 351 nm laser beams used to heat the scale-1 Nova gas-filled hohlraum and the Thomson scattering configuration are shown schematically. The interaction beam had the same pulse shape and duration as the heater beams. (b) An axial view in x-ray emission. The electron temperature (c) and the flow velocity component along the hohlraum axis (d) measured with Thomson scatter, are shown in the bottom two figures. Only with magnetic fields in LASNEX are the measurements simulated correctly [S. H. Glenzer *et al.*, Phys. Plasmas **6**, 2117 (1999)].

shift from the location of the incident beam is a consequence of beam deflection. In a gasbag hohlraum with a diameter twice as large as the scale-1, reflected SBS light was deflected as much as 10 degrees (MacGowan *et al.*, 1996). The total backscattering losses for gas-filled hohlraums with unsmoothed heater beams often exceed 15%. Time-resolved measurements show that the combined peak loss to SBS and SRS, with unsmoothed heater beams, can be as high as 40% at some times in the pulse in some targets. Sidescatter for SRS (1.9%) and SBS (1.7%) without smoothing was reduced to negligible amounts with beam smoothing.

As indicated in Fig. 3-10, the SBS gain exponents calculated for the scale-1 gas-filled hohlraums are similar to or higher than that calculated for the NIF outer beams within the Au part of the plasma. Those calculations used the plasma conditions determined from LASNEX simulations without magnetic field reduction of the heat flux out of the directly heated plasma. The time variation of the gain exponents and spectral shifts for SRS and SBS disagreed with the observed shifts and time dependence. New LIP calculations used the plasma conditions from the LASNEX simulations with magnetic fields that agreed with the measured electron temperature (Glenzer *et al.*, 1998a; Glenzer *et al.*, 2001). These LIP calculations of the SBS gain exponent for methane filled hohlraums show a peak gain late in time that is redshifted by 2 to 3 Å from 351 nm and corresponds to SBS occurring in the Au shelf that has been ablated from the Au wall by radiative and laser ablation. A time-resolved SBS spectrum and the time-dependent gain exponent from LIP is shown in Fig. 3-36. The SRS gain exponent without magnetic fields peaked after the peak of the incident laser power, ~ 1.5 ns, whereas the data showed a peak SRS reflectivity at 1 ns. The new calculations of the SRS gain exponent reproduce that peak at 1 ns because the electron temperature in the low-density gas within the laser beam is much higher with magnetic fields. Without beam smoothing, the observed SRS spectral width at 1 ns is much broader than the calculated linear gain exponent width. This broad spectrum, thought to be a consequence of self-focusing, is strongly narrowed when SSD is applied as shown in Fig. 3-37.

Another important consequence of the improved LASNEX modeling is the reduction of the calculated gain exponent in scale-1 hohlraums. It is not certain that similar reductions will occur in NIF hohlraums. The similarities in the spectral shifts and reflectivity history indicate that LASNEX is correctly calculating the hohlraum plasma conditions: the electron density n_e, the electron temperature T_e, and the flow V along the laser beam path. The LIP calculations assume a beam intensity spatially averaged in the transverse direction, while the experiments have short-wavelength speckle structure.

The SBS and SRS reflectivity from the scale-1 hohlraums dropped when beam smoothing was applied. Figure 3-38 shows peak SBS and SRS reflectivity as a function of SSD bandwidth for the scale-1 methane-filled hohlraums. Both SBS and SRS are the peak values observed during the shaped pulse experiment, during the peak of the incident pulse. The quoted reflectivities include all backscatter from 0° out to 20° from the center of the beam. The SBS backscatter with no bandwidth is quite high (15% to 20%), while the addition of 0.5 Å bandwidth reduces the SBS to about 2%. Two experiments were done at each bandwidth condition and the data are reproducible. The experimental uncertainty is $\pm 25\%$ of the quoted value of reflectivity.

Figure 3-39 shows measured time integrated SBS and SRS reflectivity as a function of SSD bandwidth for the scale-1 methane-filled hohlraums (Glenzer *et al.*, 2001). The peak SBS reflectivity is twice the time-integrated values. The interaction beam peak intensity is 2×10^{15} W/cm^2. The experimental uncertainty is $\pm 25\%$ in the reflectivity. Data taken with the earlier RPP/(3 GHz) SSD combination are shown (Moody *et al.*, 2001) as open circles. The newer data with the KPP and the 17 GHz modulator (solid circles) are

Downloaded 20 Mar 2011 to 69.181.48.121. Redistribution subject to AIP license or copyright; see http://pop.aip.org/about/rights_and_permissions

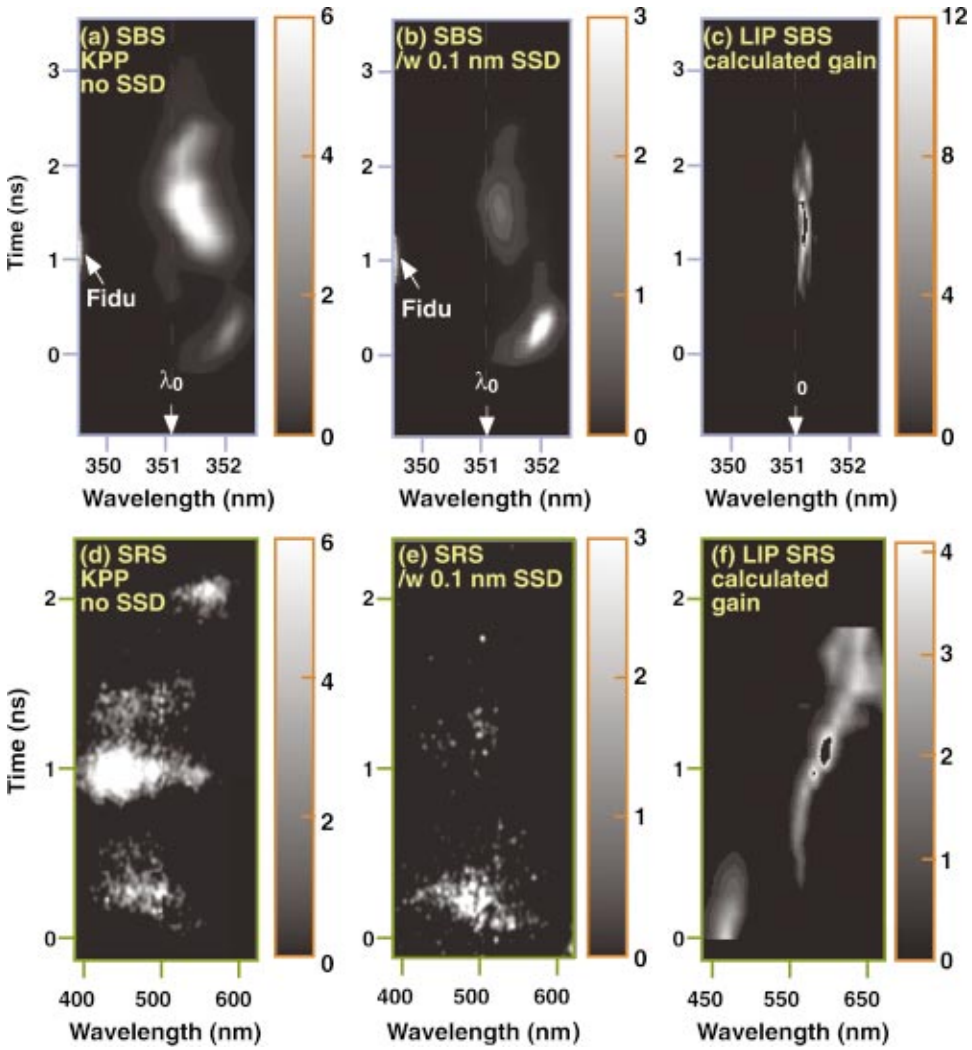

FIG. 3-36. (Color) The SBS and SRS spectrum vs time from a scale-1 Nova hohlraum without SSD (a) and (d), with SSD (b) and (e), and the calculated SBS (c) and SRS (f) gain. The SBS signal with SSD is difficult to discern but peaks at 1.5 ns and is narrower than without SSD. The spectral shift and time history agree with the SBS linear gain calculated with LIP using the mean laser intensity and LASNEX-calculated plasma parameters. The SRS spectrum is much narrower and reduced with SSD than without. It peaks at 1 ns when the calculated gain peaks. However, the SRS peaks at a shorter wavelength than the calculated gain. The late-time SRS gain arises from high-density plasma where it might be reabsorbed or inhibited by SBS competition [S. H. Glenzer *et al.*, Phys. Plasmas **8**, 1692 (2001)].

consistent. As predicted by calculations, these data indicate no significant difference between the NIF implementation of beam smoothing with KPP and 17 GHz SSD and that with RPP and 3 GHz SSD. The SRS and SBS reflectivity from scale-1 hohlraums with SSD were measured to be the same for one- or two-color cycles in agreement with the theoretical calculations discussed in Sec III B. However, the radiation temperature was 5 eV higher with two-color cycles than with one-color cycles (Kirkwood *et al.*, 1997a; Glenzer *et al.*, 2000).

Figure 3-39 also shows two data points taken with the addition of polarization smoothing (triangles) that lie among the other data, implying that, at least in this experiment, there was little benefit to polarization smoothing for the laser and plasma conditions relevant to the NIF outer beams.

Figure 3-40 shows the results of tests of beam smoothing at the higher irradiance expected in 350 eV hohlraums. The targets were scale-1 gas-filled hohlraums and the interaction beam was smoothed with a RPP and SSD, with and without

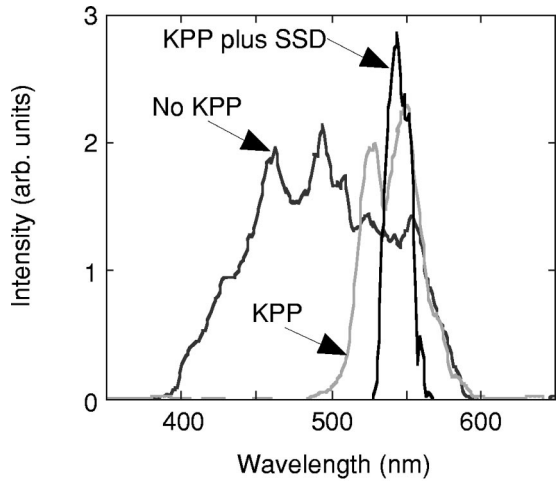

FIG. 3-37. SRS spectra from gas-filled hohlraums at 1.8 ns$<t<$2 ns for various smoothing conditions. With improved smoothing the spectra narrow from 180 nm to 30 nm.

Downloaded 20 Mar 2011 to 69.181.48.121. Redistribution subject to AIP license or copyright; see http://pop.aip.org/about/rights_and_permissions

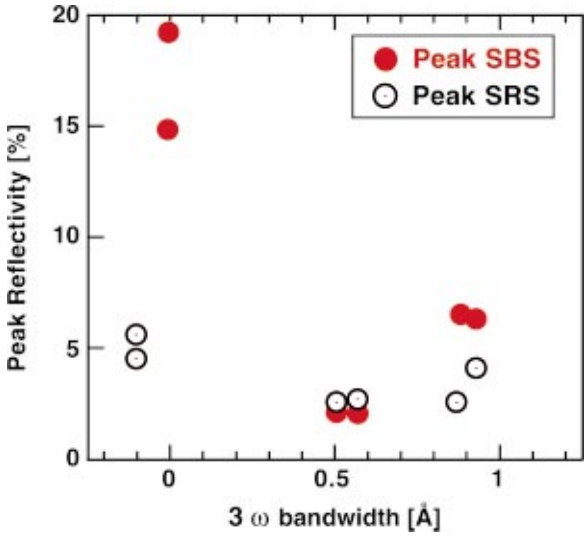

FIG. 3-38. (Color) Nova scale-1 hohlraums simulating the NIF outer beam plasma, SSD beam smoothing reduces backscatter significantly. SBS and SRS backscatter data from scale-1, methane-filled hohlraums with a Au-shelf plasma are similar to those encountered by the NIF outer beams. The reflectivity shown is the peak in time (averaged over the 50 ps diagnostic resolution) corresponding to the time of peak incident intensity (2.5×10^{15} W/cm^2). In these experiments, the interaction beam was smoothed using a 3 GHz SSD and an RPP [S. H. Glenzer *et al.*, Phys. Plasmas **8**, 1692 (2001)].

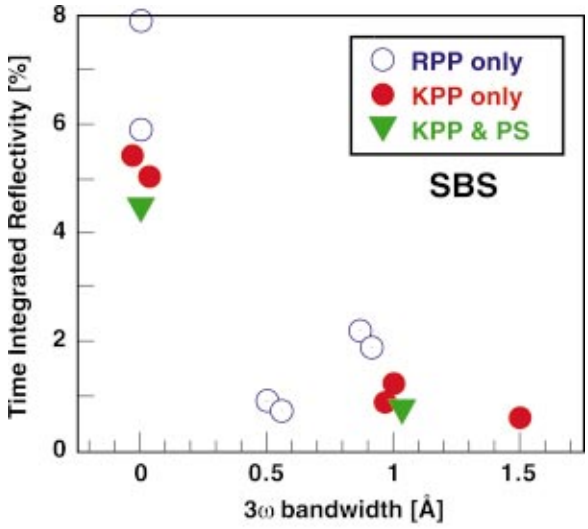

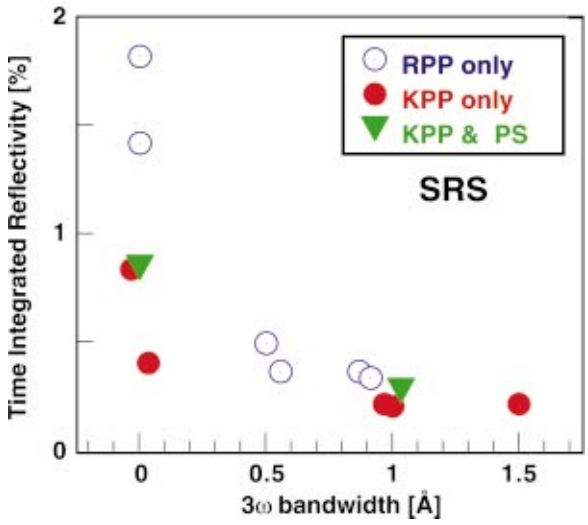

FIG. 3-39. (Color) SBS and SRS from Nova scale-1 hohlraums with NIF-like smoothing using 17 GHz SSD with a KPP. The reflectivities are similar to those from earlier Nova scale-1 hohlraum experiments using 3 GHz SSD and an RPP. Polarization smoothing does not have a significant effect for these plasma and laser conditions [S. H. Glenzer *et al.*, Phys. Plasmas **8**, 1692 (2001)].

PS. The results show a significant benefit to using PS in higher intensity applications. These hohlraum data, plus the data taken with the higher density gasbag plasmas (Fig. 3-20), show that the sum of SBS and SRS with high laser intensity can be kept below 10% with the appropriate combination of KPP, SSD, and PS. These are the plasma and laser conditions expected in 350 eV ignition-scale hohlraums. Furthermore, because the SBS and SRS of high intensity interaction beams (up to 4×10^{15} W/cm^2) are kept below 10% with beam smoothing, the KPPs that determine the shape the NIF focal spots can be designed with more latitude. That is, instead of designing for a flat intensity profile with the lowest possible peak intensity, one might allow the peak intensity to increase in order to better shape the sides of the focal spot or to allow a smaller LEH.

The scale-1 hohlraum SBS and SRS reflectivities are qualitatively different from the toroidal ones. Although the toroidal hohlraums plasmas are confined within high-Z radiating walls similar to the scale-1 hohlraums, the reflectivity behavior is more similar to high density gasbags filled with neopentane in that the SRS always dominates the reflectivity. Also, the high SRS and low SBS reflectivity is similar to that measured in gasbags after the heaters are turned off. An explanation for high SRS in toroidal hohlraums might be that the SRS is produced in regions of plasma where the electron temperature is lower than calculated. The SRS spectrum is consistent either with the nominal fill density and a lower temperature or (as suggested in the Toroidal section) with a lower density and higher temperature. The former combination produces much higher gain exponents for SRS than the latter, namely an SRS intensity gain exponent of 34 mm and 10 mm, respectively, for a laser intensity of 2×10^{15} W/cm^2. Unlike the gasbags, the heater beams do not heat directly the entire plasma. Nonetheless, the LASNEX calculations predict relatively uniform conditions inside the hohlraum because rapid electron heat conduction results with use of Bragniskii electron transport coefficients in an unmagnetized plasma (Braginskii, 1965). As noted previously, Thomson scattering measurements on Nova scale-1 gas-filled hohlraums show that temperatures near the laser entrance holes are significantly higher and interior temperatures much lower than those calculated by LASNEX without magnetic fields. When self-generated magnetic fields are included in the LASNEX calculations, the measured temperatures as well as the plasma flow velocities are in agreement with experiment. These differences could mean that conditions along the interaction beam in toroidal hohlraums differ significantly from the LASNEX calculations done to date

Downloaded 20 Mar 2011 to 69.181.48.121. Redistribution subject to AIP license or copyright; see http://pop.aip.org/about/rights_and_permissions

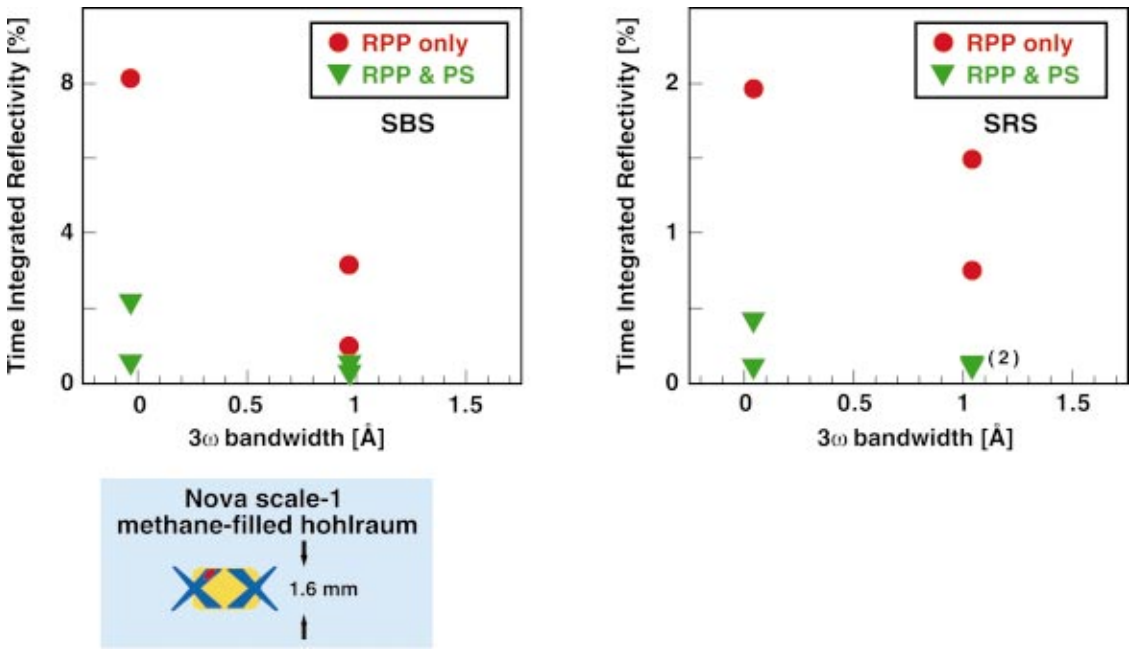

FIG. 3-40. (Color) Scale-1 hohlraum experiments at 4×10^{15} W/cm^2 using 17 GHz SSD and an RPP were designed to stress LPI for the outer NIF beams. The experiments simulate conditions for the NIF outer beams in a 350 eV hohlraum. The SBS and SRS are still low with SSD, and the addition of polarization smoothing has a clear impact [S. H. Glenzer *et al.*, Phys. Plasmas **8**, 1692 (2001)].

since the plasma intercepted by the interaction beam (along most of its propagation path) is only heated by the interaction beam and the background temperature depends on conduction from the other beams.

6. Crossing-beam energy transfer experiments

Crossing-beam experiments were carried out at Nova in both gasbag and exploding foil plasmas.

In the experiments carried out using gasbag plasmas (Kirkwood *et al.*, 1996a), the beams cross at a 53° angle and have slightly mismatched frequencies, so that the frequency difference is close to the frequency of the resonant ion–acoustic wave, and Brillouin sidescattering is seeded. The power transmitted through the plasma by the low-frequency probe beam is measured as a function of time by the TBD. The amplification is determined by comparing an experiment in which the high-frequency pump beam is present with one in which it is absent. As shown in Fig. 3-41(a), the transmitted power rises rapidly after the pump beam is turned on to a value well above what is measured when the pump is off. The experiments demonstrated that as much as several hundred joules of energy can be transferred during a 1 ns interaction time, resulting in an amplification of the probe beam by a factor of as much as 2.5. Energy transfer occurs only when the difference in the beam frequencies is as large as the frequency of the resonant ion wave, corresponding to $\Delta\lambda = 0.5$ nm in Fig. 3-41(b).

Experiments in exploding foil plasmas have shown that energy can be transferred between identical beams ($\Delta\lambda = 0$) provided there is a Mach-1 flow present to shift the frequency of the ion–acoustic wave to zero (Wharton *et al.*, 1998; Wharton *et al.*, 1999). Simulations of the NIF hohlraum show Mach-1 flow in the vicinity of the laser entrance hole. Analysis of the beam intersection geometry and flow velocities in the hohlraum (Kirkwood *et al.*, 1996a) shows that symmetry suppresses energy transfer between beams within a single cone, and that a frequency difference between beams in different cones can allow the ion wave resonance to be detuned and energy transfer between cones to be suppressed. For these reasons, the ability to operate NIF in the ''two-color'' mode is now being maintained as an option.

7. Nonlinear SBS saturation experiments

In Nova experiments, ion–acoustic wave amplitudes were observed to be saturated for conditions similar to those anticipated in future ignition experiments (Glenzer *et al.*, 2001a). The ion waves were measured with ultraviolet Thomson scattering of a 263 nm probe beam in CO_2 filled gasbag experiments with an electron temperature of $T_e = 3$ keV. The temporally resolved Thomson scattering spectra have shown simultaneously the scattering from thermal electrostatic fluctuations and ion–acoustic waves that have been excited to large amplitudes by SBS from a kilojoule interaction beam at 351 nm (cf. Fig. 3-42). The ion–acoustic waves saturate for $I > 5\times10^{14}$ W cm^{-2}. These results of the local Thomson scattering measurements are also consistent with the observed SBS reflectivity that shows saturation at the 30% level for these interaction beam intensities.

The experiments have been compared with calculations using the laser–plasma interaction code pF3D. By simulating the propagation and SBS scattering of the 3ω interaction beam through the whole length of the gasbag plasma one finds that 30% SBS corresponds to an ion–wave amplitude of $\delta n/n_e = 2\times10^{-3}$. Without nonlinear damping, the simulations show 100% reflectivity and ion–acoustic fluctuations in the Thomson scattering volume that return to the thermal

Downloaded 20 Mar 2011 to 69.181.48.121. Redistribution subject to AIP license or copyright; see http://pop.aip.org/about/rights_and_permissions

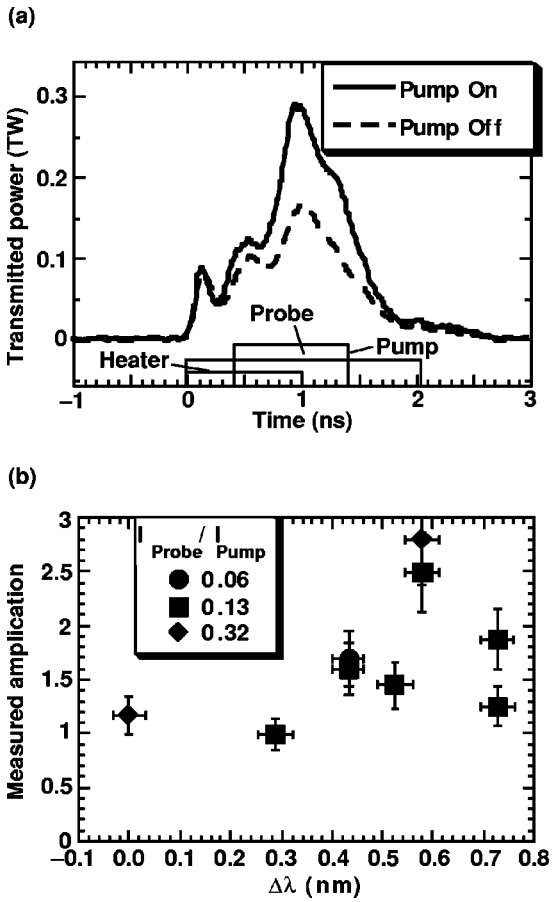

FIG. 3-41. (a) Measurement of the probe-beam power transmitted through the plasma for the case $\Delta\lambda = 0.45$ nm and $I_{\text{probe}}/I_{\text{pump}} = 0.06$. In the "pump on" case, a 2×10^{15} W/cm^2 pump beam intersects the probe between 0.4 and 1.4 ns, causing the probe to be amplified by a factor of 1.7 above the "pump off" case. (b) A series of experiments measured the amplification of the probe beam as a function of the wavelength separation of the two beams. The amplification is greatest when the frequency separation is in the vicinity of the prediction for the unshifted ion wave resonance, $\Delta\lambda = 0.45 \pm 0.04$ nm [R. K. Kirkwood *et al.*, Phys. Rev. Lett. **76**, 2065 (1996)].

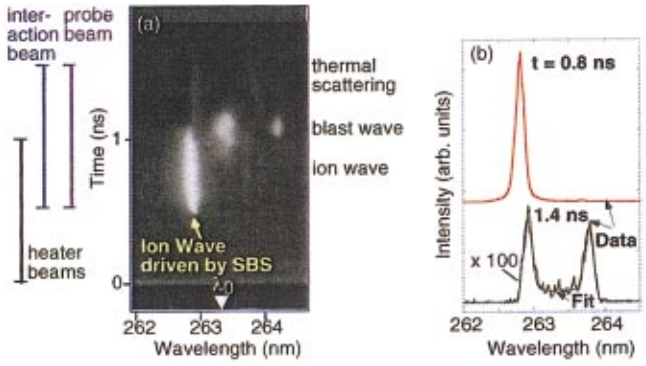

FIG. 3-42. (Color) (a) Time-resolved Thomson scattering spectrum showing coherent scattering on ion waves driven by SBS, scattering on the blast wave, and thermal incoherent scattering at late times. The time sequence of the laser beams is indicated on the left. (b) Lineouts at $t = 0.8$ ns and $t = 1.4$ ns. The earlier lineout shows 2 orders of magnitude enhanced scattering compared to the spectrum at later times. The latter is fit with the theoretical TS form factor for a gas fill CO_2 plus 1% Ar.

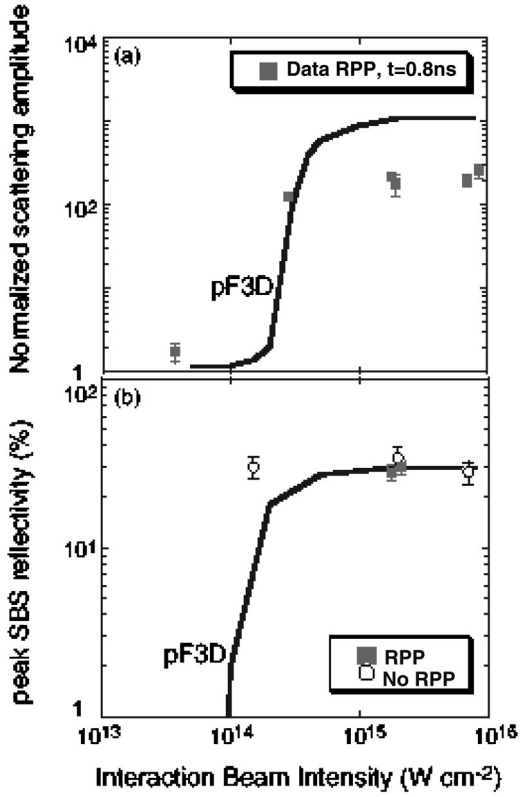

FIG. 3-43. (a) Scattering amplitude of the blueshifted ion acoustic wave normalized to the intensity of the redshifted thermal peak for various interaction beam intensities. Amplitudes are for $t = 0.8$ ns. (b) SBS reflectivity for no RPP data is observed to saturate at the 30% level. In both (a) and (b), the pF3D curves represent modeling.

level after a short initial burst, both in contradiction with experimental data. Only by including a nonlinear damping model that is based on secondary decay of the primary ion–acoustic wave into two ion waves can one find results that are consistent with the experiments. Choosing a maximum ion–wave amplitude that scales with ion–wave decay is particularly motivated by the fact that CO_2 plasmas approach low ion–wave damping conditions (similar to high-Z plasmas like Xe or Au) for which other nonlinear effects are less important. For example, the ion–wave fluctuation level observed in these experiments is significantly smaller than the threshold for ion–wave breaking by trapping, i.e., $\delta n/n_e = 0.2$.

Figure 3-43 shows that by using a nonlinear scaling, both SBS reflectivity and Thomson scattering data can be reproduced. The remaining small discrepancies might be explained by uncertainties in the absolute measured scattering power introduced by the Cassegrain telescope (alignment and incomplete sampling). However, the model assumed that two-ion-wave decay occurs at a threshold lower than suggested by theoretical linear calculations. This indicates that either our theory of the two-ion-wave decay instability is insufficient, or that other nonlinear mechanisms need to be included.

These experiments provide the first experimental evidence that the SBS instability is saturated in inertial confinement fusion plasmas. These findings further indicate that la-

Downloaded 20 Mar 2011 to 69.181.48.121. Redistribution subject to AIP license or copyright; see http://pop.aip.org/about/rights_and_permissions

ser scattering losses in future ignition experiments on the NIF might be reduced by controlling the plasma conditions together with the nonlinear wave saturation processes. Moreover, these Nova gasbag experiments have clearly shown the limits of present modeling capability. It is obvious that a first-principal understanding of the saturation process will be required to obtain a predictive modeling capability. We are planning to address the nonlinear wave physics of the high temperature, low ion wave damping plasmas that primarily occur in the high-Z wall plasma of an ignition hohlraum in the immediate future using the Thomson scattering capability that we are presently implementing on the Omega Laser Facility.

D. Summary of laser–plasma interactions in NIF-scale plasmas and future work

For the Nova plasmas which most closely approach NIF conditions, time-averaged absorption of about 90%, have been achieved. As indicated in Fig. 3-10, the Nova gasbag plasmas emulate the NIF inner beams where the long pathlength in low-Z material dominates the instability gain, while the Nova scale-1 gas-filled hohlraums emulate the outer beams where the Au plasma dominate the LPI instability gain. Figure 3-29 shows that the combined SBS and SRS scattering is less than 10% from a HeHNe gasbag plasmas, which has the most NIF-like composition and normalized ion-wave damping. For the scale-1 hohlraums, the combined SBS and SRS scattering shown in Fig. 3-39 is less than 5% with NIF levels of smoothing.

During the last decade, the understanding of filamentation effects in NIF relevant plasmas has advanced dramatically. It is now possible to calculate the impact of various beam smoothing schemes on reducing filamentation and its secondary impact on SBS and SRS. Filamentation in a flowing plasma, and its impact on hohlraum symmetry can be modeled quantitatively.

However, there is not yet a predictive capability for SBS and SRS in NIF relevant plasmas. In particular, nonlinear saturation mechanisms are incompletely understood. Therefore, the principal research activities of the LPI theory and experimental program are to investigate nonlinear saturation mechanisms for SRS and SBS, to design experiments to test their consequences, and to measure the amplitudes of the plasma waves with space and time resolved Thomson scatter. Understanding the frequent anticorrelation of SBS and SRS, such as that indicated in Figs. 3-20 and 3-21, is at an early stage. Under some conditions, which are not completely understood, large levels of scattering are observed. The toroidal hohlraum data consistently show scattering levels of 15% to 20%. Although scattering from the hydrocarbon fill gasbags is consistently below 10% while the heater beams are on, particularly with SSD beam smoothing, scattering levels can exceed 15% shortly after the heating beams are turned off. Because the Nova experiments are not an exact match to NIF plasmas, there is still uncertainty in the optimal choice of hohlraum design and drive conditions for NIF. The current plan is to further develop the understanding of LPI under NIF relevant conditions in tandem with construction and startup of NIF. Omega will be used for KPP optimization and for better understanding the scaling of SRS/SBS. The Trident laser at LANL will be used to study effects on a single speckle scale in well characterized plasmas (Montgomery *et al.*, 1999). Continued improvements are expected in modeling, which will take advantage of the massively parallel computer capability being developed in the ASCI program. As the first beams of NIF are activated, some of the first experiments will be LPI experiments on larger-scale plasmas, which will be much closer to full NIF scale. These experiments will be used to optimize the KPP, PS, and SSD combination for beam smoothing, to optimize the He/H hohlraum fill, and to look at nonlinear processes that affect SBS, SRS, crossed-beam energy exchange, and beam deflection.

IV. HOHLRAUM DRIVE AND COUPLING EFFICIENCY

Both the efficiency of coupling driver energy to a capsule and the physics of hohlraum symmetry are largely determined by the physics of x-ray production and absorption in the hohlraum. Understanding of hohlraum drive and coupling has been developed using a combination of theory, experiments at Nova and Omega, and radiation hydrodynamics simulations. In this section, the theory is reviewed in part A and the experiments compared with theory and simulations are reviewed in part B.

A. Theory

The theory for hohlraum coupling assumes the laser irradiates the hohlraum wall producing bright sources of x rays. These x rays heat the rest of the high-Z hohlraum wall. In the theory below, this heating is modeled by an ablation heat wave, or Marshak wave. A self-similar solution to the ablation heat wave problem is derived. This solution is then used to develop hohlraum energetics models based on energy balance models.

1. Hohlraum drive theory

In the following analysis (Lindl, 1998j), the hohlraum wall is approximated by a planar surface exposed to a uniform temperature of x rays, and a Lagrangian coordinate system is used for the analysis. The two independent variables are time t and a Lagrangian spatial coordinate $m = \int \rho\, dx$, which is the mass per unit area of material between the fluid particle and the surface of the hohlraum wall. Conservation of mass and momentum are given by

$$\frac{\partial U}{\partial t} = \frac{\partial v}{\partial m} \tag{4-1}$$

and

$$\frac{\partial v}{\partial t} = \frac{\partial P}{\partial m}, \tag{4-2}$$

where $U(t,m) = 1/\rho$ is the specific volume, $v(t,m)$ is the fluid velocity in the rest frame of the hohlraum wall, and $P(t,m)$ is the pressure. Conservation of energy relates the heating $T\,dS$ of a fluid particle (where T is temperature and S represents specific entropy) to the thermal energy transported out of a fluid element by the energy flux, F. Since

Downloaded 20 Mar 2011 to 69.181.48.121. Redistribution subject to AIP license or copyright; see http://pop.aip.org/about/rights_and_permissions

$T\,dS = de + P\,dU$, where $e(t,m)$ is the internal energy per unit mass in the slab, the conservation of energy may be expressed as

$$\frac{\partial e}{\partial t} + P\frac{\partial U}{\partial t} = -\frac{\partial F}{\partial m}. \tag{4-3}$$

In this analysis, it is assumed that the opacity of the matter is sufficiently high that, on the time scales of interest, matter and radiation are in LTE. More specifically, the radiation field is assumed to be nearly isotropic and of the same characteristic temperature as the matter. Although the x-ray production region, near the laser critical density, violates this assumption and must be calculated using non-LTE (NLTE) models, the hohlraum wall loss, which is at higher density and lower temperature, is near LTE conditions. The dominant heat-transport mechanism is radiation transport, and the matter is assumed to be sufficiently opaque that the diffusion approximation (Zeldovich and Razier, 1966) can be used,

$$F = -\frac{4\sigma}{3K_R}\frac{\partial T^4}{\partial m}, \tag{4-4}$$

where K_R is the Rosseland mean opacity and σ is the Stefan–Boltzmann constant. Dimensional analysis of Eqs. (4-1) to (4-4) provides useful insight. Suppose that the source temperature, applied suddenly at $t=0$, is T_S. Let $\rho_S = 1/U_S$ be the initial density of the wall, and let P_S and e_S be the pressure and energy per unit volume that the material would have if it were heated to the full source temperature T_S before it could expand to a higher specific volume than U_S.

Initially, the diffusion process described by Eqs. (4-3) and (4-4) will heat the surface of the material so rapidly that it will remain stationary in comparison to the penetration speed of the heat front. When there is no hydrodynamic motion, these equations lead to a heat front that advances into the material according to a diffusive law of the form

$$(m^2/t)_{\text{front}} \approx \frac{4\sigma T_S^4/3K_S}{e_S}.$$

The inertia of the material allows the pressure P_S to cause disturbances, which propagate with a sound (or shock) speed that can be estimated from Eqs. (4-1) and (4-2),

$$(m/t)_{\text{front}} \approx \sqrt{P_S\rho_S}.$$

At early times, the penetration speed of the thermal wave exceeds this hydrodynamic speed, but at later times, the hydrodynamic speed far exceeds the rate at which the heat wave can penetrate the wall. The critical time scale t_S at which the hydrodynamic motion begins to affect the progress of the heat front is easily estimated from the previous two relationships:

$$t_S = \left(\frac{4\sigma T_S^4}{3K_S e_S}\right)\left(\frac{1}{P_S\rho_S}\right).$$

The depth of the slab that has been heated at this ''transition time'' t_S is estimated by $m_S = t_S\sqrt{P_S\rho_S}$.

For times $t \ll t_S$, it is safe to assume that $\rho = 1/U(t,m) = \rho_S$ everywhere in the slab, which eliminates the need to solve the mass and momentum equations. [This is Marshak's ''constant density'' solution (Marshak, 1958), which is equivalent to the classical nonlinear heat conduction problem.]

Rosen (Rosen, 1979) obtained an approximate similarity solution to Eqs. (4-1)–(4-4). The following analysis closely follows his solution. A more general solution is discussed by Hammer and Rosen (Hammer and Rosen, 2003).

First, the energy Eq. (4-3) is simplified by the assumption that, for slow subsonic radiation fronts, the pressure is nearly constant near the heat front. Detailed numerical simulations are consistent with this assumption. We put P inside the time derivative and deal with the enthalpy $h = e + P/\rho$. The enthalpy and Rosseland mean opacity K are then approximated by power laws of density and temperature:

$$h = h_S\left(\frac{\rho}{\rho_S}\right)^{-\varepsilon} T^l \tag{4-5}$$

and

$$K = K_{oR}\left(\frac{\rho}{\rho_S}\right)^{R} T^{-n}. \tag{4-6}$$

The opacity and enthalpy depend primarily on temperature but the density dependence can have important effect on radiation penetration. If the opacity of the heated material decreases as the density drops, more of the radiation emitted by the source reaches the colder, deeper regions of the wall. Thus, the heat front can progress somewhat more rapidly than the $m \propto \sqrt{t}$ diffusive behavior, since the heated material becomes less effective at insulating the underlying unheated material. On the other hand, if the specific energy increases with decreasing density, the expanding material at constant temperature requires an energy input. This effect counteracts the effect of a drop in opacity with density.

As an approximate solution to the dynamics in the blowoff region, the density is set equal to that of an isothermal expansion in the blowoff region,

$$\rho = \frac{m}{C_s t}, \tag{4-7}$$

where the sound speed C_s is given by

$$C_s = C_0\left(\frac{\rho}{\rho_0}\right)^{-\varepsilon/2} T^{l/2}. \tag{4-8}$$

From the definition of m, we see that the solution to Eq. (4-7) is $\rho = \exp(-x/C_s t)$. This simple model for the blowoff is adequate for typical hohlraums because the fraction of the energy in the blowoff is generally small, and the density profiles seen in detailed numerical calculations are reasonably well approximated by an isothermal blowoff near the high density wall. With these assumptions, the energy equation has similarity solutions of the form

$$m \equiv Wt^Q \tag{4-9}$$

and

$$T(m,t) = T_0\left(\frac{t}{t_0}\right)^P f(W), \tag{4-10}$$

Downloaded 20 Mar 2011 to 69.181.48.121. Redistribution subject to AIP license or copyright; see http://pop.aip.org/about/rights_and_permissions

with $f(W=0)=1$ and $f(W=\text{front})=0$ as boundary conditions. T_0 is the temperature at the heated surface when $t=t_0$. The parameter W provides a new coordinate system in which the temperature profile is time invariant. By a suitable choice of Q, this enables us to reduce the nonlinear differential diffusion equation for heat transport to a linear differential equation. By substitution,

$$(lPZ+z\varepsilon)f^{lz}-QW\frac{\partial}{\partial W}f^{lz}$$

$$=W^{\varepsilon Z}\frac{\partial}{\partial W}\frac{D}{W^{RZ}}t^{[P\beta+r+1-Q(2+r)]}\frac{\partial}{\partial W}f^{\beta+lz}, \tag{4-11}$$

where

$$D=\frac{16\sigma C_0^r\rho_0^r T_0^\beta}{3K_0h_0t_0^{P\beta}(\beta+lZ)},$$

$$\beta\equiv n+4-l+\frac{rl}{2},$$

$$Z\equiv\left(1-\frac{\varepsilon}{2}\right)^{-1}, \tag{4-12}$$

and

$$r\equiv Z(R-\varepsilon).$$

The time dependence is eliminated by choosing

$$Q=\frac{\beta P+1+Z(R-\varepsilon)}{2+Z(R-\varepsilon)}=\frac{\beta P+1+r}{2+r}. \tag{4-13}$$

With this choice of Q, Eq. (4-11) becomes

$$\frac{D}{W^r}(f^{\beta+lZ})''-\frac{ZRD}{W^{r+1}}(f^{\beta+lZ})'+QW(f^{lZ})'$$

$$-(lpZ+Z\varepsilon)f^{lZ}=0. \tag{4-14}$$

Since W is related to the mass ablated from the surface, it increases as we move through space toward the ablation front. Near the ablation front, W will be large, R is always small, and Z and l are less than unity so that f^{lZ} is small. We expect the gradient $(f^{lZ})'$ to be large near the wavefront since the nonlinear radiation conductivity must result in a steep-fronted wave. Hence, the second and fourth terms of Eq. (4-14) are neglected. Near $W=0$,

$$f(w)=\left[1-\left(\frac{W}{W_0}\right)^\alpha\right]^{1/\beta}, \tag{4-15}$$

is used as a trial solution, where $\alpha=1+RZ$. Equation (4-14) becomes

$$\left[-\frac{D}{W^r}\frac{\beta+lZ}{\beta}\frac{\alpha}{W_0}\left(\frac{W}{W_0}\right)^{\alpha-1}+QW\right]$$

$$\times\left\{\frac{\partial}{\partial W}\left[1-\left(\frac{W}{W_0}\right)^\alpha\right]^{lZ/\beta}\right\}=0. \tag{4-16}$$

Near the front, the second term cannot be 0, because the gradient is steep. Hence, the first term must be 0. Also, near the front, $W\approx W_0$. Hence, W_0 is given by

$$W_0^{2+r}=\frac{4\sigma}{3K_0}\frac{1}{h_0}\frac{4}{Q\beta}\alpha C_0^r\rho^r\frac{T_0^\beta}{t_0^{\beta p}}, \tag{4-17}$$

and the mass penetrated by the radiation wave is then $m_0=W_0t^Q$,

$$\frac{\text{Loss}}{\text{Area}}=\frac{E_{wa}}{A_w}=\int_0^{m_0}(h)dm$$

$$=\int_0^{m_0}h_0\left(\frac{\rho}{\rho_0}\right)^{-\varepsilon}T_0^l\left(\frac{t}{t_0}\right)^{Pl}f^l(w)dm$$

$$=h_0C_0^{\varepsilon Z}t^{\varepsilon Z}(m_0)^{1-\varepsilon Z}\left(\frac{t}{t_0}\right)^{plZ}\rho_0^{\varepsilon Z}T_0^{lZ}\frac{\beta}{\beta+lZ}. \tag{4-18}$$

In carrying out the integral, we substituted for ρ/ρ_0 from Eq. (4-7) and set $m=m_0$ in the resulting term. E_{wa} is the energy into the hohlraum wall, and A_w is the hohlraum wall area. If we do not set $m=m_0$, the right-hand side of Eq. (4-18) is multiplied by $(1/\alpha)\beta[1-z\varepsilon/\alpha,(1+lz)/\beta]$, where $\beta(x,y)\equiv\Gamma(x)\Gamma(y)/\Gamma(x+y)$. Similar analytic solutions have been obtained by (Kaiser *et al.*, 1989) and by numerically integrating the equation (Pakula and Sigel, 1985) for W.

To obtain specific results for Au, we use

$$K_R=6\times10^3K_0\rho^{0.3}T_{\text{heV}}^{-1.5}\ \text{cm}^2/\text{g},$$

$$h=4.2\times10^6T_{\text{heV}}^{1.6}\rho^{-0.14}\ \text{J/g},$$

and

$$C_s=3.0\times10^6T_{\text{heV}}^{0.8}\rho^{-0.07}. \tag{4-19}$$

These results are a fit, in the temperature range of interest for laboratory ignition hohlraums, to more detailed equations of state. The Rosseland mean opacity is obtained from the STA model (Bar Shalom *et al.*, 1989) and K_0 is an overall multiplier on the opacity. Thus, $\varepsilon=0.14$, $R=0.3$, $l=1.6$, $n=1.5$, $Z=1.075$, $r=0.172$, $\beta=4.04$, and $Q=0.54+1.86P$. Although the text in this section often refers to temperatures in eV, temperatures in the equations are in hundreds of eV (heV).

If these quantities are used, the energy absorbed by the hohlraum wall after a time τ is approximated by

$$E_{wa}(MJ)=5.2\times10^{-3}K_0^{-0.39}(3.44P+1)^{-0.39}$$

$$\times T_0^{3.3}\tau^{0.62+3.3P}A_w, \tag{4-20}$$

where T_0 is the temperature at 1 ns. For a constant hohlraum temperature T_r, we have

$$E_{wa}(\text{MJ})=5.2\times10^{-3}K_0^{-0.39}T_r^{3.3}A_w\tau^{0.62}. \tag{4-21}$$

For a constant loss rate $\dot{E}_{wa}^Y/A_w=S_A$, we must have $t^{-0.38+3.3P}=t^0$. Hence, $P=0.115$ and

$$(S_A)_{15}=\frac{\dot{E}_{wa}^Y}{A_w}(\text{MJ/cm}^2/\text{ns})=4.5\times10^{-3}T_0^{3.3}/K_0^{0.39}, \tag{4-22}$$

where $(S_A)_{15}$ is the absorbed flux in units of 10^{15} W/cm^2. This form for the wall loss would be appropriate, for ex-

Downloaded 20 Mar 2011 to 69.181.48.121. Redistribution subject to AIP license or copyright; see http://pop.aip.org/about/rights_and_permissions

ample, for a constant-power laser pulse with constant x-ray conversion efficiency if we ignore hole loss. Using $T=T_0\tau^{0.115}$ and $(S_I)_{15}=0.01T^4$, we have

$$T^{3.3}=T_0^{3.3}\tau^{0.38}=44.7(S_I)_{15}^{0.825},$$

where S_I is the flux incident onto the hohlraum wall at time τ. Hence, Eq. (4-22) can be written

$$(S_I)_{15}=7.0K_0^{0.47}(S_A)_{15}^{1.21}\tau(\text{ns})^{0.46}. \tag{4-23}$$

From Eq. (4-23) it is apparent that for times on the order of 1 ns and fluxes of 10^{14} to 10^{15} W/cm^2, typical of ICF hohlraums, the incident flux onto a hohlraum wall is large compared to the absorbed flux.

The mass ablated from a hohlraum wall is approximated by

$$m_0(\text{g/cm}^2)=1.20\times10^{-3}T^{1.86}K_0^{-0.46}(3.44P+1)^{-0.46}\times\tau^{(0.54+1.86P)}. \tag{4-24}$$

If we take $P=0.115$, as required for a constant loss rate, then the depth penetrated in micrometers, for Au, is given by

$$x(\mu\text{m})=10^4\ \ \text{m(g/cm}^2)/\rho=0.53T_0^{1.86}\tau^{0.75}. \tag{4-25}$$

Thus, for times and temperatures of interest to ICF, a few microns of wall material are heated. From Eq. (4-19), the x-ray mean free path λ in Au is given by

$$\lambda(\mu\text{m})=\frac{1}{\rho K_R}=3.55\times10^{-2}T_R^{1.5}. \tag{4-26}$$

For temperatures of 200 to 300 eV typical of ICF experiments, the x-ray mean free path varies from 0.1 to 0.2 μm, so the diffusive approximation used in deriving the energy loss, Eq. (4-24), is valid for times greater than about 100 ps.

2. Hohlraum coupling efficiency theory

The approximate hohlraum coupling efficiency is obtained from

$$\eta_{ce}E_{\text{laser}}=E_{wa}+E_{ca}+E_h, \tag{4-27}$$

where η_{ce} is the laser-to-x-ray conversion efficiency. The LEH losses E_h and capsule absorbed energy E_{ca} are estimated by

$$E_h=10^{-2}T_r^4A_h\tau,\qquad E_{ca}=10^{-2}T_r^4A_c\tau. \tag{4-28}$$

The assumption made here is that the capsule absorbs the entire flux incident on it. This assumption is approximately valid for times of interest to ICF capsules for suitably chosen low-Z ablators in spherical geometry. The more general case, for which the capsule re-emits a fraction of the incident x-ray energy, is discussed below. The hohlraum wall A_w(cm^2) and entrance hole A_h(cm^2) areas used are the initial values. The capsule area A_c(cm^2) used is the initial area of the inside of the fuel layer (or the inside of the ablator if there is no fuel layer). This area is representative of the effective area during the bulk of the energy absorption. Temperature T_r(heV) is peak incident temperature, and the time τ(ns) used is typically the total energy divided by the peak power. For the case of constant hohlraum temperature, the ratio of the capsule absorbed energy E_{ca} to the energy delivered into the hohlraum by the driver E_{laser} is then given by (Lindl, 1998j)

$$\frac{E_{ca}}{E_{\text{laser}}}=\frac{\eta_{ce}}{1+\dfrac{A_h}{A_c}+\dfrac{A_w}{A_c}\dfrac{0.52}{T^{0.7}\tau^{0.38}}}=\frac{\eta_{ce}}{1+a_h+1.625a_w/N_w}=\frac{\eta_{ce}}{1+a_h+a_w/\overline{N}_w}, \tag{4-29}$$

where a_w and a_h are the ratios of the wall or entrance hole area to the capsule area, N_w is the ratio of the wall incident flux to the absorbed flux given by Eq. (4-23), and $\overline{N}_w$ is the ratio of the energy incident on the wall during the pulse to the absorbed energy. Equation (4-29) also can be written in terms of the albedo, which is defined here as the ratio of the wall re-emission to the incident flux and is closely related to N_w,

$$\frac{E_{ca}}{E_{\text{laser}}}=\frac{\eta_{ce}}{1+a_h+1.625a_w(1-\alpha)}=\frac{\eta_{ce}}{1+a_h+a_w(1-\overline{\alpha})}, \tag{4-30}$$

where α is the albedo, given by

$$\alpha=\frac{S_I-S_A}{S_I}=\frac{10^{-2}T^4-\dot{E}_W^Y}{10^{-2}T^4}=1-\frac{0.32}{T^{0.7}\tau^{0.38}}=1-\frac{1}{N}, \tag{4-31}$$

and $\overline{\alpha}$ is the average albedo over time τ, given by

$$\overline{\alpha}=\frac{10^{-2}T^4\tau-E_w}{10^{-2}T^4\tau}=1-\frac{0.52}{T^{0.7}\tau^{0.38}}. \tag{4-32}$$

Because the wall albedo is near unity for ICF conditions, or because the ratio of the incident flux to absorbed flux is large, the hohlraum wall area can be much greater than the capsule and still maintain reasonable coupling efficiency.

In the more general case with finite capsule re-emission E_{cr}, we can write (Murakami and Meyer-ter-Vehn, 1991)

$$E_{ci}=E_{ca}+E_{cr}=N_cE_{ca}=\frac{A_c}{A_w}E_{wi}=\frac{N_w}{a_w}E_{wa},$$

or

$$E_{wa}=\left(\frac{N_c}{N_w}\right)a_wE_{ca}=\frac{a_w}{n}E_{ca}, \tag{4-33}$$

and

$$E_h=\frac{A_h}{A_w}E_{wr}=N_ca_hE_{ca},$$

where N_c is the ratio of incident capsule flux to capsule absorption and $n=N_w/N_c$ is the effective ratio of incident wall flux to absorption.

From Eqs. (4-27) and (4-33), we obtain

$$\frac{E_{ca}}{E_{\text{laser}}}=\frac{\eta_{ce}}{1+(a_w/n)+N_ca_h}. \tag{4-34}$$

Downloaded 20 Mar 2011 to 69.181.48.121. Redistribution subject to AIP license or copyright; see http://pop.aip.org/about/rights_and_permissions

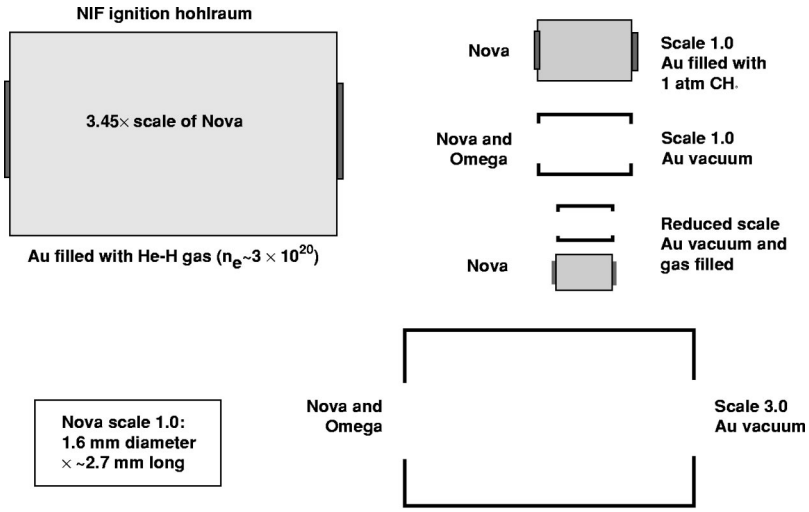

FIG. 4-1. Hohlraum x-ray drive has been studied in a wide range of hohlraums on the Nova and Omega laser.

When the capsule re-emits some fraction of the incident energy, it takes longer to absorb a given amount of absorbed energy. Hence, there is more time, essentially by the ratio N_c, for energy to be absorbed into the wall and to leak out the LEHs.

The albedos used in Eqs. (4-30)–(4-34) are slightly different than those given in (Lindl, 1998j), in which albedo was defined as the ratio of the flux emitted by the hohlraum wall to the sum of the re-emitted and absorbed flux. The temperature used in this definition was that defined by the re-emitted flux. The re-emitted flux is measured experimentally with an x-ray spectrometer looking at a region of the wall that does not include laser hot spots. In Eqs. (4-30)–(4-34), the incident flux temperature is used. The flux incident on the wall includes the reemission from the wall regions, which are not heated by laser spots, and an average contribution from the laser hot-spot sources. This temperature can be obtained experimentally by looking through the LEH at an appropriate angle as discussed below. These two definitions of albedo give very similar results for times greater than a few hundred picoseconds, for typical ICF temperatures of 200–300 eV, after which time the two temperatures differ by about 10 eV. For shorter times, the two definitions of albedo can differ significantly because the diffusion approximation breaks down at short times.

The coupling efficiency depends primarily on x-ray conversion efficiency, and the ratio of LEH and hohlraum wall area to capsule area. For ignition and high-yield hohlraums, the coupling efficiency depends only weakly on capsule energy for capsules designed to maintain an equivalent sensitivity to RT instability. As capsule size increases, the radiation temperature required for ignition decreases and the pulse length increases in such a way as to almost cancel the dependence of coupling efficiency on temperature and pulse length (Lindl, 1998k).

The LEHs must be made large enough to avoid significant absorption and refraction of the laser energy as it enters the hohlraum. The required size scales with the capsule size because the capsule size determines the pulse length. For hohlraums being investigated for ignition, the ratio of hole area to capsule area varies from about 1 to 2. The ratio of hohlraum wall area to capsule area is dictated primarily by capsule symmetry requirements, as discussed in Sec. V. For ignition hohlraums, the ratio of case area to capsule area varies from about 15 to 30. For this range of sizes for the case and the entrance holes, the coupling efficiency varies from about 10% to 20% if the x-ray conversion efficiency is about 70% to 80%. Typical Nova hohlraums, which have lower temperatures, shorter pulses and relatively larger LEHs, have a coupling efficiency of about 5%.

B. Hohlraum drive experiments

In the initial ignition hohlraum designs, the low-Z underdense plasma was produced by coating the high-Z wall with low-Z material. The laser and radiation ablate the thin low-Z coating from the wall, filling the hohlraum with low-Z plasma. More recent designs use hohlraums initially filled with low-Z gas, which, when ionized, produces the underdense low-Z plasma. Gas-filled hohlraums avoid problems with plasma stagnation and jetting, which computationally degrade capsule symmetry in the lined-hohlraum designs.

The drive experiments on Nova used a wide variety of hohlraums (Kauffman *et al.*, 1994; Suter *et al.*, 1996; Dattolo *et al.*, 2001; NTIS Document, 1998a), as shown schematically in Fig. 4-1. Nova scale-1 hohlraums are 1.6 mm diameter× 2.55–2.75 mm long. Typically, the hohlraum is made of Au with a wall thickness of 25 μm. In some experiments, the wall is thinned to about 2 μm to image keV x rays through the wall. The hohlraum length is sometimes varied for symmetry or for satisfying other experimental constraints. Different hohlraum sizes are scaled from the scale-1 size by the ratio of their diameters to those of a scale-1 size. Other dimensions sometimes vary from an exact scale. For example, a 0.75-scale hohlraum is typically 1.2 mm diameter× 2 mm long. The LEH is varied, depending on the experiment, from 50% to 100% of the hohlraum diameter. The 1 ns square pulse experiments typically used a 50% LEH, while shaped-pulse experiments had a 75% LEH. For all of the energetics studies, the hohlraums do not contain a fuel capsule.

Experiments have been done using lined, gas-filled, or

Downloaded 20 Mar 2011 to 69.181.48.121. Redistribution subject to AIP license or copyright; see http://pop.aip.org/about/rights_and_permissions

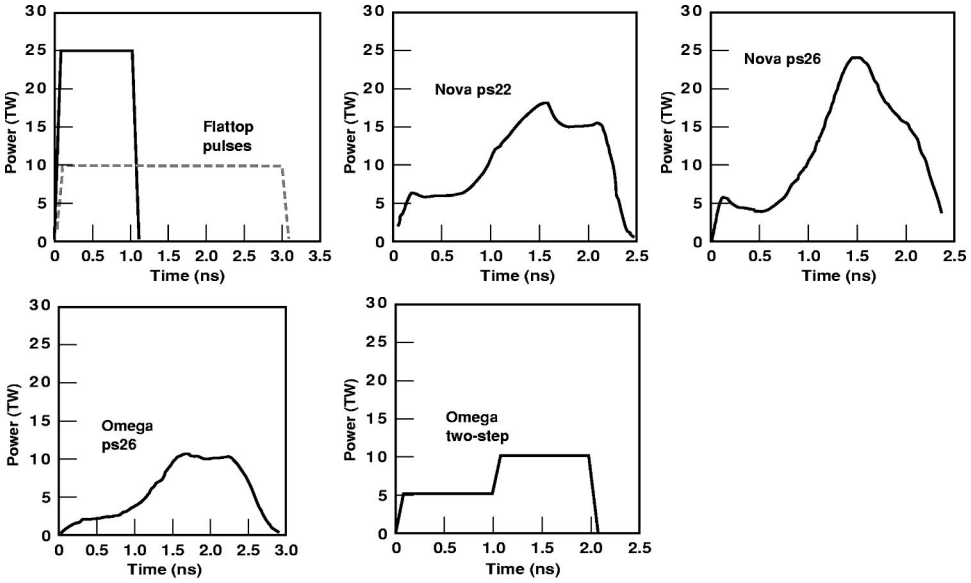

FIG. 4-2. The Nova and Omega hohlraums have been heated by a variety of pulse shapes.

vacuum hohlraums. Lined hohlraums are coated with either Ni or CH in the form of parylene. Gas-filled hohlraums for the drive experiments typically were filled with about 1 atm of methane (CH_4) but some experiments used a neopentane (C_5H_{12}) fill. Windows of 0.35 μm polyimide covered the LEHs to contain the gas. In the ensuing discussions, vacuum hohlraums refer to hohlraums without low-Z liners or gas fills. The thickness of the liners or the gas fill density is chosen so that the underdense, low-Z plasma density is about 10^{21} electrons/cm^3 when ionized and filling the hohlraum volume. The gas-filled hohlraum experiments are most directly relevant to the current NIF ignition hohlraum designs described in Sec. II.

Hohlraums are irradiated using the 10 Nova laser beams, five per side. Figure 4-2 shows the laser pulse shapes used on both Nova and the Omega laser (Suter *et al.*, 1996; Dattolo *et al.*, 2001). Experiments have been done using a shaped pulse having 29 kJ of laser energy, designated PS22, which is a 2.2 ns long pulse with a 3:1 contrast between the peak intensity and the foot intensity. Experiments in gas-filled hohlraums have also been performed with a 31 kJ pulse having a 5:1 contrast, designated PS26. Experiments on Omega used similar pulse shapes, as shown in Fig. 4-2, although they differed in detail. Experiments on both lined and unlined hohlraums have also been done using 1 ns long approximately square pulses with total powers up to 30 TW (maximum power available on Nova). The beams are pointed through the center of the LEH and defocused to reduce the intensity of the laser on the wall. For a scale-1 target, beam focus is about 1 mm outside the LEH, so the beam is expanding as it passes into the hohlraum. This allows about 100 μm clearance of the beam for a 50% LEH, assuming geometrical optics for an $f/4$ beam. The beam irradiates the wall of the hohlraum at an angle of 40° with respect to the normal of the wall and has a first bounce intensity of about

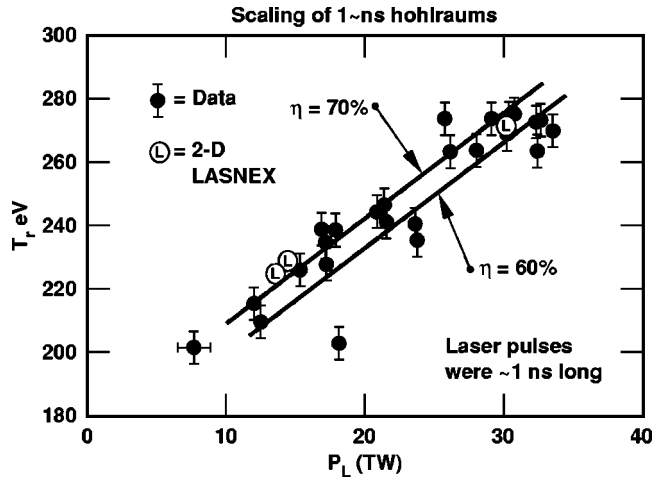

FIG. 4-3. Peak drive temperatures from Au hohlraums are in accord with 2D LASNEX simulations. The conversion efficiency inferred from hohlraum simulations for 1 ns pulses is consistent with $\eta_{ce} \sim 70\%$ from the measured TR and wall-loss measurements.

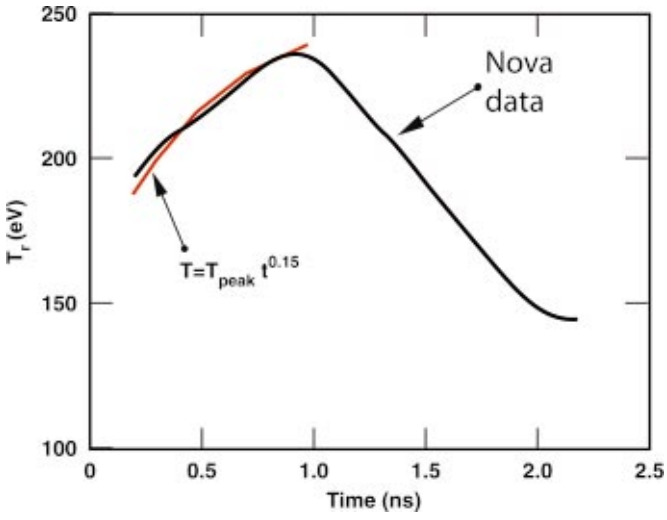

FIG. 4-4. (Color) Radiation-temperature profile obtained from soft x-ray diode measurements for a Au hohlraum driven by a 1 ns, constant-power laser pulse. The theoretical curve in red with $T = T_{1\,\mathrm{ns}} t^{0.15}$ requires a conversion efficiency $\eta = 0.7t^{0.12}$.

Downloaded 20 Mar 2011 to 69.181.48.121. Redistribution subject to AIP license or copyright; see http://pop.aip.org/about/rights_and_permissions

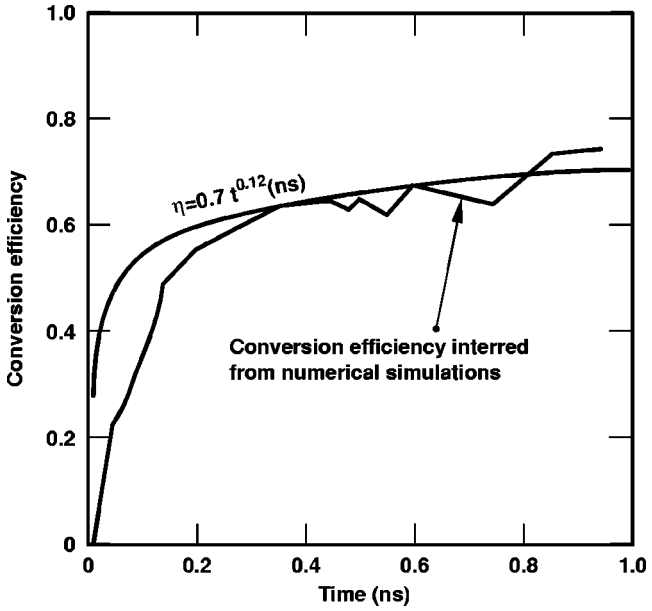

FIG. 4-5. Detailed numerical calculations of hohlraums with a 1 ns pulse predict an x-ray conversion efficiency that increases with time. A conversion efficiency given by $\eta = 0.7t^{0.12}$ is shown for comparison.

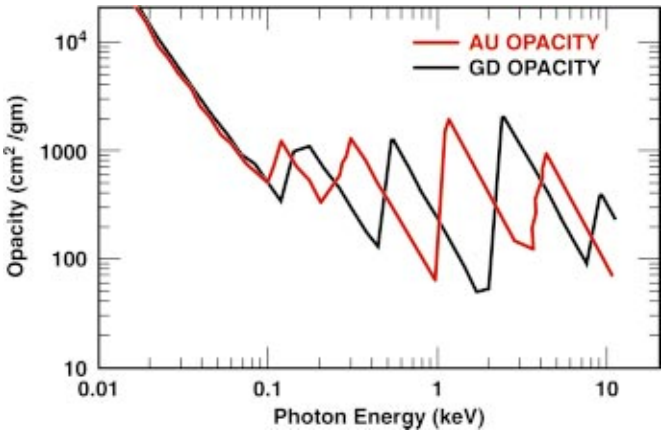

FIG. 4-7. (Color) Mixing Gd with Au results in a material (cocktail) with a higher mean opacity than pure Au. Peaks in the Gd opacity complement the windows in the Au opacity.

8×10^{14} W/cm^2 for 2 TW of laser power P_L per beam. Gas-filled hohlraum experiments have also been performed using 10 KPPs with and without smoothing by SSD (Glenzer *et al.*, 1998a; Kauffman *et al.*, 1998).

X-ray drive is measured using two complementary techniques (Kauffman *et al.*, 1995). One technique measures the shock wave generated by the absorbed x-ray flux in an Al witness plate placed over a hole in the hohlraum wall. The shock front is measured by observing optical emission produced by the emerging shock at the rear of the Al plate using an ultraviolet Cassegrain telescope coupled to an optical streak camera. X-ray drive is determined by comparing the measured shock velocity with hydrodynamic calculations. The estimated error for measuring drive is ± 5 eV, which includes the accuracy of the measurement and the uncertainty in the comparison with the calculations. The measurement is usually made in the midplane of the hohlraum between the two sets of beam cones where the witness plate is not directly irradiated by the laser.

The other technique measures the x-ray flux emitted from a hole in the hohlraum wall, using DANTE, an array of x-ray diodes (XRDs) (Kornblum *et al.*, 1986). In the XRD technique, a number of broadband channels are defined in the range from 0.1 to 1.8 keV using thin absorption filters and, for some channels, grazing incidence x-ray mirrors. Time-resolved spectra with resolution on the order of 150 ps are unfolded from the signals using calibrated channel response. The spectrally integrated flux is measured to an ac-

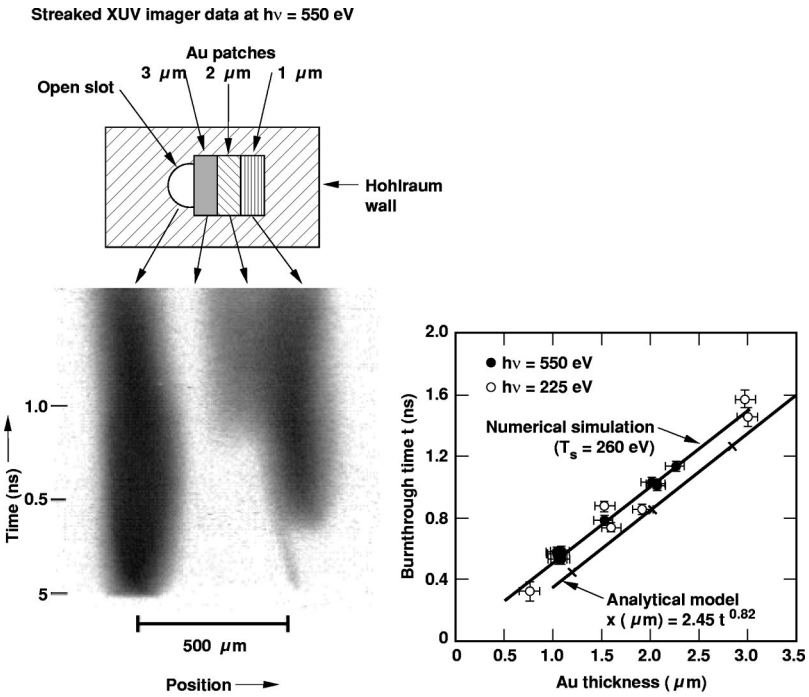

FIG. 4-6. The radiation-wave burnthrough measurements in thin Au foils agree well with numerical simulations and analytical models.

Downloaded 20 Mar 2011 to 69.181.48.121. Redistribution subject to AIP license or copyright; see http://pop.aip.org/about/rights_and_permissions

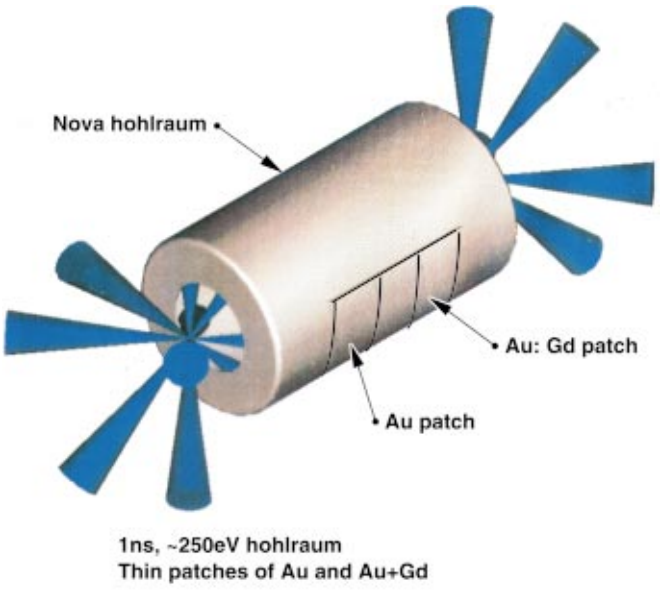

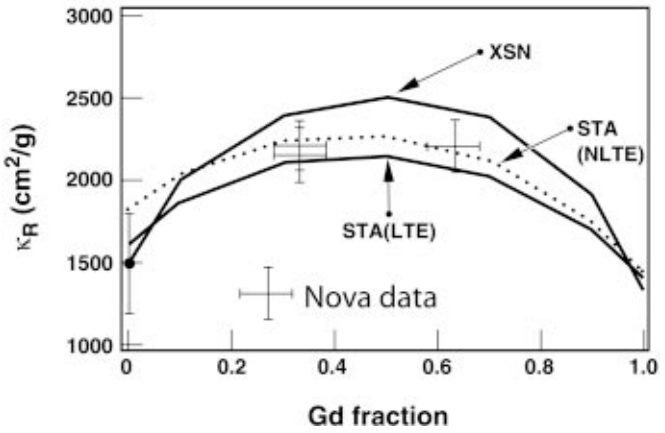

FIG. 4-8. (Color) Burnthrough measurements have shown that cocktails decrease wall losses and have a Rosseland mean opacity that depends on composition as predicted by STA models.

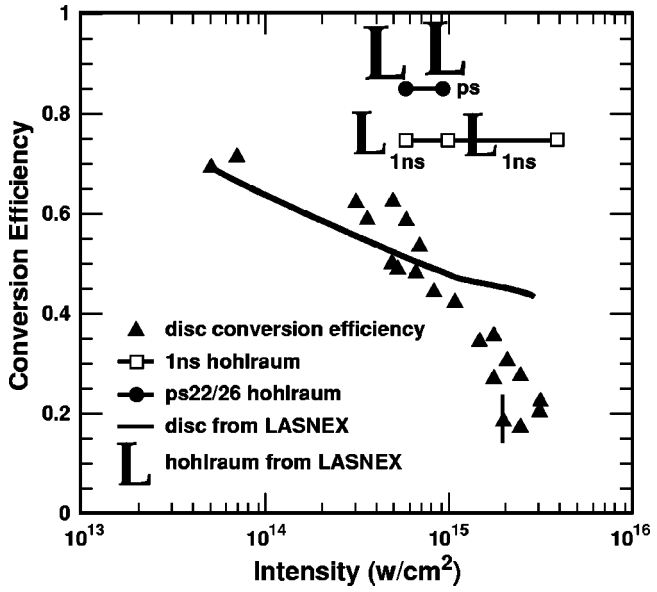

FIG. 4-9. Conversion efficiency of laser light into x rays for disks and hohlraums. Experimental number for hohlraums are inferred from wall loss data and measured temperatures.

curacy of about 20%, including calibration and unfolding uncertainties resulting in a $\pm 5\%$ uncertainty when converted to an equivalent radiation drive temperature. In some of the measurements of the x-ray flux emission from the hohlraum, photoconductive detectors (Kania *et al.*, 1990; Turner *et al.*, 1999) are used. These detectors integrate over the total spectral region.

When the diagnostic hole for the XRD measurement is placed at the midplane of the hohlraum, the two measurement techniques are complementary since the shock velocity measures the flux incident on the wall, while the XRD array measures the reradiated flux. The two measurements are related by the wall albedo, as described above.

When the XRD array or photoconductive detectors are used to measure emission from the LEH, the detectors view emission from the laser spots as well as the hohlraum wall (Decker *et al.*, 1997). If the line of sight through the LEH is chosen properly, about 30° from the hohlraum axis, the relative contributions of flux from the laser spots and the wall are comparable to that seen by a capsule at the hohlraum center. The proper angle is determined from radiation hydrodynamics calculations but the calculated sensitivity is small over a range of several degrees.

Laser absorption is determined by measuring the scattered light. Light from SBS and SRS is measured through the lens using FABS. Light scattered outside of the lens is measured by the near backscatter imaging diagnostic. Both diagnostics measure scattered light from only one beam, beam line 7, which is assumed to be representative of all of the beams. These diagnostics were described in Sec. III.

Figure 4-3 shows the measured and calculated peak Au vacuum hohlraum temperatures as a function of laser power for a series of experiments on Nova (Kauffman *et al.*, 1994). These experiments used a hohlraum that was 1600 μm diameter and 2550 μm long with a 50% LEH. The data are from experiments conducted over several years and are for constant-power 1 ns pulses. The temperatures plotted were obtained from Al witness-plate measurements, as described above. These are incident flux temperatures that are higher than temperatures inferred from looking at wall re-emission away from the laser spots. The witness plate looks at both the hot laser source regions and the cooler re-emitting wall. The incident flux temperature $T_{\rm inc}$ can be related to the re-emission flux temperature T_{re} from the definition of the albedo in Eq. (4-31):

$$T_{re}=\alpha^{1/4}T_{\rm inc}=T_{\rm inc}\left(1-\frac{0.32}{T_{\rm inc}^{0.7}\tau^{0.38}}\right)^{1/4}\approx T_{\rm inc}-0.08\frac{T_{\rm inc}^{0.3}}{\tau^{0.38}}. \tag{4-35}$$

This correction is a weak function of the source temperature. For 1 ns pulses, the source temperature is about 10 eV higher than the re-emission temperature for most cases of interest.

Equations (4-20), (4-27), and (4-28) can be used to calculate the expected hohlraum temperatures for the Nova experiments. The solid lines in Fig. 4-3 are for constant x-ray

Downloaded 20 Mar 2011 to 69.181.48.121. Redistribution subject to AIP license or copyright; see http://pop.aip.org/about/rights_and_permissions

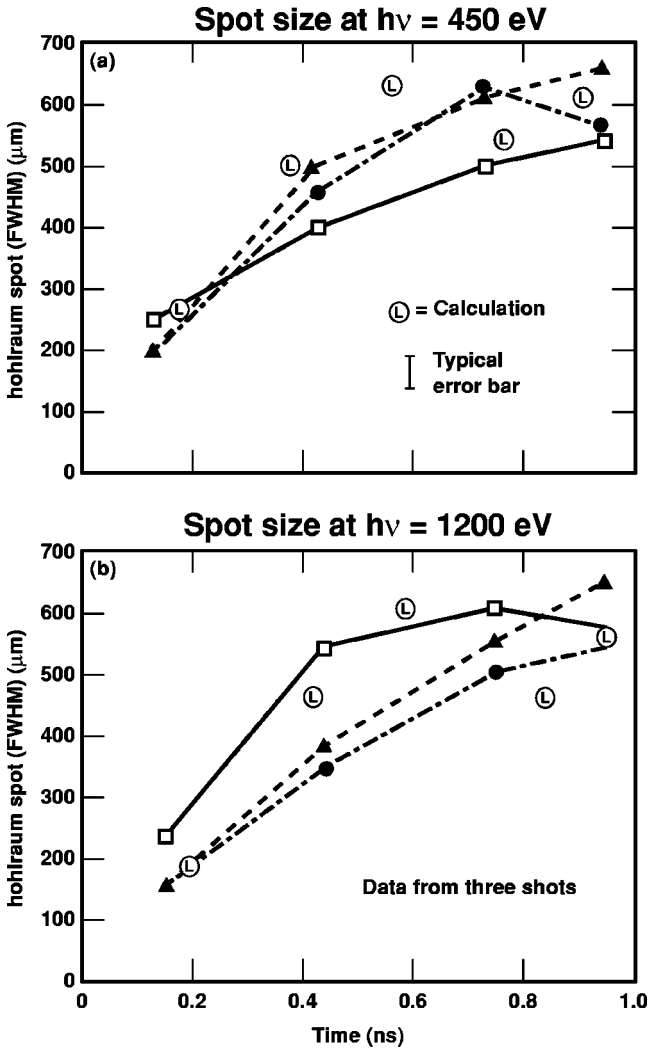

FIG. 4-10. Data and postprocessed calculations (circled L) indicate that x-ray source size in hohlraums increases with time: (a) spot size at 450 eV; (b) spot size at 1200 eV.

conversion efficiencies, η_{ce}, of 60% and 70%. Also shown are the results of detailed numerical calculations.

The experimentally measured hohlraum temperature time history—shown in Fig. 4-4 for a typical 1 ns, constant-power pulse in a Au hohlraum—implies an x-ray conversion efficiency that increases with time during the pulse. If we assume that

$$\eta_{ce} = 0.70\tau(\mathrm{ns})^{0.12} \tag{4-36}$$

and use this in Eq. (4-20), we obtain $P = 0.15$ or $T = T_0 t^{0.15}$, where T_0 is the temperature at 1 ns. As shown in Fig. 4-4, this gives a good fit to the measured hohlraum temperature-vs-time profile. The temperature history in Fig. 4-4 is a wall re-emission temperature obtained by using the Dante x-ray diode array to measure x-rays emitted from a diagnostic hole. As shown in Fig. 4-5, detailed numerical calculations also predict an x-ray conversion efficiency that increases with time. Equation (4-36), which is consistent with the numerical model results for a 1 ns pulse, is also plotted in Fig. 4-5.

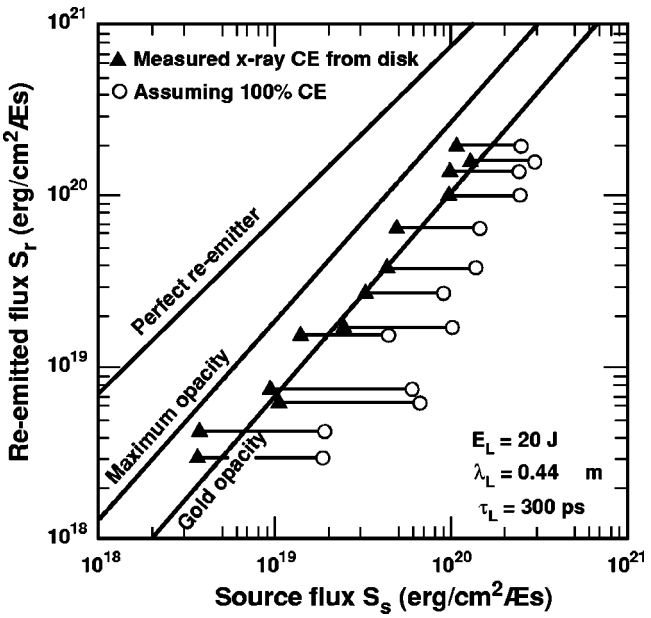

FIG. 4-11. Experiments at Garching with low energy and short pulses do not see significant enhancement of x-ray production in hohlraums compared to open-geometry measurements.

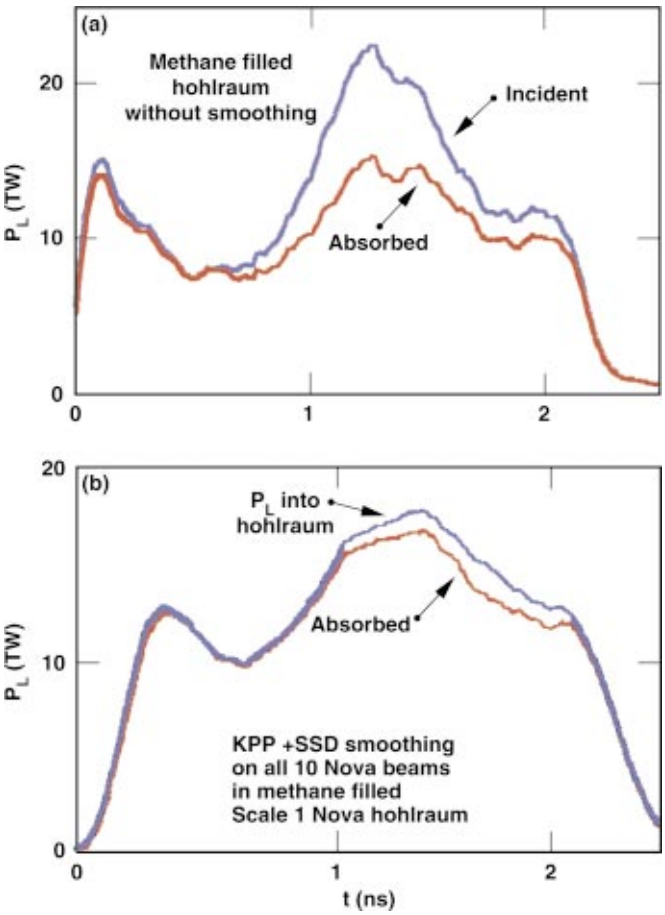

FIG. 4-12. (Color) Smooth beams are required for high absorption in gas-filled hohlraums. Similar smoothing is planned for NIF. Absorption (a) without smoothing and (b) with smoothing.

Downloaded 20 Mar 2011 to 69.181.48.121. Redistribution subject to AIP license or copyright; see http://pop.aip.org/about/rights_and_permissions

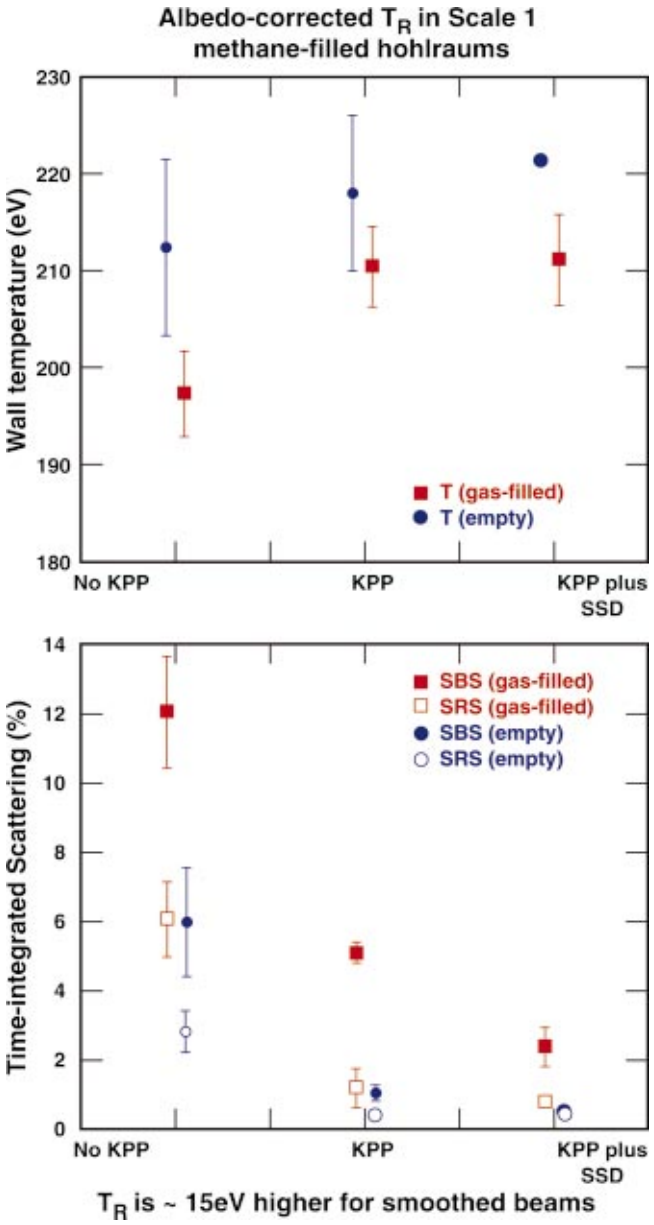

FIG. 4-13. (Color) Ten smoothed beams reduced backscatter losses and raised hohlraum temperature.

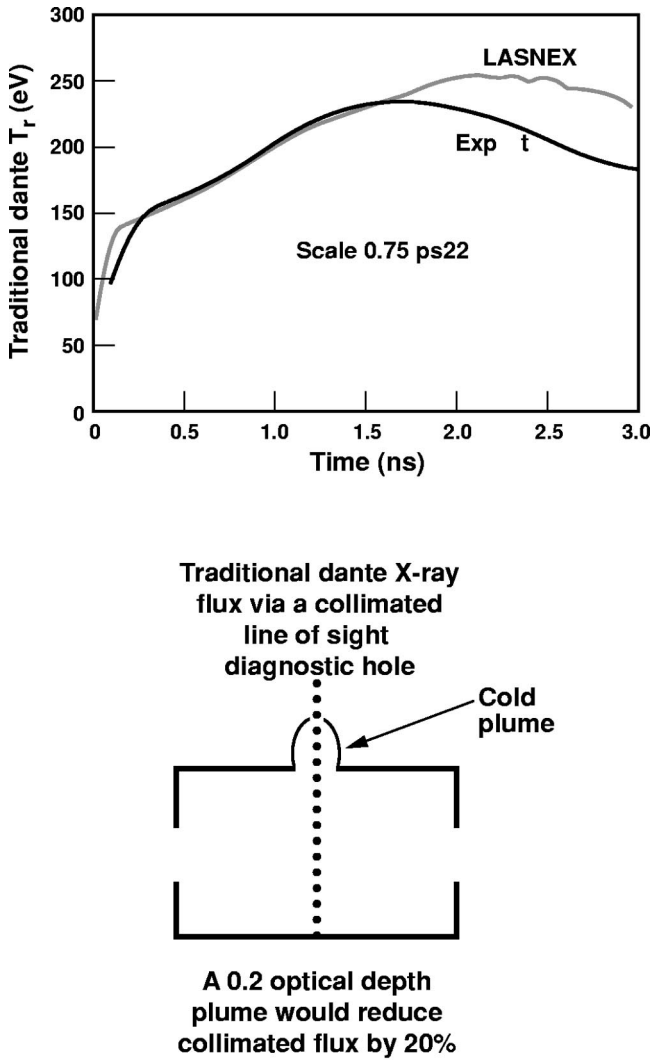

FIG. 4-14. Previous drive measurements through a diagnostic hole were often difficult to model at later times. This late-time disagreement is likely a 3D hole closure effect, which is not currently modeled in 2D hohlraum calculations.

Since the hohlraum temperature depends on both the x-ray conversion efficiency and the hohlraum wall loss, an independent measurement of the wall loss is needed in order to be confident of both elements of the hohlraum energetics model. Two independent tests of the hohlraum wall loss have been obtained in Nova experiments. In one technique (Sigel *et al.*, 1990), a thin patch of Au is placed on the wall of the hohlraum. The burnthrough time of soft x-rays is a measure of the wall loss, which scales approximately as $(K_0)^{-0.47}$ from Eq. (4-24). A second, less sensitive technique uses a wedge of Au or a series of Au steps of different thicknesses placed in the wall of the hohlraum. The shock velocity generated in the Au is approximately proportional to $(K_0)^{-0.25}$. Both techniques have been used on Nova.

Figure 4-6 shows the results of Nova experiments (Porter and Thiessen, 1992; NTIS Document, 1994d) using a thin Au patch that has 1, 2, and 3 μm thick sections and an open hole. Emission through the open hole tracks the laser pulse, while emission from the Au patch is delayed. The analytical results plotted in Fig. 4-6 use $P=0.15$, as discussed previously, in Eq. (4-24). The predicted burnthrough rate is slightly greater than observed, corresponding to about a 10 eV temperature difference. Also shown are the results of detailed numerical simulations, which accurately match the observed burnthrough rate. Both the analytical and numerical calculations of the burnthrough foils use the measured radiation temperature history. The agreement between the calculated and observed burnthrough times indicates that the wall-loss models in the numerical calculations are quite accurate.

Almost all the Nova and Omega experiments have used pure Au for the hohlraum wall. Au was chosen primarily for ease of fabrication. However, the opacity for any single material shows a wide variation as a function of photon energy. For example, the cold opacity for Au and Gd are shown in Fig. 4-7. Each of these materials has low opacity relative to the mean, just below the edges for each of the principal

Downloaded 20 Mar 2011 to 69.181.48.121. Redistribution subject to AIP license or copyright; see http://pop.aip.org/about/rights_and_permissions

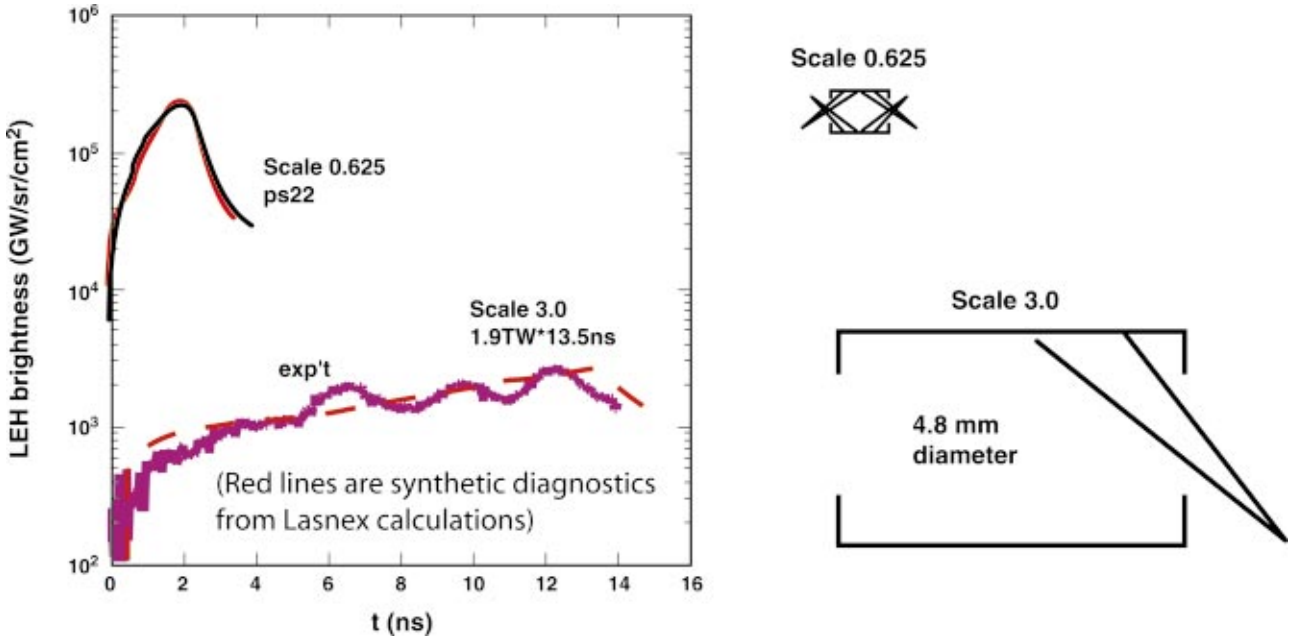

FIG. 4-15. (Color) When drive is measured through the LEH, detailed, quantitative modeling spans two orders of magnitude in radiation flux/cm^2. The experiment is shown in black and blue. LASNEX results are in the red solid and dashed lines.

quantum shells. The loss of photons into the wall is dominated by loss through these low-opacity regions. By using a mixture of materials which have overlapping edges, it is possible to reduce the wall loss (Nishimura *et al.*, 1993; Orzechowski *et al.*, 1996). Preliminary burnthrough experiments have been carried out using a Au and Gd mixture. By comparing the relative burnthrough times, the relative increase in opacity can be obtained as shown in Fig. 4-8. Optimizing the mixture of materials is an area of current research. The original NIF ignition hohlraums were designed with pure Au hohlraums in order to connect to the large Nova database. However, as discussed in Sec. II, it may be possible to substantially increase the hohlraum coupling efficiency on NIF by using these material mixtures.

The x-ray conversion efficiency inferred in hohlraums for pulses 1 ns or longer is significantly greater, in general, than that measured on flat high-Z disks in open geometry (NTIS Document, 1986; Suter *et al.*, 1996). The filled triangles of Fig. 4-9 show the x-ray conversion efficiency for a flat disk measured on Nova for 1 ns pulses. The solid line shows a typical scaling for discs from LASNEX calculations, which predict the general trends seen in the data but predict less sensitivity to intensity. For intensities of a few times 10^{14} W/cm^2 to a few times 10^{15} W/cm^2 (the intensities on the hohlraum wall for the data in Fig. 4-3), the x-ray conversion on disks is clearly lower than for hohlraums and is more intensity sensitive.

As discussed above, we infer conversion efficiency in hohlraums of about 70% for 1 ns hohlraums. For longer pulses, such as PS22 and PS26, hohlraums may be achieving conversion efficiency as high as 85%. LASNEX calculations for these different pulses, as well as the conversion efficiency inferred from the data, are also plotted on Fig. 4-9. The intensity indicated for these hohlraums corresponds to that of the vacuum spot at the hohlraum wall.

Analysis of the hohlraum simulations (Suter *et al.*, 1996) provides a rather simple explanation for the increased conversion efficiency in hohlraums. Unlike a disk, where the blowoff is free to expand, the blowoff energy and material in a hohlraum accumulates in the interior. In the hohlraum simulations, radiation production rises relative to discs initially because of conversion of kinetic energy (Massen *et al.*, 1993) and later because of radiation production by the accumulated blowoff. In the simulations at late time, radiation is produced over a substantial volume within the hohlraum.

These effects show up in experiments that look at the soft x-ray emission region around a laser spot in a hohlraum. The region of this emission becomes significantly larger than the incident spot during the laser pulse, as shown in Fig. 4-10. These data are taken by cutting a slot in the hohlraum and imaging the soft x-ray emission around a laser spot on the opposite wall (Ze *et al.*, 1993) with a soft x-ray framing camera (Ze *et al.*, 1992). This camera can take four frames in each of three different x-ray energy channels. Figure 4-10 shows the effective emission spot size measured at energies of 450 and 1200 eV. The data shown are from three shots with nominally the same conditions. A typical error bar on the spot-size measurements is 20% to 30%, based on uncertainty in film calibration and the flat-field response of the instrument. As shown in Fig. 4-10, post-processed calculations of the emission spot size in hohlraums are consistent with the observed size increase. This increase in size is not seen for a 1 ns pulse in open geometry. Experimentally, the open-geometry data are taken simultaneously with the hohlraum data by focusing one of the laser beams on the outside of the hohlraum. The brightness of the laser spot outside the hohlraum and the hohlraum laser spot are roughly equal, so that the increase in hohlraum x-ray conversion efficiency is consistent with this increase in the x-ray emission region.

Short pulse experiments by (Sigel *et al.*, 1988) at 300 ps

Downloaded 20 Mar 2011 to 69.181.48.121. Redistribution subject to AIP license or copyright; see http://pop.aip.org/about/rights_and_permissions

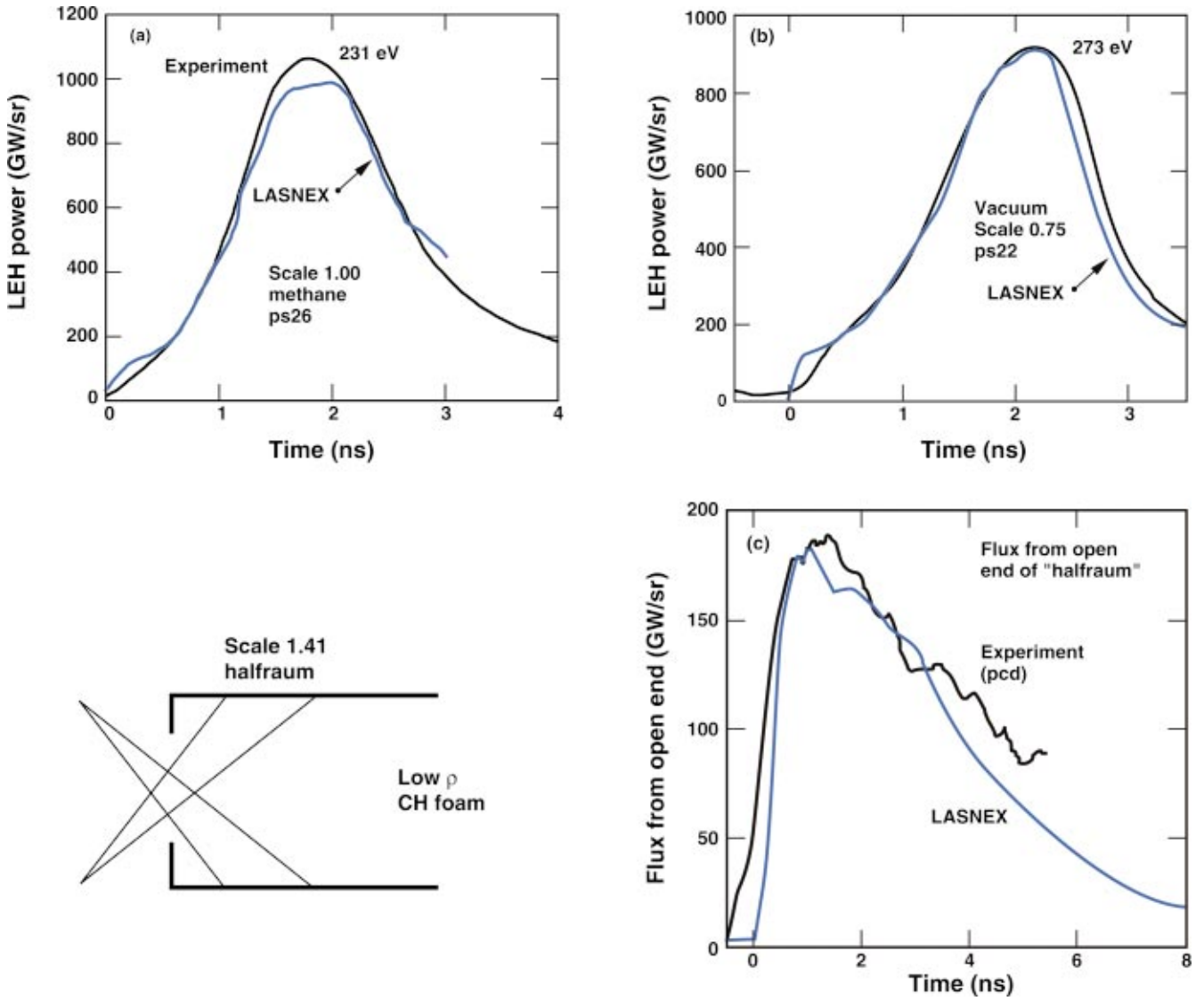

FIG. 4-16. (Color) Calculated temperature for (a) gas-filled and (b) vacuum hohlraums, as well as (c) open-ended single-sided hohlraums, are in good agreement with measurements for drive measured through the LEH.

did not show an increase in conversion efficiency relative to disk measurements. Figure 4-11 shows the re-emitted flux from their spherical cavity experiments (obtained from x-ray emission through a diagnostic hole) vs the source flux (based on disk measurements) in the hohlraum. The theoretically predicted re-emitted flux, as shown, is consistent with the disk-conversion efficiency and not with a much higher efficiency. The equivalent Nova experiments at short pulse have not been done.

To obtain an accurate quantitative comparison between the calculated and observed radiation temperature, it is important to account for stimulated scattering losses. This is particularly important for gas-filled hohlraums as indicated in Fig. 4-12. Without beam smoothing, as shown in Fig. 4-12(a), the power loss can be as much as 40% during some times in the pulse, with time integrated losses approaching 20%. With beam smoothing, the losses are reduced to a few percent, as indicated in Fig. 4-12(b). A summary of the scattering losses and the resulting hohlraums temperatures is given in Fig. 4-13 for both empty and methane-filled scale-1 hohlraums. The increase in hohlraum temperature when beam smoothing is used is consistent with the drop in scattering (Glenzer *et al.*, 1998a; Kauffman *et al.*, 1998).

All of the early drive measurements using XRDs on Nova looked through a 400 μm diameter Be-lined diagnostic hole at the hohlraum midplane. For 1 ns pulses and scale-1 hohlraums, this technique gave reasonable agreement between the Dante XRD measurements of peak drive and witness plate measurements, and between experiments and numerical calculations. However, for longer shaped pulses or for higher drive in smaller hohlraums, and at late times for almost all experiments, the XRD measurements dropped well below the calculations late in time, as indicated in Fig. 4-14 for an experiment using PS22 in a scale 0.75 vacuum hohlraum. This effect is believed to be due to a cold plume of Au emerging from the diagnostic hole (Dattolo *et al.*, 2001; NTIS Document, 1998a). However, since an accurate calculation of this effect requires a 3D hohlraum code with capabilities that are not yet available, it is not currently possible to quantitatively assess this explanation.

Downloaded 20 Mar 2011 to 69.181.48.121. Redistribution subject to AIP license or copyright; see http://pop.aip.org/about/rights_and_permissions

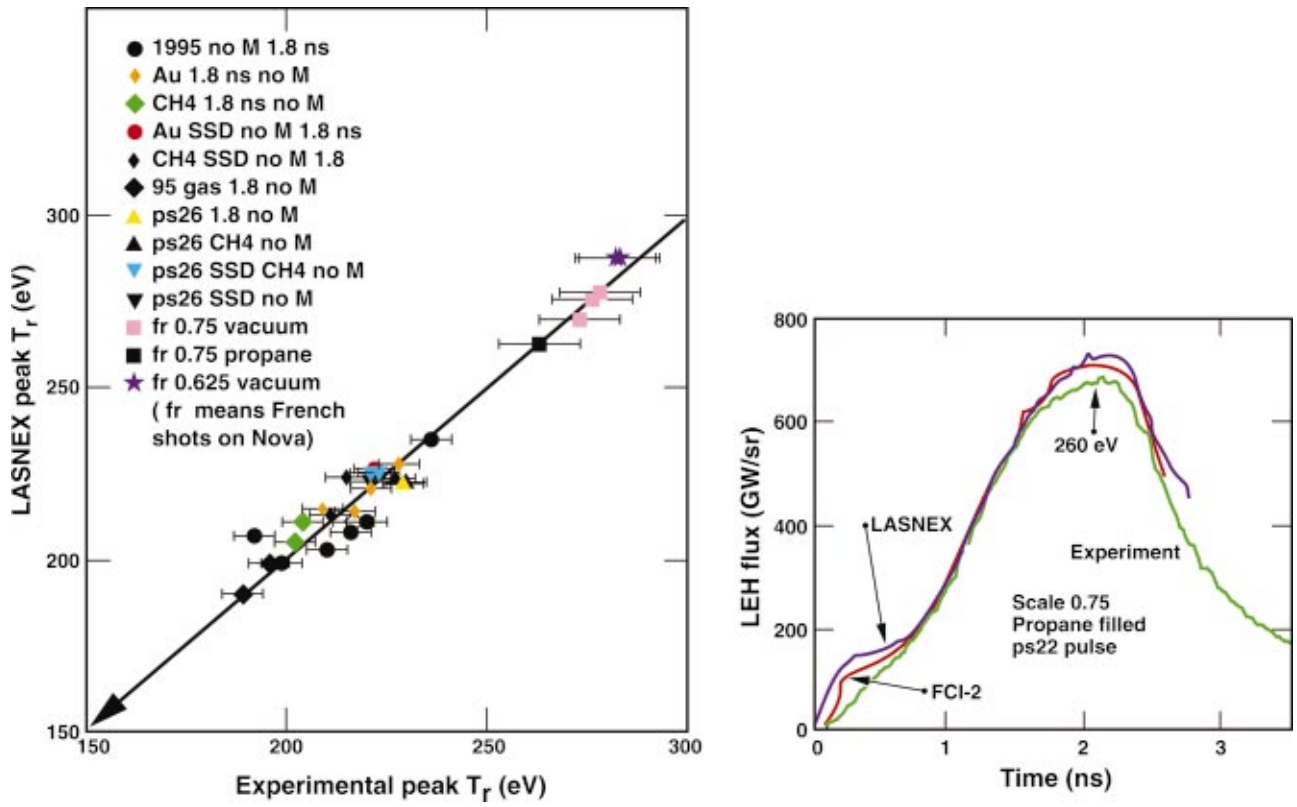

FIG. 4-17. (Color) Drive in a wide variety of ignition-relevant hohlraums agrees with detailed modeling for drive measured through the LEH.

Recently, drive measurements (Decker *et al.*, 1997) on both Nova and Omega have begun using flux from the LEH instead of flux from the unirradiated wall at the midplane. The midplane x-ray flux measurement usually measures the wall re-emission flux and needs to be adjusted by the albedo to infer the incident flux that would drive a capsule. The flux from the LEH measures flux from laser heated hot spots as well as unirradiated walls. If the appropriate view is chosen to represent the weighted average of the two areas, the measured flux is a better measure of the incident flux to drive the capsule. This has a number of experimental and computational advantages. The LEH is much larger than a diagnostic hole at the hohlraum midplane, and therefore, is less susceptible to hole-closure effects. The plasma plume in the LEH is heated by the laser pulse and is hotter and therefore more optically transparent to x rays emitted from the hohlraum interior. The LEH measurement does not require an additional hole in the hohlraum wall and a clear line of sight at the midplane to view the opposite wall making it compatible with implosion or other experimental configurations. The geometry is more nearly 2D and more readily calculated by LASNEX.

A wide variety of hohlraum sizes, gas fills, and pulse lengths have been accurately modeled using the LEH line of sight and the measured absorbed energy. These hohlraums range in size from a scale 0.65 to a scale 3.0, as indicated in Fig. 4-15 with pulse lengths from 1 to more than 10 ns. The smaller scale hohlraums have significantly more plasma filling than ignition hohlraums. Figure 4-16 shows results from a scale 0.75 vacuum hohlraum and a scale-1 methane (CH_4)-filled hohlraum. Figure 4-16 also shows a comparison with a half-open geometry. LASNEX calculations for (a) gas-filled hohlraums, (b) vacuum hohlraums, and (c) open-ended single-sided hohlraums are also shown in Fig. 4-16 showing the agreement with the results. Much of this work was done in collaboration with the French CEA, and their code FCI2 also agrees well with the data as indicated in Fig. 4-17 for a scale 0.75 hohlraum filled with propane that reaches 260 eV.

Figure 4-17 shows a comparison of the calculated and observed peak temperatures over a wide range of hohlraums. Over the full database we have

$$\frac{\text{Flux(measured thru LEH)}}{\text{Flux(LASNEX)}} = 1.04 \pm 0.07.$$

If we include the absolute calibration uncertainty of the Dante XRD system, which is about 10% in flux, in quadrature we have (Dattolo *et al.*, 2001; NTIS Document, 1998a)

$$\frac{\text{Flux(``True'')}}{\text{Flux(LASNEX)}} = 1.04 \pm 0.12.$$

This indicates that the peak flux from hohlraums can be modeled to within 12% (or a radiation temperature to 3%) at least for Omega and Nova hohlraums. This data set includes gas-filled hohlraums as well as hohlraums expected to fill significantly with high-Z plasma. As seen in Figs. 4-16 and 4-17, some differences in the model and experiment are observed in the first few hundred picoseconds. The source of this difference is still being investigated, but could be related to early time x-ray production. This should not significantly

Downloaded 20 Mar 2011 to 69.181.48.121. Redistribution subject to AIP license or copyright; see http://pop.aip.org/about/rights_and_permissions

impact understanding of NIF ignition hohlraums that use 20 ns pulses with the initial irradiation at low temperatures.

C. Summary of hohlraum drive and coupling efficiency

Understanding and predictive capability of hohlraum drive is founded on a combination of experiments, analytical models, and radiation hydrodynamics simulations. Most of the experimental database has been developed using 0.35 μm light at Nova and Omega lasers. These short wavelength experiments have shown that high temperature hohlraum conditions can be attained while maintaining low levels of preheat from fast electrons from laser plasma instabilities.

The Nova data for hohlraum drive, summarized in Fig. 4-17 for a wide range of experiments, show that the peak temperature and the time dependence of the hohlraum temperature are accurately modeled by radiation hydrodynamics codes including LASNEX and FCI2. Peak radiation flux has been predicted to $\pm 12\%$ over a wide range of hohlraum conditions. A major input into this modeling is the absorption fraction. Losses from parametric instabilities can reduce the drive, making understanding of LPI an important part of understanding NIF target performance as discussed in Sec. II.

Analytical models have been developed based on radiation ablation, or Marshak, wave heating of the high-Z walls of the hohlraum. Using the measured drive, the analytical models fit the hohlraum wall loss measurements, and LASNEX calculations. This confirms that the Marshak wave heating and ionization of the high-Z wall dominate the energetics in the targets. Given this match to the wall loss data, the drive measurements imply that the effective conversion efficiency in hohlraums for 1 ns or longer pulses in Nova scale hohlraums is 70% or greater. The LASNEX calculation of x-ray conversion efficiency is consistent with the measured temperature. The hohlraum temperature primarily depends on the wall loss and the x-ray conversion efficiency. Although the x-ray conversion efficiency is not measured directly, there is agreement with the calculated temperature and wall loss, so the accuracy of the calculated x-ray conversion efficiency follows. LASNEX accurately calculates the x-ray spot size and brightness. For a given intensity and pulse length, the size of the emission region in hohlraums is significantly larger than that from plane open-geometry targets.

In general, because of the radiation ablation and because both the radiation driven blowoff and the directly laser heated blowoff are confined, there is much more plasma in the vicinity of the laser spot in a hohlraum than in an open geometry. Conduction into this plasma can lead to an enhanced emission region. Also, the blowoff plasma can stagnate and reradiate. The higher x-ray conversion efficiency seen in hohlraums relative to those measured from plane open-geometry targets is consistent with these effects.

V. HOHLRAUM RADIATION UNIFORMITY

A. Introduction to hohlraum radiation uniformity

Understanding and controlling capsule implosion symmetry is a key requirement for ICF. The laser beam geometry and pointing into the hohlraum, as well as the optimal choice for the ratio of hohlraum case area to capsule area are strongly affected by the need to achieve a very high degree of flux uniformity on the capsule. Since hohlraum coupling efficiency is largely determined by the size of the hohlraum and the LEHs compared to the capsule size, there is a tradeoff between symmetry and efficiency. Modifications to the internal structure of the hohlraum can also be used to modify symmetry, but little work on this has been done for NIF hohlraum designs.

Symmetry requirements are determined by the capsule convergence ratio C_r, defined as the ratio of the initial outer radius of the ablator to the final compressed radius of the hot spot. Typical convergence ratios to the hot spot for an ignition or high-gain target design range from 25 to 45. If a target with an initial radius R_A, implosion v, and average acceleration g has a location on its surface with acceleration perturbation δg, then the deviation from sphericity as it implodes is given by

$$\delta R = \frac{1}{2}\delta g t^2 = \frac{\delta g}{g} r(C_r - 1), \tag{5-1}$$

where r is the compressed radius and we have substituted for t using equality $\frac{1}{2}gt^2 = R_A - r$. An asymmetric implosion will convert less of the available kinetic energy into compression and heating of the fuel. The tolerable degree of asymmetry depends on the excess of available kinetic energy above the ignition threshold. If we require that this deviation δR be less than $r/4$, then

$$\frac{\delta g}{g} \approx \frac{\delta v}{v} \approx \frac{3}{4}\frac{\delta I}{I} < \frac{1}{4(C_r - 1)}, \tag{5-2}$$

where I is the intensity. The intensity dependence comes from the rocket equation for a radiation-driven rocket (Lindl, 1998d). The tolerable degree of asymmetry depends on the ignition margin available. For the NIF ignition capsules, we have allowed a factor of about 1.4 in implosion energy relative to the minimum for ignition to account for the degradation expected from both asymmetry and mix. For long-wavelength asymmetry alone, these capsules will ignite with an imploded fuel that has $\delta R > r/2$. However, in order to tolerate both the effects of hydrodynamic instability and mix, we specify $\delta R < r/4$.

B. Theory of capsule radiation uniformity in hohlraums

If the hohlraum or case radius is large compared to the capsule radius, hohlraums are effective at smoothing all but the longest-wavelength perturbations. Analytical models can be very useful in understanding the symmetry behavior of hohlraums (Lindl, 1998c). Analytical results can readily be obtained for the example of a spherical capsule of radius R_{cap} inside a spherical hohlraum of radius R_{wall} (Haan, 1983; Caruso and Strangio, 1991). For a Legendre polynomial perturbation of order l applied on the inside of the hohlraum, the resultant perturbation on the capsule is as shown in Fig. 5-1 as a function of $R_{\mathrm{hoh1}}/R_{\mathrm{cap}}$. If the case radius is about three to four times the capsule radius, all modes but the P_2 com-

Downloaded 20 Mar 2011 to 69.181.48.121. Redistribution subject to AIP license or copyright; see http://pop.aip.org/about/rights_and_permissions

ponent are smoothed by about two orders of magnitude. When $R_{\text{wall}}/R_{\text{cap}}=5$, P_4 passes through zero. If a capsule is chosen so that it passes through this value as it implodes, very small average levels of P_4 can be achieved.

The reason for smoothing short-wavelength modes is easy to understand. If we assume that the channel between the capsule and the hohlraum wall is thin to radiation transport, then any point on the surface of the capsule averages flux from a large fraction of the hohlraum wall. In this process, all high-spatial-frequency modes are averaged out. In practice, a desire to maximize hohlraum coupling efficiency often results in $R_{\text{wall}}/R_{\text{cap}}<4$, at least at early times. Therefore, both P_2 and P_4 can be issues. Also because of RT growth after an initial imprinting, the levels of P_6 and P_8 can sometimes be an issue even at small levels. For nonspherical hohlraums, the situation is somewhat more complicated because coupling between modes (Suter, 1985) occurs for finite-size capsules. If a pure P_2 is applied to the case, P_2 and all higher even modes appear at the capsule. This occurs because different points on the capsule see different solid angles of the hohlraum wall and hence have different smoothing factors. This changes the shape of the perturbation, which is equivalent to adding harmonics of the applied mode. Figure 5-2 shows the coupling (Pollaine, 1992) between P_2 and P_4 for a cylindrical hohlraum that has a length-to-diameter ratio of 1.7, comparable to that of hohlraums on Nova or for NIF ignition hohlraum designs. Figures 5-2(a) and 5-2(b) show the P_2 and P_4 at the capsule for a P_2 (P_4) applied at the case. The principal effect of this coupling is to slightly shift the optimal pointing location for capsule symmetry in the discussion below.

In Fig. 5-2, all odd harmonics have been ignored because of an assumed left–right symmetry to the hohlraum. This imposes a power balance and pointing accuracy specification on the laser as discussed in Sec. II for NIF targets.

The long-wavelength P_2 component must be smoothed by choosing a combination of the appropriate hohlraum geometry and laser geometry. With N rings of beams, it is possible (NTIS Document, 1984) to exactly eliminate all the Legendre moments with $1<l<2N-1$. If the number of beams in each ring is equal to $2N-1$ or more, then the spherical harmonic modes Y_l^m with $m<2N-1$ are eliminated as well. In a hohlraum with no holes, the rings must be placed at the zeroes of the Legendre polynomial of order N. The beams in each ring must be uniformly spaced around the ring, and the intensities of the rings must be proportional to the Gaussian quadrature weight for that angle.

Holes in a hohlraum wall can be treated as a negative source, and a very similar analysis applies. For example, if the hohlraum wall is heated and the laser beams are suddenly turned off so that no flux comes from the beams, then a significant negative P_2/P_0 occurs because of the holes. For a typical laser hohlraum, holes cover about 5% of the solid angle and $P_2/P_0=-0.227$ from the holes. To balance this asymmetry, the centroid of the laser emission must move toward the LEHs. Because the hohlraum wall has a time-varying albedo and because of plasma blowoff from the hohlraum wall, which changes the angular position of the laser beams relative to the capsule, symmetry in hohlraums also is time varying.

Because the interior of an ICF hohlraum is initially empty or filled with a low-density, optically thin gas and remains largely optically thin during the laser pulse, the diffusion approximation used for losses into the hohlraum wall in Sec. IV does not apply to transport within a hohlraum.

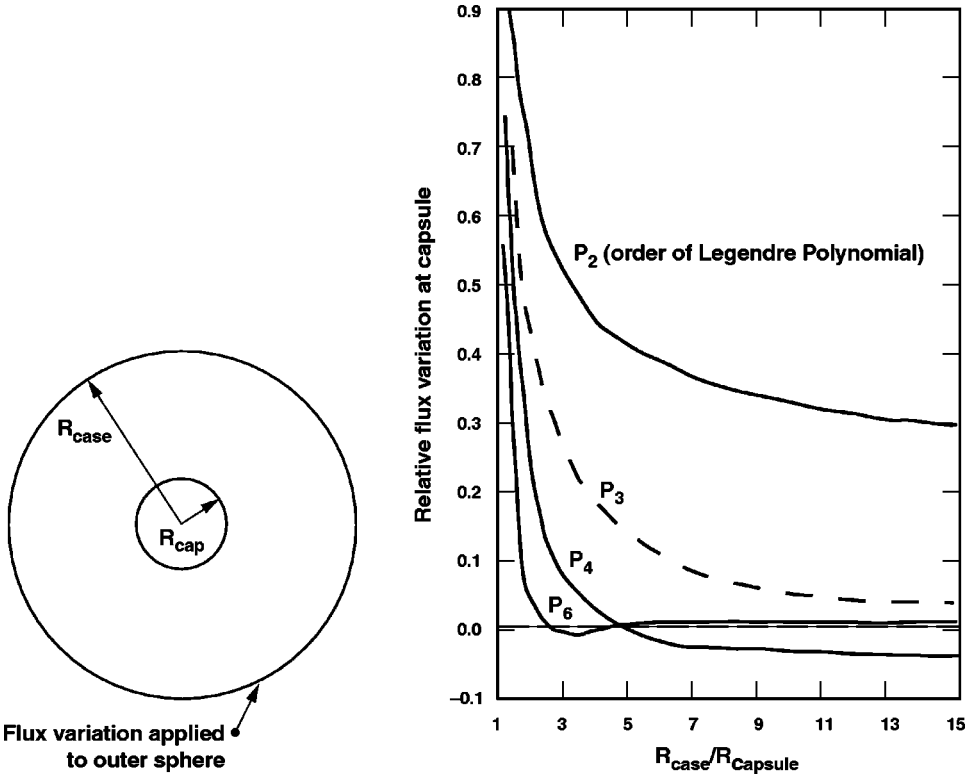

FIG. 5-1. Fraction of flux variation at wall that is imprinted at capsule as a function of ratio of case-to-capsule radius for various Legendre asymmetry modes. Hohlraums with $R_{\text{case}}/R_{\text{capsule}}$ from about 3 to 5 effectively smooth all but the P_2 Legendre polynomial flux variations.

Downloaded 20 Mar 2011 to 69.181.48.121. Redistribution subject to AIP license or copyright; see http://pop.aip.org/about/rights_and_permissions

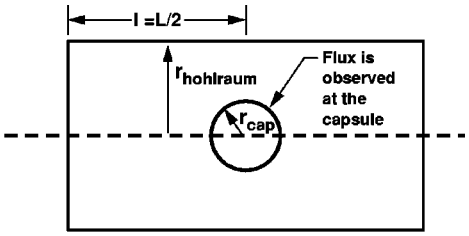

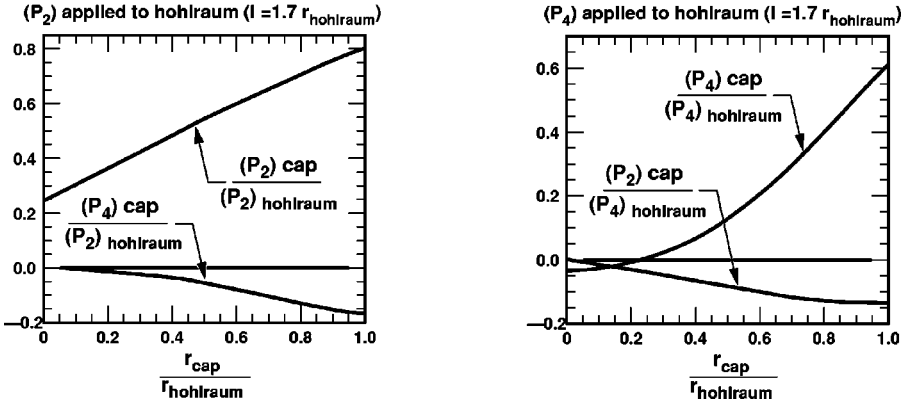

FIG. 5-2. Coupling occurs between Legendre polynomial spatial harmonic modes in nonspherical hohlraums.

When blowoff from the hohlraum wall is important in determining the spatial distribution of sources and sinks of x-ray energy in the hohlraum, or when material in the hohlraum approaches an optical depth, the coupled hydrodynamics and radiation transfer equations (Minguez, 1993) must be solved. Several models—including Monte Carlo, P_N, and S_N—have been developed to solve the radiative transfer equation. The Monte Carlo probabilistic methods, which have been considered as the main reference for comparing other approximations, were first applied by Fleck (Fleck and Cummings, 1971). The spherical harmonic method, or P_N, method (Pomraning, 1973), is based on the expansion of the specific intensity into spherical harmonics. When only the first two terms of the expansion are used, the Eddington or diffusion approximation is obtained. The discrete ordinates, or S_N method (Pomraning, 1973a), solves the transport equation for a series of specific angles.

If blowoff is unimportant, a ''viewfactor'' calculation (Kirkpatrick *et al.*, 1988; Murakami and Meyer-ter-Vehn, 1991a) can be used. This approximation assumes vacuum radiation transport between surface coupled to a wall loss model, such as that given by Eq. (4-20).

However, significant insight can be obtained from an even simpler analytical model that can be used to estimate the required location of the laser spots at various times, as well as the sensitivity of the symmetry to deviations from the optimal position (Lindl, 1998c). The hohlraum is assumed to be spherical, although the analysis also can be done for cylinders (Tabak, 1987). For purposes of this discussion, the effect of the capsule on hohlraum symmetry is small and is ignored. Although the model is readily generalized, we also assume for most of the analysis that there is a single LEH and a single ring of laser beams on each side of the hohlraum, as shown in Fig. 5-3. The laser-beam ring is located at an angular location θ_s relative to the hohlraum axis and the laser entrance hole subtends an angle Θ_H. The position or relative powers for multiple rings would be chosen so that their power-weighted P_2 is the same as that for a single ring. The flux at any point on a capsule comes from both the laser-heated region and the x-ray-heated wall. Only the flux from the laser-illuminated region is sensitive to the pointing accuracy of the laser. The flux from the x-ray-heated wall is essentially independent of exactly where the laser hits the wall. As the wall albedo increases, so does the ratio of the pointing-insensitive flux from the x-ray-heated wall to that from the laser-heated regions.

We define I_s to be the x-ray source intensity provided by the laser, and the blackbody emission from the wall to be

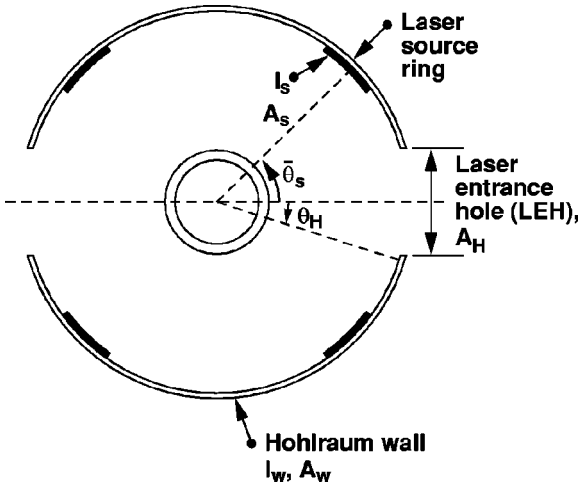

FIG. 5-3. A simplified spherical hohlraum is used to analyze hohlraum symmetry.

Downloaded 20 Mar 2011 to 69.181.48.121. Redistribution subject to AIP license or copyright; see http://pop.aip.org/about/rights_and_permissions

$I_w = 10^{-2} T_r^4$, where T_r is in units of 10^2 eV, as before, and I_w, which is in units of 10^{15} W/cm^2, is assumed to be uniform throughout the hohlraum. Although this assumption is not strictly valid, the variations within the hohlraum are relatively small for typical laser-driven hohlraums. The laser spot intensity is the excess brightness of the wall directly heated by the laser. The excess flux from the laser spots must supply the energy lost to the hohlraum wall, LEHs, and capsule. To lowest order, this flux is independent of the size or solid angle of the laser sources, but I_s clearly depends on the size of the laser spots. A smaller spot must be more intense in order to produce the required energy. The ratio of the laser spot intensity to the wall intensity depends on the wall albedo and the sizes of the LEHs and the laser spot. If we ignore the capsule, we have

$$I_s A_s = \dot{E}_w^Y + I_w A_H,$$

where A_s and A_H are the areas of the laser spots and LEHs.

The hohlraum-wall loss for Au, E_w, is given by Eq. (4-20), and the flux into the wall for constant temperature is

$$\frac{dE_w}{dt} = \dot{E}_w^Y = 3.2 \times 10^{-3} \frac{T_r^{3.3} A_w}{\tau^{0.38} K_0^{0.39}}, \tag{5-3}$$

where E_w is in megajoules, and A_w and τ are in square centimeters and nanoseconds, as before. The ratio of the laser x-ray intensity to the wall radiation intensity is then

$$\frac{I_s}{I_w} = \frac{A_w}{A_s}\left(\frac{0.32}{T_r^{0.7} \tau^{0.38} K_0^{0.39}} + \frac{A_H}{A_w}\right). \tag{5-4}$$

For a sphere, the ratio of the areas is the same as the ratio of the solid angles, so we can also write

$$\frac{I_s}{I_w} = \frac{\Omega_w}{\Omega_s}\left(1 - \alpha + \frac{\Omega_H}{\Omega_w}\right), \tag{5-5}$$

where Ω_w, Ω_H, and Ω_s are the fractional solid angles of the wall, LEHs, and laser source regions. The ratio F of the total power from the wall to that from the laser spots is given by

$$F = \frac{I_w \Omega_w}{I_s \Omega_s} = \left(\frac{1}{1 - \alpha + \dfrac{\Omega_H}{\Omega_w}}\right). \tag{5-6}$$

It is F that will determine the optimal pointing angle and the relaxation of the pointing requirements in a hohlraum. Adding a capsule to the analysis has the effect of adding a term $\Omega_{\rm cap}/\Omega_w$ to the denominator, where $\Omega_{\rm cap}$ is the solid angle of the capsule as seen from a point on the wall.

At $t = 0$, the ratio of the wall emission to the laser spot emission is zero. But the total wall emission rapidly comes to dominate the emission from the laser spots. For example, for the ignition design, the drive temperature is about 300 eV while most of the energy is being delivered, and the pulse width is about 3 ns. The drive temperature is about 100 eV during the foot, a duration of about 10 ns. Figure 5-4(a) is a plot of F vs time at 100 and 300 eV for a case with LEHs that cover 5% of the total solid angle. Even at 100 eV, the total flux from the wall exceeds that from the laser spot in less than 100 ps.

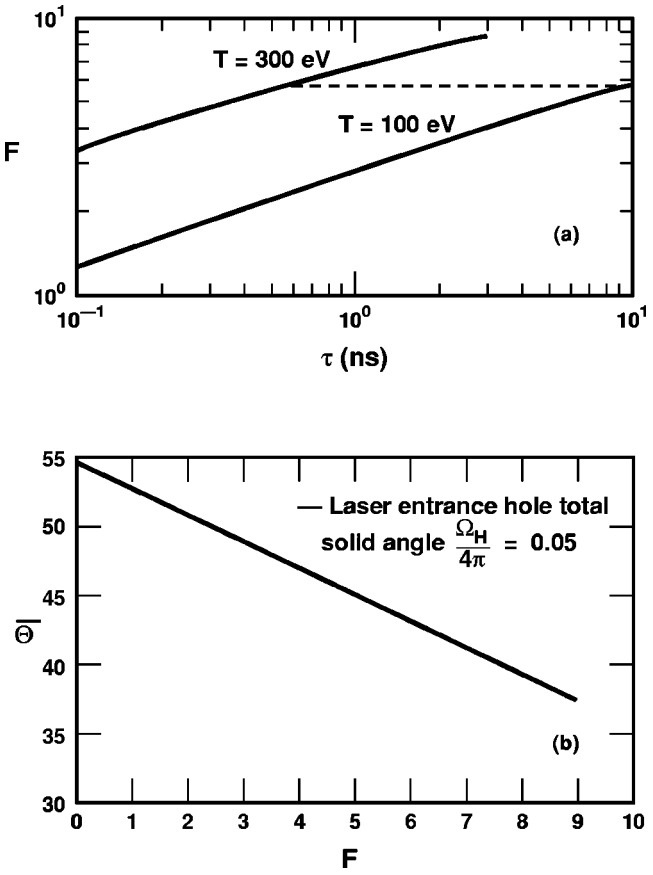

FIG. 5-4. (a) The hohlraum smoothing factor F versus pulse length. F is the ratio of the x-ray flux from the hohlraum wall to the flux from the laser hot spots. (b) The required laser source angular location $\bar{\theta}$ to zero P_2 versus hohlraum smoothing parameter F. As the hohlraum wall flux increases, the laser spot must be closer to the laser entrance hole to compensate for the deficit in flux from the LEH.

During an interval of a few hundred picoseconds, while the albedo and optimal pointing position are changing rapidly, the flux symmetry in hohlraums can vary greatly with time, but ignition capsules can tolerate a high degree of asymmetry for times this short as discussed in Sec. II.

In the case of a single ring of laser irradiation on each end of the hohlraum, the laser emission region will balance the P_2 from the hole if we have

$$\int_s I_s(x) P_2(x) dx + \int_w I_w(x) P_2(x) dx = 0, \tag{5-7}$$

where $x = \cos\theta$. Assuming that the emission from the laser sources is uniform and that loss from the LEH is uniform, Eq. (5-7) is approximately equivalent to

$$P_2(\bar{X}_s)\Omega_s I_s = P_2(\bar{X}_H)\Omega_H I_w. \tag{5-8}$$

This expression is accurate to terms of order $\Omega^3/4$ in the fractional solid angles of the laser sources and LEHs. In Eq. (5-8), $\bar{X}$ is the average value of $\cos\theta$ for the LEH or the laser source location. Using the expression for F from Eq. (5-6), we have

Downloaded 20 Mar 2011 to 69.181.48.121. Redistribution subject to AIP license or copyright; see http://pop.aip.org/about/rights_and_permissions

$$P_2(\overline{X}_s)=P_2(\overline{X}_H)\frac{\Omega_H}{\Omega_w}F=P_2(\overline{X}_H)\left(\frac{\dfrac{\Omega_H}{\Omega_w}}{1-\alpha+\dfrac{\Omega_H}{\Omega_w}}\right). \tag{5-9}$$

The effect of the capsule could be included by adding another term, Ω_c/Ω_w, to the denominator in F, as discussed earlier. Figure 5-4(b) plots the required location of the center of emission for the two-ring case as a function of F for holes that cover 5% of the solid angle. This angle is measured relative to the center of the capsule, so 0° is the axis of the hohlraum. Only the angle of one of the two rings is given. The other ring is located symmetrically on the other end of the hohlraum. If the holes were smaller, the required shift in angle would be less. One effect that is apparent from Figs. 5-4(a) and 5-4(b) is that a rapid change in hohlraum temperature results in a rapid shift in the optimal pointing angle (or power balance for multiple rings). This occurs because of a drop in albedo, or F, which accompanies a rapid temperature change. For example, as seen in Fig. 5-4(a), it would take 600 ps at 300 eV to reach the albedo, or value of F, that was achieved after 10 ns at 100 eV.

Equation (5-9) can be generalized to more rings of laser sources and to higher-order perturbations. With two rings per side, we can generalize F to be

$$F=\frac{I_w\Omega_w}{I_{s1}\Omega_{s1}+I_{s2}\Omega_{s2}}. \tag{5-10}$$

The condition for balancing P_2 is then given by

$$P_2(\overline{X}_{s1})\varepsilon+P_2(\overline{X}_{s2})(1-\varepsilon)=P_2(\overline{X}_H)\frac{\Omega_H}{\Omega_w}F=h_2, \tag{5-11}$$

where ε and $1-\varepsilon$ are the fractional powers in each ring. With two rings per side, the power in each ring can be varied in time so that the location of the centroid of emission is always at the angular location required to eliminate the P_2 flux variation. If the initial ring positions are at the zeros in P_3, at $\theta=39.23°$ and 90° relative to the capsule center, then P_4 as well as P_2 can be zeroed at time zero. For these locations, the expression for ε is given by

$$\varepsilon=\frac{10}{9}\left[0.4-P_2(\overline{X}_H)\frac{\Omega_H}{\Omega_w}F\right]. \tag{5-12}$$

At time zero, the relative powers in the beams must be the Gaussian quadrature weights. To satisfy this requirement, the ratio of the power in the inner ring from each side to that in the outer ring on each side is 0.8 at $t=0$. Then, P_2 is controlled by changing ε and can be zeroed as long as the required emission location does not move to a lower angle than the location of the ring closest to the LEH.

Hohlraums help reduce the sensitivity of asymmetry to pointing errors. To estimate the magnitude of the asymmetry at the hohlraum wall, which would occur from a pointing error, we can use

$$\frac{P_l}{P_0}=\frac{(2l+1)\int I(x)P_l(x)dx}{\int I(x)dx}=\frac{(2l+1)[\int_s I_s(x)P_l(x)dx+\int_w I_w(x)P_l(x)dx]}{\int_s I_s(x)dx+\int_w I_w(x)dx} \tag{5-13}$$

to obtain

$$(P_2/P_0)_{\text{wall}}=\frac{5\left[P_2(\overline{X}_s)-P_2(\overline{X}_H)\dfrac{\Omega_H}{\Omega_w}F\right]}{1+F}. \tag{5-14}$$

The error introduced by deviations from the optimal angle are reduced by the factor $1+F$, compared to those that would occur at $t=0$ ($F=0$) or with no hohlraum. At $F=0$, for the two-ring example used here, $P_2/P_0=1\%$ for a pointing error $\delta\theta_0=0.08°$. For the case of two rings per side, the required pointing angle of the centroid of emission is obtained by varying the ratio of power in the two rings so that a pointing error corresponds to a power imbalance between the two rings.

For the NIF ignition capsule, the time integral of P_2/P_0 must be reduced below about 1%. Because most of the energy is delivered while $1+F\approx 10$, this corresponds to about a 1° placement error in the average position of the rings. For the NIF hohlraum, a 1° ring placement error corresponds to about a 100 μm movement of the ring along the wall at the initial radius for a ring at 50° relative to the capsule. Since many beams will make up the laser rings, the pointing accuracy for individual beams is further relaxed from the average aiming accuracy by a factor of 2 or more, depending on how the pulse shaping is carried out. Detailed calculations for the NIF ignition targets were presented in Sec. II.

The time-varying albedo discussed previously causes a time variation in the optimal pointing angle for the laser beams—or a time variation in capsule flux symmetry—for a fixed pointing angle. Plasma blowoff from the hohlraum wall has the effect of changing the source angle in time, relative to the capsule, for a fixed pointing direction. As plasma blows off the wall, the laser absorption and x-ray emission also move off the wall. This has the effect of moving the angle of the laser source relative to the capsule back toward the LEH. Although the position of the critical surface never moves very far from the original hohlraum wall, the absorption position can move far from the original wall. Inverse bremsstrahlung is very efficient at absorbing the laser light in high-Z material, even at densities well below the critical density. The inverse bremsstrahlung (IB) absorption length is given approximately by (Dawson *et al.*, 1969)

$$\lambda_{\text{IB}}(\text{cm})=\frac{0.56\lambda^2T_e^{3/2}(\text{keV})}{(n/n_c)^2Z\ln\Lambda}, \tag{5-15}$$

where λ is the laser wavelength in μm. In Au or other high-Z hohlraum wall material, the absorption length is less than 0.1 cm for $n/n_c=0.1$ at a temperature of 4 keV, which is typical for the laser-propagation channel, as discussed in Sec. II. This is comparable to the scale of a Nova hohlraum, but

Downloaded 20 Mar 2011 to 69.181.48.121. Redistribution subject to AIP license or copyright; see http://pop.aip.org/about/rights_and_permissions

only about 1/4 the scale of an ignition-scale hohlraum. Absorption lengths in Au near $n/n_c \approx 1/4$ seldom exceed about 100 μm for a laser with $\lambda = 0.35$ μm.

For both the NIF hohlraum and the Nova experiments, the density along much of the laser-propagation path has $n/n_c \approx 0.1$, and the electron temperature $T_e \approx 3-5$ keV. In both cases, the laser intensity $I \approx 1-2\times 10^{15}$ W/cm^2. For Nova-scale hohlraums, the laser is able to propagate through this plasma, even in Au, and most of the laser light is absorbed fairly close to the wall in higher-density, lower-temperature Au near $n/n_c \approx 1/4$. In NIF-scale hohlraums, inverse bremsstrahlung in Au at $n/n_c \approx 0.1$ is large enough that the laser-absorption and x-ray-emission region move far from the original wall, which makes it very difficult to maintain radiation symmetry.

The fix for this effect (Lindl, 1978; Pollaine, 1988; Thiessen, 1988; Pollaine, 1991) is to displace the high-Z Au blowoff with lower-Z material. As discussed in Secs. II and IV, two approaches to this have been tried: (1) a low-Z liner on the Au, which blows off to fill the hohlraum interior with low-Z and (2) an initial gas fill of the hohlraum.

Detailed modeling of the NIF targets with LASNEX showed that the NIF capsule symmetry was adversely affected by a hydrodynamic pressure pulse on the axis of the hohlraum, when the low-Z was generated by a low-Z liner. This effect may be exaggerated because LASNEX is cylindrically symmetric, while the blowoff comes from individual laser spots that only partially fill the azimuth.

However, because a gas-filled hohlraum does not have this stagnation problem, it has been adopted as the NIF baseline design.

Capsules being designed for ignition can tolerate some time variation in symmetry without performance degradation, but the magnitude of the symmetry swings must be kept below a maximum that depends on the temporal history of the time variations as discussed in Sec. II.

There are several possible techniques for controlling time-dependent symmetry. For example, a slot could be cut in the waist of the hohlraum to exactly balance the P_2 effect of the hole. The optimum location of the beam spots is then independent of time. This strategy would cost about 20% to 30% in energy. The same effect also could be accomplished by reducing the albedo over a somewhat larger area near the waist of the hohlraum. Alternately, one could put a high-Z disk in the hohlraum between the capsule and the entrance hole. In the limit that this disk has the same albedo as the rest of the hohlraum and shields the entire capsule from the hole, this eliminates P_2 caused by the LEH and again gives a time-independent solution to the optimal beam location. Experiments of this type were done on Nova (Lindl, 1998c) as discussed in Sec. V C 2. However, neither of these approaches alone eliminates the effect of the time-dependent location of the emission region. Other approaches, such as layered hohlraum walls to provide a space and time-varying albedo, are possible, and additional internal structure can be added to eliminate P_4, if necessary, to optimize hohlraum coupling efficiency. These techniques have not been evaluated in detail. For NIF, as described above, we intend to control the time-varying flux symmetry by using two rings per side in the hohlraum and by varying the power ratio between the two rings. This approach has been called ''beam phasing.''

C. Hohlraum symmetry experiments

1. Measurement techniques

Techniques for inferring the flux asymmetries in hohlraums have included recording either the hohlraum wall emission profiles or sampling the flux at the capsule location. For the former, both thermal x-ray and hard x-ray imaging of the wall and spot emission has been used. For the latter, the ignition capsule is replaced by a variety of surrogate spheres designed to enhance and/or time resolve the effects of flux asymmetry. These x-ray techniques include measurements of re-emission patterns from high-Z spheres (Delamater *et al.*, 1996; Magelssen *et al.*, 1998), distortions of backlit images of shock-driven foam balls (Amendt *et al.*, 1997; Glendinning *et al.*, 1999) and implosions (Kalantar *et al.*, 1997), and distortions of imploded capsules viewed in self-emission (Hauer *et al.*, 1995; Hauer *et al.*, 1995a; Murphy *et al.*, 1998; Murphy *et al.*, 1998a; Turner *et al.*, 2000). For a cylindrically shaped, Nova-like hohlraum with beam rings aimed as shown in Fig. 5-5(a), an observer at the capsule location would see a collimated source flux vs angle approximately as shown in the flux vs polar-angle plot. The laser-produced hot spot causes a peak in this source at about 60° polar angle. The cold, nonemitting LEH provides zero flux at low polar angle. When this source flux vs angle is resolved into its Legendre polynomial coefficients, there is a P_0 and P_4 component of order unity and a substantial time-varying P_2 component. If we choose an initial ring position yielding a time-averaged $P_2 = 0$, time-dependent effects of spot motion, as indicated on Fig. 5-5(b), and change in hohlraum albedo cause a typical variation in the fractional P_2 pressure asymmetry from negative to positive, as shown in Fig. 5-5(c) for a standard Nova symmetry hohlraum (1.6 mm diam $\times$ 2.4 mm long with 1.2 mm diameter LEHs, driven by PS22, a 20 TW peak power, 2.2 ns long, 3:1 contrast pulse, also described in the Sec. IV drive experiments).

In thermal x-ray imaging of the hohlraum wall (Ze *et al.*, 1997; Kauffman *et al.*, 1998), a slot is cut in the side of the hohlraum and the opposing wall is viewed with a soft x-ray imager (Ze *et al.*, 1992). At Nova, imaging was performed at multiple photon energies simultaneously, typically at 250 and 450 eV. Spatial and temporal resolutions are 25 μm and 100 ps, sufficient to resolve the ring or ''spot'' motion of 100 to 200 μm/ns. The field of view includes the initial spot of a beam as well as some of the surrounding region. Figure 5-6 shows an example of the data at 450 eV for PS22 into a vacuum hohlraum. We quantitatively analyze LASNEX simulations of the experiment with a post-processor that mimics the imaging diagnostic and the analysis. Figure 5-7 shows such a comparison, plotting the position of the center of emission for the 450 eV channel from simulations and experiments. The error in determining the centroid from a single image is ± 40 μm, or ± 20 μm when averaged over several frames within ± 150 ps. The ± 20 μm error in finding the centroid contributes to a $\pm 2\%$ random error in P_2.

Downloaded 20 Mar 2011 to 69.181.48.121. Redistribution subject to AIP license or copyright; see http://pop.aip.org/about/rights_and_permissions

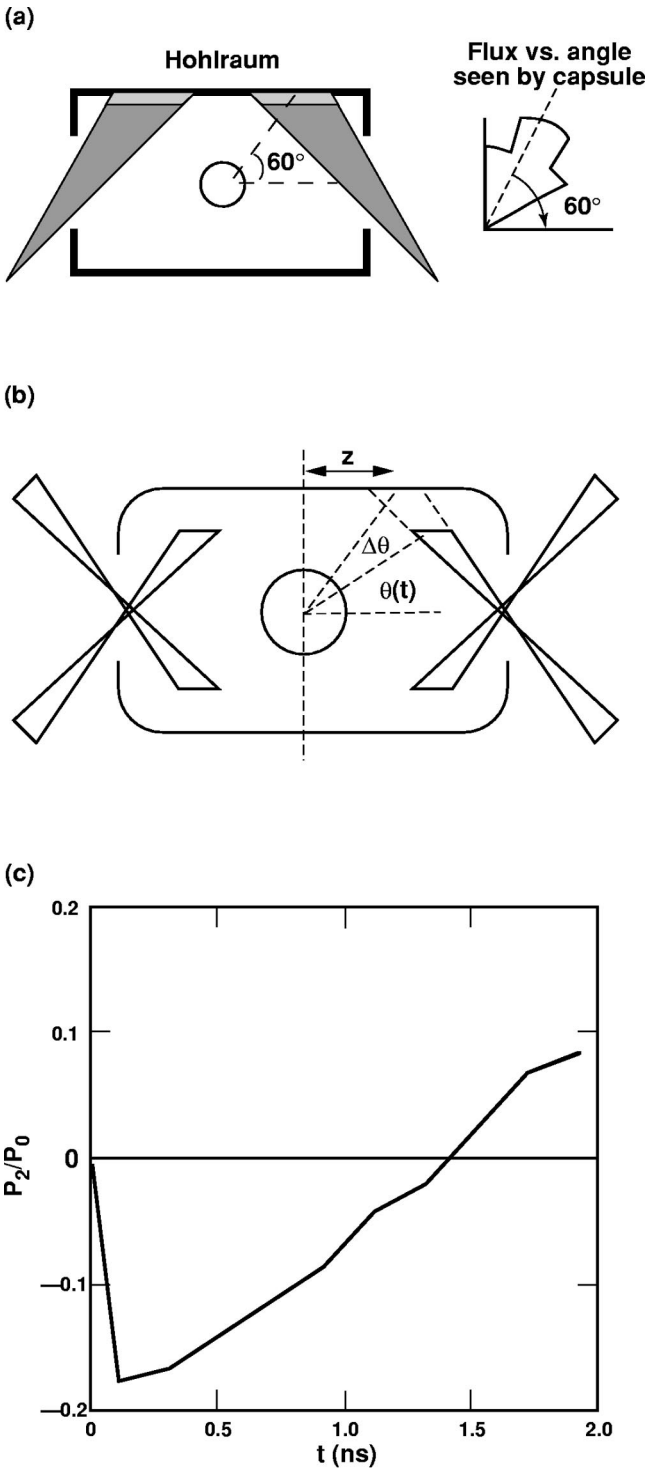

FIG. 5-5. (a) Schematic of a cylindrically shaped, Nova-like hohlraum that produces a collimated source flux vs angle approximately as shown in the flux vs polar-angle plot. (b). Schematic of laser-driven cylindrical hohlraum environment. As time evolves, the hohlraum wall blows in, intercepting the beam ring at smaller polar angle θ. In addition, the unirradiated wall emissivity increases and the capsule radius decreases. (c). Predicted P_2 pressure asymmetry variation at capsule for a standard single Nova ring/side illumination hohlraum (1.6 mm diam$\times$2.4 mm long with 1.2 mm diam LEHs, driven by a 20 TW peak power, 2.2 ns long, 3:1 contrast pulse [PS22]).

However, the full-wall profile at all photon energies is important in determining the asymmetry at the capsule, so this is a lower estimate on the random error. Nevertheless, the good comparison with LASNEX shows that we can calculate the component of spot motion observed—the component along the hohlraum wall. More recent experiments also have attempted to resolve the radial component of the wall motion by the method of triangulation (Back *et al.*, 1997) using simultaneous views. However, the views (at 22° and 0° to the hohlraum equator), besides providing useful redundancy, were not sufficiently separated in angle to make accurate radial motion measurements.

For NIF, issues with thermal x-ray imaging of the hohlraum wall include correctly assessing the 3D perturbation introduced by the slot, resolving the shallower spatial gradients in flux expected of the higher albedo NIF hohlraums (maximum albedo $\gtrsim 0.9$ vs 0.8 for Nova and Omega hohlraums), and signal strength. In addition, it may be desirable to attempt triangulation measurements again, perhaps by simultaneously viewing through the midplane and LEH. The signal strength, for a Planckian source with a fixed ratio of $h\nu/kT$ and a fixed instrument bandwidth $\Delta(h\nu/h\nu)$, is proportional to $(h\nu)^4$. Hence, the transition from studying Nova hohlraums with foot temperatures of 160 eV to NIF ignition hohlraums with foot temperatures of 80 eV leads to a 16$\times$ drop in flux. We expect that this factor can be fully recovered by averaging in the azimuthal direction (over the width of the slot).

In hard x-ray imaging, only the position of the hotter laser–plasma regions are recorded. But the viewing can be done for all spots and without perturbing the hohlraum environment, by using a thin-wall hohlraum, typically 2 μm thick Au (Suter *et al.*, 1997). These thin walls transmit >5 keV emission, which is recorded by multichannel gated pinhole imagers (Bell *et al.*, 1990; Kilkenny, 1991) with 25 μm, and 50 ps resolution. Examples of different snapshots in time from Nova and Omega thin-wall vacuum and 1 atm methane-filled hohlraums driven by unsmoothed beams are shown in Fig. 5-8. The methane is designed to emulate the gas fill required for ensuring adequate symmetry control in NIF-scale cryogenic hohlraums as discussed earlier in Sec. V B. In both cases, the hohlraums are driven with 2.2 ns long pulses with 2 or 3:1 contrast and peak powers of 10 to 20 TW. Errors in determining the spot position are ± 30 to 40 μm, 10% of the spot size.

For the Nova single-ring data, the view chosen in Figs. 5-8(a) and 5-8(b) is perpendicular to the hohlraum axis, yielding the component of motion parallel to the hohlraum axis. The distance between the centroid positions of the rings on either side of the hohlraums is plotted in time on Fig. 5-9, showing an average axial spot motion of 200 μm/ns for the vacuum hohlraum case, consistent with simulations. For the methane-filled hohlraum case, Fig. 5-9 shows that the emission centroid time-dependent position was significantly different from the vacuum case, demonstrating the sensitivity and hence utility of the hard x-ray imaging technique. The reason for this discrepancy and its resolution are discussed later in Sec. V C 2.

For the Omega data on Figs. 5-8(c) and 5-8(d), a compound view was chosen and beams were staggered in time. Figure 5-8(c) is taken at the end of the illumination from the first set of beams and Fig. 5-8(d) during the beginning of the second-set illumination. Overplotted are the expected posi-

Downloaded 20 Mar 2011 to 69.181.48.121. Redistribution subject to AIP license or copyright; see http://pop.aip.org/about/rights_and_permissions

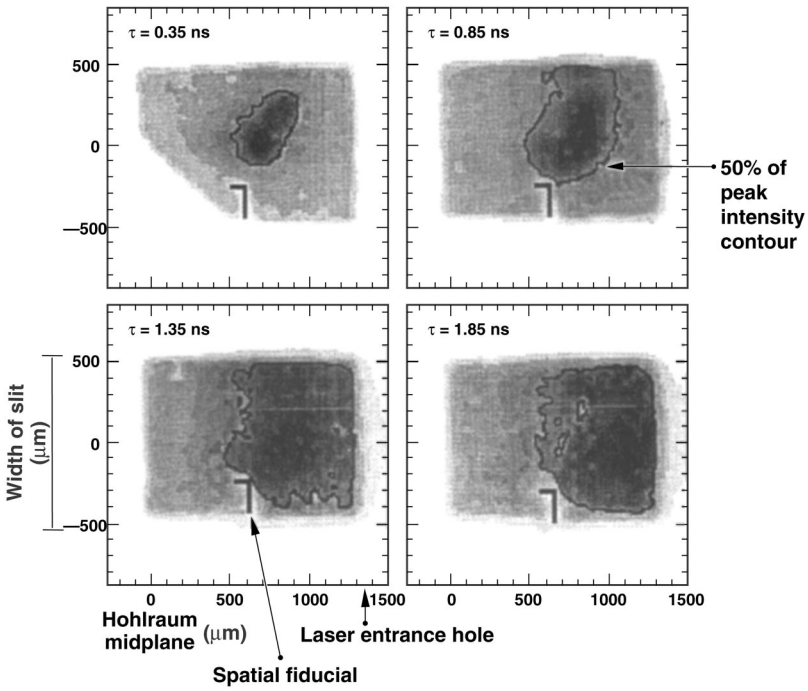

FIG. 5-6. A well-defined soft x-ray spot that moves toward the LEH is observed. Data are obtained by looking at soft x-ray emission through a 1 mm wide slot cut in the hohlraum wall.

tion of the spots if there were no wall motion. Clearly, the spots have migrated back along the incident beam path towards the LEHs, as predicted by simulations. Moreover, although the second set of beams are not incident at the same azimuthal locations as the first set, one can clearly see that these beams are interacting with a wall that has continued to move inward between Figs. 5-8(c) and 5-8(d). This proves, in accordance with LASNEX simulations, that the inward wall motion is dominated by re-radiated x-ray ablation, not by laser ablation. This also means we can treat the wall as moving radially inward at the same speed throughout the hohlraum, an approximation borne out by simulations and used below in an analytic model of the time-dependent P_2 asymmetry.

For NIF, issues with hard x-ray imaging include signal strength during the foot of the NIF ignition pulse, when the average laser intensity at the wall is only 10^{13} W/cm^2, and signal strength during the peak of the pulse, where a thicker hohlraum wall (of order 6 μm) is required to avoid burn-through of the Marshak radiation wave, and hence avoid a change in wall albedo and re-emission. Both these concerns can be alleviated by again using 1D rather than 2D imaging (i.e., averaging over spots in a ring), which could provide a 100× increase in signal strength. In addition, since the accuracy in determining centroid positions is dominated by detector noise (Glendinning *et al.*, 1999) and the width of the rings, one could relax the instrument spatial resolution to perhaps one-fifth of the ring width (200 μm), gaining another 8× in signal.

For directly measuring the time-varying flux asymmetries imposed at the capsule, surrogate spheres are required. One such surrogate consists of a nonimploding high-Z ball. The local re-emission flux from each point on the ball is a measure of the local incident flux. The re-emission from the ball limb is imaged through a diagnostic hole or LEH, pro-

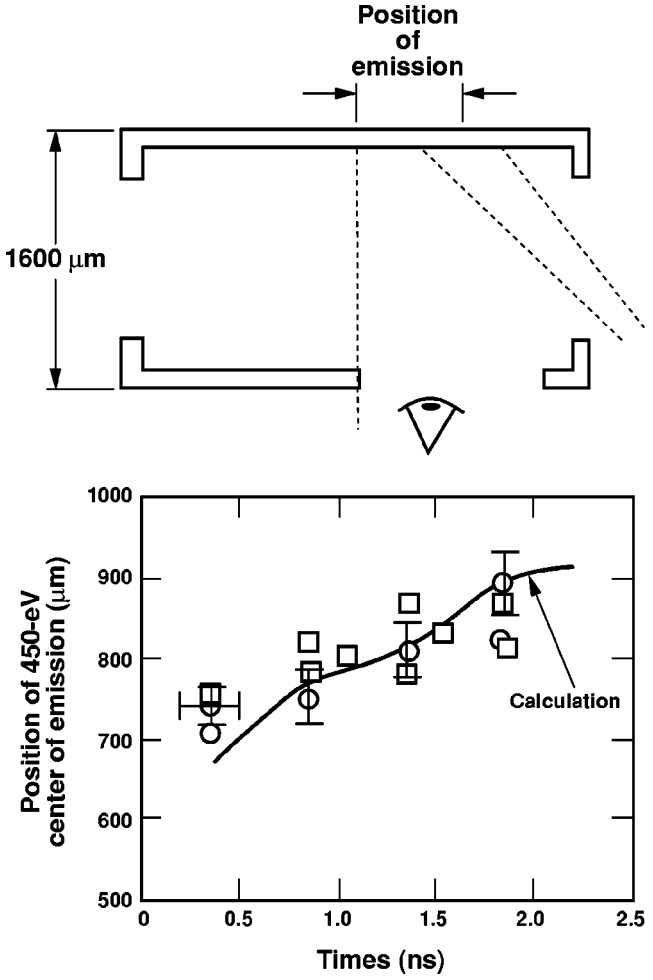

FIG. 5-7. The observed axial motion of the centroid of emission for PS22 is close to that calculated. The squares represent data from several shots with unsmoothed beams whereas the circles represent data from a shot with beams smoothed with random phase plates (RPP).

Downloaded 20 Mar 2011 to 69.181.48.121. Redistribution subject to AIP license or copyright; see http://pop.aip.org/about/rights_and_permissions

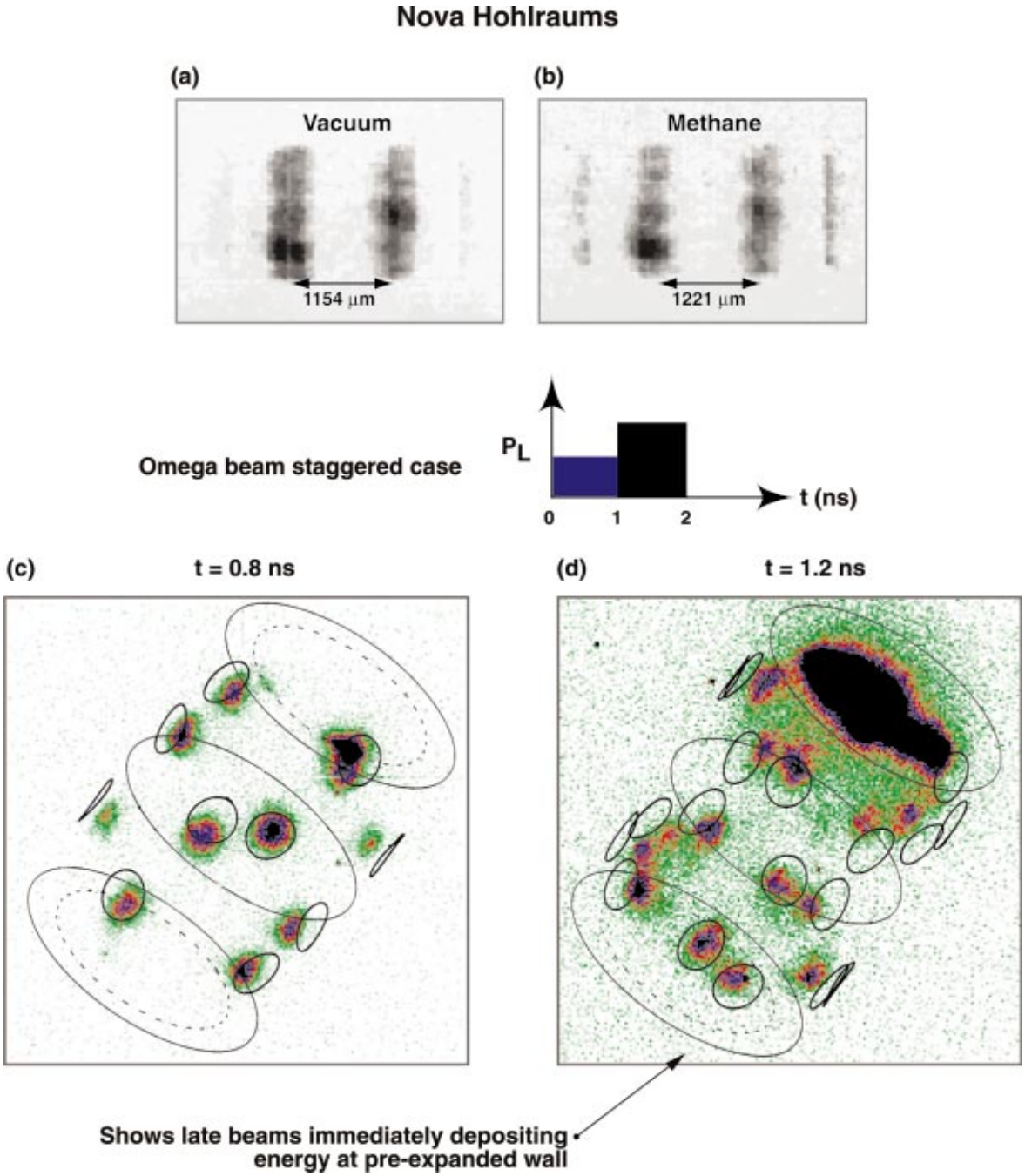

FIG. 5-8. (Color) X-ray images of laser spots from Nova and Omega hohlraums. The hohlraums have 2 μm thick walls and transmit x rays with $h\nu > 5$ keV. (a) and (b) Images from Nova hohlraums, perpendicular to the hohlraum axis, for vacuum and 1 atm methane-filled hohlraums, respectively. (c) and (d) Images from an Omega vacuum hohlraum taken from a compound angle. Image (c) is taken at the end of the first set of beams, while (d) is taken at the beginning of the second set of beams. Open circles show expected beam positions without spot motion.

viding an instantaneous measure of the flux incident on the ball vs polar or azimuthal angle, respectively. The accuracy on the measurement of the flux asymmetry is enhanced by choosing a re-emission photon energy $h\nu$ that is many times the thermal temperature kT of the hohlraum drive. In the limit of Planckian sources, an n% incident flux asymmetry results in an $n\times(h\nu/4kT)$% re-emission flux asymmetry. However, there is a practical limit to the maximum usable $h\nu$ as the re-emission flux falls off exponentially with photon energy.

Figure 5-10 shows examples of re-emission images at $h\nu = 2$ keV from a 400 μm diameter Bi sphere sampling a 200 eV, 1 ns constant-power-vacuum hohlraum drive (Hauer *et al.*, 1995a). A 2:1 left–right laser power imbalance was intentionally imposed on the hohlraum. As time progresses, the redistribution of radiation by the hohlraum reduces the left–right asymmetry in the re-emission from a left–right ratio from 7.5 to 1.4. Any uncertainties in the exact relationship between the re-emission asymmetry and the incident flux asymmetry can be experimentally calibrated by imposing intentional left–right asymmetries, as shown in Fig. 5-10.

Downloaded 20 Mar 2011 to 69.181.48.121. Redistribution subject to AIP license or copyright; see http://pop.aip.org/about/rights_and_permissions

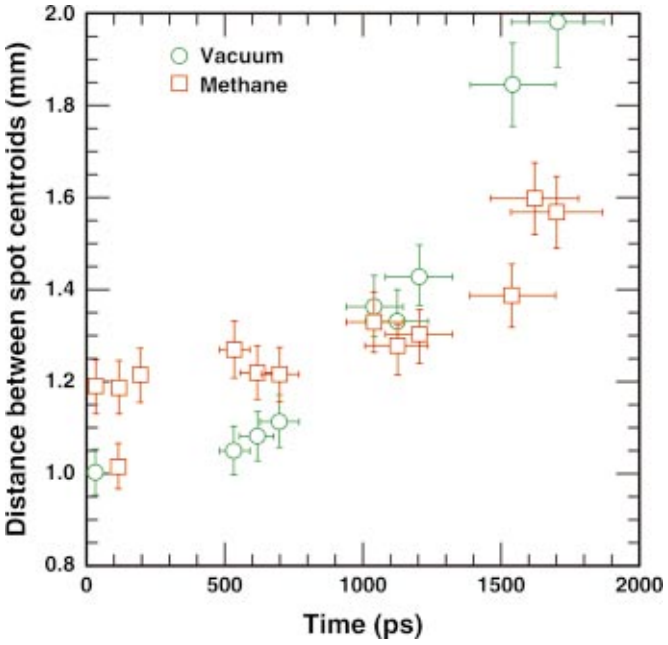

FIG. 5-9. (Color) Because of inward motion of the hohlraum wall, the separation of the two rings of laser spots in the Nova hohlraums increases with time. Circles and squares represent data from vacuum and 1 atm methane-filled Nova hohlraums, respectively.

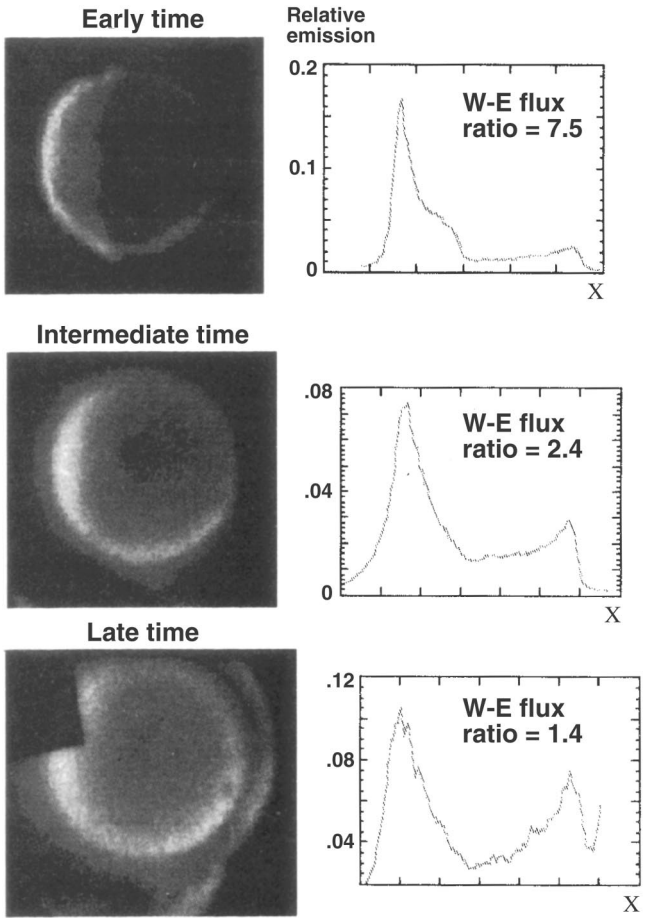

FIG. 5-10. Evolution of hohlraum environment with an intentionally imposed (east–west) laser beam imbalance of 1:2. The lineouts for each frame are taken horizontally through the center of the re-emission ball. The top frame is taken about 200 ps after the rise of a 1 ns laser drive pulse; the middle is about 400 ps after the rise and the lower about 800 ps.

We have demonstrated that the re-emission is not fluorescence stimulated by a high-photon-energy component of the hohlraum-wall flux. This component of the flux is energetically insignificant and hence not necessarily representative of the average flux asymmetry. When the high-Z sphere is overcoated with a low-Z layer only transparent to the high-photon-energy component of the hohlraum-wall radiation (specifically Au M-band radiation at 2 to 3 keV), there was no measurable reemission. Hence, the re-emission is dominated by thermal x rays.

Figure 5-11 shows the early time dependence of the pole-to-equator re-emission ratio for a left–right symmetrically driven vacuum hohlraum (PS22, with $T=160$ eV in the foot), and the inferred P_2 asymmetry. Since $h\nu/4kT\approx 3$, the $\pm 15\%$ accuracy in extracting the pole-to-equator re-emission ratio shown in Fig. 5-11 translates to a $\pm 3\%$ accuracy in inferred instantaneous P_2 asymmetry.

For NIF, issues with re-emission spheres include ablation-driven expansion of the re-emission surface, thereby limiting the duration over which the measurements can be made, signal strength for the NIF foot drive at 80 eV, and accuracy for higher modes. Later-time measurements have been demonstrated by overcoating the high-Z surface with a bleachable low-Z layer, which delays arrival of the radiation front and hence ablation of the high-Z surface. Clearly, the re-emission technique is best suited for the earliest stages of the hohlraum drive, the 10 ns long foot of the NIF pulse, and especially for the earliest times during that foot when other surrogate sphere techniques are least sensitive and applicable. The 16× drop in flux by operating at 80 eV instead of 160 eV can again be fully recovered taking advantage of the fact that the required spatial resolution can scale with hohlraum size, and hence re-emission sphere size (e.g., by imaging with 16× larger area pinholes). More experiments are required to assess accuracy of detecting higher-order asymmetry modes.

In the foam-ball technique, ablation pressure asymmetries P_n are inferred from the distortions experienced by a shock driven into a low-density foam sphere placed at the capsule location (Amendt *et al.*, 1997; Glendinning *et al.*, 1999). The pressure asymmetries produce spatial distortions in the shock position and hence out-of-round edges to the foam ball, which are recorded by radiography at high photon energy. Distortion of the shock front is approximately related to the drive-pressure nonuniformity by

$$\frac{d}{dt}(r_{\text{equator}}-r_{\text{pole}})\approx 1/2\sqrt{\frac{\bar{P}}{\rho}}\left(\frac{P_{\text{pole}}}{P_{\text{equator}}}-1\right). \tag{5-16}$$

Since the edge velocities v follow shock velocities proportional to $\sqrt{P/\rho}$, the lower the initial foam density ρ the greater the difference in edge velocities v for a given flux asymmetry, and the greater the perceived distortion after a given time interval. The limit on the minimum usable density occurs when the heat front becomes supersonic and a shock no longer forms (Amendt *et al.*, 1996). For the typical mid-Z (SiO_2) foam balls, this translates into maximum edge veloci-

Downloaded 20 Mar 2011 to 69.181.48.121. Redistribution subject to AIP license or copyright; see http://pop.aip.org/about/rights_and_permissions

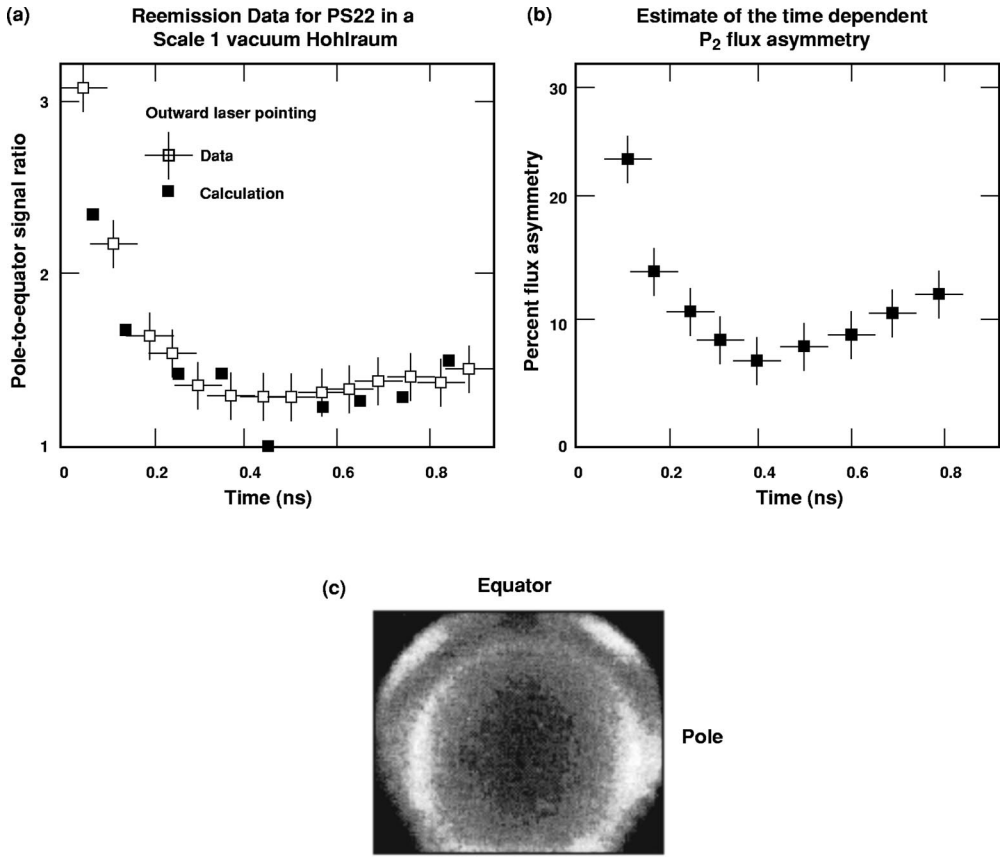

FIG. 5-11. (a) Pole-to-equator re-emission ratio for a left–right symmetrically driven vacuum hohlraum. The time average flux is pole-high in this example. (b) P_2 flux asymmetry derived from pole-to-equator re-emission ratio. (c) Typical image.

ties of 100 (180) μm/ns for hohlraum drive temperatures of 100 (300) eV, respectively. The edge speed can be maximized for a given temperature by minimizing the foam density, with the minimum ρ for SiO_2 being approximately proportional to T^2.

The distortion, decomposed into Legendre moments a_n, are related to the running integral of the applied pressure asymmetries P_n (expressed as a fraction of the zeroth-order pressure moment P_0) by

$$a_n(\tau) = -1/2 \int P_n(t) v \, dt$$

$$= -1/2 P_n a_0 \quad (\text{for constant } P_n). \tag{5-17}$$

The negative sign accounts for the fact that a larger local pressure leads to a depression on the ball. Equation (5-17) also shows that for a given measurement accuracy for a_n, the limit in accuracy in inferring P_n is only dependent on the maximum edge velocity v approximately proportional to $\sqrt{T}$.

A series of experiments were performed in single-ring-per-side Nova vacuum hohlraums driven by PS22. The distortions imposed on 0.3 g/cm^3 SiO_2 foam balls of 450 to 500 μm initial diameter were recorded as a function of the initial laser pointing by backlighting the foam balls with 4.7 keV photons. Up to 16 frames, such as that shown in Fig. 5-12, were recorded per shot with 10 to 15 μm, and 50 to 70 ps resolution. The instrument spatial resolution is set to match the intrinsic 15 μm width of the edge set by the ablation profile to maximize the signal without adding further blurring. The time-dependent distortions of the ball edge or limb, decomposed into the lowest order modes a_0, a_2, and a_4 and averaged over several frames within a ± 150 ps window are plotted in Fig. 5-13.

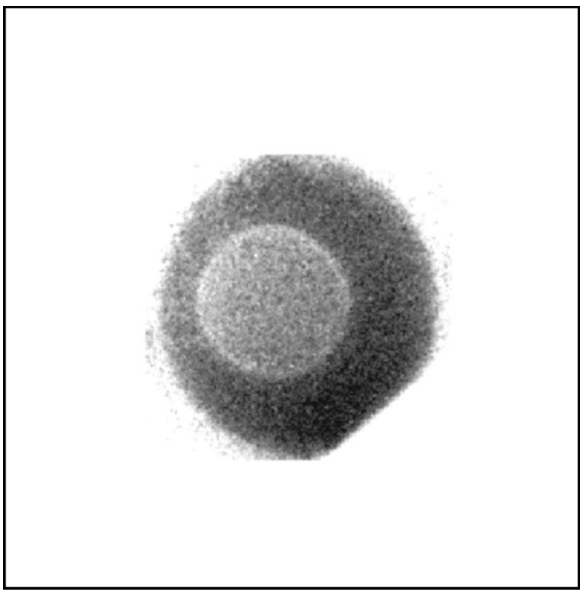

FIG. 5-12. Image of a 0.3 g/cm^3 SiO_2 foam ball, backlit by 4.7 keV x rays on Nova.

Downloaded 20 Mar 2011 to 69.181.48.121. Redistribution subject to AIP license or copyright; see http://pop.aip.org/about/rights_and_permissions

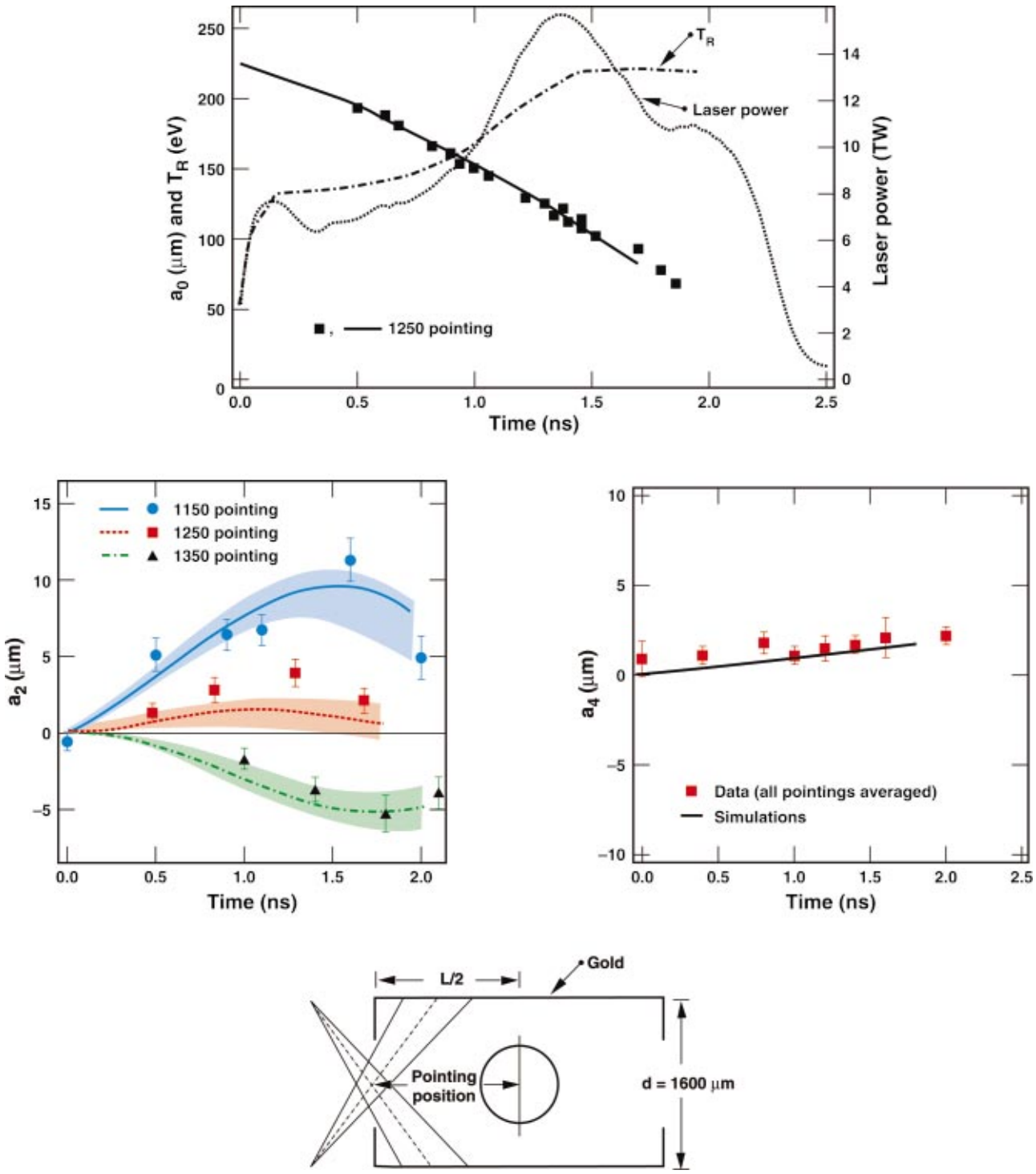

FIG. 5-13. (Color) Coefficients of zeroth, second, and fourth Legendre polynomials from the pointing scan experiment. Data are obtained from backlit foam balls of the type shown in Fig. 5-12. The laser power history and resulting radiation temperature are also shown on the a_0 plot.

In Fig. 5-13(a), the increase in edge velocity or $-da_0/dt$ as the drive increases during the pulse is evident. As expected, the only mode that depends strongly on the pointing is a_2, shown in Fig. 5-13(b) for three pointing conditions incremented in 100 μm steps. For the most inward pointed case ($z=1150$ μm), this corresponds to an initially large negative P_2 becoming more positive in time, as expected from Fig. 5-5(b). By inspection of Eq. (5-17), this should lead to a positive slope for a_2 decreasing in time but never leading to a negative value for a_2, which is in qualitative agreement with the results shown on Fig. 5-13(b). The middle pointing ($z=1250$ μm) shown in Fig. 5-13(b) corresponds closely to the pointing of best symmetry since a_2 is closest to zero by the end of the pulse. This is borne out by implosion results presented later. For the most outward pointing ($z=1350$ μm), the initial P_2 is already positive and continues to grow, which should lead to an increasingly negative slope and only negative values for a_2. This is also

Downloaded 20 Mar 2011 to 69.181.48.121. Redistribution subject to AIP license or copyright; see http://pop.aip.org/about/rights_and_permissions

in qualitative agreement with the lower data set on Fig. 5-13(b). Equation (5-17) can be applied quantitatively to the P_4 pressure asymmetry, as inferred from the a_0 and a_4 data shown in Figs. 5-13(a) and 5-13(c). From the data we have $da_4/dt = 1\ \mu$m/ns. Setting this equal to $-1/2 P_4\, da_0/dt = -1/2 \times P_4 \times 80\ \mu$m/ns, implies $P_4 = -2.5\%$. Overplotted are post-processed 2D LASNEX simulations, showing good quantitative agreement after including a systematic 40 μm pointing offset in modeling the Nova beams (Suter *et al.*, 1994).

The data error bars of $\pm 1\ \mu$m represent the standard deviation of the results of four to eight frames. The error does increase if the radiograph signal is weaker than usual (for example, limited by shot noise rather than detector noise) and hence noisier. This 1 μm error is consistent with the finding that current experiments with a variety of symmetry measurement techniques can determine the centroid of an edge, or more generally a feature, to about $\pm 10\%$ of its width, hence to much better than the instrument resolution. The instrument resolution is usually optimally set for signal strength purposes to be comparable to the feature size.

For NIF, issues with low-density foam balls include possible perturbing effects of the gas environment; hard x-ray preheat; integrity of surrogacy given that foam ball blowoff material may be different from ignition capsule blowoff; and correct modeling of the 3D hohlraum environment given that some drive beams are required for backlighting and a large area clear line of sight is required. Most of these issues will be addressed by 3D simulations in the future. Experimental tests of code predictions in these areas will be performed on the Omega Laser Facility.

For imploding backlit shells, ablation pressure asymmetries P_n are inferred from the distortions experienced by accelerating shells after shock transit. If we approximate the shell areal mass density as constant in time (i.e., the areal mass density loss through ablation is cancelled by the increase due to convergence), the shell distortion a_n is related to the fractional pressure asymmetry P_n by

$$a_n(\tau) = -a_0 \int\int P_n P_0\, dt\, dt' \Big/ \int\int P_0\, dt\, dt'. \tag{5-18}$$

Equation (5-18) also assumes a constant shell thickness as the shell converges. If the shell thickens by $x\%$, the distortion would grow by an additional $x\%$, by the Bell–Plesset effect (Plesset, 1954; Hsing and Hoffman, 1997). For a constant pressure asymmetry P_n, Eq. (5-18) simplifies to

$$a_n(\tau) = -P_n a_0(\tau). \tag{5-19}$$

For identical distances moved (identical a_0), a comparison of the constants in front of Eqs. (5-17) and (5-19) suggests an accelerated shell distortion is enhanced by $2\times$ over a shock-driven foam ball distortion. The main disadvantage of accelerating shells relative to the shock-driven foam ball is that the technique is principally useful only after shock transit and the beginning of shell acceleration. One can consider thinning the shell to either reduce the shock transit time or increase the distance traveled. However, a thin shell leads to either (a) large in-flight aspect ratios leading to undesirable shell break-up by RT instability growth of surface microroughness, or (b) secular growth of initial shell thickness variations competing with flux asymmetries. For example, a 1% initial thickness variation (e.g., 0.1 μm out of 10 μm) will lead to a similar distortion as a 1% P_n asymmetry. Hence the accelerated shell technique is best suited to delayed time-dependent measurements.

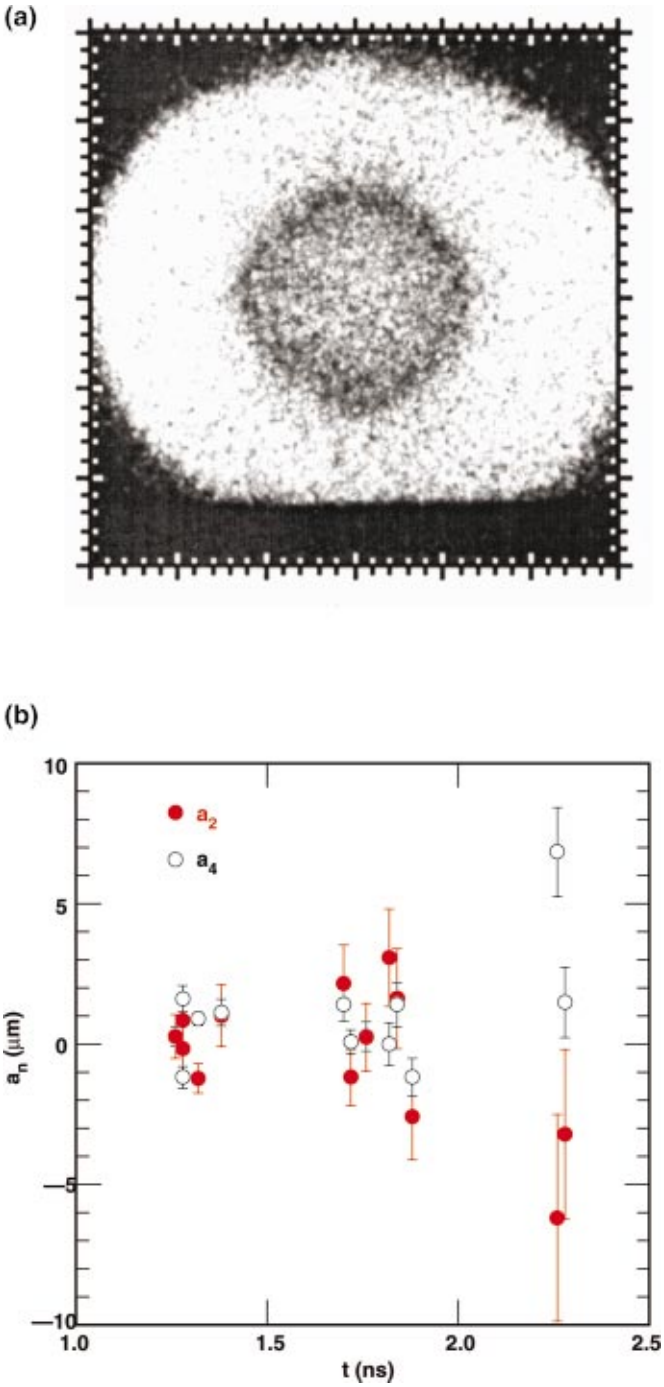

FIG. 5-14. (Color) Backlit shells also provide data on implosion symmetry. (a) A CH shell doped with 3% Ge and backlit with 4.7 keV x rays. (b) The (a_2) and (a_4) coefficients vs time.

Figure 5-14(a) shows an example (Kalantar *et al.*, 1997) of an image of a backlit shell, driven on Nova by PS26, a 6:1 contrast, 2.2 ns long, 20 TW peak power pulse. The CH shell

Downloaded 20 Mar 2011 to 69.181.48.121. Redistribution subject to AIP license or copyright; see http://pop.aip.org/about/rights_and_permissions

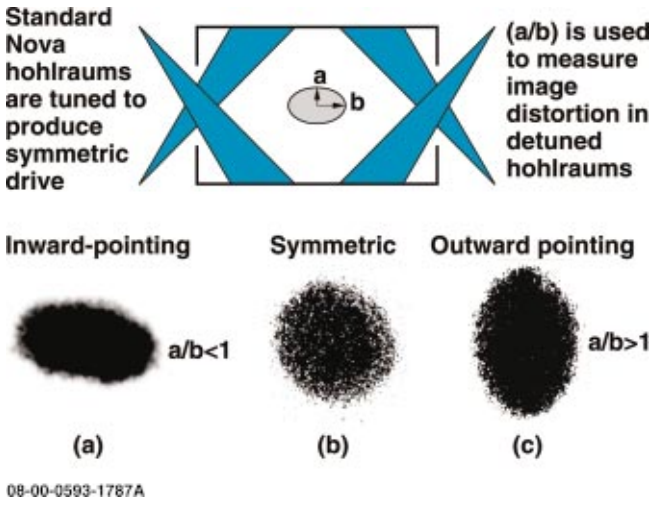

FIG. 5-15. (Color) Nova experiments have extensively used x-ray imaging of imploding capsules to test the modeling of hohlraum drive asymmetries. Observed x-ray image shapes confirm the calculated variation of the implosion shape with beam pointing: (a) inward-pointing shifts produce waist-high fluxes or ''sausaged'' images; (b) symmetric; (c) outward-pointing shifts produce pole-high fluxes or ''pancake'' images. The tilted axis in (a) shows the effects of beam imbalance and pointing errors prior to the Precision Nova improvements.

is 40 μm thick CH ablator, has a 220 μm inner radius and is doped with 3% Ge to enhance the backlit image contrast at 4.7 keV. In Fig. 5-14(b), results from initial shots for the a_2 and a_4 coefficients extracted from the images are plotted in time. A clear a_4 component emerges, and preliminary data and simulation suggest these shells are indeed at least $2\times$ more sensitive to late time asymmetries than solid foam balls. However, the error bars on a_n coefficients from preliminary data are currently about $2\times$ larger than for foam balls, principally due to the motional blurring at the faster velocities (up to 300 μm/ns vs 100 μm/ns for foam balls).

For NIF, issues with backlit shells include RT-induced shell break-up, correct modeling of the 3D hohlraum environment again, and further experimental experience with backlit shells for symmetry diagnosis.

In the most direct method of assessing the time-integrated asymmetries, a 500 μm diameter capsule (Suter *et al.*, 1994; Hauer *et al.*, 1995) filled with D_2 gas and a trace of Ar gas is placed in the center of a Nova hohlraum and is imploded by x-ray drive. Following the implosion is a bright flash of x rays produced by the hot, compressed fuel and enhanced by the mid-*Z* Ar. At that instant, snapshots are taken of the core images formed by x rays viewed perpendicular to the hohlraum axis through a hole at the midplane of the hohlraum. The resulting images show emission that is round, oblate, or prolate, depending on the beam pointing. Figure 5-15 shows three of the earliest results, from pure Au hohlraums irradiated by 1 ns flat-top pulses. A large body of evidence indicates that these capsules, which operate at a pusher convergence from 7 to 10 depending on the pulse shape, do perform as expected. There is good agreement between simulated and experimental capsule neutron yields, time of neutron production, and image sizes. Spectroscopy confirms theoretical predictions that the x rays are principally produced by the Ar and the images are, in fact, images of fuel volume. Analysis of spectroscopy data (Delamater *et al.*, 1996) and neutron data (Cable *et al.*, 1992; Nelson and Cable, 1992) confirms calculated convergences.

To a good approximation, the final distortion at peak compression time is, just as for the accelerating shells above, proportional to the fractional pressure asymmetry and distance traveled, multiplied by a constant close to unity:

$$a_n \approx -P_n a_0 . \tag{5-20}$$

Dividing by the final core diameter a_f, with $C_r \approx a_0/a_f$ for large C_r,

$$a_n/a_f \approx -P_n a_0/a_f \approx -P_n C_r . \tag{5-21}$$

Equation (5-21) states that the fractional distortion is proportional to the average fractional pressure asymmetry, magnified by the convergence ratio. For time-varying pressure asymmetries, a properly time-weighted flux asymmetry of the type shown in Eq. (5-18) is required.

Typical convergences C_r for these implosions are 7 to 10, with central emitting core diameters of 30 to 50 μm. Given current diffraction-limited spatial resolutions of 7 μm, only the lowest-order modes are accurately resolvable. To date, the images have been primarily analyzed for P_2 asymmetry, and historically quantified by their easily visible ellipticity, that is, the ratio of the core full width at half-maximum (FWHM) ''a'' at the equator at 90° to the FWHM at the pole ''b'' at 0° where

$$a/b = (1 - a_n/2a_f)/(1 + a_n/a_f) \approx 1 + (3/2)P_n C_r \tag{5-22}$$

for small values of a_n/a_f. The final relationship in Eq. (5-22) assumes that P_2 is the dominant asymmetry; for example, if the P_4 and P_2 components were equal, there would be of order 50% correction in Eq. (5-22) in relating P_2 to a/b.

The sign and magnitude of P_2 can be varied by changing either the hohlraum length or the beam pointing. Figure 5-15 shows the results of changing the beam pointing. We define the capsule pole as the portion of the capsule on the hohlraum axis of rotation. The waist is the portion of the capsule along the hohlraum midplane. When the hohlraum is elongated, as in the left image, the position of the laser beams is closer to the LEH than is required to achieve uniform average flux, resulting in a ''pancake'' implosion. As the hohlraum is shortened, as shown in the right image, the illumination from the two rings of laser beams approaches the capsule waist, and the average flux delivered to the waist begins to exceed that delivered to the poles, resulting in a ''sausage'' implosion. Between these two extremes, the laser spots are at the optimum position for which the average P_2 component is zero, and the implosion appears spherical. The center image is spherical within the measurement accuracy of a few percent in flux. An interesting feature of the sausage image is the rotation of the image axis away from the hohlraum axis. This type of nonaxial distortion occurred frequently on Nova prior to the power balance and pointing improvements achieved in the Precision Nova Project described in the Introduction.

Downloaded 20 Mar 2011 to 69.181.48.121. Redistribution subject to AIP license or copyright; see http://pop.aip.org/about/rights_and_permissions

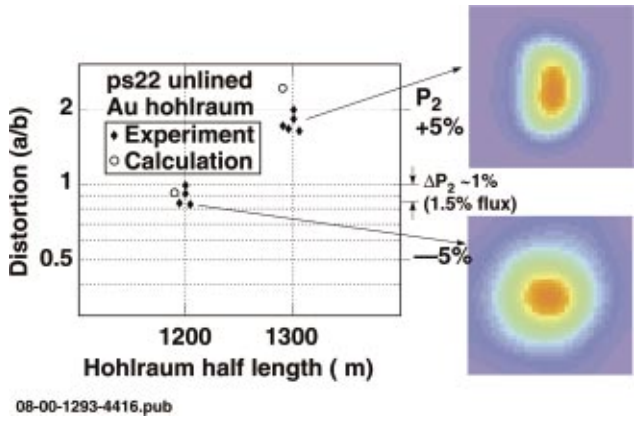

FIG. 5-16. (Color) Precision Nova implosions have shown excellent reproducibility of symmetry.

As a combined test of the reproducibility and accuracy of inferring and calculating the time-integrated P_2 asymmetry, a series of $C_r=7$ implosions were performed with Precision Nova (Caird *et al.*, 1994) and carefully selected capsules with almost identical characteristics. The capsules consisted of pure CH ablators, 45 μm thick, enclosing 50 atm of D_2 gas doped with Ar. The capsules were driven by PS22 in vacuum Nova Au hohlraums. The results of the measured and calculated core distortion a/b for two sets of implosions yielding either close-to-round or intentionally oblate images is shown in Fig. 5-16. Using Eq. (5-22), the measured ± 0.1 scatter in a/b equates to a $\pm 1\%$ variation in inferred P_2 pressure asymmetry. We note that this scatter is predominantly instrumental; for the initially larger NIF capsules yielding similar final core sizes a_f and hence higher convergence ratios, the P_2 accuracy should be even better. These experiments showed that a combination of reproducible hohlraum performance and reproducible symmetry diagnosis at a level required for NIF time-integrated symmetry tuning can be achieved.

Capsules with thinner ablators and hence shorter implosion times have also been used (Hauer *et al.*, 1995; Turner *et al.*, 2000) to vary the drive duration over which the hohlraum flux asymmetries are sampled. This provides a form of time-dependent asymmetry diagnosis at discrete time intervals, commonly known as symmetry capsules. Figure 5-17 shows an example of data from two thinner ablator capsules (35 and 20 μm thick), driven by a PS22 Nova hohlraum. One would expect thinner capsules sampling only the early, predominantly negative P_2 phase of the hohlraum illumination [see Fig. 5-5(c)] to yield prolate images ($a/b<1$), as is the case in Fig. 5-17. There was good agreement between the measured and predicted core distortions: $a/b=0.68$ and 0.92 compared to 0.71 and 0.96.

For NIF, issues with imploded capsules as symmetry capsules are few. Capsules are $4\times$ larger for NIF than for Nova and Omega, allowing either higher convergence ratio capsules for the same final core size, or, for fixed convergence ratio, larger core images, both cases allowing more accurate inferences of time-integrated asymmetries. The principal question is how early in the drive one can sample. At Omega, 10 μm thick capsule ablators have been used successfully with implosion times occurring only 300 ps after the foot portion of a 2:1 contrast, 2.2 ns long, 10 TW peak power pulse, similar to PS22. These thin ablator capsules behave as exploding pushers, and are less sensitive to hydrodynamic instability growth than if they were ablatively driven. Current estimates (Lindl, 1996a) suggest the shortest implosion time for NIF symmetry capsules will be during the second shock, roughly midway in the NIF ignition pulse. If x-ray emission strength is an issue, backlighting at maximum compression might be considered for these symmetry capsules, in the same manner as for the backlit shells discussed above.

Based on the simple analytic formulas presented above, the accuracy of the symmetry techniques for NIF ignition hohlraums can be projected from results achieved to date on a $3.5\times$ smaller scale at Nova and Omega.

The more indirect wall-based techniques (thermal and hard x-ray wall imaging) have been useful in providing independent confirmation of reasons for large (e.g., corresponding to time-averaged $\Delta P_2=15\%$) discrepancies between simulated and measured implosion distortions.

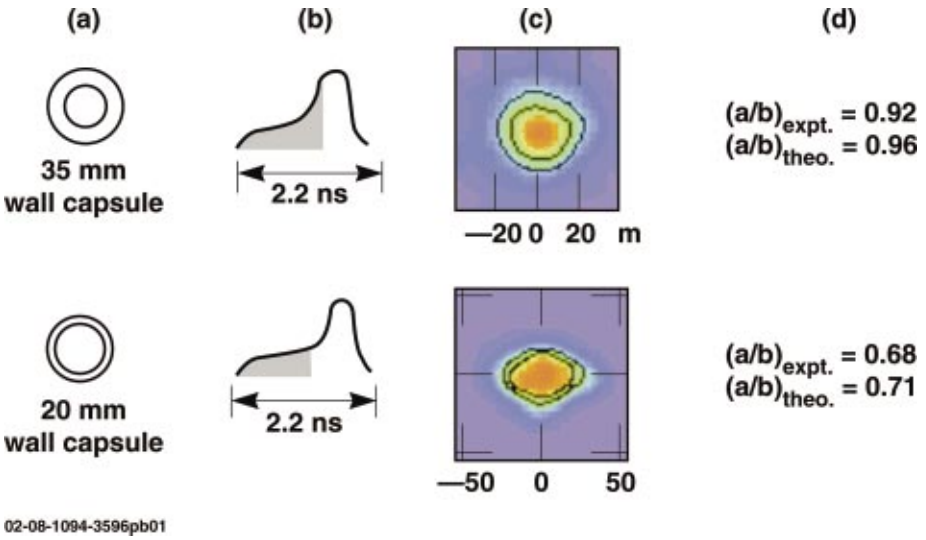

FIG. 5-17. (Color) Data from PS22 using the variation in implosion time of capsules with different wall thickness: (a) initial capsule configuration; (b) shaded portion of the drive represents the effective sampling interval for the implosion for the two cases; (c) implosion image data taken orthogonal to the hohlraum axis; (d) comparison of the measured capsule eccentricity with the calculated value.

Downloaded 20 Mar 2011 to 69.181.48.121. Redistribution subject to AIP license or copyright; see http://pop.aip.org/about/rights_and_permissions

TABLE V−1. A comparison of the required asymmetry measurement accuracy for NIF ignition hohlraums by mode number and the expected accuracy for each technique used so far. Note: The upper number in each box is for the foot of the pulse; the lower number (in parentheses) is for the peak of the pulse.

	P_2 ($t=2$ ns) measured in any 2 ns interval	$P_2 \int dt$			
NIF ignition requirement	10% (10%)	2% (1%)	1–2 % (0.5–1 %)	1–2 % (0.5–1 %)	0.50–1 % (0.50–1 %)
Re-emission sphere	3%				
Foam ball	5%	0.5%	0.6%	0.7%	0.8%
	(2.5%)	(0.5%)	(0.6%)	(0.7%)	(0.8%)
Shell	5%	0.5%	0.6%	0.7%	0.8%
	(2.5%)	(0.5%)	(0.6%)	(0.7%)	(0.8%)
Symmetry capsule		0.25% (0.25%)			

However, they are not viewed as high-precision symmetry techniques.

For assessing the sensitivity of sphere-based symmetry diagnosis techniques on NIF compared to Nova, we assume similar spatial resolution and signal to noise can be achieved. For the re-emission sphere, for fixed $h\upsilon/4kT$ ratio, the sensitivity to P_n is then independent of size or temporal scale, hence $\Delta P_2(t)=\pm 3\%$, as given above. More work remains to assess accuracy to higher order modes. For the foam ball, the accuracy over any time interval is, by Eq. (5-17), inversely proportional to the maximum sustainable edge velocity about $1.5C_s$, where C_s is the sound speed in the heated foam at the hohlraum drive temperature. For a sinusoidal $P_2(\tau)$ variation with period τ, the accuracy in inferring the P_2 amplitude is, rearranging Eq. (5-17),

$$\Delta P_2=\frac{2(\sqrt{2}\Delta a_2)(\pi/2)}{1.5C_s(\tau/2)}\approx\frac{6\Delta a_2}{C_s\tau}, \tag{5-23}$$

where the $\pi/2$ term accounts for the ratio of average-to-peak P_2, and the $\sqrt{2}$ term accounts for the fact that the difference between two statistically independent measured values of a_n is required to infer a pressure asymmetry. For the foot and peak of the NIF pulse, $C_s=55$ and 120 μm/ns. Since $\Delta a_2=1$ μm as given above, Eq. (5-23) yields, for a 2 ns period, ΔP_2 (2 ns)$=5\%$ and 2.5% for the foot and peak of the ignition pulse, respectively. Averaged over a 10 ns foot or 3.5 ns peak pulse, the edge of the foam ball moves about 1/2 of its initial radius, and the time-averaged accuracy is $\Delta P_2=0.5\%$. For higher-order modes, if we assume the same rms measurement accuracy, the accuracy in extracting an a_n coefficient is proportional to $(2n+1)^{1/2}$. Hence, for a_4, the accuracy is only $\sqrt{(9/5)}\times$ worse than for a_2, in agreement with experimental results. The projected time-averaged ΔP_4 accuracy is then 0.6%. For the backlit shells, the sensitivity over a given distance traveled is intrinsically $2\times$ better after the shock breakout, but the measurement accuracy is currently $2\times$ worse due to motional blurring. For the symmetry capsules, the accuracy according to Eq. (5-20) scales with initial capsule size, hence NIF time-integrated values for ΔP_2 of $1\%/4=0.25\%$ should be feasible. Increasing the core image sizes at the detector plane to the centimeter sizes planned for foam ball images may further improve accuracy and allow higher-order modes to be detected. This could be accomplished by ultrahigh (100 to 200×) magnification imaging with target-mounted pinholes (Koch *et al.*, 1999).

A comparison of the predicted and required asymmetry measurement accuracy for NIF ignition hohlraums, shown in Table V-1 by mode number and for each technique used so far, shows that we have met the NIF measurement requirements discussed in Sec. II.

Future work includes validating current extrapolations of measurement accuracy, at least for the foot of the NIF pulse, by performing NIF-scale hohlraum symmetry experiments at Omega. We also plan on demonstrating the feasibility of detecting higher order modes.

2. Time-integrated symmetry control

Time-integrated symmetry control has been demonstrated for a wide range of hohlraums and pulse shapes. For each of the pulse shapes and hohlraum types, a symmetry scaling was produced by varying the beam pointing or hohlraum length while observing the resulting shapes of the capsules in self-emission. Moving the beam pointing in or shortening the hohlraum produces a more prolate implosion ($a/b<1$); moving it out or lengthening the hohlraum produces a more oblate implosion ($a/b>1$).

Between 1990 and 1993, nine different symmetry scaling databases were produced with the single-ring-per-side Nova laser in pure Au and lined hohlraums (Suter *et al.*, 1994). Three scalings were done with 1 ns flat-top pulses, five scalings with the PS22 pulse shape, and one scaling with an 8:1 contrast ratio, 3.2 ns, 27 kJ pulse shape, called PS23. These pulse shapes were used to irradiate both pure Au hohl-

Downloaded 20 Mar 2011 to 69.181.48.121. Redistribution subject to AIP license or copyright; see http://pop.aip.org/about/rights_and_permissions

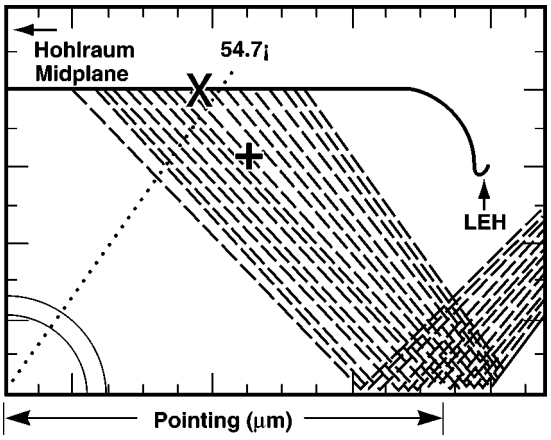

FIG. 5-18. Cutaway at $t=0$ from a 2D simulation of a hohlraum containing a pure plastic capsule with a realistic representation of Nova's beams. The calculation is cylindrically symmetric around the horizontal axis and left–right symmetric across the midplane. The beams enter through LEH's at the ends of the hohlraum. "Pointing" is the distance between the midplane and where the beams "cross" (i.e., the reflection off the horizontal, rotational axis of symmetry), generally chosen to be in the plane of the LEH.

raums and lined hohlraums, as well as gas-filled hohlraums.

With 1 ns flat-top pulses, both pure Au and Ni-lined (0.15 μm) Au hohlraums fixed in length at 2700 μm were tested. For these experiments, the beam pointing was varied so that the position of x-ray emission varied along the length of the wall. With 1 ns flat-top pulses, pure Au hohlraums were also tested in which the length of the hohlraum varied with the pointing fixed so that the beams always crossed in the plane of the LEH. The five scalings with PS22 were: fixed-length Au, and Ni-lined Au, as well as variable-length pure Au, Ni-lined Au, and CH-lined (0.75 μm) Au hohlraums. The PS23 series used pure Au hohlraums that were open cylinders.

LASNEX was used for detailed modeling of these experiments. Figure 5-18 is a cut away, at $t=0$, from a simulation of a hohlraum containing a pure-plastic capsule that is irradiated by a 2D representation of the five-beam ring of Nova beams. The wall materials, laser power vs time, etc., of a given simulation are the best estimate of what was used in each experiment modeled. To model a given symmetry scaling, simulations with a number of different beam pointings were carried out. A post-processor simulated the actual x-ray diagnostics, producing synthetic images that varied with pointing from oblate or prolate. The ratio of the image's FWHM, perpendicular to the polar axis to the FWHM along the polar axis was the distortion, which was compared with the experiment, as discussed above.

The LASNEX calculations started off fully Lagrangian. Later in time, when the absorption region in the hohlraum has evolved to a slowly varying density and temperature profile, the main part of the hohlraum interior was changed to an Eulerian grid. This allowed the calculation to deal with large shear flows that developed as the hohlraum plasma evolved and expanded out of the hohlraum entrance holes. However, most of the capsule remained Lagrangian to deal with the large change in dimensions that occurred during the implosion. The Eulerian and Lagrangian regions were joined with a stretching region that had matter flowing through it while moving slowly. Using three numerical schemes in the same calculation allowed us to simulate both main hohlraum and the capsule with the most appropriate numerical technique.

Figure 5-19 shows a comparison of the calculated and measured distortion for one of the scaling series. This series consisted of shots with Au hohlraums (1600 μm diameter with 1200 μm diameter LEHs lined with 0.15 μm Ni). In this series, the hohlraum length varied so that the beams always crossed in the plane of the LEH. This kept the LEH effects approximately the same for all of the experiments in the series. The experiments used the nominal capsules, defined earlier, and PS22. The self-emission x-ray images from the imploded capsule were the key observations made on this (and all other) scaling series. The x-ray diagnostics were time-resolved (about 100 ps frame time) and time-integrated cameras filtered to measure emission >3 keV from the Ar fuel dopant.

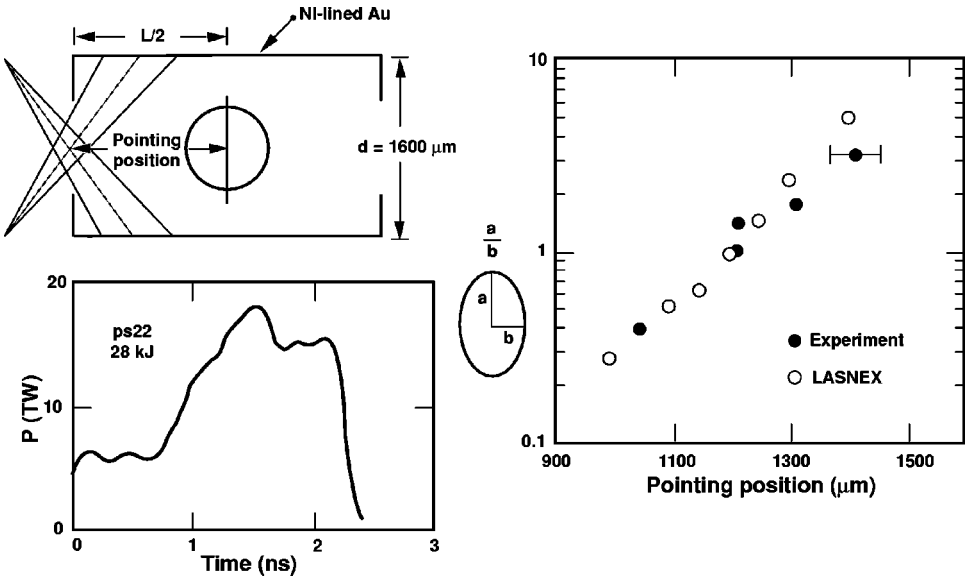

FIG. 5-19. LASNEX calculations do an excellent job of modeling symmetry for experiments in which laser pointing is kept fixed at the plane of the LEH as the hohlraum length is varied for pure Au and lined hohlraums.

Downloaded 20 Mar 2011 to 69.181.48.121. Redistribution subject to AIP license or copyright; see http://pop.aip.org/about/rights_and_permissions

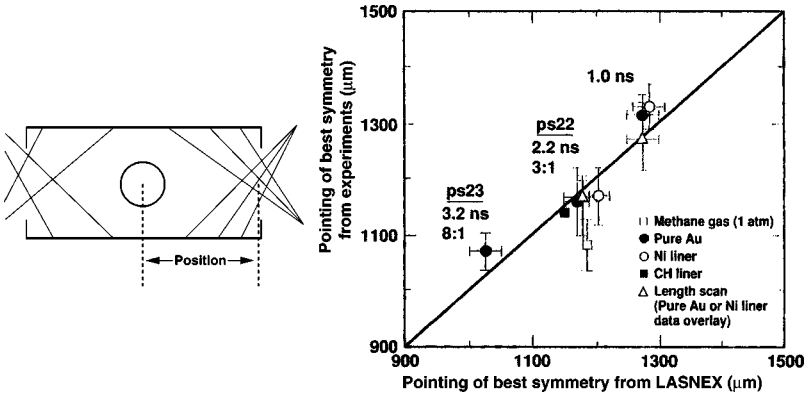

FIG. 5-20. LASNEX successfully predicts the pointing of best symmetry for almost all symmetry experiments. Beams must be moved inward for longer pulses to compensate for spot motion caused by hohlraum wall blow-off. Without beam smoothing, the experimental pointing of best symmetry is offset from the calculations by about 150 μm for the methane-gas-filled hohlraums.

The solid circles in Fig. 5-19 are distortions from the experiments as a function of beam pointing. The horizontal error bar shows an estimated $\pm 50\ \mu$m systematic uncertainty in the absolute pointing of the beams (the relative shot-to-shot pointing jitter is believed to be considerably smaller than this). The open circles are modeling distortions. Both experiment and modeling have about the same variation of distortion with pointing and produce about the same pointing of best symmetry (about $1200 \pm 50\ \mu$m in experiment and about 1150 μm in modeling).

The pointing of best symmetry changes with the pulse shape. For example, in a series that used fixed length (2700 μm), Ni-lined Au hohlraums irradiated with 1 ns flat-top pulses, the pointing of best symmetry was about 100 μm outward from the best pointing found in the PS22 series. For this 1 ns experiment, the pointing of best symmetry was about $1320 \pm 50\ \mu$m in experiment and about 1250 μm in modeling.

Figure 5-20 summarizes the pointing of best symmetry over the nine symmetry scaling databases in pure Au and lined hohlraums. It plots the pointing of best symmetry inferred from experiment against that of the integrated LASNEX simulations. Overall, there is good agreement. The vertical error bars in this plot indicate only the uncertainty in the pointing of best symmetry extracted from each experimental dataset, using the nominal pointing. The error bars do not include the systematic uncertainty in Nova's absolute pointing (about 50 μm), which would allow all the points to be moved as a group, either up or down. Figure 5-20 shows that for longer pulses, the pointing of best symmetry moves inward, to compensate for the greater outward spot motion for longer pulses.

In detailed LASNEX simulations, the pole and waist fluxes are balanced for all these Nova symmetry series when the flux-averaged center of emissivity as seen by the capsule is at about 48° relative to the hohlraum axis. At the beginning of the pulse this position is 54.7°. As the wall heats up, the optimal position moves toward the LEH, as indicated in Fig. 5-4. Because the time-averaged albedos and the size of the LEH are about the same for all of these experiments, the time-averaged optimal pointing position is also about the same. The simulations include higher l-mode components, volume emission, and mode-coupling due to having a sphere inside a cylinder. LASNEX simulations also show spot-angular velocity to be very weakly dependent on laser power P_L. Over the period when the first 50% of the laser energy is delivered, the angular velocity $d\theta/dt$ of the center of emissivity increases only as the logarithm of P_L (measured in TW) closely following

$$\frac{d\theta}{dt} = \frac{6^\circ}{\text{ns}} + \frac{3.9^\circ}{\text{ns}}(\log_{10} P_L). \tag{5-24}$$

Coupling this expression for spot motion with the requirement that the center of emissivity be at about 48° when about 50% of the laser energy has been delivered to the hohlraum results in a simple expression for the pointing of best symmetry:

$$\text{best pointing} = 671\ \mu\text{m} + \left[\frac{800\ \mu\text{m}}{\tan\left(48^\circ + \frac{d\theta}{dt} \times t_{50\%}\right)}\right]. \tag{5-25}$$

This expression is for the standard 800 μm radius hohlraums and Nova's 50° half-cone angle. The results of this very simple model are plotted as the filled triangles in Fig. 5-20 and also agree well with the database.

The role of the LEH in determining the average P_2 asymmetry was modified in another series of implosions (Amendt *et al.*, 1996a). The symmetry of imploded cores was varied by blocking the capsule's view of the LEHs by Au disks of various radii, as shown in Fig. 5-21. The data and simulations of the core distortions a/b as a function of

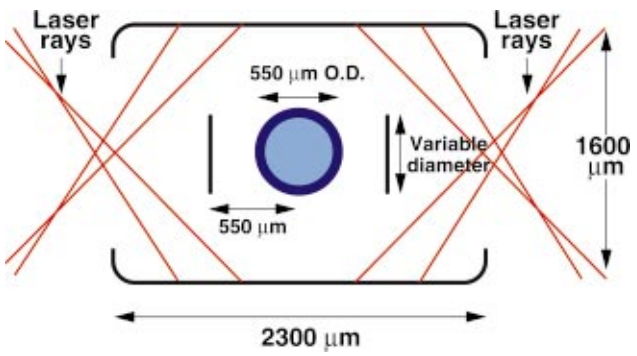

FIG. 5-21. (Color) Schematic of a Nova Au hohlraum with Au disks centered at $z = \pm 550\ \mu$m. Capsule and hohlraum dimensions are as indicated.

Downloaded 20 Mar 2011 to 69.181.48.121. Redistribution subject to AIP license or copyright; see http://pop.aip.org/about/rights_and_permissions

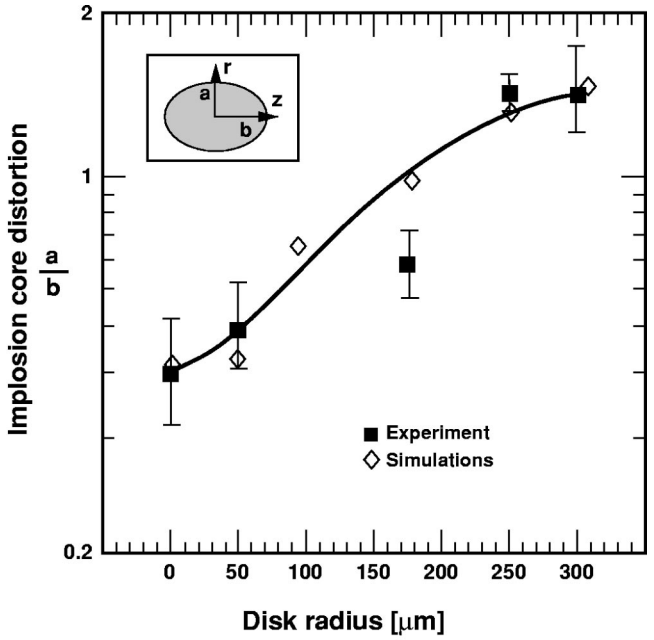

FIG. 5-22. Implosion core distortion vs disc radius for hohlraums of the type shown in Fig. 5-21.

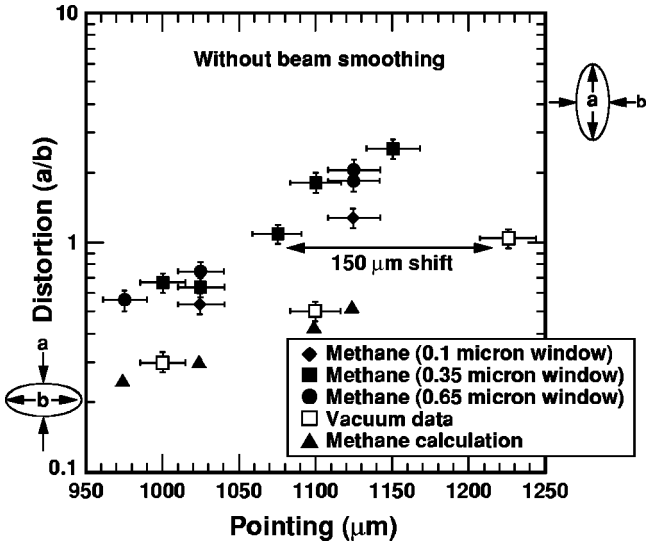

FIG. 5-23. X-ray image distortion vs laser pointing for standard capsule implosions without beam smoothing. Distortions are plotted for methane-filled hohlraums, vacuum hohlraums, and for calculations of implosions in methane-filled hohlraums. Definitions of capsule distortion are shown pictorially.

the disk radii are shown in Fig. 5-22. The images become more oblate (larger a/b ratio) as more of the LEH is blocked, in good agreement with simulations. In the limit that the Au disks completely block the LEH, essentially the entire time variation in the flux on the capsules comes from spot motion. The various series of symmetry experiments above demonstrates that we can control the combined effects of the LEH and spot motion, and that we can calculate the effects separately.

The baseline NIF ignition hohlraum is filled at cryogenic temperatures with a 1 to 2 mg/cm^3 mixture of H and He gas to control spot motion. Without this low-Z filling, inverse bremsstrahlung in Au at $n/n_c \approx 0.1$ is large enough in NIF-scale hohlraums, that the laser absorption and x-ray emission region move a significant fraction of the original hohlraum radius during the pulse, as described in Sec. II.

For Nova-scale hohlraums, which are about one-fourth 4 NIF scale, the laser is able to propagate through the low-density, high-temperature Au plasma and most of the laser light is absorbed fairly close to the wall in higher-density, lower-temperature Au. Because of this, calculations for Nova show little difference in symmetry for pure Au vacuum or gas-filled hohlraums. The principal purpose of doing the Nova gas-filled hohlraum experiments was to see if any plasma coupling effects would affect symmetry when the laser propagated through the low-Z plasma rather than a Au plasma.

Implosions and related symmetry measurements using PS22 were performed at Nova in hohlraums filled with methane or propane at 1 atm (Delamater *et al.*, 1996; Kauffman *et al.*, 1998). The gas and diagnostic holes were covered with 0.6 μm thick Mylar or from 0.1 to 0.35 μm thick polyimide windows to contain the gas. Most of the gas-filled hohlraum experiments were filled with 1 atm of methane. When ionized, this gas has $n/n_c \approx 0.03$, about the same initial electron density as the NIF baseline hohlraum. At the peak of the pulse, the gas compresses to densities of about $n/n_c \approx 0.1$, also about the same as for the NIF targets. Propane-filled hohlraums have about twice the initial electron density of methane when fully ionized.

Standard symmetry capsules were used to infer the average P_2 asymmetry from measurements of the core distortions a/b. Figure 5-23 shows the initial results of measured a/b distortion vs initial beam pointing for both vacuum and methane-filled hohlraums. The pointing position, as indicated in Figs. 5-13 and 5-20, is the distance between the plane of the LEH and the capsule center. For all these experiments, the beams cross in the plane of the LEH. The symmetry dependence on pointing is similar for vacuum and gas fill, but there is a 150 μm offset in the pointing of best symmetry, translating to a $+15\%$ average P_2 offset. Superimposed on Fig. 5-23 are the calculations for gas fill, which predicted little or no P_2 offset when including gas. The experimental offset was corroborated by a series of time-dependent measurements using thinner symmetry capsules, soft and hard x-ray imaging [see Figs. 5-8(b) and 5-9], re-emission spheres (Delamater *et al.*, 1996a), and optical imaging of the incident and transmitted beam paths (Moody *et al.*, 1996). The results from all these measurements suggest the beam is bent by up to 6° radially outward as it enters the gas-filled hohlraum.

As discussed in Sec. III, numerical simulations of filamentation in a flowing plasma (Hinkel *et al.*, 1996; Rose, 1996), reproduce this beam bending. The filamentation effects are not incorporated into LASNEX, and this results in the discrepancy in the predicted symmetry vs pointing. The effect is largest where the flow speed is near the sound speed, which occurs near the LEH.

The symmetry and implosion measurements in gas-filled hohlraums (Delamater *et al.*, 2000) were repeated with spa-

Downloaded 20 Mar 2011 to 69.181.48.121. Redistribution subject to AIP license or copyright; see http://pop.aip.org/about/rights_and_permissions

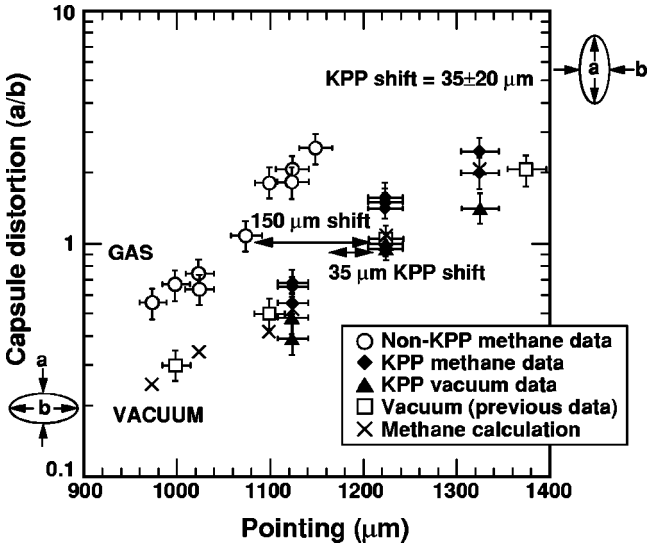

FIG. 5-24. X-ray image distortion vs laser pointing for standard capsule implosions in methane-filled hohlraums for smoothed and unsmoothed beams. LASNEX calculations and data for vacuum hohlraums are also shown. The smoothed beam data set gives a shift of 35 μm from the LASNEX results, while the unsmoothed data set gives a shift of 150 μm.

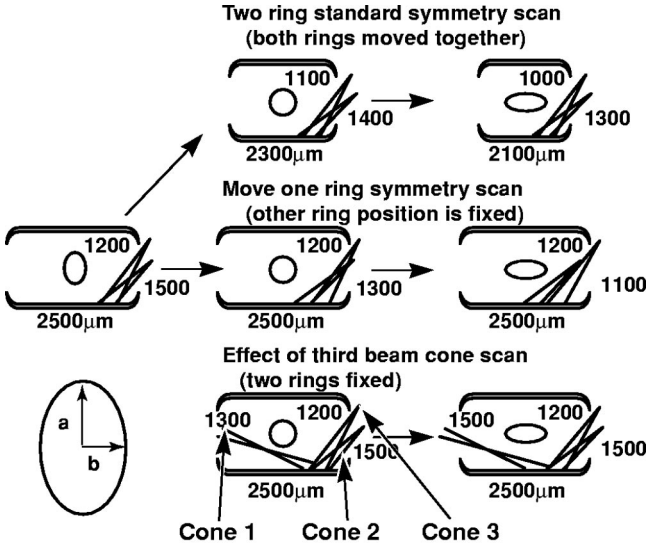

FIG. 5-25. Forty of Omega's 60 beams can be arranged in three rings per side with five, five, and 10 beams per ring at incidence angles of 21.4°, 42°, and 59°, respectively. Schematic shows the three types of symmetry scans tried and the expected effect on the imploded core.

tially smoothed beams, where the percentage of high-intensity spots susceptible to filamentation, and hence beam bending is greatly reduced. Figure 5-24 plots the results of a pointing scan taken under the identical conditions of Fig. 5-23 except for the use of smoothed beams. The results show that the 150 μm pointing offset has been reduced to 35 μm, at the level of the pointing and measurement accuracy, and once again in agreement with LASNEX. As discussed in Sec. III, the filamentation responsible for the beam bending is calculated to result in less angular deflection on NIF than in these Nova experiments.

The symmetry experiments described above have concentrated on single-ring-per-side, 10-beam, Nova hohlraums. The 60-beam Omega Laser Facility (Soures *et al.*, 1996) has made it possible to carry out symmetry experiments in a geometry with multiple rings per side.

Up to 40 of the 60 Omega beams were used to illuminate cylindrical hohlraums (Murphy *et al.*, 1998; Murphy *et al.*, 1998a). The beams were arranged in three cones of five, five and 10 beams per side with incidence angles of 21.4, 42, and 59°, respectively. Figure 5-25 schematically depicts the pointing variations tested. The core distortion results and simulations are plotted in Fig. 5-26 as a function of pointing for the different types of variations. The distortions are in excellent agreement with simulations for all types of variation, demonstrating time-integrated P_2 symmetry to 1% in multiple ring geometries. The combination of better pointing accuracy (20 μm rms) and better beam statistics (40 vs 10 beams) for equivalent beam-to-beam power imbalance, leads to smaller random asymmetries and systematic offsets relative to calculations on Omega compared to Nova.

In another series of experiments, a NIF-like multiple-ring geometry with well-separated inner and outer ring centroids was tested (Landen, 1998). The results of the measured and predicted core distortion (Landen *et al.*, 2000) for $8\times$ to $17\times$ convergence capsules are shown in Fig. 5-27. From Eq. (5-22), the measured and predicted distortions agree to 2% in average P_2. In this case with widely separated inner and outer rings, the average P_2 is being determined by the cancellation of two large P_2 components of opposite sign. The results shown in Fig. 5-27 are for optimal pointing and are further discussed in the Sec. VII HEP4-5 results from Omega.

There are several other physics issues besides beam bending for which uncertainties in modeling could poten-

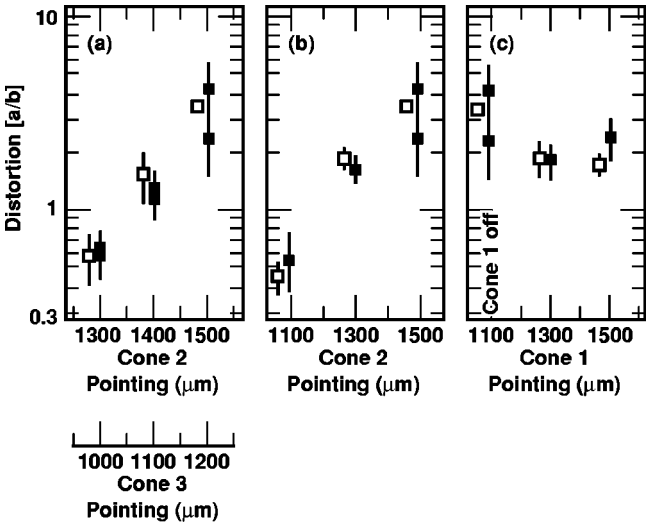

FIG. 5-26. Distortion as a function of beam pointing for the experiment (a) in which beam cones 2 and 3 formed a single ring on each side of the hohlraum, (b) in which the pointing of cone 2 was varied while that of cone 3 remained fixed at 1200 μm, and (c) in which cone 1 was added while cones 2 and 3 remained fixed at 1500 and 1200 μm, respectively. The uncertainty in the data (solid symbols) is determined by analyzing multiple images and contours on the same experiment, and that from simulations (open symbols, offset to the left for clarity) represents the range of calculations obtained from the LLNL and LANL versions of LASNEX.

Downloaded 20 Mar 2011 to 69.181.48.121. Redistribution subject to AIP license or copyright; see http://pop.aip.org/about/rights_and_permissions

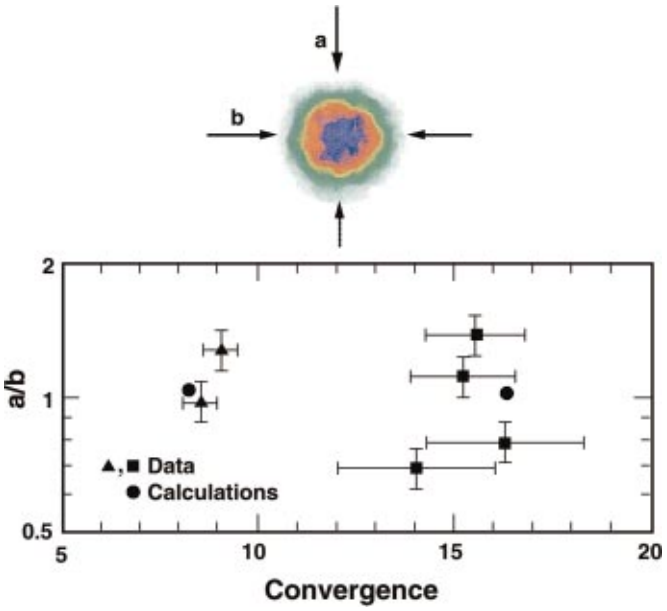

FIG. 5-27. (Color) Capsule distortion from Omega experiments using a NIF-like multiple-ring geometry with inner and outer rings well separated. The results shown are for optimal symmetry and are discussed further in Sec. VII for the HEP4-5 results.

tially cause an offset between the predicted and experimentally inferred flux asymmetry at the capsule. These include laser light directly incident on the capsule because of reflection from the hohlraum wall (glint) (Landen *et al.*, 1996; Honda *et al.*, 1998), the crossed beam energy transfer by three-wave mixing, discussed in Sec. III, and inhibited heat conduction (Glenzer *et al.*, 1997a).

The level of glint measured in vacuum hohlraums is 10% of the incident power over the first 150 ps, dropping rapidly after that as the hohlraum-wall plasma develops, in agreement with LASNEX simulations. For a gas-filled NIF ignition hohlraum, the effects of glint are small because the reflected laser light has to bleach through a cold (<100 eV) absorptive H/He plasma to reach the capsule. Only 1% of the glint is transmitted through this low temperature gas, and only after a 2 to 3 ns delay, by which time the capsule x-ray ablation surface is separated by 200 μm from the lower-density laser-absorption surface. Hence, an upper level on the contribution of glint to low-mode flux asymmetries is estimated by multiplying 1% transmission by 10% reflectivity, a negligible 0.1% contribution for a fraction of 1 ns.

Energy transfer between crossing beams by stimulated Brillouin scattering in flowing and stationary plasmas will change the power balance between beam rings and hence the lowest-order asymmetries. For example, a 20% transfer of energy from an inner to an outer cone, as demonstrated in the recent Nova experiments discussed in Sec. III, would lead to a 5% offset in P_2. If the P_2 offset is large enough, the target or laser geometry would not have enough flexibility to correct for it. It is also possible that the beam-to-beam variations could be larger than the NIF target could tolerate. The NIF laser design mitigates this energy transfer, eliminating potential resonances by using small variations in laser wavelength for inner and outer rings, as discussed in Sec. III.

Recent Thomson scattering measurements of plasma temperatures in gas-filled Nova hohlraums (Glenzer *et al.*, 1997a; Glenzer *et al.*, 1999) were higher than expected from LASNEX simulations without self-generated magnetic fields. The higher temperatures, are reproduced in LASNEX simulations that include the self-generated fields (Lindl, 1998d). Simulations of NIF targets, which include the greater heat transport inhibition and higher matter temperatures in the hohlraum interior caused by B-fields, lead to a proportionately larger increase in laser light transmission over the longer path taken by the inner ring. This change in transmission leads to a change in the hohlraum flux pattern and asymmetries. The effect is roughly equivalent to a 2% change in average P_2, easily correctable by a small change in pointing or ring-to-ring power balance.

3. Time-dependent symmetry control

It is possible to describe the time-dependent symmetry for the Nova experiments with an analytic formula (Landen *et al.*, 1999) based on the observed spot motion given by Eq. (5-24), the pointing sensitivity of the source flux given by Eq. (5-14), and the geometric smoothing of asymmetry for a capsule in a cylindrical hohlraum shown in Fig. 5-2. For a foam ball driven by a hohlraum illuminated by a single ring/side pointed near the P_2 node, we have

$$\frac{P_2}{P_0}=5\left[0.25+0.67\left(\frac{r_f-v_f t}{r}\right)\right]\left[\frac{\dfrac{0.18T^{0.5}t}{\sqrt{z^2+r^2}}+1.2(z-0.71r)-P_2(X_H)\left(\dfrac{1.5(A_H/A_w)T_1^{0.7}t^{0.38}}{1+1.5(A_H/A_w)T_1^{0.7}t^{0.38}}\right)}{1+\left(\dfrac{2.2T_1^{0.7}t^{0.38}}{1+1.5(A_H/A_w)T_1^{0.7}t^{0.38}}\right)}\right], \tag{5-26}$$

where z is the axial distance in millimeters between the initial ring centroid position at the hohlraum wall (of area A_w) and the hohlraum mid-plane [see Fig. 5-5(a)], r is the hohlraum radius in millimeters, r_f is the initial foam ball radius in millimeters, v_f is in millimeters per nanosecond, t is the time in nanoseconds after the drive starts, and T_1 is the hohlraum re-emission temperature in heV after 1 ns. Equation (5-26) is essentially Eq. (5-14) modified to apply to the capsule surface location rather than the source location. The first term in square brackets represents the smoothing factor for a

Downloaded 20 Mar 2011 to 69.181.48.121. Redistribution subject to AIP license or copyright; see http://pop.aip.org/about/rights_and_permissions

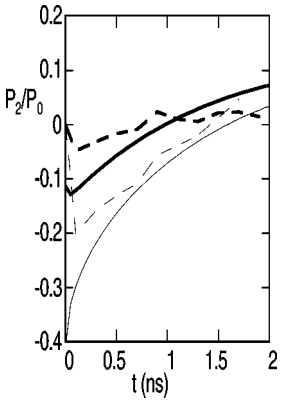

FIG. 5-28. Time dependence of P_2/P_0 pressure asymmetry at a foam ball calculated by the simplified analytical model (dashed curves) and by 2D Lasnex simulations (solid curves). The lower and upper curves are for an initial beam ring position from the hohlraum midplane of $z=430$ μm and 530 μm, respectively.

spherical foam ball in a cylindrical hohlraum of typical length-to-diameter ratio$=1.5$. Variations of $\pm 20\%$ around this hohlraum aspect ratio value cause a negligible change in the smoothing factor ($<\pm 3\%$) for a typical initial ratio $r_f/r=0.3$. The three terms in the numerator in the second set of square brackets represent the variation in the hot-spot P_2 coefficient as the wall, and hence laser spots move in time (a weak function of hohlraum flux, and hence laser intensity from Eq. (5-24); the initial hot-spot P_2 coefficient determined by the initial laser beam positions, and the P_2 coefficient due to the laser entrance hole of area A_H, respectively). The denominator represents the smoothing by the factor F shown in Fig. 5-4 due to the recirculating flux in a hohlraum. The smoothing is a function of the hohlraum losses, and is a weak function of the hohlraum flux and hence of the laser pulse shape. Equation (5-26) can be easily extended to the case of multiple ring illumination or high contrast pulse shapes.

The time-dependent P_2/P_0 asymmetry as derived from Eq. (5-26) for two initial beam pointing conditions in standard PS22 Nova hohlraum drives are plotted in Fig. 5-28. The model results are in good agreement with overplotted predictions from 2D radiation hydrodynamic LASNEX simulations. At the earliest times, the negative P_2 swing is due to the rising albedo. The later positive P_2 swing is due to the decrease in ring polar angle due to wall motion. Both P_2 curves flatten and converge at late time, as expected when hohlraums become increasingly dominated by wall fluxes and are relatively insensitive to pointing position. The P_2 sensitivity to pointing is greatest at early times when F is small. The 5% to 10% P_2/P_0 offset between simulations and the analytic model can be attributed to a positive P_2 contribution at the capsule due to a near-unity P_4 wall component, which affected the measured ratio of a/b but is not included in the analytic model.

Three experimental series conducted at the Omega (Turner *et al.*, 2000) and Nova (Glendinning *et al.*, 1999) laser facilities have extended the symmetry studies by demonstrating time-dependent control of P_2 and P_4 flux asymmetries. A NIF-like multiple ring illumination has been used at Omega to reduce both P_2 and P_4 asymmetry swings to levels below those required for ignition. All of these series used from 2.1 to 2.5 mm long, 0.8 mm radius hohlraums with 0.6 to 0.8 mm radius LEHs. The hohlraums were driven by 2.2 ns long, pulse-shaped 3ω beams, with peak powers of 10 to 20 TW, similar to PS22, reaching peak temperatures of 180–200 eV. Time-dependent flux asymmetries were inferred from the shapes of shock-compressed, 0.25 mm radius, backlit, 0.3 g/cm^3 SiO_2 foam balls.

In initial time-dependent symmetry control experiments on Omega, a single correction in time for the P_2 asymmetry was applied by turning off one set of beam rings midway through the pulse (at 1 ns) and turning on another set appropriately pointed to either enhance or reduce the P_2 asymmetry swing due to spot motion as indicated in Fig. 5-29(a). Both cases were designed for zero-time integrated P_2 asymmetry for implosion times of 2 ns. The results in Fig. 5-30(a) show a large excursion in a_2 for the case where the asymmetry swing was intentionally enhanced, reaching a peak of about 4 μm, 2% of the average radius at that time. For the case attempting to reduce the asymmetry swing, a_2 stays within ± 2 μm at all times. Figure 5-30(b) shows that a_4, which is not controlled here, monotonically increases in accordance with simulations. The a_2 data are well-matched by the overplotted semiempirical model combining Eqs. (5-26) and (5-17). The residual discrepancies between this simplified model and code calculations, also overplotted, are partially due to the exclusion of mode-coupling terms in the simple model (i.e., P_4 at a cylindrical hohlraum wall imprinting P_2 at a spherical foam ball).

At Nova, time-dependent symmetry control was achieved by a combination of (a) sending different pulses down each half of each beam-line and (b) defocusing beams,

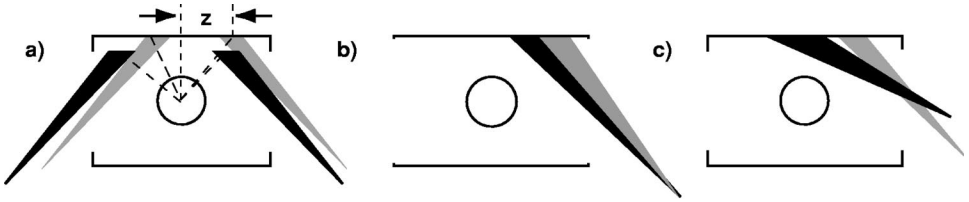

FIG. 5-29. Schematic hohlraum illumination geometries used for time-dependent symmetry studies. (a) 42° and 59° $f/6.5$ Omega beams are staggered in time (gray ring first). The delayed beam rings (in black) interact with a converged hohlraum wall. The dashed lines show the angular swing in the laser ring positions as seen by the capsule (left-hand side showing enhanced swing, right-hand side showing reduced swing). (b) 50° $f/4.2$ Nova beams are split in half, with each half (black and gray) equipped with different pulse shape. (c) Omega beam rings at 21° and from 42° to 59° provide simultaneous, multiple ring, NIF-like geometry.

Downloaded 20 Mar 2011 to 69.181.48.121. Redistribution subject to AIP license or copyright; see http://pop.aip.org/about/rights_and_permissions

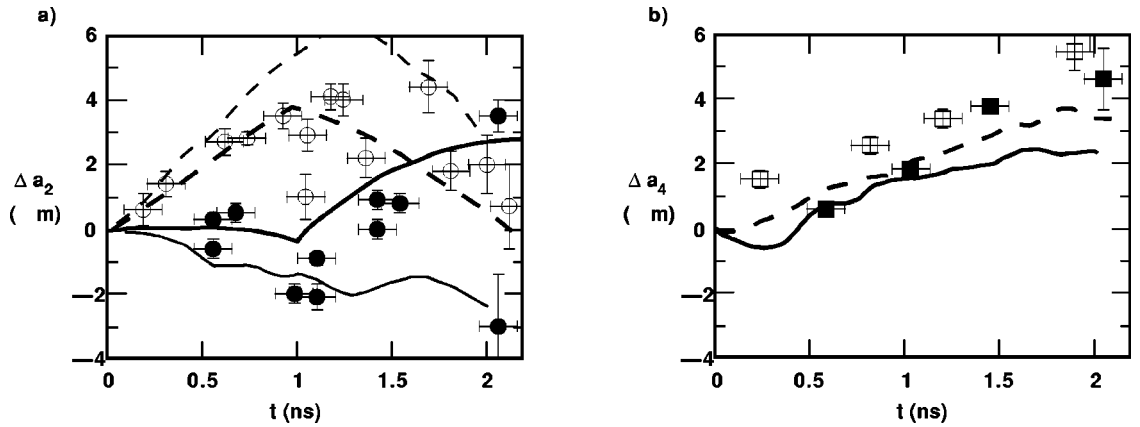

FIG. 5-30. Results from Omega symmetry experiments with staggered beams. (a) Foam ball second-order Legendre distortions for reduced (filled circles) and enhanced (open circles) P_2 asymmetry swings. (b) Foam ball fourth-order Legendre distortions for reduced (filled squares) and enhanced (open squares) P_2 asymmetry swings. Solid and dashed, bold curves are simulation predictions for reduced and enhanced swing cases. Thin curves are simplified analytic model predictions.

thus creating two rings of illumination with a time-varying power ratio, but with limited adjustability in ring separation, as indicated in Fig. 5-29(b) (Ehrlich *et al.*, 1997). The ratio of inner to outer half-ring power is increased in time to compensate for the hohlraum wall inward motion. The measured second order Legendre foam ball distortions are plotted in Fig. 5-31 for cases with and without different pulse shapes on each half-ring. To enhance the effects of the asymmetry swing in the absence of beam phasing, an inner pointing has been deliberately chosen that does not yield a round image at the end of the drive. While both illumination geometries yield the same final distortion as designed, Fig. 5-31 clearly shows a smaller swing in distortion for the foam ball experiencing beam-phased drive. A comparison of the inferred P_2 asymmetry with and without beam phasing shows a $3\times$ reduction in the P_2 asymmetry swing to levels below 5%/ns.

For the most recent Omega experiments, a NIF-like multiple ring illumination with adjustable ring separation was exercised as indicated in Fig. 5-29(c). Since the presence of two rings pointed far from the P_2 node position naturally reduces the P_2 symmetry swing, no beam phasing was required; beam phasing is currently a requirement for NIF ignition because the ratio of pulse length to hohlraum scale is greater, leading to greater relative wall motion. The measured and code-predicted second and fourth order Legendre foam ball distortions are plotted in Figs. 5-32(a) and 5-32(b). The improvement in P_4 control by using simultaneous multiple rings rather than single ring illumination is evident by comparing Figs. 5-30(b) and 5-32(b). Differentiating the a_n data following Eq. (5-17), we infer $<5\%$ P_2 and P_4 pressure asymmetries over any 1 ns interval, below the maximum level tolerable for ignition on NIF. In addition, Fig. 5-32 shows that the final a_2 and a_4 are zero within the ± 1 μm measurement accuracy, implying the average P_2 and P_4 asymmetry has been limited to 2%. This is to be compared with the larger 20%/ns P_2 swings shown in Fig. 5-28 and 4% average P_4 for traditional unphased and unstaggered, single-ring illumination.

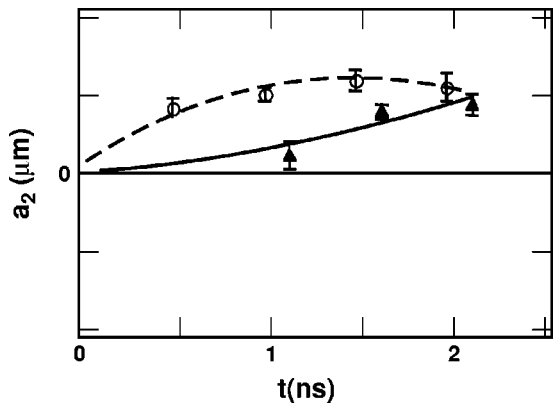

FIG. 5-31. Results from Nova split-ring symmetry experiments. Foam ball second P_2 order Legendre distortions for phased (triangles) and unphased (open circles) drive. Curves are fits to the data.

D. Summary of hohlraum radiation uniformity and future work

There is quantitative agreement between data, analytic models and code simulations of time-averaged and time-dependent low-order flux asymmetries in cylindrical hohlraums. This includes measurement and calculation of the laser spot motion. The agreement now extends from vacuum to gas-filled and to multiple-ring hohlraums. Current symmetry diagnostic techniques developed at Nova meet the accuracy requirements for assessing and controlling low-mode asymmetries in NIF-scale ignition hohlraums.

Symmetry experiments on Nova have been a good test of many of the features that will affect symmetry on the NIF:

- The minimum case-to-capsule ratio (ratio of hohlraum radius to initial capsule radius) is comparable on Nova (2.8) and the NIF (2.5). As described in Figs. 5-1 and 5-2, this ratio determines the geometric smoothing of source flux nonuniformities in a hohlraum. It also determines the coupling efficiency of x rays to the capsule.
- The LEH effect on the flux uniformity at the capsule is comparable on Nova experiments and the NIF hohlraum. The P_2/P_0 at the capsule, due to the LEH, is about 10%

Downloaded 20 Mar 2011 to 69.181.48.121. Redistribution subject to AIP license or copyright; see http://pop.aip.org/about/rights_and_permissions

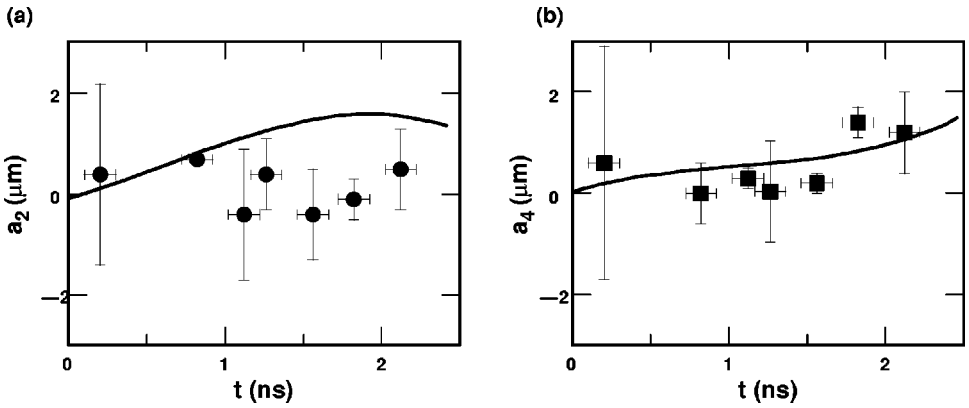

FIG. 5-32. Foam ball distortions from Omega multiple ring illumination in cylindrical hohlraums driven by PS26. (a) Foam ball second-order and (b) fourth-order Legendre distortions. Curves are code simulations of expected distortions.

for the NIF design. Depending on the size of the LEH, this effect ranges from 10 to 20% for the Nova experiments.

- The angular change in the location of the source emission due to wall blowoff, which determines the magnitude of flux asymmetry due to spot motion, is about 10 to 15° on both Nova experiments with the 2.2 ns PS22 pulse and for the gas-filled NIF ignition hohlraum.
- Refraction effects for both the Nova experiments and the NIF hohlraum are generally fairly small. The refraction angle is given approximately by (Born and Wolf, 1975)

$$\frac{d\theta}{dx_s}=\frac{d}{dx_p}\sqrt{1-\frac{n}{n_c}}\Rightarrow\Delta\theta\approx\frac{1}{2}\frac{n}{n_c}\frac{L_s}{L_p}, \tag{5-27}$$

where $x_s(L_s)$ is distance (scale length) along the beam path, and $x_p(L_p)$ is distance (scale length) perpendicular to the beam path. Because $n/n_c\approx 0.1$ and electron conduction results in $L_s\approx L_p$, refraction is limited to a few degrees.

- Implosion symmetry reproducibility for Precision Nova, as shown in Fig. 5-16, meets the 1% uniformity requirements for ignition experiment time-averaged flux. Time-dependent control of low-order asymmetries has been accomplished to the levels required for NIF ignition.

Ongoing work includes validating current extrapolations of measurement accuracy by performing, for the foot of the pulse, NIF-scale hohlraum symmetry experiments at Omega (Landen *et al.*, 2000). These experiments also test out new, more efficient backlighting techniques (Landen *et al.*, 2001) for imaging NIF-scale foam balls and shells. We are also in the process of demonstrating the feasibility of detecting higher-order modes (Pollaine *et al.*, 2001) such as P_6 and P_8 to the required 0.5 to 1% level. In addition, any issues that arise from simulations concerning the applicability of the foam ball technique in a gas-filled hohlraum environment will be addressed at Omega Laser Facility.

VI. PLANAR AND CONVERGENT RAYLEIGH–TAYLOR INSTABILITY

A. Introduction

The indirect-drive ignition targets for NIF have been designed to operate in the weakly nonlinear regime of Rayleigh–Taylor (Rayleigh, 1899; Taylor, 1950; Chandrasekhar, 1961) and Richtmyer–Meshkov (Richtmyer, 1960; Meshkov, 1969) growth. At the laser energy that will be available and at the drive temperatures and implosion pressures that we expect to achieve, operation in this regime is necessary to successfully prevent shell breakup during the implosion and subsequent compression of the fuel. The hydrodynamic instability program was designed to study the ablation stabilization that is responsible for reduced growth rates. The program also carried out experiments designed to look at the transition between linear and nonlinear growth and at the difference between 2D and 3D saturation. This work is reviewed below. There has also been a large body of recent work (Read, 1984; Youngs, 1984; Freed *et al.*, 1991; Alon *et al.*, 1994; Hecht *et al.*, 1994; Alon *et al.*, 1995; Shvarts *et al.*, 1995; Ofer *et al.*, 1996; Oron *et al.*, 1998; Dimonte and Schneider, 2000; Cook and Dimotakis, 2001; Oron *et al.*, 2001) exploring the transition and evolution of Rayleigh–Taylor and Richtmyer–Meshkow instabilities into the fully turbulent regime. Although of great interest to many situations in high energy density physics, this work is of less relevance to the indirect-drive ignition goal and is not reviewed here.

B. Implosion dynamics

As discussed below, the hydrodynamic instability effects in ICF implosions are strongly connected to the implosion pressure or radiation temperature that can be generated on laboratory facilities, and to the implosion velocity that is required for ignition. The relations between implosion pressure and implosion velocity determine the shell aspect ratio, the ratio of the shell radius to its thickness, which is directly related to instability growth as discussed in Sec. VI C.

The implosion of an ICF capsule can be described by a rocket equation. In an ablation-driven rocket, the exhaust, which is the target corona, is continually heated so that it remains nearly isothermal as it expands, instead of having no internal energy as assumed for the ideal rocket. The implosion velocity $V_{\rm imp}$ can be written

$$V_{\rm imp}=\frac{P}{\dot{m}}\ln\frac{m_0}{m}\equiv V_{\rm ex}\ln\frac{m_0}{m}, \tag{6-1}$$

where P is the ablation pressure, $\dot{m}$ the mass ablation rate, m_0 the initial mass, and m the final mass.

Downloaded 20 Mar 2011 to 69.181.48.121. Redistribution subject to AIP license or copyright; see http://pop.aip.org/about/rights_and_permissions

For indirect-drive (Hatchett and Rosen, 1982; Rosen and Lindl, 1983; NTIS Document, 1991b), we have, approximately,

$$P(\text{Mbar})_{\text{ID}} = 3T_r^{3.5} = 170I_{15}^{7/8}, \tag{6-2}$$

$$\dot{m}(\text{g/cm}^2/\text{s})_{\text{ID}} = 3\times 10^5 T_r^3 = 10^7 I_{15}^{3/4}. \tag{6-3}$$

From these two equations, we then have

$$V_{\text{imp}}(\text{cm/s})_{\text{ID}} = 10^7\sqrt{T_r}\ln\frac{m_0}{m} = 1.8\times 10^7 I_{15}^{1/8}\ln\frac{m_0}{m}. \tag{6-4}$$

The ablation velocity—V_{abl}, the velocity with which the ablation front moves through the shell—is given by the mass ablation rate divided by the shell density,

$$V_{\text{abl}}(\text{cm/s})_{\text{ID}} = 2.35\times 10^5 \alpha^{3/5} T_r^{9/10} = 6.6\times 10^5 \alpha^{3/5} I_{15}^{9/40}. \tag{6-5}$$

We have used the relationship between pressure and density given by

$$P_{\text{DT}}(\text{Mbar}) = 2\alpha\rho^{5/3}(\text{g/cm}^3), \tag{6-6}$$

where α is the ratio of the pressure at a given density to the Fermi pressure P_F.

These equations, which are written both in terms of the radiation temperatures T_r (in hundreds of eV, or heV) and an equivalent intensity in units of 10^{15} W/cm^2, are reasonable approximations for capsules for which the capsule ablator albedo (the ratio of the re-emitted x-ray flux to the incident flux) is near zero. Because it is usually possible to choose a low-Z ablator that has sufficiently high opacity in its cold state to absorb the incident radiation but still have low opacity in the heated blowoff region, this approximation is reasonable for much of the capsule implosion history. This approximation is valid longer for a sphere with diverging flow than for a planar sample. When the albedo of the capsule blowoff starts becoming significant, Eqs. (6-2) through (6-5) become time dependent.

Subsonic ablation implosion experiments on Nova, which are described by Eqs. (6-2) through (6-5), have been very successful in the 200 to 300 eV radiation-temperature regime predicted to be required for laboratory capsules that would ignite and burn when driven by 1 to 10 MJ lasers.

The shell in-flight aspect ratio (IFAR), the ratio of the shell radius R to its thickness ΔR, can be related to V_{imp}, V_{abl}, and V_{ex} by integrating the rocket equation. The work W done on the imploding fuel by the pressure P generated from ablation is given by

$$W = \int_{\text{Vol}} P\, dV.$$

Most of the work is done while the shell is still at a large fraction of its initial radius. Shell velocities typically approach their peak values by the time the shell reaches half its initial radius. By the time the shell has moved this far, the volume inside the shell has been reduced by almost an order of magnitude, and little more $P\,dV$ work can be done on the shell.

If we assume that the shell is accelerated over half its radius, we have (Lindl, 1998d)

$$\int_0^{t_1} v\, dt = \frac{1}{2}R = \int_0^{t_1} V_{\text{ex}}\ln\frac{m_0}{m}dt, \tag{6-7}$$

where

$$\ln\frac{m_1}{m_0} = \ln\left(1-\frac{V_{\text{abl}}t_1}{\Delta R}\right) = \frac{V_{\text{imp}}}{V_{\text{ex}}},$$

$$\Rightarrow \frac{R}{\Delta R} = 2\frac{V_{\text{ex}}}{V_{\text{abl}}} f_1\left(\frac{V_{\text{imp}}}{V_{\text{ex}}}\right), \tag{6-8}$$

where $f_1(x) = [1-(1+x)\exp(-x)]$.

In numerical simulations, $R/\Delta R$ varies in time. The maximum in $R/\Delta R$ typically occurs just as the compressed shell begins to accelerate. This maximum is not a representative value for $R/\Delta R$, because the shell has not moved very far, and the density has not relaxed to a more steady-state distribution. For most high-gain targets, a more representative value of $R/\Delta R$, for use in comparison with the analysis presented here, is the value at a time when the shell has moved about 1/4 of the initial radius. At this time, the shell has moved about 1/2 of the total acceleration distance and has experienced $1/\sqrt{2}$ of the total number of e-foldings of growth for constant acceleration.

For implosions in which most of the mass is ablated, or in other words, if the implosion velocity is greater than the rocket exhaust velocity V_{ex}, then f_1 is approximately linear in x. Because typical implosion velocities range from 2 to 4×10^7 cm/s, this case generally applies to radiation drive, as seen from Eq. (6-4), for radiation temperatures of a few hundred electron volts. With this approximation, $(R/\Delta R)_{\text{ID}}$ (or in-flight aspect ratio) for indirect-drive is given by

$$\left(\frac{R}{\Delta R}\right)_{\text{ID}} \approx 0.56\frac{V_{\text{imp}}}{V_{\text{abl}}} \quad \text{for } 4 > \frac{V_{\text{imp}}}{V_{\text{ex}}} > 0.8. \tag{6-9}$$

Equation (6-9) was obtained by assuming an ice block model for the shell density (constant density across the entire shell thickness). In an actual ICF capsule, pressure and density gradients are necessary for the shell to have a uniform acceleration. Within the accelerating shell, we have

$$\rho a = \nabla P = \frac{dP}{dr}. \tag{6-10}$$

If the material across the shell has constant entropy, we can use Eq. (6-6) to obtain

$$\frac{d}{dr}\rho^{2/3} = \text{constant}. \tag{6-11}$$

With the boundary conditions $\rho = \rho_0$ at $r = 0$ and $\int \rho\, dr = \rho_0 \Delta R$, we obtain

$$\frac{\rho}{\rho_0} = \left(1-\frac{2}{5}\frac{r}{\Delta R}\right)^{2/3}, \tag{6-12}$$

where ρ_0 is the peak density in the shell. The shell thickness is usually defined as the distance between densities that are $1/e$ times the peak density. From Eq. (6-12) this is about $1.2\times$ that of the ice block model.

From Eqs. (6-6) and (6-9), the achievable implosion velocity for radiation-driven capsules at fixed $R/\Delta R$ will be

Downloaded 20 Mar 2011 to 69.181.48.121. Redistribution subject to AIP license or copyright; see http://pop.aip.org/about/rights_and_permissions

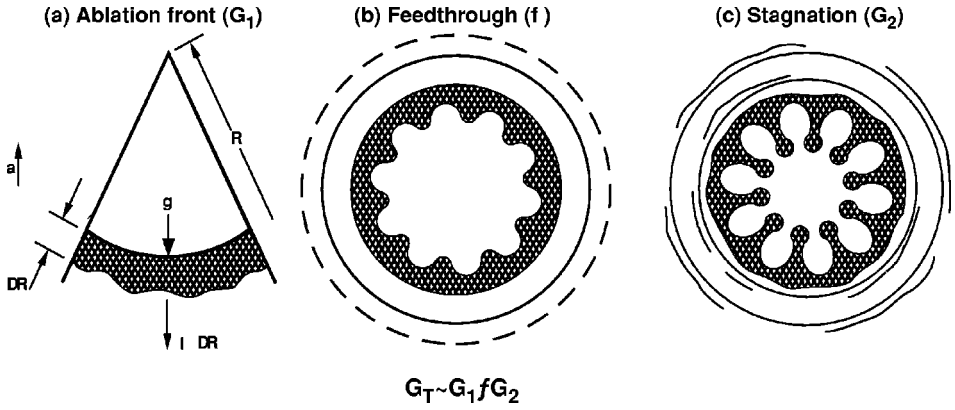

FIG. 6-1. Schematic showing how RT perturbation growth affects an implosion. The designations G_T, G_1, f, and G_2 correspond to the total growth factor, growth factor at the outer surface during acceleration, feedthrough to the inner surface, and growth factor at the inner surface during deceleration.

linearly proportional to the ablation velocity or nearly linearly proportional to the radiation temperature:

$$(V_{\mathrm{imp}})_{\mathrm{ID}} \approx \frac{R/\Delta R}{0.56} V_{\mathrm{abl}} = 5.1\times 10^5 \alpha^{3/5} \frac{R}{\Delta R} T_R^{0.9}$$

$$= 1.4\times 10^6 \alpha^{3/5} \frac{R}{\Delta R} I_{15}^{9/40}. \qquad (6\text{-}13)$$

Because the minimum energy for ignition depends strongly on the achievable implosion velocity (Levedahl and Lindl, 1997; Basko and Johner, 1998; Herrmann *et al.*, 2001), the ignition threshold is set by the achievable values of hohlraum temperature and $R/\Delta R$.

In general, the plasma physics constraints discussed in Sec. III limit the peak radiation temperature and the RT hydrodynamic instability sets an upper limit to the value of the shell $R/\Delta R$.

C. Hydrodynamic instability theory in indirect-drive ICF implosions

The RT (Rayleigh, 1899; Taylor, 1950; Chandrasekhar, 1961) instability and its shock-driven analog, the Richtmyer–Meshkov (RM) instability (Richtmyer, 1960; Meshkov, 1969) have been a focus of research in ICF capsule physics. In smoothly accelerated shells, the RT instability is the dominant source of perturbation growth and the focus of the work discussed below. In some capsules which are more impulsively driven (Lindl and Mead, 1975; Haan, 1989; Tabak, 1989), the RM instability can be a significant contributor to the growth. The ablation front is RT unstable, and outer surface imperfections grow during the shell implosion. This growth can seed perturbations in the capsule interior that in turn grow by the RT instability during the deceleration and stagnation phase, and because of convergence effects (Bell, 1951; Plesset, 1955). The total growth at the hot spot–main fuel interface, as illustrated in Fig. 6-1, can be approximated as $G_T = G_1 \cdot f \cdot G_2$, where the total growth factor (G_T) has been decomposed into growth at the ablation front or outer surface (G_1), fractional feed through (f) to the inner hot spot/cold fuel boundary or to the pusher–fuel interface in capsules without a cryogenic fuel layer, and growth at the hot spot boundary during deceleration (G_2).

Simplified analytical models provide some insight into the evolution of hydrodynamic instabilities in ICF capsules. A widely used formula for the growth of RT perturbations at the ablation front is given by

$$\gamma = \sqrt{\frac{ka}{1+kL}} - \tilde{\beta} k V_a. \qquad (6\text{-}14)$$

In this equation, k is the mode wave number, a is the acceleration, L is the density-gradient scale length in the ablation front, and $\tilde{\beta}$ is a constant between 1 and 3. Since the RT modes are localized near the ablation front, the advection of perturbed material away from the front by ablation was recognized as a stabilization effect early in the ICF program (Bodner, 1974; Lindl and Mead, 1975). The RT instability is a surface mode with a depth $1/k$, so density gradients have the effect of reducing the density contrast at the ablation front and this reduces the growth (Munro, 1988; NTIS Document).

Equation (6-14) with $\tilde{\beta} \approx 1$ was first obtained in 1983 from numerical simulations for radiation-driven implosions (Lindl, 1983). Equation (6-14) also compared quite well to numerical simulations of direct-drive (Tabak *et al.*, 1990) with $\tilde{\beta} \sim 3$.

Although $\tilde{\beta}$ is smaller for radiation drive than for direct-drive, ablation velocities at a typical intensity of 10^{15} W/cm^2 are about a factor of 10 larger for radiation drive (Lindl, 1998d) so that the stabilizing effects of ablation are larger for radiation drive. The higher ablation rates also result in thicker shells and larger density scale lengths L for radiation-driven capsules. Thicker shells have less feedthrough from outer surface growth to the inner surface. In optimized capsules, ablation and density scalelength are about equally important stabilizing effects.

For direct-drive, Eq. (6-14) is a generalization of the Takabe formula obtained by Takabe (Takabe *et al.*, 1985) for a DT target, which has very small density gradients,

$$\gamma = 0.9\sqrt{ka} - \tilde{\beta} k V_a, \qquad (6\text{-}15)$$

where $\tilde{\beta}$ varies in numerical simulations but is usually 3 to 4. Ablation of DT by thermal conduction results in very steep density gradients at the ablation front so Eq. (6-15) differs little from Eq. (6-16) in this case.

Downloaded 20 Mar 2011 to 69.181.48.121. Redistribution subject to AIP license or copyright; see http://pop.aip.org/about/rights_and_permissions

Equation (6-15) is similar to a form obtained by Bodner (Bodner, 1974) from an analytical model of ablation with a density discontinuity at the ablation front and other authors observed stabilization in simulations of ICF implosions early in the ICF program (Henderson *et al.*, 1974; Fraley *et al.*, 1975).

Recently, Betti *et al.* (Betti *et al.*, 1996; Goncharov *et al.*, 1996; Betti *et al.*, 1998) have developed a model for RT instability in the presence of ablation that obtains the density and velocity equilibrium profiles self-consistently from a model of thermal conduction. The model of Betti *et al.* solves the mass, and momentum equations in the frame of the ablation front

$$\frac{\partial \rho}{\partial t} + \nabla \cdot (\rho \mathbf{V}) = 0, \tag{6-16}$$

$$\rho\left(\frac{\partial \mathbf{V}}{\partial t} + \mathbf{V} \cdot \nabla \mathbf{V}\right) = -\nabla P + \rho \mathbf{g}. \tag{6-17}$$

The energy equation is given by

$$\rho T \frac{dS}{dt} + \nabla \cdot \mathbf{Q} = 0, \tag{6-18}$$

where

$$\frac{d}{dt} = \frac{\partial}{\partial t} + \mathbf{V} \cdot \nabla.$$

S is the entropy and Q is the heat flow. Following Kull and Anisimov (Kull and Anisimov, 1986), the energy equation can be written as

$$\nabla \cdot \left(\frac{\gamma}{\gamma - 1} P\mathbf{V} - \kappa \nabla T\right) = -\left(\frac{1}{\gamma - 1}\frac{\partial P}{\partial t}\right) + \mathbf{V} \cdot \nabla P \approx 0, \tag{6-19}$$

where $\mathbf{Q} = -\kappa \nabla T$ has been used and

$$T\frac{dS}{dt} = \frac{dW}{dt} - \frac{1}{\rho}\frac{dP}{dt}$$

is used to relate entropy, pressure and specific internal energy $W = C_P T$. Here C_P is the specific heat at constant pressure. The coefficient of thermal conductivity is given by $\kappa = \kappa_a (T/T_a)^v$ where κ_a is the thermal conductivity at the ablation front temperature T_a. The right-hand side of Eq. (6-19) can usually be ignored in subsonic ablation fronts of interest to ICF (Kull and Anisimov, 1986).

Using conservation of mass,

$$U = |V| = \rho_a V_a / \rho = V_a / \xi \tag{6-20}$$

and assuming that the pressure is slowly varying compared to variations in the density and temperature so that we can relate temperature variations to density variations, Eq. (6-19) is used to obtain an equation for the density variation,

$$\frac{d}{dy}\left[\frac{1}{\xi}\left(-1 + \frac{K_a}{C_P \rho_a V_a}\frac{1}{\xi^{v+1}}\frac{d\xi}{dy}\right)\right] = \frac{d}{dy}\left[\frac{1}{\xi}\left(-1 + L_0 \frac{1}{\xi^{v+1}}\frac{d\xi}{dy}\right)\right] = 0 \tag{6-21}$$

or

$$\frac{d\xi}{dy} = \frac{1}{L_0}\xi^{v+1}(1 - \xi). \tag{6-22}$$

L_0 is the effective scale height of the energy deposition layer in the ablation front obtained from setting the heat flux from conduction approximately equal to the internal energy flux,

$$-\kappa \nabla T \equiv \frac{\kappa_a T_a}{L_0} \approx C_P \rho_a T_a V_a. \tag{6-23}$$

Equation (6-21) shows that the density profile is determined by the two parameters L_0 and v. L_0 is related to the minimum of the density (or temperature) gradient scale by the relationship (Kull and Anisimov, 1986):

$$L_\rho = \min\left[\rho \Big/ \frac{d\rho}{dy}\right] = L_0 (v+1)^{v+1}/v^v. \tag{6-24}$$

For $v \to 0$, $L_\rho \approx L_0$ while for $v > 0$, $L_\rho > L_0$. For example, for $v = 2.5$, $L_\rho \approx 8L_0$. This occurs because for heat conduction that is a strong function of temperature, the energy deposition that drives the ablation actually occurs in a region that is much narrower than the temperature (or density) scale length. When the coefficient of heat conduction is a constant $(v = 0)$, the thickness of the heat deposition layer is the same as the temperature scalelength. The energy transport equation used in this model is a simple conduction model with a heat transport coefficient that has a power law dependence on temperature. In an ICF capsule, the energy transport can be quite complex. It is a combination of electron conduction and radiation transport, which frequently cannot be described by a simple power law in temperature. However, since the Rayleigh–Taylor instability is mainly a hydrodynamic instability process, depending on density, pressure, and velocity profiles, it turns out to be possible to describe most situations of interest by using a power law conduction equation as long as the value of v and L_0 used are those obtained from detailed 1D simulations which include the more accurate transport models.

Using Eqs. (6-20) and (6-22), the equilibrium momentum Eq. (6-17), can be written

$$\frac{dP}{dy} = -\rho g\left[1 - \frac{U}{g}\frac{dU}{dy}\right] = -\rho g\left[1 - \xi^{v-2}(1-\xi)\frac{V_a^2}{L_0 g}\right] = -\rho g[1 - \xi^{v-2}(1-\xi)\mathrm{Fr}]. \tag{6-25}$$

The Froude number $\mathrm{Fr} = V_a^2/gL_0$ plays a central role in the instability because it determines the location of the pressure peak relative to the density peak. For $\mathrm{Fr} \gg 1$, the pressure peak is very near the density peak while for $\mathrm{Fr} \ll 1$, the pressure peak is in the blowoff region well away from the density peak.

The linearized conservation equations for mass momentum and energy can be combined into a fifth-order differential equation. Using a boundary layer analysis for modes with $\varepsilon \ll 1$ and a WKB approximation for $\varepsilon \gg 1$ where $\varepsilon = kL_0$ and k is the mode number, it is possible to find approximate solutions for $\mathrm{Fr} \gg 1$ and $\mathrm{Fr} \ll 1$ and for $\varepsilon \ll 1$ and $\varepsilon \gg 1$ and an asymptotic dispersion relation which covers the

Downloaded 20 Mar 2011 to 69.181.48.121. Redistribution subject to AIP license or copyright; see http://pop.aip.org/about/rights_and_permissions

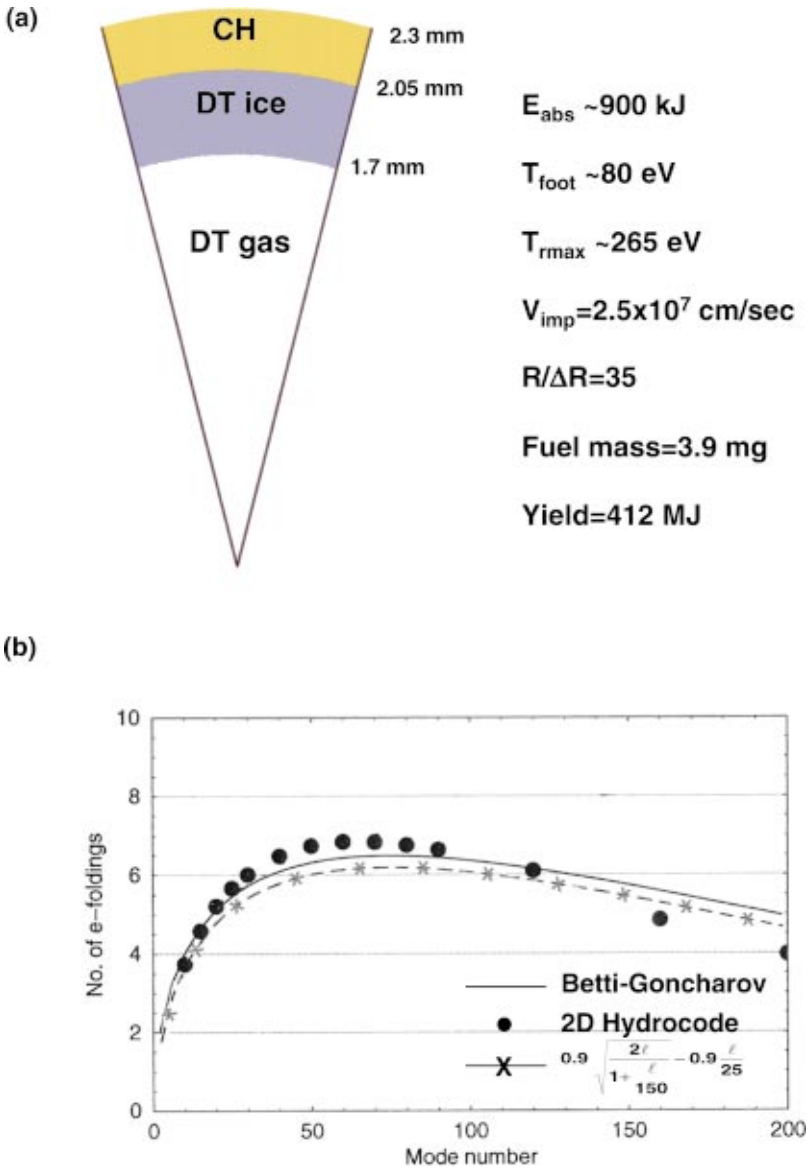

FIG. 6-2. (Color) (a) 1 MJ plastic ablator capsule used for the 2D instability study. It is a good test of the Betti–Goncharov (BG) model for indirect-drive because the density discontinuity at the ablator/DT fuel interface is small until late time so most of the growth is at the ablation front in the CH. (b) RT instability growth versus mode number. The dots are from 2D hydrodynamic instability calculations. The solid line is from the BG model with the analytic profiles fit to 1D hydrocode calculations at each time step. The dashed line is from an approximate integral of the BG model using average values of the density gradient, shell aspect ratio, and ablation rate.

full range of Fr, and ε has been obtained (Betti *et al.*, 1998). The analysis for all of this is quite complex and the asymptotic dispersion relation requires a half page of algebra. Fortunately, over a wide range of conditions of interest to ICF, the asymptotic dispersion relation has the same behavior as Eqs. (6-14) or (6-15) with coefficients that depend on Fr and v:

$$\lambda_1 = \alpha_1(\mathrm{Fr},v)\sqrt{kg} - \beta_1(\mathrm{Fr},v)kV_a\,, \tag{6-26}$$

$$\lambda_2 = \alpha_2(\mathrm{Fr},v)\sqrt{\frac{kg}{1+kL_\rho}} - \beta_2(\mathrm{Fr},v)kV_a\,. \tag{6-27}$$

Equation (6-26) works well for large Froude numbers while Eq. (6-27) works well for small Froude numbers (Betti *et al.*, 1998). The values of Fr and v are determined by fitting the analytic hydro-profiles given in Eqs. (6-22) and (6-25) with those obtained from 1D simulations including multigroup radiation transport. For a typical indirect-drive implosion, the Froude number varies significantly between the foot of the pulse and the peak of the pulse. During the foot Fr$>$1 and Eq. (6-26) would apply. However, during the peak of the pulse, when most of the growth occurs, Fr$<$1 and Eq. (6-27) applies. Figure 6-2(a) shows a plastic ablator capsule that is driven at 265 eV and absorbs about 0.9 MJ of energy. This capsule is being evaluated for inertial fusion energy applications and is slightly larger than the largest capsule that might be tested on NIF with the enhanced efficiency hohlraum discussed in Sec. II. During the peak of the pulse, Fr$\sim$0.4 and the effective $v\sim$1.5–2. These are typical parameters for indirect-drive. For this set of parameters, an approximate dispersion relation is given by (Betti *et al.*, 1998)

$$\gamma = 0.9\sqrt{\frac{kg}{1+kL_\rho}} - 1.4kV_a\,. \tag{6-28}$$

The growth factors predicted by the full Betti–Goncharov dispersion relation compare quite well with those obtained from 2D simulations (Herrmann *et al.*, 2001a; Tabak *et al.*) as shown in Fig. 6-2(b). In calculating the growth factors predicted by the Betti–Goncharov model, the appropriate

Downloaded 20 Mar 2011 to 69.181.48.121. Redistribution subject to AIP license or copyright; see http://pop.aip.org/about/rights_and_permissions

values of Fr, L_ρ, and v are determined by fitting the analytic hydro-profiles to a detailed 1D simulation at a continuous series of points and integrating the growth rates.

An approximate integral of Eq. (6-28), in which the number of e-foldings of RT growth depends only on the shell in-flight aspect ratio, can also be compared to the 2D calculations. This expression is given by

$$n=\int \gamma\, dt \approx 0.9\sqrt{\frac{2lx/R}{1+0.2l\dfrac{\Delta R}{R}}}-1.4l\frac{\Delta R}{R}(1-m/m_0)$$

$$\approx 0.9\sqrt{\frac{2.0l}{1+0.2l\dfrac{\Delta R}{R}}}-1.25l\frac{\Delta R}{R}, \qquad (6\text{-}29)$$

where $l=kR$ is the Legendre polynomial mode number. $L_\rho = 0.25\Delta R$ is the average density gradient at the ablation front. For indirect-drive, values for L_ρ typically range from 0.1 to $0.5\Delta R$, depending on the ablator material and the x-ray drive spectrum. $L_\rho \approx 0.5\Delta R$ is the largest gradient scale length consistent with maintaining a given peak shell density and fuel adiabat. The value for $R/\Delta R$ in Eq. (6-29) is an average value during the implosion. A value near 3/4 the initial radius is representative and we use $R/\Delta R=35$ for the capsule in Fig. 6-2(a). The effect of convergence has been ignored in the integral. For constant acceleration, the number of e-foldings increases in the first term in Eq. (6-29) because of the decrease in wavelength with convergence but the stabilization from the second term also increases with convergence. Within the accuracy of this model, these effects nearly cancel. In doing the integral, a constant acceleration over a distance d equal to the initial radius R is assumed. Peak velocity in a typical implosion occurs after a distance of about 2/3 of the initial radius. Using a larger distance in this planar approximation compensates for the spherical convergence.

Because of the relatively low exhaust velocity, most of the shell mass is ablated in indirect-drive implosions to achieve the required implosion velocity. Hence, we take $(1-m/m_0)\approx 0.9$ in the integral.

With these parameter, Eq. (6-29) gives a number of e-foldings very close to the 2D calculations or the full Betti–Goncharov calculation as seen in Fig. 6-2(b).

Figure 6-3 is a plot of e-foldings vs l-number predicted by Eq. (6-29) for a variety of values for $R/\Delta R$. If we limit the maximum number of e-foldings during acceleration to about six, then we are limited to $R/\Delta R \approx 35$.

Instabilities during the deceleration phase also must be controlled. For the case of greatest interest in high-gain ICF targets, the instability during deceleration occurs between the DT hot spot, at high temperature and relatively low density, and the DT main fuel. Electron conduction provides some ablation stabilization as the hot/cold boundary moves into the cold fuel during compression, and stabilization also occurs because electron conduction establishes a density gradient between the hot and cold material. The same analysis done at the ablation surface of the shell during acceleration can be applied during the deceleration (Lobatchev and Betti, 2000) and Eq. (6-28) also works well here. The density gradient is typically $0.02-0.04r_h$, where r_h is the final compressed radius. Without deceleration, the hot/cold interface would arrive at the origin at about ignition time or slightly later depending on the pulse shaping of the implosion, so the effective deceleration distance is about equal to $\sim 0.5-1.0r_h$. For NIF capsules, most of the mass in the hot spot comes from ablation of the cold material in the imploding shell during compression. Since the cold shell density is about 10 times the density of the hot spot, we can estimate the depth of material ablated during deceleration Δr_{cold} as $(4\pi/3)\,\rho_{\text{hot}} r_h^3 \approx 4\pi r^2 \Delta r_{\text{cold}}$ or $\Delta r_{\text{cold}}/r_h \sim \rho_h/3\rho_c \sim 1/30$.

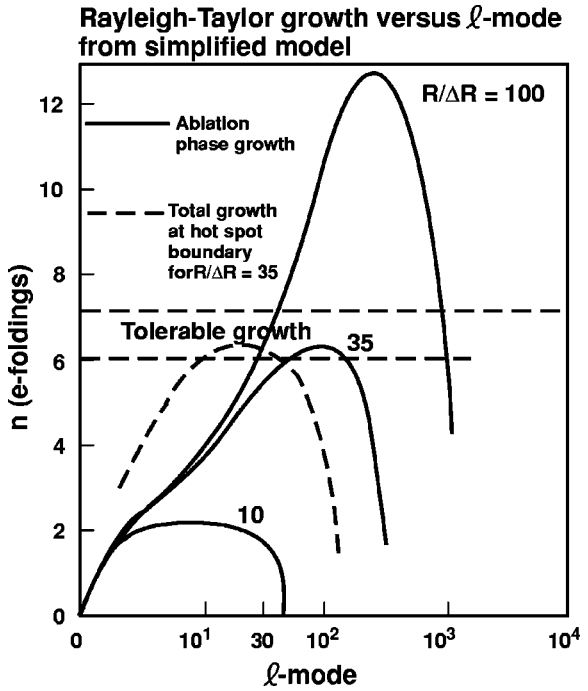

FIG. 6-3. The ratio of capsule radius to shell thickness, the capsule aspect ratio, largely determines hydrodynamic instability growth. Simple analytic models can be used to estimate the amplification of perturbations as a function of mode number.

The approximate integral of Eq. (6-28) during acceleration, using $L_\rho \sim 0.02r_h$ is then given by

$$n_{\text{decel}} \sim 0.9\sqrt{\frac{\ell}{1+0.02\ell}}-1.4\ell/30. \qquad (6\text{-}30)$$

Growth during deceleration typically is limited to about three e-foldings as seen from Eq. (6-30).

The source of perturbation at the hot/cold interface can be either initial perturbations on the inside of the shell or perturbations that feedthrough from the outside of the shell. The RT modes are surface modes that decrease away from the surface approximately as

$$\eta=\eta_0 e^{-k\Delta R}=\eta_0 e^{-l\Delta R/R}. \qquad (6\text{-}31)$$

Hence, the number of e-foldings on the inner surface due to feedthrough is reduced from the number on the outer surface by

$$n_{\text{feedthrough}}=-l\frac{\Delta R}{R}. \qquad (6\text{-}32)$$

Downloaded 20 Mar 2011 to 69.181.48.121. Redistribution subject to AIP license or copyright; see http://pop.aip.org/about/rights_and_permissions

Because feedthrough decreases exponentially with l, it will be dominated by lower order modes.

In this simple model, the combined effects of acceleration, feedthrough, and deceleration result in a total number of e-foldings of amplification of perturbations given by

$$n_{\text{accel}}+n_{\text{feedthrough}}+n_{\text{decel}} \approx 0.9\sqrt{\frac{2l}{1+0.25l\frac{\Delta R}{R}}}-2.25l\frac{\Delta R}{R} +0.9\sqrt{\frac{l}{1+0.02l}}-0.05l. \quad (6\text{-}33)$$

When the effects of growth during acceleration, feedthrough, and deceleration are combined with the fact that the spectral distribution of perturbations for typical capsules falls off as l increases, the principal modes that contribute to perturbations in the fuel are spherical harmonic mode numbers less than about 30 or 40. For $R/\Delta R=35$, the number of e-foldings predicted by Eq. (6-33) is plotted in Fig. 6-3.

Equation (6-33) applies to the amplification of perturbations that grow initially on the outside of the shell during acceleration. Perturbations initially present on the inside also must be taken into account. The growth of these perturbations during deceleration is limited by Eq. (6-30). However, inside defects can feed out to the ablation surface on the outside of the shell after passage of the initial shock through the shell. This effect is a major contributor in determining the required cryogenic layer uniformity. Also, x-ray preheat can result in an ablator density that is less than the fuel density during acceleration of the shell. There is then an interior interface between the fuel and the ablator, which can also grow. This is a significant effect for some of the NIF capsules, especially the NIF PT shown in Fig. 6-4(a) (see also Fig. 2-3). Figure 6-4(b) shows the growth of perturbations at both the ablation front in the plastic ablator and at the DT fuel/ablator interface (Perkins and Herrmann, 2002). The Betti–Goncharov model does a good job of predicting the growth at the ablation front. However, late in time the Atwood number at the fuel-ablator interface approaches unity. This results in substantial additional late time growth, which is particularly important for the shorter wavelength modes. Growth at this interface is seeded by feedthrough from the ablation front and is not included in the Getti–Goncharov models. This short wavelength growth contributes substantially to the sensitivity of the PT to ablator roughness as discussed in Sec II. To reduce this effect, the PT capsule is currently being re-optimized with a thicker ablator and/or thicker fuel and possibly a graded ablator preheat dopant to concentrate more preheat shielding near the ablator-fuel interface.

The above analysis considered only purely exponential growth of perturbations in which the mode amplitude is proportional to the initial amplitude. Beyond a certain amplitude, the perturbation enters the nonlinear regime. The shape of the perturbation changes from sinusoidal to broad thin bubbles and narrow thick spikes. This transition corresponds in Fourier space to the generation of higher harmonics

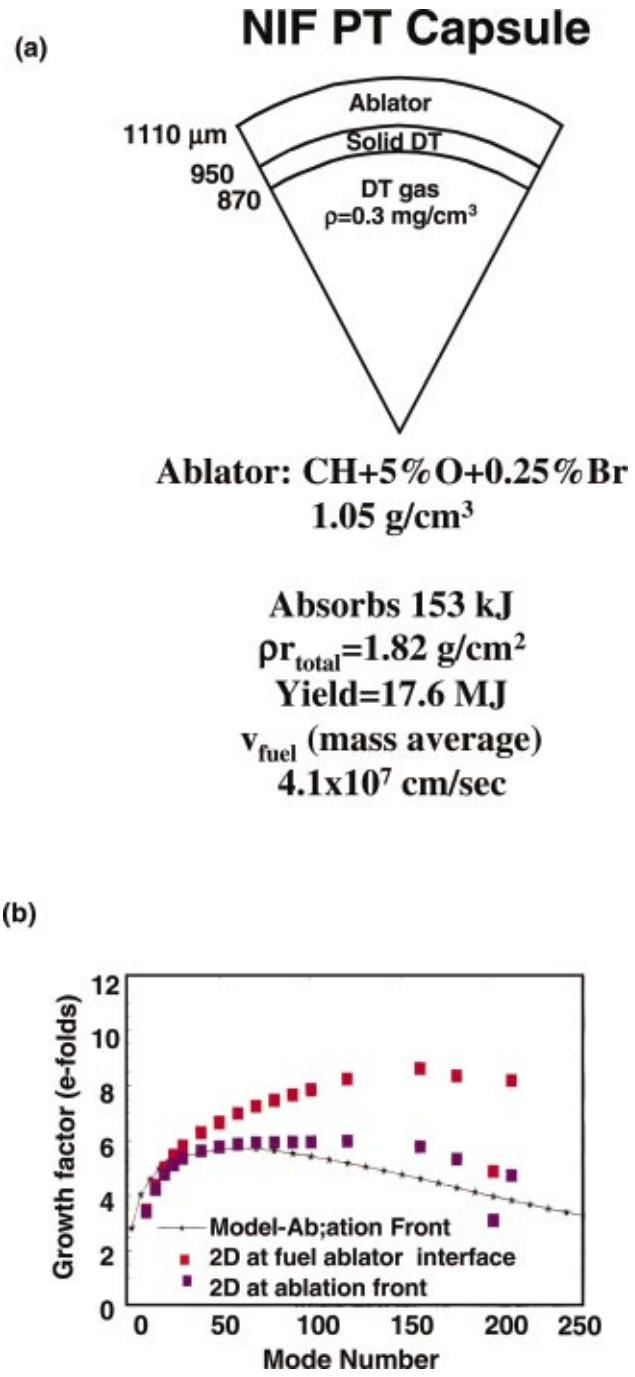

FIG. 6-4. (Color) (a) NIF PT capsule. (b) RT instability growth vs mode number. Solid squares are growth from the 2D hydrodynamic instability calculation at the ablation front in the CH. The solid line is the BG model. The open squares are growth at the CH/DT interface from the 2D calculations. The enhanced growth for the higher modes is due to a density discontinuity at the CH/DT interface caused by x-ray preheat in the CH.

(McCrory *et al.*, 1981). Within the framework of third-order perturbation theory (Jacobs and Catton, 1988; Jacobs and Catton, 1988a), the amplitudes of the perturbation fundamental mode (first harmonic) η_1 second harmonic η_2, and third harmonic η_3 can be written as

$$\eta_1 \approx \eta_L(1-\tfrac{1}{4}k^2\eta_L^2), \quad (6\text{-}34)$$

$$\eta_2 \approx \tfrac{1}{2}k\eta_L^2, \quad (6\text{-}35)$$

Downloaded 20 Mar 2011 to 69.181.48.121. Redistribution subject to AIP license or copyright; see http://pop.aip.org/about/rights_and_permissions

$$\eta_3 \approx \tfrac{3}{8} k^2 \eta_L^3, \tag{6-36}$$

where η_L is the linear regime spatial amplitude. The wave numbers of the first three harmonics correspond to $k = 2\pi/\lambda$, $2k$, and $3k$. At third order, we see in Eq. (6-34) that the growth of the fundamental is decreased. In the asymptotic limit of the nonlinear regime, the bubble amplitude can be written as

$$\int \eta(t) \approx \int \sqrt{Fg\lambda}\, dt \tag{6-37}$$

which corresponds to a perturbation growing at its terminal bubble velocity (Davies and Taylor, 1950; Layzer, 1955; Baker *et al.*, 1980),

$$v_B = (Fg\lambda)^{1/2}, \tag{6-38}$$

where F is a dimensionless constant that depends only on the shape of the perturbation. As derived by Layzer, $(F)^{1/2} = 1/(6\pi)^{1/2} = 0.23$ in 2D and 0.36 in 3D for an axisymmetric bubble. If we define the transition into the nonlinear regime to occur when the growth in the fundamental mode is reduced by 10%, then from Eq. (6-34) we have $\eta_L/\lambda \approx 0.1$, which is the widely used threshold for nonlinearity given by Layzer.

When more than one mode is initially present, the modes become coupled in the nonlinear regime (Verdon *et al.*, 1982; Dahlburg and Gardner, 1990; Gamaly *et al.*, 1990; Haan, 1991; Ofer *et al.*, 1992), leading to the appearance of ''beat'' modes $k_i \pm k_j$. At second order, this can be written as

$$\eta_{k_i \pm k_j} \approx \mp \tfrac{1}{2} (k_i \pm k_j)\, \eta^L_{k_i} \eta^L_{k_j}. \tag{6-39}$$

This mode coupling causes a redistribution of a multimode perturbation to longer and shorter wavelengths and affects the saturation of individual modes.

Shocks and convergence effects modify the model given above. When the drive first turns on, an initial strong shock is launched through the foil during compression. The shock front will typically be deformed, bearing the imprint of any initial surface imperfections. This perturbed or rippled shock front is dynamically similar to the RM instability. As the shock travels through the foil, material behind the shock develops a lateral velocity component, initially moving material from regions where the foil was thinner (initial perturbation valley) towards regions where the foil was thicker (initial perturbation peak), causing the areal density modulation to increase. However, the shape of the shock front is not constant, but evolves with time (Munro, 1989; Endo *et al.*, 1995) and can cause the areal density modulation to decrease or even reverse phase if the foil is thick enough compared to the perturbation wavelength. After the shock breaks out the undriven side of the foil, a rarefaction also perturbed in space returns to the ablation front, and the compressed foil accelerates as a unit. During the ablative acceleration phase, convergence introduces a different threshold for nonlinear effects due to a decrease of perturbation wavelength (Haan, 1989a) and because of thin shell effects (McCrory *et al.*, 1981; Verdon *et al.*, 1982; Baker *et al.*, 1987). There can also be a change in perturbation amplitude due to the combination of convergence and compressibility (Hattori *et al.*, 1986). Feedthrough is decreased because the pusher shell thickens during convergence. Convergence effects are magnified during the deceleration phase because of the large fractional change in radius (Hattori *et al.*, 1986; Haan, 1989a; Sakagami and Nishihara, 1990; Sakagami and Nishihara, 1990a; Town and Bell, 1991). An accurate quantitative description of the growth of individual modes generally requires the use of numerical simulations.

The effect of a whole spectrum of modes, when all of the modes remain in the linear or only weakly nonlinear regime, can be calculated analytically by using the theory of Haan (Haan, 1989a). This is the case of greatest interest for high-gain ICF capsules. In this regime, the primary nonlinearity is a transition from exponential growth in time to linear growth in time for those modes that exceed an amplitude

$$S(k) = \frac{2}{k^2 \chi_L} \approx \left(1/2 \frac{\lambda}{\chi_L}\right)(0.1\lambda). \tag{6-40}$$

This criterion, which is valid in 3D when a full spectrum of modes is present, is a generalization of the single-mode criterion of Layzer (1955), which is given above. The factor $\lambda/2\chi_L$, compared to the single-mode saturation criterion, accounts for the number of similar modes about k that can contribute to the saturation of mode k, including a density-of-states factor with periodic boundary conditions of length χ_L. In amplitude or physical space, this correction occurs because a wave packet with small but finite spectral width cannot be distinguished over short distances from a single mode at k. We expect saturation to occur at roughly the same amplitude in both cases, or when the amplitude of each spectral component of the multimode case is given by the Haan criterion. Except for this transition to growth linear in time, all of the modes in a full spectrum of perturbations for most single-shell high-gain ICF capsules with realistic surface finishes can be treated as growing independently. The amplitude generated by a full spectrum of modes with random phases can then be calculated by taking an rms sum over all modes. The best estimates of these effects require the use of detailed numerical simulations to calculate the growth factors for a large number of individual modes.

For quantitative application to a spherical implosion, we define the spherical harmonic modes as

$$R_{lm}(t) = \int d\Omega\, Y^*_{lm}(\Omega) R(\Omega, t), \tag{6-41}$$

where $R(\Omega,t)$ is the radius at solid angle Ω and time t, and Y^*_{lm} is the complex conjugate of the l,m spherical harmonic. Initial surface characterization is used to determine $R_{lm}(0)$.

Numerical simulations of one mode at a time throughout the linear regime are used to define $R^{\mathrm{lin}}_{lm}(t)$, the amplitude to which mode l would have grown if the evolution were entirely linear. This quantity is directly proportional to $R_{lm}(0)$, with the proportionality factor determined from the simulation. These simulations capture all of the effects of the initial shock phase and spherical convergence effects on the mode growth. Sufficient simulations are run to interpolate to all

Downloaded 20 Mar 2011 to 69.181.48.121. Redistribution subject to AIP license or copyright; see http://pop.aip.org/about/rights_and_permissions

contributing modes. Given the set of quantities $R_{lm}^{\mathrm{lin}}(t)$, we determine whether the spectrum is nonlinear by comparing $R_{lm}^{\mathrm{lin}}(t)$ to

$$S(l)=2R/l^2, \tag{6-42}$$

where R is the mean radius. If any modes $R_{lm}^{\mathrm{lin}}(t)$ have amplitude larger than $S(l)$, they are replaced with an estimated nonlinear amplitude. That is,

$$R_{lm}(t)=\begin{cases} R_{lm}^{\mathrm{lin}}(t) & \text{if } R_{lm}^{\mathrm{lin}}(t)<S(l), \\ S(l)\{1+\ln[R_{lm}^{\mathrm{lin}}(t)/S(l)]\} & \text{if } R_{lm}^{\mathrm{lin}}(t)>S(l). \end{cases} \tag{6-43}$$

If $R_{lm}^{\mathrm{lin}}(t)$ grows exponentially, this construction gives growth linear in time at large amplitude, with the generalization of the bubble terminal velocity given in Eq. (6-25) appropriate for a full spectrum of modes. The mix amplitude at any time of interest is determined from the rms sum of the modes,

$$\sigma^2(t)=\frac{1}{4\pi}\sum_{l,m}|R_{lm}(t)|^2\approx\frac{R^2}{2\pi}\int_0^\infty k|R_{lm}|^2dk$$

$$=\frac{1}{4\pi}\int[R(\Omega)-R_0]^2\,d\Omega. \tag{6-44}$$

The bubble amplitude is taken to be $\sqrt{2}\sigma$, and the spike amplitude to be $(1+A)\sqrt{2}\sigma$, where A is the Atwood number (Youngs, 1984).

Haan has developed a second-order mode coupling theory (Haan, 1991) that can be used to determine when this approximation breaks down. As discussed below, this theory is in generally good agreement with experiments that impose multiple initial modes on samples and look at the growth of sum and difference modes. These results confirm that mode coupling is not important for most cases of interest in indirect-drive ICF.

D. Experimental configuration and measurement techniques

The dominant source for the total perturbation growth and subsequent mixing is the growth of outer surface perturbations during the acceleration phase. The perturbations in areal density can be precisely measured by radiography in planar geometry (Grun *et al.*, 1987; Kilkenny, 1990; Remington *et al.*, 1991; Glendinning *et al.*, 1992; Remington *et al.*, 1992; Dimonte and Remington, 1993; Hammel *et al.*, 1993; Remington *et al.*, 1993; Hammel *et al.*, 1994; Hammel *et al.*, 1994a; Remington *et al.*, 1994; Marinak *et al.*, 1995; Remington *et al.*, 1995; Marinak *et al.*, 1998) for both direct-drive and indirect-drive RT instability and RM instability. Relatively few experiments to study convergent RT instability have been performed because of the difficulty in diagnosis. Some experiments have been carried out in which a planar foil is replaced by a sphere with perturbations on one hemisphere (Cherfils *et al.*, 1999; Glendinning *et al.*, 2000). The growth of perturbations on the surface of the sphere can be measured by using radiography through the sphere. The integral effect of outer surface growth, feedthrough, and inner surface growth can be measured in cylindrical implosion experiments (Hsing *et al.*, 1997; Hsing and Hoffman, 1997).

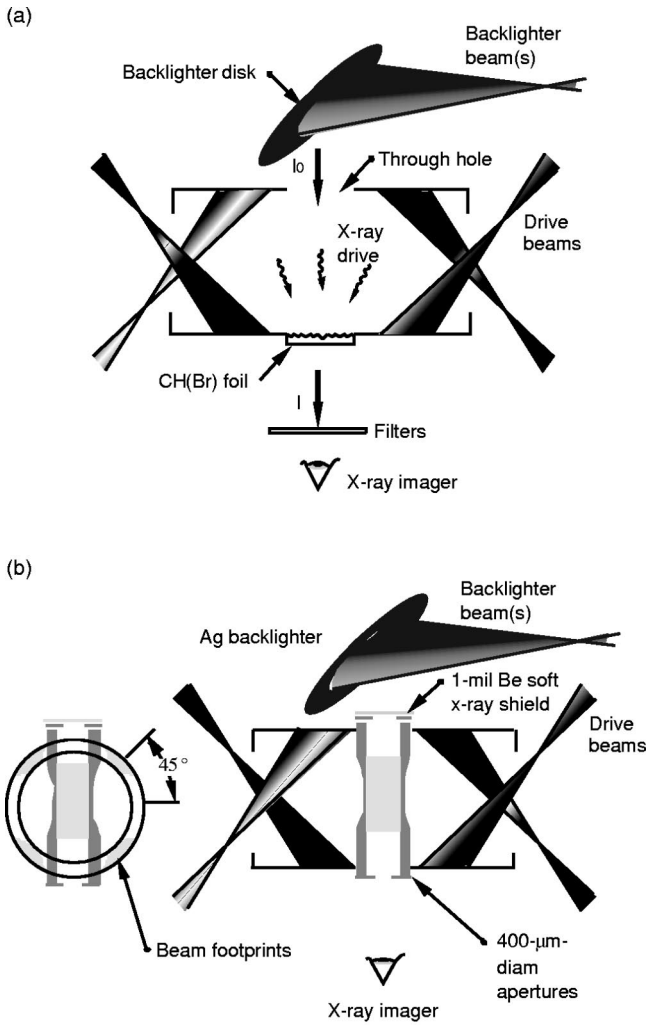

FIG. 6-5. (a) Modulated planar CH(Br) foils or modulated CH(Ge) capsules were mounted on the hohlraum wall. (b) The cylindrically convergent experiment was mounted perpendicular to the hohlraum axis.

This geometry allows diagnostic access and superior control of the shell's inner surface during target fabrication, although questions arise concerning edge effects and implosion symmetry.

The experimental configuration for the indirect-drive planar experiments using a shaped, low-adiabat drive is illustrated in Fig. 6-5. Surface perturbations are molded onto one side of a planar 750 μm diameter CH(Br) foil ($C_{50}H_{47}Br_{2.7}$) of density $\rho=1.26$ gm/cm^3. This material was chosen for most of the RT experiments (Kilkenny, 1990; Remington *et al.*, 1991; Remington *et al.*, 1992; Dimonte and Remington, 1993; Hammel *et al.*, 1993; Remington *et al.*, 1993; Hammel *et al.*, 1994; Hammel *et al.*, 1994a; Remington *et al.*, 1994; Marinak *et al.*, 1995; Remington *et al.*, 1995; Marinak *et al.*, 1998) because it behaves in a way similar to ablators in high gain capsules in which both ablation and density gradient effects are important in determining the growth of the RT instability. The foil is mounted across a hole in the wall of a 3000 μm long, 1600 μm diameter Au cylindrical hohlraum with the perturbations facing inwards, as shown in Fig. 6-5(a). The foil is diagnosed by radiography with an 800 μm diameter spot of x rays created

Downloaded 20 Mar 2011 to 69.181.48.121. Redistribution subject to AIP license or copyright; see http://pop.aip.org/about/rights_and_permissions

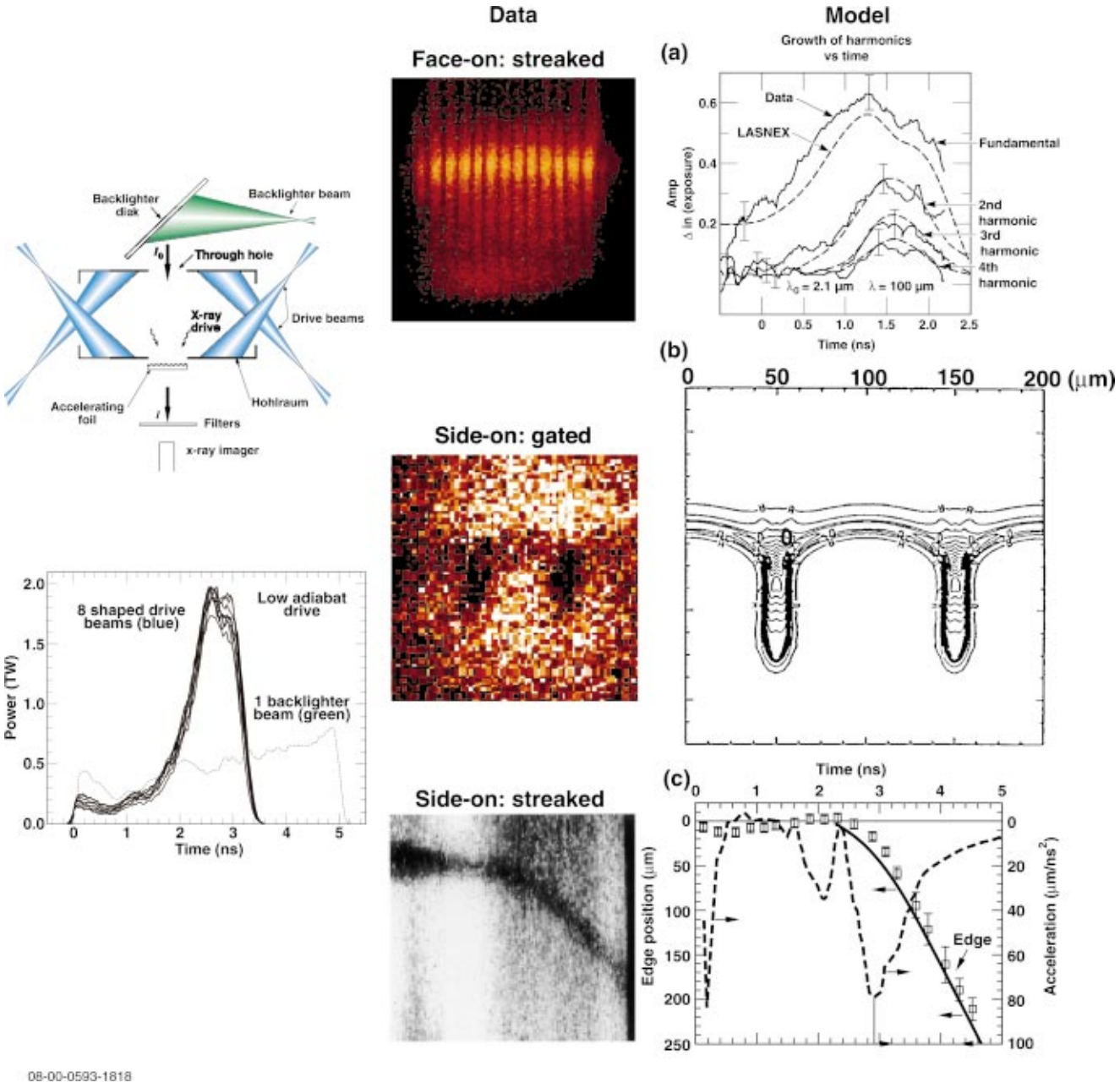

FIG. 6-6. (Color) Experiments on planar targets have allowed quantitative evaluation of the growth of RT instability in the presence of radiation ablation. (a) Face-on streaked images provide a 1D history of the time variation in the spatial distribution of the x-ray backlighter transmission through the perturbed sample. (b) Side-on gated images provide a 2D record of the spatial distribution of the perturbed foil. (c) Side-on streaked images provide a record of the foil position as a function of time.

by irradiating a disk of Rh, Mo, Ag, or Sc (depending on the experiment) with one or two Nova beams. The modulations in foil areal density cause modulations in the transmitted backlighter x-ray flux, which are recorded as a function of time with either gated (Budil *et al.*, 1996) (FXI) or streaked x-ray imaging diagnostics. Typical images are shown in Fig. 6-6. Table VI-1 shows the various laser energies, modulation amplitudes, wavelengths, and backlighters for the planar experiments discussed below. This table also shows the results of experiments with fluorosilicone (FS) and undoped CH. The FS foils had the largest growth of the materials used, approaching NIF-like growth factors with shaped pulses. Undoped CH has the highest level of ablation stabilization and the least growth.

The setup for spherical experiments (Cherfils *et al.*, 1999; Glendinning *et al.*, 2000) was identical to that for the planar experiments, with the foil replaced by a modulated Ge-doped plastic capsule. This was a 500 μm diameter, CH(1.3% Ge) capsule with a 50–55 μm thick wall, mounted in the hole in the hohlraum wall. This is the same type of capsule used in the HEP4 experiments discussed in the Sec. VII. The side of the capsule towards the drive had sinusoidal surface modulations, 70 μm wavelength and 2.5 μm initial amplitude. In both of these categories of experiments, the

Downloaded 20 Mar 2011 to 69.181.48.121. Redistribution subject to AIP license or copyright; see http://pop.aip.org/about/rights_and_permissions

TABLE VI−1. Planar geometry experimental details, including the fundamental wavelength, initial amplitude, mean foil thickness, laser energy, and backlighter material. The maximum observed and predicted growth factors are given in the last two columns.

Foil material	Drive	Perturbation wavelength λ (μm)	Initial amplitude η_0 (μm)	Foil thickness (μm)	E_{Laser}(kJ)	Backlighter	Observed growth	Calculated growth
Single-mode perturbations								
CH(Br)	Shaped	100	2.4	48	16.1	Rh	3.8	5.8
CH(Br)	Shaped	70	2.4	50	18.5	Rh	6.5	7.3
CH(Br)	Shaped	50	0.42	57	17.4	Mo	19.9	24.0
CH(Br)	Shaped	30	1.5	53	15.1	Rh	7.2	9.7
FS	Shaped	50	4.5	57.5	19.3	Rh	6	4
FS	Shaped	50	0.8	56.0	16.6	Rh	22	20
FS	Shaped	50	0.16	65.5	16.7	Rh	75	75
FS	Ins Sq.	50	2.2	28		Dy	2.9	2.8
CH	Ins Sq.	50	2.5	28		Dy	1.7	1.9
Two-mode perturbations								
CH(Br)	Shaped	75	1.8	54	17.3	Rh	3.7	3.9
		50	1.8				4.7	6.2
Eight-mode perturbations								
CH(Br)	Shaped	180	−0.294	50	17.1	Rh	−8.2	−7.9
		90	−0.277				7.7	11.8
		60	−0.315				15.6	22.3
		45	−0.316				25.7	32.7
		36	0.232				11.4	18.1
		30	0.183				−37.8	−34.2
		25.7	0.133				−30.0	−43.0
		22.5	−0.059				−38.2	43.0

hole on the back wall of the hohlraum was covered with 100 μm thick CH to prevent Au from obscuring the backlighter x rays.

The experiment geometry for the cylindrical implosions (Hsing *et al.*, 1997; Hsing and Hoffman, 1997) is also shown in Fig. 6-5(b). The hohlraum had an inside length of 2750 μm and an inside diameter of 1600 μm. A cylindrical polystyrene tube was mounted orthogonal to the hohlraum axis. This orientation allows a direct line-of-sight to the diagnostics, avoids interference with laser beams, and avoids radiation flow into the ends of the cylinder, which can occur in a cylinder oriented along the hohlraum axis. A 25 μm Be foil was placed between the backlighter and cylinder to filter out soft x rays and prevent light reflected from the backlighter from entering the cylinder. The outer diameter of the cylinder was tapered toward the center, allowing the central region of the cylinder to implode before the ends, minimizing edge effects. The central 400 μm long region of the cylinder had perturbations machined on the outer surface in a dodecagon shape (fundamental mode number $m=12$). A 4 μm thick, 160 μm long dichlorostyrene ($C_8H_6Cl_2$) belt was placed around the center of the cylindrical shell, flush with the shell's inner surface. The belt served as a marker layer, because it was opaque to the x-ray backlighter, whereas the polystyrene cylinder was relatively transparent except late in time. Because the marker layer was on the inner surface of the cylinder and had no perturbations initially, any perturbations observed indicate feedthrough of the initial outer-surface perturbations to the inner surface. The marker layer had a density relatively close to that of the unchlorinated polystyrene ($1.4\,\text{g/cm}^3$ vs $1.0\,\text{g/cm}^3$), and calculations showed that this density mismatch did not cause significant RT growth. A $60\,\text{mg/cm}^3$ microcellular triacrylate foam ($C_{15}H_{20}O_6$) was placed inside the shell to provide a backpressure as the cylinder imploded. The foam had a cell size of about 1 to 3 μm and was shorter than the cylinder to minimize opacity to the backlighter. On each end of the cylinder, a 400 μm diameter circular aperture made of 25 μm thick Au concentric with the cylinder axis provided a centering fiducial for each frame on the pinhole camera. The cylinder was viewed along its axis with a time-resolved gated x-ray pinhole camera (GXI) (Kilkenny *et al.*, 1988).

The instrumental spatial resolution is expressed as the point spread function (PSF). The PSF for the magnification-22 grazing incidence Wölter x-ray microscope (Ellis *et al.*, 1990) used for the streaked imager experiments is given by (Morales *et al.*, 1995)

$$R_{W1}(x)=e^{-w/\sigma} \tag{6-45}$$

with $\sigma=6.7\pm1.4$ μm. In one experiment, a different section of the optic was used with resolution given by

$$R_{W2}(x)=\frac{1}{1+\alpha}(e^{-x/\sigma_1}+\alpha e^{-x/\sigma_2}), \tag{6-46}$$

with α, σ_1, and, σ_2 given by 0.22, 3.5, and 18 μm, respectively. The resolution for both framing cameras (FXI and GXI) is given by

Downloaded 20 Mar 2011 to 69.181.48.121. Redistribution subject to AIP license or copyright; see http://pop.aip.org/about/rights_and_permissions

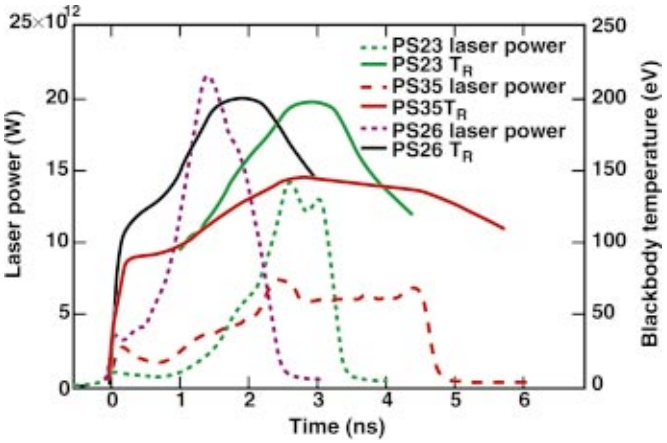

FIG. 6-7. (Color) Drive history for the three laser pulse shapes used in these experiments. The total laser power as a function of time for the drive beams is shown (left axis) in each case (the backlighter power history is not shown). The corresponding x-ray blackbody temperature is also shown for each pulse (right axis).

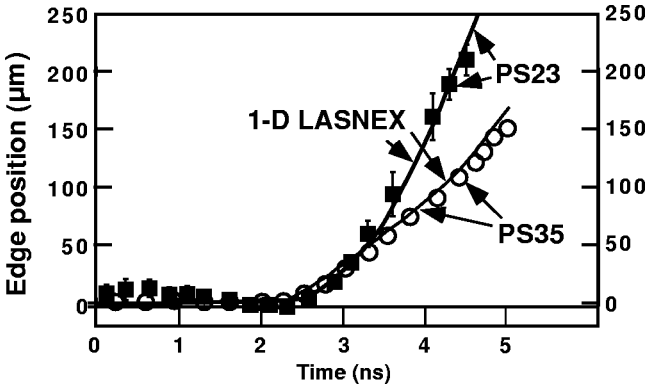

FIG. 6-8. Foil trajectory for the planar geometry experiments. The plotting symbols represent the measured position of the rear edge (side away from the x-ray drive) of the foil as a function of time. The two pulse shapes used for planar geometry experiments are represented as PS23 and PS35 (see Fig. 6-5). The error bars arise from the uncertainties in defining the edge. The solid curves are the results of 1D LASNEX simulations. Note that the rear edge of the foil does not start to move until after shock breaks out.

$$R_{\mathrm{FC}}(x)=\frac{1}{1+a_0}\left(e^{-x^2/2a_1^2}+a_0e^{-x/a_2}\right) \tag{6-47}$$

with $a_0=0.05\ \mu$m, $a_1=3.6\ \mu$m, and $a_2=28.8\ \mu$m.

The low-adiabat laser drives used in these experiments are shown in Fig. 6-7. They were generated by focusing eight 0.351 μm, 2–3 kJ, temporally shaped Nova beams into the Au hohlraum. The total power for each of the four drives is shown. The x-ray drives were measured with an array of time-resolved x-ray diodes and are also shown in Fig. 6-7.

The trajectory is a measure of the gross hydrodynamics. In planar geometry, the trajectory was measured by viewing across the foil. The trajectory of the convergent cylinder is given by the average radius of the cylinder in each image, and that of the sphere is determined by the wavelength as a function of time. The trajectories are reproduced very well with LASNEX (Zimmerman and Kruer, 1975) simulations and are shown in Fig. 6-8. The error bars represent the uncertainty in defining the edge of the foil.

E. Instability experiments in planar geometry

Figure 6-9 shows typical streaked data, from a single-mode face-on planar experiment (Remington *et al.*, 1995) with $\lambda=100\ \mu$m, $\eta_0=2.4\ \mu$m initial perturbation on a 48-μm-thick CH(Br) foil. The image is shown in Fig. 6-9(a), and profiles of modulations in optical depth $\Delta\mathrm{OD}=-\ln(\text{exposure})$ at early, intermediate, and late times are given in Fig. 6-9(b). The real components of the Fourier transform for the three ΔOD profiles are shown in Fig. 6-9(c). At early time, only the η_1 fundamental mode (first harmonic) exists, while at late time, higher Fourier harmonics—up to the fifth—are observed, forming the bubble and spike shape of the top lineout in Fig. 6-9(b).

Figure 6-10 shows the results of wavelength scaling experiments (Remington *et al.*, 1995) with single-mode CH(Br) foils for the two different x-ray drives. For these single-mode ($m=1$) experiments, the wavelengths investigated were $\lambda=30$, 50, 70 (for PS23 only), and 100 μm. The plotting symbols represent the experimental results for the

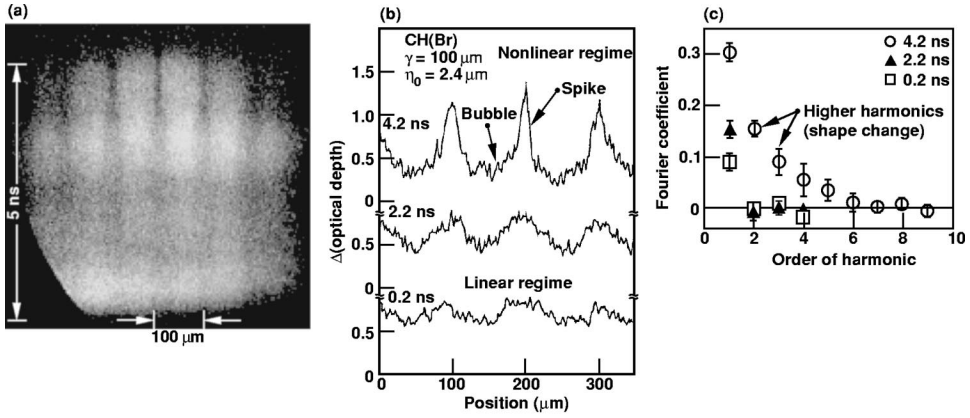

FIG. 6-9. Various representations are shown for the single-mode face-on data for a $\lambda=100\ \mu$m, $\eta_0=2.4\ \mu$m perturbation imposed on a 48 μm thick CH(Br) foil. (a) The "raw" streaked image is shown as film density. The film response is removed using a calibrated exposure across a precision "P20" optical density wedge. (b) Profiles of Δ (optical depth) $\approx\Delta\ \ln$(exposure) are shown at 0.2 ns, 2.2 ns, and 4.2 ns. (c) The real components of the Fourier transforms are given for the three profiles shown in (b). Note that at late time, the perturbation enters the nonlinear regime, and up to the fifth harmonic of the perturbation Fourier composition is observed.

Downloaded 20 Mar 2011 to 69.181.48.121. Redistribution subject to AIP license or copyright; see http://pop.aip.org/about/rights_and_permissions

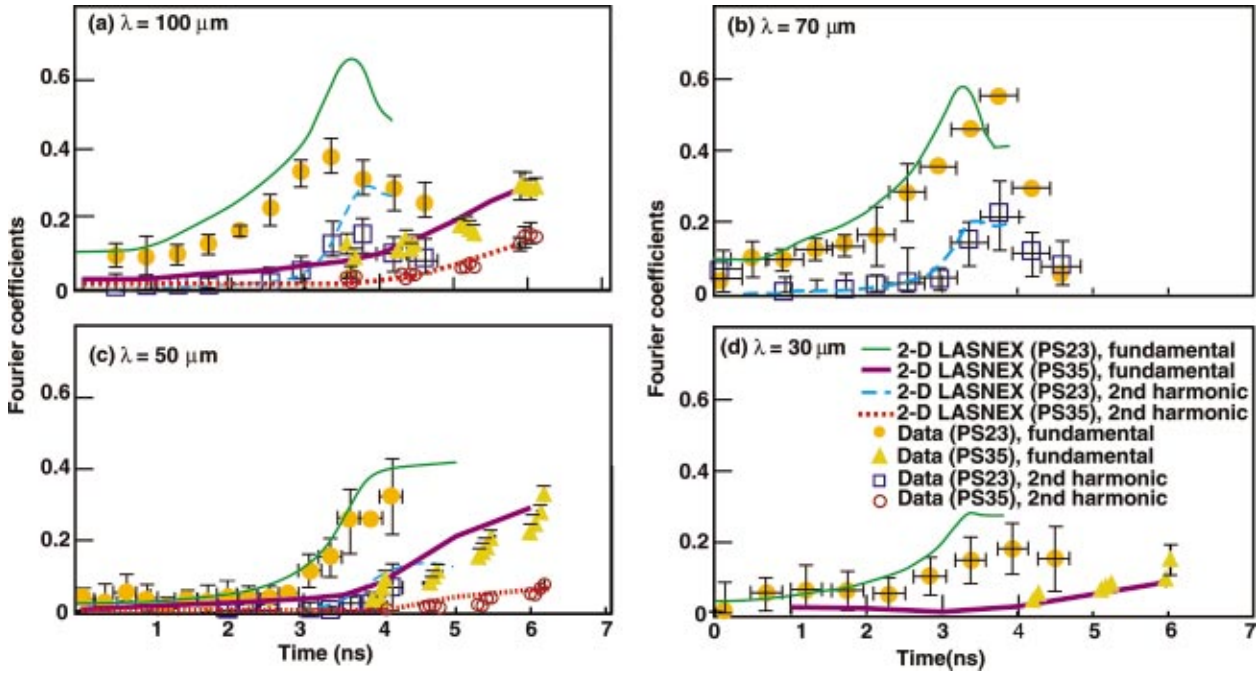

FIG. 6-10. (Color) Results of the wavelength scaling experiments (single mode). (a) $\lambda = 100\ \mu$m, (b) $\lambda = 70\ \mu$m (for the PS23 drive only), (c) $\lambda = 50\ \mu$m, and (d) $\lambda = 30\ \mu$m.

fundamental mode (circles) and the second harmonic (squares). The error bars represent the standard deviation of the ensemble formed by treating each individual period of the perturbations as independent data. The growth factor (GF) is defined as the ratio of peak to initial contrast. In these experiments, GF varied from 4 to 20.

The curves in Fig. 6-10 represent the corresponding results from 2D LASNEX simulations after convolving the simulated image exposure with the appropriate instrumental resolution function. The 100 μm data with the PS23 drive do not agree with the simulation, although the 100 μm data with PS35 drive do. Data obtained with the Wölter optic had a larger uncertainty in the PSF determination than that obtained with the FXI.

In the 2D multimode planar experiments (Remington *et al.*, 1993; Remington *et al.*, 1994; Remington *et al.*, 1995), the initial perturbations investigated were of the form $\eta(x) = \Sigma_{n=1}^{m} \eta_n \cos(k_n x)$, where $k_n = 2\pi/\lambda_n$. The multimode perturbations investigated are shown in Fig. 6-11. The modes are harmonics of the longest repeating pattern. Figure 6-11(a) shows a large amplitude two-mode perturbation given by $\lambda_2 = 75\ \mu$m and $\lambda_3 = 50\ \mu$m, with $\eta_2 = \eta_3 = 2\ \mu$m. Figure 6-11(b) shows a small-amplitude eight-mode ($m = 8$) perturbation given by $\lambda_n = (180\ \mu\text{m})/n$, $n = 1-8$.

The resulting time dependence of the modulations for the two-mode experiment is shown in Figs. 6-12(a) and 6-12(b), along with the corresponding LASNEX simulations. The presence of the coupled modes in the two-mode experiment, arising as the modulations enter the nonlinear regime, is correctly predicted by LASNEX. Had only a single mode been initially present, the simulations would have predicted quite different behavior. The eight-mode results are also shown in Figs. 6-12(c)–6-12(j), and again the effects of mode coupling are apparent.

The second-order perturbation model can be quantitatively applied to the eight-mode experiment, using

$$\eta_k \approx \eta_k^L + \frac{1}{2}k\left[\sum_{k'} \eta_{k'}^L \eta_{k+k'}^L - \frac{1}{2}\sum_{k'<k} \eta_{k'}^L \eta_{k-k'}^L\right] \quad (6\text{-}48)$$

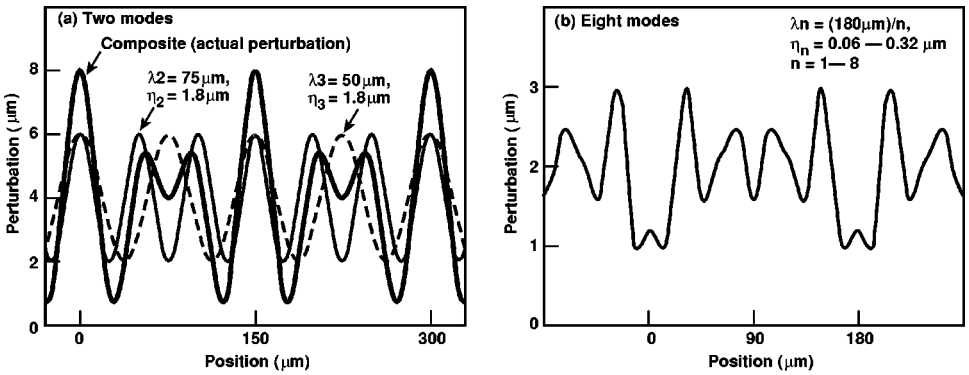

FIG. 6-11. The multimode perturbation patterns investigated are shown. (a) The curves correspond to $\lambda_2 = 75\ \mu$m, $\eta_2 = 2\ \mu$m (dashed), $\lambda_3 = 50\ \mu$m, $\eta_3 = 2\ \mu$m (dotted), and their superposition (solid), which represents the actual perturbation. (The actual measured amplitudes were $\eta_{2,3} = 1.8\ \mu$m.) (b) The 8-mode perturbation is given by the solid curve and corresponds to the sum of wavelengths $\lambda_n = (180\ \mu\text{m})/n$, $n = 1-8$.

Downloaded 20 Mar 2011 to 69.181.48.121. Redistribution subject to AIP license or copyright; see http://pop.aip.org/about/rights_and_permissions

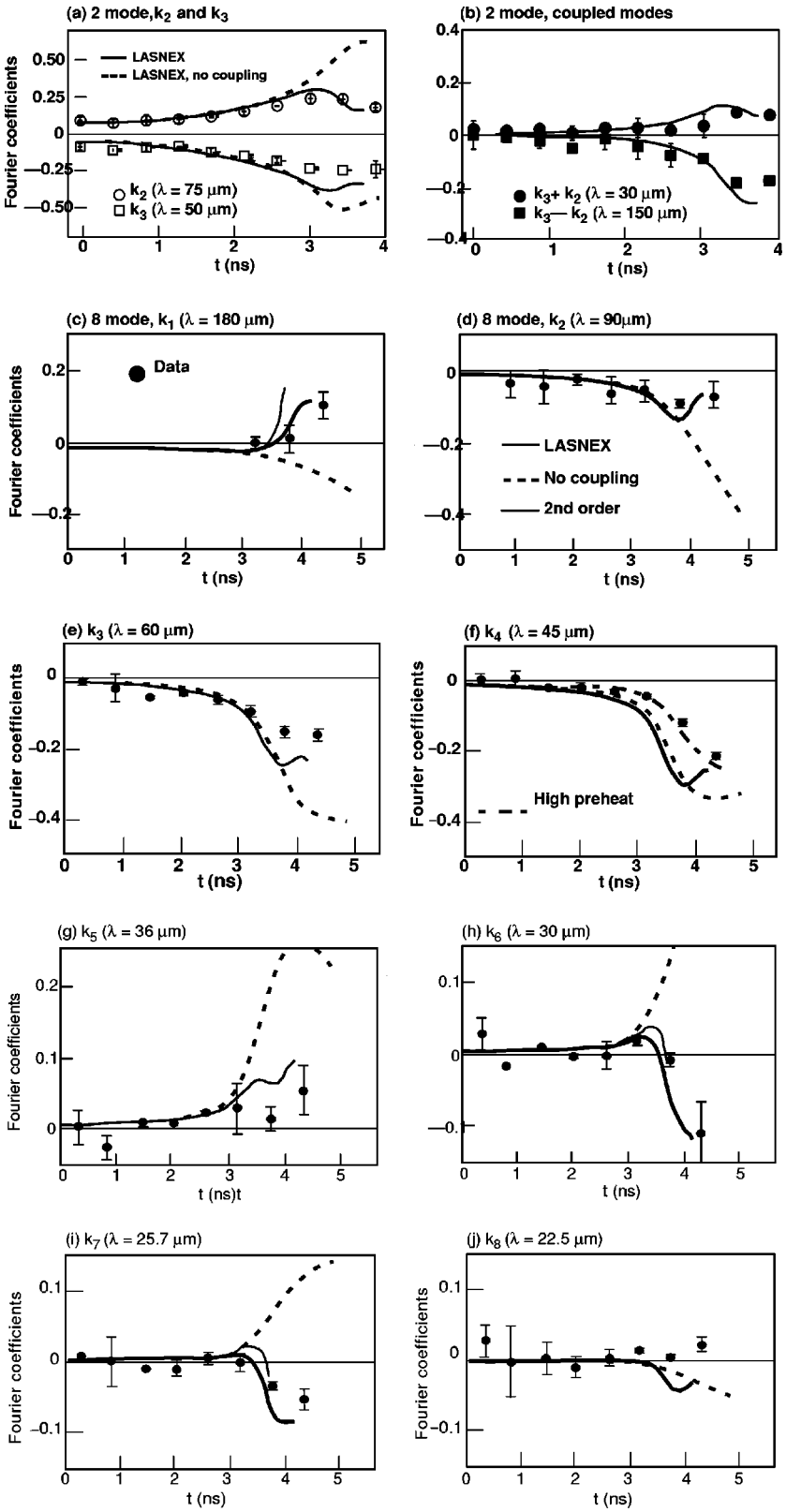

FIG. 6-12. The time dependence for the two- and eight-mode data. (a) The open circles represent k_2 (the $\lambda = 75\ \mu$m component of the pre-existing perturbation), and the open squares correspond to k_3 (the $\lambda = 50\ \mu$m component of the perturbation) for the 2-mode foil. (b) The solid circles correspond to the $k_3 + k_2$, $\lambda = 30\ \mu$m coupled term, and the solid squares to the $k_3 - k_2$, $\lambda = 150\ \mu$m coupled term. The smooth solid curves are the results of 2D LASNEX simulations for this two-mode foil, and the dashed curves correspond to assuming that only one of the two initial perturbations was present at a time. In (c)–(j), the growth of modes $\lambda_n = (180\ \mu\text{m})/n$ is shown vs time, where $n = 1$ to 8. The thin curves for modes k_1, k_6, and k_7 correspond to the results of a weakly nonlinear, second-order perturbation theory. The long dashed curve for mode k_4 corresponds to a simulation with assumed enhanced preheat in the foot of the drive.

by summing over the couplings from all pairs of modes whose sum or difference equals the k of interest. The η_{k_n} represent spatial amplitudes defined from the LASNEX simulations by dividing the modulations in areal density by the foil peak density. For each λ_n in the eight-mode foil, 2D LASNEX simulations are run for very small initial amplitude perturbations, which remain in the linear regime. The $\eta^L_{k_n}(t)$ are then obtained by scaling by the ratio of actual to the linear initial amplitude. The results from this perturbation analysis are shown by the dotted curves in Fig. 6-12 for $t \leqslant 3.7$ ns. Beyond this time, the central assumption of the model (dominant modes not affected by the coupling terms)

Downloaded 20 Mar 2011 to 69.181.48.121. Redistribution subject to AIP license or copyright; see http://pop.aip.org/about/rights_and_permissions

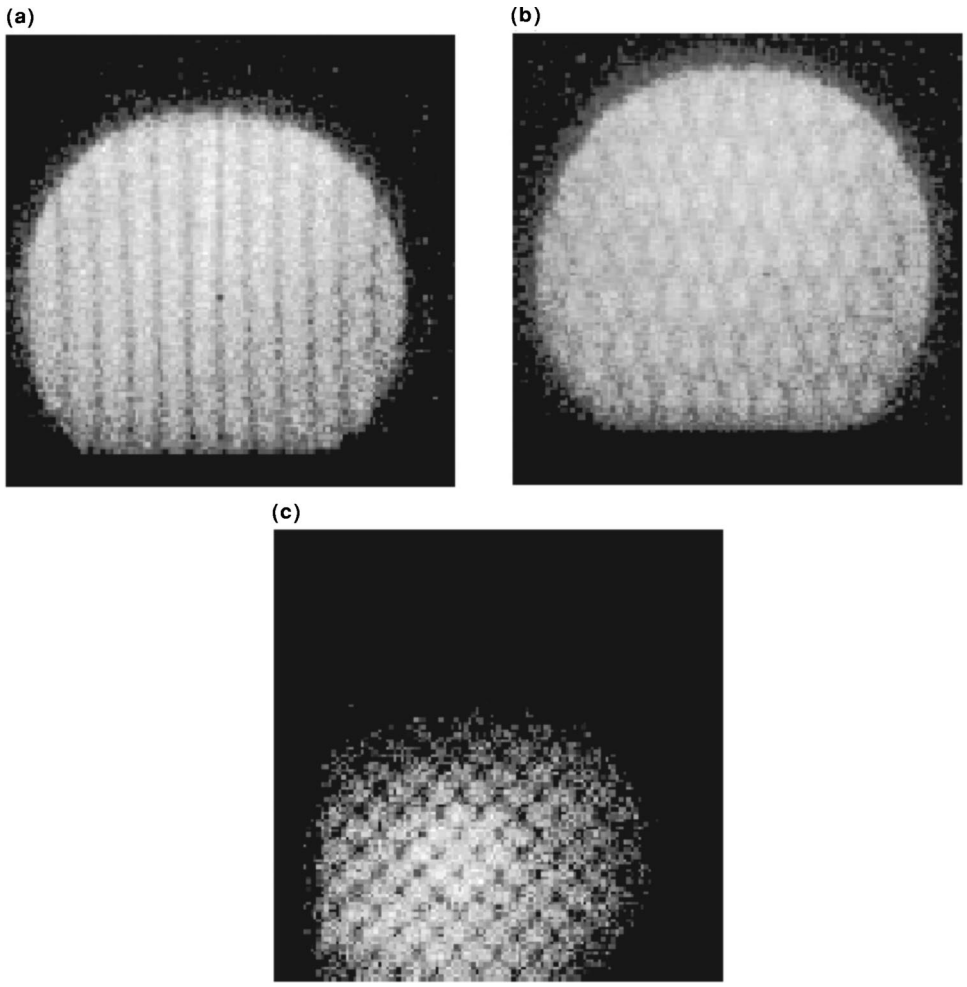

FIG. 6-13. Images from the 3D single-mode Nova experiments are shown in (a)–(c). The perturbations correspond to (a) 2D $\lambda = 50\ \mu$m, $\eta_0 = 2.5\ \mu$m, (b) 3D $k_x = 3k_y$: $\lambda_x = 53\ \mu$m, $\lambda_y = 158\ \mu$m, $\eta_0 = 2.4\ \mu$m, and (c) 3D $k_x = k_y$, $\lambda_x = \lambda_y = 71\ \mu$m, $\eta_0 = 2.7\ \mu$m.

is violated, and the model is no longer applicable. In each case, second-order perturbation theory predicts the phase reversals.

The behavior of a 3D perturbation is different from that of a 2D one. Perturbations of the same wave number $|k| = (k_x^2 + k_y^2)^{1/2}$ can have different shape and evolve differently in the nonlinear phase while having the same linear-regime RT growth rate. Single-mode experiments (Marinak *et al.*, 1995) were used to examine the effect of mode shape on growth. The foils were made from molds formed by laser ablation of a Kapton substrate (NTIS Document, 1994e). The perturbed foils all had the same magnitude wave vector $|\mathbf{k}| = (k_x^2 + k_y^2)^{1/2}$ and nominally the same amplitude. The ''2D'' foil (1D wave vector $\mathbf{k} = k_x$) was a simple $\lambda = 50\ \mu$m sinusoid with initial amplitude $\eta_0 = 2.5\ \mu$m. One of the ''3D'' foils [2D wave vector $\mathbf{k} = (k_x, k_y)$] corresponded to a ''stretched'' $k_x = 3k_y$ perturbation, and the other was a square $k_x = k_y$ mode. Images from the Nova shots at 4.3 ns, which is near peak growth, are shown in Fig. 6-13. The gated x-ray pinhole camera for these images was run at $8\times$ magnification with 10 μm pinholes, and 150 μm Be filtering. The backlighter was Sc at 4.3 keV.

Each image from the Nova shots was reduced to modulation in optical depth. The experiments were simulated with the 3D radiation-hydrodynamics code HYDRA (Marinak *et al.*, 1996). The images are Fourier analyzed, and the amplitudes corresponding to the fundamental mode are extracted. The results for the evolution of the fundamental mode are shown in Fig. 6-14. The $k_x = k_y$ square 3D mode grows the largest, the $\lambda = 50\ \mu$m 2D mode grows the least, and the $k_x = 3k_y$ stretched 3D mode falls in between. Simulations of the same mode structure with identical drive and sample thickness are also shown in Fig. 6-14, showing that the most symmetric shapes grow the fastest.

An actual ICF capsule will have a full spectrum of 3D modes growing simultaneously and interacting through mode coupling. To approach this situation, an experiment (Marinak *et al.*, 1998) was performed with the PS35 drive and a foil modulated with a locally random, isotropic perturbation, shown in Fig. 6-15. Perturbations on this foil span nearly a decade in Fourier space. Because weakly nonlinear mode coupling occurs over a bubble width, the short length scale random variation in the perturbations sets conditions for bubble formation and saturation. Over the largest transverse length scales of the system, the pattern possesses reflection symmetry; each 150 μm square is symmetric about its boundaries. The length scale of the reflection symmetry is too long for the lowest modes to determine weakly nonlinear saturation of the bubbles. The pattern is continued on the foil for an extra half-period beyond the 300 μm square that defines the fundamental wavelength. This enabled rigorous treatment of the boundary conditions in the code simulation.

Downloaded 20 Mar 2011 to 69.181.48.121. Redistribution subject to AIP license or copyright; see http://pop.aip.org/about/rights_and_permissions

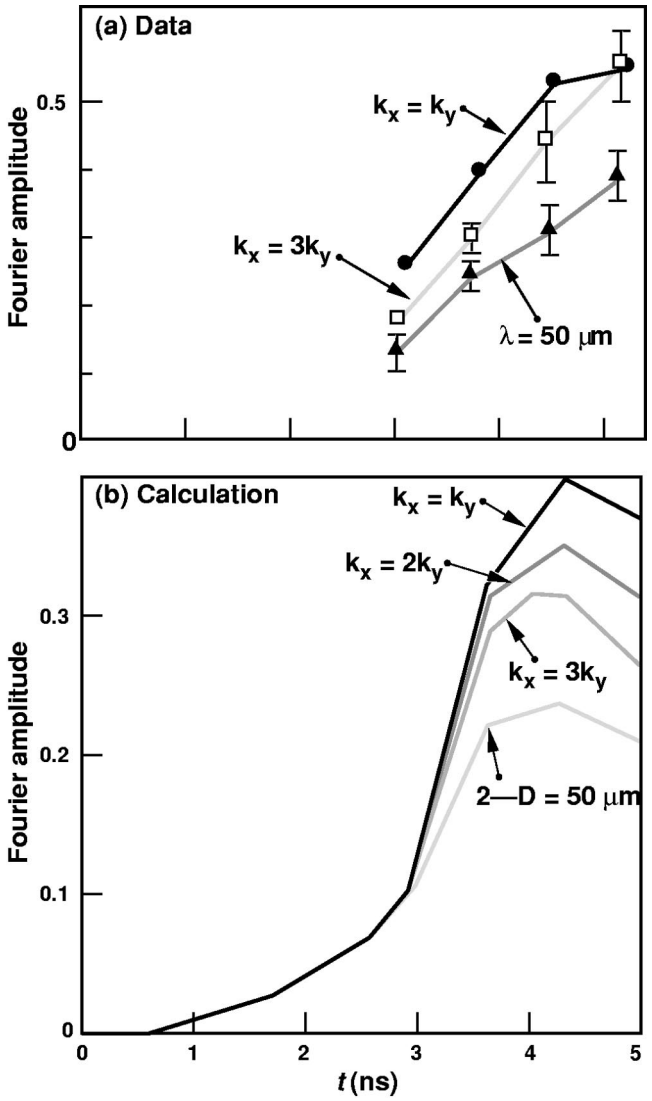

FIG. 6-14. (a) Results of the evolution of the fundamental mode Fourier amplitude of ln(exposure) for the 3D $k_x = k_y$ (solid circles), $k_x = 3k_y$ (open squares), and 2D $\lambda = 50$ μm (solid triangles) perturbations. The connecting lines are meant only to guide the eye. (b) Predicted Fourier amplitude of ln(exposure) from 3D simulations for the evolution of four different perturbation shapes all with the same magnitude $k = (k_x^2 + k_y^2)^{1/2}$ wave vector, for drive conditions slightly different from those of (a). The most symmetric ($k_x = k_y$) mode is predicted to grow the largest, the 2D $\lambda = 50$ μm mode grows the least, and the 3D stretched cases fall in between, in agreement with the experiments.

The specified surface perturbation consisted of modes of the form $\cos(k_x x)\cos(k_y y)$, where $(k_x, k_y) = 2\pi(m,n)/\chi_L$ with $(m,n) = (0-12, 0-12)$ and $\chi_L = 300$ μm. The total rms of the pattern was measured by contact radiography to be 0.66 μm.

The simulation of this experiment predicts a period of substantial linear-regime RT growth, followed by the usual formation of broad bubbles and spikes. Figure 6-16(a) shows an experimental image obtained at 6.0 ns. Under the influence of mode coupling, the pattern has evolved into broad bubbles in close packing surrounded by narrow, interconnecting spike sheets with local spike maxima occurring at the intersections of spike sheets, similar to the bubble and spike sheets from the single wavelength experiments of Fig. 6-13.

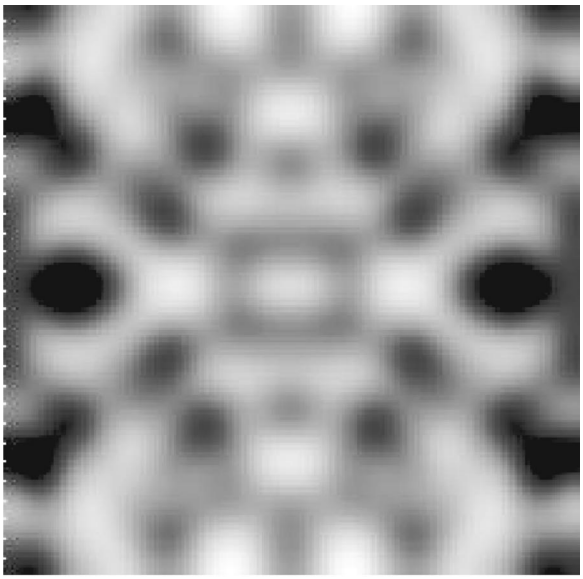

FIG. 6-15. Contours of the designed initial 3D multimode pattern shown on a 300 μm square. Darkest regions correspond to greatest foil thickness.

The average diameter of the bubbles at 6 ns is about 50 μm, corresponding to the wavelength at the peak of the growth factor spectrum. The simulated radiograph from the HYDRA calculation at 6.0 ns is shown in Fig. 6-16(b). The quantitative comparison of the Fourier spectra with the data is shown in Fig. 6-17. The simulation quantitatively matches the measured evolution of the spectrum.

The onset of nonlinear saturation as predicted by HYDRA is well estimated by the Haan model given in Eq. (6-40). Perturbation amplitudes obtained from the simulation exceed $(\lambda_n/2\chi_L)(\lambda_n/10)$ over a broad range by 6 ns, but are much less than $\lambda_n/10$. Thus the collective nonlinearity observed in the experiment, seen by the presence of the broad bubbles, is occurring for individual mode amplitudes much smaller than 10% of the wavelength.

F. Instability experiments in convergent geometry

In the cylindrical geometry (Hsing *et al.*, 1997; Hsing and Hoffman, 1997), the central 400 μm section of the cylinder had perturbations machined on the outer surface in a dodecagon shape (fundamental mode number $m = 12$), with a peak-to-valley modulation of 9 μm. Figure 6-18 shows a typical frame at 2.11 ns from the imploding cylinder. The $m = 12$ perturbation is clearly observed in the image. The perturbation amplitude grows in time, and the wavelength is seen to decrease as the radius decreases. According to calculations, the ablation front has not yet burned through to the marker layer, so the existence of an observed $m = 12$ feature is due to feedthrough of the initial perturbation to the marker layer. The tips of the dodecagon have grown into spikes at the ablation front. Figure 6-19 shows the results of a Fourier analysis of a contour at the outer edge at about the 50% exposure level. Mode 12 has a value of 10 ± 2 μm, which is a factor of 2.9 ± 0.6 greater than its initial value. At $t = 2.30$ ns, just about the time that the deceleration phase begins, the Fourier analysis of the outer edge gives an 11.5

Downloaded 20 Mar 2011 to 69.181.48.121. Redistribution subject to AIP license or copyright; see http://pop.aip.org/about/rights_and_permissions

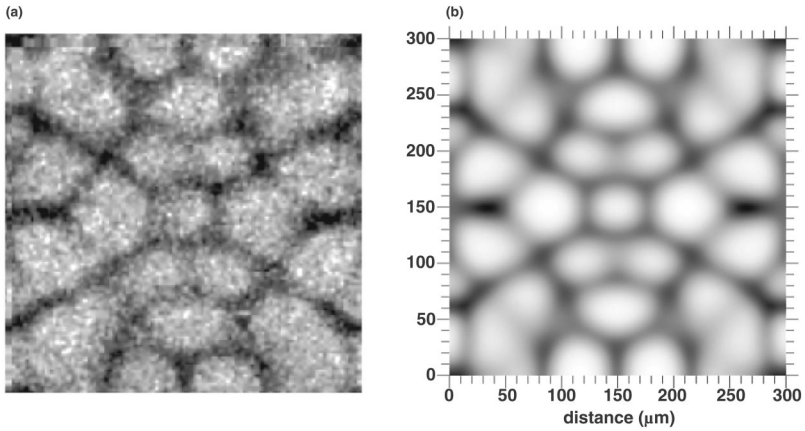

FIG. 6-16. (a) Experimental radiograph of the 3D multimode foil at 6.0 ns. Darkest regions correspond to greatest foil thickness (spikes). (b) Simulated radiograph at 6.0 ns, which includes the diagnostic resolution. Gray scales for (a) and (b) cover the same change in optical depth.

μm amplitude, and for the inner edge, a 2 μm, $m=12$ amplitude, or an attenuation of 0.18. Using attenuation equal to $e^{-k\Delta x}$ for a Rayleigh–Taylor mode, $k=0.12\ \mu\text{m}^{-1}$ for mode 12 at a radius of $\sim 100\ \mu$m, and a marker layer thickness from the simulation of $\Delta\chi=17\ \mu$m results in an attenuation of 0.14, consistent with the measurement.

Mode 0 is the average diameter of the cylinder, and the radius vs time derived from this is shown in Fig. 6-19(a). The positions are correctly predicted by simulations using the 1D radiation hydrodynamics code HYADES (Larsen, 1990). The $m=4$ seen in the data is the result of radiation asymmetry.

During deceleration, the inner surface becomes RT unstable and perturbations on the inside surface grow without ablative stabilization. In the frame in Fig. 6-18 at 2.72 ns, visible spikes protrude into the core. This is due to the Bell–Plesset (Bell, 1951; Plesset, 1955) growth, which includes a purely geometric effect. The growth can be estimated by considering a compressible fluid without acceleration. The amplitude change, which in cylindrical geometry varies about as $1/\rho r$, essentially arises from conservation of mass within the perturbed layer as it converges. Using values of ρ and r in the center of the marker layer from the 1D simulation and normalizing the amplitude to 10 μm at 2.11 ns, the resultant growth is plotted in Fig. 6-19(b).

The spherical experiments (Cherfils *et al.*, 1999; Glendinning *et al.*, 2000) produced the images shown in Fig. 6-20. The perturbation was a square patch $350\times350\ \mu$m.

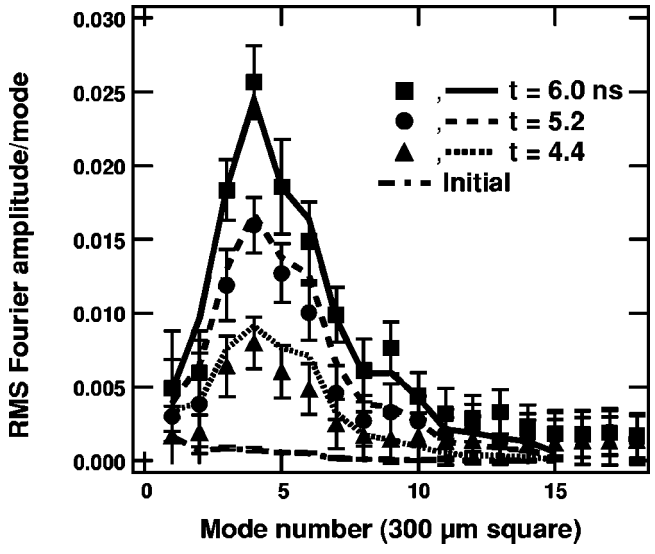

FIG. 6-17. Fourier spectra of ln(exposure) vs time for the 3D multimode foil. The curves are from the HYDRA 3D simulations and include the effect of finite instrumental resolution. The symbols are results from analyzing the experimental radiograph.

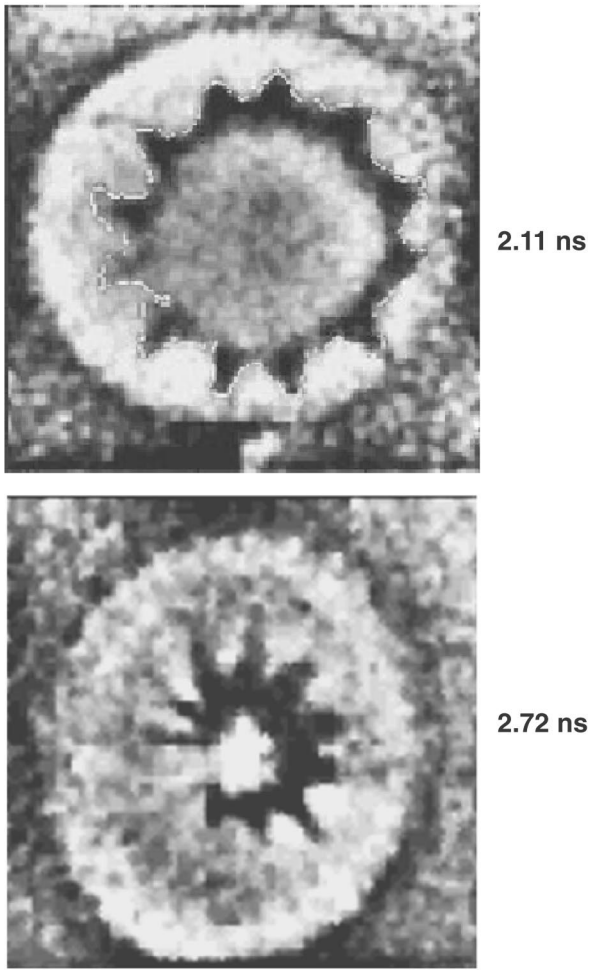

FIG. 6-18. (a) An outer contour of the cylindrical implosion experiment taken at 50% peak exposure, superposed over an x-ray image taken at 2.11 ns. (b) Cylinder at 2.72 ns.

Downloaded 20 Mar 2011 to 69.181.48.121. Redistribution subject to AIP license or copyright; see http://pop.aip.org/about/rights_and_permissions

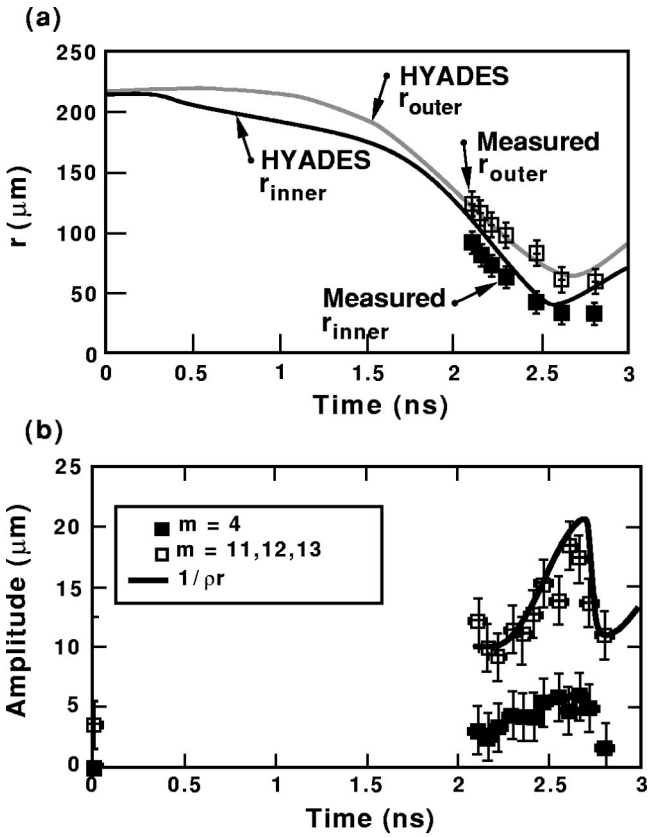

FIG. 6-19. (a) The measured outer and inner diameters of the tracer layer in the cylindrical experiment as a function of time compared with the trajectories from a HYADES calculation. (b) The Fourier modal amplitudes as a function of time. The value $1/\rho r$ is superposed. Cylindrical modes grow at this rate purely from convergence effects.

The shock driven by ablation reaches the interior of the capsule wall at 1.4 ns. As the hemisphere accelerates from 1.5 to 2.25 ns, it also converges by over a factor of 2, as seen by the shrinking of the wavelength shown in Fig. 6-21(a). The experiment was simulated with the 2D radiation hydrodynamics code FCI2 (Buresi *et al.*, 1986; Busquet, 1993). The simulations of the wavelength with FCI2 are also shown in Fig. 6-21(a).

Figure 6-21(b) shows the Fourier analysis of the data. The peak observed growth factor of optical depth modulation is about 6, and the modulation shows that it has entered the nonlinear regime with the appearance of the second harmonic. The dramatic drop in modulation after 2 ns is due partly to the drop in instrument MTF as the wavelength decreases, partly to the motional blurring as the velocity increases, and partly to nonlinear saturation of the growth of the fundamental. The FCI2 simulations, post-processed to include the radiography and diagnostic resolution, correctly predict the wavelength and amplitude as a function of time. The light curves are coefficients of the Fourier transform of the spatial amplitude extracted from the simulations, based on an isodensity contour at the perturbed ablation front.

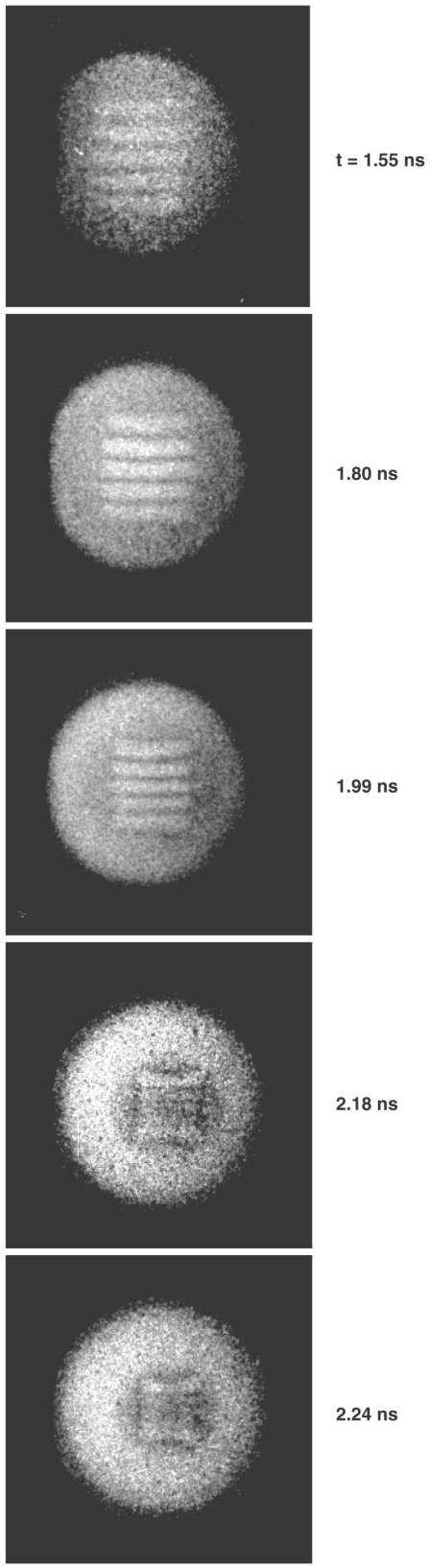

FIG. 6-20. Radiographs of a capsule with $\lambda_0 = 70\ \mu$m perturbations, at $t = 1.55$, 1.80, 1.99, 2.18, and 2.24 ns.

G. Summary of planar and convergent RT instability

In indirect-drive ICF, the achievable implosion velocity, which determines the minimum ignition energy, is approximately proportional to the product of the radiation temperature and the ratio of the shell radius to its thickness, the shell aspect ratio. In the linear phase of Rayleigh–Taylor instability, which dominates indirect drive ignition capsules, the to-

Downloaded 20 Mar 2011 to 69.181.48.121. Redistribution subject to AIP license or copyright; see http://pop.aip.org/about/rights_and_permissions

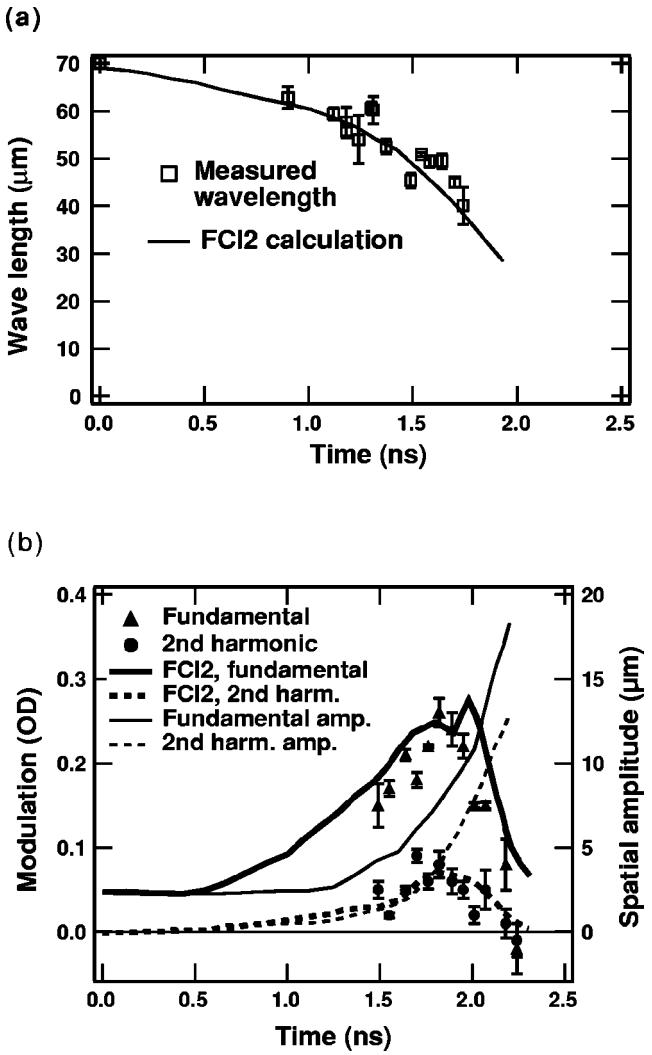

FIG. 6-21. (a) Wavelength determined from the images in Fig. 6-18 as a function of time. (b) Modulation amplitude of the fundamental and first harmonic for the radiographs and simulated radiographs, and simulated modulation at the ablation front.

tal growth of perturbations is a strongly increasing function of the shell aspect ratio. The analytic theory of linear RT growth in the presence of ablation has advanced to the point that there is excellent agreement between detailed numerical calculations and analytic theory. Calculation of a full spectrum of modes into the weakly nonlinear regime in spherical geometry still requires the use of detailed numerical models.

An extensive series of experiments and simulations to examine the growth of single modes over a range of wavelengths, as well as the effect of multiple modes on perturbation growth, has been carried out. For single modes, the perturbation evolves prior to shock breakout due to the rippled shock dynamics. After shock breakout, the perturbations grow rapidly with time in the linear regime and saturate in the nonlinear regime, with the appearance of higher harmonics. For the multimode foils, the individual modes grow independently in the linear regime. In the nonlinear regime, the modes become coupled and the $k_i \pm k_j$ terms are clearly observed, in agreement with simulations and second-order perturbation theory. Mode coupling leads to a redistribution of the existing perturbations in Fourier space, which in physical space results in a change in the perturbation shape. The bubbles become broader and flatter and the spikes narrower. In general there is excellent agreement between the simulations and experiments. However, a small but systematic discrepancy exists between simulations and experiments, with the simulations showing slightly larger growth than observed. This could be caused by greater than expected preheat in the foot of the drive, a less compressible equation of state for CH(Br), or a degraded instrumental modulation transfer function.

Single-mode experiments very clearly indicate the differences in growth between 2D and 3D perturbation shape. Axisymmetric 3D bubbles grow the largest, consistent with a simple buoyancy vs drag argument, with third-order perturbation theory, and with full 3D radiation-hydrodynamics simulations. The evolution of a pattern with a full spectrum of 3D modulations, including the range of modes predicted to be most dangerous for ignition capsules, was measured. This pattern grew into the weakly nonlinear regime and evolved into round, closely packed bubbles separated by narrow, interconnecting spike sheets, correctly simulated with the 3D radiation-hydrodynamics code HYDRA. The experiment and simulation demonstrated that collective nonlinearity occurs in the multimode target when individual mode amplitudes are close to values from the Haan model, much less than the saturation amplitude for a single mode.

Radiation-driven cylindrical and spherical convergent experiments were also performed. In the cylindrically convergent experiments, we observed the RT instability seeded by feedthrough from the outer surface to the inner surface and the presence of Bell–Plesset growth during the stagnation phase. Spherical experiments showed the onset of nonlinearity, in agreement with numerical simulations.

VII. IMPLOSION EXPERIMENTS

A. Introduction to implosion experiments

The indirect-drive implosion experiments in the Hydrodynamic Equivalent Physics (HEP) program, were developed as integral tests of drive, pulse shaping, symmetry, and hydrodynamic instability. Some early implosion experiments (HEP1 and HEP3) had key implosion diagnostic development objectives as well as target physics objectives. The later experiments (HEP4 and HEP5) carried out on Nova and Omega were designed to have a NIF-like hohlraum-to-capsule-size ratio and instability growth similar to that expected on NIF. The HEP4 experiments were limited to convergence ratios of $C<10$ while the HEP5 goal was to get good capsule performance at as large a convergence as possible with the symmetry achievable on the experimental facility being used. The goal in both cases was to develop confidence in the computational capability to model the results so that projections of NIF performance could be tested.

HEP1 was initiated as an experimental series designed to develop quantitative neutron diagnostics for inferring fuel density and mix from measurements of fuel areal density ρR and the secondary neutron spectrum. However, the density of $20-40$ g/cm^3 specified in the HEP1 goal could only be met

Downloaded 20 Mar 2011 to 69.181.48.121. Redistribution subject to AIP license or copyright; see http://pop.aip.org/about/rights_and_permissions

with capsules that had a convergence of greater than 20, where convergence is defined as the initial outer ablator radius divided by the final fuel radius. Achieving this objective required the precision Nova improvements to power and energy balance discussed in Sec. I. Also, the HEP1 experiments (Cable *et al.*, 1994) achieved better symmetry because they utilized a smaller capsule relative to the hohlraum size than planned for NIF. This results in reduced time-dependent asymmetry variations, because of the shorter laser pulses required for the smaller capsule, and increases geometric hohlraum smoothing. These experiments achieved a hot fuel density of 20 g/cm^3, the analog of the hot spot in NIF capsules. These experiments also achieved a density of 150 to 200 g/cm^3 in the material surrounding and compressing the hot fuel, the analog of the dense cold fuel in the NIF targets. Both of these densities were the highest achieved in the Nova experiments. The comparable NIF densities, as discussed in Sec. II, are 70 to 100 g/cm^3 in the hot spot and 900 to 1200 g/cm^3 in the surrounding cold fuel.

The goal of HEP3 was to develop x-ray spectroscopy as a technique for measuring the effects of hydrodynamic instability on implosions. The HEP3 implosions (Dittrich *et al.*, 1994) used constant power 1 ns pulses and the experimental goals required implosions that did not pose a serious challenge to Nova's power and energy balance. The targets were low-growth (perturbations grew by a factor-of-about-10), low-convergence ($C<10$) plastic capsules with a multimode spectrum of initial surface perturbations.

The key implosions of the indirect-drive ignition program (HEP4/HEP5) are intended to be an integral test of the effects of short-wavelength hydrodynamic instability growth combined with long-wavelength variations in x-ray flux.

The capsules in these experiments have been designed to have 4 to 5 e-foldings of Rayleigh–Taylor (RT) instability growth. For Nova capsule sizes and surface finish, this level of RT growth results in mix penetration comparable to that predicted for NIF capsules.

To be as NIF-like as possible, these experiments utilized hohlraums which have the ratio of the hohlraum radius to the capsule radius comparable to that of NIF targets. This ratio governs the geometric smoothing of short-wavelength radiation flux variations as discussed in Sec. IV. The goal of these experiments was to get as close to NIF convergence ratios as was feasible given the symmetry limitations of current experimental facilities. With Nova's basic 10-beam geometry, even capsules with a convergence ratio of $C<10$ are degraded in yield in hohlraums with a hohlraum–to–capsule-radius ratio comparable to that planned for NIF. Current experiments with increased convergence ratio utilize the flexible geometry of the 60-beam Omega laser. On Omega, convergence 10 capsules achieve near ''clean 2D'' yield, where clean 2D refers to a two-dimensional (2D) integrated hohlraum simulation that includes intrinsic flux asymmetry (see Sec. IV) but neglects random flux asymmetry and atomic mix between the pusher and fuel. In recent experiments, convergence-22 HEP5 capsule performance on Omega approaches 40% of clean 2D yield. Most of the performance degradation in these higher convergence implosions can be quantitatively explained by pusher–fuel mix and low-order capsule asymmetries.

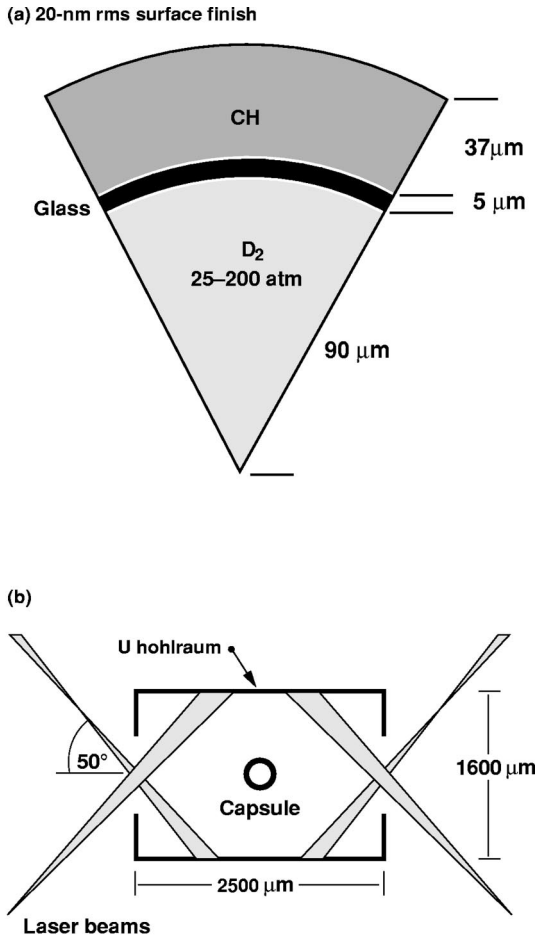

FIG. 7-1. (a) Capsule and (b) hohlraum geometry used for HEP1.

B. HEP1 experiments: Development of quantitative neutron diagnostics for fuel ρr

The HEP1 capsules were indirectly driven gas-filled microballoons as shown in Fig. 7-1(a). The glass capsules were filled with D_2 or an equimolar DT mix. Capsule fill pressures were varied from 25 to 200 atm, which changed the capsule convergence for constant-drive conditions. The capsule was relatively small, with a diameter 16% of the hohlraum diameter. This small capsule helps minimize radiation flux asymmetry. The short pulse required for the HEP1 experiments, because of the small capsule size, also helps minimize time-dependent asymmetry by reducing plasma motion. Even without considering the symmetry benefits, a small capsule was needed so that secondary neutrons could be used for the determination of the imploded fuel areal density. We found that 10 Nova beams (2.1 kJ each at 0.35 μm wavelength) were incident on the interior of a U hohlraum at 2×10^{15} W/cm^2. The hohlraum, shown in Fig. 7-1(b), had a diameter of 1600 μm and length of 2500 μm with a pair of 1200 μm diameter laser entrance holes (LEH). Use of a glass shell and a U hohlraum minimizes the x-ray preheating of the capsule.

Downloaded 20 Mar 2011 to 69.181.48.121. Redistribution subject to AIP license or copyright; see http://pop.aip.org/about/rights_and_permissions

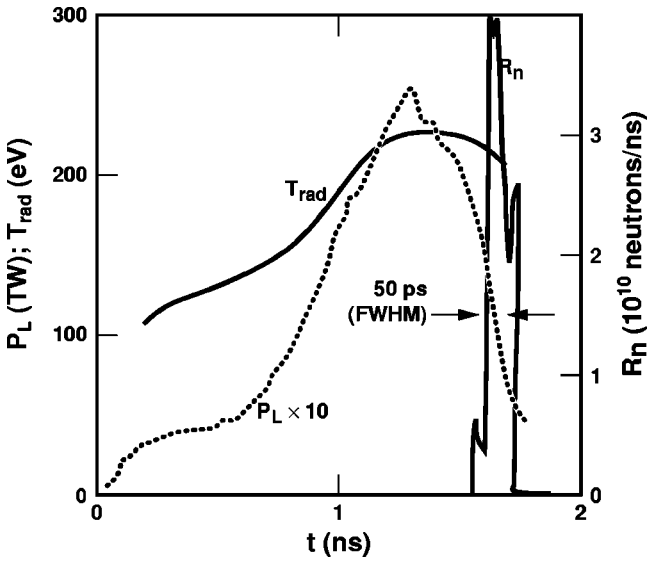

FIG. 7-2. Observed laser power P_L, hohlraum temperature T_r, and neutron production rate R_n for 100 atm DT-filled HEP1 capsules.

The x-ray drive was measured using the Dante diagnostic, described in Sec. IV, looking into the hohlraum at both directly illuminated laser spots and the indirectly illuminated wall (Kornblum *et al.*, 1986); observed spectra were nearly Planckian. Figure 7-2 shows the measured laser power P_L, the corresponding brightness temperature of the x-ray drive T_r, and the neutron production rate R_n. Pulse shaping is required to limit pusher entropy generation by shocks and to keep the pusher dense during inward acceleration.

The small capsule and short pulse help minimize, but do not eliminate, the intrinsic hohlraum asymmetry for these experiments. The time varying wall albedo and spot motion result in a time variation of P_2 with a peak value of 8% even though the time-average is near zero. Random variations in beam power balance and pointing also contribute to asymmetry. The precision Nova improvements (NTIS Document, 1994f), discussed in Sec. I, made it possible to maintain tolerances of 8%-rms beam-to-beam power balance during the foot of the laser pulse and 4% power balance during the peak. Pointing tolerance is $\pm 30\ \mu$m rms. This control gives a power balance on the capsule, from viewfactor simulations, that is uniform to within 2% rms at peak power and 4% in the foot.

Convergence and peak compression are affected by the RT instability at the pusher–fuel interface. Calculations show that perturbations on the interface are primarily seeded by the feedthrough of growing perturbations at the ablation front, which in turn are seeded by initial ablator surface-finish perturbations. Haan's multimode, weakly nonlinear mix model (Haan, 1989a), discussed in Sec. VI C, was applied to calculations of the implosions of the 25 and 100 atm fill capsules. Growth factors (defined as final amplitude at pusher–fuel interface divided by initial amplitude at ablator surface) are calculated in the linear regime at a number of l modes. The rms depth of mix penetration is calculated by multiplying the initial surface-finish mode spectrum by the growth factors, applying the saturation model described in Sec. VI C, and then adding the saturated mode amplitudes in quadrature. With mode saturation applied, most of the quadrature sum of amplitudes at bang time comes from $l \leqslant 20$ for either fill pressure. The growth is almost the same for both fill pressures over this range of modes.

The burn-averaged fuel density and capsule convergence were determined by measuring the burn-averaged fuel areal density $\rho R \equiv \int_{\text{fuel}} \rho(r)dr$. If ρ is uniform, then $\rho = \rho_0(\rho R/\rho_0 R_0)^{3/2}$; thus, a determination of ρR gives both ρ and R. The fuel convergence-C is defined as the ratio of initial outer ablator radius R_{a0} to the final fuel radius R. The uniform-ρ assumption gives a slight underestimate of the actual convergence and density since the actual density must increase with radius as the temperature decreases for an approximately isobaric fuel configuration. From simulations, this correction represents about a 15% effect in the average density for the 25 atm capsules and about a 25% effect in the 100 atm capsules.

Fuel ρR is determined from the secondary-neutron spectrum (Gamalii *et al.*, 1975; Blue and Harris, 1981; Azechi *et al.*, 1986; Cable *et al.*, 1986; Cable and Hatchett, 1987). This technique relies on the observation of 12 to 17 MeV secondary neutrons produced via the $D(T,n)^4He$ reaction in an initially pure D_2 fuel. The 1.01 MeV T nuclei, or tritons, are produced in the primary fusion reaction $D(D,p)T$. If the tritons do not slow significantly as they traverse the fuel, then the fraction of tritons producing secondary neutrons is proportional to the fuel ρR. For the fuel conditions in the HEP1 implosions (low temperature with mixed pusher material), ρR values above a few mg/cm^2 cause significant triton slowing, and corrections must be made for the energy dependence of the $D(T,n)^4He$ cross section (Lindl, 1998b). Since the cross section rises with decreasing triton energy, this correction typically results in a ρR value lower than that calculated for the case of little slowing. The secondary-neutron energy spectrum is measured with an array of neutron time-of-flight detectors referred to as a large neutron scintillator array (LaNSA) (Nelson and Cable, 1992). Figure 7-3 shows a spectrum obtained by summing all the 25 atm capsule data; the figure also shows the spectrum obtained from calculations of these implosions with the Haan mix model.

Observed fuel areal densities, which ranged up to 16 mg/cm^2, resulted in the densities and convergences plotted in Fig. 7-4. For this figure, observed values were averaged over several implosions (two at 200 atm, six at 100 atm, and 10 at 25 atm), and the errors were dominated by statistics related to the number of observed secondary neutrons. Figure 7-4 (a) shows that the observed convergence and (b) density vs capsule fill pressure values are consistent with or better than those expected from simulations if the effects of pusher–fuel mixing are included. Early HEP1 experiments demonstrated that the precision Nova improvements were required to achieve the high convergence ratios indicated in Fig. 7-4. Without the precision Nova improvements, observed convergence decreased as the initial fill was decreased. The calculations labeled ''clean 1D'' do not include mix and assume perfect spherical symmetry. Pusher–fuel mixing introduces two important effects: mixing of higher-Z matter into the fuel enhances the triton slowing, and mixing

Downloaded 20 Mar 2011 to 69.181.48.121. Redistribution subject to AIP license or copyright; see http://pop.aip.org/about/rights_and_permissions

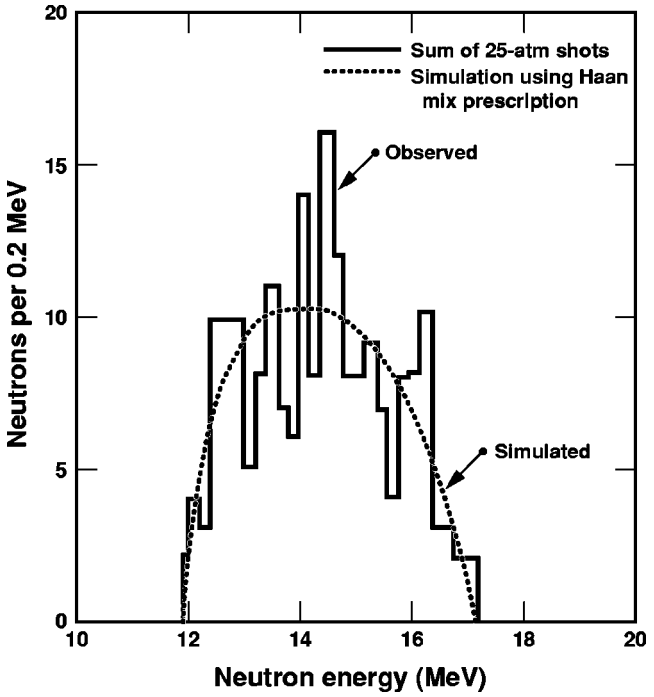

FIG. 7-3. Secondary-neutron energy spectrum measured with array of neutron time-of-flight detectors (LaNSA). Observed is sum of spectra from all 25 atm HEP1 capsules. The shape of the neutron spectrum is well-matched with the Haan mix model.

of fuel outward into the pusher decreases the fuel convergence. Secondary-neutron spectroscopy allows us to quantify these effects since the secondary-neutron energy spectrum is dependent on the rate of triton slowing. Figure 7-3 shows that the calculated and observed secondary spectra are in good agreement, which further validates the mix modeling.

C. HEP3 experiments: Spectroscopic diagnosis of pusher–fuel mix in low-growth-factor implosions

The HEP3 series of Nova experiments used plastic-shelled capsules. A typical capsule shell in the experiment had a 420 μm inside diameter and a 55 μm thick wall, and consisted of three layers as shown in Fig. 7-5. The inner layer was about 3 μm thick and consisted of polystyrene doped with 1.0 at. % Cl. The middle layer was a 3 μm thick permeation barrier made of polyvinyl alcohol (PVA), which sealed in the fuel gas. An outer layer of plasma polymer ($CH_{1.3}$) was deposited over the inner layers (Letts *et al.*, 1981), forming the ablator. The capsule interior was filled with 50 atm D_2 and doped with 0.1 atm Ar. The Cl tracer in the shell and Ar in the fuel are spectroscopic tracers (Hauer *et al.*, 1991; Keane *et al.*, 1993; Hammel *et al.*, 1994a) for x-ray radiographic imaging and spectroscopy of the imploded core.

All 10 beams of the Nova laser were used to indirectly drive the imploding capsules. A square pulse of laser light with duration of 1 ns heated the Au cylindrical hohlraum with nominally 17 kJ of laser energy. The hohlraum had a diameter of 1600 μm and length of 2750 μm with a pair of 1200 μm diameter laser entrance holes. A peak radiation temperature of 230 eV was reached.

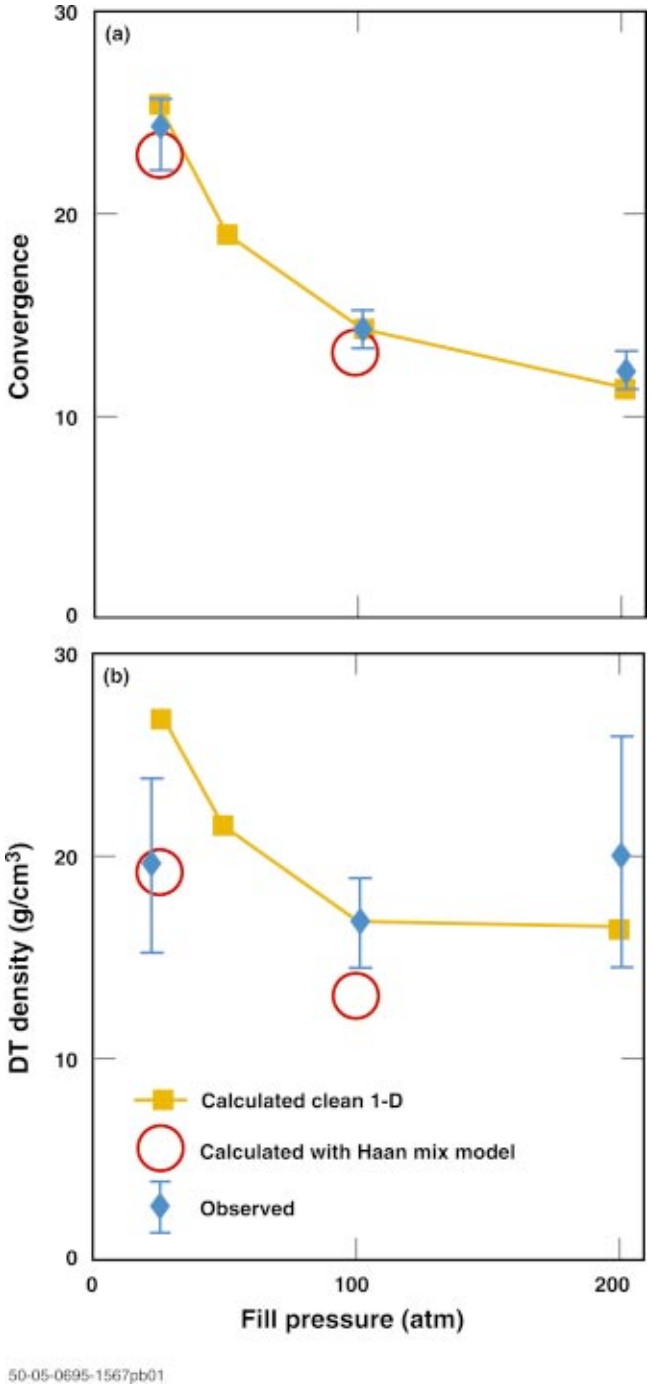

FIG. 7-4. (Color) Observed and calculated (a) convergence and (b) density vs capsule fill pressure for the HEP1 experiments. The experimental measurements and calculations of convergence are in good agreement. Density, expressed as equivalent DT fill even when the capsule has a pure D_2 fill, is proportional to the cube of the convergence ratio and is highly sensitive to errors in the measurement.

The capsules had relatively low convergence (about 8) and had considerably less sensitivity to growth of surface perturbations compared to that predicted for the NIF. The implosions were designed with low convergence and short pulse lengths so that asymmetries in the x-ray drive would have little impact on the implosions.

To make capsules with various degrees of surface roughness, many polystyrene beads, ranging in diameter from 0.6

Downloaded 20 Mar 2011 to 69.181.48.121. Redistribution subject to AIP license or copyright; see http://pop.aip.org/about/rights_and_permissions

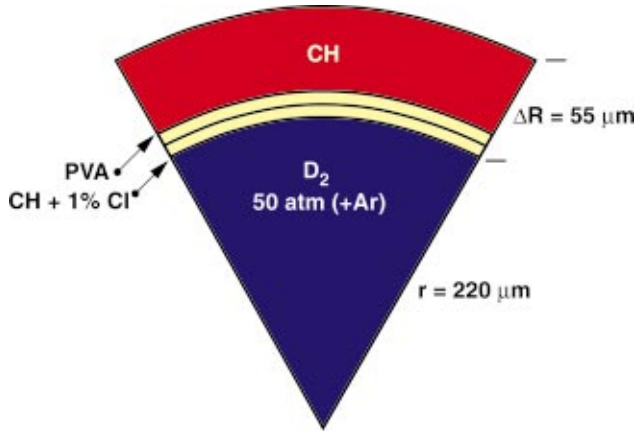

FIG. 7-5. (Color) Schematic of the capsules used in the HEP3 experiments.

to 7 μm, were embedded in the PVA layer. When the ablator layer was deposited onto this rough PVA surface, the perturbations were imprinted on the outer surface as shown in Fig. 7-6(a). This approach to varying the surface roughness was used prior to the development of the more precise laser surface ablation technique used in the HEP4 experiments.

Atomic force microscope (AFM) (NTIS Document, 1994f) equatorial traces were taken of capsules from the capsule production runs used for these experiments. The equatorial AFM traces are converted to power spectra and combined to form ensemble averages. By assuming that the surface bumpiness is isotropic, these 1D average power spectra are transformed into 2D (spherical surface) power spectra (NTIS Document, 1994c):

$$P_{2D}(l)=\left(l+\frac{1}{2}\right)\sum_{n=l,l+2}^{\infty}[P_{1D}(n)-P_{1D}(n+2)]\times\frac{(n+l)!!(n-l-1)!!}{(n-l)!!(n+l+1)!!},\qquad(7\text{-}1)$$

where l is the perturbation mode number, P_{1D} is the 1D power spectrum and P_{2D} is the 2D power spectrum. Figure 7-6(b) shows 2D (spherical surface) power spectra of capsules with rms=0.03, 0.31, and 1.75 μm.

Diagnosis of enhanced pusher–fuel mix due to these surface perturbations was performed primarily by looking at the variation with roughness of the Ar and Cl dopant x-ray self-emission (Hammel *et al.*, 1993a). The Cl x-ray emission from the dense shell or pusher surrounding the fuel, is expected to increase relative to the x-ray emission of the fuel dopant, Ar, as the surface roughness is increased. In the temperature and density regime of this experimental series, the variation of x-ray line radiation from these dopants is strongly dependent on temperature. During the implosion, $P\,dV$ work heats the fuel and the Ar, but the Cl is heated via conduction enhanced by mixing of the fuel and the surrounding shell. To track the dynamics of the mix region, the x-ray emission was monitored by means of a crystal spectrometer coupled to an x-ray streak camera. This diagnostic had a temporal resolution of about 30 ps and a spectral resolving power $(\lambda/\delta\lambda)\approx 700$ (Hammel *et al.*, 1990).

Figures 7-7(a) and 7-7(b) show the observed and simulated spectra at peak x-ray emission for the implosion of a smooth (0.03 μm rms) capsule. Very little Cl Ly-α emission, relative to Ar Ly-α, is evident in either of these spectra. The simulations indicate that 6% of the total Cl mass has reached at least 600 eV. The simulated Ly-α satellite line strengths, on the low-energy side of the Ly-α lines, differ from those observed, and the large absorption feature evident in Fig. 7-7(b) at 2.75 to 2.80 keV is probably due to errors in calculating the opacity of the Cl He-α line in the colder plastic away from the pusher–fuel interface. Figures 7-7(c) and 7-7(d) show the spectra from an intermediate-roughness (0.31 μm rms) capsule. In this case, the Ly-α emission from both the Cl and Ar is comparable in strength, and 10% of the total Cl mass (according to simulations) has reached at least 600 eV. Figures 7-7(e) and 7-7(f) show the spectra from a very rough (1.75 μm rms) capsule. In this case, the Cl Ly-α emission is stronger than the Ar Ly-α emission, and 15% of the simulated total Cl mass has reached at least 600 eV. The simulations show that between the smooth and rough surface capsules, the Cl Ly-α emission increased by 350% but the Ar Ly-α emission decreased by only 30%.

The temporal history of the emission also differs between the smooth and bumpy capsules. For the smooth cap-

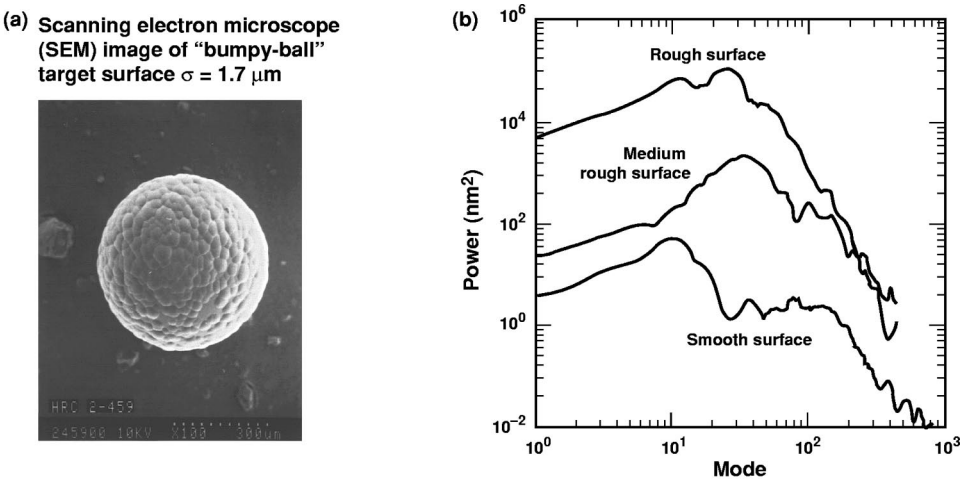

FIG. 7-6. (a) Scanning electron microscope (SEM) image of ''bumpy-ball'' target with a target surface $\sigma=1.7$ μm. (b) The 2D (spherical surface) power spectra characterizing the outer surface of three representative HEP3 capsules with rms=0.03, 0.31, and 1.70 μm.

Downloaded 20 Mar 2011 to 69.181.48.121. Redistribution subject to AIP license or copyright; see http://pop.aip.org/about/rights_and_permissions

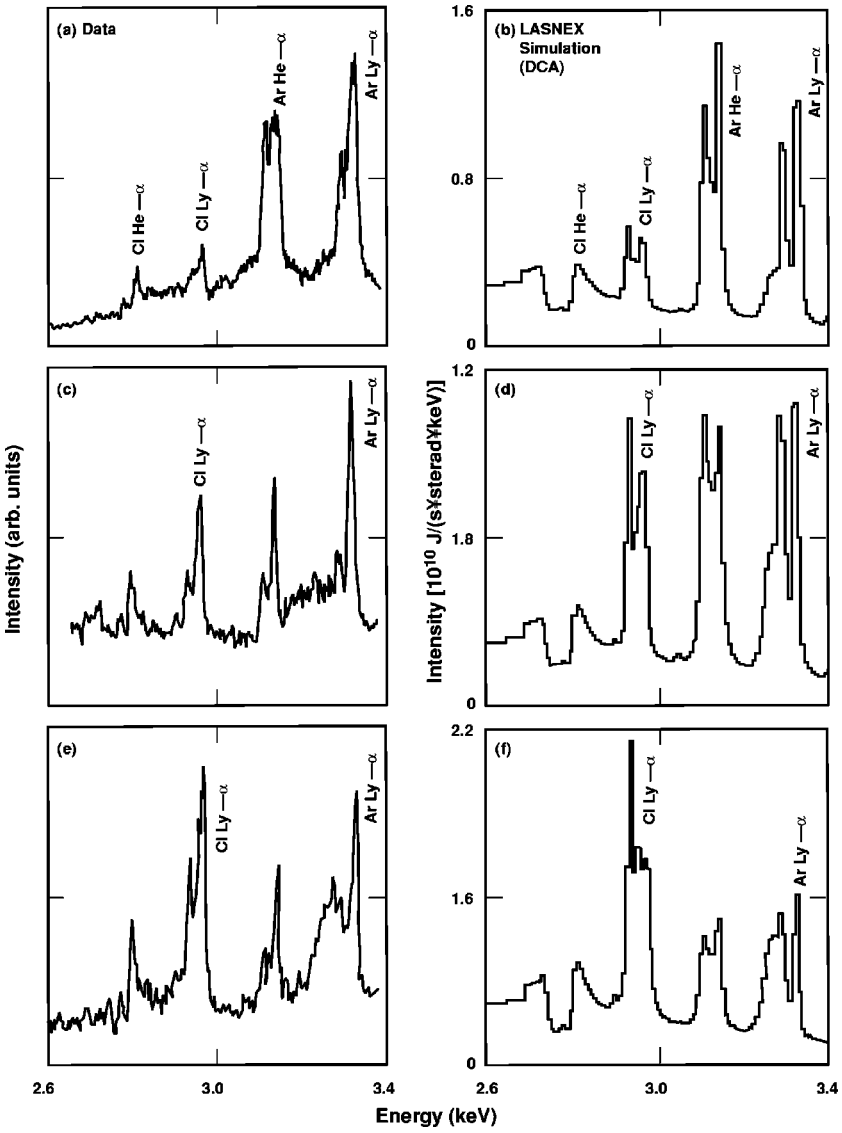

FIG. 7-7. (a) Data as observed by the streaked crystal spectrometer and (b) 1D LASNEX calculation using detailed configuration accounting of the spectra at peak x-ray emission from the implosion of a smooth-surface capsule ($\sigma = 0.03\ \mu$m). Relevant emission lines of Cl and Ar are labeled. Intensity units are 10^{10} J/s/ster/keV; (c) data and (d) calculation for an intermediate-roughness capsule ($\sigma = 0.3\ \mu$m); (e) data and (f) calculation for a rough ($\sigma = 1.7\ \mu$m) capsule.

sule, the Ar emission is strong and starts early while the Cl emission is weak and starts later, when electron conduction from the fuel region heats up the pusher. For the most strongly perturbed capsules, the Ar and Cl emission come on almost at the same time with weaker Ar emission and stronger Cl emission.

D. Nova HEP4 experiments: Diagnosis of pusher–fuel mix and capsule performance in high-growth-factor implosions with convergence $C<10$

The HEP4 experiments use plastic capsules with a mid-Z dopant to suppress preheat, as well as a shaped laser pulse. These changes, relative to the HEP3 capsules, result in the implosion of denser, thinner shells, which more efficiently couple kinetic energy into compression. The peak calculated hydrodynamic instability growth factor of about 100 is within about one e-folding of that expected for NIF capsules.

Figure 7-8 shows the mix amplitudes vs surface roughness calculated using the Haan mix model for the low-growth-factor HEP3 implosions, the Nova HEP4 implosions, and the anticipated NIF conditions. These mix widths are obtained from the Haan mix model using the growth-factor spectrum calculated for the different implosions. A typical intrinsic surface roughness power spectrum from a nominally smooth Nova capsule was used for these calculations. The gray lines with constant slope correspond to the absence of saturated growth. The departure from constant slope for each black curve is the result of growth saturation. As discussed in Sec. II, ignition for NIF will require that the final mix amplitude not exceed about one-third of the converged capsule radius. This criterion is equivalent to a yield reduction of 1/3 to 1/2 for nonigniting target designs such as those used in HEP4. If there were no growth saturation, NIF capsules would need to be smoother by a factor of 2–3. The HEP4 experiments were designed to span both sides of the saturation threshold by varying initial surface roughness from 0.01 μm rms upward. A specific goal of the HEP4 campaign was to test the validity of the growth-saturation model. Although a 1D atomic mix model has proved successful in interpreting many features of ICF implosions, the shell material in 2D and 3D calculations of the effect of perturbations feeding through the shell is not physically mixed with the fuel, as the

Downloaded 20 Mar 2011 to 69.181.48.121. Redistribution subject to AIP license or copyright; see http://pop.aip.org/about/rights_and_permissions

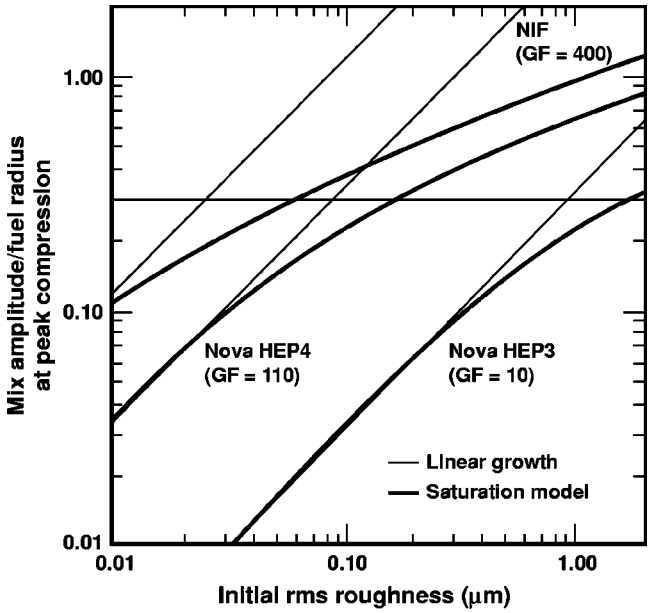

FIG. 7-8. Calculated mix amplitude (normalized to fuel radius at peak neutron emission time) vs initial surface roughness. Starting from the right, the three curves correspond to the low-growth HEP3 design, the higher-growth HEP4 design, and the NIF design. Black and gray curves correspond to calculations with and without growth saturation, respectively. The section of the NIF curve above a normalized mix amplitude of 0.33 corresponds to loss of ignition for the baseline ignition capsule discussed in Sec. II.

term ''mix'' usually implies. Instead, the pusher–fuel interface consists of well-developed bubbles and spikes that penetrate the pusher and fuel, respectively. Nonlinear saturation effects, ablation stabilization and reduced shell ''feedthrough'' result in small amplitudes for very-short-wavelength perturbations. The growth-factor for long-wavelength features is relatively small. Because of this combination of effects, as discussed in Sec. II on NIF target design, the bubble and spike features that dominate during the implosion phase are typically in modes $l=15$ to 30. For perturbations in this wave-number range, as discussed in Sec. II, the heat loss from the fuel to the surrounding dense shell is essentially the same for a 1D atomic mix model as for a 2D or 3D multimode calculation with the same depth perturbed region. However, some features of the implosion require detailed modeling of the interface, and the effects of long-wavelength perturbations with $l<10$ are not well approximated by atomic mix. With recent increases in computer speed and memory, it is now routine to directly model the full spectrum of modes that affect ICF implosions in 2D. It is now possible to cover a wide range of modes in 3D calculations, including both long-wavelength asymmetry effects and shorter-wavelength instability effects in an integrated 3D calculation. Both 2D and 3D calculations have been used in the modeling of the HEP4 experiments.

Figure 7-9 shows the cross section of a typical capsule used in the HEP4 experiments. The ablator is plasma-polymerized plastic ($CH_{1.3}$), typically 39 μm thick, and is doped (Cook *et al.*, 1994) with up to 3 at. % Br or Ge. The inner few microns of the shell consist of a CH mandrel, doped with 0.07% Ti for the spectroscopy experiments. A 3 μm polyvinyl alcohol (PVA) intermediate layer serves as a

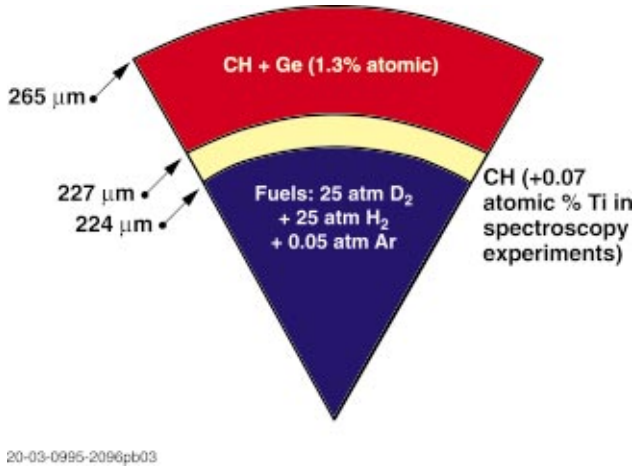

FIG. 7-9. (Color) Cross section of a typical capsule design for the HEP4 campaign. For spectroscopy experiments, the inner CH shell had a Ti dopant. The D_2 fuel was diluted with H_2 to limit the yield in order to avoid saturation of the LANSA neutron detector array.

diffusion barrier for the fuel. The fuel consists of 25 atm each of D_2 and H_2, doped with 0.05 at. % Ar. Dilution of the D_2 with H_2 was necessary to reduce the neutron yield in order to avoid saturation in the secondary-neutron detector. Figure 7-10 shows the initial shell optical depth vs photon energy and demonstrates, for example, that 1.3 at. % Ge doubles the initial capsule optical depth above the Ge ($n=2$) bound-free absorption edge at 1.2 keV. Simulations using the measured photon flux above 1.2 keV indicate that such shielding reduces the entropy of the inner-shell surface relative to the undoped case by 20% before the first shock arrives at 1 ns. The Ar serves as a noninvasive emission diagnostic of electron temperature and electron density and of the spatial profile of the fuel during the burn phase. The Ar and Ti concentrations are calculated to be low enough that they do not appreciably affect the implosion hydrodynamics of these moderate convergence (8–10) capsules.

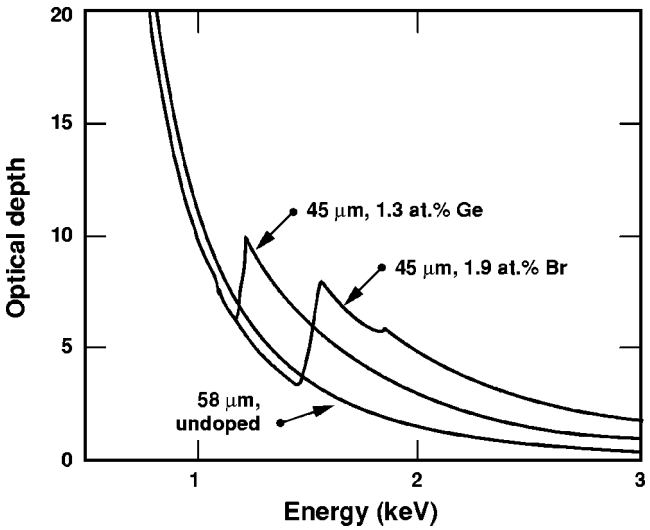

FIG. 7-10. Initial capsule ablator opacity vs photon energy for 58 μm thick undoped plastic ablators and for 45 μm thick ablators doped with either 1.3 at. % Ge or 1.9 at. % Br.

Downloaded 20 Mar 2011 to 69.181.48.121. Redistribution subject to AIP license or copyright; see http://pop.aip.org/about/rights_and_permissions

The RT seeding is provided by preroughening the capsule surface by UV laser ablation (NTIS Document, 1994e) of 200 randomly distributed 75 μm diameter pits of equal depths. This process yields a continuous distribution of perturbation wave numbers. The surface roughness is quantified by averaging a series of circumferential depth profiles obtained by atomic force microscopy. The profiles are Fourier-transformed to yield 1D power spectra, which are found to be in excellent agreement with spectra predicted by a model assuming randomly located pits of the measured shape. By assuming that the surface bumpiness is isotropic, these 1D average power spectra are transformed into 2D (spherical surface) power spectra as discussed for HEP3. These spectra serve as input to simulations of instability growth. The surface roughness is defined to be the square root of the summed power spectra, expressed as a rms roughness. For the purposes of defining roughness, the lowest-order modes ($l<10$), which grow the least, are not included. The baseline capsule has an rms surface perturbation of 175 Å on both its inner and outer surfaces, corresponding to the best capsules available for Nova experiments. In addition to the baseline capsule, capsules with outer-surface rms perturbations of 0.1, 0.2, 0.4, and 1.0 μm were fielded. (The inner surface was not modified and was assumed to have a surface finish of 175 Å, equivalent to the outer surface of an unmodified capsule.)

The capsules are mounted in the center of a 2400 μm long, 1600 μm diameter Au hohlraum with 1200 μm diameter LEHs on each end. A hohlraum of pentagonal cross section was used to avoid line focusing of reflected laser light onto the capsule surface, as is observed with cylindrical hohlraums. X-ray and optical measurements indicate that such line foci reach irradiances of 10^{14} W/cm^2 over the first 200 ps, which could seed RT-unstable perturbations of similar magnitude to some of the smaller-amplitude ablated pits.

The soft x-ray drive was generated by irradiating the inner hohlraum walls with all 10 beams having the ''precision Nova'' accuracy described earlier. Figure 7-11(a) shows the absorbed power (accounting for measured time-dependent SRS and SBS laser backscatter) from a ramped five-to-one contrast ratio pulse shape (PS26), chosen to provide reduced shock preheating which approximates ignition-scale drive. The average x-ray flux at the capsule, plotted in Fig. 7-11(a) as a blackbody flux temperature, was inferred from filtered, time-resolved, multichannel (Dante) measurements of x-ray re-emission from the hohlraum walls. Measurements were performed on both laser-irradiated and unirradiated walls. The drive was independently inferred from simultaneous UV shock breakout measurements (Kauffman *et al.*, 1995) using Al wedges [Fig. 7-11(b)] as described in Sec. IV; the results are in good agreement with simulations based on the measured drive shown in Fig. 7-11(a). The peak drive temperature was 237 ± 7 eV. The uncertainty in drive is primarily a systematic uncertainty due to calibration uncertainty in the Dante channels.

Harder x rays from the high-temperature, low-density Au laser plasmas (principally Au $n=4$ to $n=3$ and $n=5$ to $n=3$ transitions between 2 and 4 keV) directly heated by the laser beams are also present. Figure 7-10 shows that the ablator optical depth is only 1 to 2 for these x rays, making

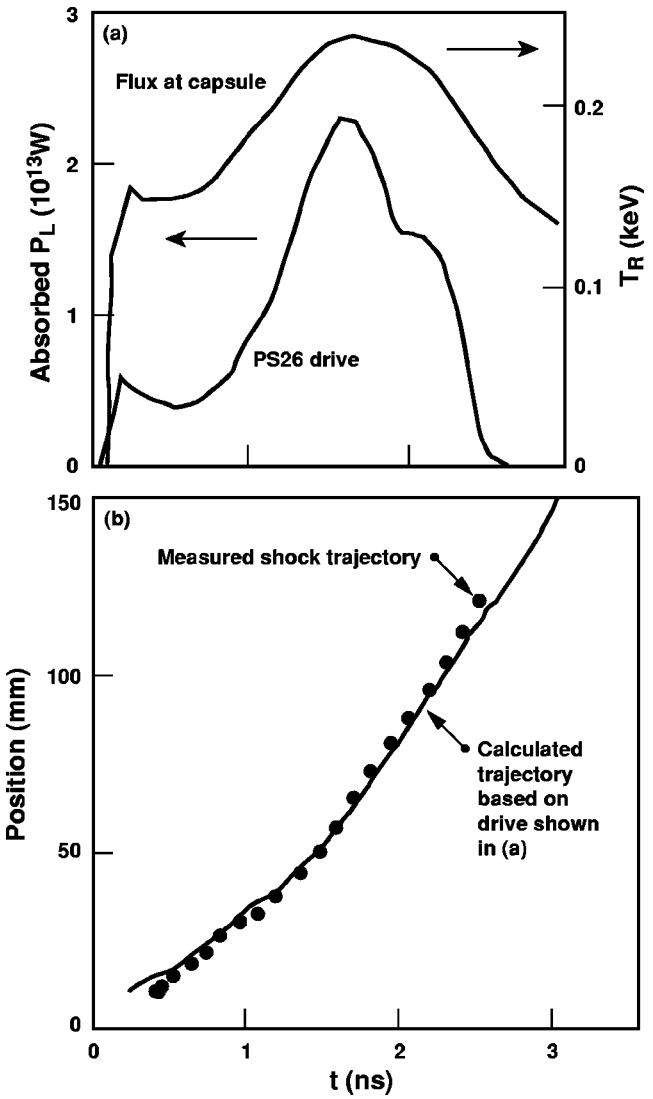

FIG. 7-11. (a) Measured absorbed laser power and measured soft x-ray flux (plotted as a blackbody flux temperature) for the Nova HEP4 experiments from absolutely calibrated filtered diode array (Dante). (b) Measured shock trajectory in Al wedge and corresponding predicted trajectory based on the x-ray drive in (a).

them an important source of preheating of the inner shell. Their fractional contribution to the total drive at the capsule (shown in Fig. 7-12) was determined from a solid-angle average formed by combining the Dante localized absolute flux measurements with 2D spatially resolved x-ray images of the hohlraum wall. The error bars represent only Dante uncertainties; the assumption of an optically thick Lambertian source for the harder x rays may result in an additional factor-of-2 underestimate of their fraction. However, simulations show that admitting a total factor-of-3 underestimate in hard x-ray fraction will decrease yields for 1.3 at.% Ge-doped capsules by only 30%.

The implosions are diagnosed by primary and secondary neutron yields (Cable and Hatchett, 1987), neutron production times (Lerche *et al.*, 1993), time-resolved x-ray imaging (Kilkenny, 1991), and time-resolved x-ray spectroscopy of tracer dopants in the shell and fuel (Campbell, 1991; Hammel *et al.*, 1994a; Keane *et al.*, 1994; Keane *et al.*, 1995;

Downloaded 20 Mar 2011 to 69.181.48.121. Redistribution subject to AIP license or copyright; see http://pop.aip.org/about/rights_and_permissions

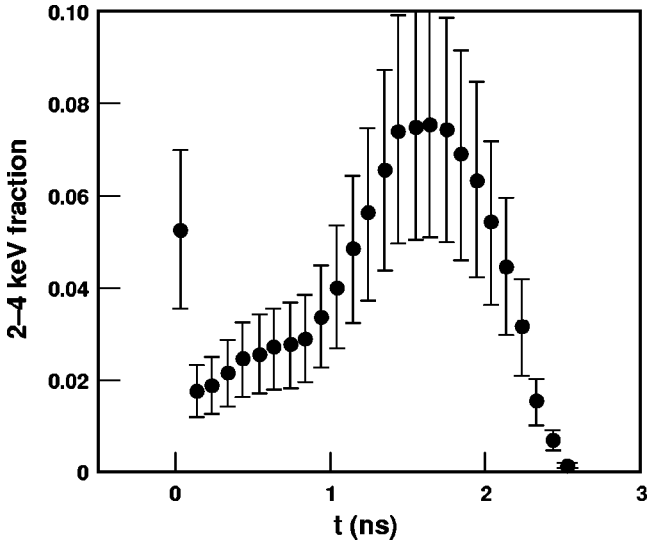

FIG. 7-12. Estimated 2–4 keV flux on the Nova HEP4 capsule as a fraction of total x-ray power. Error bars represent only the uncertainty in Dante calibration and spectral unfold; additional uncertainty in the angular distribution could result in another factor-of-2 uncertainty. Capsule preheat largely arises from photons in this region of the x-ray spectrum which come from Au M-lines.

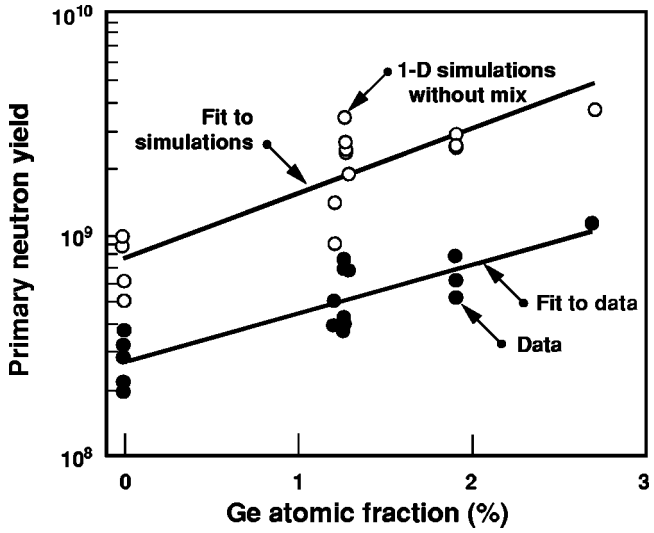

FIG. 7-13. Measured and calculated primary (DD) neutron yields from 1D simulations without mix or asymmetry vs doping for smooth capsules. Solid lines are linear fits to data and simulations. Doping the capsules to suppress radiative preheat results in denser implosions. Capsule yield increases with doping as expected but absolute yields are degraded by mix and asymmetry.

Keane *et al.*, 1995a; Keane *et al.*, 1995b; Landen *et al.*, 1995). Results are compared with predictions from LASNEX (Zimmerman and Kruer, 1975) and the 3D radiation hydrodynamics code HYDRA (NTIS Document, 1995b; Marinak *et al.*, 1995; Marinak *et al.*, 1996).

The first HEP4 implosions were used to test the behavior of the smoothest available plastic capsules as the ablator doping was increased. The doping decreases the preheat, which results in lower entropy and a higher shell density. In the limit of negligible RT growth, the increase of in-flight shell density increases the coupling of shell energy into the fuel (Meyer-ter-Vehn, 1982; Lindl *et al.*, 1992), resulting in increased final fuel areal density and neutron yield.

Figure 7-13 shows that the measured yield does indeed increase with Ge doping, with a slope about nearly 70% of that of the corresponding 1D simulations. Peak neutron production times (2.2 ± 0.1 ns) and hence implosion velocities were kept fixed by varying the initial ablator thicknesses (from 44 μm at 2 at. % Ge to 58 μm for undoped ablators) to compensate for changes in initial shell density and opacity when incorporating Ge in the ablator. Capsules were selected for best surface finish (<0.03 μm rms roughness). The simulations used the measured drive flux and spectrum at each time as baseline input, with slight modifications for ($<10\%$) shot-to-shot variations in laser energy and capsule dimensions. The systematic factor-of-3-to-4 difference between calculated 1D yields and measured yields for smooth capsules is largely reproduced by 3D calculations discussed below. These calculations account for intrinsic hohlraum asymmetry and long-wavelength variations in capsule thickness.

Figure 7-14 displays 4 keV x-ray snapshots showing a reduction in imploded core image size as the ablator doping is successively increased from (a) zero to (b) 1.3 to (c) 2.7 at. % Ge. The imploded cores, imaged with 7 μm and 80 ps resolution by gated pinhole cameras, are dominated by Ar free-bound emission from the doped fuel. Figure 7-14(d) shows the azimuthally averaged 50% contour diameters extracted from such images. The average measured x-ray radii decrease monotonically with increasing Ge doping, with a slope about 80% of that calculated from post-processed 2D integrated hohlraum and capsule simulations of the image size, but with an overall 30% reduction in size. Fuel areal densities and (by invoking particle conservation) fuel convergences were also inferred from the fraction of secondary DT reactions and the resultant secondary-neutron energy spectrum (Cable and Hatchett, 1987) measured by the LaNSA (NTIS Document, 1994) diagnostic. At all values of Ge doping, the inferred fuel convergences from secondary neutrons are within 10% of the values obtained from simulations. To reconcile the x-ray size discrepancy with the agreement in neutron-inferred convergence, we note that emissivity for keV x-ray photons is sensitive to sub-keV variations in plasma temperature, while the secondary reaction between MeV tritons and deuterons is not. Hence the 30% overprediction in x-ray core image size shown in Fig. 7-14(d) may be evidence that the 2D simulations without mix, while correctly predicting the final fuel radius, overpredict the plasma temperature in the outer regions of the compressed fuel. Such increased cooling is seen in 3D calculations that include long-wavelength variations in capsule wall thickness. Moreover, predicted H-like emission from Ti dopant in the inner portion of the shell was not observed during the spectroscopy-based series of implosions, again suggesting that the volume comprising the outer regions of the fuel and the inside of the shell is cooler than predicted in 2D calculations.

Figure 7-15 shows primary neutron yield for undoped and doped capsules vs initial surface roughness. Between best surface finish (<0.03 μm rms) and 1 μm rms rough-

Downloaded 20 Mar 2011 to 69.181.48.121. Redistribution subject to AIP license or copyright; see http://pop.aip.org/about/rights_and_permissions

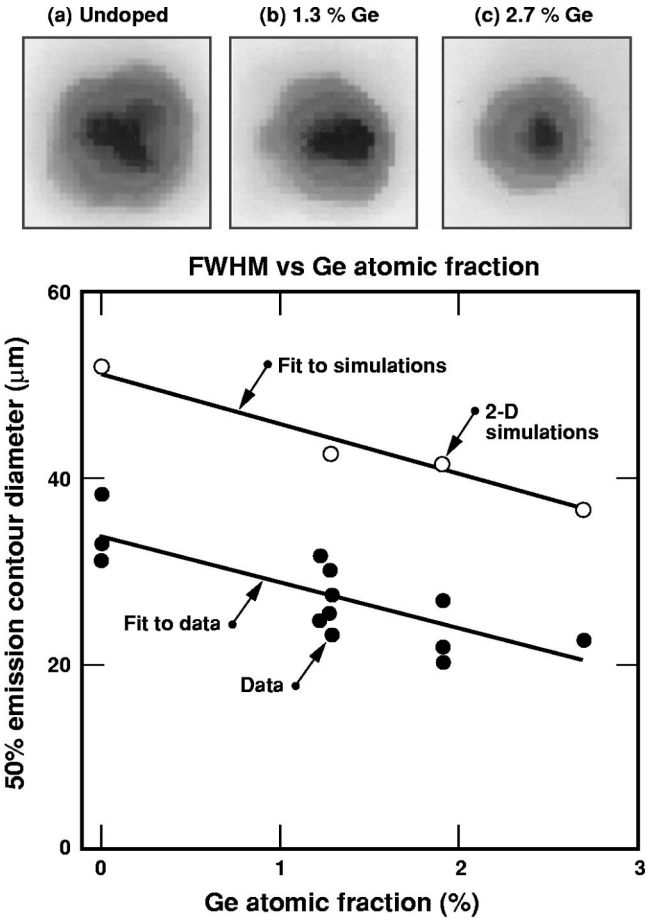

FIG. 7-14. X-ray images at 4 keV of imploded cores from smooth capsules at peak emission time for (a) no doping, (b) 1.3 at. % Ge, and (c) 2.7 at. % Ge. (d) Measured (solid circles) and calculated (open circles) azimuthally averaged diameters of 50% x-ray emission contours vs Ge doping. Solid lines are linear fits to data and simulations. The predicted smaller size of the x-ray emitting region as doping increases is consistent with the observations, although the absolute size of the emitting cores is smaller than calculated.

ness, the yields of undoped capsules drop by a factor of only 1.5, while those of 1.3 at. % Ge-doped capsules drop by a factor of 6. This finding is qualitatively consistent with the transition from low-growth-factor (about 10) to high-growth-factor (about 110) behavior expected with doping the ablator. Moreover, there is a statistically significant factor-of-2 yield degradation between doped capsules with best surface finish and doped capsules with 0.2-μm rms roughness; from Fig. 7-8, the latter correspond closely to the 33% mix penetration depth that marks the ignition threshold in typical NIF ignition capsule designs.

Figure 7-16 compares the averaged doped capsule yields vs surface finish with various simulation results. The lowest curve, which represents the atomic mix model with no saturation, severely overestimates the yield degradation for large initial surface roughness. The other curves represent the same model corrected for the different saturation behavior predicted for 3D or 2D multimode growth (Keane *et al.*, 1995b). The 3D atomic mix model is in fairly good agreement with data at the rough end, i.e., rms roughness >0.2 μm. The larger yield degradation calculated for the 3D saturation model is a consequence of the later onset of saturation (Haan, 1989a) and of the higher terminal velocity of low-density 3D fuel bubbles rising into the shell as discussed for planar experiments in Sec. VI. The atomic mix model with the 2D saturation prescription, although not consistent

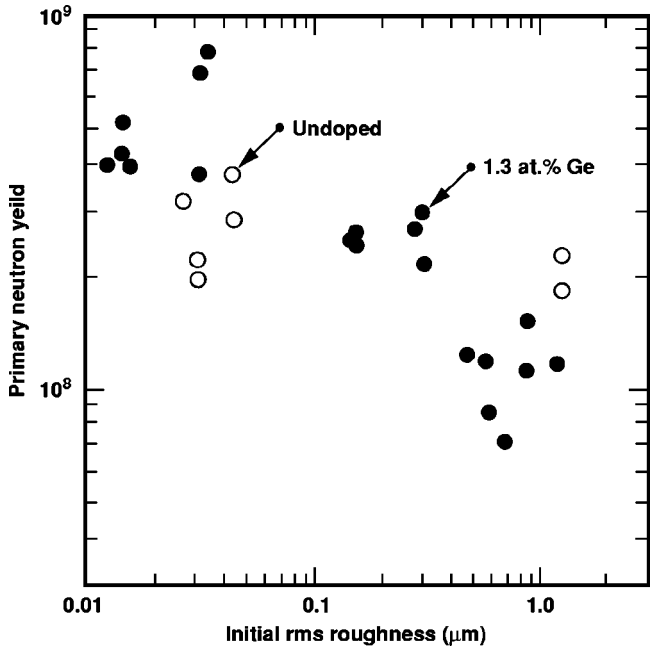

FIG. 7-15. Measured primary neutron yields for 1.3 at. % Ge-doped (solid circles) and undoped (open circles) capsules vs initial rms surface roughness. As expected, the yield of the denser more unstable doped capsules, is more sensitive to surface roughness than the undoped capsules.

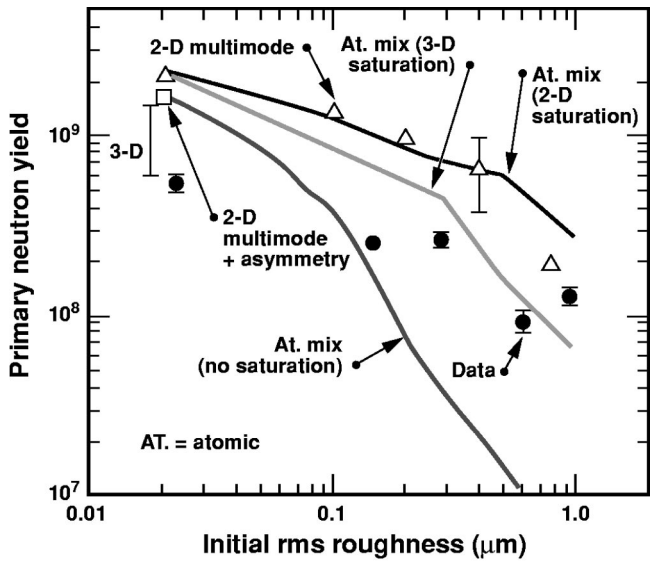

FIG. 7-16. Measured and calculated primary neutron yields for 1.3 at. % Ge-doped capsules vs initial surface roughness. Solid circles are averaged data points from Fig. 7-22. Solid curves are predictions from the atomic mix model with no saturation, with 2D saturation, and with a 3D saturation prescription. The square and the triangles are predictions from 2D multimode simulations with and without intrinsic long-wavelength hohlraum flux nonuniformities. The vertical line at the upper left-hand side represents the range of yields calculated by the 3D HYDRA code for a smooth capsule by varying the relative orientation between low-order capsule and radiation flux nonuniformities.

Downloaded 20 Mar 2011 to 69.181.48.121. Redistribution subject to AIP license or copyright; see http://pop.aip.org/about/rights_and_permissions

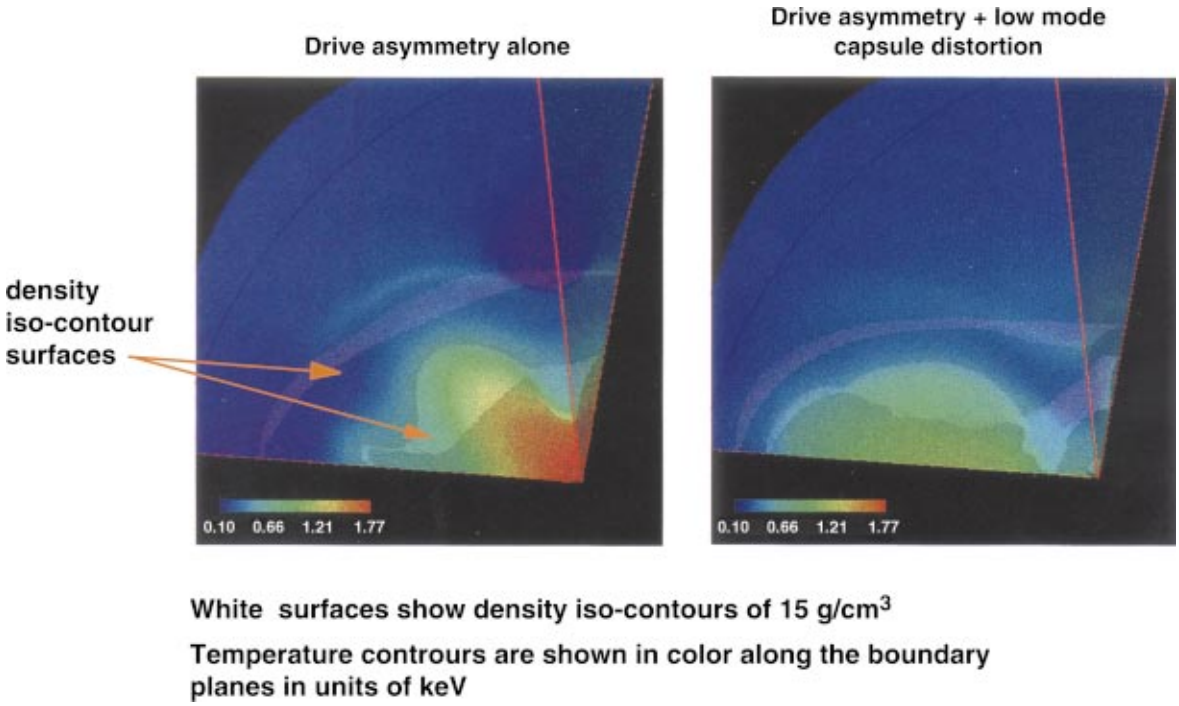

FIG. 7-17. (Color) 3D calculations of the HEP4 capsule implosions on Nova: (a) The distortion of an implosion due to Nova's intrinsic hohlraum radiation asymmetry. Nova's fivefold radiation pattern can be calculated with the 36° slice shown. Although the distortions shown are significant, the yield degradation from an unperturbed calculation is only about 30%. (b) The enhanced distortion which results from including a 2 μm offset between the inner and outer plastic shell surfaces, which was typical in the targets used in the HEP4 experiments, provides enough additional distortion that the temperatures are significantly lowered and the yield is reduced by about an additional factor of 2. With this level of degradation, the calculated and observed yields for smooth capsules are in agreement.

with the 3D nature of perturbation growth in the experiment, is included to show good agreement with 2D finely zoned multimode simulations (shown as triangles).

In the 2D multimode simulations, the 3D nature of the perturbations is accounted for by adjusting the 2D surface power spectra so that each mode makes the same relative contribution to the total rms roughness as in 3D. Since 2D simulations are carried out on a 90° quadrant of the capsule, power in odd modes is ''aliased'' into the adjacent even modes. At peak neutron emission time, the 2D simulations show classic ''bubble and spike'' saturated RT growth for the dominant modes at the pusher–fuel interface for initial surface roughnesses greater than 0.1 μm. The effects of low-mode drive nonuniformities, which distort the pusher–fuel interface, were included in some 2D multimode calculations. For example, the predicted extra yield degradation due to flux nonuniformities for a smooth, doped capsule is about 30%, as shown by the square in Fig. 7-16. The remaining factor-of-2-to-3 yield discrepancy, which remains for smooth capsules, can be largely accounted for in 3D calculations by long-wavelength capsule wall thickness variations coupled to the intrinsic hohlraum asymmetry.

In these 3D capsule-only calculations, the azimuthal variation associated with Nova's five laser spots on each end of the hohlraum has a fundamental period corresponding to $m=5$, which can be simulated over a 1/20 sphere that covers 90° in polar angle and 36° in azimuthal angle. Time-varying $m=0$ components of drive asymmetry imposed on the capsule in the HYDRA simulation are obtained from a LASNEX integrated hohlraum simulation. The azimuthally varying $m=5$ components of the drive asymmetry are obtained from an analytic estimate that uses a calculated time-varying albedo. Contributions to asymmetry due to pointing errors and beam power imbalance are not modeled. The imploded shape is shown in Fig. 7-17(a). In this figure, the $\rho=15$ g/cm^3 contour is shaded white, and the color shading represents the fuel temperature, which reaches a peak of about 1.7 keV. The time chosen is near the time of peak burn rate for an unperturbed calculation and is also near the peak burn rate for this 3D calculation. Bubbles are rising halfway between the hohlraum equator and the pole, nearest the locations of the laser spots. Spikes are rapidly approaching the center of the hot spot near the equator. These spikes reach the center of the hot spot after the calculated bang time for an unperturbed, spherical implosion and thus have only a modest effect on the yield. The calculated yield, 1.44×10^9, is equal to 59% of that for a perfectly spherical implosion, and 92% of the yield obtained when only $m=0$ terms are included.

In addition to the imposed short-wavelength surface perturbations and drive asymmetry, there are long-wavelength asymmetries associated with the fabrication of Nova capsules. The surface roughness of ''smooth'' capsules, i.e., those without imposed laser-ablated patterns, is quantified from a series of circumferential depth profiles recorded by atomic force microscopy and from interferometry measurements. These techniques provide reliable measurements of the low-mode components ($l<10$) of intrinsic capsule asymmetry. The measurements show that the smooth capsules can

Downloaded 20 Mar 2011 to 69.181.48.121. Redistribution subject to AIP license or copyright; see http://pop.aip.org/about/rights_and_permissions

have significant low-l mode components in thickness. Interferometry indicates that a $P1$ perturbation in the concentricity of shell inner and outer surfaces of 4 μm peak to valley is typical. Individually, these long-wavelength thickness variations cause gross asymmetries in the capsule shape, but have only a modest impact on the yield. However, the effect of these long-wavelength perturbations can be much more significant when coupled to the spikes that develop from shorter-wavelength surface perturbations or variations from flux asymmetry. This coupling to other sources of long wavelength asymmetry depends upon how the very-low-mode surface perturbations are oriented relative to the hohlraum axis. This can lead to a stochastic variation in the experimental yields as seen in the data.

Two 3D simulations were performed to compare the results of no coupling and unfavorable coupling with low modes. For the first case—the absence of low-mode intrinsic capsule asymmetries—the simulation included the capsule intrinsic surface roughness resulting from modes with $l > 10$ only and drive asymmetry. A yield of 1.37×10^9 was produced, shown as the top of the vertical line at 0.02 μm rms in Fig. 7-16. In a second simulation, low-mode capsule asymmetries were also included, giving a peak-to-valley amplitude typical of measured values. These modes were oriented so as to enhance the effect of coupling with drive asymmetry. In the latter case, the spikes reached the center of the capsule 50 ps sooner than in the former case, significantly cooling the hot spot shown in Fig. 7-17(b), and reducing the yield to 6.0×10^8, as shown in Fig. 7-16. This calculation suggests that coupling between low-mode capsule shell perturbations and drive asymmetry can explain much of the variability in the yields of the smooth capsules and brings these simulated yields close to the experimental values. The addition of low-mode intrinsic asymmetries reduces the simulated yield for a capsule with 0.15 μm rms perturbations as well. In the simulation with 1 μm rms perturbation amplitude that included drive asymmetry, the RT growth of the multimode perturbation dominated the overall perturbation evolution. Thus the addition of low mode intrinsic perturbations has a relatively small effect on the yields calculated for the roughest capsules.

The primary and secondary neutron yields are best suited to inferring large mix fractions. This occurs because the yield for these capsules is dominated by the hottest (central) region, which is furthest from the pusher–fuel interface and least affected by conduction cooling.

One technique that is in principle more sensitive to shell perturbations is measurement of the neutron yields from capsules with deuterated shells and an inert gas fill (Chrien *et al.*, 1998). Figure 7-18 shows a cross section of the capsule design. The only differences with respect to the usual capsule shown in Fig. 7-9 are a 75 atm H_2 fill, which has the same fuel mass as the 50 atm D_2-H_2 fill shown in Fig. 7-9 and a 4 μm thick deuterated polystyrene inner shell. Simulations predict a similar fuel convergence for the 75 atm H_2 filled capsule, despite the 50% higher atomic number density, because of a lower value of fuel entropy (per atom) in the implosion of this capsule. In addition, peak growth factors are predicted to be a factor-of-2 higher than for the D_2-H_2 gas-filled capsules. This is principally the result of a delay in the yield from the deuterated shell, which depends on thermal conduction from the central hydrogen gas fill, rather than occurring directly in the gas. This delay allows more time for perturbation growth during compression.

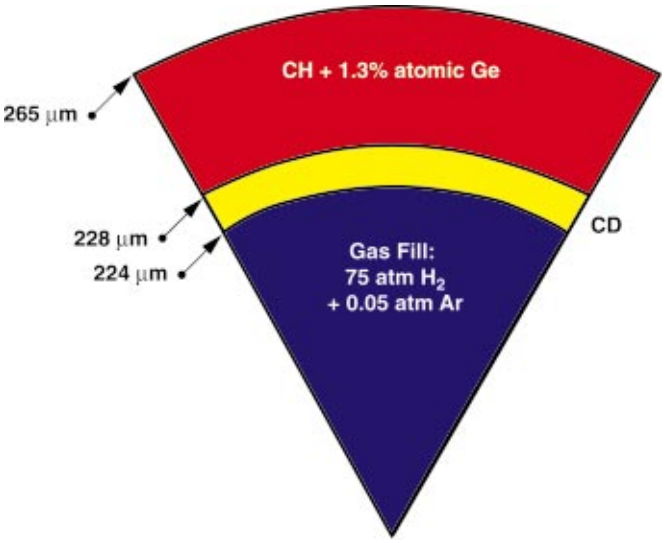

FIG. 7-18. (Color) Cross section of a typical deuterated-shell capsule design. Since the gas fill is inert, all the yield arises from conduction to the deuterated layer making these capsules more sensitive to mix at the fuel–pusher boundary than capsules whose yield comes from the gas fill.

Figure 7-19 shows the observed dependence of shell primary yield on surface roughness. The implosion conditions were identical to those in the D_2-H_2 gas-filled target implosions except for a 7% lower drive temperature designed to reduce ultrahard x-ray contamination of the neutron diagnos-

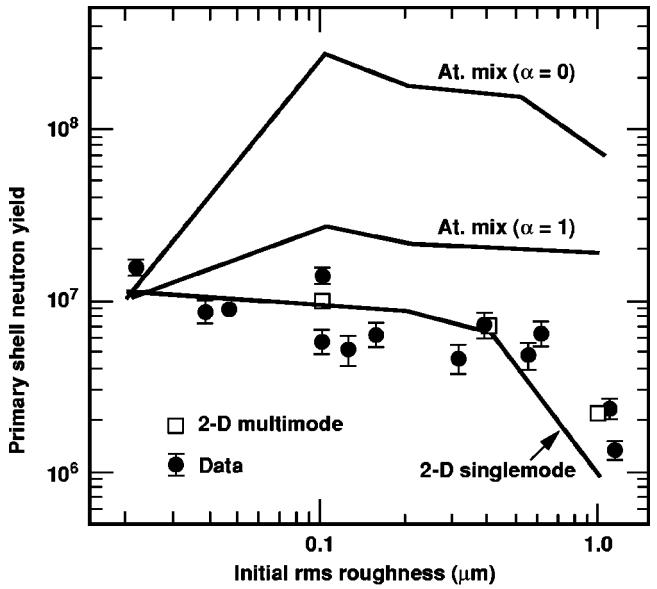

FIG. 7-19. Measured and calculated primary yields for 1.3 at. % Ge-doped deuterated-shell capsules vs initial surface roughness. Solid circles are the data with indicated experimental uncertainties. The middle and top curves are predictions from the 1D atomic mix model with ($\alpha=1$) and without ($\alpha=0$) enhanced heat diffusion. The lower curve and squares are predictions from 2D single-mode ($l=24$) and multimode ($l=2, 4, 6,..., 48$) simulations.

Downloaded 20 Mar 2011 to 69.181.48.121. Redistribution subject to AIP license or copyright; see http://pop.aip.org/about/rights_and_permissions

tics measuring the low yields. The yield remains nearly constant with increasing surface roughness up to 0.5 μm and finally falls for rougher surfaces. Figure 7-19 shows predictions of 2D multimode ($l=2$, 4, 6,..., 48) and single-mode ($l=24$) calculations, which are in good agreement with the data. The simpler single-mode simulations assume that all the roughness is concentrated in a dominant mode. The predicted yields fall rapidly at about 0.4 μm rms roughness, at which point the increased heat losses to the deuterated layer are insufficient to raise or even maintain the D_2 temperature because of the reduced compressional heating of the gas. The peak compressional heating power in the implosion of a capsule with 1 μm rms roughness is only 72% of the unperturbed value. The simulations indicate shell breakup for capsules above 0.4 μm rms roughness.

Figure 7-19 also shows the results of calculations using the atomic mix model with and without the enhanced thermal conductivity across the mix region (as described in Sec. II). The deuterated shells are quite sensitive to heat flow in the mix region since all the yield comes from there. The 1D mix model with enhanced heat conduction matches the data fairly well, while the model without mix-enhanced heat conduction is far from the experiments.

The HEP3 implosions successfully utilized x-ray spectroscopy as a technique for diagnosing the effects of RT instability on the pusher–fuel interface. This technique was further explored for the moderate-growth-factor HEP4 implosions which used an inner layer of Ti dopant in the shell and Ar dopant in the fuel for the target shown in Fig. 7-9.

Line emission was modeled (Langer *et al.*, 1997) using LASNEX, to obtain the temperature and density of the imploding capsule, and the atomic kinetics code CRETIN (Scott and Mayle, 1994) was used in both 1D and 2D. However, this technique had limited utility for the HEP4 experiments. For smooth or rough capsule surfaces, the emission is rather weak in one or the other of the two spectral lines of interest; hence line ratios are sensitive to small variations in conditions in the vicinity of the mix region. This leads to ambiguous results and spectroscopic tracers have not played a major role in the assessment of high performance implosions. These experiments (Keane *et al.*, 1993) and modeling (Langer *et al.*, 1997) are not reviewed here.

E. Omega HEP4 and HEP5 implosions

In hohlraums with NIF-like ratios of the hohlraum size to capsule size, the Nova laser, with only five beams per side, provides radiation symmetry that is inadequate for high-performance capsules with convergence ratios larger than about 10. Even for the convergence-10 implosions discussed above, the combination of long-wavelength flux asymmetry and capsule asymmetry resulted in a yield degradation of about a factor of 4 from a spherical 1D implosion. The high-convergence HEP1 campaign on Nova, utilized a large case-to-capsule ratio, and the resultant short pulse length to reduce the effects of flux asymmetry. Even with these improvements, the performance of the high-convergence HEP1 capsules was significantly degraded from 1D performance. To achieve a significant fraction of the yield calculated for a 1D implosion in hohlraums with NIF-like case-to-capsule ratios and capsules with convergence ratios >10, some form of time-dependent flux asymmetry control, as well as improved azimuthal symmetry control, are required.

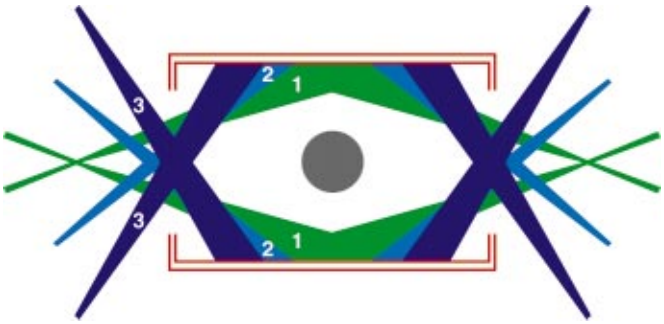

FIG. 7-20. (Color) Shown is the HEP4 hohlraum geometry with multicone irradiation used on the Omega laser. Cone 1 enters hohlraum at 22°, cone 2 at 42°, and cone 3 at 58°.

For hohlraum experiments, Omega (Soures *et al.*, 1996) has four times the number of beams available on Nova, and the beams can be arranged in a NIF-like multicone geometry. Since all beams on Omega are constrained to have identical pulse shapes, the beam phasing planned for NIF is not a current option on Omega, but the symmetry is still significantly improved compared to Nova. The HEP4 experiments were repeated to take advantage of this improved symmetry. These experiments achieve yields near those calculated for a 1D implosion. Experiments have also been carried out on Omega with convergences exceeding 20.

The hohlraums used on Omega were 1600 μm diameter and 2500 μm length with 1200 μm diameter laser-entrance-holes, the same dimensions as the HEP4 hohlraums used on Nova. All of the hohlraums were made with 2 μm Au on 100 μm CH backing for structural support. These thin-walled hohlraums allow direct high-energy x-ray imaging of the laser spots (as discussed in Sec. V). The pulse shape used was the five-to-one contrast laser pulse PS26, as in the Nova HEP4 campaign [see Fig. 7-11(a)]. The energy available in 40 beams on Omega for this 2.5 ns pulse shape was just under 15 kJ. This is less energy than was available on Nova but is adequate for studying the implosion dynamics. The 40 beams were divided into three rings of either five or 10 beams on each side: five beams per side at 21.4°, five beams per side at 42°, and 10 beams per side at 58.9° relative to the hohlraum axis. The pointings of the beams were arranged to have a NIF-like configuration (Lindl, 1998b) with an inner cone and an outer cone (see Fig. 7-20). This configuration was achieved by having cone 1 (21.4°) irradiate the hohlraum wall near the midplane of the hohlraum, and having cones 2 and 3 pointed closer to the hohlraum endcaps. For PS26, simulations and analysis show that this cone geometry maintains good time-dependent symmetry control without the need for beam phasing (Amendt *et al.*, 1997) or beam staggering (Turner *et al.*, 2000).

In the initial implosion campaign on Omega in 1998, four types of implosion targets were shot: (1) 50 atm D_2 fill capsules with 1.1% Ge-doped ablators; (2) 50 atm D_2 fill capsules with undoped ablators; (3) 10 atm D_2 fill capsules

Downloaded 20 Mar 2011 to 69.181.48.121. Redistribution subject to AIP license or copyright; see http://pop.aip.org/about/rights_and_permissions

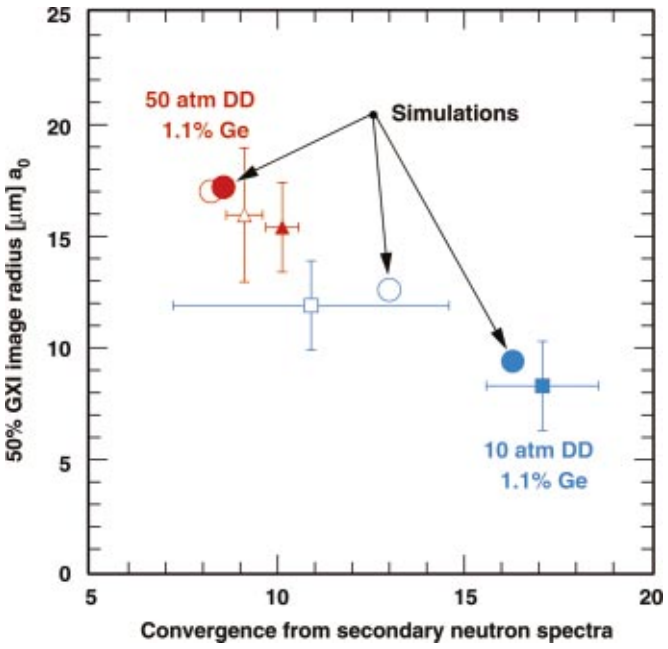

FIG. 7-21. (Color) The 50% gated-x-ray image sizes vs neutronically inferred convergence for doped (solid) and undoped (open), low- (red) and high- (blue) convergence targets. Simulations are represented by circles.

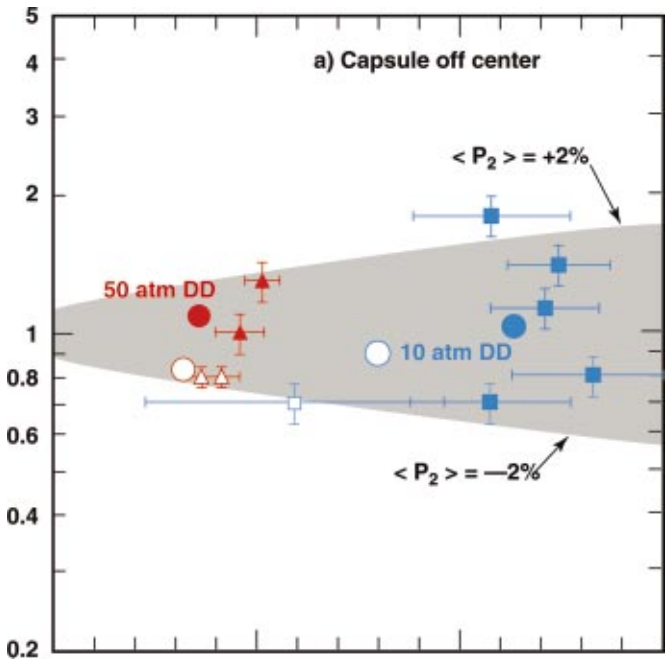

FIG. 7-22. (Color) The 50% gated-x-ray image distortions (a/b) vs neutronically inferred convergence for doped (solid) and undoped (open), low- (red) and high- (blue) convergence targets. Simulations are represented by circles. Gray shading indicates time- averaged $P2$ asymmetry of $<2\%$.

with 1.1% Ge-doped ablator; and (4) 10 atm D_2 fill capsules with undoped capsules. All capsules were nominally 510 μm outer diameter with 30 μm thick shells. In this first series, the fuel was doped with 0.1 atm Ar to facilitate imaging of the imploded fuel shape. The undoped 50 atm targets were designed with slightly thicker shells (35 μm) in order to closely match the bang times of the doped targets.

Figure 7-21 shows the average radius a_0 of the 50% gated x-ray image (Kilkenny *et al.*, 1988) (GXI) contour vs the inferred fuel convergence from secondary neutron measurements. The inferred fuel convergence is obtained from the ratio of secondary (DT) neutron yield, as recorded by a time-resolved neutron sensitive scintillator array—Medusa (Knauer *et al.*, 1995), to the DD neutron yield (see Sec. VII B). The 50% contour has traditionally correlated well with the pusher–fuel boundary on earlier 1 ns flattop pulses used on Nova (Suter *et al.*, 1994). Four representative targets are shown along with the predicted performance. For the doped ablator data, the factor-of-2 decrease in a_0 for the higher-convergence targets mirrors the factor-of-2 increase in neutronic convergence. Moreover, the a_0 for the high-convergence doped target matches closely the simulated fuel radius at bangtime.

Figure 7-22 displays the 50% GXI distortions of the imploded cores for the various targets. The distortions are shown in terms of a/b, the ratio of the principal axes of the imploded core image as in the symmetry experiments described in Sec. V. The shaded gray region in Fig. 7-22 is identified with a distortion that would be produced by a time-averaged flux uniformity of 2% or less. Almost all targets showed satisfactory symmetry control according to this criterion. Adequate control of a_4 is also indicated from the implosion data. The average measured a_4/a_0 distortion of the doped high-convergence targets was about 7%, compared with the predicted level of 4%. This result is consistent with the foamball and backlit implosion data showing acceptably small levels of a_4 flux asymmetry resulting from multicone irradiation of the hohlraum wall as discussed in Sec. V.

Figure 7-23 shows the measured convergences compared with predicted convergences with no mix. Except for the misaligned high-convergence target, agreement is good. The

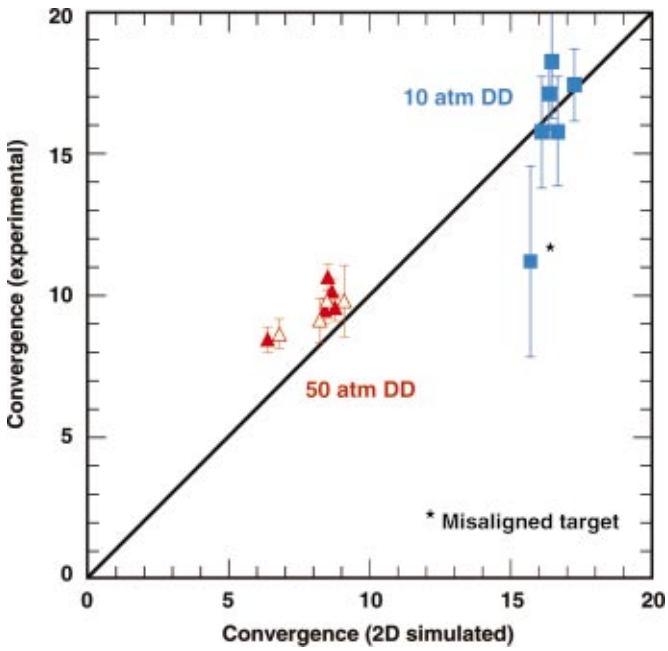

FIG. 7-23. (Color) Experimental neutron convergence vs predicted neutron convergence based on 2D simulations for doped (solid) and undoped (open), low- (red) and high- (blue) convergence targets.

Downloaded 20 Mar 2011 to 69.181.48.121. Redistribution subject to AIP license or copyright; see http://pop.aip.org/about/rights_and_permissions

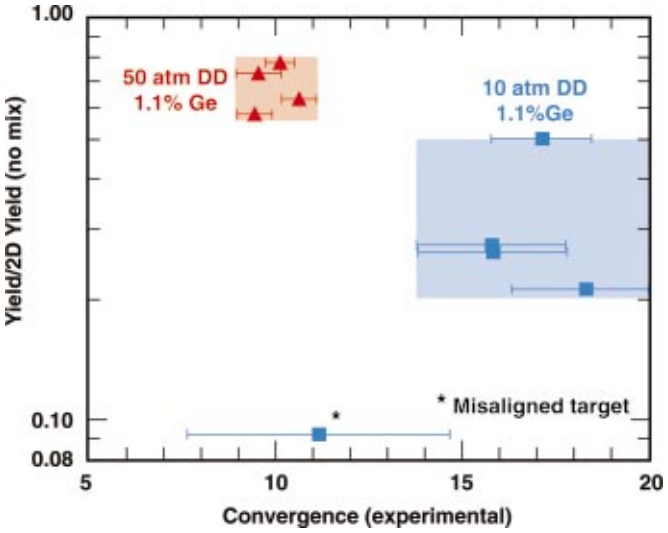

FIG. 7-24. (Color) Measured neutron yield normalized to yield calculated in 2D without mix and including intrinsic hohlraum asymmetry with perfect power balance and pointing accuracy vs experimental convergence for doped, low- (red) and high- (blue) convergence targets.

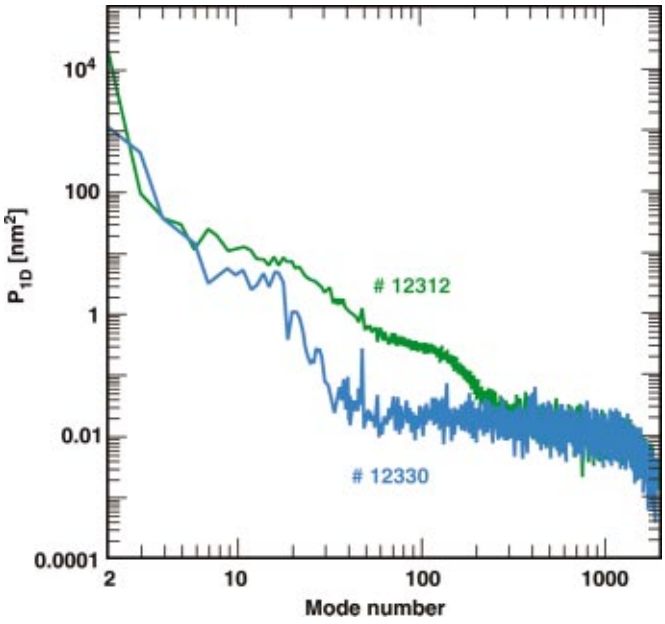

FIG. 7-25. (Color) Measured 1D Fourier power spectrum of surface roughness for two targets: (a) ''Rough'' is identified with target #12312 (green). (b) ''Smooth'' with target #12330 (cyan).

role of mix is to cool the fuel and thereby cause further slowing of the tritons from their birth energy at 1.01 MeV. Because the DT cross section increases with decreasing triton energy, the ratio of secondary neutrons to primary neutrons may actually increase with mix, resulting in higher inferred convergence. However, simulations suggest that the role of mix on convergence for the four types of targets considered is minimal, giving at most a few percent difference.

Figure 7-24 shows the ratio of measured to 2D simulated yields vs measured convergence. The doped low-convergence targets performed on average nearly twice as well as the doped high-convergence capsules. The data in both cases are grouped as shown (in boxes) to indicate that the targets in each category have nearly identical fabrication.

Figure 7-25 shows two 1D surface roughness spectra that were measured during this initial HEP4/5 campaign on Omega. Only two of the targets were scanned with atomic force microscopy. The analysis below assumes that this pair of spectra brackets the true spectra for the experiments. Figure 7-26 shows the calculated linear growth-factors obtained for the high- and low-convergence doped targets. For both low- and high-convergence targets, the peak growth factors exceed 100 as in the HEP4 campaign on Nova. The low-mode growth factors, although small, are important since the amplitudes of the low-mode-number perturbations can be significant, particularly for $P1$ and $P2$. In the calculations discussed here, the effects of capsule perturbations are divided between ''surface roughness'' perturbations with mode number $\geqslant 10$ (for which 1D atomic mix of cool pusher material and hot fuel is a reasonable approximation), and the longer-wavelength perturbations. For the low-convergence implosions, the effect of surface roughness gives 8% (14%) yield degradation for the smooth (rough) spectrum shown in Fig. 7-25. The high-convergence implosion is predicted to have 15% (27%) yield degradation for the same spectra.

Figures 7-27(a) and 7-27(b) summarize the calculated yield degradation for varying amounts of initial target distortion in $P1$ and $P2$. The amount of $P1$ on each capsule was interferometrically measured along one axis, but neither control nor selection was exercised in this initial series of implosions. Although the average amount of $P1$ for the high- and low-convergence capsules was about one-third of a micron, the scatter is considerable from target to target. From Fig. 7-27(a) the high-convergence target is about twice as sensitive to $P1$ as the lower-convergence target for $P1 < 1\ \mu$m. Simulations show the clear presence of a jet of

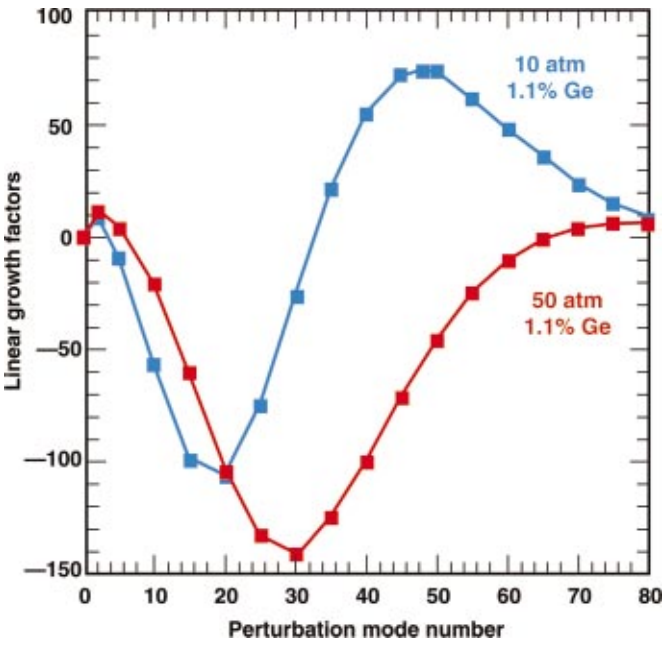

FIG. 7-26. (Color) Calculated small-amplitude growth factors vs Legendre mode number for doped, low- (red) and high- (blue) convergence targets.

Downloaded 20 Mar 2011 to 69.181.48.121. Redistribution subject to AIP license or copyright; see http://pop.aip.org/about/rights_and_permissions

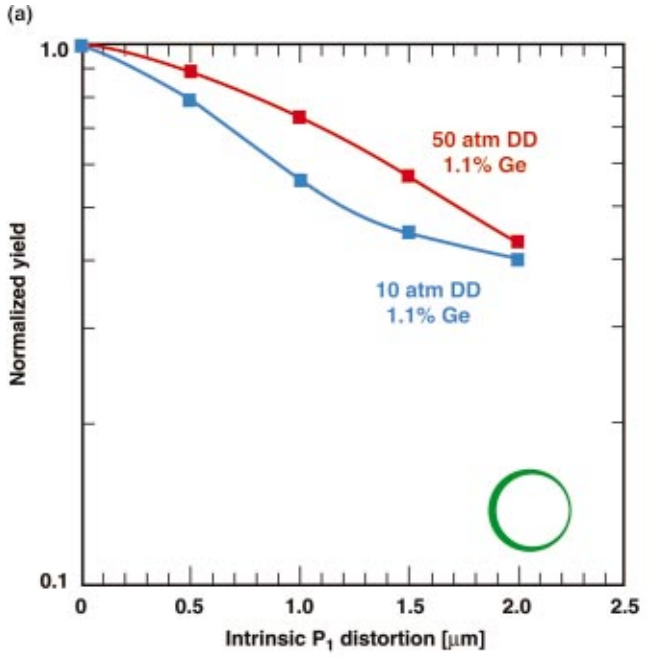

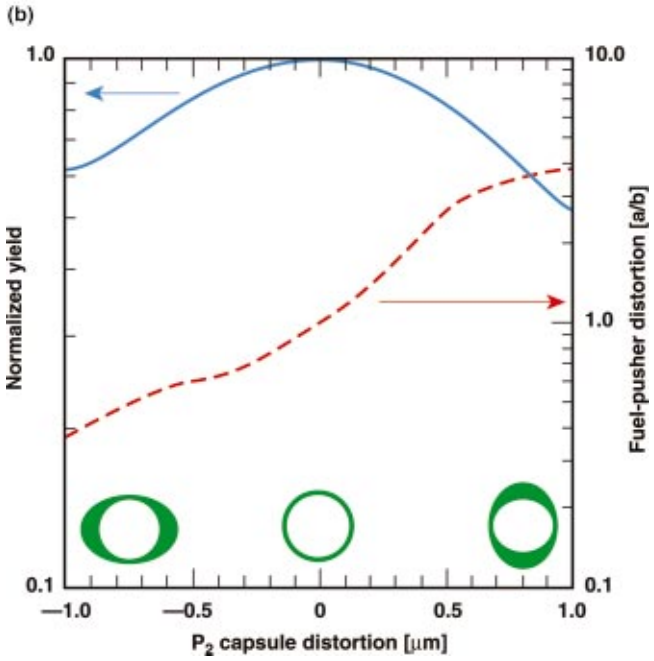

FIG. 7-27. (Color) (a) Predicted yield degradation vs intrinsic capsule $P1$ distortion for doped, low- (red) and high- (blue) convergence targets. (b) Predicted yield degradation (blue solid line) and 50% gated-x-ray image distortion (red dashed line) vs $P2$ capsule distortion for high-convergence doped targets. Capsule distortion is pictorially represented at the bottom of the figure.

colder fuel material along the symmetry axis of the hohlraum, which laterally displaces the target several microns from the center of the hohlraum near bang time. For a $P1$ oriented along the axis of the hohlraum, a ring of fuel is evident in the simulations which suggests that axial x-ray imaging may enable detection of this $P1$ signature. Sidehole or lateral views of the imploded core show a ''kidney bean'' shape in the simulations, but post-processing of this image

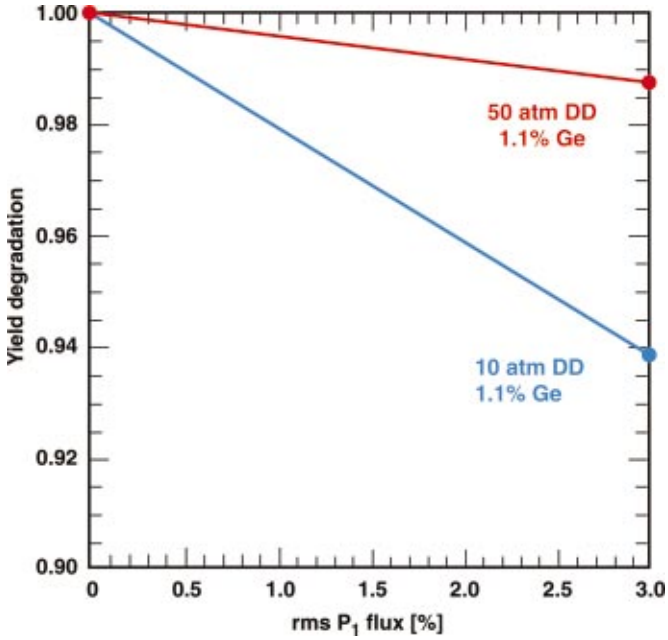

FIG. 7-28. (Color) Calculated neutron yield degradation vs rms $P1 \equiv (Y_{1,-1}^2 + Y_{1,0}^2 + Y_{1,1}^2)^{1/2}$ laser flux for doped, low- (red) and high- (blue) convergence targets.

with 5 μm instrumental resolution shows a mostly round image over a large range of $P1$. Thus, the image resolution is not sufficient to distinguish the effects of $P1$ on core distortion when viewed side on.

Figure 7-27(b) shows the predicted effect of capsule $P2$ on distortion and yield degradation. In contrast to the case of $P1$, modest levels of $P2$ can result in large observable distortions in the imploded core when viewed transversely. The observed range of a/b distortions in the database from Fig. 7-22 from about 3/5 to 5/3 help constrain the allowed levels of capsule $P2$. Based on the simulations and the demonstrated time-dependent symmetry control in the experiment, $P2$ is not expected to be a major source of yield degradation. This conclusion is consistent with the measured levels of capsule $P2$ of less than 0.2 μm for the two roughness spectra shown in Fig. 7-25.

For all but three shots during this early campaign, the rms laser energy imbalance was about 8% on both the foot and the peak of PS26. On two occasions, one beam misfired, resulting in a nearly 16% rms laser energy imbalance. To estimate the effect of random laser energy imbalance on capsule performance, 3D viewfactor calculations were carried out. For 8% rms energy imbalance, the principal random flux asymmetry was a $\langle P1 \rangle \equiv \mathrm{rms}[Y_{1,m=-1,0,1}]$ of nearly 3.8% (2.9%) on the foot (peak). LASNEX 2D simulations of a capsule with a 3% $\langle P1 \rangle$ intrinsic x-ray flux asymmetry imposed for all time were carried out. Figure 7-28 displays the amount of degradation as a function of rms laser energy imbalance. The high-convergence target is more susceptible to laser energy imbalance, but the level of yield degradation is only at the 6% level. For the low-convergence target, the amount of yield degradation is only about 1%.

Throughout this campaign, the cone #1 beam powers ran about 5% higher than average on one side while the cone #2

Downloaded 20 Mar 2011 to 69.181.48.121. Redistribution subject to AIP license or copyright; see http://pop.aip.org/about/rights_and_permissions

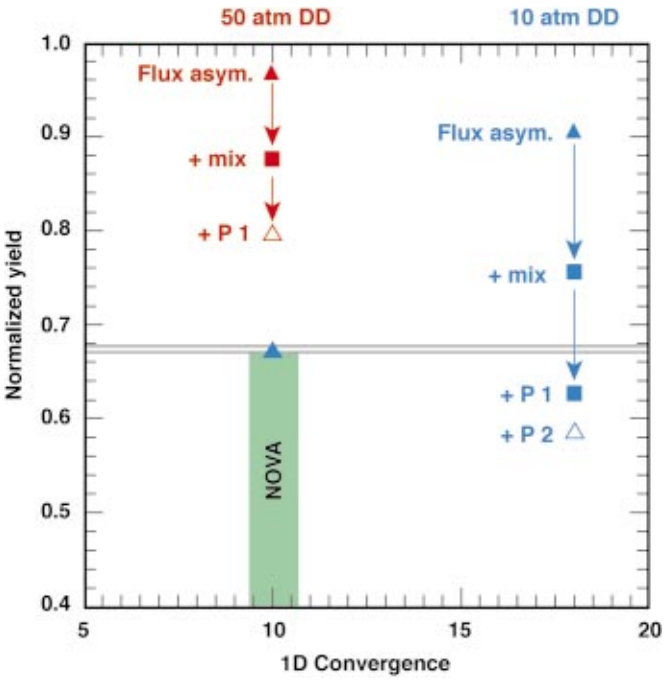

FIG. 7-29. (Color) Calculated normalized yield for the initial Omega indirect drive implosion series vs neutronic convergence for doped, low- (red) and high- (blue) convergence target. Range of HEP4 Nova data is shown in green. Horizontal blue line is calculated normalized yield for the high-convergence target subject to 1/3 mix penetration fraction of fuel. The baseline NIF ignition capsules fail to ignite with mix above this level. Solid diamonds represent cumulative (multiplicative) effect of simulated intrinsic flux asymmetry and random laser power imbalance. Multiplicative effects of capsule $P1$, $P2$ distortions and surface roughness are as indicated.

beams ran about 6% lower than average on the same side. This systematic one-sided inner-outer cone laser power imbalance is simulated using two-sided (180°) integrated hohlraum calculations. For the high-convergence capsules, this asymmetry results in an additional 10% yield degradation.

Although the Omega geometry provides significant control of both the intrinsic time-averaged and time-dependent flux variations, there are some residual effects. For the higher-convergence implosions, the calculated 2D yield degradation from intrinsic hohlraum asymmetry in the Omega multicone geometry is less than 40%, an improvement over the factor of 2 or more degradation calculated for a single cone geometry. Since the Omega geometry has four times as many beams as the Nova geometry, the contributions to asymmetry from intrinsic azimuthal variations are expected to be significantly less. In 3D viewfactor calculations, the largest flux asymmetry comes from $Y_{10,-10}$, but the amplitude of this mode is only 0.05%.

Many of the important effects considered above can be modeled in a single integrated calculation. However, a single calculation incorporating all of the above effects cannot be carried out at present. An estimate of the impact of multiple effects can be obtained by simply multiplying the individual effects. For the low-convergence target, the effects of surface roughness, random laser power imbalance, and $P1$ capsule distortion give $0.90\times0.99\times0.90=0.80$, or 20% total yield degradation. The same effects for the higher-convergence target give $0.80\times0.94\times0.80=0.60$. Figure 7-29 graphically illustrates the relative importance of the degradation effects and their relevance for NIF-like mix studies. The horizontal line at 67% normalized yield indicates the amount of Omega high-convergence yield degradation (33%) corresponding to a 1/3 mix-penetration depth. As discussed in Sec. II, this is the largest mix penetration depth tolerable for the NIF ignition targets with a 40% ignition margin. The lower-convergence HEP4 implosion targets perform well above the NIF failure threshold. The initial high-convergence targets on Omega perform close to the NIF failure threshold for pusher–fuel mix.

To incorporate several degradation effects in a single calculation, two-sided integrated hohlraum calculations that include left–right laser power imbalance, surface roughness-induced mix, and capsule $P1$ were carried out. These simulations include the observed left–right laser power imbalance of $+5\%$ (-6%) on the innermost (intermediate) cones. The effects of capsule surface roughness are incorporated using atomic mix along each grid angle in the 2D simulation. The mix depth is obtained from the Haan saturation model. A capsule $P1$ of 0.5 μm was assumed for both the higher- and lower-convergence targets. Sensitivity of alignment of the capsule $P1$ with the laser $P1$ was tested by reversing the sign of the capsule $P1$; little difference was seen between the two cases. The integrated calculation for the high-convergence target showed a 43% yield degradation, while the low-convergence target experienced a 26% reduction. Both of these integrated calculations give yield degradations somewhat larger than found by simply multiplying the individual effects together.

In both calculational approaches, the yield degradation for the higher-convergence target is roughly twice that of the lower-convergence target with the former target experiencing about a factor-of-2 yield degradation. The predicted yield agrees with the measured yield to within 10% for the best performing target at each convergence. However, the remaining targets in this first series had poorer performance as shown in Fig. 7-24.

The higher convergence implosions on Omega in 2000–2001 had better characterized and smoother capsule surfaces, improved laser performance and a greater assortment of capsule types than the initial experiments (Amendt *et al.*, 2002). The laser-power imbalance was also improved as part of an overall effort to improve the performance of the Omega laser for both direct- and indirect-drive capsules.

These experiments included both capsules with and without 0.05 atm. Ar dopant in the fuel. Figure 7-30 summarizes the results of these experiments. The Ar-free capsules systematically achieved more than a factor of two higher fraction of the calculated clean yield than the capsules with Ar dopant. Also, the Ar doped capsules show considerably more scatter in neutron yield independent of the rms surface roughness. This implosion series included 5 atm D_2 filled capsules for the first time and these capsules performed at a significant fraction of (2D) clean yield. The effect of a 0.1 atm. Ar fill is calculated and observed to be small at 50 atm fill. Current calculations do not predict the large effect observed for the 0.05 atm. Ar dopant for the lower fill capsules and work is ongoing to understand this discrepancy.

Downloaded 20 Mar 2011 to 69.181.48.121. Redistribution subject to AIP license or copyright; see http://pop.aip.org/about/rights_and_permissions

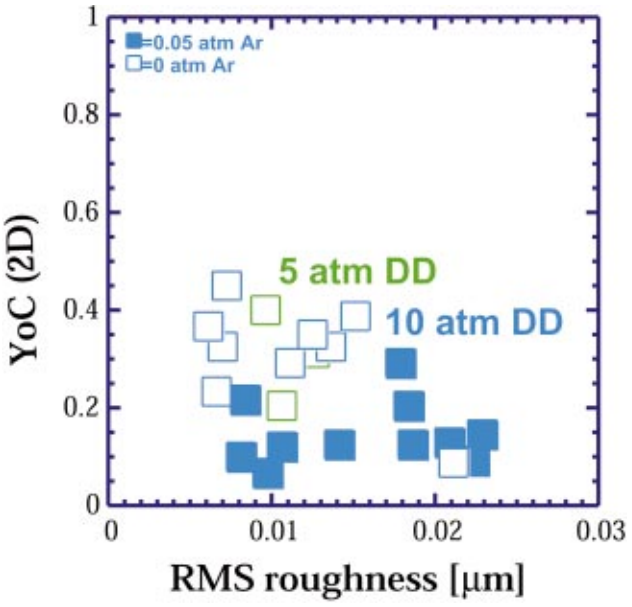

FIG. 7-30. (Color) Yield over clean (2D) DD neutron yield vs rms surface roughness for 5 atm (green) and 10 atm (blue) fill with (solid squares) and without (open squares) 0.05 atm Ar dopant for Omega HEP5 targets fielded in 2000–2001.

The following analysis focuses on the Ar free implosions.

Because the yield is a sensitive function of the x-ray drive, a close match between measured and simulated drive is necessary for calculating absolute yields. Figure 7-31 shows the measured and simulated (Dante) x-ray drive from 2D hohlraum simulations alongside the measured laser pulseshape for a representative laser shot in the Ar-free implosion campaign. There is an excellent match between simulated and measured drive. In Sec. IV, we concluded that over a wide range of hohlraums, we have:

$$\frac{\text{Flux(``True'')}}{\text{Flux(LASNEX)}} = 1.04 \pm 0.12.$$

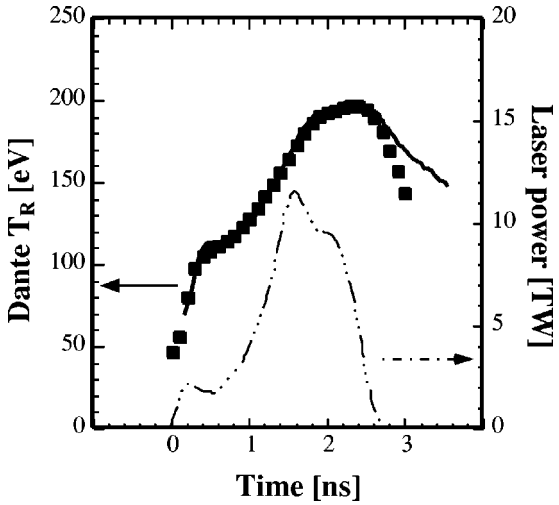

FIG. 7-31. Measured (filled squares) and simulated (solid line) Dante drive temperature vs time for the Omega high convergence implosions done in 2000–2001; laser power history (dashed–dotted) vs time.

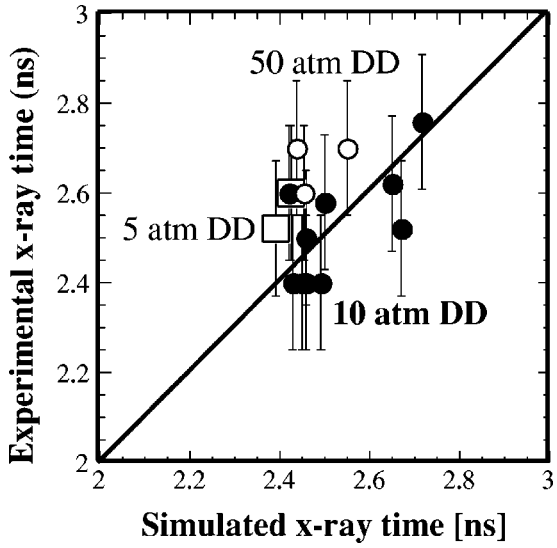

FIG. 7-32. Measured vs simulated instant of peak x-ray self-emission for 5 atm D_2-filled capsules (open squares), 10 atm D_2-filled capsules (filled circles), and 50 atm D_2-filled capsules (open circles).

A few percent error in flux would lead to about a 10% error in the calculated yield while a 15% error in flux would lead to about a factor of 2 error in the yield. Given the close correspondence between the measured and calculated yield indicated in Figs. 7-24 and 7-29, it appears that the systematic uncertainty in DD yield due to drive uncertainty may be as little as 10% or less. Backscatter has not been included in the simulation shown in Fig. 7-31. However, full-aperture backscatter measurements on (outer) cones 2 and 3 show total backscatter levels into the $f/6$ lens cones generally less than 200 J; near backscatter outside of the monitoring lenses is estimated to be at a similar level based on near-backscatter imaging experience on Nova. Cone 1 FABS monitoring is not yet available on Omega but the length of hohlraum plasma traversed and wall intensity is similar to cone 2 so we estimate that the total backscatter would also be about 200 J. Thus, we infer a total backscatter level of only ≈ 600 J or 4% of the incident laser energy, corresponding to an ≈ 3 eV deficit in peak drive temperature which is within the measurement error.

Measured peak x-ray emission times from the imploded core provide a further check on the hohlraum x-ray drive. Figure 7-32 shows a comparison of the measured and simulated peak x-ray emission times for three capsule D_2 fill pressures (5, 10, 50 atm). The times agree within the error bars further confirms that the hohlraum drive is properly modeled in the calculations.

Figure 7-33(a) shows the measured DD neutron yields, normalized to calculated clean DD neutron yields from two-dimensional (2D) integrated hohlraum simulations, versus the fuel convergence which is inferred from the ratio of secondary (DT) neutron yield to the DD neutron yield. These 2D calculations only include degradation due to intrinsic long-wavelength hohlraum radiation flux variations whose effects were described above. Figure 7-33(a) shows that the 50 atm capsules achieve 75% of the yield predicted by this ''clean 2D'' calculation (YoC_{2D}) while the highest conver-

Downloaded 20 Mar 2011 to 69.181.48.121. Redistribution subject to AIP license or copyright; see http://pop.aip.org/about/rights_and_permissions

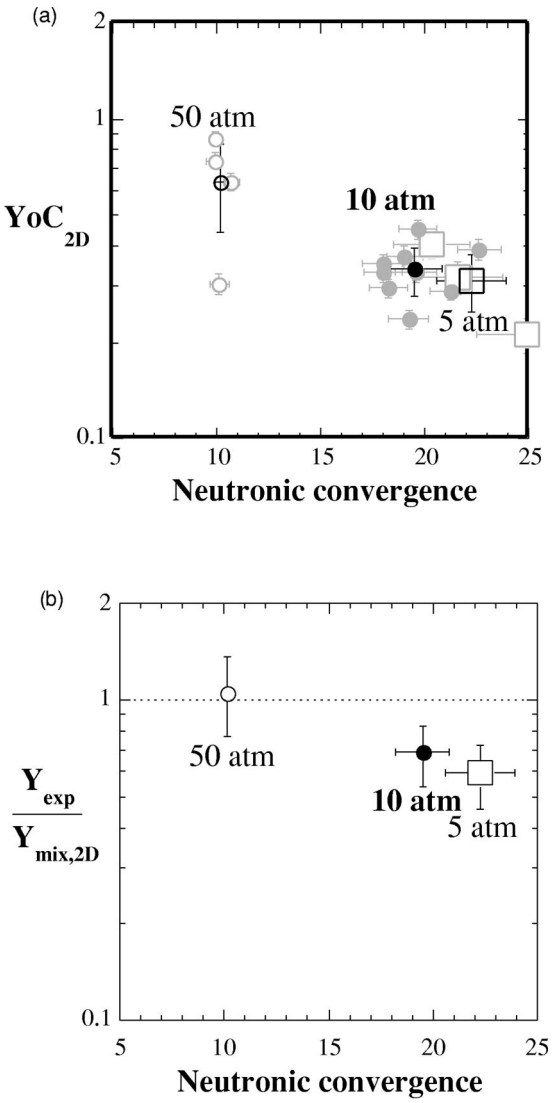

FIG. 7-33. (a) Ratio of measured primary (DD) neutron yield over clean 2D simulated yield vs inferred fuel convergence from secondary (DT) neutrons for 5 atm D_2-filled capsules (open squares), 10 atm D_2-filled capsules (filled circles), and 50 atm D_2-filled capsules (open circles). Bold symbols denote averaging over each target type. (b) Averaged ratio of measured primary (DD) neutron yield to 2D simulated yield with 1D mix model vs inferred fuel convergence from secondary (DT) neutrons.

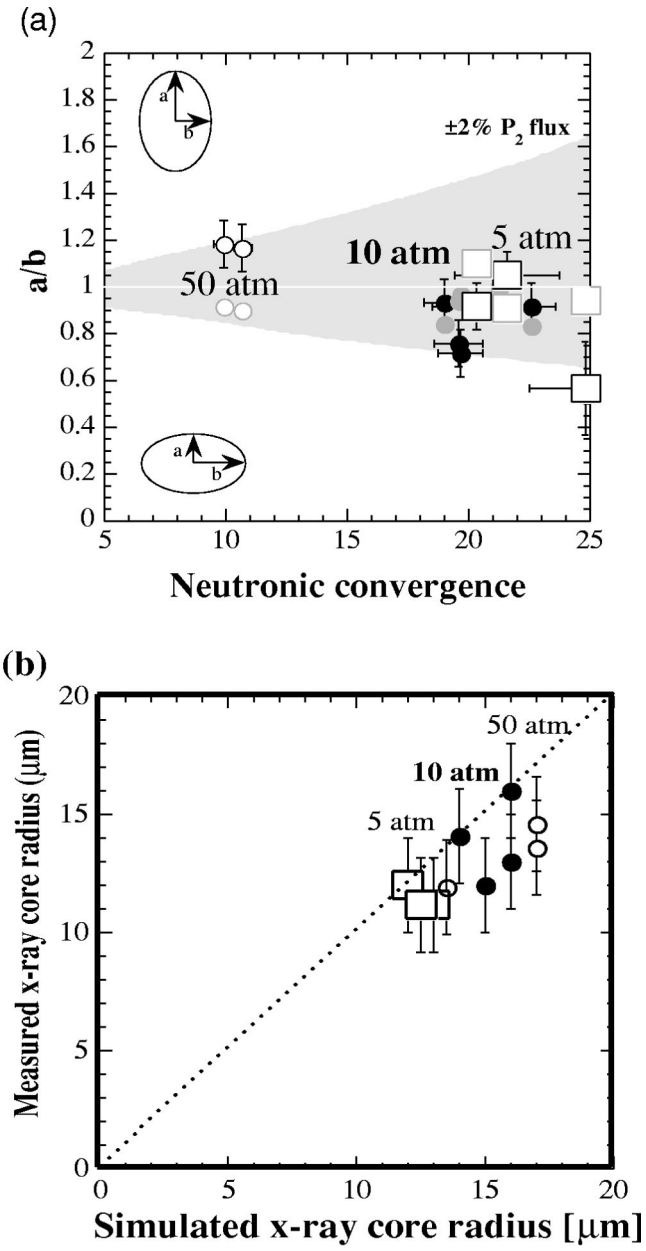

FIG. 7-34. (a) Measured and simulated "a/b" distortion of 50% x-ray self-emission contour vs inferred fuel convergence for 5 atm D_2-filled capsules (open squares), 10 atm D_2-filled capsules (filled circles), and 50 atm D_2-filled capsules (open circles); simulation points are indicated in gray; (b) measured vs simulated average radius of 50% x-ray self-emission contour.

gence targets, at 5 atm D_2 fill, had a mean YoC_{2D} yield near 30%.

Figure 7-33(b) shows the result of including a Haan-type mix to the three different capsule fills. The performance of the moderate-convergence targets (50 atm D_2) compares well with the predicted DD neutron yields. Other sources of degradation such as long-wavelength capsule nonuniformities and random flux asymmetry from laser power imbalances exist as in the earlier Ar-doped implosion campaign but are estimated to contribute less than 10% in total. For the higher convergence targets Fig. 7-33(b) shows that only a 20–30 % yield degradation is remaining when mix and intrinsic hohlraum radiation flux nonuniformity is calculated. Here, the effects of a plausible 0.5 μm, $\ell = 1$ shell thickness variation alone can contribute a 20% degradation in yield [see Fig. 7-27(a)].

Figure 7-34(a) shows the measured distortions "a/b" of the 50% emission contour versus convergence obtained from secondary neutron measurements, where a (b) is the radius of the 50% contour along the hohlraum waist (axis). The shaded region corresponds to a time-integrated lowest-order flux asymmetry of $<2\%$. The data show effective symmetry control near the level required for the NIF for convergences up to 20, as obtained from secondary neutron measurements.

Demonstration of even higher convergences (>30) using secondary neutron measurements is not possible with the yields obtained on Omega implosions. For example, the same CH capsules filled with only 2 atm of pure D_2 are predicted to reach a convergence greater than 30 according

Downloaded 20 Mar 2011 to 69.181.48.121. Redistribution subject to AIP license or copyright; see http://pop.aip.org/about/rights_and_permissions

to (clean) 1D simulations, but the sampling errors for secondary neutron detection become too large for reliably inferring a fuel convergence.

X-ray core imaging techniques are still possible, but the convergence measured this way may be more model dependent. Multiple 4–6 keV x-ray images of the imploded cores for the 5, 10, and 50 atm fills were obtained using an array of 5 μm pinholes and 70 ps resolution framing cameras. Adequate signal was recorded despite the absence of Ar dopant in the fuel. Figure 7-34(b) shows the comparison between the measured and expected 50% self-emission contour sizes for fuel bremsstrahlung x rays. This contour correlates well with the calculated fuel–pusher interface for the higher convergence 5 and 10 atm D_2-fill capsules, according to the simulations. For the 50 atm D_2 fill, the core conditions are less isothermal and the calculated 50% x-ray emission contour occurs inside the fuel–pusher interface. A lower intensity contour could be chosen to better match the location of the fuel–pusher interface, but these calculations illustrate the model dependence of using the x-ray emission for inferring fuel convergence. Mix and other effects which modify the temperature profile near the pusher–fuel interface will also change the size of the x-ray image and these effects can be substantial for the small core sizes obtained at high convergence, further complicating the comparison between the x-ray emission size and the fuel size.

F. Summary of implosion experiments

The HEP1 implosion series on Nova was used to develop quantitative neutron diagnostics for inferring fuel density and mix using the secondary DT neutron spectrum from DD fuel implosions. This technique has been used on the HEP4 and HEP5 implosions on both the Nova and Omega lasers.

The HEP3 implosions successfully demonstrated the use of x-ray spectroscopy as a technique for obtaining mix information on implosions.

The goal of the HEP4 implosion experiments was to demonstrate a quantitative understanding of implosion experiments for convergences of about 10 with overall hydrodynamic instability growth of 100 or more for a NIF-like perturbation spectrum. This goal was achieved on Nova. However, the smoothest capsules had yields degraded by about a factor of 3 from 1D because of intrinsic hohlraum flux and long-wavelength capsule asymmetry. Quantitative calculations of the performance of the convergence 10 capsules on Nova required the development of 3D capsule implosion codes. The observed level of degradation, although calculable, implies a level of asymmetry significantly exceeding that which would be acceptable for ignition experiments. On the Omega laser, which has improved symmetry relative to Nova, the HEP4 capsules have achieved 70% to 80% of the idealized or clean 2D yield, which is within the range required for ignition.

The higher-convergence goals (HEP 5) are being successfully pursued on Omega. At convergence-17, the best performing capsules achieved close to 50% of the idealized 2D yield, somewhat less than would be required for ignition but still higher than achieved with the convergence 7–10 HEP4 capsules on Nova. Recent work with Ar-free implosions has exploited further improvements in target quality and laser-power balance on Omega to demonstrate significant performance of convergence-22 capsules which is consistent with hydrodynamic implosion calculations when the effects of intrinsic hohlraum asymmetry and hydrodynamic instability are included. Even higher convergence capsules may achieve reasonable performance on Omega. However, the full level of independent pulse shaping planned for NIF will be required to demonstrate convergence ratio 30 or more implosions as required by current ignition designs for NIF.

ACKNOWLEDGMENTS

One of the authors (John Lindl) was responsible for the overall content and integration of the material in this review. As in any review, this document covers only a subset of the work that has been carried out since 1990 in developing the physics basis for ignition using indirect-drive ICF. The other authors were primarily involved in developing content for the following individual sections: Steve Haan, Sec. II; Dick Berger and Siegfried Glenzer, Sec. III; Larry Suter and Bob Kauffman, Sec. IV; Nino Landen, Sec. V; Gail Glendinning, Sec. VI; and Peter Amendt, Sec. VII. A few of the references in this review are to Livermore or Los Alamos internal documents that are not yet publicly available. Most of these are still in the process of review for declassification as a result of the December 1993 decision by DOE to declassify large portions of the U.S. ICF Program.

Besides the authors, who have all been active in the program on Nova and Omega, the work reported here required the efforts of many hundreds of people who cannot all be mentioned. Authors of the scientific work reviewed here are credited in the references. However, the scientific leadership and management of the large teams of people required to successfully carry out this research deserve acknowledgment. Erik Storm was the head of the LLNL ICF Program from 1984 to 1992, during the time when Nova became operational and the Nova Technical Contract was developed. During this early period, Mike Campbell was the Nova Experiments Program Leader. Mike followed Erik as the ICF Program Leader. Upon becoming the LLNL laser programs Associate Director in 1994, Mike played the central role in establishing NIF as a key element in the Stockpile Stewardship Program. One of the authors, John Lindl, was the leader of the ICF Program theory and code development work from 1984–1990, was leader of the overall Nova Target Physics Program from 1990 to 1995, and the ICF Program Scientific Director since 1995. Joe Kilkenny was the Nova Experiments Program leader from 1992–1995. He was the ICF Target Physics Program Leader from 1995–1997 and the Deputy Associate Director for ICF and NIF from 1997 to 1999. Bruce Hammel has been the LLNL Ignition Program Leader from 1998 to the present. Mordy Rosen was the leader of the LLNL theory and code development work from 1990–1997 and Tom Bernat has been the long time leader of the target fabrication work at LLNL. During much of the time involved in the work on Nova, Melissa Cray was the

Downloaded 20 Mar 2011 to 69.181.48.121. Redistribution subject to AIP license or copyright; see http://pop.aip.org/about/rights_and_permissions

LANL ICF Program Leader, a job held by Alan Hauer since 1999. All of these people held major management responsibility, and played an essential role in the success of the work on indirect-drive on Nova.

This work was performed under the auspices of the U.S. Department of Energy by the Lawrence Livermore National Laboratory under Contract No. W-7405-Eng-48.

APPENDIX: THE NOVA TECHNICAL CONTRACT (NTC)

The Nova Technical Contract (NTC), as spelled out in the 1990 review of the ICF Program (NAS Review, 1993a) comprises the HLP physics goals, and the HEP goals.

The HLP program addresses laser–plasma coupling, x-ray generation and transport, and the development of energy-efficient hohlraums that provide the appropriate spectral, temporal, and spatial x-ray drive. The HLP program was divided into seven subgoals:

(1) HLP1: Demonstrate acceptable coupling of laser light to x rays in low-Z-lined hohlraums using shaped laser pulses and peak radiation temperatures up to $T_R \approx 210$ eV.
(2) HLP2: Demonstrate acceptable coupling of laser light to x rays in lined hohlraums with peak radiation temperature $T_R \geqslant 270$ eV with 1 ns square pulses.

Acceptable coupling for HLP1 and HLP2 was defined as follows:

- Absorption fraction $f_{\text{abs}} > 90\%$.
- Stimulated Brillouin scattering (SBS) fraction $f_{\text{SBS}} < 5-10\%$.
- Suprathermal-electron fraction $f_{\text{hot}} < 5\%$ at $T_{\text{hot}} \geqslant 50$ keV.
- Stimulated Raman scattering (SRS) fraction $f_{\text{SRS}} < 5-10\%$.

(3) HLP3: Demonstrate an ability to measure and calculate energy balance in a hohlraum with emphasis on wall loss and albedo and an ability to diagnose and predict the (time-dependent) position of the laser-produced x-ray source within the hohlraum. Demonstrate an ability to characterize and model plasma evolution in a hohlraum.
(4) HLP4: Demonstrate symmetry control with low- and intermediate-Z-lined hohlraums. Achieve low-order, l-mode (P_2, P_4) time-integrated symmetry $\leqslant 2$ to 4%.
(5) HLP5: Demonstrate acceptable levels of scattering in large-scale plasmas that match the plasma conditions, beam geometry, and beam smoothing of ignition hohlraums as closely as possible. The plasmas should have density and velocity scalelengths ≈ 2 mm, electron temperature > 1.5 keV, and $n/n_c < 0.15$.
Acceptable levels of scattering were defined as follows:

- SBS fraction $f_{\text{SBS}}(\text{back, side}) < 5-10\%$.
- SRS fractions fSRS(back, side) $< 5-10\%$ and $f\text{SRS}(\text{forward}) < 5\%$.

(6) HLP6: Evaluate the impact of laser beam filamentation on SBS and SRS and develop control techniques to the extent necessary to ensure acceptable levels of scattering.
(7) HLP7: Develop an improved understanding of x-ray conversion efficiency in hohlraums under conditions appropriate for NIF ignition targets.

Evolution of the NIF target designs and completion of the 60-beam Omega laser at the University of Rochester (Soures *et al.*, 1991) resulted in modifications and extension to the NTC. These changes affected principally the HLP goals.

The most notable change to the NIF targets has been a change in the NIF hohlraum. Ignition-scale hohlraums require some sort of a low-Z fill to control the position of laser beam absorption and x-ray emission. At the time of the NAS report, ignition targets used low-Z liners on the inside of the hohlraum wall to create a plasma. These ''lined hohlraum'' targets, spelled out in the NTC, worked well in the Nova experiments. Later, however, more detailed NIF-target calculations predicted a significant asymmetric pressure pulse on the capsule when the liner plasma collapsed onto the hohlraum axis. This pulse may be an artifact of calculations that are currently constrained to be axisymmetric, or it may be possible to mitigate this pulse by intentional 3D hohlraum design features. To avoid the on axis pressure pulse, the baseline NIF target design has been switched from a liner to a low-Z gas fill (Haan *et al.*, 1995; Krauser *et al.*, 1996).

Although not part of the original NTC, symmetry control and x-ray drive in gas-filled targets became a major focus on Nova and the later Omega experiments.

HLP1 and HLP2 specify temperature goals in hohlraums with shaped and unshaped laser pulses. The temperature goals for shaped pulses result in plasma conditions inside the hohlraum that are comparable to those for NIF targets. Higher temperatures are possible for unshaped pulses because there is less time for the buildup of plasma. These higher temperatures provide a test of x-ray wall loss at NIF-like temperatures. These HLP goals were achieved in lined hohlraums. The experiments were extended to gas-filled hohlraums where the temperature goals were also achieved. These results are discussed in Sec. IV.

A quantitative understanding of x-ray absorption by high-Z hohlraum-wall material is essential for understanding hohlraum-coupling efficiency. This was a major objective of HLP3 and was accomplished in the Nova experiments as discussed in Sec. IV.

The goal of HLP4 was to demonstrate NIF-level control of the time average of the long-wavelength P_2 and P_4 radiation flux asymmetry. Nova's basic 10-beam geometry, with five beams in a ring on each end of the hohlraum, only al-

Downloaded 20 Mar 2011 to 69.181.48.121. Redistribution subject to AIP license or copyright; see http://pop.aip.org/about/rights_and_permissions

lows control of the time average radiation asymmetry. An average P_2 flux asymmetry of 1% has been achieved, as described in Sec. V. NIF has two rings of beams on each side; this allows control of the time variation of P_2 as well as the time-average P_4 and P_6. In general, the time variation of the P_2 asymmetry on Nova exceeds the requirements of the NIF capsules. The larger number of beams on Omega allows control of the time variation of flux asymmetry. In addition, changes to Nova that allowed propagation of a separate pulse in each half of each beam also provided a means for controlling the time variation of asymmetry. The NTC was extended to include experiments that have demonstrated this control. Although the time average asymmetry of P_2 has met the NIF requirement, the rms variation in flux asymmetry over all modes exceeds that required for NIF capsules. With the level of power balance and pointing accuracy achieved on Nova (Omega), the rms flux variations are a factor of 4 (2) greater than expected on NIF.

HLP5 and HLP6 address various aspects of LPI in hohlraums. Although significant progress has been made in understanding these effects, there is not yet a true predictive capability for use in hohlraum design. However, by going to short-wavelength laser light, it has been possible to identify conditions under which the LPI effects play only a minor role in target performance. Under these conditions, it has then proven possible to accurately predict ICF capsule performance. The purpose of the HLP5 and HLP6 goals is to identify the limits of this safe operating regime for ignition targets and to increase this regime as much as possible by incorporating various types of coherence control on the laser beams and by target design choices. Because we do not yet have a predictive capability for LPI in hohlraums, the utility of the conclusions of the HLP5 and HLP6 experiments relies on being able to produce NIF-like plasma conditions with the Nova laser. The Nova plasma conditions approach those expected on NIF but are not identical. The Nova plasmas are typically 3–4 keV while much of the NIF hohlraum interior is 5–6 keV. Scale sizes on Nova were typically a factor of 2–3 shorter than expected on NIF and the ratio of electron to ion temperature is higher on Nova than on NIF. Average absorptions of 90%, which meet the NTC goals, have been achieved in many of the experiments designed to emulate NIF plasmas. However, some of the experiments discussed in Sec. III have total scattering levels which exceed the NTC goals by a factor of 2 and instantaneous scattering can exceed even that level. Experiments are continuing with the goal of achieving an improved predictive capability.

The HEP experiments address the issues of hydrodynamic instability and mix, as well as the effects of flux asymmetry on capsules that are scaled as closely as possible to ignition capsules (hydrodynamic equivalence). The HEP program addresses capsule-physics issues associated with ignition. This includes the physics associated with ignition (energy gain and energy loss to the fuel during implosion) in the absence of α-particle deposition. The HEP program was subdivided into five subgoals:

(1) HEP1: Demonstrate fuel densities of $20-40$ g/cm^3 using high-contrast pulse shaping with noncryogenic targets. The fuel density will be inferred from measurements of fuel areal density ρr using advanced neutron-based diagnostics.
(2) HEP2: Measure the reduced linear growth and early nonlinear behavior of the RT instability at the ablation surface for x-ray-driven targets. Using planar targets, observe single-mode growth at the ablation surface by factors of >30, from which reductions by factors of 2 to 3 from the classical RT growth rate are inferred. Targets of various compositions will be used to confirm the modeling of plasma opacity as it affects x-ray-driven hydrodynamics.
(3) HEP3: Using x-ray spectroscopy, demonstrate pusher/fuel mixing that is dependent on initial target surface quality. The targets will be low-growth (perturbations grow by a factor of about 10), low-convergence ($C_r<10$) plastic capsules with a multimode spectrum of initial surface perturbations.
(4) HEP4: Demonstrate quantitative understanding of implosion experiments to convergence ratios $C_r\approx 10$ with overall hydrodynamic instability growth factors of 100 to 500 for an l-mode spectrum similar to that characteristic of ignition target designs (for which maximum growth occurs for mode numbers $l\approx 30$).
(5) HEP5: Extend HEP4 experiments to convergence ratios $C_r=20-40$ with capsule performance consistent with Nova's symmetry limitations.

HEP1 and HEP3, covered in Sec. VII, were initially viewed as experiments designed to develop quantitative neutron and x-ray techniques for measuring the effects of hydrodynamic instability on implosions. The HEP3 goals required implosions that did not pose a serious challenge to Nova's power and energy balance. However, the density specified in the HEP1 goal could only be met with capsules that had a convergence >20. Success of this objective required the precision Nova improvements to power and energy balance. HEP1 experiments utilized reduced-scale capsules which decreases time-dependent asymmetry variations and increases geometric hohlraum smoothing. These experiments achieved hot fuel density of 20 g/cm^3, the analog of the hot spot in NIF capsules. These experiments also achieved a density of $150-200$ g/cm^3 in the material surrounding and compressing the hot fuel, the analog of the dense cold fuel in the NIF targets. Both of these densities were the highest achieved in the NTC experiments. The comparable NIF densities are $70-100$ g/cm^3 in the hot spot and $900-1200$ g/cm^3 in the surrounding cold fuel.

In general, it is difficult to accurately measure the RT growth of perturbations on a spherical shell. The HEP2 experiments in planar geometry were designed to obtain quantitative growth rates in planar geometry. Since most of the growth of perturbations in an ICF implosion occurs during the first factor-of-2 change in capsule radius, planar experiments capture most of the relevant physics. Planar experiments have been carried out with up to 4–5 e-foldings of growth. Because of its importance to the success of an ICF implosion, the level of experiments actually far exceeded the initial objective of HEP2. Experiments were carried out that

Downloaded 20 Mar 2011 to 69.181.48.121. Redistribution subject to AIP license or copyright; see http://pop.aip.org/about/rights_and_permissions

looked at a variety of nonlinear effects including mode coupling and 2D and 3D mode saturation as well as some convergent geometry experiments. These results are covered in Sec. VI.

The HEP4 and HEP5 experiments are an integral test of the effects of short-wavelength hydrodynamic-instability growth combined with long-wavelength variations in x-ray flux. To be as NIF-like as possible, these experiments require the ratio of the hohlraum radius to the capsule radius to be comparable to those of NIF targets. This ratio governs the geometric smoothing of short-wavelength-radiation flux variations. With Nova's basic 10-beam geometry, even capsules with a convergence ratio of 10 are somewhat degraded in yield. Good capsule performance for higher convergence ratios requires a more sophisticated beam geometry. Current experiments with increased convergence ratio utilize the flexible geometry of the 60-beam Omega laser. The HEP4 and HEP5 experiments on Nova and Omega have been designed to have 4–5 e-foldings of instability growth. For Nova capsule sizes and surface finishes, this level of RT growth results in a mix penetration comparable to that predicted for NIF capsules. The HEP4 goal of predictable performance for convergence-10 capsules was completed on Nova. However, the yield of these capsules was degraded by a factor of 3–4 from an ideal implosion and we have found that it is necessary to include the 3D effects of capsule perturbations and radiation-flux asymmetry in order to quantitatively model the capsule performance in these experiments. HEP4 experiments on Omega, with better radiation symmetry achieve near ideal capsule performance. Capsules with convergence ratios of 20 or more, the HEP5 goal, have also been successfully carried out on Omega. Calculations which include the effects of hydrodynamic instability and hohlraum radiation-flux asymmetry predict the performance of these capsules as indicated in Sec. VII.

Afeyan, B. B., Chou, A. E., Matte, J. P., Town, R., and Kruer, W. L., "Kinetic theory of electron-plasma and ion-acoustic waves in nonuniformity heated laser plasmas," Phys. Rev. Lett. **80**, 2322 (1998).

Albritton, J. R., Williams, E. A., Bernstein, I. B., and Swartz, K. P., "Nonlocal electron heat transport by not quite Maxwell-Boltzmann distributions," Phys. Rev. Lett. **57**, 1887 (1986).

Alon, U., Hecht, J., Mukamel, D., and Shvarts, D., "Scale invariant mixing rates of hydrodynamically unstable interfaces," Phys. Rev. Lett. **72**, 2867 (1994).

Alon, U., Hecht, J., Ofer, D., and Shvarts, D., "Power laws and similarity of Rayleigh–Taylor and Richtmyer–Meshkov mixing fronts at all density ratios," Phys. Rev. Lett. **74**, 534 (1995).

Amendt, P. A., Turner, R. E., and Landen, O. L., "Hohlraum-driven high-convergence implosion experiments with multiple beam cones on the Omega laser facility," Phys. Rev. Lett. **89**, 165001 (2002).

Amendt, P., Glendinning, S. G., Hammel, B. A. *et al.*, "Direct measurement of x-ray drive from surrogate targets in Nova hohlraums," Phys. Rev. Lett. **77**, 3815 (1996).

Amendt, P. A., Murphy, T. J., and Hatchett, S. P., "Novel symmetry tuning in Nova hohlraums using axial gold disks," Phys. Plasmas **3**, 4166 (1996a).

Amendt, P., Glendinning, S. G., Hammel, B. A., Landen, O. L., Murphy, T. J., Suter, L. J., Hatchett, S., Rosen, M. D., Lafitte, S., Desenne, D., and Jadaud, J. P., "New methods for diagnosing and controlling Hohlraum drive asymmetry on Nova," Phys. Plasma **4**, 1862 (1997).

Anderson, D. and Bonnedal, M., "Variational approach to nonlinear self-focusing of Gaussian laser beams," Phys. Fluids **22**, 105 (1979).

Andreev, A. A. and Tikhonchuk, V. T., "Effect of trapped particles on stimulated Brillouin scattering in a plasma," Sov. Phys. JETP **68**, 1135 (1989).

Azechi, H., Miyanaga, N., Stapf, R. O. *et al.*, "Experimental determination of fuel density-radius of inertial confinement fusion targets using secondary nuclear fusion reactions," Appl. Phys. Lett. **49**, 555 (1986).

Back, C. A., Berger, R. L., Estabrook, K. G., Failor, B. H., Hsing, W. W., Hsieh, E. J., Hockaday, R., Kalantar, D. H., Kauffman, R. L., Keane, C. J., Klem, D. E., MacGowan, B. J., Montgomery, D. S., Moody, J. D., Powers, L. V., Shapard, T. D., Stone, G. F., Suter, L. J., and Turner, R. E., "Use of large scale-length plasmas to study parametric plasma instabilities," J. Quant. Spectrosc. Radiat. Transf. **54**, 27 (1995).

Back, C. A., Kalantar, D. H., Kauffman, R. L., Lee, R. W., MacGowan, B. J., Montgomery, D. S., Powers, L. V., Shepard, T. D., Stone, G. F., and Suter, L. J., "Measurements of electron temperature by spectroscopy in hohlraum targets," Phys. Rev. Lett. **77**, 4350 (1996).

Back, C. A., Glenzer, S. H., Landen, O. L. *et al.*, "X-ray diagnostics of hohlraum plasma flow," Rev. Sci. Instrum. **68**, 831 (1997).

Bailey, D. S. (private communication, 1981).

Baker, K. L., Drake, R. P., Bauer, B. S., Estabrook, K. G., Rubenchik, A. M., Labaune, C., Baldis, H. A., Renard, N., Baton, S. D., Schifano, E., Michard, A., Seka, W., and Bahr, R. E., "Observation of the Langmuir decay instability driven by stimulated Raman scattering," Phys. Plasmas **4**, 3012 (1997).

Baker, G. R., Meiron, D. I., and Orszag, S. A., "Vortex simulations of the Rayleigh–Taylor instability," Phys. Fluids **23**, 1485 (1980).

Baker, G. R., McCrory, R. L., Verdon, C. P., and Orszag, S. A., "Rayleigh–Taylor instability of fluid layers," J. Fluid Mech. **178**, 161 (1987).

Baldis, H. A., Villeneuve, D. M., LaFontaine, B., Enright, G. D., Labaune, C., Baton, S., Mounaix, Ph., Pesme, D., Casanova, M., and Rozmus, W., "Stimulated Brillouin scattering in picosecond time scales: Experiments and modeling," Phys. Fluids B **5**, 3319 (1993).

Baldis, H. A., Labaune, C., Moody, J. D., Jalinaud, T., and Tikhonchuk, V. T., "Localization of stimulated Brillouin scattering in random phase plate speckles," Phys. Rev. Lett. **80**, 1900 (1998).

Bar Shalom, A., Oreg, J., Goldstein, W. H., Shvarts, D., and Zigler, A., "Super-transition-arrays: a model for the spectral analysis of hot, dense plasma," Phys. Rev. A **40**, 3183 (1989).

Basko, M. and Johner, J., "Ignition energy scaling of inertial confinement fusion targets," Nucl. Fusion **38**, 1779 (1998).

Bell, A. R., "Electron energy transport in ion waves and its relevance to laser-produced plasmas," Phys. Fluids **26**, 279 (1983).

Bell, G. I., Los Alamos National Laboratory, Report No. LA-1321, 1951.

Bell, P. M., Hammel, B. A., Kilkenny, J. D. *et al., Ultrahigh Speed and High Speed Photography, Photonics and Videography '89*, Proc. SPIE, Int. Soc. Opt. Eng. (USA), 1990, pp. 415–421.

Berger, R. L. (private communication, 2001). Millimeter length simulations of gasbags in two dimensions with mean laser intensities between 0.2 and 2×10^{15} W/cm^2 with similar plasma conditions show increased reflectivity at low intensity but less than a factor of 2 increase at 2×10^{15} W/cm^2 R.

Berger, R. L., "Nonlinear competition between stimulated Brillouin-scattered light waves in plasmas," Phys. Rev. Lett. **51**, 1554 (1983).

Berger, R. L., Williams, E. A., and Simon, A., "Effect of plasma noise spectrum on stimulated scattering in inhomogeneous plasma," Phys. Fluids B **1**, 414 (1989); LIP is a LASNEX postprocessor that computes the kinetically correct gain exponent along the laser ray trajectory. It includes multiple species effects in inhomogeneous plasma.

Berger, R. L., Lasinski, B. F., Kaiser, T. B., Williams, E. A., Langdon, A. B., and Cohen, B. I., "Theory and three-dimensional simulation of light filamentation in laser-produced plasma," Phys. Fluids B **5**, 2243 (1993).

Berger, R. L., Lasinski, B. F., Langdon, A. B., Kaiser, T. B., Afeyan, B. B., Cohen, B. I., Still, C. H., and Williams, E. A., "Influence of spatial temporal laser beam smoothing on stimulated Brillouin scattering in filamentary laser light," Phys. Rev. Lett. **75**, 1078 (1995); **76**, 3239(E) (1996).

Berger, R. L., Still, C. H., Williams, E. A., and Langdon, A. B., "On the dominant and subdominant behavior of stimulated Raman and Brillouin scattering driven by nonuniform laser beams," Phys. Plasmas **5**, 4337 (1998).

Berger, R. L., Lefebvre, E., Langdon, A. B., Rothenberg, J. E., Still, C. H., and Williams, E. A., "Stimulated Raman and Brillouin scattering of polarization-smoothed and temporally smoothed laser beams," Phys. Plasmas **6**, 1043 (1999).

Betti, R., Goncharov, V. N., McCrory, R. L., Sorotokin, P., and Verdon, C. P.,

Downloaded 20 Mar 2011 to 69.181.48.121. Redistribution subject to AIP license or copyright; see http://pop.aip.org/about/rights_and_permissions

''Self-consistent stability analysis of ablation fronts in inertial confinement fusion,'' Phys. Plasmas **3**, 2122 (1996).
Betti, R., Goncharov, V. N., McCrory, R. L., and Verdon, C. P., ''Growth rates of the ablative Rayleigh-Taylor instability in inertial confinement fusion,'' Phys. Plasmas **5**, 1446 (1998).
Bezzerides, B., DuBois, D. F., and Rose, H. A., ''Saturation of stimulation Raman scattering by the excitation of strong Langmuir turbulence,'' Phys. Rev. Lett. **70**, 2569 (1993).
Bezzerides, B., ''Intrinsic bending of a laser beam in a flowing plasma,'' Phys. Plasmas **5**, 2712 (1998).
Birdsall, C. K. and Langdon, A. B., *Plasma Physics via Computer Simulation* (McGraw-Hill, New York, 1985).
Blue, T. E. and Harris, D. B., ''The ratio of D–T to D–D reactions as a measure of the fuel density-radius product in initially tritium-free inertial confinement fusion targets,'' Nucl. Sci. Eng. **77**, 463 (1981).
Bodner, S. E., Colombant, D. G., Gardner, J. H., Lehmberg, R. H., Obenshain, S. P., Phillips, L., Schnitt, A. J., Sethian, J. D., McCrory, R. L., Seka, W., Verdon, C., Knauer, J. P., Afeyan, B. B., and Powell, H. T., ''Direct-drive laser fusion: Status and prospects,'' Phys. Plasmas **5**, 1901 (1998).
Bodner, S. E., ''Rayleigh–Taylor instability and laser-pellet fusion,'' Phys. Rev. Lett. **33**, 761 (1974).
Boehly, T. R. *et al.*, ''Reduction of laser imprinting using polarization smoothing on a solid-state fusion laser,'' J. Appl. Phys. **85**, 3444 (1999).
Bonnaud, G., Pesme, D., and Pellat, R., ''Nonlinear Raman scattering behavior with Langmuir and sound waves coupling in a homogeneous plasma,'' Phys. Fluids B **2**, 1618 (1990).
Born, M. and Wolf, E., *Principles of Optics*, 5th ed. (Pergamon, New York, 1975), Sec. 3.2.1.
Braginskii, S. I., ''Transport processes in plasmas,'' *Reviews of Plasma Physics* (Consultants Bureau, New York, 1965), Vol. 1, pp. 205–311.
Brantov, A., Bychenkov, V. Yu., Tikhonchuk, V. T., and Rozmus, W., ''Nonlocal plasma electron hydrodynamic,'' JETP **83**, 716 (1996).
Brantov, A., Bychenkov, V. Yu., Tikhonchuk, V. T., and Rozmus, W., ''Nonlocal electron transport in laser heated plasmas,'' Phys. Plasmas **5**, 2742 (1998).
Brunner, S. and Valeo, E., ''Trapped-particle instability leading to bursting in stimulated Raman scattering simulations,'' Phys. Rev. Lett. (submitted).
Brunner, S. and Valeo, E., ''Simulations of electron transport in laser hot spots,'' Phys. Plasmas **9**, 923 (2002).
Budil, K. S., Perry, T. S., Bell, P. M., Hares, J. D., Miller, P. L., Peyser, T. A., Wallace, R., Louis, H., and Smith, D. E., ''The flexible x-ray imager,'' Rev. Sci. Instrum. **67**, 485 (1996).
Buresi, E., Coutant, J., Dautray, R., Decroisette, M., Duborgel, B., Guillaneux, P., Launspach, J., Nelson, P., Patou, C., Reisse, J. M., and Watteau, J. P., ''Laser program development at CLE-V: Overview of recent experimental results,'' Laser Part. Beams **4**, 531 (1986).
Busquet, M., ''Radiation-dependent ionization model for laser-created plasmas,'' Phys. Fluids B **5**, 4191 (1993).
Bychenkov, V. Yu., Rozmus, W., and Tikhonchuk, V. T., ''Nonlocal electron transport in a plasma,'' Phys. Rev. Lett. **75**, 4405 (1995).
Bychenkov, V. Yu., Rozmus, W., Brantov, A., and Tikhonchuk, V. T., ''Theory of filamentation instability and stimulated Brillouin scattering with nonlocal hydrodynamics,'' Phys. Plasmas **7**, 1511 (2000).
Bychenkov, V. Yu., Rozmus, W., and Tikhonchuk, V. T., ''Stimulated Raman scattering in non-Maxwellian plasmas,'' Phys. Plasmas **4**, 1481 (1997).
Cable, M. D., Hatchett, S. P., and Nelson, M. B., ''Neutron spectroscopy with a large neutron time-of-flight detector array (Lansa),'' Rev. Sci. Instrum. **63**, 4823 (1992).
Cable, M. D., Lane, S. M., Glendinning, S. G. *et al.*, ''Implosion experiments at Nova,'' Bull. Am. Phys. Soc. **31**, 1461 (1986).
Cable, M. D. and Hatchett, S. P., ''Neutron spectra from inertial confinement fusion targets for measurement of fuel areal density and charged particle stopping powers,'' J. Appl. Phys. **62**, 2233 (1987).
Cable, M., Hatchett, S. E., Caird, J. A., Kilkenny, J. D., Kornblum, H. N., Lane, S. M., Laumann, C. W., Lerche, R. A., Murphy, T. J., Murray, J., Nelson, M. B., Phillion, D. W., Powell, H. T., and Ress, D. B., ''Indirect driven, high convergence inertial confinement fusion implosions,'' Phys. Rev. Lett. **73**, 2316 (1994).
Caillard, J. and Lefebvre, E. (private communication, 1999).
Caird, J. A., Ehrlich, R. B., Hermes, G. L. *et al.*, *11th International Workshop on Laser Interaction and Related Plasma Phenomena*, AIP Conf. Proc. 244–245 (1994).
Campbell, E. M. *et al.*, ''Recent results from the Nova program at LLNL,'' Laser Part. Beams **9**, 209 (1991).
Caruso, A. and Strangio, C., ''The quality of the illumination for a spherical cavity enclosed in a radiating cavity,'' Jpn. J. Appl. Phys., Part 1 **30**, 1095 (1991).
Chandrasekhar, S., *Hydrodynamic and Hydromagnetic Stability*, The International Series of Monographs on Physics (Clarendon, Oxford, 1961).
Cherfils, C., Glendinning, S. G., Galmiche, D., Remington, B. A., Richard, A. L., Haan, S., Wallace, R., Dague, N., and Kalantar, D. H., ''Convergent Rayleigh–Taylor experiments on the Nova laser,'' Phys. Rev. Lett. **83**, 5507 (1999).
Chrien, R. E., Hoffman, N. M., Colvin, J. D., Landen, O. L., and Hammel, B. A., ''Fusion neutrons from the gas-pusher interface in deuterated-shell inertial confinement fusion implosions,'' Phys. Plasmas **5**, 768 (1998).
Cobble, J. A., Fernandez, J. C., Kurnit, N. A., Montgomery, D. S., Johnson, R. P., Renard-LeGalloudec, N., and Lopez, M. R., ''The spatial location of laser-driven, forward-propagating waves in a National-Igntion-Facility-relevant plasma,'' Phys. Plasmas **7**, 323 (2000). The temporal history of SRS and SBS do not always support anticorrelation as shown in Trident experiments. The Thomson scatter measurements of the plasma waves in these experiments do indicate an anticorrelation in space possibly caused by nonlinear interaction.
Coggeshall, S., Mead, W., and Jones, R., ''Flicker in small scale laser-plasma self-focusing,'' Phys. Fluids **31**, 2750 (1988).
Cohen, B. I., Lasinski, B. F., Langdon, A. B., and Cummings, J. C., ''Dynamics of ponderomotive self-focusing in plasmas,'' Phys. Fluids B **3**, 766 (1991).
Cohen, B. I., Baldis, H. A., Berger, R. L., Estabrook, K. G., Williams, E. A., and Labaune, C., ''Modeling of the competition of stimulated Raman and Brillouin scatter in multiple beam experiments,'' Phys. Plasmas **8**, 571 (2001).
Cohen, B. I. and Kaufman, A. N., ''Effects of beat-wave electron trapping on stimulated Raman and Thomson scattering,'' Phys. Fluids **21**, 404 (1978).
Cohen, B. I., Lasinski, B. F., Langdon, A. B., and Williams, E. A., ''Resonantly excited nonlinear ion waves,'' Phys. Plasmas **4**, 956 (1997).
Cohen, B. I., Lasinski, B. F., Langdon, A. B., Williams, E. A., Wharton, K. B., Kirkwood, R. K., and Estabrook, K. G., ''Resonant stimulated Brillouin interaction of opposed laser beams in a drifting plasma,'' Phys. Plasmas **5**, 3408 (1998).
Collins, G. W., Bernat, T. P., Mapoles, E. R., and Duriez, C., ''Heat-flux induced changes to multicrystalline D_2 surfaces,'' LLNL Report No. UCRL-JC-124261.
Cook, A. W. and Dimotakis, P. E., ''Transition stages of Rayleigh–Taylor instability between miscible fluids,'' J. Fluid Mech. **443**, 66 (2001).
Cook, R., Overturf, G. E., Buckley, S. R., and McEachern, R., ''Production and characterization of doped mandrels for inertial confinement fusion experiments,'' J. Vac. Sci. Technol. A **12**, 1275 (1994).
Corman, E. G., Loewe, W. B., Cooper, G. E., and Winslow, A. M., ''Multigroup diffusion of energetic charged particles,'' Nucl. Fusion **15**, 377 (1975).
Dahlburg, J. P. and Gardner, J. H., ''Ablative Rayleigh–Taylor instability in 3-dimensions'' Phys. Rev. A **41**, 5695 (1990).
Dattolo, E., Suter, L. J., Monteil, M-C., Jaudad, J.-P. *et al.* ''Status of our understanding and modeling of x-ray coupling efficiency in laser heated hohlraums,'' Phys. Plasmas **8**, 260 (2001).
Davies, R. M. and Taylor, G. I., Proc. R. Soc. London, Ser. A **200**, 375 (1950).
Dawson, J., Kaw, P., and Green, B., ''Optical absorption and expansion of laser-produced plasmas,'' Phys. Fluids **12**, 875 (1969).
Decker, C., Turner, R. E., Landen, O. L. *et al.*, ''Hohlraum radiation drive measurements on the Omega laser,'' Phys. Rev. Lett. **79**, 1491 (1997).
Delamater, N. D., Lindman, E. L., Magelssen, G. R. *et al.*, ''Observation of reduced beam deflection using smoothed beams in gas-filled hohlraum symmetry experiments at Nova,'' Phys. Plasmas **7**, 1609 (2000).
Delamater, N. D., Murphy, T. J., Hauer, A. A. *et al.*, ''Symmetry experiments in gas-filled hohlraums at NOVA,'' Phys. Plasmas **3**, 2022 (1996).
Delamater, N. D., Magelssen, G. R., and Hauer, A. A., ''Re-emission technique for symmetry measurements in hohlraum targets containing a centered high-Z ball,'' Phys. Rev. E **53**, 5240 (1996a).
Depierreux, S., Fuchs, J., Labaune, C., Michard, A., Baldis, H. A., Pesme, D., Huller, S., and Laval, G., ''First observation of ion-acoustic waves produced by the Langmuir decay instability,'' Phys. Rev. Lett. **84**, 2869 (2000).

Downloaded 20 Mar 2011 to 69.181.48.121. Redistribution subject to AIP license or copyright; see http://pop.aip.org/about/rights_and_permissions

Dimonte, G. and Schneider, M., ''Density ratio dependence of Rayleigh–Taylor mixing for sustained and impulsive acceleration histories,'' Phys. Fluids **12**, 304 (2000).
Dimonte, G. and Remington, B., ''Richtmyer-Meshkov experiments on the Nova laser at high comparison,'' Phys. Rev. Lett. **70**, 1806 (1993).
Dittrich, T. R., Haan, S. W., Marinak, M. M., Pollaine, S. M., Hinkel, D. E., Munro, D. H., Verdon, C. P., Strobel, G. L., McEachern, R., Cook, R. C., Roberts, C. C., Wilson, D. C., Bradley, P. A., Foreman, L. R., and Varnum, W. S., ''Review of indirect-drive ignition design options for the National Ignition Facility,'' Phys. Plasmas **6**, 2164 (1999).
Dittrich, T. R., Hammel, B. A., Keane, C. J., McEachern, R., Turner, R. E., Haan, S. W., and Suter, L. J., ''Diagnosis of pusher-fuel mix in indirectly driven Nova implosions,'' Phys. Rev. Lett. **73**, 2324 (1994).
Dixit, S. N., Lawson, J. K., Manes, K. R., Powell, H. T., and Nugent, K. A., ''Kinoform phase plates for focal plane irradiance profile control,'' Opt. Lett. **19**, 417 (1994).
Dixit, S. N., Thomas, I. M., Woods, B. W., Morgan, A. J., Henesian, M. A., Wegner, P. J., and Powell, H. T., ''Random phase plates for beam smoothing on the Nova laser,'' Appl. Opt. **32**, 2543 (1993).
Drake, R. P. and Batha, S. H., ''The influence of subsidiary Langmuir ceday on the spectrum of stimulated Raman scattering,'' Phys. Fluids B **3**, 2936 (1991).
DuBois, D. F. and Goldman, M. V., ''Radiation-induced instability of electron plasma oscillations,'' Phys. Rev. Lett. **14**, 544 (1965); Phys. Rev. **164**, 207 (1967).
DuBois, D. F. and Goldman, M. V., ''Parametrically excited plasma fluctuations,'' Phys. Rev. **164**, 207 (1967).
DuBois, D. F. (private communication, 1998).
Ehrlich, R. B., Amendt, P. A., Dixit, S. N., *et al.*, ''Solid state lasers for application to inertial confinement fusion: Second Annual International Conference,'' Proc. SPIE, Int. Soc. Opt. Eng. (USA), 1997, pp. 819–824.
Eliseev, V. V., Rozmus, W., Tikhonchuk, V. T., and Capjack, C. E., ''Interaction of crossed laser beams with plasmas,'' Phys. Plasmas **3**, 2215 (1996).
Ellis, R. J., Trebes, J. E., Phillion, D. W., Kilkenny, J. D., Glendinning, S. G., Wiedwald, J. D., and Levesque, R. A., ''Four frame gated Wolter x-ray microscope,'' Rev. Sci. Instrum. **61**, 2759 (1990).
Emmett, J. L., Krupke, W. F., and Trenholme, J. B., ''Future development of high-power solid-state laser systems,'' Sov. J. Quantum Electron. **13**, 1 (1983).
Endo, T., Shigemori, K., Azechi, H., Nishiguchi, A., Mima, K., Sato, M., Nakai, M., Nakaji, S., Miyanaga, N., Matsuoka, S., Ando, A., Tanaka, K. A., and Nakai, S., ''Dynamic behavior of rippled shocks and subsequently-induced areal-density-perturbation growth in laser-induced foils,'' Phys. Rev. Lett. **74**, 3608 (1995).
Epperlein, E. M., ''Kinetic theory of laser filamentation in plasmas,'' Phys. Rev. Lett. **65**, 2145 (1990).
Epperlein, E. M., ''Kinetic simulations of laser filamentation in plasmas,'' Phys. Fluids B **3**, 3082 (1991).
Epperlein, E. M., ''Effect of electron collisions on ion-acoustic waves and heat flow,'' Phys. Plasmas **1**, 109 (1994).
Epperlein, E. M. and Short, R. W., ''Nonlocal heat transport effects on the filamentation of light in plasmas,'' Phys. Fluids B **4**, 2211 (1992).
Epperlein, E. M. and Short, R. W., ''Comment on 'Theory and three-dimensional simulation of light filamentation in laser-produced plasmas,' '' Phys. Plasmas **1**, 1364 (1994).
Epperlein, E. M., Short, R. W., and Simon, A., ''Damping of ion-acoustic waves in the presence of electron-ion collisions,'' Phys. Rev. Lett. **69**, 1765 (1992).
Estabrook, K., Kruer, W. L., and Haines, M. G., ''Nonlinear features of stimulated Brillouin and Raman scattering,'' Phys. Fluids B **1**, 1282 (1989).
Estabrook, K. G., Kruer, W. L., and Lasinski, B. F., ''Heating by Raman backscattering and forward scatter,'' Phys. Rev. Lett. **45**, 1399 (1980).
Farley, D. R., Estabrook, K. G., Glendinning, S. G., Glenzer, S. H., Remington, B. A., Shigemori, K., Stone, J. M., Wallace, R. J., Zimmerman, G. B., and Harte, J. A., ''Radiative jet experiments of astrophysical interest using intense lasers,'' Phys. Rev. Lett. **83**, 1982 (1999).
Fernandez, J. C., Cobble, J. A., Failor, B. H., DuBois, D. F., Montgomery, D. S., Rose, H. A., Vu, H. X., Wilde, B. H., Wilke, M. D., and Chrien, R. E., ''Observed dependence of stimulated Raman scattering on ion-acoustic damping in hohlraum plasmas,'' Phys. Rev. Lett. **77**, 2702 (1996).
Fernandez, J. C., Cobble, J. A., Montgomery, D. S., Wilke, M. D., and Afeyan, B. B., ''Observed insensitivity of stimulated Raman scattering on electron density,'' Phys. Plasmas **7**, 3743 (2000).
Fernandez, J. C., Berggren, R. R., Bradley, K. S., Hsing, W. W., Gomez, C. C., Cobble, J. A., and Wilks, M. D., ''Improved optical diagnostics for the Nova laser,'' Rev. Sci. Instrum. **66**, 626 (1995).
Fernandez, J. C., Cobble, J. A., Failor, B. H., Hsing, W. W., Rose, H. A., Wilde, B. H., Bradley, K. S., Gobby, P. L., Kirkwood, R., Kornblum, H. N., Montgomery, D. S., and Wilke, M. D., ''Dependence of stimulated Brillouin scattering on laser intensity, laser f number, and ion species in hohlraum plasmas,'' Phys. Rev. E **53**, 2747 (1996a).
Fernandez, J. C., Bauer, B. S., Cobble, J. A., DuBois, D. F., Kyrala, G. A., Montgomery, D. S., Rose, H. A., Vu, H. X., Watt, R. G., Wilde, B. H., Wilke, M. D., Wood, W. M., Failor, B. H., Kirkwood, R., and MacGowan, B. J., ''Measurements of laser-plasma instability relevant to ignition hohlraums,'' Phys. Plasmas **4**, 1849 (1997).
Fleck, Jr., J. A. and Cummings, J. D., ''An implicit Monte Carlo scheme for calculating time and frequency dependent nonlinear radiation transport,'' J. Comput. Phys. **8**, 313 (1971).
Foord, M. E., Glenzer, S. H., Thoe, R. S., Wong, K. L., Fournier, K. B., Wilson, B. G., and Springer, P. T., ''Ionization processes and charge-state distribution in a highly ionized high-z laser-produced plasma,'' Phys. Rev. Lett. **85**, 992 (2000).
Forslund, D. W., Kindel, J. M., and Lindman, E. L., ''Theory of stimulated scattering processes in laser-irradiated plasmas,'' Phys. Fluids **18**, 1002 (1975); **18**, 1017 (1975).
Forslund, D. W., Kindel, J. M., and Lindman, E. L., Phys. Fluids **18**, 1017 (1975a).
Fourkal, E., Bychenkov, V. Yu., Rozmus, W., Sydora, R., Kirkby, C., Capjack, C. E., Glenzer, S. H., and Baldis, H. A., ''Electron distribution function in laser-heated plasmas,'' Phys. Plasmas **8**, 550 (2001).
Fraley, G. S., Gula, W. P., Henderson, D. B., McCrory, R. L., Malone, R. C., Mason, R. J., and Morse, R. L., ''Implosion, stability, and burn of multi-shell fusion pellets,'' *Plasma Physics and Controlled Nuclear Fusion Research II* (International Atomic Energy Agency, Vienna, 1975), pp. 543–555.
Freed, N., Ofer, D., Shvarts, D., and Orszag, S. A., ''2-Phase flow analysis of self-similar turbulent mixing by Rayleigh–Taylor instability,'' Phys. Fluids A **3**, 912 (1991).
Froula, D. H., Divol, L., and Glenzer, S. H., ''Measurements of nonlinear growth of ion-acoustic waves in two-ion-species plasmas with Thomson scattering,'' Phys. Rev. Lett. **88**, 105003 (2002).
Fusion Policy Advisory Committee Final Report, DOE/S0081 (U.S. Department of Energy, Washington, DC, 1990)
Gamalii, E. G., Guskov, S. Yu., Krokhin, O. N., and Rozanov, V. B., ''Possibility of determining the characteristics of laser plasma by measuring the neutrons of the DT reaction,'' JETP Lett. **21**, 70 (1975).
Gamaly, E. G., Lebo, I. G., Rozanov, V. B., Favorsky, A. P., Fedyanin, A. O., Myshetskaya, E. E., and Tishkin, V. F., ''Nonlinear stage in the development of hydrodynamic instability in laser targets,'' Laser Part. Beams **8**, 173 (1990).
Geddes, C. G. R., Kirkwood, R. K., Glenzer, S. H., Estabrook, K. G., Cohen, B. I., Young, P. E., Joshi, C., and Wharton, K. B., ''Observation of ion wave decay products of Langmuir waves generated by stimulated Raman scattering in ignition scale plasmas,'' Phys. Plasmas **10**, 3422 (2003).
Ghizzo, A., Bertrand, P., Shoucri, M. M., Johnston, T. W., Fijalkow, E., and Feix, M. R., ''A Vlasov code for the numerical simulation of stimulated Raman scattering,'' J. Comput. Phys. **90**, 431 (1990).
Ghosal, S. and Rose, H. A., ''Two-dimensional plasma flow past a laser beam,'' Phys. Plasmas **4**, 2376 (1997).
Glendinning, S. G., Amendt, P., Cline, B. D. *et al.*, ''Hohlraum symmetry measurements with surrogate solid targets,'' Rev. Sci. Instrum. **70**, 536 (1999).
Glendinning, S. G., Colvin, J., Haan, S., Kalantar, D. H., Landen, O. L., Marinak, M. M., Remington, B. A., Wallace, R., Cherfils, C., Dague, N., Divol, L., Galmiche, D., and Richard, A. L., ''Ablation front Rayleigh–Taylor growth experiments in spherically convergent geometry,'' Phys. Plasmas **7**, 2033 (2000).
Glendinning, S. G., Weber, S. V., Bell, P., DaSilva, L. B., Dixit, S. N., Henesian, M. A., Kania, D. R., Kilkenny, J. D., Powell, H. T., Wallace, R. J., Wegner, P. J., Knauer, J. P., and Verdon, C. P., ''Laser driven planar Rayleigh–Taylor instability experiments,'' Phys. Rev. Lett. **69**, 1201 (1992).

Downloaded 20 Mar 2011 to 69.181.48.121. Redistribution subject to AIP license or copyright; see http://pop.aip.org/about/rights_and_permissions

Glenzer, S. H., Rosmej, F. B., Lee, R. W., Back, C. A., Estabrook, K. G., MacGowan, B. J., Shepard, T. D., and Turner, R. E., ''Measurements of suprathermal electrons in hohlraum plasmas with x-ray spectroscopy,'' Phys. Rev. Lett. **81**, 365 (1998).

Glenzer, S. H., Suter, L. J., Berger, R. L., Estabrook, K. G., Hammel, B. A., Kauffman, R. L., Kirkwood, R. K., MacGowan, B. J., Moody, J. D., Rothenberg, J. E., and Turner, R. E., ''Hohlraum energetics with smoothed laser beams,'' Phys. Plasmas **7**, 2585 (2000).

Glenzer, S. H., Fournier, K. B., Decker, C., Hammel, B. A., Lee, R. W., Lours, L., MacGowan, B. J., and Osterheld, A. L., ''Accuracy of K-shell spectra modeling in high-density plasmas,'' Phys. Rev. E **62**, 2728 (2000a).

Glenzer, S. H., Contrib. Plasma Phys. **40**, 36 (2000).

Glenzer, S. H., Berger, R. L., Divol, L. M., Kirkwood, R. K., MacGowan, B. J., Moody, J. D., Rothenberg, J. E., Suter, L. J., and Williams, E. A., ''Reduction of stimulated scattering losses from hohlraum plasmas with laser beam smoothing,'' Phys. Plasmas **8**, 1692 (2001).

Glenzer, S. H., Divol, L. M., Berger, R. L., Geddes, C., Kirkwood, R. K., Moody, J. D., Williams, E. A., and Young, P. E., ''Thomson scattering measurements of saturated ion waves in laser fusion plasmas,'' Phys. Rev. Lett. **86**, 2565 (2001a).

Glenzer, S. H., Back, C. A., Estabrook, K. G., Wallace, R., Baker, K., MacGowan, B. J., Hammel, B. A., Cid, R. E., and De Groot, J. S., ''Observation of two ion-acoustic waves in a two-species laser-produced plasma with Thomson scattering,'' Phys. Rev. Lett. **77**, 1496 (1996).

Glenzer, S. H., Back, C. A., Estabrook, K. G., and MacGowan, B. J., ''Thomson scattering in the corona of laser-produced gold plasmas,'' Rev. Sci. Instrum. **68**, 668 (1997).

Glenzer, S. H., Back, C. A., Suter, L. J. *et al.*, ''Thomson scattering from inertial-confinement-fusion hohlraum plasmas,'' Phys. Rev. Lett. **79**, 1277 (1997a).

Glenzer, S. H., Back, C. A., Estabrook, K. G., MacGowan, B. J., Montgomery, D. S., Kirkwood, R. K., Moody, J. D., Munro, D. H., and Stone, G. F., ''Electron temperature and density measurements in laser-produced large-scale-length gas-bag plasmas by x-ray spectroscopy,'' Phys. Rev. E **55**, 927 (1997b).

Glenzer, S. H., Back, C. A., Suter, L. J. *et al.*, ''Thomson scattering from inertial confinement fusion plasmas,'' *13th Laser Interaction and Related Plasma Phenomena*, AIP Conf. Series **406**, 95 (1997c).

Glenzer, S. H. (private communication, 1998).

Glenzer, S. H., Suter, L. J., Turner, R. E., MacGowan, B. J., Estabrook, K. G., Blain, M. A., Dixit, S. N., Hammel, B. A., Kauffman, R. L., Kirkwood, R. K., Landen, O. L., Monteil, M.-C., Moody, J. D., Orzechowski, T. J., Pennington, D. M., Stone, G. F., and Weiland, T. L., ''Energetics of inertial confinement fusion hohlraum plasmas,'' Phys. Rev. Lett. **80**, 2845 (1998a).

Glenzer, S. H., Rozmus, W., MacGowan, B. J., Estabrook, K. G., De Groot, J. D., Zimmerman, G. B., Baldis, H. A., Harte, J. A., Lee, R. W., Williams, E. A., and Wilson, B. G., ''Thomson scattering from high-z laser-produced plasmas,'' Phys. Rev. Lett. **82**, 97 (1999).

Glenzer, S. H., Weiland, T. L., Bower, J., MacKinnon, A. J., and MacGowan, B. J., ''High-energy 4 omega probe laser for laser-plasma experiments at Nova,'' Rev. Sci. Instrum. **70**, 1089 (1999a).

Glenzer, S. H., Alley, W. E., Estabrook, K. G. *et al.*, ''Thomson scattering from laser plasmas,'' Phys. Plasmas **6**, 2117 (1999b).

Goncharov, V. N., Betti, R., McCrory, R. L., and Verdon, C. P., ''Self-consistent stability analysis of ablation fronts with small Froude numbers,'' Phys. Plasmas **3**, 4665 (1996).

Grun, J., Emery, M. E., Manka, C. K., Lee, T. N., McLean, E. A., Mostovych, A., Stamper, J., Bodner, S., Obenschain, S. P., and Ripin, B. H., ''Rayleigh–Taylor instability growth rates in targets accelerated with a laser beam smoothed by induced spatial incoherence,'' Phys. Rev. Lett. **58**, 2672 (1987).

Haan, S., Dittrich, T., Marinak, M., and Hinkel, D., ''Design of ignition targets for the National Ignition Facility,'' *Proceeding of the Conference on Inertial Fusion Science and Applications '99* (Elsevier, Paris, France, 2000).

Haan, S. W., ''Radiation transport between concentric spheres,'' Lawrence Livermore National Laboratory, Livermore, CA, COPD 83-64, 1983.

Haan, S., ''Stability analysis of a direct drive ignition capsule,'' ICF Program Annual Report UCRL-116901-88/89, 1989, p. 130.

Haan, S., ''The onset of non-linear saturation for Rayleigh–Taylor growth in the presence of a full spectrum of modes,'' Phys. Rev. A **39**, 5812 (1989a).

Haan, S. W., ''Weakly nonlinear hydrodynamic instabilities in inertial fusion,'' Phys. Fluids B **3**, 2349 (1991).

Haan, S. W., Pollaine, S. M., Lindl, J. D., Suter, L. J., Berger, R. L., Powers, L. V., Alley, W. E., Amendt, P. A., Futterman, J. A., Levedahl, W. K., Rosen, M. D., Rowley, D. P., Sacks, R. A., Shestakov, A. I., Strobel, G. L., Tabak, M., Weber, S. V., Zimmerman, G. B. from LLNL and Krauser, W. J., Wilson, D. C., Coggeshall, S., Harris, D. B., Hoffman, N. M., and Wilde, B. H. from LANL, ''Design and modeling of ignition targets for the National Ignition Facility,'' Phys. Plasmas **2**, 2480 (1995).

Hammel, B. A., Bell, P., Keane, C. J., Lee, R. W., and Lewis, C. L. S., ''High Z x-ray spectroscopy on laser-imploded capsules,'' Rev. Sci. Instrum. **61**, 2774 (1990).

Hammel, B. A., Griswold, D., Landen, O. L., Perry, T. S., Remington, B. A., Miller, P. L., Peyser, T. A., and Kilkenny, J. D., ''X-ray radiographic measurements of radiation driven shock and interface motion in solid density material,'' Phys. Fluids B **5**, 2259 (1993).

Hammel, B. A., Keane, C. J., Cable, M. D., Kania, D. R., Kilkenny, J. D., Lee, R. W., and Pasha, R., ''X-ray spectroscopic measurements of high densities and temperatures from indirectly driven inertial fusion capsules,'' Phys. Rev. Lett. **70**, 1263 (1993a).

Hammel, B. A., Kilkenny, J. D., Munro, D., Remington, B. A., Kornblum, H. N., Perry, T. S., Phillion, D. W., and Wallace, R. J., ''X-ray radiographic imaging of hydrodynamic phenomena in radiation driven materials—shock propagation, material compression and sheer flow,'' Phys. Plasmas **1**, 1662 (1994).

Hammel, B. A., Keane, C. J., Dittrich, T. R., Kania, D. R., Kilkenny, J. D., Lee, R. W., and Levedahl, W. K., ''K- and L-shell x-ray spectroscopic measurements and pusher dopants in indirectly driven ICF implosions,'' J. Quant. Spectrosc. Radiat. Transf. **51**, 113 (1994a).

Hammer, J. H., Tabak, M., Wilks, S. C., Lindl, J. D., Bailey, D. S., Rambo, P. W., Toor, A., Zimmerman, G. B., and Porter, Jr., J. L., ''High yield inertial confinement fusion target design for a z-pinch-driven hohlraum,'' Phys. Plasmas **6**, 2129 (1999).

Hammer, J. H. and Rosen, M. D. ''A consistent approach to solving the radiation diffusion equation,'' Phys. Plasmas **10**, 1829 (2003).

Hatchett, S. P., Lawrence Livermore National Laboratory, Livermore, CA (private communication, 1993).

Hatchett, S. P. and Rosen, M. D., ''Analysis of radiation-driven rocket efficiency,'' Laser Program Annual Report 1981/1982, Lawrence Livermore National Laboratory, Livermore, CA, UCRL-50055-81/82, 1982, pp. 2-15–2-20.

Hattori, F., Takabe, H., and Mima, K., ''Rayleigh–Taylor instability in a spherically stagnating system,'' Phys. Fluids **29**, 1719 (1986).

Hauer, A. A., Suter, L., Delamater, N. *et al.*, ''The role of symmetry in indirect-drive laser fusion,'' Phys. Plasmas **2**, 2488 (1995).

Hauer, A. A., Delamater, N. D., and Koenig, Z. M., ''High-resolution x-ray spectroscopic diagnostics of laser-heated and ICF plasmas,'' Laser Part. Beams **9**, 3 (1991).

Hauer, A., Delamater, N., Ress, D. *et al.*, ''Review of drive symmetry measurement and control experiments on the Nova laser system,'' Rev. Sci. Instrum. **66**, 672 (1995a).

Hecht, J., Alon, U., and Shvarts, D., ''Potential flow models of Rayleigh–Taylor and Richtmyer–Meshkov bubble fronts,'' Phys. Fluids **6**, 4019 (1994).

Heikkinen, J. A., Karttunen, S. J., and Salomaa, R. R. E., ''Ion acoustic nonlinearities in stimulated Brillouin scattering,'' Phys. Fluids **27**, 707 (1984).

Hemker, R. G. *et al.*, *Proceedings of the 1999 Particle Accelerator Conference, New York* (IEEE, Piscataway, NJ, 1999), Vol. 5, p. 3672.

Hemker, R. G., Ph.D. dissertation, UCLA, 2000.

Henderson, D. B., McCrory, R. L., and Morse, R. L., ''Ablations stability of laser-driven implosions,'' Phys. Rev. Lett. **33**, 205 (1974).

Herrmann, M., Tabak, M., and Lindl, J. D., ''A generalized scaling law for the ignition energy of inertial confinement fusion capsules,'' Nucl. Fusion **41**, 99 (2001).

Herrmann, M. C., Tabak, M., and Lindl, J. D., ''Ignition scaling laws and their application to capsule design,'' Phys. Plasmas **8**, 2296 (2001a).

Hinkel, D. E., Haan, S. W., Dittrich, T. R., and Marinak, M. M., ''National Ignition Facility targets driven at high radiation temperature: Ignition, hydrodynamic stability, and laser–plasma interactions,'' Phys. Plasmas (to be published).

Hinkel, D. E. (private communication, 1996).

Hinkel, D. E., Williams, E. A., and Still, C. H., ''Laser beam deflection induced by transverse plasma flow,'' Phys. Rev. Lett. **77**, 1298 (1996).

Downloaded 20 Mar 2011 to 69.181.48.121. Redistribution subject to AIP license or copyright; see http://pop.aip.org/about/rights_and_permissions

Hinkel, D. E., Williams, E. A., Berger, R. L., Powers, L. V., Langdon, A. B., and Still, C. H., ''Propagation of realistic beams in underdense plasma,'' Phys. Plasmas **5**, 1887 (1998).
Hinkel, D. E., Berger, R. L., Williams, E. A., Langdon, A. B., Still, C. H., and Lasinski, B. F., ''Stimulated Brillouin backscatter in the presence of transverse plasma flow,'' Phys. Plasmas **6**, 571 (1999).
Hiob, E. and Barnard, A. J., ''Vlasov simulation of stimulated Raman scattering in one dimension,'' Phys. Fluids **26**, 3119 (1983).
Hoffer, J. K. and Foreman, L. R., ''Radioactively-induced sublimation in solid tritium,'' Phys. Rev. Lett. **60**, 1310 (1988).
Hoffer, J. K., Foreman, L. R., Mapoles, E. R., and Simpson, J. D., ''Forming a uniform shell of solid DT fusion fuel by the beta-layering process,'' *Nuclear Fusion Research 1992* (International Atomic Energy Agency, Vienna, 1992), Vol. 3, p. 443.
Hoffer, J. K., Foreman, L. R., Mapoles, E. R. (private communication, 1995).
Honda, H., Nishimura, H., Miyamoto, S. *et al.*, ''Influence of specularly reflected laser light on uniformity of implosion of indirect-drive fusion capsule,'' Plasma Phys. Controlled Fusion **40**, 1097 (1998).
Hsing, W. W., Barnes, C. W., Beck, J. B., Hoffman, N. M., Galmiche, D., Richard, A., Edwards, J., Graham, P., Rothman, S., and Thomas, B., ''Rayleigh–Taylor instability evolution in ablatively driven cylindrical implosions,'' Phys. Plasmas **4**, 1832 (1997).
Hsing, W. W. and Hoffman, N. M., ''Measurement of feedthrough and instability growth in radiation-driven cylindrical implosions,'' Phys. Rev. Lett. **78**, 3876 (1997).
Hüller, S., Mounaix, Ph., and Tikhonchuk, V. T., ''SBS reflectivity from spatially smoothed laser beams: Random phase plates versus polarization smoothing,'' Phys. Plasmas **5**, 2706 (1998).
Hunt, J. T. and Speck, D. R., ''Present and future performance of the Nova laser system,'' Opt. Eng. **28**, 461 (1989).
Iglesias, C. A. and Rogers, F. J., ''Updated opal opacities,'' Astrophys. J. **464**, 943 (1996).
Jacobs, J. W. and Catton, I., ''Three-dimensional Rayleigh–Taylor instability—Part 1: Weakly nonlinear theory,'' J. Fluid Mech. **187**, 329 (1988).
Jacobs, J. W. and Catton, I., ''Three-dimensional Rayleigh–Taylor instability—Part 2: Experiment,'' J. Fluid Mech. **187**, 353 (1988a).
Jones, O. S., Bull. Am. Phys. Soc. **43**, 1896 (1998).
Kaiser, N., Meyer-ter-Vehn, J., and Sigel, R., ''The x-ray driven heating wave,'' Phys. Fluids B **1**, 1747 (1989).
Kalantar, D. H., Haan, S. W., Hammel, B. A. *et al.*, ''X-ray backlit imaging measurement of in-flight pusher density for an indirect drive capsule implosion,'' Rev. Sci. Instrum. **68**, 814 (1997).
Kalantar, D. H., MacGowan, B. J., Bernat, T. P., Klem, D. E., Montgomery, D. S., Moody, J. D., Munro, D. H., Stone, G. F., Hsing, W. W., and Failor, B. H., ''X-ray imaging of uniform large scale-length plasmas created from gas-filled targets on Nova,'' Rev. Sci. Instrum. **66**, 782 (1995).
Kalantar, D. H., Klem, D. E., MacGowan, B. J., Moody, J. D., Montgomery, D. S., Munro, D. H., Shepard, T. D., Stone, G. F., Failor, B. H., and Hsing, W. W., ''Production and characterization of large plasmas from gas bag targets on Nova,'' Phys. Plasmas **2**, 3161 (1995a).
Kania, D. R., Pan, L., Kornblum, H. *et al.*, ''Soft x-ray detection with diamond photoconductive detectors,'' Rev. Sci. Instrum. **61**, 2765 (1990).
Kato, Y., Mima, K., Miyanaga, N., Arinaga, S., Kitagawa, Y., Nakatsuka, M., and Yamanaka, C., ''Random phasing of high-power lasers for uniform target acceleration and plasma-instability suppression,'' Phys. Rev. Lett. **53**, 1057 (1984).
Kauffman, R., Suter, L., Darrow, C. B., Kilkenny, J. D., Kornblum, H. N., Montgomery, D. S., Phillion, D. W., Rosen, M. D., Thiessen, A. R., Wallace, R. J., and Ze, F., ''High temperatures in inertial confinement fusion radiation cavities heated with 0.35 μm light,'' Phys. Rev. Lett. **73**, 2320 (1994).
Kauffman, R. L., Kornblum, H. N., Phillion, D. W., Darrow, C. B. *et al.*, ''Drive characterization of indirect drive targets on the Nova lasers,'' Rev. Sci. Instrum. **66**, 678 (1995).
Kauffman, R. L., Powers, L. V., Dixit, S. N. *et al.*, ''Improved gas-filled hohlraum performance on Nova with beam smoothing,'' Phys. Plasmas **5**, 1927 (1998).
Keane, C. J., Hammel, B. A., Kania, D. R., Kilkenny, J. D., Lee, R. W., Osterheld, A. L., Suter, L. J., Mancini, R. C., Hopper, Jr., C. F., and Delamater, N. D., ''X-ray spectroscopy of high-energy density inertial confinement fusion plasmas,'' Phys. Fluids B **5**, 3328 (1993).
Keane, C. J., Hammel, B. A., Osterheld, A. L., Lee, R. W., Kania, D. R., Suter, L. J., Mancini, R. C., Hopper, Jr., C. F., and Delamater, N. D., ''Analysis of K- and L-shell spectra from indirectly driven implosions,'' J. Quant. Spectrosc. Radiat. Transf. **51**, 147 (1994).
Keane, C. J., Cook, R. C., Dittrich, T. R., Hammel, B. A. *et al.*, ''Diagnosis of pusher-fuel mix in spherical implosions using x-ray spectroscopy,'' Rev. Sci. Instrum. **66**, 689 (1995).
Keane, C. J., Pollak, G. W., Cook, R. C., Dittrich, T. R., Hammel, B. A., Landen, O. L., Langer, S. H., Levedahl, W. K., Munro, D. H., Scott, H. A., and Zimmerman, G. B., ''X-ray spectroscopic diagnostics of mix in high growth factor spherical implosions,'' J. Quant. Spectrosc. Radiat. Transf. **54**, 207 (1995a).
Keane, C. J., Landen, O. L., Hammel, B. A., Amendt, P. *et al.*, ''Observation of large-growth-factor behavior in indirectly driven spherical implosions,'' Lawrence Livermore National Laboratory, Livermore, CA, UCRL-JC-123022, 1995b.
Kessler, T., Lin, Y., Iwan, L., Castle, W., Kellogg, C., Barone, J., Kowaluk, E., Schmidt, A., Marshall, K., Smoth, D., Rigatti, A., Warner, J., and Staley, A., ''Laser phase conversion using high-efficiency continuous distributed phase plates,'' SPIE Proceedings of the Second Annual International Conference on Solid-State Lasers for Application to Inertial Confinement Fusion (ICF) Paris, France, 22–25 October 1996.
Kilkenny, J. D., ''High speed proximity focused x-ray cameras,'' Laser Part. Beams **9**, 49 (1991).
Kilkenny, J. D., Bell, P., Hanks, R., Power, G., Turner, R. E., and Wiedwald, J., ''High-speed gated x-ray imagers,'' Rev. Sci. Instrum. **59**, 1793 (1988).
Kilkenny, J. D., ''Experimental results on hydrodynamic instabilities in laser accelerated planar packages,'' Phys. Fluids B **2**, 1400 (1990).
Kim, K., Mok, L., Erlenborn, M. J., and Bernat, T., ''Non-contact thermal gradient method for fabrication of uniform cryogenic inertial fusion targets,'' J. Vac. Sci. Technol. A **3**, 1196 (1985).
Kirkpatrick, R. C., and Wingate, C. A. (private communication, 1980).
Kirkpatrick, R. C., Tabor, J. E., Lindman, E. L., and Cooper, A. J., ''Indirect solar loading of waste heat radiators,'' in *Proceedings of Space 88*, edited by S. W. Johnson and J. P. Wetzel (American Society of Civil Engineers, New York, 1988), pp. 964–973.
Kirkwood, R. K., MacGowan, B. J., Montgomery, D. S., Afeyan, B. B., Kruer, W. L., Moody, J. D., Estabrook, K. G., Back, C. A., Glenzer, S. H., Blain, M. A., Williams, E. A., Berger, R. L., and Lasinski, B. F., ''Effect of ion-wave damping on stimulated Raman scattering in high-Z laser-produced plasmas,'' Phys. Rev. Lett. **77**, 2706 (1996).
Kirkwood, R. K., Afeyan, B. B., Kruer, W. L., MacGowan, B. J., Moody, J. D., Montgomery, D. S., Pennington, D. M., Weiland, T. L., and Wilks, S. C., ''Observation of energy transfer between frequency-mismatched laser beams in a large-scale plasma,'' Phys. Rev. Lett. **76**, 2065 (1996a).
Kirkwood, R. K., MacGowan, B. J., Montgomery, D. S., Moody, J. D., Afeyan, B. B., Kruer, W. L., Back, C. A., Estabrook, K. G., Glenzer, S. H., Blain, M. A., Rousseaux, C., Williams, E. A., Berger, R. L., and Lasinski, B. F., ''Observation of multiple mechanisms for stimulating ion waves in ignition scale plasmas,'' Phys. Plasmas **4**, 1800 (1997).
Kirkwood, R. K., Back, C. A., Blain, M. A., Desenne, D. E., Dulieu, A. G., Glenzer, S. H., MacGowan, B. J., Montgomery, D. S., and Moody, J. D., Rev. Sci. Instrum. **68**, 636 (1997a).
Kirkwood, R. K., Montgomery, D. S., Afeyan, B. B., Moody, J. D., MacGowan, B. J., Glenzer, S. H., Kruer, W. L., Estabrook, K. G., Wharton, K. B., Williams, E. A., and Berger, R. L., ''Observation of the nonlinear saturation of Langmuir waves driven by ponderomotive force in a large scale plasma,'' Phys. Rev. Lett. **83**, 2965 (1999).
Kishony, R. and Shvarts, D., ''Ignition condition and gain prediction for perturbed inertial confinement targets,'' Phys. Plasmas **8**, 4925 (2001).
Klem, D. E., Lawrence Livermore National Laboratory, Livermore, CA (private communication, 1995).
Knauer, J. P., Kremens, R. L., Russotto, M. A., and Tudman, S., ''Using cosmic rays to monitor large scintillator arrays,'' Rev. Sci. Instrum. **66**, 926 (1995).
Koch, J. A., Landen, O. L., Hammel, B. A. *et al.*, ''Recent progress in high-energy, high-resolution x-ray imaging techniques for application to the National Ignition Facility,'' Rev. Sci. Instrum. **70**, 525 (1999).
Kolber, T., Rozmus, W., and Tikhonchuk, V. T., ''Saturation of backward stimulated Raman scattering and enhancement of laser light scattering in plasmas,'' Phys. Plasmas **2**, 256 (1995).
Kornblum, H. N., Kauffman, R. L., and Smith, J. A., ''Measurement of

Downloaded 20 Mar 2011 to 69.181.48.121. Redistribution subject to AIP license or copyright; see http://pop.aip.org/about/rights_and_permissions

0.1–3-keV x rays from laser plasmas,'' Rev. Sci. Instrum. **57**, 2179 (1986).

Krauser, W. J., Hoffman, N. M., Wilson, D. C., Wilde, B. H., Varnum, W. S., Harris, D. B., Swenson, F. J., Bradley, P. A., Haan, S. W., Pollaine, S. M., Wan, A. S., Moreno, J. C., and Amendt, P. A., ''Ignition target design and robustness studies for the National Ignition Facility,'' Phys. Plasmas **3**, 2084 (1996).

Kruer, W. L., *Physics of Laser Plasma Interactions* (Addison-Wesley, Redwood City, CA, 1988).

Kruer, W. L., ''Intense laser plasma interactions: From Janus to Nova,'' Phys. Fluids B **3**, 2356 (1991); ''Interaction physics for megajoule laser targets,'' in *Laser Interaction and Related Plasma Phenomena* (Plenum, New York, 1993), Vol. 10, p. 503.

Kruer, W. L., Campbell, E. M., Decker, C. D., Wilks, S. C., Moody, J., Orzechowski, T., Powers, L., Afeyan, B. B., and Dague, N., ''Strongly driven laser-plasma coupling,'' Plasma Phys. Controlled Fusion **41**, A409 (1999).

Kruer, W. L., Dawson, J. M., and Sudan, R. N., ''Trapped-particle instability,'' Phys. Rev. Lett. **23**, 838 (1969).

Kruer, W. L., Valeo, E. J., and Estabrook, K. G., ''Limitation of Brillouin scattering in plasmas,'' Phys. Rev. Lett. **35**, 1076 (1975).

Kruer, W. L., Wilks, S. C., Afeyan, B. B., and Kirkwood, R. K., ''Energy transfer between crossing laser beams,'' Phys. Plasmas **3**, 382 (1996).

Kull, H. J. and Anisimov, S. I., ''Ablative stabilization in the incompressible Rayleigh–Taylor instability,'' Phys. Fluids **29**, 2067 (1986).

Kyrala, G. A., Evans, S., Jimerson, J., and Fernandez, J. C., ''Time resolved side scatter diagnostics at Nova,'' Rev. Sci. Instrum. **68**, 664 (1997).

Labaune, C., Baldis, H. A., Renard, N., Schifano, E., and Michard, A., ''Location of ion-acoustic waves from back and side stimulated Brillouin scattering,'' Phys. Rev. Lett. **76**, 3727 (1996).

Labaune, C., Baldis, H. A., Bauer, B. S., Tikhonchuk, V. T., and Laval, G., ''Time-resolved measurements of secondary Langmuir waves produced by the Langmuir decay instability in a laser-produced plasma,'' Phys. Plasmas **5**, 234 (1998).

Labaune, C., Baldis, H. A., Cohen, B., Rozmus, W., Depierreux, S., Schifano, E., Bauer, B. S., and Michard, A., ''Nonlinear modification of laser-plasma interaction processes under crossed laser beams,'' Phys. Plasmas **6**, 2048 (1999).

Landen, O. L., Amendt, P. A., Turner, R. B. *et al.*, ''High convergence implosion symmetry in cylindrical hohlraums,'' in *Proceedings of the Inertial Fusion Science and Applications 99*, edited by C. Labaune, W. J. Hogan, and K. A. Tanaka (Elvesier, Paris, 2000), pp. 178–181.

Landen, O. L., Bradley, D. K., Pollaine, S. M., *et al.*, ''Indirect-drive time-dependent symmetry diagnosis at NIF-scale,'' in *Proceedings of the Inertial Fusion Science and Applications 99*, edited by C. Labaune, W. J. Hogan, and K. A. Tanaka (Elvesier, Paris, 2000a), pp. 174–179.

Landen, O. L., Farley, D. R., Glendinning, S. G. *et al.*, ''X-ray backlighting for the NIF,'' Rev. Sci. Instrum. **72**, 627 (2001).

Landen, O. L., Keane, C. J., Hammel, B. A., Cable, M. D., Colvin, J., Cook, R., Dittrich, T. R., Haan, S. W., Hatchett, S. P., Hay, R. G., Kilkenny, J. D., Lerche, R. A., Levedahl, W. K., McEachern, R., Murphy, T. J., Nelson, M. B., Suter, L., and Wallace, R. J., ''Indirectly driven, high growth Rayleigh–Taylor implosions on Nova,'' J. Quant. Spectrosc. Radiat. Transf. **54**, 245 (1995).

Landen, O. L., Keane, C. J., Hammel, B. A. *et al.*, ''Effects of variable x-ray preheat shielding in indirectly driven implosions,'' Phys. Plasmas **3**, 2094 (1996).

Landen, O. L., ''Time-dependent indirect-drive symmetry control on the Nova and Omega laser facilities,'' Proceedings of 17th International Symposium on Plasma Physics and Controlled Nuclear Fusion Research 1998 (IAEA, Vienna, Austria, 1999).

Landen, O. L., Amendt, P. A., Suter, L. J. *et al.*, ''A simple time-dependent analytic model of the P2 asymmetry in cylindrical hohlraums,'' Phys. Plasmas **6**, 2137 (1999).

Langdon, A. B., ''Nonlinear transverse bremsstrahlung and heated-electron distributions,'' Phys. Rev. Lett. **44**, 575 (1980).

Langdon, A. B. and Lasinski, B. F., ''Filamentation and subsequent decay of laser light in plasmas,'' Phys. Rev. Lett. **34**, 934 (1975).

Langdon, A. B. and Lasinski, B. F., in *Methods of Computer Physics*, edited by B. Alder, S. Fernbach, M. Rotenberg, and J. Killeen (Academic, New York, 1976), Vol. 16, pp. 327–366.

Langdon, A. B., Lasinski, B. F., and Kruer, W. L., ''Nonlinear saturation and recurrence of the two-plasmon decay instability,'' Phys. Rev. Lett. **43**, 133 (1979).

Langer, S. H., Scott, H. A., Keane, C. J., Landen, O. L., and Marinak, M. M., ''Yield and emission line ratios from ICF target implosions with multi-mode Rayleigh–Taylor perturbations,'' J. Quant. Spectrosc. Radiat. Transf. **58**, 709 (1997).

Larsen, J. T., in *HYADES—A Radiation Hydrodynamics Code for Dense Plasma Studies*, edited by B. Goldstein, C. Hooper, J. Gauthier, J. Seely, and R. Lees, 4th International Workshop on Radiative Properties of Hot Dense Matter (World Scientific, Sarasota, FL, 1990), p. 321.

Laval, G., Pellat, R., Pesme, D., Ramani, A., Rosenbluth, M. N., and Williams, E. A., ''Parametric instabilities in the presence of space-time random fluctuations,'' Phys. Fluids **20**, 2049 (1977).

Layzer, D., ''On the stability of superposed fluids in a gravitational field,'' Astrophys. J. **122**, 1 (1955).

Lee, Y. T., ''A model for ionization balance and L-Shell spectroscopy of non-LTE plasmas,'' J. Quant. Spectrosc. Radiat. Transf. **38**, 131 (1987).

Lee, R. W., Whitten, B. L., and Strout, II, R. E., ''Spectra—A model for K-Shell spectroscopy,'' J. Quant. Spectrosc. Radiat. Transf. **32**, 91 (1984).

Lefebvre, E., Berger, R. L., Langdon, A. B., MacGowan, B. J., Rothenberg, J. E., and Williams, E. A., ''Reduction of laser self-focusing in plasma by polarization smoothing,'' Phys. Plasmas **5**, 2701 (1998).

Lehmberg, R. H. and Obenschain, S. P., Opt. Commun. **46**, 27 (1983). Induced spatial incoherence (ISI), not used at Nova, is another temporal smoothing technique where each RPP element is temporally incoherent with each other.

Lerche, R. A., Phillion, D. W., and Tietbohl, G. L., ''Neutron detector for fusion reaction-rate measurements,'' in Proceedings of SPIE 2002, edited by P. W. Roehrenbech (San Diego, CA, 1993), p. 153.

Lessler, T. J., Lin, Y., Armstrong, J. J., and Velazquez, B., ''Phase conversion of lasers with low-loss distributed phase plates,'' in *Laser Coherence Control: Technology and Applications*, edited by H. T. Powell and T. J. Kessler (SPIE, Bellingham, WA, 1993), Vol. 1870, p. 95104.

Letts, S. A., Meyers, D. W., and Witt, L. A., ''Ultrasmooth plasma poymerized coatings for laser fusion targets,'' J. Vac. Sci. Technol. **19**, 739 (1981).

Levedahl, W. K. and Lindl, J. D., ''Energy scaling of inertial confinement fusion targets for ignition and high gain,'' Nucl. Fusion **37**, 165 (1997).

Lin, Y., Kessler, T. J., and Lawrence, G. N., ''Distributed phase plates for super-Gaussian focal-plane profiles,'' Opt. Lett. **20**, 764 (1995).

Lin, Y., Kessler, T. J., and Lawrence, G. N., ''Design of continuous-surface-relief phase plates for surface-based simulated annealing to achieve control of focal plane irradiance,'' Opt. Lett. **21**, 1703 (1996).

Lindl, J. D., *Inertial Confinement Fusion* (Springer-Verlag, New York, 1998); ''Development of the indirect-drive approach to inertial confinement fusion and the target physics basis for ignition and gain,'' Phys. Plasmas **2**, 3933 (1995).

Lindl, J. D. and Mead, W. C., ''Two-dimensional simulation of fluid instability in laser-fusion pellets,'' Phys. Rev. Lett. **34**, 1273 (1975).

Lindl, J. D., ''Apollo targets for Nova and KrF-driven reactors,'' Laser Program Annual Report (1978), Lawrence Livermore National Laboratory, Livermore, CA, UCRL-50055-78, 1978, pp. 2-77–2-88.

Lindl, J. D., ''Hydrodynamic and plasma stability limitations on the choice of laser wavelength for radiation driven ICF implosions,'' Laser Program Annual Report (1983), Lawrence Livermore National Laboratory, Livermore, CA, UCRL-50055-83, 1983, pp. 2-40–2-46.

Lindl, J. D., McCrory, R. L., and Campbell, E. M., ''Progress toward ignition and propagating burn in inertial confinement fusion,'' Phys. Today **45**, 32 (1992).

Lindl, J. D., and Marinak, M. M., ''Progress on the physics of ignition for radiation driven inertial confinement fusion targets,'' *The Proceedings of the 16th International Conference on Plasma Physics and Controlled Fusion Research 1996, Montreal Canada, October 7–11, 1996* (International Atomic Energy Agency, Vienna, 1996), pp. 43–56.

Lindl, J. D., ''Time-dependent asymmetries in laser-fusion hohlraums: A response. I,'' Comments Plasma Phys. Controlled Fusion **17**, 221 (1996).

Lindl, J. D., *Inertial Confinement Fusion* (Springer-Verlag, New York, 1998).

Lindl, J. D., *Inertial Confinement Fusion* (Springer-Verlag, New York, 1998a), Chap. 13.

Lindl, J. D., *Inertial Confinement Fusion* (Springer-Verlag, New York, 1998b), Chap. 2.

Lindl, J. D., *Inertial Confinement Fusion* (Springer-Verlag, New York, 1998c), Chap. 8.

Downloaded 20 Mar 2011 to 69.181.48.121. Redistribution subject to AIP license or copyright; see http://pop.aip.org/about/rights_and_permissions

Lindl, J. D., *Inertial Confinement Fusion* (Springer-Verlag, New York, 1998d), Chap. 5.
Lindl, J. D., *Inertial Confinement Fusion* (Springer-Verlag, New York, 1998e), Chap. 10.
Lindl, J. D., *Inertial Confinement Fusion* (Springer-Verlag, New York, 1998f), Chap. 3.
Lindl, J. D., *Inertial Confinement Fusion* (Springer-Verlag, New York, 1998g), Chap. 11.
Lindl, J. D., *Inertial Confinement Fusion* (Springer-Verlag, New York, 1998h), Chap. 12.
Lindl, J. D., *Inertial Confinement Fusion* (Springer-Verlag, New York, 1998i), Chap. 4.
Lindl, J. D., *Inertial Confinement Fusion* (Springer-Verlag, New York, 1998j), Chap. 7.
Lindl, J. D., *Inertial Confinement Fusion* (Springer-Verlag, New York, 1998k), Chap. 6.
Lobatchev, V. and Betti, R., "Ablative stabilization of the deceleration phase Rayleigh–Taylor instability," Phys. Rev. Lett. **85**, 4522 (2000).
Luciani, J. F., Mora, P., and Virmont, J., "Nonlocal heat transport due to steep temperature gradients," Phys. Rev. Lett. **51**, 1664 (1983).
MacGowan, B. J., Berger, R. L., Cohen, B. I., Decker, C. D., Dixit, S., Glenzer, S. H., Hinkel, D. E., Kirkwood, R. K., Langdon, A. B., Lefebvre, E., Moody, J. D., Rothenberg, J. E., Rousseaux, C., Suter, L. J., Still, C. H., and Williams, E. A., "Laser beam smoothing and backscatter saturation processes in plasmas relevant to National Ignition Facility hohlraums," in Proceedings of the IAEA, 17th International Conference on plasma physics and controlled nuclear fusion, Yokahama, Japan, 18–24 October 1998, Vol. 3, pp. 1107–1110 (1999).
MacGowan, B. J., Afeyan, B. B., Back, C. A., Berger, R. L., Bonnaud, G., Casanova, M., Cohen, B. I., Desenne, D. E., DuBois, D. F., Dulieu, A. G., Estabrook, K. G., Fernandez, J. C., Glenzer, S. H., Hinkel, D. E., Kaiser, T. B., Kalantar, D. H., Kauffman, R. L., Kirkwood, R. K., Kruer, W. L., Langdon, A. B., Lasinski, B. F., Montgomery, D. S., Moody, J. D., Munro, D. H., Powers, L. V., Rose, H. A., Rousseaux, C., Turner, R. E., Wilde, B. H., Wilks, S. C., and Williams, E. A., "Laser plasma interactions in ignition-scale hohlraum plasmas," Phys. Plasmas **3**, 2029 (1996).
MacGowan, B. J., Berger, R. L., Afeyan, B. B., Back, C. A., Blain, M. A., Canaud, B., Cohen, B. I., Desenne, D. E., Estabrook, K. G., Glenzer, S. H., Hinkel, D. E., Kirkwood, R. K., Kruer, W. L., Langdon, A. B., Lasinski, B. F., Montgomery, D. S., Moody, J. D., Rousseaux, C., Still, C. H., and Williams, E. A., "Laser scattering in large-scale-length plasmas relevant to National Ignition Facility hohlraums," *Proceedings of the IAEA, 16th International Conference on Plasma Physics and Controlled Nuclear Fusion, Montreal, Quebec, Canada, Oct. 1996* [Fusion Energy **3**, 181 (1997)].
Magelssen, G. R., Delamater, N. D., Lindman, E. L. *et al.*, "Measurements of early time radiation asymmetry in vacuum and methane-filled hohlraums with the reemission ball technique," Phys. Rev. E **57**, 4663 (1998).
Marinak, M. M., Glendinning, S. G., Wallace, R. J., Remington, B. A., Budil, K. S., Haan, S. W., Tipton, R. E., and Kilkenny, J. D., "Nonlinear Rayleigh–Taylor evolution of a three-dimensional multimode perturbation," Phys. Rev. Lett. **80**, 4426 (1998).
Marinak, M. M., Remington, B. A., Weber, S. V., Tipton, R. E., Haan, S. W., Budil, K. S., Landen, O. L., Kilkenny, J. D., and Wallace, R., "Three-dimensional single mode Rayleigh–Taylor experiments on Nova," Phys. Rev. Lett. **75**, 3677 (1995).
Marinak, M. M., Tipton, R. E., Landen, O. L., Murphy, T. J., Amendt, P., Haan, S. W., Hatchett, S. P., Keane, C. J., McEachern, R., and Wallace, R., "Three-dimensional simulations of Nova high growth factor capsule implosions," Phys. Plasmas **3**, 2070 (1996).
Marjoribanks, R. S., Budnik, F., Kulcsar, G., and Zhao, L., "Isoelectronic line intensity ratios for plasma electron temperature measurement," Rev. Sci. Instrum. **66**, 683 (1995).
Marjoribanks, R. S., Richardson, M. C., Jaanimagi, P. A., and Epstein, R., "Electron-temperature measurement in laser-produced plasmas by the ratio of isoelectronic lin intensities," Phys. Rev. A **46**, 1747 (1992).
Marshak, R. E., "Effect of radiation on shock wave behavior," Phys. Fluids **1**, 24 (1958).
Martin, A. J., Simms, R. J., and Jacobs, R. B., "Beta energy driven uniform deuterium–tritium ice layer in reactor-size cryogenic inertial fusion targets," J. Vac. Sci. Technol. A **6**, 1885 (1988).
Massen, J., Tsakiris, G. D., and Sigel, R., "Modeling of plasma dynamics in x-ray confining cavities," Phys. Rev. E **48**, 2073 (1993).
Matte, J. P., Lamoreux, M., Moller, C., Yin, R. Y., Delettrez, J., Virmont, J., and Johnston, T. W., "Non-Maxwellian electron distributions and continuum x-ray emission in inverse bremsstrahlung heated plasmas," Plasma Phys. Controlled Fusion **30**, 1665 (1988).
Max, C. E., "Strong self-focusing due to ponderomotive force in plasmas," Phys. Fluids **19**, 74 (1976).
McCrory, R. L., Montierth, L., Morse, R. L., and Verdon, C. P., "Nonlinear evolution of ablation-driven Rayleigh–Taylor instability," Phys. Rev. Lett. **46**, 336 (1981).
McKinstrie, C. J., Li, J. S., Giacone, R. E., and Vu, H. X., "Two-dimensional analysis of the power transfer between crossed laser beams," Phys. Plasmas **3**, 2686 (1996).
McKinstrie, C. J., Smalyuk, V. A., Giacone, R. E., and Vu, H. X., "Power exchange between crossed laser beams and the associated frequency cascade," Phys. Rev. E **55**, 2044 (1997).
McMullin, J. N., Capjack, C. E., and James, C. R., "HFATER: A 2D laser propagation subroutine for underdense plasmas," Comput. Phys. Commun. **23**, 31 (1981).
Meshkov, Y. Y., "Instability of a shock wave accelerated interface between two gases," Izv. Akad. Nauk SSSR, Mekh. Zhidk. Gaza **5**, 151 (1969) (translation, NASA TTF-13-074, 1970).
Meyer-ter-Vehn, J., "On energy gain of fusion targets: The model of Kidder and Bodner improved," Nucl. Fusion **22**, 561 (1982).
Minguez, E., "Radiation transport in ICF targets," in *Nuclear Fusion by Inertial Confinement*, edited by G. Velarde, Y. Ronen, and J. M. Martinez-Val (CRC, Boca Raton, FL, 1993), Chap. 8.
Montgomery, D. S., Johnson, R. P., Rose, H. A., Cobble, J. A., and Fernandez, J. C., "Flow-induced beam steering in a single laser hot spot," Phys. Rev. Lett. **84**, 678 (2000).
Montgomery, D. S., Cobble, J. A., Fernandez, J. C., Focia, R. J., Johnson, R. P., Renard-LeGalloudec, N., Rose, H. A., and Russell, D. A., "Recent Trident single hot spot experiments: Evidence for kinetic effects, and observation of the Langmuir decay instability cascade," Phys. Plasmas **9**, 2311 (2002).
Montgomery, D. S., Afeyan, B. B., Cobble, J. A., Fernandez, J. C., Wilke, M. D., Glenzer, S. H., Kirkwood, R. K., MacGowan, B. J., Moody, J. D., Lindman, E. L., Munro, D. H., Wilde, B. H., Rose, H. A., DuBois, D. F., Bezzerides, B., and Vu, H. X., "Evidence of plasma fluctuations and their effect on the growth of stimulated Brillouin and stimulated Raman scattering in laser plasmas," Phys. Plasmas **5**, 1973 (1998).
Montgomery, D. S., Johnson, R. P., Cobble, J. A., Fernandez, J. C., Lindman, E. L., Rose, H. A., and Estabrook, K. G., "Characterization of plasma and laser conditions for single hot spot experiments," Laser Part. Beams **17**, 349 (1999).
Moody, J. D., Lours, L., Sanchez, J. J., Williams, E. A., Berger, R. L., Collins, G. A., Decker, C. B., Divol, L., Glenzer, S. H., Hammel, B. A., Jones, R., Kirkwood, R. K., Kruer, W. L., MacGowan, B. J., Pipes, J., Suter, L. J., Thoe, R., Unites, W., and Young, P. E.,"First measurement of backscatter dependence on ion acoustic damping in a low-Z, high density helium/hydrogen laser-plasma," Phys. Plasmas (submitted).
Moody, J. D., MacGowan, B. J., Rothenberg, J. E., Berger, R. L., Divol, L. M., Glenzer, S. H., Kirkwood, R. K., Williams, E. A., and Young, P. E., "Backscatter reduction using combined spatial, temporal, and polarization beam smoothing in a long-scale-length laser plasma," Phys. Rev. Lett. **86**, 2810 (2001).
Moody, J. D., MacGowan, B. J., Munro, D. H., Berger, R. L., Kirkwood, R. K., and Montgomery, D. S., "Experimental studies of the light transmitted through a large scalelength plasma," Bull. Am. Phys. Soc. **39**, 1753 (1994).
Moody, J. D., MacGowan, B. J., Hinkel, D. E., Kruer, W. L., Williams, E. A., Estabrook, K., Berger, R. L., Kirkwood, R. K., Montgomery, D. S., and Shepard, T. D., "First optical observation of intensity dependent laser beam deflection in a flowing plasma," Phys. Rev. Lett. **77**, 1294 (1996).
Moody, J. D., MacGowan, B. J., Kirkwood, R. K., and Montgomery, D. S., "Measurements of high intensity laser beam transmission through a large scalelength plasma," Rev. Sci. Instrum. **68**, 1725 (1997).
Moody, J. D., MacGowan, B. J., Glenzer, S. H., Kirkwood, R. K., Kruer, W. L., Pollaine, S. M., Williams, E. A., Stone, G. F., Afeyan, B. B., and Schmitt, A. J., "Measurements of near forward scattered laser light in a large inertial confinement fusion plasma," Rev. Sci. Instrum. **70**, 677 (1999).
Moody, J. D., MacGowan, B. J., Glenzer, S. H., Kirkwood, R. K., Kruer, W.

Downloaded 20 Mar 2011 to 69.181.48.121. Redistribution subject to AIP license or copyright; see http://pop.aip.org/about/rights_and_permissions

L., Schmitt, A. J., Williams, E. A., and Stone, G. F., ''First measurement of short length-scale density fluctuations in a large laser plasma,'' Phys. Rev. Lett. **83**, 1783 (1999a).

Morales, G. J. and O'Neil, T. M., ''Nonlinear frequency shift of an electron plasma wave,'' Phys. Rev. Lett. **28**, 417 (1972).

Morales, R. I., Remington, B. A., and Schwinn, T., ''High precision Wolter optic calibration facility,'' Rev. Sci. Instrum. **66**, 700 (1995).

More, R. M., Warren, K. H., Young, D. A., and Zimmerman, G. B., ''A new quotidian equation of state (QEOS) for hot dense matter,'' Phys. Fluids **31**, 3059 (1988).

Morse, R. L. and Nielson, C. W., ''Numerical simulation of the Weibel instability in one and two dimensions,'' Phys. Fluids **14**, 830 (1970).

Mounaix, P., Divol, L., Huller, S., and Tikhonchuk, V. T., ''Strong self-focusing in quasi-stationary laser plasmas,'' Phys. Plasmas **7**, 4259 (2000).

Mourenas, D., ''Saturation of stimulated Raman backscatter in strongly turbulent plasmas,'' Phys. Plasmas **6**, 1258 (1999).

Munro, D. H., ''Rippled shock front solutions for testing hydrodynamic stability simulations,'' Phys. Fluids B **1**, 134 (1989).

Munro, D. H. (private communication, 1998).

Munro, D. H., ''Analytic solutions for Rayleigh–Taylor growth rates in smooth density gradients,'' Phys. Rev. A **38**, 1433 (1988).

Munro, D. H., Cellier, P. M., Collins, G. W., Gold, D. M., Da Silva, L. B., Haan, S. W., Cauble, R. C., Hammel, B. A., and Hsing, W. W., ''Shock timing technique for the National Ignition Facility,'' Phys. Plasmas **8**, 2245 (2001).

Munro, D. H. and Zimmerman, G. B. (private communication, 1993).

Murakami, M. and Meyer-ter-Vehn, J., ''Indirectly driven target for inertial confinement fusion,'' Nucl. Fusion **31**, 1315 (1991).

Murakami, M. and Meyer-ter-Vehn, J., ''Radiation symmetrization in indirectly driven ICF targets,'' Nucl. Fusion **31**, 1333 (1991a).

Murphy, T. J., Wallace, J. M., Delamater, N. D. *et al.*, ''Hohlraum symmetry experiments with multiple beam cones on the Omega laser facility,'' Phys. Rev. Lett. **81**, 108 (1998).

Murphy, T. J., Wallace, J. M., Delamater, N. D. *et al.*, ''Indirect drive experiments utilizing multiple beam cones in cylindrical hohlraums on OMEGA,'' Phys. Plasmas **5**, 1960 (1998a).

National Academy of Sciences Review of the Department of Energy's Inertial Confinement Fusion Program, Final Report (National Academy Press, Washington, DC, 1990).

National Technical Information Service Document UCRL 5002175 (The B-integral is the nonlinear phase accumulated by the pulse propagating through the laser amplifier, ''Laser Annual Report—1975'' UCRL-50021-75, p. 238). Copies may be obtained from the National Technical Information Service, Springfield, VA 22161.

National Technical Information Service Document No. DE95017708 (D. S. Kershaw, ''Flux limiting in nature's own way,'' Lawrence Livermore National Laboratory, Livermore, CA, UCRL-78378, 1976). Copies may be obtained from the National Technical Information Service, Springfield, VA 22161.

National Technical Information Service Document No. UCRL-52276 (W. A. Lokke and W. H. Grasberger, ''XSNQ-U: A Non-LTE emission and absorption coefficient subroutine,'' Lawrence Livermore National Laboratory, Livermore, CA, UCRL-52276, 1977). Copies may be obtained from the National Technical Information Service, Springfield, VA 22161.

National Technical Information Service Document No. DE86005297 (J. W.-K. Mark, ''Reduction of deposition asymmetries in directly driven ion beam and laser targets,'' 1984 Laser Program Annual Report, Lawrence Livermore National Laboratory, Livermore, CA, UCRL-50021-84, 1984, pp. 3-24–3-28). Copies may be obtained from the National Technical Information Service, Springfield, VA 22161.

National Technical Information Service Document No. DE88014097 (R. L. Kauffman, ''X-ray conversion efficiency,'' Laser Program Annual Report 1986, Lawrence Livermore National Laboratory, Livermore, CA, UCRL-50021-86). Copies may be obtained from the National Technical Information Service, Springfield, VA 22161.

National Technical Information Service Document No. DOE/DP 40200-149 [''Phase conversion using distributed polarization rotation,'' LLE Rev. **45**, 1 (1990)]. Copies may be obtained from the National Technical Information Service, Springfield, VA 22161.

National Technical Information Service Document No. DE91009750 (G. B. Zimmerman, ''Recent developments in Monte-Carlo techniques,'' Lawrence Livermore National Laboratory, Livermore, CA, UCRL-105616, 1990a). Copies may be obtained from the National Technical Information Service, Springfield, VA 22161.

National Technical Information Service Document No. DE 91017920 [H. T. Powell, S. N. Dixit, and M. A. Henesian, ''Beam smoothing capability of the Nova laser,'' *Laser Program Annual Report—1991*, Lawrence Livermore National Laboratory, Livermore, CA, UCRL-LR-105820-91 (1991), pp. 28–38]. Copies may be obtained from the National Technical Information Service, Springfield, VA 22161.

National Technical Information Service Document No. DE91017920 [T. P. Bernat, E. R. Mapoles, and J. J. Sanchez, ''Temperature and age-dependence of redistribution rates of frozen deuterium-tritium,'' ICF Quart. Rep. **1**, 443 (1991a), Lawrence Livermore National Laboratory, UCRL-LR-105821-91-2]. Copies may be obtained from the National Technical Information Service, Springfield, VA 22161.

National Technical Information Service Document No. DE92006882 [S. Hatchett, ''Ablation gas dynamics of low-Z materials illuminated by soft x rays,'' Lawrence Livermore National Laboratory, Livermore, CA, UCRL-JC-108348 (1991b)]. Copies may be obtained from the National Technical Information Service, Springfield, VA 22161.

National Technical Information Service Document No. DE93014373 [*Laboratory Microfusion Capability Study: Phase II Report*, DOE/DP-0017 U.S. Department of Energy, Washington, DC (1993), NTIS Doc. No. DE93014373]. Copies may be obtained from the National Technical Information Service, Springfield, VA 22161.

National Technical Information Service Document No. DE94010835 (Precision Nova ICF Quart. Rep. 4, edited by H. T. Powell, Lawrence Livermore National Laboratory, UCRL-LR-105821-94-1, 1994). Copies may be obtained from the National Technical Information Service, Springfield, VA 22161.

National Technical Information Service Document Nos. DE95017671 through DE95017673 and DE95017676 through DE95017700 (J. A. Paisner, E. M. Campbell, and W. J. Hogan, *The National Ignition Facility Project*, UCRL-JC-117397 and UCRL-PROP-117093, May 1994a). Copies may be obtained from the National Technical Information Service, Springfield, VA 22161.

National Technical Information Service Document No. DE94016700 (J. T. Hunt, K. R. Manes, J. R. Murray, P. A. Renard, R. W. Sawicki, J. B. Trenholme, and W. Williams, ''Laser Design Basis for the National Ignition Facility,'' Lawrence Livermore National Laboratory, Livermore, CA, UCRL-JC-117399, 1994b). Copies may be obtained from the National Technical Information Service, Springfield, VA 22161.

National Technical Information Service Document No. DE 95-011970 [S. M. Pollaine, S. P. Hatchett, and S. H. Langer, ''Spectral analysis of ICF capsule surfaces,'' ICF Quarterly Report **4**, 87 (1994c) UCRL LR105821-94-3]. Copies may be obtained from the National Technical Information Service, Springfield, VA 22161.

National Technical Information Service Document No. DE95011969 [J. L. Porter, T. J. Orzechowski, M. D. Rosen, A. R. Thiessen, L. J. Suter, and J. T. Larsen, ''The albedo of gold at high temperatures,'' ICF Quarterly Report **4**, 125 (1994d), Lawrence Livermore National Laboratory, UCRL-LR-105821-94-4]. Copies may be obtained from the National Technical Information Service, Springfield, VA 22161.

National Technical Information Service Document No. DE95000314 [R. J. Wallace, R. L. McEachern, and W. W. Wilcox, ''Laser ablation machining of ICF capsules,'' ICF Quarterly Report **4**, 79 (1994e), Lawrence Livermore National Laboratory, UCRL-LR-105821-94-3]. Copies may be obtained from the National Technical Information Service, Springfield, VA 22161.

National Technical Information Service Document No. DE94010835 [R. L. McEachern, C. Moore, G. E. Overturf III, S. R. Buckley, and R. Cook, ''Precision target for precision Nova,'' ICF Quarterly Report **4**, 25 (1994f), Lawrence Livermore National Laboratory, Livermore, CA, UCRL-LR-105821-94-1]. Copies may be obtained from the National Technical Information Service, Springfield, VA 22161.

National Technical Information Service Document No. DE96004569 [R. L. Berger, T. B. Kaiser, B. F. Lasinski, C. H. Still, A. B. Langdon, and E. A. Williams, ''Modeling the effects of laser-beam smoothing on filamentation and stimulated Brillouin scattering,'' ICF Quarterly Report **5**, 130 (1995), Lawrence Livermore National Laboratory, Livermore, CA, UCRL-LR-105821-95-3 (1995)]. Copies may be obtained from the National Technical Information Service, Springfield, VA 22161.

National Technical Information Service Document No. DE96010473 [B. MacGowan, R. Berger, J. Fernandez, B. Afeyan *et al.*, ''Laser-plasma interactions in NIF-scale plasmas,'' ICF Quarterly Report **5**, 305 (1995),

Downloaded 20 Mar 2011 to 69.181.48.121. Redistribution subject to AIP license or copyright; see http://pop.aip.org/about/rights_and_permissions

Lawrence Livermore National Laboratory, Livermore, CA, UCRL-LR-105821-95-4 (1995a)]. Copies may be obtained from the National Technical Information Service, Springfield, VA 22161.

National Technical Information Service Document No. DE96004569 [M. M. Marinak, R. E. Tipton, B. A. Remington, S. W. Haan, and S. V. Weber, ''Three-dimensional simulations of ablative hydrodynamic instabilities in indirectly driven targets,'' ICF Quarterly Report **5** (1995b), Lawrence Livermore National Laboratory, Livermore, CA, UCRL-LR-105821-95-3]. Copies may be obtained from the National Technical Information Service, Springfield, VA 22161.

National Technical Information Service Document No. DE96004569 [D. Pennington, M. A. Henesian, R. B. Wilcox, T. L. Weiland, and D. Eimerl, ''Four-color laser irradiation system for laser-plasma interaction experiments,'' ICF Quarterly Report **5**, 130 (1995), Lawrence Livermore National Laboratory, Livermore, CA, UCRL-LR-105820-95-2 (1996)]. Copies may be obtained from the National Technical Information Service, Springfield, VA 22161.

National Technical Information Service Document [D. E. Hinkel, E. A. Williams, and C. H. Still, ''Laser-beam deflection induced by transverse plasma flow,'' ICF Quarterly Report **7**, 63 (1997), Lawrence Livermore National Laboratory, Livermore, CA, UCRL-LR-105821-97-2 (1997)]. Copies may be obtained from the National Technical Information Service, Springfield, VA 22161.

National Technical Information Service Document No. DE000008491 [O. S. Jones, ''Sensitivity studies of power imbalance and asymmetry for NIF indirect drive,'' ICF Quarterly Report **8**, 140 (1998), Lawrence Livermore National Laboratory, UCRL-LR-105821-98-4]. Copies may be obtained from the National Technical Information Service, Springfield, VA 22161.

National Technical Information Service Document No. DE00008491 [L. J. Suter, E. Dattolo, S. Glenzer *et al.* ''Status of our understanding and modeling of ignition hohlraum x-ray conversion efficiency,'' (1998a) UCRL-LR-105821-98-4, pp. 171–178]. Copies may be obtained from the National Technical Information Service, Springfield, VA 22161.

National Technical Information Service Document No. DE86002577 (R. Lelevier, G. Lasher, and F. Bjorklund, ''Effect of a Density Gradient on Taylor Instability''). Copies may be obtained from the National Technical Information Service, Springfield, VA 22161.

National Technical Information Service Document No. DE95011969 [S. N. Dixit, I. M. Thomas, M. Rushford, R. Merrill, M. D. Perry, H. T. Powell, and K. A. Nugent, ''Kinoform phase plates for tailoring focal plane intensity profiles,'' (1994g) Lawrence Livermore National Laboratory, Livermore, CA, UCRL-LR-105821-94-4]. Copies may be obtained from the National Technical Information Service, Springfield, VA 22161.

Nelson, M. B. and Cable, M., ''LaNSA: A large neutron scintillator array for neutron spectroscopy at Nova,'' Rev. Sci. Instrum. **63**, 4874 (1992).

Nishimura, H., Endo, T., Shiraga, H., Kato, Y., and Nakai, S., ''X-ray emission from high-*Z* mixture plasmas generated with intense blue laser light,'' Appl. Phys. Lett. **62**, 1344 (1993).

Nuckolls, J. H., Wood, L., Thiessen, A., and Zimmerman, G. B., ''Laser compression of matter to super-high densities: thermonuclear (CTR) applications,'' Nature (London) **239**, 139 (1972).

Oberman, C. and Auer, C., ''General theory of enhanced induced emission in plasmas,'' Phys. Fluids **17**, 1980 (1974).

Ofer, D., Shvarts, D., Zinamon, Z., and Orszag, S. A., ''Mode coupling in nonlinear Rayleigh–Taylor instability,'' Phys. Fluids B **4**, 3549 (1992).

Ofer, D., Alon, U., Shvarts, D., McCrory, R. L., and Verdon, C. P., ''Modal model for the nonlinear multimode Rayleigh–Taylor instability,'' Phys. Plasmas **3**, 3073 (1996).

Oron, D., Alon, U., and Shvarts, D., ''Scaling laws of the Rayleigh–Taylor ablation front mixing zone evolution in inertial confinement fusion,'' Phys. Plasmas **5**, 1467 (1998).

Oron, D., Arazi, L., Kartoon, D., Rikanati, A., Alon, U., and Shvarts, D., ''Dimensionality dependence of the Rayleigh–Taylor and Richtmyer–Meshkov instability late-time scaling laws,'' Phys. Plasmas **8**, 2883 (2001).

Orzechowski, T. J., Rosen, M. D., Kornblum, H. N., Porter, J. L., Suter, L. J., Thiessen, A. R., and Wallace, R. J., ''The Rosseland mean opacity of a mixture of gold and gadolinium at high temperatures,'' Phys. Rev. Lett. **77**, 3545 (1996).

Pakula, R. and Sigel, R., ''Self-similar expansion of dense matter due to heat transfer by nonlinear conduction,'' Phys. Fluids **28**, 232 (1985).

Pau, S., Dixit, S. N., and Eimerl, D., J. Opt. Soc. Am. B **11**, 1498 (1994).

Pennington, D. *et al.*, Tech. Dig. Ser.-Opt. Soc. Am. **8**, 161 (1994).

Perkins, J. L. and Herrmann, M. (private communication, 2002).

Plesset, M. S., ''On the stability of fluid flows with spherical symmetry,'' J. Appl. Phys. **25**, 96 (1954).

Plesset, M., ''On the stability of the spherical shape of a vapor cavity in a liquid,'' Q. Appl. Math. **13**, 419 (1955).

Pollaine, S. M., Bradley, D. K., Landen, O. L. *et al.*, ''NIF-scale hohlraum asymmetry studies by thin shell radiography,'' Phys. Plasmas **8**, 2357 (2001).

Pollaine, S., ''Helium-filled hohlraum for foam-ablator capsules,'' 1988 Laser Program Annual Report: Target Design, Lawrence Livermore National Laboratory, Livermore, CA, XDIV-90-0054, 1988, pp. 246–259.

Pollaine, S., ''Nova Upgrade symmetry design,'' 1990/1991 LLNL Laser Program Annual Report, Lawrence Livermore National Laboratory, Livermore, CA, UCRL-LR-116901-90/91, 1991, pp. 214–234.

Pollaine, S. M. (private communication, 1992).

Pomraning, G. C., *Equations of Radiation Hydrodynamics* (Pergamon, New York, 1973a), Chap. 5, Sec. 5.

Pomraning, G. C., *Equations of Radiation Hydrodynamics* (Pergamon, New York, 1973a), Chap. 5, Sec. 6.

Porter, J. and Thiessen, A. R., ''Summary of albedo experiment,'' Lawrence Livermore National Laboratory, Livermore, CA, CLY-92-059, 1992.

Powers, L. V., Berger, R. L., Kauffman, R. L., MacGowan, B. J., Amendt, P. A., Back, C. A., Bernat, T. P., Dixit, S. N., Eimerl, D. I., Estabrook, K. G., Harte, J. A., Kalantar, D. H., Klem, D. E., Lasinski, B. F., Montgomery, D. S., Moody, J. D., Munro, D. H., Shepard, T. D., Suter, L. J., Turner, R. E., Williams, E. A., Fernandez, J. C., Hsing, W. W., Wilde, B. H., and Failor, B. H., ''Gas-filled targets for large scale-length plasma interaction experiments on Nova,'' Phys. Plasmas **2**, 2473 (1995).

Powers, L. V., Turner, R. E., Kauffman, R. L., Berger, R. L., Amendt, P., Back, C. A., Bernat, T. P., Dixit, S. N., Eimerl, D., Harte, J. A., Henesian, M. A., Kalantar, D. H., Lasinski, B. F., MacGowan, B. J., Montgomery, D. S., Munro, D. H., Pennington, D. M., Shepard, T. D., Stone, G. F., Suter, L. J., and Williams, E. A., ''Low stimulated Brillouin backscatter observed from large, hot plasmas in gas-filled hohlraums,'' Phys. Rev. Lett. **74**, 2957 (1995).

Rambo, P. W., Wilks, S. C., and Kruer, W. L., ''Hybrid particle-in-cell simulations of stimulated Brillouin scattering including ion-ion collisions,'' Phys. Rev. Lett. **79**, 83 (1997).

Rayleigh, J. W. S., *Scientific Papers* (University Press, Cambridge, 1899).

Read, K. I., ''Experimental investigation of turbulent mixing by Rayleigh–Taylor instability,'' Physica D **12**, 45 (1984).

Remington, B. A., Haan, S. W., Glendinning, S. G., Kilkenny, J. D., Munro, D. H., and Wallace, R. J., ''Large growth Rayleigh–Taylor experiments using shaped laser pulses,'' Phys. Rev. Lett. **67**, 3259 (1991).

Remington, B. A., Haan, S. W., Glendinning, S. G., Kilkenny, J. D., Munro, D. H., and Wallace, R. J., ''Large growth, planar Rayleigh–Taylor experiments on Nova,'' Phys. Fluids B **4**, 967 (1992).

Remington, B. A., Weber, S. V., Haan, S. W., Kilkenny, J. D., Glendinning, S. G., Wallace, R. J., Goldstein, W. H., Wilson, B. G., and Nash, J. K., ''Laser driven hydrodynamic instability experiments,'' Phys. Fluids B **5**, 2589 (1993).

Remington, B. A., Weber, S. V., Marinak, M. M., Haan, S. W., Kilkenny, J. D., Wallace, R., and Dimonte, G., ''Multimode Rayleigh–Taylor experiments on Nova,'' Phys. Rev. Lett. **73**, 545 (1994).

Remington, B. A., Weber, S. V., Marinak, M. M., Haan, S. W., Kilkenny, J. D., Wallace, R. J., and Dimonte, G., ''Single-mode and multimode Rayleigh–Taylor experiments on Nova,'' Phys. Plasmas **2**, 241 (1995).

Renard, N., Labaune, C., Baldis, H. A., Bauer, B. S., Quesnel, B., Schifano, E., Michard, A., Seka, W., and Estabrook, K. G., ''Detailed characterization of electron plasma waves produced by stimulated Raman scattering,'' Phys. Rev. Lett. **77**, 3807 (1996).

Riazuelo, G. and Bonnaud, G., ''Coherence properties of a smoothed laser beam in a hot plasma,'' Phys. Plasmas **7**, 3841 (2000). The results have been confirmed independently in this paper.

Richtmyer, R. D., ''Taylor instability in shock acceleration of compressible fluids,'' Commun. Pure Appl. Math. **13**, 297 (1960).

Riconda, C., Huller, S., Myatt, J., and Pesme, D., ''Kinetic effects on the ion sound waves generated by stimulated Brillouin scattering of a spatially smoothed laser beam,'' Phys. Scr., T **T84**, 217 (2000).

Rose, H. A., ''Laser beam deflection by flow and nonlinear self-focusing,'' Phys. Plasmas **3**, 1709 (1996).

Rose, H. A., ''Saturation of stimulated Brillouin scatter by self-consistent flow profile modification in laser hot spots,'' Phys. Plasmas **4**, 437 (1997).

Downloaded 20 Mar 2011 to 69.181.48.121. Redistribution subject to AIP license or copyright; see http://pop.aip.org/about/rights_and_permissions

Rose, H. A. and DuBois, D. F., ''Modification of stimulated Brillouin, saturated Raman scattering and strong Langmuir turbulence by nonlocal heat transport,'' Phys. Fluids B **4**, 1394 (1992).

Rose, H. A. and DuBois, D. F., ''Laser hot spots and the breakdown of linear instability theory with application to stimulated Brillouin scattering,'' Phys. Rev. Lett. **72**, 2883 (1994).

Rose, H. A. and Ghosal, S., ''Effect of smoothing by spectral dispersion on flow induced laser beam deflection: The random phase modulation scheme,'' Phys. Plasmas **5**, 775 (1998).

Rose, H. A. and Ghosal, S., ''Nonlinear theory of power transfer between multiple crossed laser beams in a flowing plasma,'' Phys. Plasmas **5**, 1461 (1998a).

Rosen, M. D., ''Scaling law for radiation temperature,'' Laser Program Annual Report, 1979, Lawrence Livermore National Laboratory, Livermore, CA, UCRL-50055-79, pp. 2-37–2-46.

Rosen, M. D., and Lindl, J. D., ''Model for gain vs. laser energy for x-ray driven targets,'' Laser Program Annual Report 1983, Lawrence Livermore National Laboratory, Livermore, CA, UCRL-50055-83, 1983, pp. 2-17–2-20.

Rosen, M. D. and Nuckolls, J. H., ''Exploding pusher performance—A theoretical model,'' Phys. Fluids **22**, 1393 (1979).

Rosenbluth, M. N. and Sagdeev, R. Z., in *Handbook of Plasma Physics, Volume 3: Physics of Laser Plasma*, edited by A. M. Rubenchik and S. Witkowski (Elsevier, Amsterdam, 1991), Chap 9, and references therein.

Rothenberg, J. E., ''Comparison of beam-smoothing methods for direct-drive inertial confinement fusion,'' J. Opt. Soc. Am. B **14**, 1664 (1997).

Russell, D. A., DuBois, D. F., and Rose, H. A., ''Nonlinear saturation of stimulated Raman scattering in laser hot spots,'' Phys. Plasmas **6**, 1294 (1999).

Sacks, R. A. and Darling, D. H., ''Direct-drive cryogenic ICF capsules employing DT wetted foam,'' Nucl. Fusion **27**, 447 (1987).

Sakagami, H. and Nishihara, K., ''Rayleigh–Taylor instability on the pusher-fuel contact surface of stagnating targets,'' Phys. Fluids B **2**, 2715 (1990).

Sakagami, H. and Nishihara, K., ''Three-dimensional Rayleigh–Taylor instability of spherical systems,'' Phys. Rev. Lett. **65**, 432 (1990a).

Salcedo, A., Focia, R.J., Ram, A.K., and Bers, A., ''Studies of stimulated Raman backscattering and associated nonlinear laser–plasma interactions,'' Nucl. Fusion **43**, 1759 (2003).

Sanbonmatsu, K. Y., Vu, H. X., DuBois, D. F., and Bezzerides, B., ''New paradigm for the self-consistent modeling of wave-particle and wave-wave interactions in the saturation of electromagnetically driven parametric instabilities,'' Phys. Rev. Lett. **82**, 932 (1999).

Sanbonmatsu, K. Y., Vu, H. X., Bezzerides, B., and DuBois, D. F., ''Quantitative comparison of reduced-description particle-in-cell and quasilinear-Zakharov models for parametrically excited Langmuir turbulence,'' Phys. Plasmas **7**, 2824 (2000).

Schmitt, A. and Afeyan, B. B., ''Time-dependent filamentation and stimulated Brillouin forward scattering in inertial confinement fusion plasmas,'' Phys. Plasmas **5**, 503 (1998).

Schurtz, G. P., Nicolai, Ph. D., and Busquet, M. *et al.*, ''A nonlocal electron conduction model for multidimensional radiation hydrodynamics codes,'' Phys. Plasmas **7**, 4238 (2001).

Scott, H. A. and Mayle, R. W., ''GLF—A simulation code for x-ray lasers,'' J. Appl. Phys. **58**, 36 (1994).

Seka, W., Williams, E. A., Craxton, R. S., Goldman, L. M., Short, R. W., and Tanaka, K., ''Convective stimulated Raman scattering instability in laser plasmas,'' Phys. Fluids **27**, 2181 (1984); Oberman, C. and Auer, C., ''General theory of enhanced induced emission in plasmas,'' *ibid.* **17**, 1980 (1974). Because the amplitudes of light waves and plasma waves in thermal equilibrium are very small, many efoldings are necessary to deplete the incident light power.

Short, R. W. and Simon, A., ''Landau damping and transit-time damping of localized plasma waves in general geometries,'' Phys. Plasmas **5**, 4124 (1998). If the wave is spatially localized, the linear Landau damping is properly done by Fourier transform where the wavenumber dependence of the damping can be accounted for. Such a spatial localization may have an important effect on the Langmuir wave damping.

Short, R. W., Bingham, R., and Williams, E. A., ''Filamentation of laser light in flowing plasmas,'' Phys. Fluids **25**, 2302 (1982).

Short, R. W. and Simon, A., ''Collisionless damping of localized plasma waves in laser-produced plasmas and application to stimulated Raman scattering in filaments,'' Phys. Plasmas **5**, 4134 (1998a).

Shvarts, D., Alon, U., Ofer, D., McCrory, R. L., and Verdon, C. P., ''Nonlinear evolution of multimode Rayleigh–Taylor instability in two and three dimensions,'' Phys. Plasmas **2**, 2465 (1995).

Sigel, R., Tsakiris, G. D., Lavarenne, F., Massen, J., Fedosejevs, R., Meyer-ter-Vehn, J., Murakami, M., Eidman, K., Witkowski, S., Nishimura, H., Kato, Y., Takabe, H., Endo, T., Kondo, K., Shiraga, H., Sakabe, S., Jitsuno, T., Takagi, M., Yamanaka, C., and Nakai, S., ''Experimental observation of laser-induced radiation heat waves,'' Phys. Rev. Lett. **65**, 587 (1990).

Sigel, R., Pakula, R., Sakabe, S., and Tsakiris, G. D., ''X-ray generation in a cavity heated by 1.3- or 0.44-mm laser light: III Comparison of the experimental results with theoretical predictions for x-ray confinement,'' Phys. Rev. A **38**, 5779 (1988).

Skupsky, S., Short, R. W., Kessler, T., Craxton, R. S., Letzring, S., and Soures, J. M., ''Improved laser-beam uniformity using the angular dispersion of frequency-modulated light,'' J. Appl. Phys. **66**, 3456 (1989).

Skupsky, S. and Craxton, R. S., ''Irradiation uniformity for high-convergence laser-fusion experiments,'' Phys. Plasmas **6**, 2157 (1999).

Sodha, M. S., Ghatak, A. K., and Tripathi, V. K., in *Progress in Optics*, edited by E. Wolf (North-Holland, Amsterdam, 1976), Vol. 13, p. 169.

Soures, J. M., McCrory, R. L., Verdon, C. P. *et al.*, ''Direct-drive laser-fusion experiments with the Omega, 60-beam, greater-than-40 kJ, ultraviolet laser system,'' Phys. Plasmas **3**, 2108 (1996).

Soures, J., McCrory, R., Boehly, T., Craxton, R., Jacobs, S., Kelly, J., Kessler, T., Knauer, J., Kremens, R., Kumpan, S., Letzring, S., Seka, W., Short, R., Skeldon, M., Skupsky, S., and Verdon, C., ''Omega upgrade laser for direct-drive target experiments,'' Laser Part. Beams **11**, 317 (1991).

Still, C. H., Berger, R. L., Langdon, A. B., Hinkel, D. E., Suter, L. J., and Williams, E. A., ''Filamentation and forward Brillouin scatter of entire smoothed and aberrated laser beams,'' Phys. Plasmas **7**, 2023 (2000).

Still, C. H. (private communication, 2002). Simulation of the propagation and self-focusing of an entire NIF $f/8$ cluster (Fig. 3-14) in a plasma 4 mm long would require about 10^9 cells and 6 terabytes of memory with spatial resolution of 1.25 wavelengths transverse and 2 wavelengths parallel to the propagation direction. A 100 ps simulation would take about 80 hours on 370 nodes and 1850 processors of the ASCI White.

Stoeckl, C., Chiritescu, C., Delettrez, J. A., Epstein, R., Glebov, V. Yu., Harding, D. R., Keck, R. L., Loucks, S. J., Lund, L. D., McCrory, R. L., McKenty, P. W., Marshall, F. J., Meyerhofer, D. D., Morse, S. F. B., Regan, S. P., Radha, P. B., Roberts, S., Sangster, T. C., Seka, W., Skupsky, S., Smalyuk, V. A., Sorce, C., Soures, J. M., Town, R. P. J., Frenje, J. A., Li, C. K., Petrasso, R. D., Seguin, F. H., Fletcher, K., Paladino, S., Freeman, C., Izumi, N., Lerche, R., and Phillips, T. W., ''First results from cryogenic target implosions on OMEGA,'' Phys. Plasmas **9**, 2195 (2002).

Suter, L. J., ''Cross talk between modes in cylindrical hohlraums,'' Laser Program Annual Report 1985, Lawrence Livermore National Laboratory, Livermore, CA, UCRL-50055-85, 1985, pp. 30–31.

Suter, L. J., Hauer, A. A., Powers, L. V., Ress, D. B., Delameter, N., Hsing, W. W., Landon, O. L., Thiessen, A. R., and Turner, R. E., ''Modeling and interpretation of Nova's symmetry scaling data base,'' Phys. Rev. Lett. **73**, 2328 (1994).

Suter, L. J., Kauffman, R. L., Darrow, C. *et al.*, ''Radiation drive in laser-heated hohlraums,'' Phys. Plasmas **3**, 2057 (1996).

Suter, L. J., Rothenberg, J., Munro, D., Van Wonterghem, B., and Haan, S., ''Exploring the limits of the National Ignition Facility's capsule coupling,'' Phys. Plasmas **7**, 2092 (2000).

Suter, L. J., Thiessen, A. R., Ze, F. *et al.*, ''Use of thin wall imaging in the diagnosis of laser heated hohlraums,'' Rev. Sci. Instrum. **68**, 838 (1997).

Tabak, M. and Callahan-Miller, D., ''Design of a distributed radiator target for inertial fusion driven from two sides with heavy ion beams,'' Phys. Plasmas **5**, 1895 (1998).

Tabak, M., ''Symmetry properties of reactor scale hohlraums,'' Laser Program Annual Report (1986/1987), Lawrence Livermore National Laboratory, Livermore, CA, UCRL-50055-86/87, 1987, pp. 2-169–2-182.

Tabak, M., ''Stability properties of a directly driven laser capsule absorbing 1.7 MJ,'' ICF Program Annual Report UCRL-116901-88/89, 1989, p. 141.

Tabak, M., Munro, D. H., and Lindl, J. D., ''Hydrodynamic instability and the direct drive approach to laser fusion,'' Phys. Fluids B **2**, 1007 (1990).

Tabak, M., Callahan-Miller, D., Herrmann, M. C., Hatchett, S. P., Lindl, J. D., and Perkins, J. L., Target design activities for inertial fusion energy at Lawrence Livermore National Laboratory, 18th IAEA Fusion Energy

Downloaded 20 Mar 2011 to 69.181.48.121. Redistribution subject to AIP license or copyright; see http://pop.aip.org/about/rights_and_permissions

Conference Proceedings: (http://www.iaea.org/programmes/ripc/physics/index.html).
Takabe, H., Mima, K., Montierth, L., and Morse, R. L., "Self-consistent growth rate of the Rayleigh–Taylor instability in an ablatively accelerating plasma," Phys. Fluids **28**, 3676 (1985).
Taylor, G. I., "The instability of liquid surfaces when accelerated in a direction perpendicular to their plans," Proc. R. Soc. London, Ser. A **201**, 192 (1950).
Thiessen, A. R., "Some aspects of LMF hohlraum design," 1988 Laser Program Annual Report: Target Design, Lawrence Livermore National Laboratory, Livermore, CA, XDIV-90-0054, 1988.
Tikhonchuk, V. T., Fuchs, J., Labaune, C., Depierreux, S., Huller, S., Myatt, J., and Baldis, H. A., "Stimulated Brillouin and Raman scattering from a randomized laser beam in large inhomogeneous collisional plasmas. II. Model description and comparison with experiments," Phys. Plasmas **8**, 1636 (2001).
Tikhonchuk, V. T., Pesme, D., and Mounaix, Ph., "Stimulated Brillouin scattering reflectivity in the case of a spatially smoothed laser beam interacting with an inhomogeneous plasma," Phys. Plasmas **4**, 2658 (1997).
Town, R. P. J. and Bell, A. R., "3-dimensional simulations of the implosion of inertial confinement fusion targets," Phys. Rev. Lett. **67**, 1863 (1991).
Tsubakimoto, K., Nakatsuka, M., Nakano, H., Kanabe, T., Jitsuno, T., and Nakai, S., Opt. Commun. **91**, 9 (1992).
Tsubakimoto, K., Jitsuno, T., Miyanaga, N., Nakatsuka, M., Kanabe, T., and Nakai, S., Opt. Commun. **103**, 185 (1993).
Turner, R. E., Landen, O. L., Bell, P., Costa, R., and Hargrove, D., "Achromatically filtered diamond photoconductive detectors for high power soft x-ray flux measurements," Rev. Sci. Instrum. **70**, 656 (1999).
Turner, R. E., Amendt, P., Landen, O. L., Glendinning, S. G. *et al.*, "Demonstration of time-dependent symmetry control in hohlraums by drive-beam staggering," Phys. Plasmas **7**, 333 (2000).
Verdon, C. P., McCrory, R. L., Morse, R. L., Baker, G. R., Meiron, D. I., and Orszag, S. A., "Nonlinear effects of multifrequency hydrodynamic instabilities on ablatively accelerated thin shells," Phys. Fluids **25**, 1653 (1982).
Vu, H. X., "An adiabatic fluid electron particle-in-cell code for stimulating ion-driven parametric instabilities," J. Comput. Phys. **124**, 417 (1996).
Vu, H. X., "Three dimensional particle-in-cell simulations of ion-driven parametric instabilities," Phys. Plasmas **4**, 1841 (1997).
Vu, H. X., "Laying a foundation for laser plasma modeling for the National Ignition Facility," Comput. Phys. Commun. **127**, 71 (2000).
Vu, H. X., DuBois, D. F., and Bezzerides, B., "Transient enhancement and detuning of laser-driven parametric instabilities by particle trapping," Phys. Rev. Lett. **86**, 4306 (2001).
Vu, H. X., Wallace, J. M., and Bezzerides, B., "An analytical and numerical investigation of ion acoustic waves in a two-ion plasma," Phys. Plasmas **1**, 3542 (1994).
Wharton, K. B., Kirkwood, R. K., Glenzer, S. H., Estabrook, K. G., Afeyan, B. B., Cohen, B. I., Moody, J. D., and Joshi, C., "Observation of energy transfer between identical-frequency laser beams in a flowing plasma," Phys. Rev. Lett. **81**, 2248 (1998).
Wharton, K. B., Kirkwood, R. K., Glenzer, S. H., Estabrook, K. G., Afeyan, B. B., Cohen, B. I., Moody, J. D., MacGowan, B. J., and Joshi, C., "Observation of resonant energy transfer between identical-frequency laser beams," Phys. Plasmas **6**, 2144 (1999).
White, R. M., Resler, D. A., and Warshaw, S. I., "Evaluation of charged-particle reactions for fusion applications," in *Proceedings of the International Conference on Nuclear Data for Science and Technology 1991, Julich, Germany*, edited by S. M. Qaim (Springer-Verlag, Berlin, 1992), p. 834.
Wilde, B. H., Fernandez, J. C., Hsing, W. W., Cobble, J. A., Delamater, N. D., Failor, B. H., Krauser, W. J., and Lindman, E. L., "The design and characterization of toroidal-shaped nova hohlraums that simulate national ignition facility plasma conditions for plasma instability experiments," *Proceedings of the 12th International Conference on Laser Interaction and Related Plasma Phenomena, Osaka, 1995*, edited by G. H. Miley (AIP Press, New York, 1996), Conf. Proc. No. 369, Part 1, p. 255.
Wilks, S. C., Kruer, W. L., Denavit, J., Estabrook, K. G., Hinkel, D. E., Kalantar, D., Langdon, A. B., MacGowan, B., Montgomery, D. S., and Williams, E. A., "Nonlinear theory and simulations of stimulated Brillouin backscatter in multispecies plasmas," Phys. Rev. Lett. **74**, 5048 (1995).
Wilks, S. C., Kruer, W. L., Estabrook, K. G., and Langdon, A. B., "Theory and simulation of stimulated Raman scatter at near-forward angles," Phys. Fluids B **4**, 2794 (1992).
Williams, E. A., "Scaling of SRS and SBS with speckle size," Bull. Am. Phys. Soc. **44**, 179 (1999).
Williams, E. A. (private communication, 2000).
Williams, E. A. (private communication, 2002).
Williams, E. A., Berger, R. L., Drake, R. P., Rubenchik, A. M., Bauer, B. S., Meyerhofer, D. D., Gaeris, A. C., and Johnston, T. W., "The frequency and damping of ion acoustic waves in hydrocarbon (CH) and two-ion-species plasmas," Phys. Plasmas **2**, 129 (1995).
Williams, E. A., Cohen, B. I., Lasinski, B. F., Berger, R. L., Langdon, A. B., and Still, C. H., "Ion wave saturation and stimulated Brillouin scattering," Bull. Am. Phys. Soc. **42**, 1998 (1997).
Willis, G. E. and Deardorf, J. W., "Measurement on the development of thermal turbulence in air between horizontal plates," Phys. Fluids **8**, 2225 (1965).
Wilson, D. C., Bradley, P. A., Hoffman, N. M., Swenson, F. J., Smitherman, D. P., Chrien, R. E., Margevicus, R. W., Thoma, D. J., Foreman, L. R., Hoffer, J. K., Goldman, S. R., Caldwell, S. E., Dittrich, T. R., Haan, S. W., Marinak, M. M., Pollaine, S. M., and Sanchez, J. J., "The development and advantages of beryllium capsules for the National Ignition Facility," Phys. Plasmas **5**, 1953 (1998).
Young, P. E., Berger, R. L., Decker, C., Divol, L., *et al.*, in *Proceedings of the Inertial Fusion Sciences and Applications 99, Bordeaux, France, 1999*, edited by C. Labaune, W. Hogan, and K. Tanaka (Elsevier, Paris, 2000), p. 307.
Young, P. E., Still, C. H., Hinkel, D. E., Kruer, W. L., Williams, E. A., Berger, R. L., and Estabrook, K. G., "Observations of laser-beam bending due to transverse plasma flow," Phys. Rev. Lett. **81**, 1425 (1998).
Youngs, D. L., "Numerical simulation of turbulent mixing by Rayleigh-Taylor instability," Physica D **12**, 32 (1984).
Ze, F., Kauffman, R. L., Kilkenny, J. D., Wiedwald, J., Bell, P. M., Hanks, R., Stewart, J., Dean, D., Bower, J., and Wallace, R., "A new multichannel soft x-ray framing camera for fusion experiments," Rev. Sci. Instrum. **63**, 5124 (1992).
Ze, F., Kauffman, R., Kilkenny, J., Langer, S., More, D., Powers, L., Ress, D., Rosen, M., Suter, L., Wallace, R., and Wiedwald, J., "Investigation of x-ray conversion in hohlraums," *1993 Topical Conference on Physics of Radiatively Driven ICF Targets, 1993, Monterey, California* [Def. Res. Rev. **6**, 103 (1993)].
Ze, F., Langer, S. H., Kauffman, R. L. *et al.*, "A comparative study of x-ray emission from laser spots in laser-heated hohlraums relative to spots on simple disk targets," Phys. Plasmas **4**, 778 (1997).
Zeldovich, Ya. B. and Razier, Yu. P., *Physics of Shock Waves and High-Temperature Phenomena* (Academic, New York, 1966), Sec. II.10.
Zimmerman, G. B. and Kruer, W. L., "Numerical simulation of laser-initiated fusion," Comments Plasma Phys. Controlled Fusion **2**, 51 (1975).
Zimmerman, G. B. and More, R. M., "Pressure ionization in laser-fusion target simulation," J. Quant. Spectrosc. Radiat. Transf. **23**, 517 (1980).

Downloaded 20 Mar 2011 to 69.181.48.121. Redistribution subject to AIP license or copyright; see http://pop.aip.org/about/rights_and_permissions